

**A Thesis Submitted for the Degree of PhD at the University of Warwick**

**Permanent WRAP URL:**

<http://wrap.warwick.ac.uk/97372>

**Copyright and reuse:**

This thesis is made available online and is protected by original copyright.

Please scroll down to view the document itself.

Please refer to the repository record for this item for information to help you to cite it.

Our policy information is available from the repository home page.

For more information, please contact the WRAP Team at: [wrap@warwick.ac.uk](mailto:wrap@warwick.ac.uk)

Random Load Fatigue Damage  
Accumulation in Mild Steel.

by

B. C. Fisher. B.Sc.

A Dissertation submitted for the Degree of  
Doctor of Philosophy.

School of Engineering Science,  
University of Warwick, Coventry.

May 1971.

MEMORANDUM

This dissertation is submitted in support of an application for the Degree of Doctor of Philosophy in Engineering Science, from the University of Warwick, Coventry.

No part of the work contained in this thesis has been submitted for other Degrees or Diplomas from this University or any other Institution.

Any help received in the preparation of this document has been fully acknowledged in the text.

I declare that the statements in this Memorandum are true in every respect.

B. C. Fisher

May, 1971.

## ACKNOWLEDGEMENTS

Firstly, I should like to express my appreciation to my supervisor, Dr. Frank Sherratt, for the continued support and encouragement which he has given throughout this project. I also wish to acknowledge the help of Dr. J. Monk, given by writing a data logging program for the School's process control computer.

Thanks are due to Mr. A. Redhead, Senior Technician, for his help mainly with those aspects concerning equipment maintenance and administration, and to Mr. J. Hawkins, Technician, for his valuable assistance in specimen preparation and experimental testing. The University's Engineering Workshop, under the supervision of Mr. L. Whittingham, is also to be acknowledged for the manufacture of test equipment and fatigue specimens.

For their assistance in the preparation of this thesis I should like to thank Mrs. M. King who has carefully typed the manuscript, and Miss T. Page and Mr. R. Hinkinson for the production of graphs and diagrams.

The British Railways Board is to be thanked for their financial support during the last one and a half years of this work.

Finally, I should like to thank my wife for the understanding which she has shown throughout the duration of the research project.

## S U M M A R Y

The work reported in this thesis was carried out in the School of Engineering Science, University of Warwick, between October 1967 and April 1971.

It establishes that by using high sensitivity eddy current crack detection, fatigue damage accumulation for both random and constant amplitude loading can be represented as occurring in two stages:-

Stage A:- Microcrack Initiation and Propagation.

Stage B:- Macrocrack Propagation.

The results of specimen sectioning and optical microscope work suggest that there is some correlation between the observed stage behaviour and that proposed by Forsyth (17).

An empirical relationship is restated for constant amplitude loading whereby the proportion of life spent in either stage can be estimated from the elastic stress concentration factor. This relationship is based on the behaviour observed from a wide range of specimen configurations.

It is established under random loading that for a given specimen configuration the proportion of time spent in Stage A behaviour for a given fatigue life remains unaltered for changes in waveform irregularity factor. This statement applies to two series of tests for loading waveforms of unaltered fundamental p.s.d. shapes and Gaussian amplitude probability density distributions. It is suggested that the signal maximum peak/rms. ratio is a significant factor in determining the proportion of life spent in crack initiation.

On-line computer techniques are described which enable data acquisition for the accurate definition of the statistical properties of random loading waveforms. The computer programs which perform off-line analysis of data and provide power spectral density, peak probability density and amplitude probability density descriptions of random signal properties are described.

Cumulative damage predictions are made using Miner's Hypothesis on a basis of positive peak stresses to failure for Stage A and Stage B lives, and overall fatigue life. The results confirm that Miner seriously underestimates the damage contribution of low stresses on fatigue life as a whole, and they also show that the damage contribution of low stresses is underestimated for the crack initiation phase of life. It is suggested that the inadequacies in Miner's Hypothesis cannot always be accounted for by adopting the "hypothetical S/N curve" concept.

An investigation into size effect behaviour under random and constant amplitude loading is presented, and indicates a striking similarity in Stage A/Total life behaviour for both large and small geometrically similar specimens.

The fundamentals involved in the design of electro-hydraulic servo controlled fatigue test rigs are outlined and applied to the three servohydraulic rigs which were built in order to carry out the described experimental program.

LIST OF CONTENTS

	<u>PAGE NO.</u>
Memorandum	
Acknowledgements	
Summary	
Chapter 1	
Fatigue Damage Accumulation - A Survey of Literature and the Presentation of Research Objectives	1
Chapter 2	
Experimental Techniques	37
Chapter 3	
Measurement & Analysis of Random Signals	61
Chapter 4	
Random Signal Synthesis and Statistical Definition	81
Chapter 5	
Flat Strip Cantilever Specimen Fatigue Test Results	90
Chapter 6	
Flat Strip Axial Specimen Fatigue Test Results	97
Chapter 7	
Small Round Cantilever Specimen Fatigue Test Results	106
Chapter 8	
Size Effect Investigation - Large Round 3-Point Bending Specimen Fatigue Test Results	116
Chapter 9	
Analysis and Discussion of Results	128

References.

- Appendix A - Fundamentals of Electro Hydraulic  
Servo Controlled Fatigue Test Rig Design.
- Appendix B - The Autocorrelation Function Method of  
Power Spectral Density Estimation from  
a Discrete Sample Record of data.
- Appendix C - Statistical Measurements on Servo-Hydraulic  
Fatigue Machines.
- Appendix D - A list of papers which were presented or  
published during this work.

Notes - Figures and tables are presented at the end of  
each chapter in the order to which they are  
referred in the text, and prefixed by the  
chapter number, e.g. table 6.3 and Fig. 6.3.

C H A P T E R 1

FATIGUE DAMAGE ACCUMULATION - A SURVEY OF LITERATURE  
AND THE PRESENTATION OF RESEARCH OBJECTIVES

1.	INTRODUCTION	2
2.	CUMULATIVE FATIGUE DAMAGE THEORIES	5
3.	THE MECHANISM OF FATIGUE FAILURE	14
4.	FATIGUE CRACK PROPAGATION THEORIES	17
5.	SIGNIFICANT FATIGUE PARAMETERS OF RANDOM WAVEFORMS	20
6.	RANDOM WAVEFORM ANALYSIS FOR FATIGUE DAMAGE EVALUATION	26
7.	OBJECTIVES OF RESEARCH PROJECT	35

## 1. INTRODUCTION

The problem of failure of engineering components from metal fatigue has confronted engineers for over one hundred years. The prevention of fatigue failure forms an integral part of the complete design process and related investigations have been carried out across the whole science discipline in an effort to gain fuller understanding of the phenomenon. The total amount of existing literature is immense but, even so, a reliable approach to the application of fatigue data to component life prediction does not yet exist. This does not preclude engineering solutions of the problem but, for accurate life prediction, there is no completely satisfactory substitute for component testing under realistically simulated service loading.

Metal fatigue is a process by which dynamic loading can weaken and break a component at a much lower load than the static breaking load. There are four main classifications of factors which influence this process: loading effects, e.g. random or periodic loading waveform; environmental effects, e.g. temperature or corrosive atmosphere; processing effects, e.g. component design shape and manufacturing techniques; and, metallurgical effects, e.g. fatigue resistance of material microstructure. Such factors constitute the variables of the design problem which, out of practicality, are analysed by design procedures which make assumptions about the nature of service loading and offer solutions based on material homogeneity and its treatment as a continuum.

But apart from these more practical considerations, fundamentals have to be established on which to base a fatigue life prediction method. A realistic attempt at analysing the damaging effect of a complex loading waveform must use

existing basic data and also quantify the accumulation of damage during the fatigue process. However, there are anomalies in deciding what constitutes fatigue damage. A metal physicist viewing the process at an atomic level would account for fatigue damage in terms of dislocation movements. Such a fundamental approach is hardly satisfactory in an engineering context which is more likely to acknowledge that damage has occurred when some process is underway which eventually will lead to component malfunction, for example, the onset of continuous and steady fatigue crack propagation.

The first systematic fatigue investigations were carried out in Germany by Wöhler towards the end of the nineteenth century and the principles which he established have been widely adopted. His name is often used to describe the universal S/N curve presentation of fatigue data, which describes the number of constant amplitude sinusoidal stress cycles that a fatigue specimen withstands before failure.

A characteristic of these curves is that some ferrous metals show a fatigue limit when tested in this manner, i.e. a stress at which an infinite number of stress cycles can be endured. This has led to an "infinite life" approach to design in which the estimated component service stresses are kept below the fatigue limit. Clearly, weight and economic penalties render this an impractical method of dynamic load design, and a "limited life" criterion has to be adopted. Component design life is then based on a chosen probability of failure level with the scatter inherent to fatigue results described by a probability of failure distribution.

The majority of S/N type fatigue data has been generated in full realisation that dynamic loading patterns are far from sinusoidal in nature, but at a time when equipment

limitations prevented the full simulation of service type loadings. When data capture methods were used to define service loading patterns as frequency distributions of stress levels, attempts at realistic testing consisted of applying blocks of stress sinusoids with due regard being paid to their relative statistical frequencies of occurrence. Associated decisions involved in formulating the block programme include choosing the number and level of the stress blocks, the number of stress cycles in each block and the sequence of blocks in order to avoid introducing coaxing and over-stressing effects. The attractiveness of these sinusoidal test procedures lies in their simplicity, and reliability and cost comparisons with complex loading waveform test facilities are much in their favour. Nevertheless there are limitations, especially in the way in which these tests simulate the damaging effect of a random signal and, therefore, over recent years considerable emphasis has been placed on random fatigue testing installations. In part, this continued interest in realistic testing has resulted from the inability of cumulative damage theories to accurately predict fatigue life. The development of these random loading facilities owes a lot to stimulation from the aerospace industry, as do the associated advances in random data measurement and analysis.

But it is clearly impractical for a design process to require full service testing as proof of component integrity. The ultimate aim is to carry out component fatigue life evaluation at the drawing board, with only small scale back-up testing. In this respect, the main advantage of random load test systems lies in their ability to apply loading

waveforms of known statistical parameters so that experimental data can be generated in an effort to identify relevant fatigue characteristics.

A parallel development has been taking place in the field of fractography. The limitations in resolution of the optical microscope have been largely overcome by electron microscopy and much more accurate examination of fracture surfaces is now possible.

Thus, to some extent there has been a revolution during recent years in the experimental techniques adopted in fatigue research studies. It is the intention of this chapter to review the significant aspects of studies which are relevant to the area of cumulative fatigue damage.

## 2. CUMULATIVE FATIGUE DAMAGE THEORIES

Cumulative damage theories are ultimately concerned with predicting the fatigue lives of components subjected to variable amplitude dynamic loading which is essentially random in form. They propose a mechanism for damage growth and state a rule for adding the damage produced by different amplitude stress cycles. Further, damage theories can be divided into those which are applicable to high-strain/low-cycle fatigue conditions, and those applicable to high-cycle fatigue conditions. High cycle fatigue implies that failure occurs only after a large number of cycles, usually greater than  $10^3$ , and macroscopic plasticity or yielding does not occur. The elastic relationship between stress and strain then applies and fatigue data is represented by the conventional stress amplitude/cycles to failure curve. The work of this project is concerned with high cycle fatigue life prediction.

Damage theories require some experimental support, and most rely on sinusoidal fatigue data in the form of S/N curves. Certainly the majority of fatigue design data is presented in this manner. For a given specimen form, the main factors which influence the shape of the S/N curve are the particular material tested, mean stress, mode of loading (i.e. axial or bending) and surface finish. Frequency and waveform oscillatory shape have secondary effects, and extreme environmental conditions (temperature and corrosion) usually require separate evaluation. Nevertheless, identical testing conditions do not produce identical fatigue lives. Scatter is inherent in fatigue results and statistical distribution functions are introduced to define lives through probability of failure levels. The lognormal distribution is commonly assumed in general fatigue work, although at very low probabilities of failure the distribution is certainly not lognormal. (The work here adopts the lognormal presentation of fatigue lives and is not fundamentally concerned with the statistical presentation of fatigue data). The number of cycles to failure is given when a crack has been produced of the order of the specimen cross section in length, usually resulting in complete separation into two parts. Thus, the form of S/N curve data presentation is one which does not account for the composite nature of the fatigue process, for example, by discriminating between phases of crack initiation and propagation.

The literature on cumulative damage is extensive and an unbiased assessment of rival theories is very difficult. One hypothesis dominates the whole topic, though, and a convenient way of bringing some perspective to the field is to take this first. In the western world this cumulative

damage theory is attributed to Miner who proposed it in 1945 (1). It is a simple theory, needs a minimum amount of test information and is widely used. It has been incorporated in several well-respected codes of practice. Unfortunately, it has been shown by countless investigators to be wrong!

Miner assumed that damage accumulates linearly when constant amplitude stress cycles are applied, each cycle doing the same amount of damage as any other cycle of the same amplitude. If the S/N curve shows that at stress  $S_i$  failure occurs in  $N_i$  cycles, then the fraction of life used by applying  $n_i$  cycles of  $S_i$  is  $n_i/N_i$ . Failure will occur when all the life has been accounted for in this way. In general terms the theory states that failure will occur for  $m$  stress levels when:-

$$\sum_{i=1}^m \frac{n_i}{N_i} = D \quad (1.1)$$

where  $N_i$  = life when subjected to  $S_i$  alone

$n_i$  = number of cycles of  $S_i$  applied

$D$  = a constant, called the life fraction.

Miner sets  $D = 1$ , although tests have been conducted which report values of the life fraction from about 0.2 to 10.

But attempts to replace Miner with a theory which is better in all circumstances have not been very successful. There are many alternatives, and one of the best reviews is by Kaechele (2), who establishes fundamental concepts around which cumulative damage theories are structured. Also, Stallmeyer and Walker (3) and Booth (4) have produced broader but less detailed reviews using these fundamentals.

Kaechele sets his comparisons against Miner's theory from considerations based on the concepts of stress independence and stress interaction. Stress independence means that equal amounts of fatigue damage are produced by equal fractions of life for all stress amplitudes. This is illustrated by fig. 1.1, whereas the effect of a stress dependent theory on cycles to failure is shown by fig. 1.2. These plots have been normalised so that equal ordinates represent the same amount of damage. Kaechele suggests, as a reference, the damage - strength loss or crack length - at failure for the highest encountered stress. There must be less damage at failure in tests of higher stress levels than lower stress levels. The applied number of cycles are normalised to the number of cycles producing that damage at the particular stress level.

An interaction free theory assumes that the course of damage due to a particular stress amplitude remains unaltered regardless of whether other stress cycles are present in the loading spectrum. For example, if stresses below the fatigue limit reduce life, this is either a direct effect of those stresses or an interaction effect due to the presence of other stress amplitudes. There are effects due to the sequence of application of stress cycles and effects due to relative magnitudes of the stress cycles, and either effect might be dominant. For example, sequencing of stress cycles is the dominant interaction effect during coxing. But with stationary random stress histories it is likely that sequence effects are small, since stresses are applied in a completely random manner. Interaction is then more probably a stress magnitude effect, for example, when high peak loads create residual stresses which affect the subsequent crack growth

rate. Some experimental support is given to this theory by fig. 1.3. which presents the work on aluminium alloy specimens of Hardrath (5). It shows the effect of applying test loads of simple sequences in contrast to a random sequence of identical load levels and frequencies of occurrence.

Miner's theory is stress-independent and interaction free, and Kaechele shows that other similarly structured theories reduce to being directly equivalent to Miner. The significant aspects of several cumulative damage theories are now presented. A rigorous analysis in the context of the fundamentals outlined previously is given by Kaechele.

Valluri (6) bases his cumulative damage rule on dislocation theory and plastic deformation at the crack tip - through consideration of a narrowing hysteresis loop. Three constants are required to be determined from actual fatigue tests. The approach is stress-independent and interaction free and is essentially equivalent to Miner's criterion. The form of the equation gives an exponential growth of crack length with increasing numbers of stress cycles and, on the basis of assumptions made, could not be used to design to the appearance of first cracking.

Shanley (7) proposed a mechanism of failure from considerations of reversed slip occurring on one slip plane. This cyclic slip causes progressive unbonding of atoms at a free surface, and failure is defined as the attainment of a critical crack length. Crack growth is expressed through an exponential function. Several modified theories have been presented although the fundamental approach is one of stress-dependence and postulates interaction effects to result from varying amounts of initial damage produced by the first

cycles of each stress amplitude. Shorter fatigue lives are predicted than by Miner, although this does not imply that the actual fatigue life will be longer than that predicted.

The original presentation of Corten and Dolan (8) included both stress-dependence and interaction effects, but subsequent experimental work (9, 10) which can be considered as an investigation of the original concepts led to the formulation of a stress-independent, interaction theory. In its final form the approach is simple. It accounts for interaction effects through a modified S/N curve, fig. 1.4. The parameter  $d$  defines the slope of the curve and is determined from two level sinusoidal tests. This parameter is shown to be relatively insensitive to the percentage of cycles in the repetitive blocks applied at each of the two stress levels. Marsh and Mackinnon (11) do not substantiate this finding however. The reference stress  $S_h$  is defined as the most severe stress in the loading history. The feasibility of this approach has not been proven for complex stress histories, and it can be envisaged that a great deal of testing would be involved, since  $d$  would probably vary with different mean stresses and stress conditions having no common stress ratio.

A similar approach has been adopted by Freudenthal and Heller (12) who present a stress-independent theory and account for interaction effects again through a straight line modification to the S/N diagram, fig. 1.4. The defined reference stress  $S_h$  is unrelated to the applied stress history, but is specified at a stress level within the  $10^3$  to  $10^4$  cycles life range. The slope parameter  $d$  of the modified S/N curve is obtained from multilevel sinusoidal tests arranged to simulate the actual design stress history, as

compared with the simple two level testing of Corten and Dolan. The feasibility of this approach for complex waveforms has not yet been shown.

Grover (13) proposes a two stage damage process consisting of an initial stage during which cracks are initiated and a second stage consisting of propagation of these cracks to failure, see fig. 1.5. The boundary between the two stages is defined at some fraction  $a$  of the total life. If the fraction is the same for all stress levels the theory becomes stress independent and equivalent to Miner, since it is interaction free. However, as proposed, it is stress dependent. Grover's theory is based upon being able to determine the magnitude of the fraction  $a$  as a function of the stress level, and its use has been limited because no method has been reported whereby the number of cycles required to initiate a crack could be accurately determined.

Many other cumulative damage theories have been proposed, and just as those outlined, they all conform in their general approach to observed experimental behaviour. Nevertheless, there is no indication that any one theory gives predictions significantly better than the other proposed theories. In a lot of cases new basic data is required to prove the theories absolutely, but to achieve this the indications are that substantial experimental programmes would have to be mounted. Kaechele concludes that no radical "breakthroughs" have yet appeared in the area of cumulative fatigue damage theory, and this conclusion still applies.

Thus, although it is desirable that a more accurate method of life prediction should be found, evidence suggests that any proposed alternative must retain some of the characteristics of Miner's theory. It must be simple to use,

have a wide range of applicability and offer major improvements in damage prediction.

Certainly Miner's theory is inexact, but it is adequate for a lot of design situations, particularly if it is used in the modified form:-

$$\sum \frac{n}{N} = D \quad (1.2)$$

where the value of D is chosen from experience, e.g. equal to 0.3 for conservative applications. But it is important in this context to consider consistency of accuracy rather than absolute accuracy. If the fatigue life achieved in practice was always about two or three times less than the predicted life, due allowance could be made for this and Miner's theory could be used with confidence. However, the evidence is that this is not always the case.

In these circumstances one approach to the problem is to consider the situations where cumulative damage prediction needs improving. Miner's theory is particularly unsatisfactory when loading histories have infrequent applications of high stresses, and when there are large numbers of low stress amplitudes which alone would do little damage, but which may become significant when higher peaks are present to initiate damage. High stresses are very variable in their effect and may extend life rather than doing any damage at all. Service stress histories are often of this form when components are designed to meet the demands of reliability engineering, as with agricultural machinery and motor cars. In these circumstances one solution is to suggest a cumulative damage theory which is essentially a modification of Miner's theory. There are two notable in-

vestigations which adopt this approach.

An attempt was made by Marsh and Mackinnon (11) to allow for the damaging effect of stresses below the constant amplitude fatigue limit. Tests were conducted on mild steel sharply notched bending specimens, and the results were compared against life predictions made from a hypothetical S/N curve constructed with a fatigue limit chosen at 0.8 times the original constant amplitude fatigue limit, and a slope modified in a similar way to that suggested by Corten and Dolan. Accurate life predictions for these particular results were obtained by means of this hypothetical S/N curve concept, but later Marsh and Frost (14) stated that considerable experience is necessary with the use of this (and similar) methods, particularly for stress histories with a small number of very high stress peaks, and the method was not claimed as being readily applicable to all situations.

Kirkby and Edwards (15) indicate stress dependence and interaction effects as the probable causes of error in Miner's theory, and suggest that stress amplitudes below the fatigue limit may make a significant contribution to total damage when distributed in a random manner amongst higher stress amplitudes, as in aircraft loading. A method is proposed which makes some allowance for these effects whereby basic fatigue data is generated in the form of RMS/N curves using Gaussian random signals with a Rayleigh distribution of peak stresses. It is shown, using a graphical method, that a service loading spectrum can be synthesised to a good approximation by three such waveforms of different rms. stress levels. The appropriate lives can then be read from the basic RMS/N data and life estimation

made using Miner's theory. The results do show a significant increase in accuracy for this method of prediction, but it is concluded that further allowance for interaction effects is necessary if more accurate life predictions are to be obtained. It is also emphasised that the adoption of this method would entail the generation of a considerable amount of experimental design data.

Generally studies in cumulative damage theory formulation have not attempted to quantify the composite nature of the fatigue process, for example, by distinguishing between the phases of microcrack initiation and growth to the first detectable crack, and macrocrack propagation. It is possible that there are fundamental errors in making such generalised approaches to damage calculation. In this respect, therefore, it is of value to examine investigations which have been concerned with the initiation and growth of fatigue cracks.

### 3. THE MECHANISM OF FATIGUE FAILURE

The general way in which fatigue cracks are initiated and grow from free surfaces of ductile metals is now established. At room temperatures and stresses less than those causing general yielding, microcracks originate in persistently active slip bands which are spaced irregularly over surface grains and most closely aligned with the directions of maximum shear stress. To-and-fro slip movement occurs on neighbouring slip planes and creates surface roughening and steps within a slip band. Surface roughening becomes more intense as more stress cycles are applied, and grooves or intrusions are formed. These grooves deepen with continued to-and-fro slip movement and develop into microcracks.

Microcrack initiation is confined to surface grains and periodic removal of the surface layer extends fatigue life (16). Initial microcrack development takes place along the line of the slip plane as a continuation of the slip process, and is governed by the range of resolved shear stress acting along the slip plane. Ultimately, though, opening and closing of the microcrack is caused by resolved cyclic stresses normal to the crack faces and a localised zone of plastically deformed material is created immediately ahead of the crack tip which is large enough for the crack to grow as if in a continuum. Crack propagation then becomes independent of slip and associated with the magnitude of tensile strain existing in the stress field immediately ahead of the crack. The direction of propagation deviates from its slip path and becomes normal to the nominal maximum cyclic tensile stress axis and the crack is then termed a macrocrack.

Thus there are basically two modes of crack growth, and the change from one to the other is a natural division of behaviour. Forsyth (17) calls the two types of behaviour Stage 1 and Stage 2 crack growth. The changeover from one to the other is not necessarily sudden. Slip band cracking may decrease in a gradual manner, and some stress conditions favour one form of growth, e.g. a mean tensile stress will encourage the changeover to Stage 2 growth. It is a general classification of behaviour; for example, grain boundary crack initiation is an exception.

Early studies in fatigue tended to emphasise the period of life spent in crack initiation rather than crack propagation. It was not realised that different fundamental mechanisms constituted the fatigue cracking process

and it was the general belief that crack formation occurred late in life. Thus, crack growth was considered relatively unimportant. It is now known that crack initiation can occur quickly but, even so, it is incorrect to make the general assumption that the majority of life is taken in either initiating or propagating fatigue cracks.

The criterion associated with fatigue macrocrack growth - Forsyth's Stage 2 process - is the principal tensile stress at the crack tip. This period of growth is characterised by striation markings on the fracture surfaces. Striation patterns vary with the loading and material, but are usually shown most clearly in ductile materials. This is probably because ductility allows more plastic deformation at the crack tip. Certainly harder materials tend to show less plastic deformation and more cleavage characteristics. However, the exact mode of macrocrack propagation is not clear, and both ductile and cleavage mechanisms of material separation occur.

A typical characteristic of sheet or plate crack growth is crack front advance by alternate periods of Stage 2 growth and tensile-fracture jumps (17). Tensile crack tunnelling, down the centre of the sheet, is encouraged by triaxial stress conditions while fatigue crack growth favours the surface layers. The crack runs at right angles to the plane of the sheet, later forming double  $45^\circ$  shear lips which change to a single  $45^\circ$  fracture.

Generally, beneficial compressive residual stresses are induced at the crack tip by high tensile loads which are not large enough to intrinsically damage the material, and this reduces the subsequent crack growth rate (18).

The associated plastically deformed zone of residual stress is larger for longer cracks. High compressive stresses do not have the detrimental effect of inducing equivalent tensile residual stresses because the crack faces come together and reduce the stress concentration at the root of the crack. Thus, only a slight increase in growth rate is observed after compressive loads. An uncracked component, however, would realise the notch stress concentration for compressive loads and harmful residual tensile stresses would be induced. Nevertheless, this behaviour does depend on the permanence of the residual stresses and they are likely to fade in materials with low yield stresses, such as mild steels.

#### 4. FATIGUE CRACK PROPAGATION THEORIES

Aerospace studies have stimulated a number of investigations into crack growth in high strength aluminium alloys with tests usually carried out on centrally slotted sheets loaded so that Stage 2 growth starts early in the fatigue life. Probably the most significant development in crack propagation theory has resulted from work in this field by Paris (19), based on the study of continuum mechanics and the elastic crack tip stress intensity factor, K. These investigations show good correlation for a wide range of work between observed crack growth rate and value of K represented by the relationship:-

$$\frac{da}{dn} = C (\Delta K)^4$$

where a = crack length;

$\Delta K$  = range in K, describing the cyclic change  
in the stress field surrounding the crack tip;

$C$  = constant depending on material and mean load. The studies apply to both random and constant amplitude loading.

The correlation offered by the stress intensity factor with crack growth rates appears most promising. However, there is an important limitation imposed in the use of this concept by the stressed state of the material surrounding the crack. Linear elastic behaviour is assumed to dominate and the plastic zone size at the crack tip must be small, e.g. in comparison with the crack length. This condition is called small scale yielding. It raises particular problems when extending a continuum mechanics analysis to account for residual stresses caused by plastic deformation and when dealing with low strength ductile materials. The stress intensity factor concept has yet to be established as a general approach for these cases.

The conditions governing the growth or dormancy of small macrocracks in notched specimens of various materials has been established empirically by Frost and Greenan (20). The information was obtained from constant amplitude tests of edge-cracked plate specimens about tensile mean loads. Crack growth was defined by the parameter  $s^3l$ , where  $s$  = nominal gross area alternating stress, and  $l$  = edge crack length. If  $s^3l > c$  a crack will grow, and if  $s^3l < c$  the crack will lie dormant, where  $c$  = a constant whose value depends on the material and ratio of mean to alternating stresses.

Earlier work by Frost (21) establishes the way in which  $c$  can be used to interpret notched fatigue data. The results apply to specimens with deep vee-notches where the initial effective crack length is taken equal to the notch

depth. A crack formed at the notch root will only grow to cause complete failure if the nominal alternating stress lies in the area marked "fracture" shown in fig. 1.6. Thus, for values of  $K_t$  below  $K_t$  crit, the nominal initiation stress is higher than the minimum propagation stress and all cracks will grow to cause failure of the specimen. A constant minimum propagation stress is therefore shown to exist.

Harrison (22) has reassessed the published results of non-propagating fatigue cracks on a stress intensity factor basis. Since  $K$  dictates the rate of crack propagation it seems reasonable to suppose that the value of  $\Delta K$  will determine whether or not cracks propagate. The low values of stress considered made the approach valid for ductile materials, such as mild steel, and little correction was needed for crack tip plastic zone size. The work showed that cracks would only propagate if  $\Delta K$  exceeded a certain value represented by a law with  $\frac{\Delta K}{E}$  as the significant parameter, where  $E$  is the material modulus of elasticity. Certainly the work forms a basis for an experimental programme to verify this approach, but it does not completely establish the validity of the concept in dealing with small cracks. Schijve's (23) work with aluminium shows good agreement of crack growth rate as a function of the stress intensity factor for cracks as small as 0.1 mm (0.004 ins.) in notched and unnotched sheet material, but unsatisfactory results were obtained for estimates of fatigue life taken to reach this value.

The influence of the notch stress concentration on the propagation of small cracks cannot be discounted. It can be imagined that macrocrack growth is initially very dependent

on the stress field of the notch. For a sharp notch, typically one in which non-propagating cracks are found, the stress gradient drops away very quickly from the base of the notch. Thus, the crack may not grow long enough to influence the gross elastic stress field in a way necessary for its continued propagation, so that the stress field due to the notch itself remains dominant.

Although it has not been the intention to review completely the field of crack propagation, the information presented illustrates a movement throughout engineering design which has developed over recent years. Quantitative efforts are now made to account for the crack resistance of engineering structures. It is possible to use fracture mechanics design methods to establish the critical crack (or flaw) size that would cause catastrophic failure. For the case of fatigue cracks, it is then possible to arrange inspection intervals based on crack growth data so that a crack is not allowed to propagate to the critical size. In this context therefore, there is strong evidence to suggest that cumulative damage theory formulation should concentrate on the prediction of that period of fatigue life spent in crack initiation.

##### 5. SIGNIFICANT FATIGUE PARAMETERS OF RANDOM WAVEFORMS

The problem of random load cumulative damage prediction would be eased somewhat if it were known exactly which waveform parameters caused fatigue damage. The present number of publications describing random load fatigue investigations is fairly limited and the work only extends over the last fifteen years or so. There is some ambiguity in the findings of this work. A comprehensive survey of the lit-

crature has been made (24), but here investigations are reviewed which have been concerned only with the fatigue damaging effect of analogue stress histories from stationary Gaussian processes.

Generally random load tests tend to show less scatter and initiate more fatigue cracks than constant amplitude tests. Without exception a given rms. intensity random load produces shorter fatigue lives than the equivalent rms. constant amplitude waveform. But apart from rms. loading intensity, the signal parameters which have been considered most significant in describing the effect of random loading on fatigue life are:-

- (1) Irregularity Factor, defined as the ratio of the number of positive going signal zero crossings to the number of peaks  $\left(\frac{N_0}{N_p}\right)$ .
- (2) Power Spectrum Shape, or Power Spectral Density Function.
- (3) Clipping Ratio, or Crest Factor, defined as the ratio of maximum encountered peak stress to the signal rms. value.

Signal zero crossings and peaks are determined by the power spectral density function, and theoretically therefore it is not possible to vary the irregularity factor independently of the power spectrum shape. However the power spectrum shape can be kept qualitatively the same, e.g. a band pass spectrum, and variations in  $N_p$  achieved without altering its fundamental form. But it is possible to produce the same irregularity factor values from different fundamental power spectral shapes.

Fatigue life comparisons have usually been made on the basis of zero crossings or peaks to failure. The effect of

plotting results on a peaks to failure basis is to shift the results to the right with respect to a zero crossings plot, by an amount proportional to  $\frac{N_p}{N_0}$ . Thus, those signals with Rayleigh-like peak distributions are shifted less to the right than others.

Theoretical prediction of the occurrence of signal peaks and zero crossings can be made from the power spectrum shape, although an accurate estimate of the shape is required since these parameters are determined through higher moments. In the majority of cases reported below, reference is made to the fact that direct counting from recorded waveform traces was preferred because of its more accurate results.

Clevenson and Steiner (25) conducted two series of tests to determine the effect of p.s.d. shape and value of  $\frac{N_0}{N_p}$  using circular, notched ( $K_t = 4$ ) 2024-T4 aluminium alloy specimens loaded axially about zero mean. The series of tests at  $\frac{N_0}{N_p} = 0.82$  showed no significant difference between the fatigue lives for three different power spectra. Also, the tests carried out with one fundamental p.s.d. shape and  $\frac{N_0}{N_p}$  ratios of 0.66, 0.75, 0.79 and 0.82 showed no significant difference for lives expressed as total peaks or zero crossings to failure.

Kowalewski (26) used extruded 2024 aluminium circular specimens loaded in cantilever bending and excited by what was essentially a peaked band pass power spectrum to obtain  $\frac{N_0}{N_p}$  values of 0.98, 0.91 and 0.75. He concluded that fatigue lives were not affected very much by the value of the signal irregularity factor.

Fuller (27) carried out investigations with aluminium 2024-T3 strip cantilever specimens for three p.s.d. shapes

of measured  $\frac{N_o}{N_p}$  values 0.96, 0.95 and 0.75. The results, fig. 1.7, show no significant differences between the fatigue lives of the three loading waveforms. However, the qualitative display of these results was secondary to the main object of establishing a fatigue life prediction method based on signal rise and fall distributions.

Similar specimens to those used by Fuller were employed by Hillberry (28) in his broad band and narrow band power spectrum investigations. The band width of the broad band power spectrum was approximately 200Hz., and the narrow band spectrum was centred on 220Hz. The two values of  $\frac{N_o}{N_p}$  were 0.79 and 1 respectively. Equivalent fatigue lives were obtained under both loadings, see fig. 1.8.

The  $\frac{N_o}{N_p}$  values used by Bussa (29) for his investigations on SAE 1006 steel strip specimens ( $K_t = 2.6$ ), loaded axially about 1000 lbf. mean load, were measured at 0.75, 0.85 and 0.98. Two fundamental p.s.d. shapes were used. An analysis of his results, whether made on a basis of peaks or zero crossings to failure shows, fig. 1.9, that the higher ratios are always more damaging. A difference in life also occurs for the two power spectral shapes.

Work has been carried out by Carse (30) with round, notched ( $K_t = 1.7$ ), SAE 5130 steel cantilever specimens. Two fundamental power spectrum shapes were used, each with two irregularity factors and signal clipping ratios of 4. Neglecting the effect of power spectrum shape, no consistent trend emerged from the fatigue lives produced by the signals. The most damaging signal had the highest  $\frac{N_o}{N_p}$  value, 0.93, and was then followed in order by the values 0.68, 0.73 and 0.81. However, within each p.s.d. shape, the higher irregularity factor produced the shorter

fatigue lives.

Broch (31) used cantilever epoxy paper printed circuit boards excited by single resonance and double resonance power spectra, with measured irregularity factors of 1.0 and 0.53 respectively. One series of 50 specimens was tested for each p.s.d. shape. Both tests were performed at equal rms. stress levels with an equal occurrence of zero crossings. Therefore the actual number of high stress peaks (say above 2.5 x rms.) was basically the same for each loading, and the essential difference was the distribution of stress waveform half cycles or rises and falls, see fig. 1.10. For the single resonant waveform only one stress half cycle occurs between successive maximum and minimum stress excursions, whereas for the double resonant waveform successive stress excursions consist of a series of rises or falls. Broch found that there was a statistically significant difference between the means of the two tests, and that the higher value of  $\frac{N_o}{N_p}$  was more damaging.

To some extent the work of Booth et al (32) on the effect of high loads can be considered to support Broch's findings. Small En15 steel round specimens were fatigued in cantilever bending with a random load of constant power spectrum shape and  $\frac{N_o}{N_p}$  value of 0.78, but which was clipped to four different peak/rms. ratios. The results are shown in fig. 1.11. The fatigue lives for 5.5, 4.0 and 3.5 x rms. clipping were very similar, whereas the tests with clipping at 2.5 x rms. level were considerably longer, particularly at lower load intensities. This suggests that the few short duration high loads had little effect on overall fatigue life, whereas the greater quantity of medium high loads had a significant effect.

It is important, though, to realise that this may not apply when extremely high clipping ratios are encountered, for example, in service loading patterns. From an engineering standpoint, service load simulation experience has shown that naturally occurring random phenomena - a given sea state, patch of atmospheric turbulence, or road roughness - can be represented as a stationary Gaussian process of given intensity or rms. level. However, the total service loading is usually termed quasi-stationary since it will be built up from a particular distribution of loading intensities of different durations. Thus, the resulting stress peak distribution will not be predicted as for stationary Gaussian processes. This concept leads to programmed rms. testing in which the load spectrum is controlled by the power spectrum shape and a distribution of rms. load levels, each with a particular peak distribution and duration. Jaeckel and Swanson (33) present results of fatigue tests under random loading, synthesised from Gaussian noise with an exponential distribution of rms. levels, each with Rayleigh peak distributions clipped to  $4 \times$  rms. level. The specimens were identical to those used by Bussa. The overall clipping ratio was much higher than that of the individual stress levels -  $10.4 \times$  signal rms. level. Tests were conducted for stationary random and programmed rms. waveforms. The fatigue lives of the programmed rms. test series were much less than would have been assumed by extrapolation from the stationary random tests, and the authors felt that a large contribution to the increased damage rate was made by the high overall clipping ratio.

In summarising, it is possible to present the above

results in two groups according to the material tested. The investigations with aluminium alloys have shown a negligible effect on fatigue life of signal power spectrum shape and irregularity factor. The results for steels, however, do show a general trend of decreasing fatigue life with an increasing value of the signal irregularity factor. There are also power spectrum shape and clipping ratio effects. It does not appear that the general assumption (24) that p.s.d. shape and  $\frac{N_0}{N_p}$  ratio have no effect on fatigue life is true. If it were true, the implication would be that fatigue life is primarily a function of r.m.s. stress level. With the results presently available, however, it can only be concluded that the effect of varying the statistical properties of Gaussian waveforms has not yet been established with any degree of certainty.

## 6. RANDOM WAVEFORM ANALYSIS FOR FATIGUE DAMAGE EVALUATION

The fundamental object of random stress waveform analysis is to present data in a form which is easily incorporated into a cumulative damage theory. Essentially, the analysis constitutes measurement of the various amplitude domain characteristics of a signal. There are two main approaches. The first involves direct waveform counting techniques which were established before the second method, statistical processing of signals by random vibration theory, became more generally adopted. The applications discussed are again limited here to stationary Gaussian waveforms.

### 6.1 Direct Waveform Counting Methods

Comprehensive reviews have been made by Haas (34) and Schijve (35). Counting methods use combinations of peaks,

ranges and level-crossings, the main forms of which are presented below.

#### Level Crossing Counting

A count is made for a particular load level each time the waveform crosses that level with a positive slope. (The counting result would be the same for negative level crossings). A count of positive going zero crossings is included, and the method is illustrated in fig. 1.12. The level crossing method does not retain the classic "cycles to failure" fatigue parameter and it is insensitive to variations in the frequency content of the random signal. Only the statistical frequencies of load occurrences are presented. Also, it is not correct to assume that the number of peaks between two successive levels can be obtained by subtracting the number of counts at adjacent levels.

#### Peak Counting

The method of peak counting is shown in fig. 1.13. A count is made for a particular load level when the waveform slope passes through zero, with the instrument discriminating between peaks (maxima) and troughs (minima). Load sequence information is not retained. This technique also does not account for any variations in signal frequency content. Signals may have identical peak distributions but quite different power spectra.

#### Range-Mean Counting

A range or "half cycle" of load occurs between successive signal peaks and troughs. A positive range, when the peak is preceded by the trough, is termed a rise and a negative range is termed a fall. The range-mean counting

method is shown in fig. 1.14. Individual ranges are recorded with the associated means. In the past the adoption of this counting procedure has not been as widespread as peak or level counting. Instrumentation required to record the data is complex, and testing facilities have not always been able to reproduce the recorded loading statistics. Today, these drawbacks are not such a handicap. Fatigue test equipment is capable of response to random loading waveforms and digital computers can be applied to data analysis (36).

Since two variables are counted the resulting distribution function is two dimensional, and much more information is obtained than with other counting methods. It is possible, for example, to present rise and fall statistics as independent of mean loads, or as mean load dependent distributions. Signal frequency content and load sequence information is not retained, though. There is also the advantage that, given the necessary constant amplitude information, fatigue damage evaluation could be readily made using Miner's law with signal data in this form.

Nevertheless, there is a fundamental difficulty with this counting procedure in its application to waveforms which have a significant number of low amplitude components, as shown by fig. 1.15. It may be desirable to neglect these small load variations since it is likely that they cause little fatigue damage and may grossly distort the range-mean distribution in this respect. Some judgement is therefore necessary with the use of this procedure.

Fatigue damage evaluations which rely on counting methods as a means of establishing loading waveform characteristics have applied mainly to narrow band random signals (28, 37,

38, 39). The general procedure has been to take chart traces of the waveform to determine the value of the irregularity factor, and then use the equation describing the theoretical peak probability density distribution, which for the case of a narrow band signal is usually the Rayleigh distribution. Then the concept of a fatigue load cycle can be retained and it is straightforward to apply Miner's theory.

The usual technique is to approximate the S/N curve to an equation of the form:-

$$N S^b = C \quad (1.3)$$

where  $N$  = number of cycles to failure,

$S$  = peak alternating stress,

$b, C$  = constants.

For many materials this is a good approximation, although errors are inherent in the necessary data extrapolation which is involved. Also, no allowance is made for a fatigue limit, and it incorrectly represents material behaviour when very high peak stresses are applied. The value of  $C$  and  $b$  are given by a least squares fit of data to a  $\log S - \log N$  plot.

A Rayleigh signal has a peak probability density distribution defined by:-

$$p(S) = \frac{S}{\sigma^2} \exp\left(-\frac{S^2}{2\sigma^2}\right) \quad (1.4)$$

where  $S$  = value of stress peak,

$\sigma$  = rms. value of signal.

If the signal has a centre frequency of  $f$  Hz. the total number of peaks (and therefore stress cycles in the range  $S$  to  $S+ds$ ) in a time  $t$  sec. is given by:-

$$n = f.t.p(S) . dS.$$

The fractional damage in N cycles is:-

$$\frac{n}{N} = \frac{\text{f.t.p.}(S) \Delta S}{N}$$

The total damage then becomes :-

$$D = \text{f.t.} \int \frac{D(S)}{N} dS$$

and using equation 1.4:-

$$D = \frac{Nf}{\sigma^b C} \int S^{b+1} \exp\left(\frac{-S^2}{2\sigma^2}\right) dS \quad (1.5)$$

where  $Nf$  = total cycles to failure.

Thus, for the case of no fatigue limit and no clipping of peaks the limits of integration are 0 and  $+\infty$ , and the resulting integral is a gamma function expressed as:-

$$D = \frac{Nf}{C} (\sqrt{2}\sigma)^b \Gamma\left(1 + \frac{b}{2}\right) \quad (1.6)$$

Using Miner's theory, D is set equal to unity for fatigue failure.

White and Lewszuk (39) extend this damage expression to the practical case of a clipped loading waveform. Their tests on welded joints indicate that b generally lies between 2 and 5. For values of b not greater than about 5 they show that waveforms with peak/rms. ratios greater than 4 negligibly affect (mathematically) the fatigue damage prediction of equation 1.6.

Several investigations have been carried out which adopt similar approaches of fatigue damage evaluation to that outlined. Hillberry (28) made life comparisons against Miner predictions based on the damage caused only by positive peaks for broad band ( $\frac{N_o}{N_p} = 0.79$ ) and narrow band loading, and showed that Miner overestimated the actual life by about  $1\frac{1}{2}$  to 5 times, see fig. 1.8. Fralich (37)

presents a Miner life prediction method based on the rms. value of peak stresses and shows the estimates to be about twice those in practice, but this error increases at lower stress levels, see fig. 1.16. Williams (39) makes similar findings.

Fuller (27) made a counting analysis of three random loading waveforms from chart traces to give rise and fall information from one thousand peaks and one thousand troughs. The data was processed to give the two dimensional range-mean distributions, but because of the relatively small sample size and necessary smoothing, the information was not considered reliable enough in this form for fatigue evaluation. It was therefore reworked independent of mean levels to provide true range distributions, and in addition range distributions based on the greatest peak and succeeding least trough between positive zero crossings. Peak distributions were not extracted because it was felt that stress excursion was the meaningful parameter for fatigue damage calculations. The S/N curve was defined by a Stussi-type curve:-

$$\frac{S - S_f}{S_u - S} = a.N^{-b} \quad (1.7)$$

where    S = value of the stress peak,  
          N = number of cycles to failure,  
          S<sub>u</sub> = material ultimate tensile stress,  
          a, b = constants,  
          S<sub>f</sub> = fatigue limit peak stress.

This equation makes allowance for a fatigue limit and for very high peak loads approaching the material ultimate tensile strength. However, complete account is not taken of bending loads in fatigue where stresses in excess of the

ultimate tensile stress can be sustained without fracture. In these conditions it is probably more realistic that  $S$  should represent the static collapse stress. The values of  $a$  and  $b$  are given by a least squares fit of data to a  $\log \left( \frac{S - S_f}{S_u - S} \right) - \log N$  plot for an assumed value of  $S_f$ .

Fuller's work was principally concerned with determining which signal range distribution would provide a best fit to data when used with a proposed fatigue damage prediction method. The method was based on a geometric relationship which was established between the particular range distribution and material  $S/N$  curve from a signal loading intensity factor and a load distribution factor. But life predictions made from a Miner summation using the range distribution data essentially showed no difference between the two range distributions for all three waveforms, and fatigue life was particularly overestimated at low stress levels - by about six times. The results are presented in Table 1.1. During these calculations, however, stresses above the material U.T.S. were disregarded. This meant that signal clipping ratio values varied from about 3 to 6 for the stress levels considered, and they were not those actually experienced.

## 6.2. Random Signal Analysis Methods

In actual practice it is often necessary to analyse large quantities of data. The application of direct counting methods under such circumstances would be extremely laborious and this has led to attempts to use statistical parameters which are more common to random vibration analysis as the relevant characteristics in fatigue damage evaluation.

Practical applications of power spectral analysis techniques can be found in aircraft gust load design

procedures. In recent years fundamental advances have been made in the representation of atmospheric turbulence as a stationary random process, and gust load criteria have become based on power spectral concepts. These criteria have been integrated into existing design procedures, and stress analysis is carried out under statistically defined loading patterns (see introduction to reference 40). But the essential process of establishing a design strength is based on an analysis which uses as a criterion the strength of existing satisfactory aircraft combined with encountered service gust loading patterns. These procedures make no attempt to correlate at a fundamental level, power spectral density parameters with cumulative fatigue damage.

Rice et al (41) suggest that the principal cause of fatigue damage is the rise and falls, or stress excursions, in the loading waveform rather than other statistical quantities, and their work concentrates on the problem of rise and fall distribution estimation. An approximate method of calculation for rise and fall distribution is presented for the case of a stationary Gaussian waveform and applied to an idealised band pass power spectrum shape. Four values of cut off frequencies are used to vary the spectrum shape between narrow band (Rayleigh peak distribution) and low pass, and the results of the computed rise and fall density distributions are favourably compared with measurements from experimental data. The approach is also extended to show the correlation for aluminium sheet between fatigue crack growth and the average rise and fall height in the variation of the crack tip stress intensity factor. Nevertheless, the work points out that the exact theoretical determination of the rise and fall distribution is a very

difficult problem, and previous approaches to the subject (26, 42) are found to be in error. Thus, it can only be concluded that solutions for the estimation of rise and fall distributions of stationary Gaussian waveforms are not yet readily available for incorporation into fatigue damage evaluation methods.

It can be concluded that fatigue damage evaluation calculation using direct waveform counting methods have mainly been limited to signals with Rayleigh peak distributions. The characteristics of this particular loading are not representative of the general case. Fatigue life predictions using the basic form of Miner's theory show a general trend to overestimate actual life, usually by a factor of two or three. This overestimation does vary however, particularly with low stress signals which have a significant number of stresses below the constant amplitude fatigue limit. With Miner's hypothesis low stresses contribute little to damage accumulation, but this is not to suggest that this is the sole error in Miner's law. Nevertheless, fatigue damage calculations using Miner in the form presented by equation 1.5 have the advantage of providing a quick indication of whether a fatigue problem exists with a particular component under random loading.

As an objective for further work in this field waveform analysis methods should concentrate on identifying those parameters which are necessary to provide an adequate statistical description of the signal, and present the data so that relevant fatigue characteristics can be extracted. For statistical definition, the form of the amplitude probability density distribution must be established, and

the power spectral density function is necessary to describe, at least qualitatively, the frequency distribution of waveform energy. From a fatigue damage evaluation standpoint it is certainly desirable to adopt a data capture method which permits extraction of signal range-mean information. The concept of a fatigue cycle is thus retained. This method would also allow calculation of the signal irregularity factor so that peak distribution functions can be defined (for Gaussian signals), and consistent comparisons with published random fatigue data can then be made.

#### 7. OBJECTIVES OF RESEARCH PROJECT

The assessment of research investigations which have been primarily concerned with improving cumulative fatigue damage estimation suggests two main avenues of approach, through which worthwhile contributions to the problem might be made.

Firstly, there is no overriding evidence to suggest that the adoption of any one alternative cumulative damage theory in preference to Miner's theory would give a major improvement in life prediction. In this situation it is therefore reasonable to accept the basic form of Miner's rule but with some modification to take account of certain inadequacies, for example, to assess the effect of infrequent high stresses and allow for damage caused by stresses below the constant amplitude fatigue limit. One way of doing this is to adopt Grover's (13) approach and attempt to quantify the various phases of fatigue life so that fatigue damage can be apportioned accordingly. Previous work (43) along these lines for constant amplitude loading showed that it was possible to quantify the fatigue process into two

stages, but the lengths of crack present in each stage for these particular tests did not indicate any correlation with the stage behaviour proposed by Forsyth (17). Thus, the first principal objective of this work can be stated:-

"To investigate the possibility of quantifying the fatigue process for random loading in terms of accepted two-stage behaviour and establish the realism of a life evaluation method based on an assessment of fatigue damage accumulation in these stages".

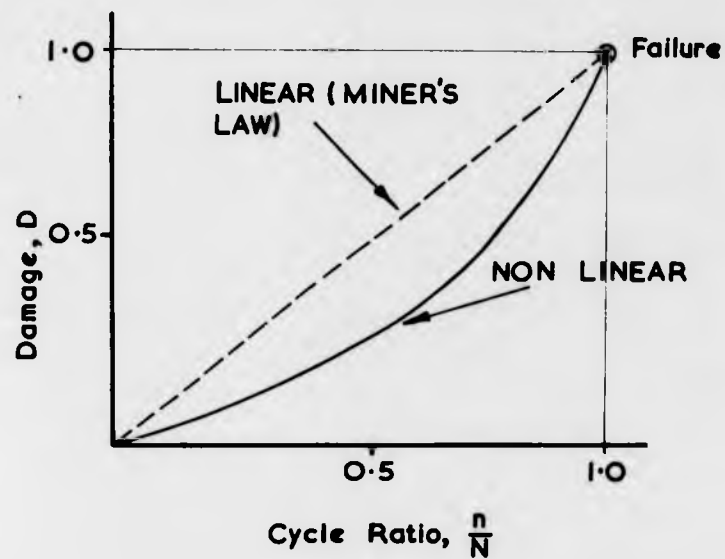
The second area of study is closely linked with cumulative damage and involves the measurement and analysis of experienced stress histories. Usually dynamic loading varies in some random manner and the problem is one of specifying and measuring those parameters which influence the accumulation of fatigue damage. The amount of data to be handled is very large if accurate measurements are to be obtained and it becomes practical to consider the data handling capacity of digital computers. Thus, the second objective of this work can be stated:-

"To make estimates of fatigue life using established computer techniques (36, 44) which enable accurate data acquisition from random stress waveforms".

Irregularity Factor	RMS. Stress KSI	Miner Life/Test Life for Rise and Fall Distribution	Miner Life/Test Life for Rise and Fall Distribution for Max. Peak and Min. Trough
0.96	22	3.66	3.63
	19.3	4.15	4.26
	15	5.7	6.05
	13.5	7.03	8.44
0.95	23.2	3.59	3.37
	18	2.63	2.58
	15	3.94	4.00
	12	6.2	6.94
0.75	22	3.38	2.40
	18	3.79	3.25
	15	6.16	5.31
	12	5.42	5.03

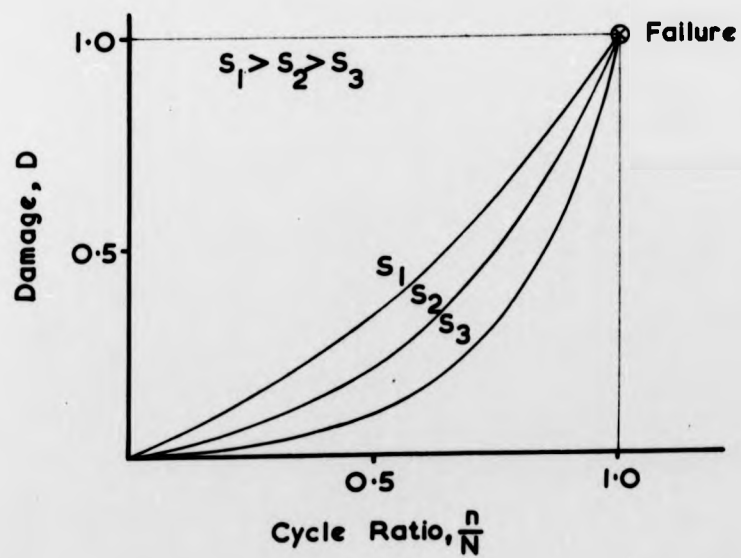
Constant Amplitude Fatigue Limit = 28.1 KSI Peak  
(reference 27)

Table 1.1



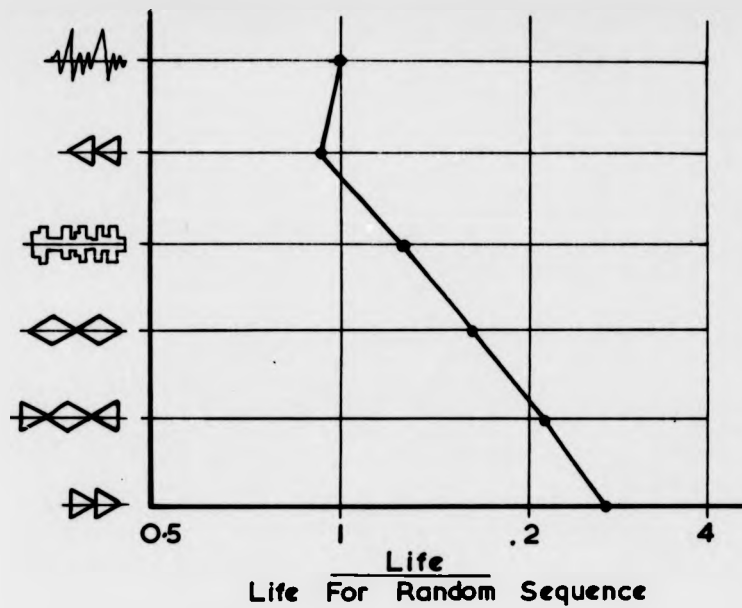
Stress - independent damage - cycle relationship

FIG. 1.1.



Stress - dependent damage - cycle relationship

FIG. 1.2.



Load Sequence Effect (ref.5)

FIG. 1.3.

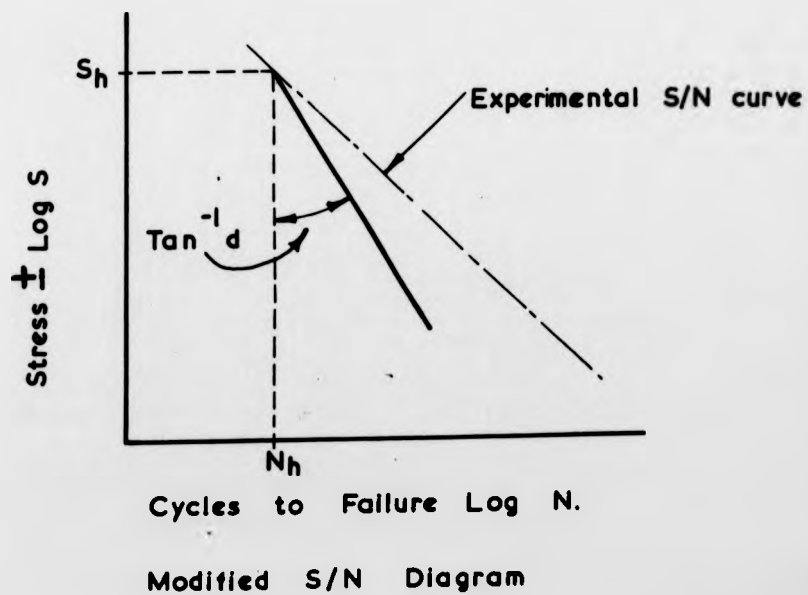
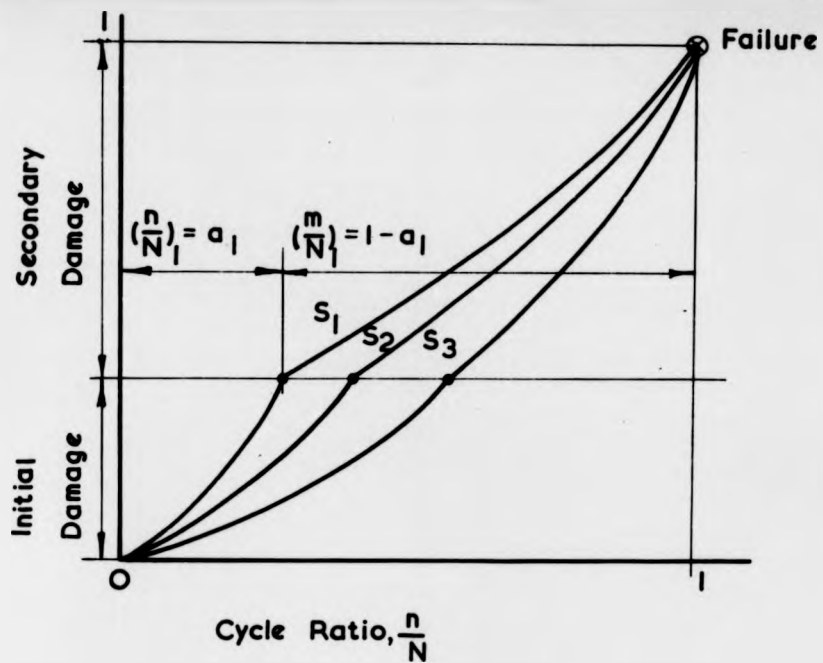
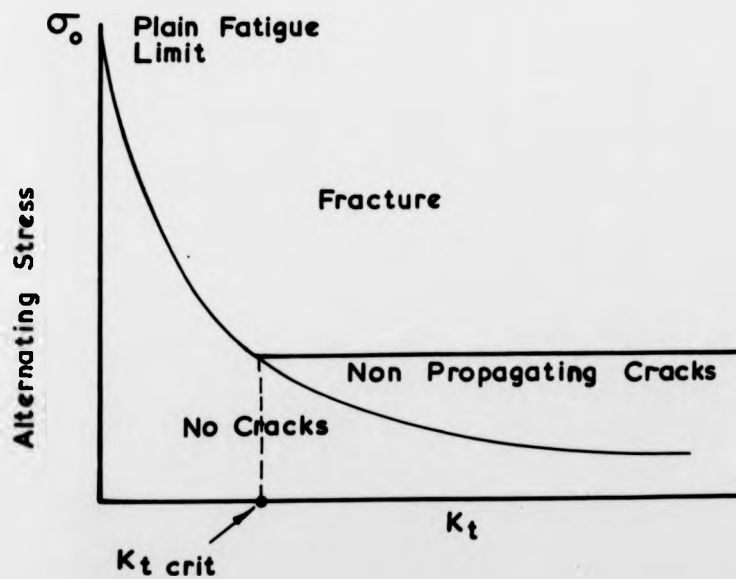


FIG. 1.4.



Stress dependent damage - cycle relationship  
for Grover's Theory (ref. 13)

FIG. 1.5.



Generalised alternating stress versus  $K_t$  diagram for  
notched specimens having different root radii but  
the same notch depth (ref. 21)

FIG. 1.6.

Signal Irregularity Factor

x 0.96  
· 0.95  
o 0.75

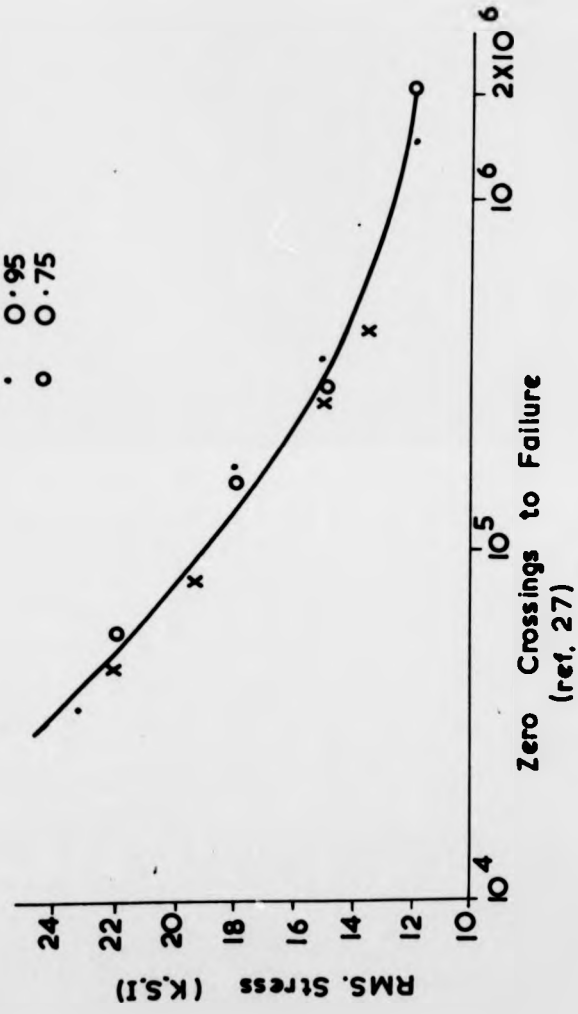


FIG. 1.7.

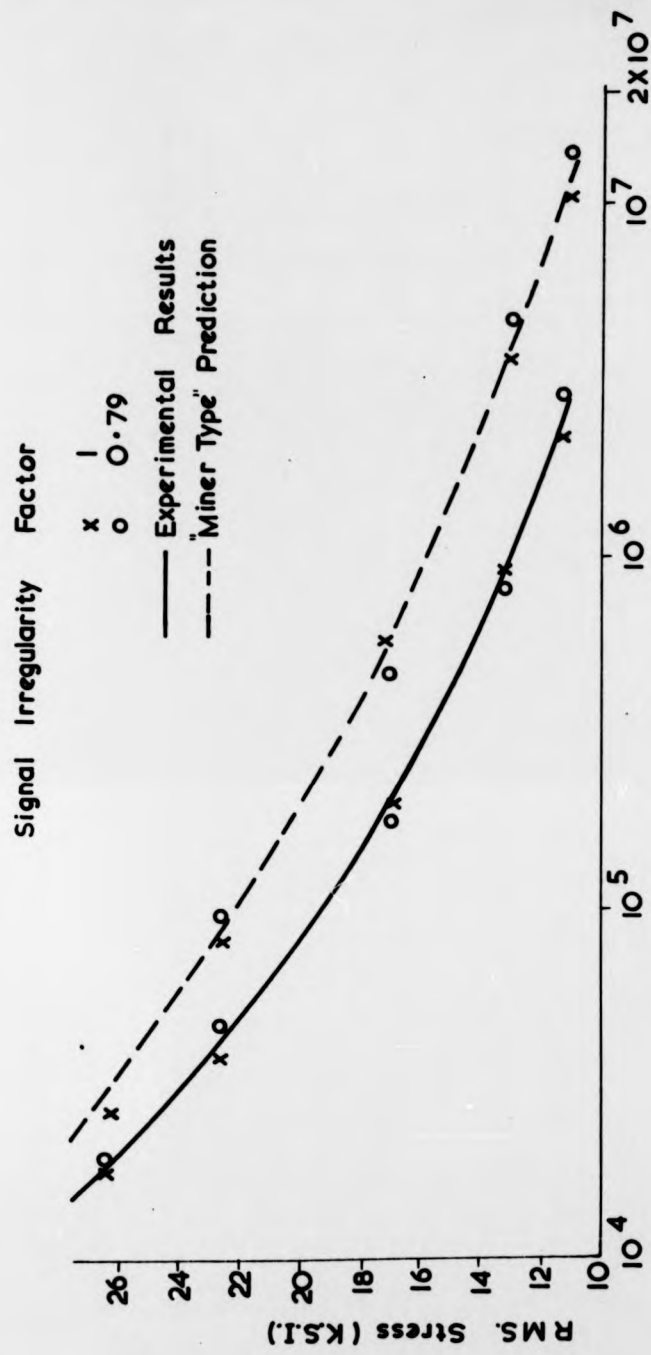
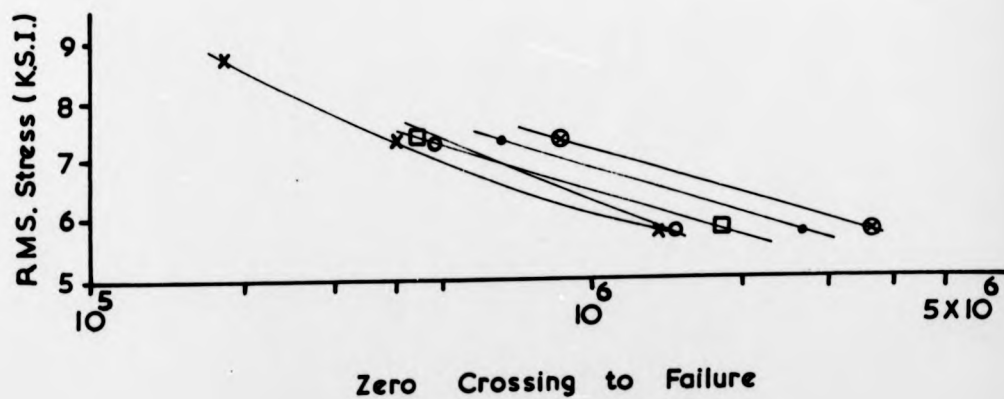
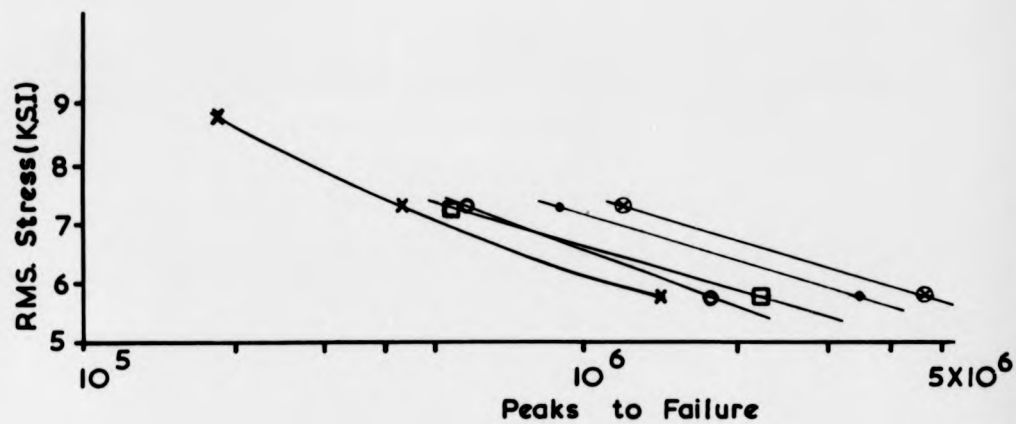


FIG 1.8.



Signal Irregularity Factor

'Band Pass' Spectrum

x 0.98

□ 0.85

• 0.75

'Double Resonance' Spectrum

○ 0.85

⊙ 0.75

(ref. 29)

FIG. 1.9.

$$\frac{N_o^+}{N_p} = 1$$

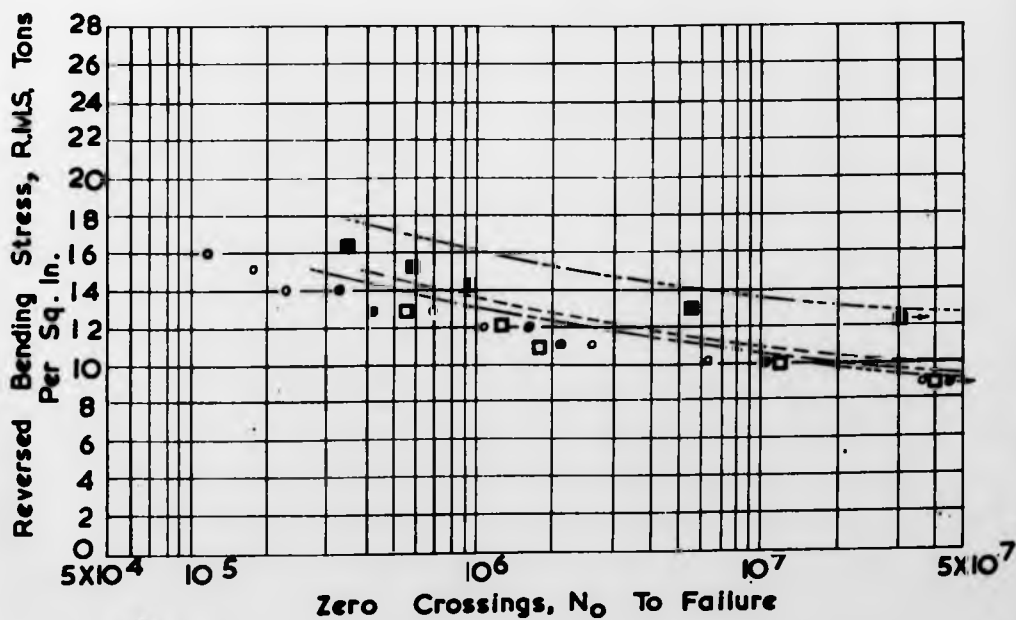


$$\frac{N_o^+}{N_p} = 0.53$$



Waveform Traces (ref. 31)

FIG. I. 10.



$$\frac{N_o^+}{N_p} = 0.78$$

(reference 32)

Test Results	
■	2.5 Sigma cut-off
○	4.0 Sigma cut-off
□	5.5 Sigma cut-off
Predicted Results With Miner's Law	
---	2.5 Sigma cut-off
---	4.0 Sigma cut-off
---	5.5 Sigma cut-off

FIG. III.

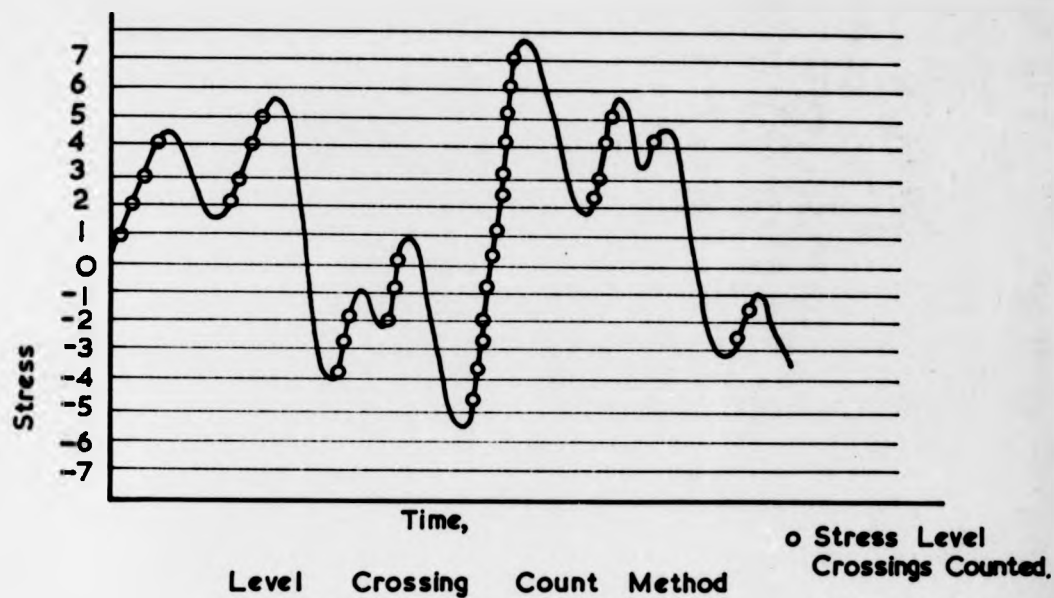


FIG. I.12.

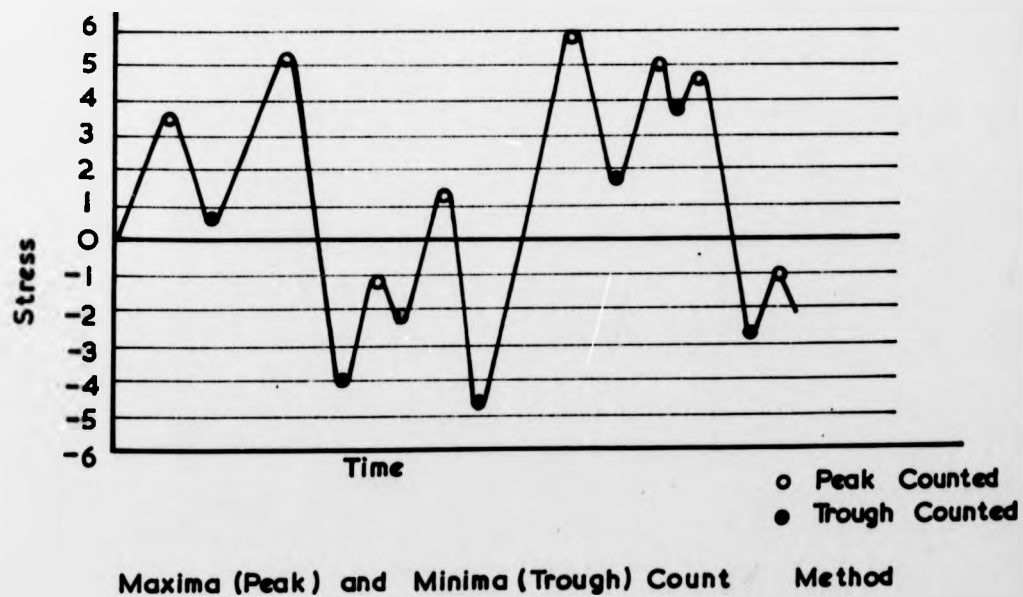
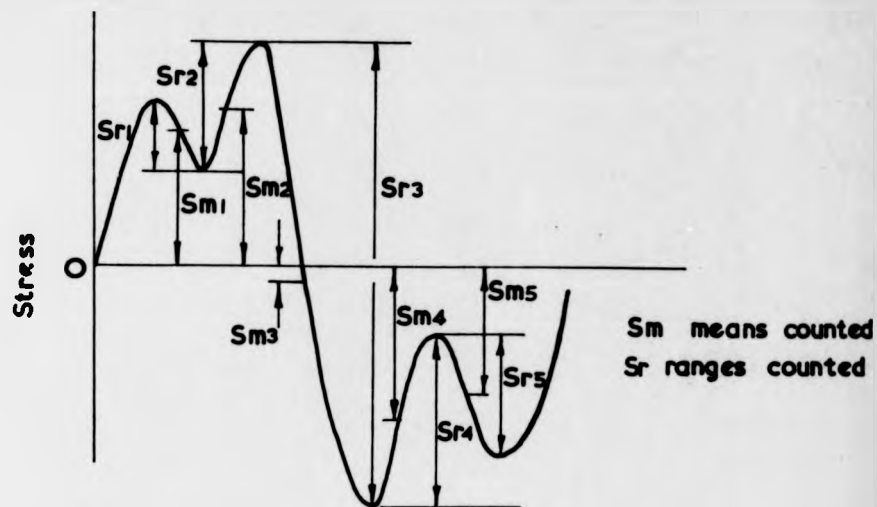
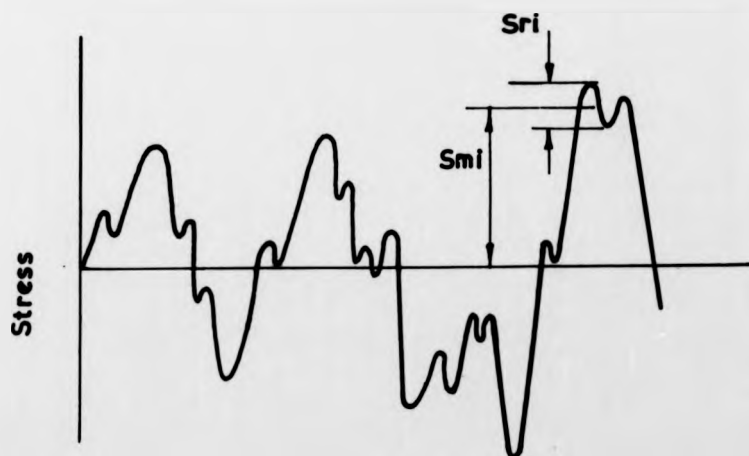


FIG. I. 13.



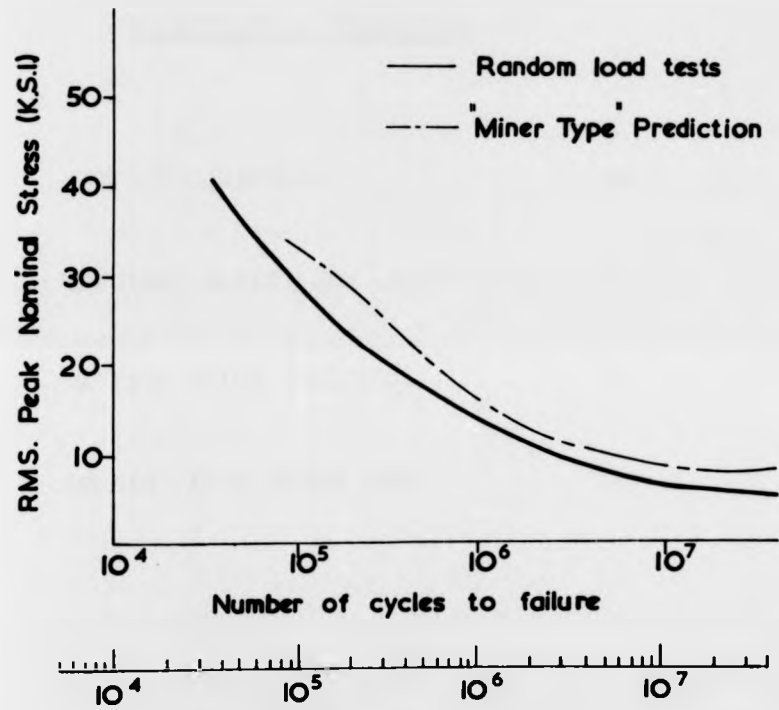
Range - Mean Count Method.

FIG. I. 14.



Range - Mean Count Method Applied to Random  
Waveform containing Small and Large Amplitude  
Variations.

FIG. I. 15.



(ref. 37.)

FIG. I.16.

CHAPTER 2

EXPERIMENTAL TECHNIQUES

1.	FATIGUE EQUIPMENT	38
2.	SPECIMEN DESIGN AND MANUFACTURE	50
3.	FATIGUE CRACK DETECTION	56
4.	STRAIN GAUGE TECHNIQUES	59

### 1. FATIGUE EQUIPMENT

Fatigue testing was carried out using three electrohydraulic servo controlled test rigs and two electromagnetic vibrator test rigs.

Initially work started with a test rig which was designed around a proprietary electrohydraulic system of power pack, hydraulic ram and electronic control module. The test specimen was loaded in cantilever bending by the ram which was rated at  $\pm 1100$  lbf. Early commissioning work showed that the dynamic performance and accuracy of force control of this system were not good enough for the testing envisaged and that changes in the design of the ram and control module were necessary. So that testing could get underway while modifications were made, it was decided to instal another electrohydraulic system but driven from the same hydraulic power pack. A ram and control module were ordered from a different servo hydraulic equipment manufacturer and a test rig was designed and constructed. This system was rated at  $\pm 3\frac{1}{2}$  tf. and the specimen was loaded in axial tension/compression. Later in the test programme a third servo system was commissioned which had a larger capacity hydraulic power supply and a more sophisticated electronic control module. The system was rated at  $\pm 10$  tf. and a test rig was designed and constructed to fatigue specimens in three point bending.

The basic principles behind the design and commissioning of electrohydraulic servo controlled fatigue test rigs are presented in Appendix A. Detailed calculations were made for each rig for the stress analysis of parts to withstand dynamic loading and the vibration analysis of resonant behaviour. Engineering drawings were prepared and all com-

ponents were manufactured by the University Workshop. Including all these design and drawing details here would be lengthy so reference is only made to drawings now held by the University Workshop Drawing Office.

Also, two electromagnetic vibrators rated at  $\pm 40$  lbf. thrust were used to fatigue specimens in cantilever bending. The majority of development work for these two rigs was associated with instrumenting specimen force measurement and specimen failure trip circuits.

#### 1.1. Fairley Air Surveys $\pm 1100$ lbf. Servo Rig

This rig was designed to fatigue specimens machined from strip mild steel in cantilever bending about a zero mean force level. The photograph, fig. 2.1, shows the general layout of the rig, and design details are given by drawings ES/2/209/1 - 5. The framework was fabricated from structural steel sections. The hydraulic ram was bolted to the base of the rig and the specimen was bolted to a rigid platform cantilevered from one leg of the framework. To prevent any twisting during loading, the plane of the specimen was aligned accurately to lie in the line of thrust of the ram by shimming the plate onto which the specimen was bolted. The method of specimen mounting is shown in fig. 2.2, and loading was through a spring steel strip bolted to the end of the specimen and driven by a steel shaft which screwed into the top of the load cell. The spring steel was stiff enough to withstand the maximum ram force but was sufficiently flexible to reduce ram side loading and give only a small carry over moment at the specimen. Also, the steel shaft was constrained by linear bearings to reduce ram side loading. The hydraulic power

supply was 12 g.p.m. from two constant pressure variable delivery pumps at 3000 p.s.i. and the servo valve was a Moog Series 22 type.

Initial commissioning work with this rig proved to be very disappointing because of the poor reliability and dynamic performance of the proprietary equipment. Some industrial and research users of this equipment were also experiencing similar troubles at this time. Problems were encountered both with the hydraulic and electronic components, and it is relevant to briefly list these faults and the measures taken to remedy them because of the large amount of time which this took.

#### Hydraulic Equipment

Initially, the main filter on the hydraulic power pack had not been correctly assembled. This caused severe contamination of the servo valve which had to be replaced. A new main filter was fitted and a secondary filter was introduced into the hydraulic circuit immediately before the valve.

Misalignment of the electric motor/hydraulic pump drive had occurred during assembly and pump failure resulted after approximately 200 hours running. This necessitated a major overhaul of the power pack and replacement of electric motor bearings, drive coupling and pump drive shaft and seals.

Despite accurate alignment and elimination of hydraulic ram side loading, test waveforms monitored at the load cell amplifier showed distortion which indicated two faults with the ram:-

(a) The step in the waveform shown when loading from tension to compression suggested mechanical backlash and

was traced to a poor fit of the taper coupling to the piston rod. The taper faces were marked by "cocoa" fretting stains. The taper was reground and the coupling refitted.

(b) The raggedness of the waveform for command signals of an amplitude much larger than the system dead zone indicated stick-slip movement of the piston rod. Examination showed scoring of the piston rod, suggesting metal to metal contact in the ram bearings. The bearings were bronze and designed to provide controlled hydraulic leakage, but commissioning work questioned whether adequate bearing lubrication was being achieved. The Motor Industry Research Association, Nuneaton, had experienced similar trouble, and in consultation with them the bearings were redesigned to incorporate p.t.f.e. bushes and the scavenge ports were blocked.

This resulted in considerably improved waveform shape.

#### Electronic Equipment

A diagram of the original electronic control circuit components is shown in fig. 2.3.

Before proceeding with testing, it was decided to check the order of variation of load cell amplifier output drift due to laboratory temperature variations. A thermistor sensing probe was hung near the fatigue rig and the sensed temperature was recorded in one minute durations over 24 hours using a Grant Instruments Ltd. Model B reading unit and a Smiths' Multiscript Model 3 chart recorder. The load cell amplifier voltage was data logged in 30 minute intervals with a Dynamco Microscan 6300 Data Logging Unit. The results are shown in fig. 2.4, and they indicate an apparent mean force drift of the order of 80 lbf. over

twelve hours, which was unacceptable for the testing envisaged.

Other aspects of the control module design were unsatisfactory. One chopper stabilised amplifier using voltage feedback combined the functions of control amplifier and servo valve drive amplifier. Loop gain adjustment was provided only by the variable gain of the load cell amplifier. The load cell rating was  $\pm 15,000$  lbf. against the  $\pm 1100$  lbf. maximum thrust of the hydraulic ram. There was a 50 mV. peak ripple on the output of the stabilised power supply, and no specification was available for voltage stability.

In order to establish a sound instrumentation footing it was decided to redesign the control loop electronics. This is shown in fig. 2.5. Loop gain adjustment is independent of load cell amplifier gain, and the control and valve drive functions are achieved by separate amplifiers. The load cell was regauged to increase its sensitivity, and the original stabilised voltage supply replaced. Drift measurements of the load cell amplifier output are shown in fig. 2.6, resulting in an acceptable error of apparent mean load variation during twelve hours of about 5 lbf. The gains of the loop components were:-

Specimen Stiffness	=	5000 lbf./in.
Summing Amplifier Gain	=	2
Servo Amplifier Gain	=	7mA/V
Servo Valve Gain	=	2.67 in <sup>3</sup> /s/mA
Load Cell/Amplifier Gain	=	6.5mV/lbf.
Hydraulic Ram Gain	=	0.42 $\frac{1}{\text{in}^2}$

A frequency response of the rig with modified hydraulic ram and control electronics is shown in fig. 2.7.

The load cell/load cell amplifier calibration was made using an Amsler 2,000 lbf. testing machine. Achieved test rig static and dynamic specimen stresses were measured over the test range by strain gauging a specimen and using a dead weight calibration to check the stresses calculated from the load cell output. Alignment test results showed that transverse bending amounted to 1% of the applied load and achieved cantilever stresses were 4% less than for the calibration cantilever static loading. Fatigue test stress levels were set using specimen stress/load cell amplifier voltage data presented in tabular form and calculated from a least squares fit to the calibration information.

The electronic trip circuit which was used is shown in fig. 2.8. The circuit was mechanically triggered by a micro switch. As the specimen failed the increased deflection caused the specimen to strike the micro switch, thus opening the contacts. The principle of operation of the electronic circuit is described in the section dealing with Electromagnetic Vibrator Test Rigs.

#### 1.2 Keelavite Hydraulics $\pm 3\frac{1}{2}$ tf Servo Rig

This rig was designed to fatigue specimens machined from strip mild steel in axial tension/compression, and is shown by the photograph in fig. 2.9. Design details are given by drawings ES2/210/1 - 2. The framework was fabricated from structural steel sections and the load cell fastened to the crossbar of the framework. The ram was bolted to the base of the rig. The specimen was held in grips between the load cell and the ram (see fig. 2.10) and, to prevent buckling in compression, was loaded dynamically about a mean tensile load of 800 lbf. Alignment of the hydraulic ram and load cell to give accurate axial

loading was achieved by shimming and using the mandrel and collar system shown in fig. 2.11. The mandrel was quite free when the load cell and ram had finally been bolted in position.

One modification to the electronic control module had to be made during rig commissioning. Electrical noise, mainly from the switching transients of an overhead crane and workshop machinery, was picked up by the load cell and associated cable and amplified by the load cell amplifier. This interference was not noticeable when amplifier common mode balance had been restored by achieving reactive and resistive balance in the amplifier feedback circuits (see Appendix A).

Loading pulses could also be felt on the specimen by switching electrical equipment on/off the mains supply which powered the control module. To avoid this trouble, the module mains power was taken from a separate clean mains circuit.

Further modifications were made to the electronic control circuit to improve the rig frequency response as described in Appendix A, which also gives the gains of the components within the loop. Details of the control circuit electronics are given in fig. 2.12. Drift measurements of the load cell amplifier output are shown in fig. 2.13, giving an apparent mean load variation of 15 lbf. or  $1\frac{1}{2}\%$  of the set mean level. This was acceptable for the testing here. The test rig frequency response is shown in fig. 2.14.

To maintain a high degree of axial alignment both ends of test specimens were first located in each grip by a dowel which was a slide fit through brass bushes in the grip and a reamed hole in the specimen. The eccentricity of the reamed

hole from the specimen test section was not greater than 0.005". Then the 800 lbf. mean tensile load was applied and the specimen clamped by bolts, tightened using two spanners to minimise any twisting effect. All testing was carried out at a mean load of 800 lbf.

The load cell/load cell amplifier calibration was made using the 5 Tf. range of an Amsler 40 Tf. testing machine. Achieved test rig static and dynamic specimen stresses were measured over the test range by strain gauging 4 specimens and using dead weight calibrations to check the stresses calculated from the load cell output. The results are summarised in Table 2.1.

A factor complicating any rational analysis of these results was the condition of the specimens themselves. Since the material was supplied in the hot rolled condition it was doubted if any one specimen was perfectly flat. During clamping in the grips the straightening of a curved specimen would induce transverse bending stresses along its length and in-plane bending stresses along its width. The alignment test results indicated that at the worst there might be a variation in the mean tensile stress across the specimen of about 20% from the nominal applied, and that the dynamic stress across the specimen could vary by up to about 8%. It is questionable whether the order of variation of static mean stress indicated by these tests would significantly affect the results. Work with sheet mild steel specimens by Frost & Greenan (20) has indicated that for mild steel the mean load has no effect on crack propagation rate. The fatigue results showed no more scatter than that expected from polished specimens, and out of 70 specimens tested, 21 fractured from one side, 23 from the other and

26 specimens fractured from cracks initiated from both notches. It was thought that the bending stresses introduced during the testing were not exceptionally high, and that they in no way detracted from the validity of the results.

An electronic trip circuit similar to the one shown in fig. 2.8 was used during testing with a micro switch being triggered at failure by increased extension of the cracked specimen.

### 1.3 Derritron $\pm$ 40 lbf. Electromagnetic Vibrator Rigs

Two electromagnetic 40 lbf. thrust vibrators were used to fatigue  $\frac{1}{4}$ " diameter specimens in cantilever bending. The majority of development work was associated with instrumenting specimen force measurement and specimen failure trip circuits. Minor structural modifications required to the existing test rigs to accommodate the test specimen were a repositioning of the vibrator unit and the manufacture of new specimen clamping plates. One test rig is shown by the photograph of fig. 2.15.

An integral diaphragm type load cell was designed to bolt to the vibrator table and the specimen force was applied through the load cell/ball joint assembly, see fig. 2.16. Initially the ball joints showed a tendency to chatter during testing because of the play in the bearing, but this was eliminated by fixing a small rigid clamp to the ball joint which deformed the outer race slightly to remove any bearing backlash.

There are certain general rules which are applicable to diaphragm transducer design (45). The deflection at the centre of the diaphragm should not be greater than about

one quarter of the thickness for good strain linearity (of the order of 0.25%) and to achieve an accurate response to dynamic forces the diaphragm resonant frequency should be at least five times the highest applied frequency. The designed diaphragm load cells had a fundamental resonance of  $2\frac{1}{2}$  KHz and the centre deflection at 40 lbf. was 0.01 ins., or 40% of the thickness. The load cells were manufactured from En.8 steel. The strain gauge bridge consisted of eight gauges each with a nominal 120 ohm resistance and arranged to eliminate signal components due to bending across the load cell. The load cell amplifier circuits are shown in fig. 2.17.

Achieved specimen stresses were measured by strain gauging a specimen and using a static calibration to check the stresses achieved dynamically and calculated from the load cell output. Linearity of rig response to increases in signal input was checked up to the highest 4 x signal r.m.s. stress excursion encountered in the test programme by taking U.V. traces of the load cell output from short bursts of constant amplitude cycles.

Initially the actual frequency response for both rigs was as shown by fig. 2.18, peaked about a frequency of 47 Hz. This resonant frequency was determined by the load cell/specimen stiffness and effective mass on the vibrator table. Constant amplitude testing was carried out at this frequency and the 10Hz. bandwidth narrow band testing was centred on this frequency. However, the response of each rig was subsequently modified to accommodate broader band testing by shaping the input signal with two networks of the form shown in fig. 2.19, so that the achieved test rig response then had the form shown in fig. 2.20.

The electromagnetic vibrators were run open loop and therefore provided a table displacement directly proportional to the command signal. Thus, when the stiffness of a specimen was significantly reduced by a fatigue crack the load cell output voltage dropped until at specimen fracture load cell voltage was zero. This principle was used in the design of the electronic trip circuit, shown in fig. 2.21. The load cell signal is rectified and amplified by a differential input operational amplifier to drive a transistor which provides the necessary current to energize a number of relay coils. For random testing the time constant of the feedback resistor/capacitor can be increased to prevent the circuit from tripping as the amplifier voltage falls during a period of low load signal.

#### 1.4 Keelavite Hydraulics $\pm$ 10 Tf. Servo Rig

This rig was designed to fatigue round specimens in three point bending and is shown by the photograph in fig. 2.22. Design details are given by drawings ES2/241/1 - 7. The rig provided a testing facility which would enable the investigation of size effect under random loading and allow a comparison with the results obtained under similar loading from the 0.25" nominal diameter cantilever specimens of the electromagnetic rigs.

The hydraulic system comprised a power pack supplied by Keelavite Hydraulics Ltd. and a Sperry 3600L servo valve coupled to a L8senhausen hydraulic ram mounted in a testing table. The power pack flow rating was 22 gpm. and that of the servo valve 35 gpm. The control electronics, supplied by Keelavite Hydraulics Ltd., were coupled to a Sangamo Type D90 load transducer of 25,000 lbf. maximum rated load.

A block diagram of the complete system is shown by fig. 2.23. Drift measurements of the load cell demodulator/amplifier output indicated no significant voltage variation.

The hydraulic ram was not rated to take severe side loads and it was felt that with the large forces to be used in this testing a cantilever bending mode of loading may have led to side loading problems, especially since the ram was rigidly bolted into a testing table and not mounted on a swivel at its base. Therefore, a three point bending rig was built which also enabled loading from compression to tension.

Apart from establishing an overall strength integrity, there were two main considerations to be taken into account during the design. Firstly, it was necessary to ensure that there was minimal restraint from the end fixings to both longitudinal and rotational movement of the specimen ends, and in addition to allowing this freedom of movement it was important to prevent bearing backlash. These conditions were met by designing what was essentially a trunnion end fixing, mounted in plummer blocks which were free to slide horizontally but restrained vertically. All bearing clearances were controlled by shimming. The principle is shown by the photograph of fig. 2.24.

The second consideration essentially arose from the specimen design. It was necessary to achieve a bending span long enough to enable a significant size increase over the cantilever specimens, taking into account the force capacity of the hydraulic ram and the resonant behaviour of the rig. A simply supported three point bending configuration does not give particularly high fundamental resonant frequencies. For this test rig the resonant frequency was associated with

the bending stiffness and mass of the specimen, and the weight of the loading head, load cell and piston rod at the specimen centre span. This frequency was calculated at 40 Hz. The test rig frequency response is shown in fig. 2.25. Constant amplitude testing was carried out at 10 Hz. and the 3 Hz. bandwidth narrow band testing was centred on this frequency.

The load cell/load cell demodulator-amplifier calibration was made using the 10 Tf. range of an Amsler 40 Tf. testing machine. Two strain gauge pairs were mounted on a plain specimen to measure maximum bending stresses, one pair at the position of each notch, and a voltage calibration was made for static simply supported three point bending, using the 15 Tf. Transverse Unit of a Denison Model T60CT testing machine. Achieved test rig static and dynamic specimen stresses were compared with the bending calibration for applied force levels measured by the load cell. The results are shown in fig. 2.26. There is good correspondence between the achieved test rig loading and the three point bending condition, and for the purposes of specimen stress calculation it was taken that simply supported three point bending was achieved in the test rig.

An electronic trip circuit similar to the one shown by fig. 2.8 was used to indicate specimen failure. The circuit was mechanically triggered by a microswitch from the increased deflection during specimen failure.

## 2. SPECIMEN DESIGN AND MANUFACTURE

It was in an effort to give the results of this work a degree of general applicability in an engineering design sense that the fatigue specimens were machined from mild

steel and given elastic stress concentration factor values of about two. Low carbon steels are widely used throughout the engineering industry and frequently design stress concentration factors fall in the  $K_t = 2$  region.

Specimens for the two small servohydraulic rigs were machined from  $\frac{1}{8}$ " and  $\frac{1}{4}$ " thick steel strip. These dimensions were governed by test rig force capacity and the achievement of realistically sized specimen test sections. Cold drawn bright steel strip was more attractive as specimen material than hot rolled strip from the aspects of surface finish and more accurate production tolerances, but it was felt that residual stresses from the drawing process would have a gross effect across the material section for these thicknesses. Therefore, steel was ordered to En 3A, B.S.970 specification and supplied in the hot rolled and normalised condition. All specimens were machined from one batch of steel and no further heat treatment was carried out. No material grain distortion was apparent at the notch during subsequent specimen sectioning and fatigue crack examination work.

Later in the test programme, as work merged into the British Rail Contract and the electromagnetic and  $\pm 10$  Tf. servohydraulic test rigs were used, specimens were machined from cold drawn bright round steel bar to En 3B, B.S.970 specification. British Rail felt that this was the most suitable steel for their cumulative fatigue damage research programme, but being aware of gross residual stress effects, the steel was ordered from B.I.S.R.A. where precautions were taken to reduce the passes during cold drawing. No heat treatment was carried out during specimen production, and

again no grain distortion was apparent at the notch during subsequent specimen sectioning and fatigue crack examination work.

Sample test pieces were chosen from the batches of steel and analysed to determine chemical composition and mechanical properties. The results are shown in Table 2.2 and all material conformed to the respective B.S. Specifications.

### 2.1 Fairey Air Surveys $\pm$ 1,100 lbf. Servo Rig Specimen

The low force rating of the hydraulic ram dictated fatigue testing in bending and a cantilever bending rig was manufactured. Specimens were designed to be held in the rig by bolted clamping attachments.

Specimens were machined by the University Workshops from one batch of 18 ft. lengths of 2" x  $\frac{1}{4}$ " section En 3A steel strip. The nominal value for the notch stress concentration factor was  $K_t = 1.94$ . Unfortunately, specified machining tolerances were not achieved during machining but, subsequently, all specimens were checked and those were used which conformed to the dimensions shown by fig. 2.27. The maximum variation of  $K_t$  from the nominal value was  $\pm 2\%$  because of these dimensional changes. Test stress levels were set to suit each individual specimen test section.

Jigs were made to clamp the specimens during manufacture. Notch forms were carefully machined by first drilling to just under size and finally reaming to size taking a light finishing cut. Machine feeds were low and an adequate supply of coolant was used to minimise the development of residual surface stresses.

The polishing of notch forms for flat specimens has

not been nearly so well standardised as for cylindrical specimens, but the same principles apply. Notch polishing is a cutting and not a buffing process. The object is to produce a smooth surface and remove machine marks without cold working with a view to producing uniformity of test conditions rather than with the thought of producing a highly polished or buffed surface.

After machining it was found with some specimens that hand operations were required to remove feather edges from the corners of the notch. Notch polishing was achieved with a slurry of machine oil and carborundum valve grinding paste, using a soft steel rod just less than the notch diameter, held in a drilling machine chuck. Two grades of grinding paste - coarse and fine - were used. Also prior to testing, the faces of the specimen test sections were lightly sanded with emery cloth and machine oil in the longitudinal direction to remove surface rolling scale. The specimens were thoroughly cleaned of oil before testing with clean rag.

The following dimensional and notch form checks were made for each tested specimen:-

1. Specimen width at notch throat.
2. End face to notch centre line (moment arm).
3. Specimen overall width at test section.
4. Specimen thickness.
5. Notch profile for radius and general regularity of profile using a Nikon profile projector on X 50 magnification.

Also, a number of specimens were chosen at random and their notch surfaces examined for pits and scratches at a magnification of X 100.

### 2.2 Keelavite Hydraulics $\pm 3\frac{1}{2}$ Tf. Servo Rig Specimen

The force capacity of this test rig permitted axial fatigue testing and specimens were designed to be held in the rig by bolted clamping attachments.

Specimens were machined by the University Workshop from one batch of 18 ft. lengths of 2" x  $\frac{1}{8}$ " section En 3A steel strip. The nominal value for the notch stress concentration factor was  $K_t = 2.26$ . Unfortunately, specified machining tolerances were not achieved during machining but, subsequently, all specimens were checked and only those were used which conformed to the dimensions shown by fig. 2.28. The maximum variation of  $K_t$  from the nominal value was  $\pm 3\%$  because of these dimensional changes. Test stress levels were set to suit each individual specimen test section.

Specimen machining and polishing techniques followed the procedures adopted for the cantilever strip specimens, but during machining additional care was taken to ensure accurate positioning of the reamed locating holes at the ends of each specimen.

Dimensional and notch form checks were made in a similar way to those of the cantilever strip specimens, with an additional measurement being taken of the eccentricity of the dowel locating hole from the test section.

### 2.3 Derritron $\pm 40$ lbf. Electromagnetic Vibrator Rig Specimen

The two electromagnetic vibrators had been incorporated in fatigue rigs which loaded specimens in cantilever bending. Specimen design had been made at an earlier stage of the British Rail Contract than the work reported here, but no testing had been carried out.

A batch of 4000 specimens was machined by A. Blundell

& Co. Ltd., Coventry. The material was En 3B bright steel, cold drawn as a special batch by B.I.S.R.A. Half of the batch was available for this work.

Specimens were prepared for testing in groups of 20. Each specimen was initially lightly polished with oil and grade 320 aluminium oxide emery cloth, and finish polished with a slurry of oil and fine silicon carbide valve grinding compound using a thin piece of string. The following dimensional and notch form checks were then made on 5 specimens chosen at random from each batch:-

1. Notch throat diameter.
2. Spigot end face to notch centre line.
3. Specimen outside diameter.
4. Notch profile for radius and general regularity of profile using a Nikon profile projector set to X50 magnification.
5. Notch surface for pits and scratches at a magnification of X100.

It was found that polishing reduced the throat diameter slightly from the nominal as machined dimension, but all tested specimens conformed to the dimensions and tolerances shown in fig. 2.29. Test stress levels were based on nominal dimensions.

#### 2.4 Keelavite Hydraulics $\pm$ 10 Tf. Servc Rig Specimen

The principal object of the testing with these specimens was to investigate the presence of any size effect under random loading compared with the results from the small electromagnetic vibrator cantilever specimens. Therefore, it was necessary to retain an equivalent mode of loading and achieve essentially the same notch stress distribution as

for the small specimens. The larger specimen was therefore loaded in three point bending and its size was determined by the available hydraulic force which allowed a geometric scaling up of the small specimen form by a factor of ten.

Approximately fifty specimens were machined by the University Workshops from one batch of 18 ft. lengths of  $2\frac{1}{2}$ " diameter En 3B steel bar. The nominal value for the notch stress concentration factor was  $K_t = 1.59$ . Unfortunately, specified machining tolerances were not achieved during machining. However, all the specimens were checked and they conformed to the dimensions shown in fig. 2.30. The maximum variation of  $K_t$  from the nominal value was  $\pm 1\%$  because of these dimensional changes. Test stress levels were set to suit each individual specimen test section.

Polishing and dimensional checks were made in a similar way to those of the small cantilever specimens, with the exception that the notch form could not be accurately checked on the Nikon projector because the specimens were too large. However, because form tools were used to machine the notches and because of previous experience in specimen machining, it was not expected that significant notch form errors would be present.

### 3. FATIGUE CRACK DETECTION

#### 3.1 Förster Defectometer Type 2.154

Fatigue tests were interrupted briefly at regular intervals to monitor the growth of fatigue cracks in specimens using an eddy current instrument, the Defectometer Type 2.154 manufactured by Institut Dr. Förster in Germany, and shown by the photograph of fig. 2.31.

The probe comprises a single coil wound round a ferrite rod and supplied with a high frequency constant current amplitude signal. During the initial setting up of the instrument, a balancing network is adjusted to provide a reference voltage which is made equal in amplitude and phase to the voltage across the probe coil when the probe is in contact with a virgin specimen. The voltage across the probe coil is directly proportional to its impedance, which in turn is influenced by changes in the specimen. The difference between these voltages is indicated by a meter, or by voltage terminals at the back of the instrument. The balancing procedure also enables the "lift-off" effect to be suppressed, since eddy current measurement can be very much affected by a variation of the distance between probe coil and specimen. All adjustments were made with a high instrument defect sensitivity to achieve a linear instrument response for the range of crack depths of interest.

Apart from specimen geometry, the significant factors which influence eddy current induction by a particular test coil and current frequency are the material electrical conductivity, magnetic permeability and the presence of discontinuities such as cracks. The instrument does respond to material changes such as work hardening because of the associated changes in conductivity and permeability, but this is small compared with the response to specimen cracking. The instrument is only suitable for the detection of cracks which are close to the surface, since the extremely high frequency results in a "skin effect" which only allows the eddy currents to penetrate to a relatively small depth.

The physical meaning of a given defectometer response

was established by sectioning and optically examining part fatigued specimens. Detected fatigue cracks were usually in the range 0.0005" to 0.050" long.

### 3.2 Specimen Sectioning & Optical Microscope Examination

Cylindrical specimens were sectioned by sawing across the notch at the point of maximum crack depth. With flat specimens both sides of each notch were examined for fatigue cracks and, in addition, specimens were sometimes sectioned through the centre of the notch in the plane of the specimen to more accurately define the crack front.

Sectioned faces were filed lightly to remove saw marks, and specimens mounted in bakelite for ease of holding during polishing. Mechanical polishing was carried out using wet and dry emery paper - grades 220, 320, 400 and 600 - finishing off on 10 micron and 1 micron diamond wheels. Specimens were held so that scratches were formed in one direction only and rotated through 90° when moving onto the next grade of paper. Polishing pressure was light and specimens were rubbed until scratches from the previous paper were removed.

Mechanical polishing tended to flow metal into any fatigue cracks which were present and, therefore, specimens were chemically etched or electrolytically polished before micro examination.

Chemical etching was achieved by dipping the mounted specimen into a 2% nital solution for several seconds:-

98% Concentrated Nitric Acid

2% Alcohol or Methylated Spirits.

The solution was mixed by slowly adding the nitric acid to the alcohol.

Electrolytic polishing was carried out by hanging a dry unmounted specimen in a stainless steel beaker containing the electrolyte. The specimen formed the anode and polishing was continued for 2-3 minutes at 20v. and a current of 0.1/0.15 amps. The electrolyte composition was:-

133 cc Glacial Acetic Acid (99.5% conc. min.)

25 g Chromium Trioxide

7 cc Water

The solution was mixed in a conical flask placed in a 60°/70°c water bath standing in a fume cupboard. First the chromium trioxide was added to the acid, followed by the water. When not being used the solution was stored in an airtight bottle, but it usually started to deteriorate after about three weeks.

After preparation optical examination of specimens and the measurement of fatigue crack lengths was made on a Vickers 55 m. microscope using magnifications up to X1000.

#### 4. STRAIN GAUGE TECHNIQUES

In anticipation of the involvement with strain gauging during this work it was decided at the outset to adopt a straightforward, reliable and quick technique for strain gauge bonding. The procedure followed was recommended by the Strain Measurements & Equipment Division of Welwyn Electric Ltd. and essentially involved obtaining a chemically clean surface before bonding with Eastman 910 adhesive.

Strain gauges were used for load cell instrumentation and fatigue rig calibration. The gauges were T.M.L. Polyester backed resistance wire strain gauges marketed by Electromechanisms Ltd. Printed circuit copper terminal strips supported strain gauge lead wires and aided wiring up bridge circuits. Particular attention was paid to the

positioning of load cell gauges to achieve temperature compensation and the cancellation of any bending strains across load cells. During fatigue rig calibration the output of both two arm and four arm bridges were amplified by a Fenlow ZA2 transducer amplifier, a low drift d.c. amplifier with 0.01% linearity. The gain was variable to any value between 100 and 1600 and it contained its own variable bridge power supply. The output current adequately drove ultraviolet galvanometers. An S.E.2800 U.V. recorder, together with suitable galvanometers, were used for detailed examination of test rig waveform shape.

Specimen		B22	A22	G22	B21	Average
Eccentricity of dowel holes from test section (ins.)		0.001	0.009	0.001	0.007	-
% of applied static mean stress induced with grips free	Transverse	22	22	not measured		22
	Inplane	9	3	"	"	6
% of applied static mean stress induced with grips bolted	Transverse	9	2	14	24	12
	Inplane	12	3	9	3	7
% of applied dynamic stress induced with grips bolted and loaded with static mean stress	Transverse	9	7	7	6	7
	Inplane	0	0	0	1	1

Static Mean Stress = 3.0 Tsi (800 lbf. mean load)

Induced Dynamic Stresses are averages from tests with constant amplitude peak nominal stresses of 1.5, 3.0, 4.5, and 6.0 Tsi.

Table 2.1

Specimen Identifi- cation	% C Max.	% Si Max.	% Mn Max.	% S Max.	% P Max.	Tensile Strength Tsi (Min)	Elongation % Min.
fig.2.27	0.22	0.15	0.55	0.035	0.026	30	36
fig.2.28	0.11	0.20	0.47	0.045	0.036	27	37
En 3A	0.25	0.35	0.90	0.05	0.06	28	25
fig.2.29	0.11	0.14	0.59	0.03	0.025	38	20
fig.2.30	0.16	0.18	0.79	0.027	0.027	34	22
En 3B	0.25	0.35	1.00	0.06	0.06	28	17

Specimen Material was supplied to B.S. 970; 1955.  
 Tabulated specimen properties are averages from  
 3 specimens chosen at random.

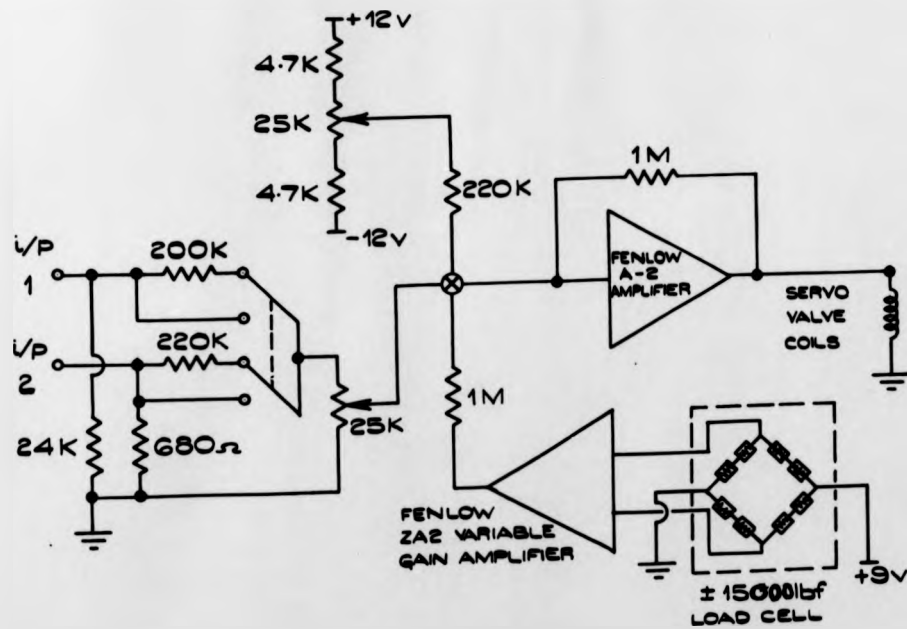
Table 2.2



Fig. 2.1.

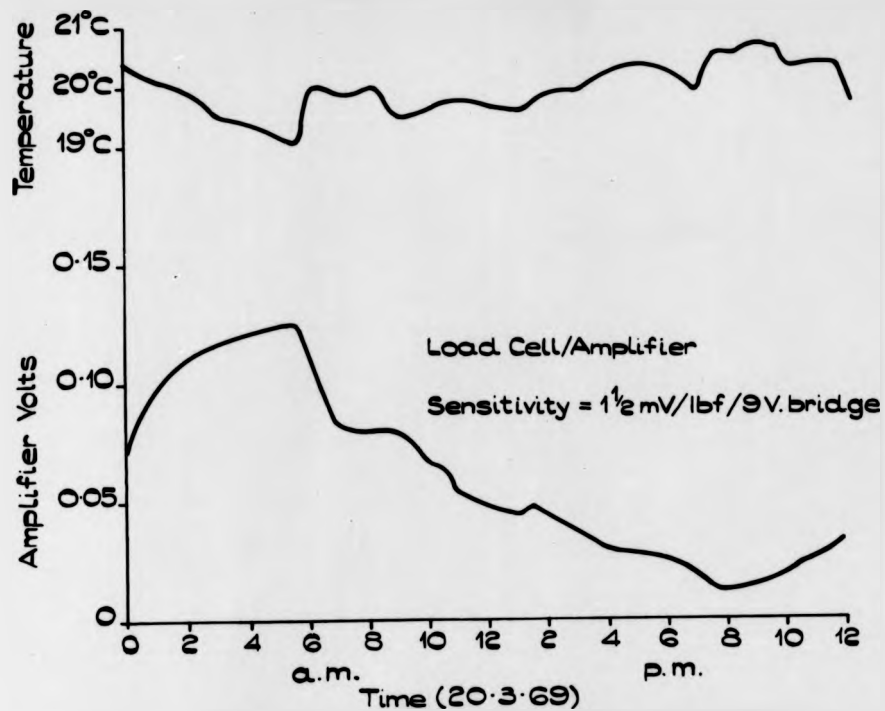


FIG. 2.2.

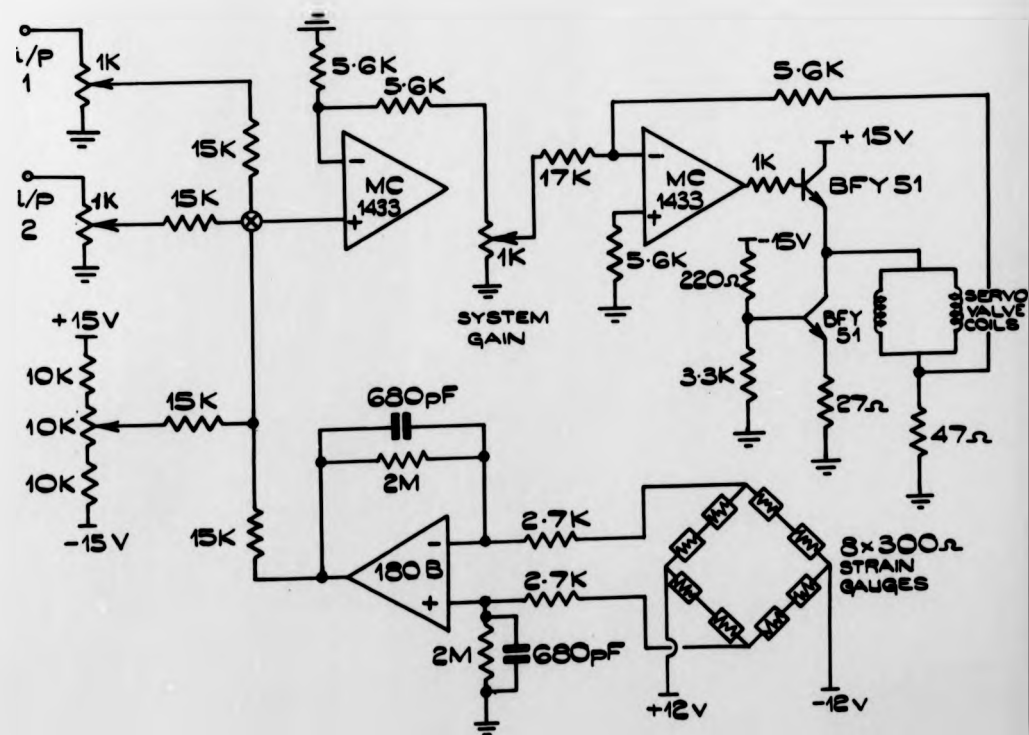


ORIGINAL ELECTRONIC CONTROL MODULE CIRCUIT.

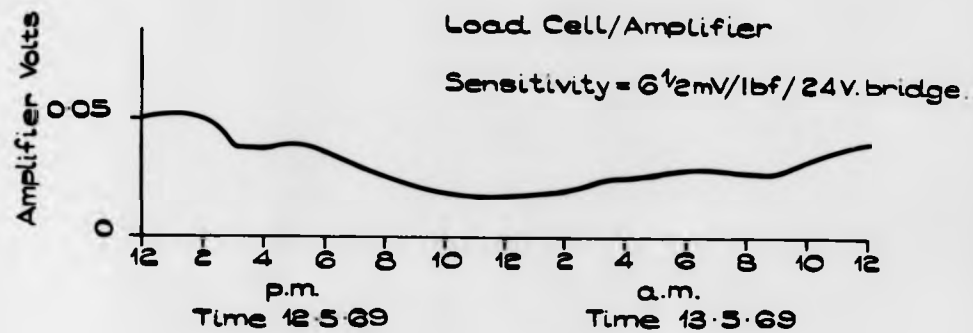
FIG. 2.3.



LOAD CELL/AMPLIFIER VOLTAGE DRIFT  
FIG. 2.4.

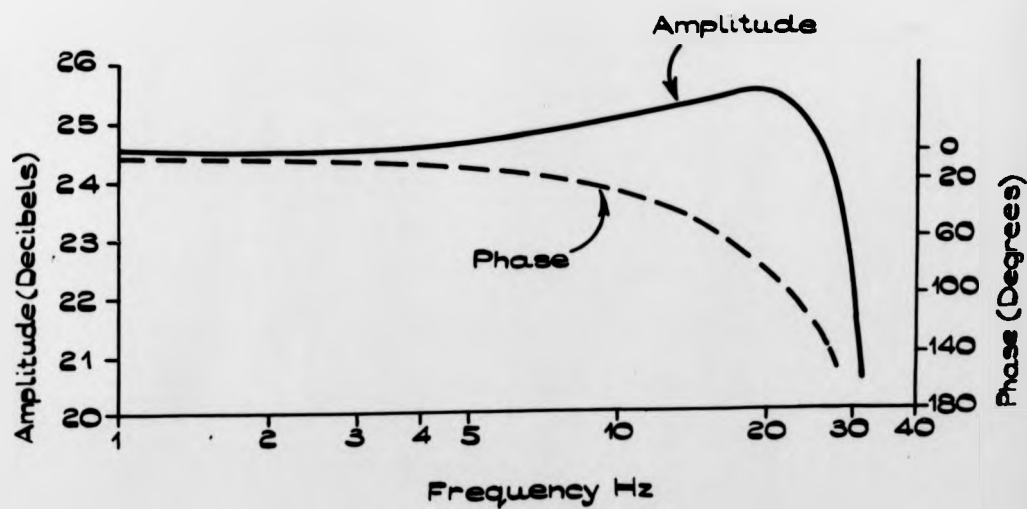


REDESIGNED ELECTRONIC CONTROL MODULE CIRCUIT.  
FIG. 2.5.



LOAD CELL / AMPLIFIER VOLTAGE DRIFT.

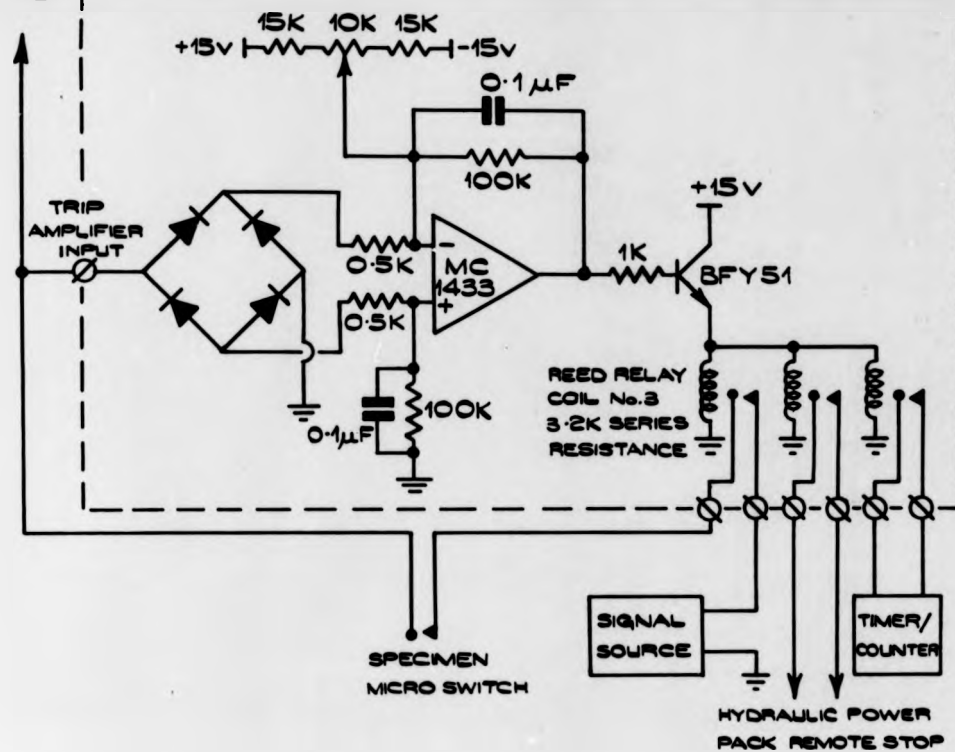
FIG. 2.6.



CLOSED LOOP FREQUENCY RESPONSE.

FIG. 2.7.

COMMAND SIGNAL  
TO CONTROL  
MODULE



SPECIMEN FAILURE TRIP CIRCUIT.

FIG. 2.8.

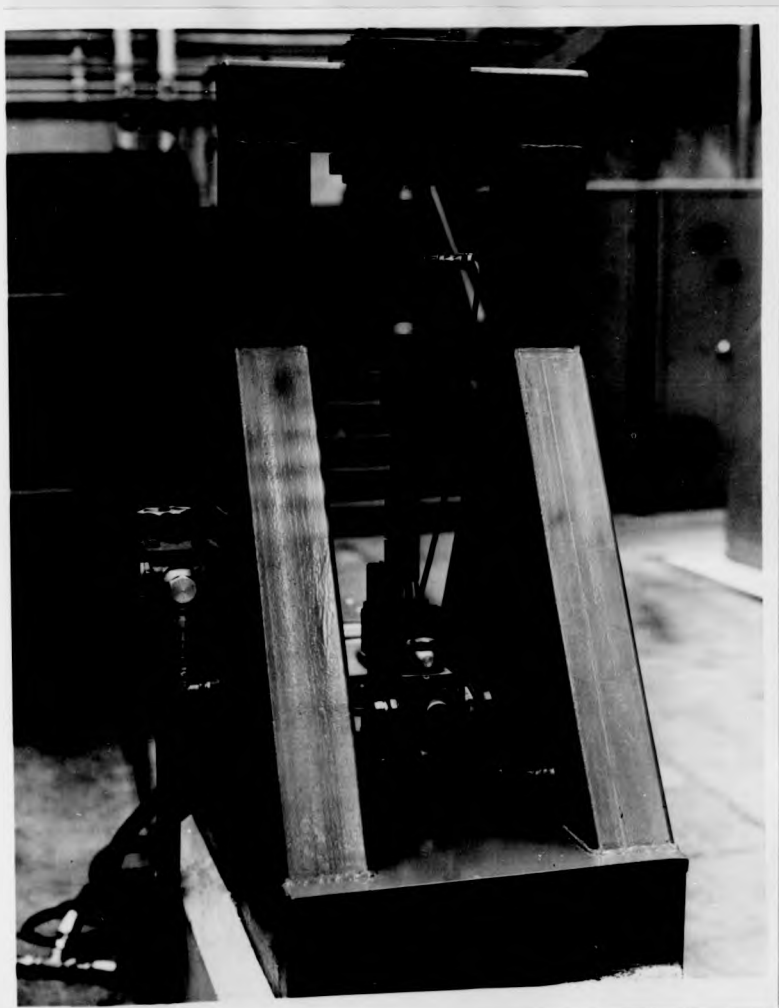


FIG. 2.9.

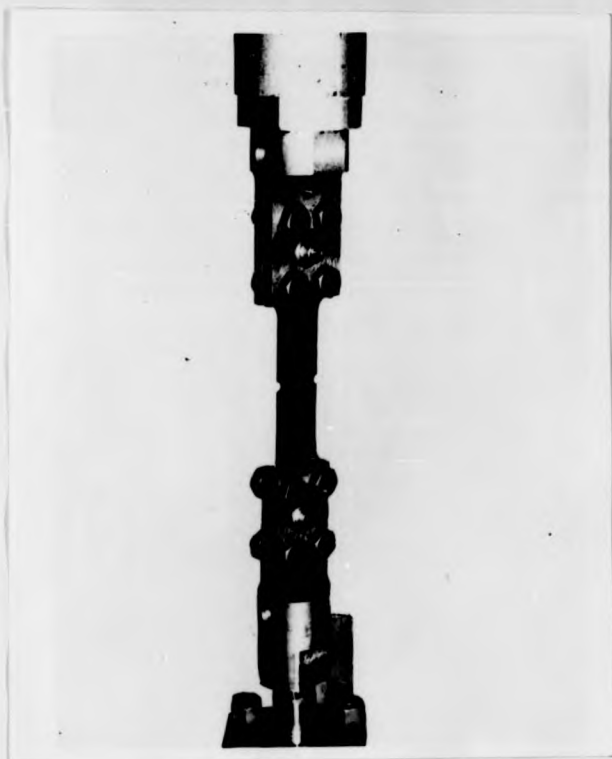
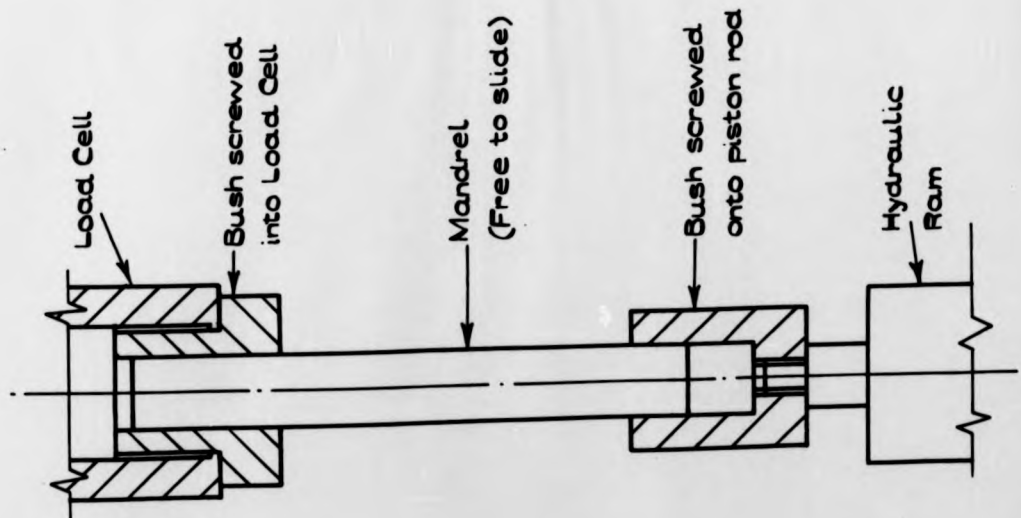
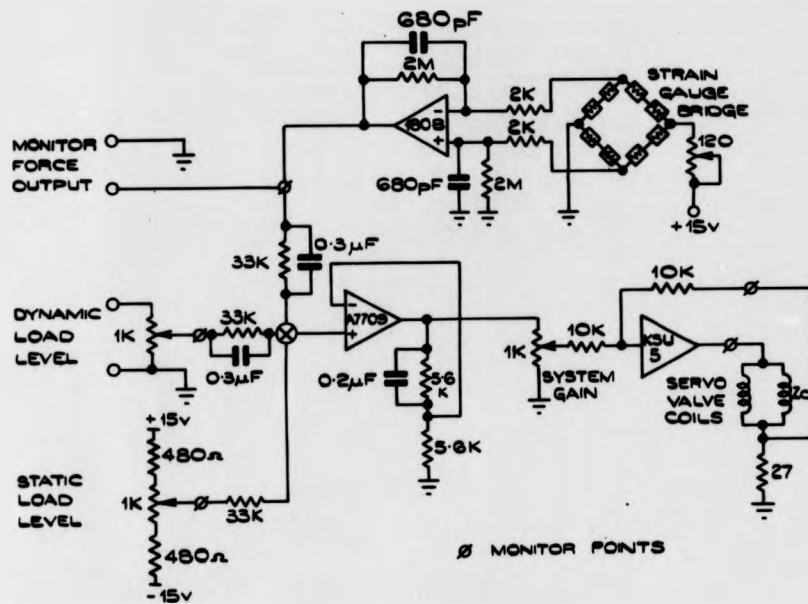


FIG. 2.10.



TEST RIG ALIGNMENT PROCEDURE

FIG. 2.11.



ELECTRONIC CONTROL MODULE CIRCUIT

FIG. 2.12.

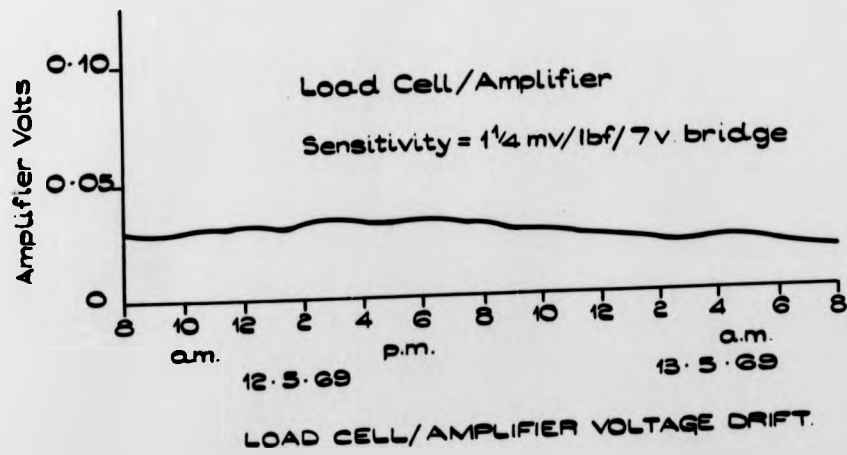
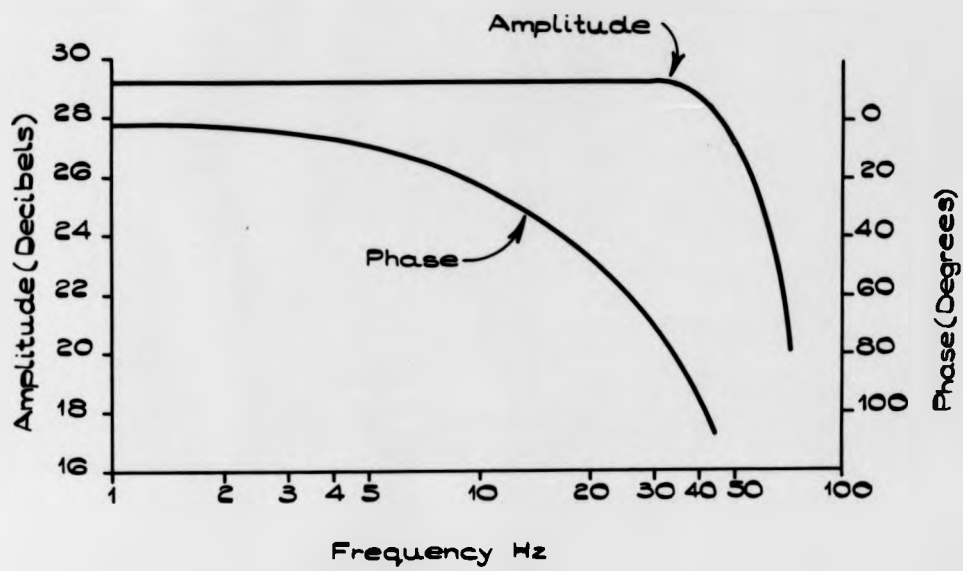


FIG. 2.13.



CLOSED LOOP FREQUENCY RESPONSE.

FIG. 2.14.

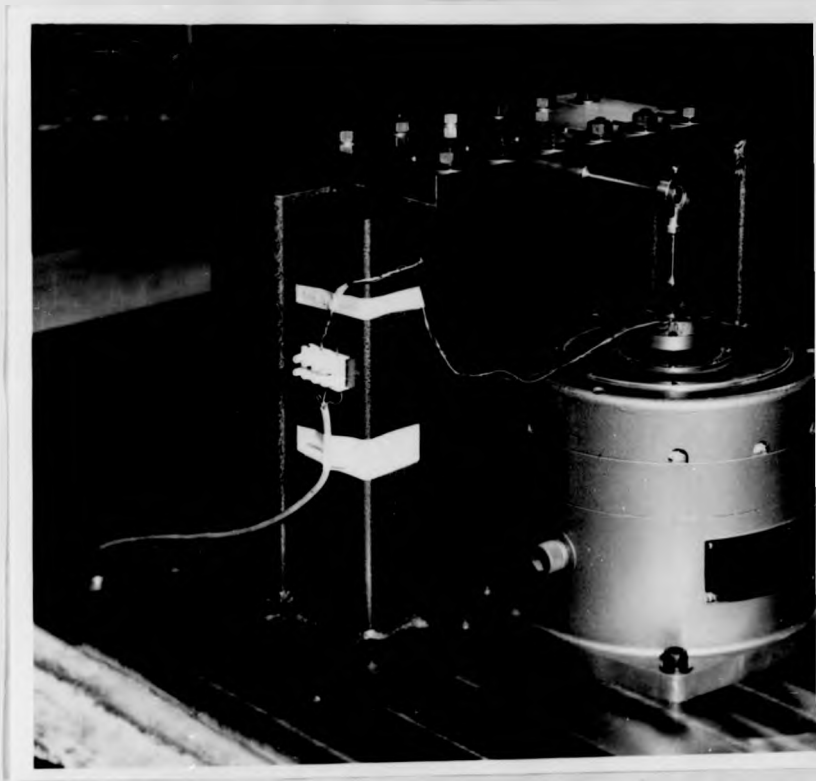
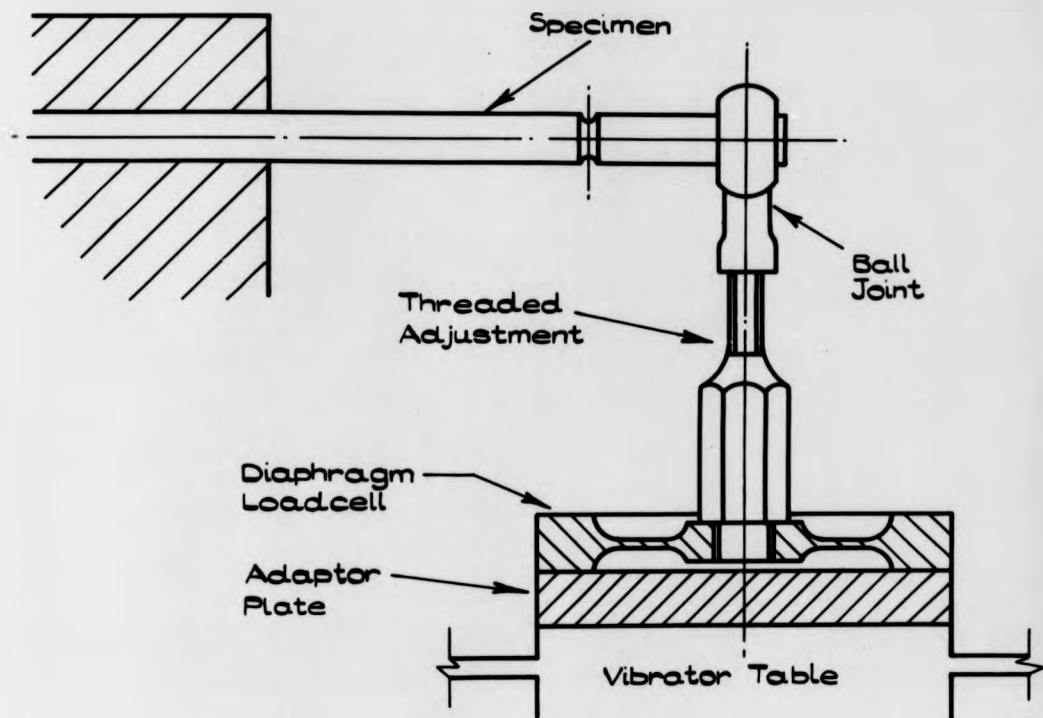
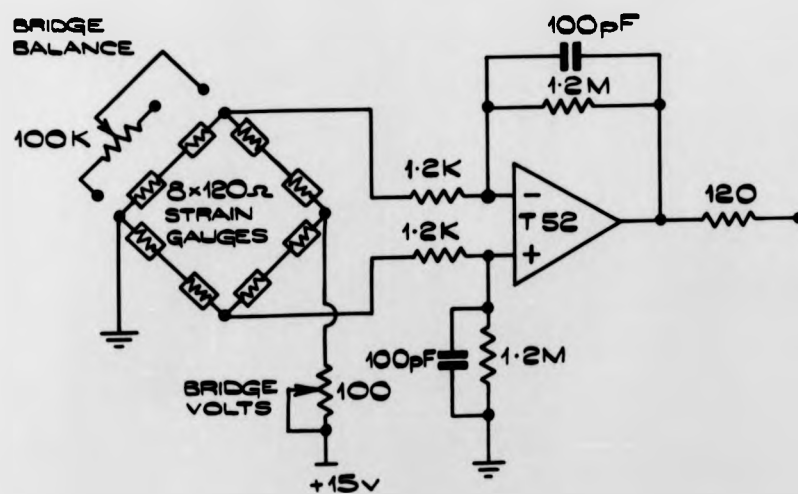


FIG. 2.15.



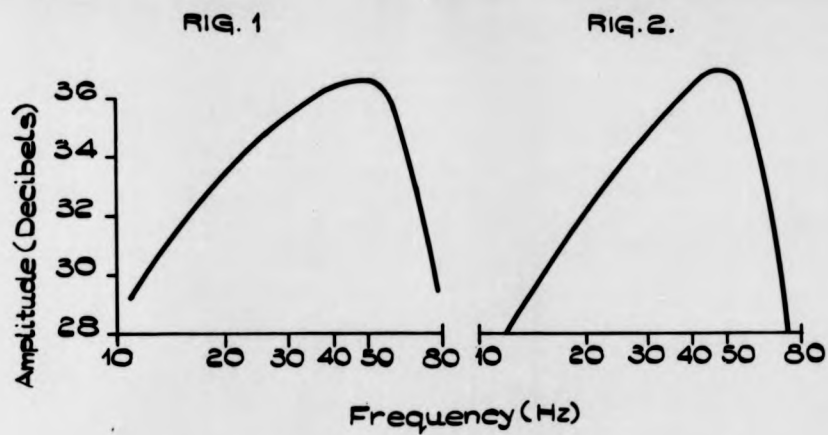
SPECIMEN MOUNTING AND DRIVE DETAILS.

FIG. 2.16.



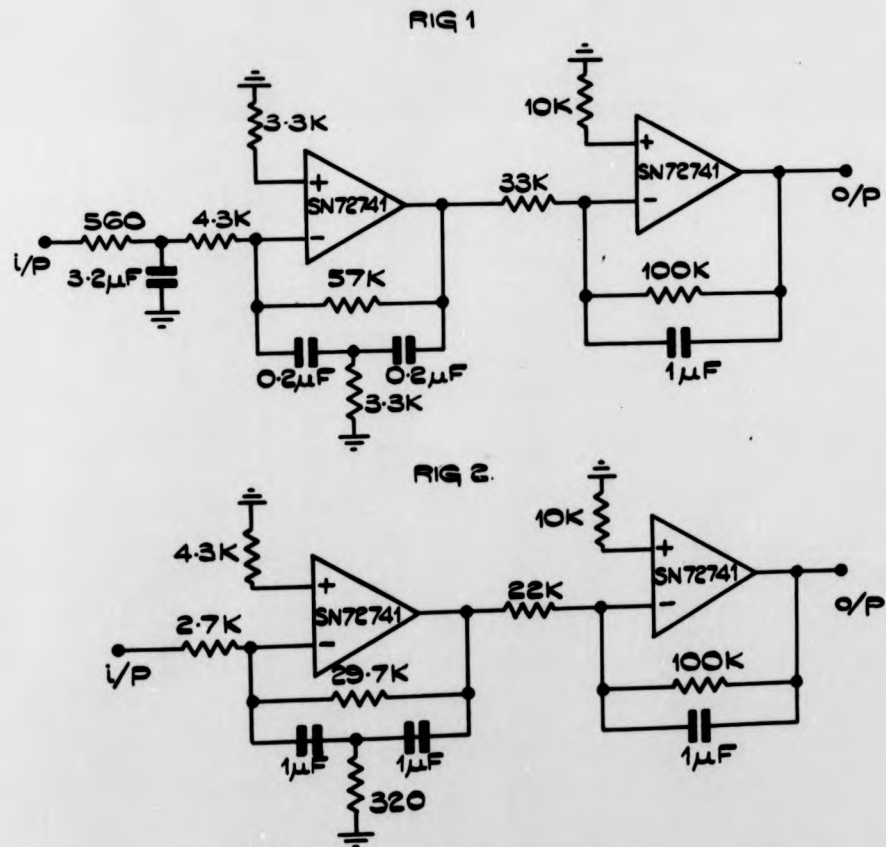
LOAD CELL AMPLIFIER CIRCUIT.

FIG. 2.17.



OPEN LOOP FREQUENCY RESPONSE.

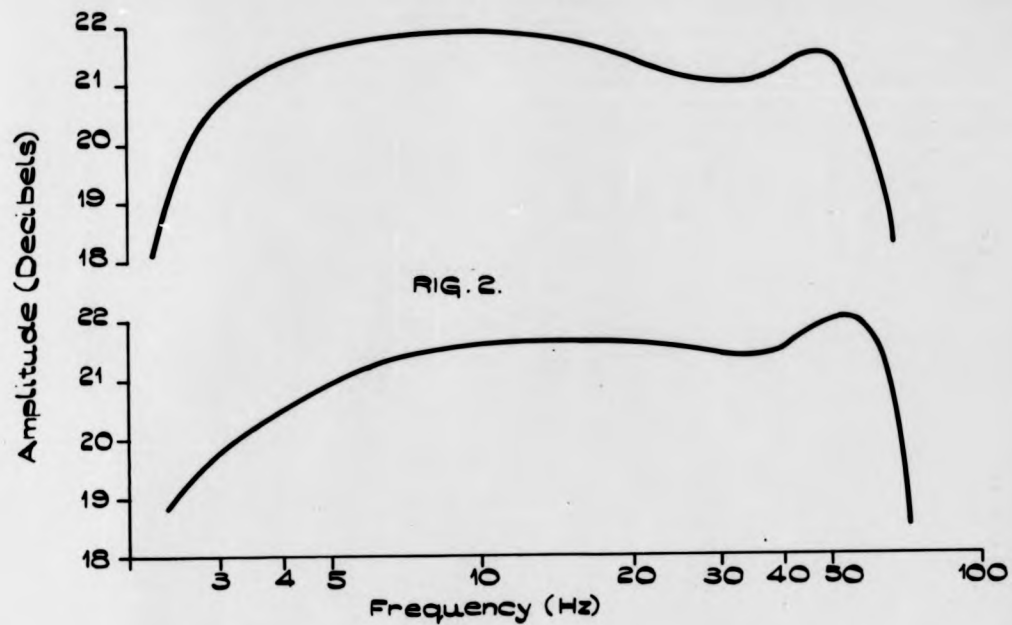
FIG. 2.18.



FREQUENCY RESPONSE MODIFYING NETWORKS

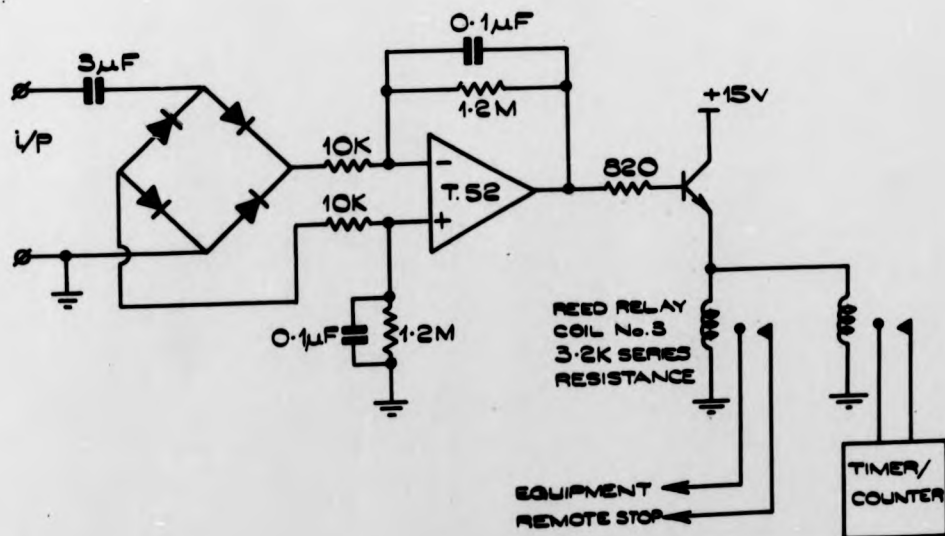
FIG. 2.19.

FIG 1.



MODIFIED OPEN LOOP FREQUENCY RESPONSE.

FIG. 2.20.



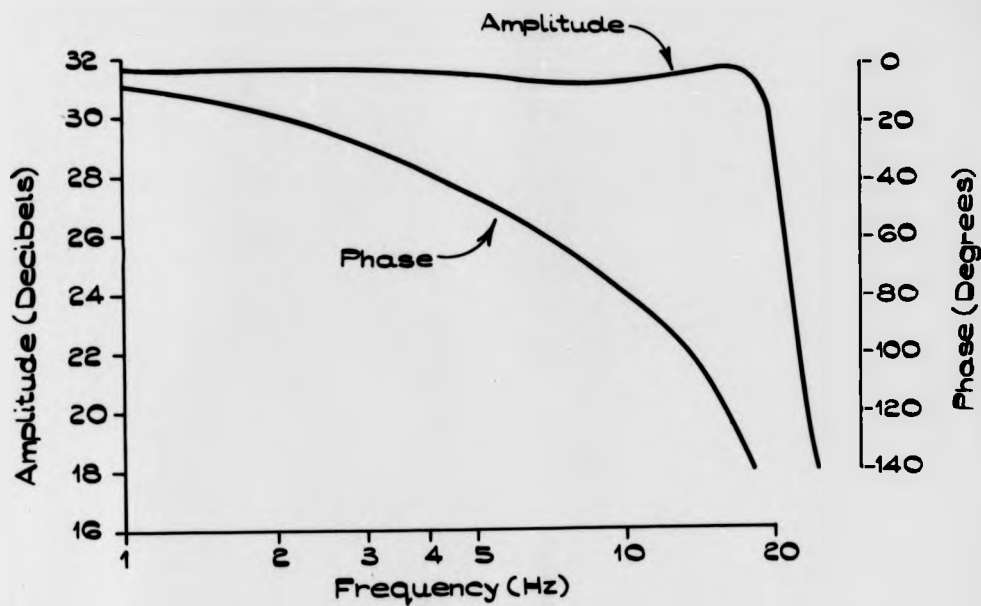
SPECIMEN FAILURE TRIP CIRCUIT

FIG. 2.21.



FIG. 2.22.





CLOSED LOOP FREQUENCY RESPONSE

FIG. 2.25.

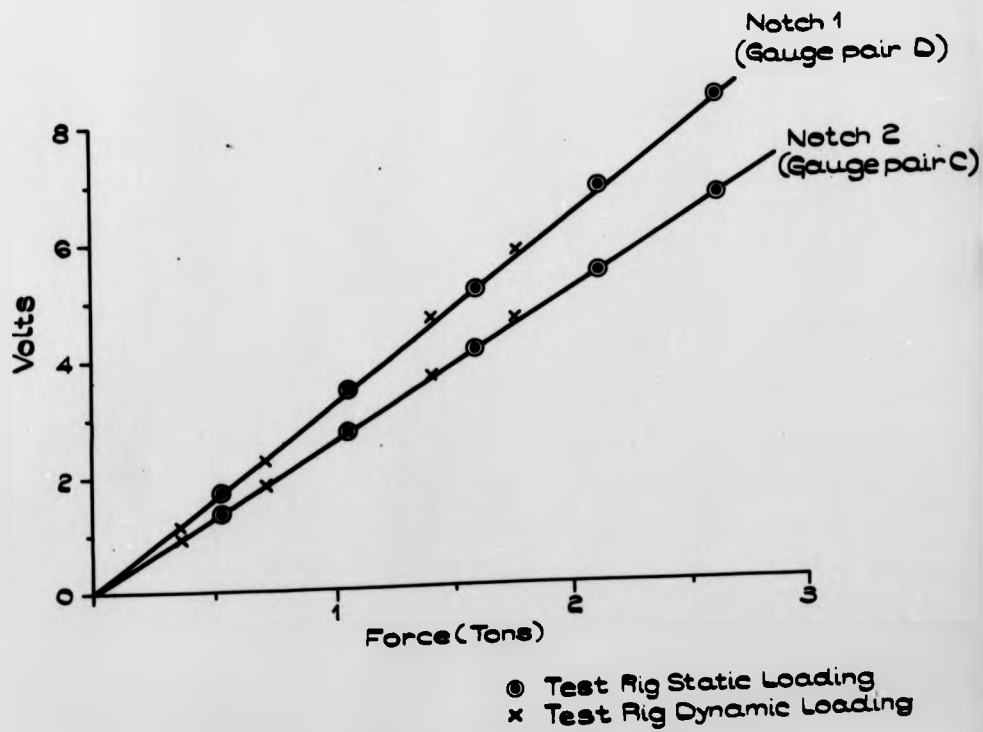
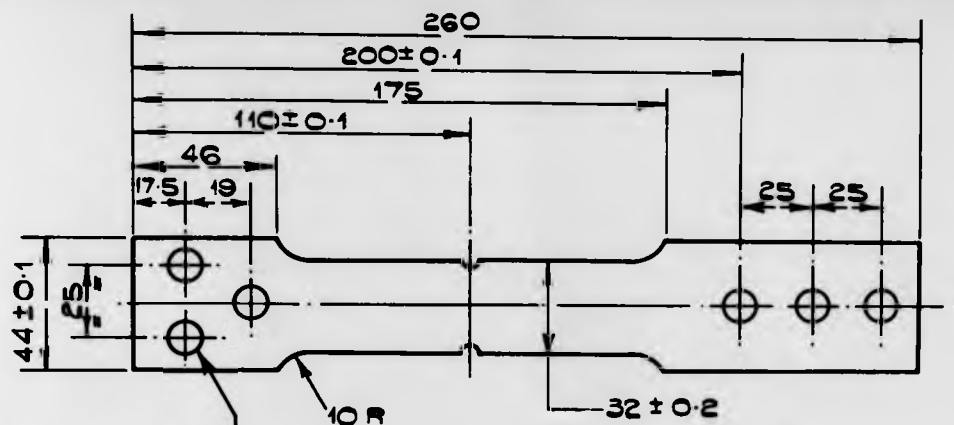
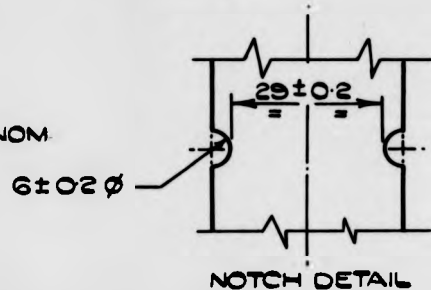


FIG. 2.26.

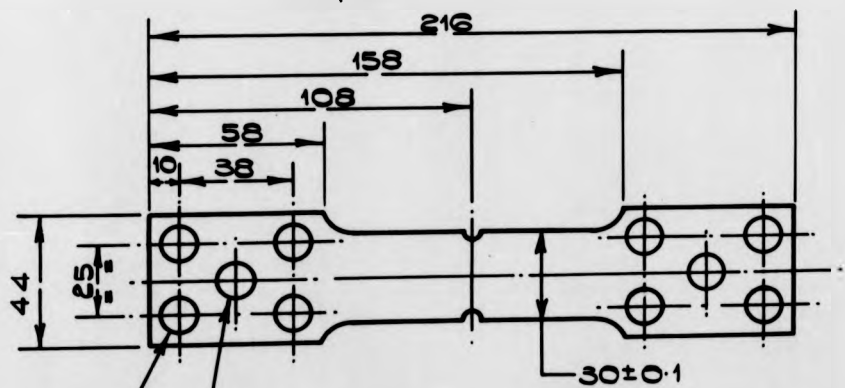


6 HOLES  
10.5  $\phi$  CLEARANCE

AS ROLLED THICKNESS = 0.25" NOM.  
 $K_t = 1.94$   
DIMS. IN MM.

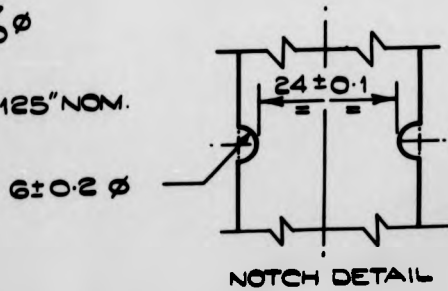


CANTILEVER SPECIMEN  
FIG. 2.27

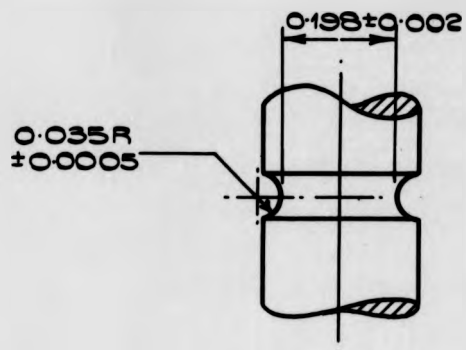
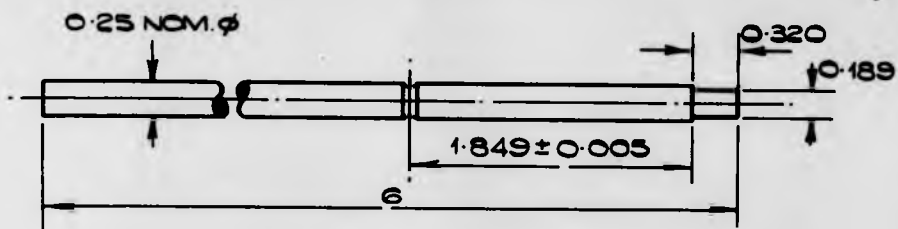


4 HOLES  
10.5  $\phi$  CLEARANCE  
12.027  $\phi$   
12.000  $\phi$

AS ROLLED THICKNESS = 0.125" NOM.  
 $K_t = 2.26$   
DIMS. IN MM.

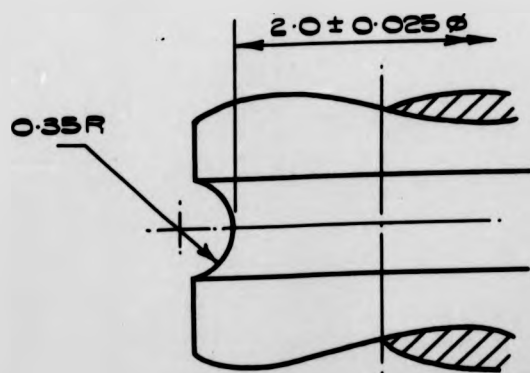
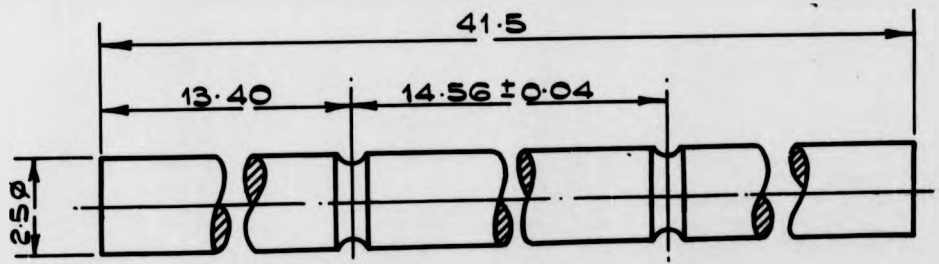


AXIAL SPECIMEN  
FIG. 2.28



$K_t = 1.593$   
DIMS. IN INS.

CANTILEVER BENDING SPECIMEN  
FIG. 2.29.



$K_t = 1.593$   
DIMS. IN IN.

3PT. BENDING SPECIMEN  
FIG. 2.30



FIG. 2.31.

C H A P T E R 6

MEASUREMENT & ANALYSIS OF RANDOM SIGNALS

1.	INTRODUCTION	62
2.	DIGITAL ANALYSIS OF DATA	64
3.	MEAN SQUARE VALUE (VARIANCE)	65
4.	AMPLITUDE PROBABILITY DENSITY FUNCTION	67
5.	POWER SPECTRAL DENSITY FUNCTION	71
6.	STATISTICAL FUNCTIONS RELEVANT TO FATIGUE	74

## MEASUREMENT & ANALYSIS OF RANDOM SIGNALS

### 1. INTRODUCTION

Metal fatigue is a process by which dynamic loading weakens and eventually breaks a component. The dynamic loading can be described by deterministic or random time varying stress data. Deterministic data can be represented by explicit mathematical relationships, whereas random data must be described in terms of probability statements and mathematical averages.

The majority of fatigue test data has been collected under sinusoidal stress-time varying loading in the form of stress amplitude - cycles to failure curves or S/N curves. This data can be used straightforwardly for the design of components receiving predominately such a loading, e.g. rotary machines. The stress history is deterministic and mathematically defined by the stress amplitude and loading frequency. All the signal power exists at one frequency. The stress amplitude describes the intensity of the fatigue loading and is the significant fatigue parameter.

In practice, however, many fatigue producing stress histories exist as random phenomena, e.g. noise from jet and rocket engines, buffeting forces on aircraft at gust wind velocities, motor vehicle suspension vibration and acoustic pressure in nuclear power station cooling gas circulators. These random processes may be further classified as stationary or non-stationary. A signal is non-stationary when the time averaged statistical properties vary throughout an ensemble of <sup>sample records.</sup>  $\lambda$  For example, non-stationary vehicle suspension vibration is caused by overall variations in road roughness and vehicle speed. Stationary random data is described as being ergodic or non-ergodic. The time

averaged statistical properties of an ergodic signal computed from a **continuous** sample record are the same as **the ensemble averaged properties**. In actual practice, random data representing stationary physical phenomena are generally ergodic. In addition, it is often justifiable to further classify this data as conforming to the Gaussian amplitude probability density distribution. It is this form of random signal which is considered here.

Statistical functions are used to define the basic properties of random data. They can also provide relevant fatigue characteristics. Apart from the intensity of the loading itself, parameters which can be associated with the overall physical raggedness of the signal have relevance to the fatigue data reduction process. These parameters include signal level crossings, maxima and minima, and rise and fall heights. The basic signal properties are described by mean square values, amplitude probability functions and power spectral density functions. The mean square value provides the description of loading intensity, the probability density function provides information in the amplitude domain, and the power spectral density function describes the distribution of power in the frequency domain.

The measurement and analysis of random data can be achieved by analog or digital methods. Digital analysis was carried out for the work reported here. Extensive reference has been made to the work by Bendat and Piersol (46), although the intention has not been to make a rigorous mathematical approach to the subject. For certain aspects of fatigue work it is only necessary to achieve what is essentially a qualitative description of the random process.

## 2. DIGITAL ANALYSIS OF DATA

Digitizing converts a continuous random signal to a set of discrete random data so that basic statistical calculations can be carried out in digital form over the time interval of the record. A set of data which represents a random signal time history in this form is called a discrete sample record.

Sampling defines the points at which data values are determined. Enough points are required to describe the signal properly over its entire frequency range without sampling at points which are too close, which would give correlated and highly redundant data. But if sample points are too far apart, these points could represent either low or high frequency elements of the data. This is called aliasing and the sampling rate should be chosen so that aliasing errors are avoided.

If the time interval between samples is  $h$  seconds, the sampling rate is  $\frac{1}{h}$  samples per second. Useful data will lie from 0 to  $\frac{1}{2h}$  Hz. and any data at frequencies which are higher than  $\frac{1}{2h}$  Hz. is folded into and confused with data in this frequency range. Therefore,  $h$  is chosen such that it is physically unreasonable for data to exist above  $\frac{1}{2h}$  Hz. The frequency:-

$$f_c = \frac{1}{2h} \quad (3.1)$$

is called the Nyquist frequency.

Analog-to-digital conversion of the random signal also involves defining the sampled values numerically. Round off errors are incurred which depend on the bit length of the A - D converter register. This operation is called quantization and the round off error is referred to as quantization noise. Signals considered here were quantized

over an input range of 2046 scale units, corresponding to a rounding off of approximately 10mV. on a  $\pm 10V.$  input range. For the purpose of analysis, signal rms. values were of the order of  $1\frac{1}{2}/2$  volts, and thus it was considered that quantization errors in voltage measurements were negligible.

Achieved test specimen stress histories were sampled and some statistical analysis was carried out on line. The computer used was the School's S.D.S. 90-2 which has 8K of 12 bit core store and is linked to a fast A - D converter. For fatigue work the A - D converter was locked to one input channel so that the maximum sampling rate of 50 KHz could be used. The converter represented the sampled value as 10 binary digits plus sign in twos-complement form. All programming was carried out in Symbol at assembler level, and three programs were written which were used by the author. One program was written by J. Monk, formerly of the School, which sampled an incoming signal at a rate selected as an integer number of 1 msec. intervals with a maximum of 8000 samples. Dr. F. Sherratt provided a program which analysed a waveform into a joint peak/trough probability density distribution and P. Wellstead wrote a program which performed on-line power spectral density analysis. Subsequent data processing was then carried out using the University's ICL 4130 computer with Algol programming.

### 3. MEAN SQUARE VALUE (VARIANCE)

The general intensity of a random time history  $x(t)$  is described by the mean square value  $\psi_x^2$ , which is the average of the squared values of the time history.

$$\psi_x^2 = \lim_{T \rightarrow \infty} \frac{1}{T} \int_0^T x^2(t) dt$$

The root mean square or rms. value is the square root of the mean square value.

When a signal combines a dynamic component about a static or time-invariant component, the static component is described by a mean value  $\mu_x$  which is the average of all values of the time history.

$$\mu_x = \lim_{T \rightarrow \infty} \frac{1}{T} \int_0^T x(t) dt$$

The signal variance  $\sigma_x^2$  describes the signal dynamic component and is the mean square value about the mean.

$$\sigma_x^2 = \lim_{T \rightarrow \infty} \frac{1}{T} \int_0^T [x(t) - \mu_x]^2 dt$$

The standard deviation is the square root of the variance. The variance, mean and mean square values are related by:-

$$\sigma_x^2 = \psi_x^2 - \mu_x^2$$

For a random signal represented by a discrete sample record of N independent data samples, an unbiased estimate of the sample true mean value is given by:-

$$\bar{x} = \frac{1}{N} \sum_{i=1}^N (x_i) \quad (3.2)$$

The normalised standard error of this measurement is  $\frac{1}{\sqrt{N}}$

Transforming data to zero mean value simplifies digital calculations, so that an unbiased estimate of the variance is then given by:-

$$\hat{\sigma}_x^2 = \frac{1}{N-1} \sum_{i=1}^N (x_i)^2 \quad (3.3)$$

The normalised standard error of this measurement is  $\frac{2}{\sqrt{N}}$

$$\psi_x^2 = \lim_{T \rightarrow \infty} \frac{1}{T} \int_0^T x^2(t) dt$$

The root mean square or rms. value is the square root of the mean square value.

When a signal combines a dynamic component about a static or time-invariant component, the static component is described by a mean value  $\mu_x$  which is the average of all values of the time history.

$$\mu_x = \lim_{T \rightarrow \infty} \frac{1}{T} \int_0^{\infty} x(t) dt$$

The signal variance  $\sigma_x^2$  describes the signal dynamic component and is the mean square value about the mean.

$$\sigma_x^2 = \lim_{T \rightarrow \infty} \frac{1}{T} \int_0^T [x(t) - \mu_x]^2 dt$$

The standard deviation is the square root of the variance. The variance, mean and mean square values are related by:-

$$\sigma_x^2 = \psi_x^2 - \mu_x^2$$

For a random signal represented by a discrete sample record of N independent data samples, an unbiased estimate of the sample true mean value is given by:-

$$\bar{x} = \frac{1}{N} \sum_{i=1}^N (x_i) \quad (3.2)$$

The normalised standard error of this measurement is  $\frac{1}{\sqrt{N}}$

Transforming data to zero mean value simplifies digital calculations, so that an unbiased estimate of the variance is then given by:-

$$\hat{\sigma}_x^2 = \frac{1}{N-1} \sum_{i=1}^N (x_i)^2 \quad (3.3)$$

The normalised standard error of this measurement is  $\frac{2}{\sqrt{N}}$

An unbiased estimate of the standard deviation,  $s$ , is given by the square root of  $\hat{\sigma}_x^2$ . It is also convenient to further transform the data to unit standard deviation, so that:-

$$Z_i = \frac{X_i}{s} \quad i = 1, 2, \dots, N \quad (3.4)$$

During fatigue testing the measurement of random signal test stress levels was made using the true averaging facility of a Solartron JM 1860 Time Domain Analyser. The exponential averaging technique normally used by rms. volt-meters often may be unsuitable for measuring random signals because the measurement output is then essentially independent of signal values which occurred more than about seven time constants in the past. This can be overcome by using long time constants but the accuracy of the result will always be influenced by an associated variance and, in practice, a compromise is necessary between measurement time and accuracy. The Time Domain Analyser enables a continuous measurement of the signal true average to be made, with a continued reduction in the associated variance. Instrument accuracy is  $\pm 1\%$  with a crest factor rating of 5 x full scale rms. reading. When D.C. coupled the dynamic range is 0 - 10 KHz, and is 3 Hz - 10 KHz with a 0.1 Hz. 3db frequency when A.C. coupled.

#### 4. AMPLITUDE PROBABILITY DENSITY FUNCTION

The amplitude probability density function describes the probability that the random signal will assume a particular value at any instant of time.

The probability that the random time history  $x(t)$  will fall within the range  $x$  and  $x + \Delta x$  is:-

$$\text{Prob } (x < x(t) \leq x + \Delta x) = \lim_{T \rightarrow \infty} \frac{\Delta x}{T}$$

where,

$\Delta x$  is the width of the amplitude window,

$T_x$  is the time spent by  $x(t)$  in  $\Delta x$ , and,

$T$  is the total observation time.

It is more convenient to describe probability density since probability depends upon the width of the amplitude window. Therefore:-

$$p(x) = \lim_{\Delta x \rightarrow 0} \frac{\text{Prob}(x < x(t) \leq x + \Delta x)}{\Delta x} = \lim_{\Delta x \rightarrow 0} \lim_{T \rightarrow \infty} \frac{1}{T} \left( \frac{T_x}{\Delta x} \right)$$

The amplitude probability density function  $p(x)$  is always real valued and non-negative. It is termed a first order probability density function because it does not depend on the behaviour of the random signal before (or after) passing through the amplitude window. If restrictions are made on the behaviour of the signal outside the amplitude window, the function becomes a higher order probability density function, e.g. the probability distribution of signal maxima.

The probability that  $x(t)$  takes a value which is less than or equal to a value  $x$  is determined from the cumulative probability distribution function  $P(x)$ :-

$$P(x) = \text{Prob}(x(t) \leq x) = \int_{-\infty}^x p(x) dx$$

The probability that  $x(t)$  takes a value within the range  $x_1$  to  $x_2$  is:-

$$P(x_2) - P(x_1) = \text{Prob}(x_1 < x(t) \leq x_2) = \int_{x_1}^{x_2} p(x) dx$$

The probability distribution function is bounded by zero and unity since the probability of  $x(t)$  being less than  $-\infty$  is zero, while the probability of  $x(t)$  being less than  $+\infty$  is unity.

The shape of the probability density curve is affected by the nature of the random process and the presence of any non linearities. The most well known probability density curve is obtained from a normal (Gaussian) random process giving the familiar bell shaped curve represented mathematically:-

$$p(z) = \frac{1}{\sqrt{2\pi}} \exp \left( -\frac{z^2}{2} \right) \quad (3.5)$$

where  $z(t)$  has unit standard deviation (standardised variable). The functions for the probability density and cumulative probability of a Gaussian random process are shown in fig. 3.1.

The mean and mean square values of  $x(t)$  can be presented in terms of the probability density function:-

$$\begin{aligned} \mu_x &= \int_{-\infty}^{+\infty} x p(x) dx \\ \psi_x^2 &= \int_{-\infty}^{+\infty} x^2 p(x) dx \end{aligned}$$

An estimate of the probability density function of a random signal can be obtained from a discrete sample record of standardised data by dividing the range of  $z$  into an appropriate number of equal width class intervals. The percentage of data in each class interval gives the probability density histogram. The goodness of fit of the observed data to the expected can then be tested using the chi-square distribution. Any deviation of the estimated probability density from the expected value will cause the sample chi-square value to increase and, therefore, a one-sided (upper tail) test is used. The power of the chi-square goodness-of-fit test is influenced by the choice of the number of class intervals. Table 3.1 shows the recommended minimum optimum number for tests carried out at the 5% level of significance (47). In order to obtain measurements which

do not have a significant bias error it is suggested that the width of the class interval should not be greater than  $0.2 \times$  signal rms. level (46).

The sample probability density function is not unique but determined by the end points of the class intervals and the number of class intervals. The end points should be chosen so that extreme class intervals contain a minimum of about four occurrences. Sample probability density estimates are made at the midpoints of each of the  $K$  class intervals and defined by:-

$$P_i = \frac{N_i}{N} \left( \frac{K}{Z_{\max} - Z_{\min}} \right) \quad (3.6)$$

where,

$$i = 1, 2 \dots K$$

$N_i$  = number in each class interval, and,

$Z_{\max}$  and  $Z_{\min}$  are chosen end points.

For normally distributed signals these results can then be compared with the Gaussian probability density function. The number of degrees of freedom of the chi-square test for normality is  $K-3$ . One degree of freedom is taken since the final class interval frequency is determined by the frequencies in the previous intervals, and two degrees of freedom are taken because the mean and standard deviation must be used to fit the Gaussian function.

The amplitude probability density distributions for achieved test specimen stress histories were analyzed on-line using a data logging program which digitized the waveform with a sampling period chosen as an integer multiple of 1 msec. intervals. Any number of samples up to 3,000 could be taken in one run and then output to paper tape. Subsequent analysis was carried out using an Algol program

which tested the data for goodness of fit to the Gaussian amplitude probability density distribution. The program output compared the expected class interval frequencies with the observed, plotted the sample probability density histogram and Gaussian curve, and computed the sample and actual chi-square values. The flow diagram for the program is shown in fig. 3.2.

### 5. POWER SPECTRAL DENSITY FUNCTION

The power spectral density function describes the general frequency composition of data in terms of the frequency density of its mean square value. It separates out the frequency composition of the data. The important property of the power spectral density function is its relation to the autocorrelation function.

The autocorrelation function describes the general dependence of values of the data at one time on the values at a future time. An estimate of the autocorrelation between values of  $x(t)$  at times  $t$  and  $t + \tau$  is given by:-

$$R_x(\tau) = \lim_{T \rightarrow \infty} \frac{1}{T} \int_0^T x(t) x(t + \tau) dt$$

where  $\tau$  is the lag time.  $R(\tau)$  is always real valued with a maximum at  $\tau = 0$ .

The autocorrelation function and power spectral density function form a fourier transform pair, so that a two sided power spectrum is defined as function of frequency  $f$  by:-

$$S_x(f) = \int_{-\infty}^{+\infty} R_x(\tau) \exp(-j2\pi f\tau) d\tau \quad (-\infty < f < \infty)$$

Physically realisable power spectra are one sided functions, and are related to two sided functions:-

$$G_x(f) = 2 S_x(f) \quad (0 \leq f < \infty)$$

The power spectrum is a real positive function of frequency. The static mean value of a signal appears in its power spectral density function as a Dirac delta function at zero frequency. Thus, for power spectral measurements the signal mean level has to be removed. The variance of  $x(t)$  with zero mean is given by:-

$$\sigma_x^2 = \int_0^{\infty} G_x(f) df$$

Hence, the variance is equal to the total area under the power spectral density - frequency curve.

Initially, it was intended to estimate signal power spectral density functions by fourier transformation of their autocorrelation function, and a computer program was developed accordingly. Signals were analysed on-line using the previously mentioned data logging program to provide punched paper tape data for analysis by an Algol program. This program calculated mean, mean square and discrete power spectral density estimates. The fundamental formulae of the analysis and the flow diagram for the program are presented in Appendix B.

The disadvantage of the autocorrelation function/discrete fourier transform method of p.s.d. calculation is the large amount of required computing time. In 1965 Cooley and Tukey (48) reported an algorithm which makes significant computational savings, and it is widely known as the Fast Fourier Transform. It is usual to choose  $N$ , the number of points in the discrete sample record, as an integer power of two. The f.f.t. algorithm is then called the radix-2 algorithm, and the d.f.t. requires approximately  $N^2$  operations (operation meaning complex multiplication) compared with the  $N \log_2 N$  for the f.f.t. The saving in computational

effort is shown in fig. 3.3, from reference 49, where the ratio of the d.f.t. operations to f.f.t. operations rises sharply as the number of sampled points increases.

Shortly before fatigue testing began a computer program using the f.f.t. algorithm was developed in the School and which enabled on-line power spectral density measurement (44). Therefore, all p.s.d. analysis reported here was carried out using this program. The program uses the radix-2 decimation-in-time algorithm and can take a maximum number of points,  $N$ , in each discrete sample record of 256 ( $= 2^8$ ). Stress histories are sampled at a frequency determined by a square wave signal generator, and the useful frequency range of the program extends from D.C. to approximately 500 Hz. The sampled data are read into an input array of size  $N$  and transferred to a working array to compute the power spectral density estimate. This estimate is added to an accumulator array and the average of the accumulated spectral estimates is then displayed on an oscilloscope screen. This process is repeated and can be terminated when the shape of the displayed p.s.d. estimate is stable. The variance of the final estimate depends on the number of estimates averaged. The program described here can average 8192 independent estimates without overflow. Subsequent analysis of the accumulated spectrum can then be made off-line from a punched paper tape record.

Stress histories were analysed using the program set to read data blocks of 256 points. The facility for D.C. suppression, whereby the sample mean is calculated and subtracted from the working array, was always used. The additional program facilities of linear modification of data and further spectrum smoothing by Hanning were not used.

## 6. STATISTICAL FUNCTIONS RELEVANT TO FATIGUE

At present no statistical function can be applied universally to quantitative estimates of fatigue damage under random loading. In a qualitative sense, though, it is certain that overall raggedness of the signal waveform is significant. In this respect, differences between waveforms are described by the differences in occurrence of signal peaks (or troughs since these form a complementary distribution), the differences in occurrence of signal rises and falls (or "half cycles"), and the way in which these are related within the signal to the overall mean level. With Gaussian signals these "waveform" effects can be related to the power spectral density function and, thus, power spectrum shape becomes prominent in fatigue damage analysis, suggesting frequency as a significant variable. But this is not borne out by constant amplitude testing which proves frequency effects to be secondary.

Rice et al (41) present rise and fall distributions as the significant fatigue parameter, whereas Bendat (50) is more concerned with the prediction of peak probability density functions in an analysis of the fatigue damaging effect of a random signal. Both references contain important equations and these are presented in this section.

The occurrence of crossings at a signal level  $x$ , for Gaussian signals, is given by:-

$$N_x = \frac{1}{\pi} \sqrt{\frac{-R''(0)}{R(0)}} \exp\left(\frac{-x^2}{2R(0)}\right)$$

This can be applied to the case of signal zero crossings:-

$$N_0 = \frac{1}{\pi} \sqrt{\frac{-R''(0)}{R(0)}}$$

which, since there are as many positive going zero crossings

as negative going, can be rewritten to give positive crossings:-

$$N_0^+ = \frac{1}{2\pi} \sqrt{\frac{-R''(0)}{R(0)}}$$

The expected number of signal peaks in a Gaussian process is given by:-

$$N_p = \frac{1}{\pi} \sqrt{\frac{R^4(0)}{-R''(0)}}$$

where,

$$R(0) = \int_0^\infty G_x(f) df = \sigma_x^2$$

$$-R''(0) = \int_0^\infty (2\pi f)^2 G_x(f) df = \text{2nd moment of power spectrum}$$

$$R^4(0) = \int_0^\infty (2\pi f)^4 G_x(f) df = \text{4th moment of power spectrum}$$

The probability of the occurrence of signal peaks (or maxima) can be established from the ratio of the expected number of zero crossings per unit time to the expected number of peaks per unit time. The general form of the peak probability density function for Gaussian signals is something between a Rayleigh and Gaussian curve. A series of these curves is shown in fig. 3.4 whose shapes are determined by the irregularity factor:-

$$F = \frac{N_0^+}{N_p} = \frac{N_0}{2 \cdot N_p} \quad (3.18)$$

In terms of a standardised variable, the peak probability density function is defined by:-

$$p(z) = \frac{K_1}{\sqrt{2\pi}} \exp\left(\frac{-z^2}{2K_1^2}\right) + Fz \exp\left(\frac{-z^2}{2}\right) \left[1 - P_n\left(\frac{z}{K_2}\right)\right] \quad (3.19)$$

where,

$$K_1 = \sqrt{1 - F^2} \quad (3.20)$$

$$K_2 = \frac{K_1}{F} \quad (3.21)$$

and,

$$P_n \left( \frac{z}{K_2} \right) = \frac{1}{\sqrt{2\pi}} \int_{\frac{z}{K_2}}^{\infty} \exp \left( -\frac{y^2}{2} \right) dy \quad (3.22)$$

$P_n \left( \frac{z}{K_2} \right)$  is the probability for a standard normal distribution with zero mean and unit variance that the value  $(z/K_2)$  will be exceeded.

When  $F$  is zero  $p(z)$  reduces to the standardised Gaussian probability density function:-

$$p(z) = \frac{1}{\sqrt{2\pi}} \exp \left( -\frac{z^2}{2} \right) \quad (3.23)$$

which is the case for wideband noise where the expected number of maxima is much larger than the expected number of zero crossings. When  $F$  is unity  $p(z)$  becomes a standardised Rayleigh probability density function:-

$$p(z) = z \exp \left( -\frac{z^2}{2} \right) \quad (3.24)$$

which is the case for narrow band noise where the expected number of peaks (or troughs) is equal to the expected number of positive zero crossings.

The probability that a peak chosen at random will be greater than some value  $z$  can be expressed in terms of  $p(z)$ :-

$$\begin{aligned} P(z) &= \int_z^{\infty} p(z) dz \\ &= P_n \left( \frac{z}{K_1} \right) + F \exp \left( -\frac{z^2}{2} \right) \left[ 1 - P_n \left( \frac{z}{K_2} \right) \right] \end{aligned} \quad (3.25)$$

where  $P_n \left( \frac{z}{K_1} \right)$  and  $P_n \left( \frac{z}{K_2} \right)$  are as previously defined.

Interpreting a random signal as a distribution of rises and falls or ranges is useful in that each range can be equated to half of a sine wave cycle. This presents the random signal as a collection of constant amplitude stress cycles which can be associated with constant amplitude design data for life calculations. If the signal has a Rayleigh

distribution of peaks, with one peak for each zero crossing, a single load cycle is simply identifiable. But general theoretical solutions for rise and fall distributions in a continuous random process are not as readily available as peak distributions, although the average height of the rises and falls in a Gaussian signal is straightforward to determine (41):-

$$\bar{h} = -R''(0) \sqrt{\frac{2\pi}{R^4(0)}}$$

This parameter has been shown to have particular relevance to the crack propagation phase of the fatigue damage process.

The statistical parameters derived from power spectral density functions will be significantly in error if the power spectra are not accurately defined. Accurate definition cannot always be readily achieved and, even so, meaningful cumulative damage calculations are difficult if parameters do not give recourse to the signal waveform. Generally direct measurements of signal data have to be introduced and the most commonly encountered recording methods are chart traces of waveforms and level crossing meters. Some level crossing meters do not retain all signal information, and there is the disadvantage of instrument inflexibility. High measurement errors can result from data extracted from chart recordings and the subsequent analysis of large quantities of data is tedious unless done by computer. It therefore becomes attractive to use on-line digital analysis and to process signals so that fatigue information is retained. One compact way of doing this is to specify the joint probability density of peak/trough pairs (36).

In the realisation of the random waveform in fig. 3.5 the excursion from the peak at A to the trough at B may be

regarded as a half cycle of load. Other peaks will occur at level A at different times but will generally be followed by troughs at different levels to B, e.g.  $A_2 - B_2$ . The total probability of peaks occurring at level A can therefore be subdivided into those associated with a subsequent trough B, and those associated with a trough  $B_2$ . Similarly, the ascending half cycle C -  $A_2$  will contribute to the probability count, although no distinction is made by the computer program, described in reference 36, between "rises" or "falls".

It is important to note, though, that basing fatigue data capture on signal rise and fall heights can, in some cases, lead to substantially incorrect results if applied without judgement. For example, for a loading waveform of a sine wave carrying an extremely small amplitude high frequency component, it would be expected that the fatigue life would be essentially the same as for the sine wave alone. But the distribution of rises and falls would be markedly changed for, in place of a relatively large rise and fall, there would now be a series of rises and falls.

The way in which a joint probability plot of peaks and troughs is built up can be visualised from fig. 3.6. The data is presented with increments of peak value on the y-axis, and of trough value on the x-axis. In choosing x and y intervals, the x-y plane is effectively divided into a series of squares and each square represents a range or half cycle of load with specified peak and trough values. The length of the z ordinate erected on this square is then a measure of the number of times this half cycle occurs in either a specified time or in a specified total number of half-cycles. If the probability distributions are reasonably continuous functions the plot will develop into a z-surface, and all

the information of this type contained in a signal can be characterised by giving the shape of the surface. Since a peak must always be greater than the troughs on either side, all the non-zero probabilities will lie on one side of the line  $y=x$ , so that the final figure is a volume lying mainly over the  $(+y, -x)$  quadrant, and cut off by a  $z$  plane containing  $y=x$ . The portion lying over the  $(+x, +y)$  quadrant represents half cycles lying entirely in the positive (tension) region, and those over the  $(-x, -y)$  plane mean half-cycles in the negative (compression) region.

Peak/trough pair data capture is achieved by using a program which operates by fast digitization of the signal and compares successive samples until a peak is found. The value of this peak is held and tracking continues to a trough. An indirect address is then made up from the leading six bits of the peak value and similarly for the trough value, and one digit is added to that location in store. The total voltage field is therefore divided into  $\pm 32$  intervals and when signals are analysed over the  $\pm 10V.$  range, this gives a voltage class interval of  $\frac{1}{3.2}V.$  A clock interrupt records elapsed run time and a cross section of the probability surface on the  $y = -x$  plane can be displayed during run time on an oscilloscope screen. Stress histories were analysed using the program set to a sampling rate of 1 msec.

Other typical data can also be obtained from the joint peak/trough (or range/mean) presentation by appropriate summation. Zero crossings per unit time can be extracted by summing over the  $(+y, -x)$  quadrant. The occurrence per unit time of peaks at a given level is given by summing over  $(+x, -x)$  at a constant  $y$  ordinate, and the total number of peaks (or troughs) to occur is simply half the total

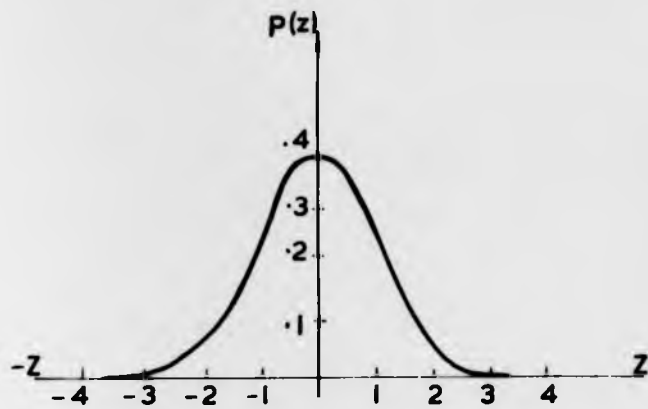
recorded peak/trough pairs. The signal irregularity factor can therefore be calculated.

The peak probability density distributions for achieved test stress histories were analysed on-line using this program. The data was then processed by the University's ICL 4130 computer to extract signal irregularity factor information and the peak probability densities in each of the 64 class intervals. The program output compared graphically the experimentally recorded data with the theoretical peak distribution calculated from equation 3.19 using the irregularity factor. Also, the expected peak frequencies in each class interval were listed together with the observed values. The flow diagram for the program is shown in fig. 3.7.

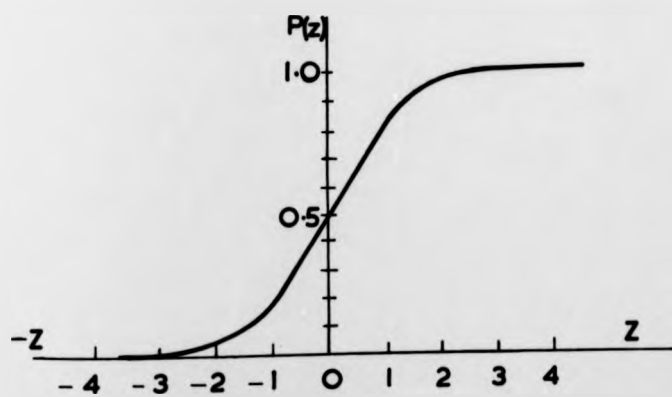
Number of Samples (N)	0-300	300 500	501 700	701 900	901 1250	1251 1750	1751 ∞
Number of Class Intervals (K)	16	20	24	27	30	35	39

Number of Class Intervals for Chisquare Test at  
5% level of significance (reference 47)

Table 3.1

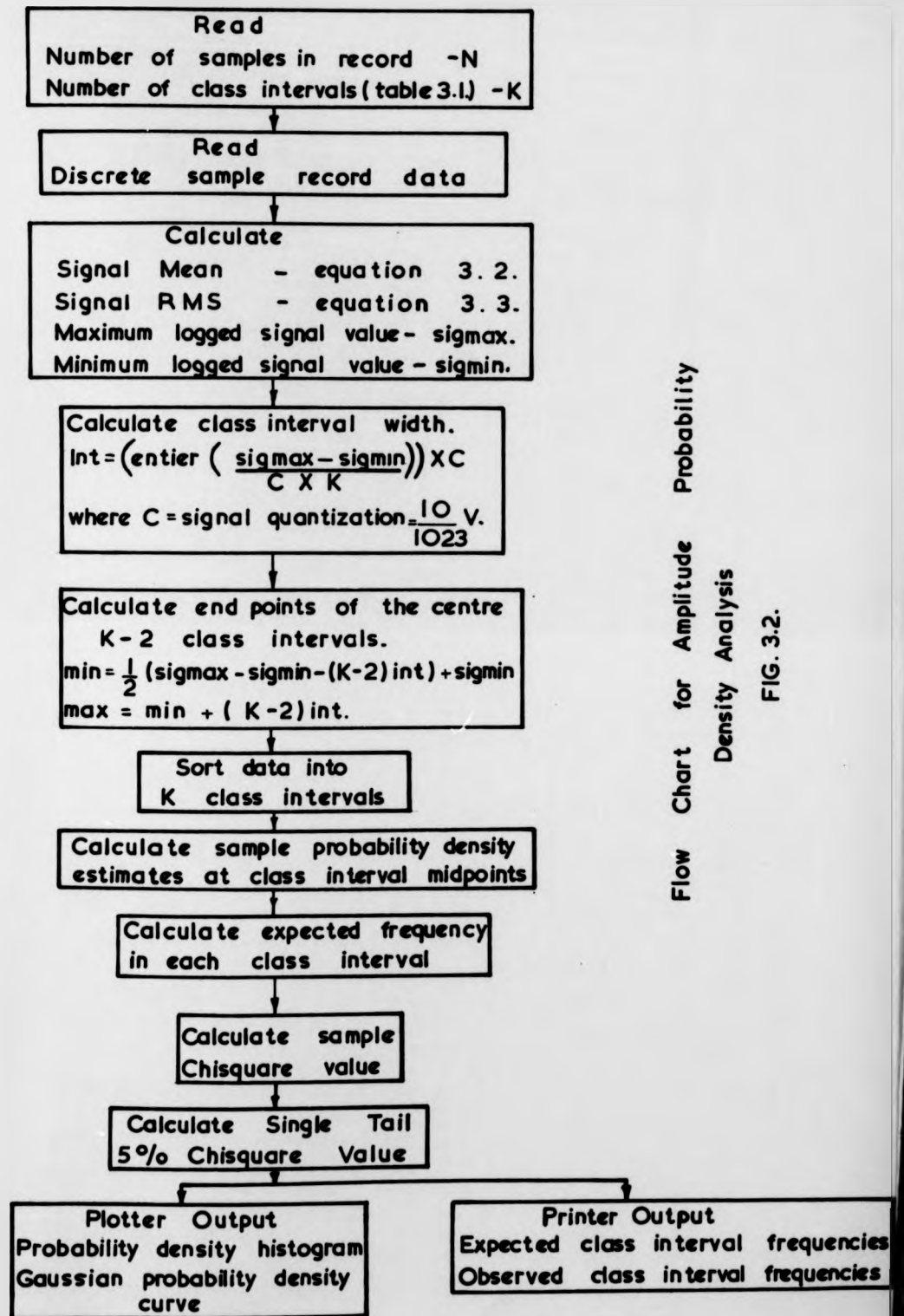


Gaussian Probability Density Function



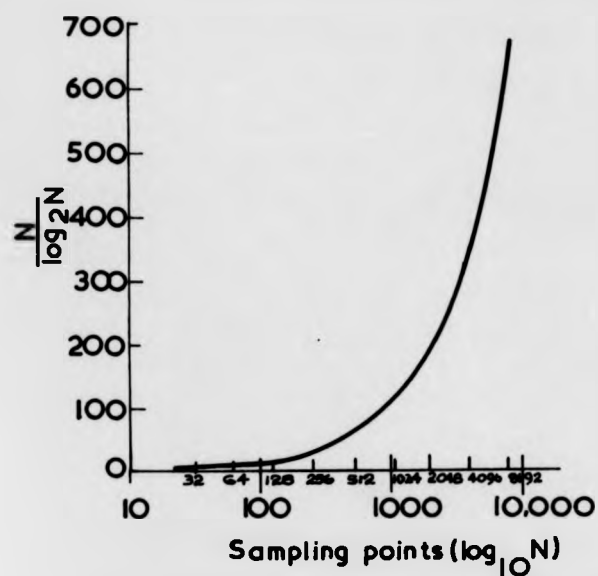
Gaussian Probability Distribution Function

FIG. 3.1.



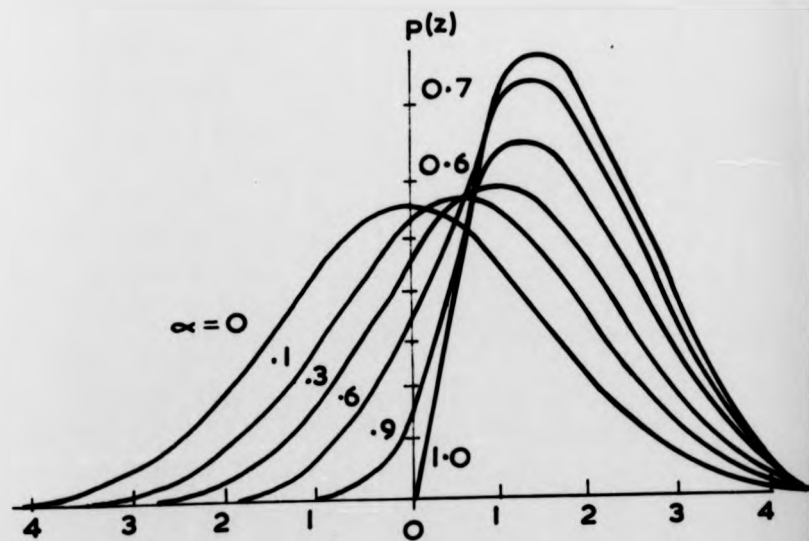
Flow Chart for Amplitude Probability  
Density Analysis

FIG. 3.2.



Saving in Computation Time from  
use of Fast Fourier Transform (ref 49)

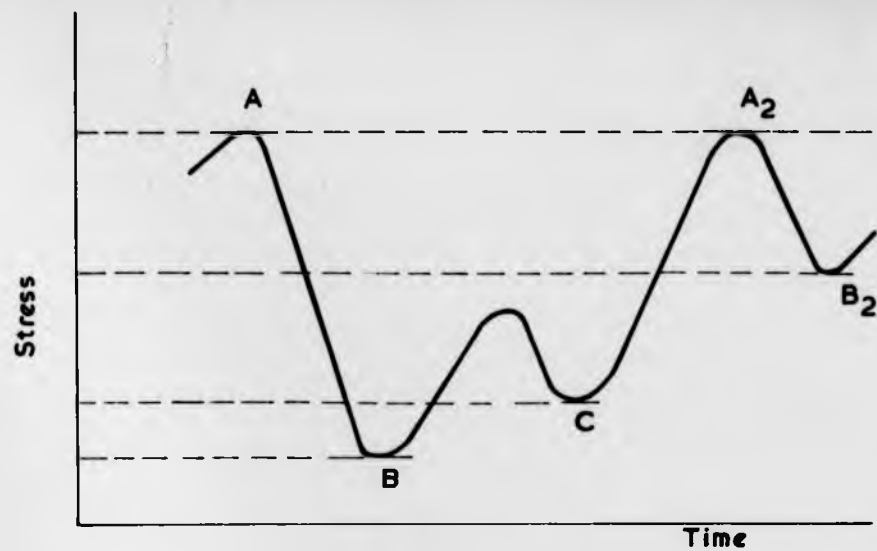
FIG. 3.3.



Set of normalized peak probability density  
curves plotted with  $\alpha (=F^2)$  as parameter

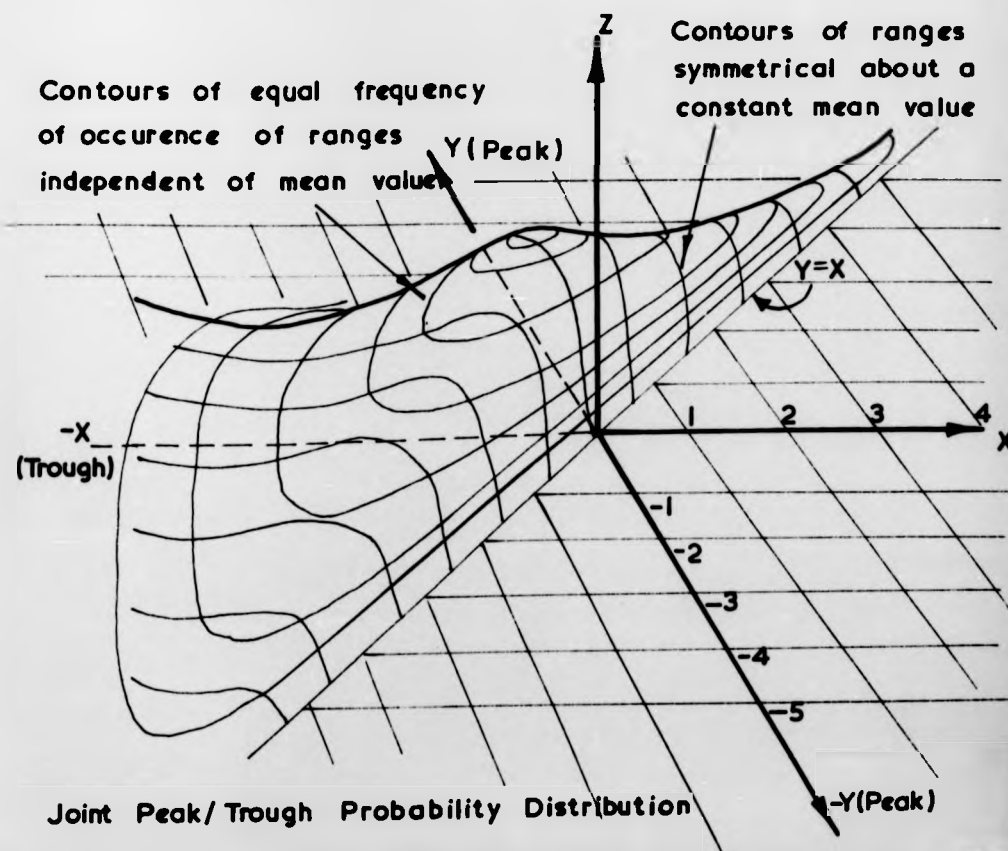
(ref 52)

FIG. 34.



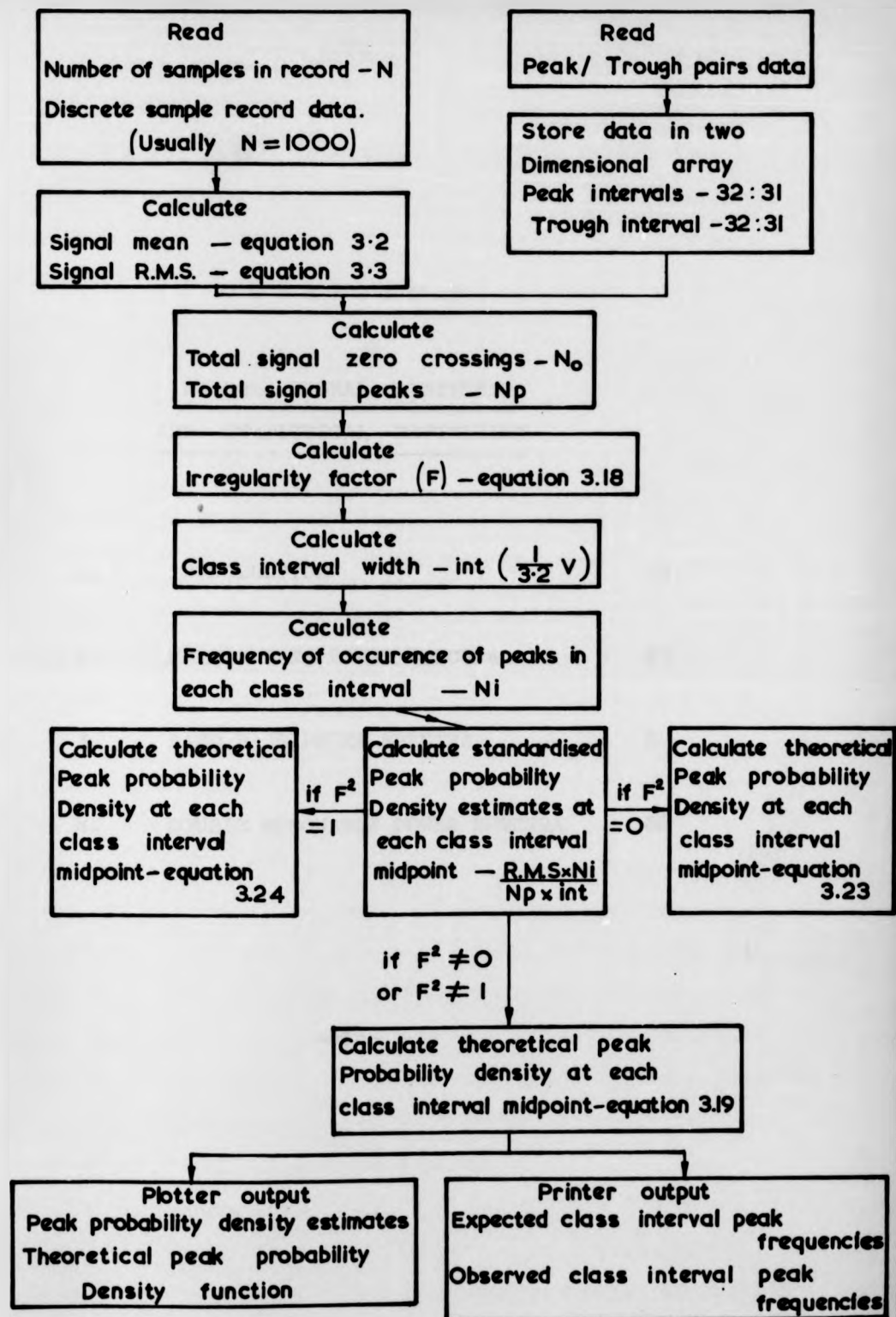
Joint Peak / Trough Pair Counting

FIG. 3.5.



Joint Peak/Trough Probability Distribution

FIG. 3.6.



Flow Chart for Peak Probability  
Density Analysis

Fig. 3.7.

C H A P T E R 4

RANDOM SIGNAL SYNTHESIS  
AND STATISTICAL DEFINITION

1.	INTRODUCTION	82
2.	NARROW BAND POWER SPECTRA	83
3.	BAND PASS POWER SPECTRA	84
4.	DOUBLE RESONANCE POWER SPECTRA	86

## 1. INTRODUCTION

Random waveforms were synthesised from active linear filters and two random signal generators with wide band noise outputs conforming to the Gaussian distribution up to defined crest factors, i.e. peak to rms. ratios. As a function of frequency,  $f$ , the relation between the filter input and output signals is given by:-

$$G_{out}(f) = |H(f)|^2 \cdot G_{in}(f)$$

where,

$H(f)$  = filter transfer function,

$G_{in}(f)$  = filter input power spectral density function,

$G_{out}(f)$  = filter output power spectral density function.

Output signals were Gaussian since the filter transfer functions were linear. Filter dynamic ranges accommodated signal variations at least to four times rms. levels.

Filter characteristics were chosen to provide loading waveforms with different peak distributions, and thus different rise and fall distributions. Peak values are greatly influenced by the shape of the signal power spectrum, and Rice (51) has given a general formula for the peak distribution as a function of spectrum shape for filters which behave linearly in amplitude response. Broch (52) has checked this formula experimentally and some of the principles behind his work have been applied here to design filter characteristics which provided signals of different peak distributions while still retaining essentially the same power spectral density form. One series of loading waveforms was synthesised by filtering wide band noise to provide bandpass spectra of differing cut off frequency ratios, and another series was realised by varying the energy ratio

between the resonant peaks of a two degree of freedom, or double resonance, filter characteristic.

Signal statistical definition was achieved by measurements of amplitude probability density, peak probability density and power spectral density functions using the programs described in Chapter 3.

## 2. NARROW BAND POWER SPECTRA

A narrow bandwidth type of power spectrum can be regarded as the limiting case of a band pass signal. Initial testing with the electromagnetic rigs was carried out using a 10 Hz. half power bandwidth random signal centred on 47 Hz. A similar signal was used to drive the  $\pm 10$  Tf. servohydraulic three point bending rig, although here the centre frequency was 10 Hz. with a 3 Hz. half power bandwidth. The waveforms are shown in fig. 4.1.

A Brüel & Kjaer sine-random generator type 1040 provided the signals. This signal generator uses a 5 Hz. - 10 KHz. wide band noise source of constant power spectral density, flat to within  $\pm 1$  db. The noise is defined as having a Gaussian amplitude distribution up to a crest factor of 4 at full instrument output voltage. The noise is amplified before passing to a selective frequency amplifier which has variable 3 db. bandwidths of 3, 10, 30 and 100 Hz. Modulation circuits then further process the noise before it appears at the output of a cathode follower stage as a continuously variable centre frequency, narrow band signal.

Amplitude probability measurements were made as set out in Tables 4.1 and 4.2. Signal values were sorted into 39 equal width class intervals and a chi-square goodness-of-fit test to the normal distribution was made at the 5% level of

significance. Both signals are compared graphically with the expected distributions in figs. 4.2 and 4.3. The results of Tables 4.1 and 4.2 show that the hypothesis of normality can be accepted.

The distributions of peak scresses were measured using the joint peak/trough probability program but only peak data was extracted during subsequent processing. The recorded signal details are listed together with expected and observed peak frequencies in Tables 4.3 and 4.4. Comparative graphs of the theoretical and experimental peak probability density distributions are shown in figs. 4.4 and 4.5. The 47 Hz. centre frequency signal conformed accurately to a Rayleigh distribution for peak excursions up to 4 x signal rms., although the lower frequency signal proved to be not quite Rayleigh in its peak distribution.

A fast fourier transform power spectral density analysis was made according to the details in Table 4.5 to determine the frequency content of the random signals. The results are shown in figs. 4.6 and 4.7, which show narrow band type power spectra. Both plots are normalised to give unit area under the curve.

### 3. BAND PASS POWER SPECTRA

Later in the electromagnetic test rig programme opportunity arose to extend the testing to other band pass power spectral shapes.

The Brüel and Kjaer generator also provided a wide band noise output in the range 5 Hz. - 10 KHz. directly from the first amplifier stage. This noise was shaped to provide two band pass power spectra using a Barr & Stroud Variable Filter Type EF2.

The filter consists of two independent low pass/high pass sixth order R-C active filter units which for the band pass mode are connected in cascade. The pass band insertion loss lies within  $\pm 1$  db. There is digital selection of the 3 db. cut off frequencies to within 5%. Stop band attenuation is 36 db./octave and the distortion factor is 0.25%. Signals up to 8.5v peak to peak can be handled.

Thus, the power spectra of both signals were essentially flat over the pass bands. The 3 db. upper cut off frequencies were 52 Hz. with lower cut off frequencies of 5 Hz. and 25 Hz. The signal peak distribution is influenced by the cut off frequency ratio, stop band attenuation and spectrum shape within the pass band, tending towards Rayleigh as the band width decreases for flat spectra. The two waveforms are shown in fig. 4.8.

Amplitude probability density, peak probability density and power spectral density estimates were made for both filtered signals in a manner similar to that previously outlined. Amplitude probability measurements are summarised in Tables 4.6 and 4.7 and graphical comparisons between the expected and actual distributions are shown in figs. 4.9 and 4.10. The hypothesis of normality was accepted for the 5% level of significance. The graphs in figs. 4.11 and 4.12 show an accurate comparison between the theoretical and experimental peak probability density distributions. The expected and observed peak frequencies are given in Tables 4.8 and 4.9. The details of power spectral density measurements are presented in Table 4.10 and figs. 4.13 and 4.14.

The response of each test rig was modified to accommodate this band pass testing by the addition of shaping networks at the inputs (see Chapter 2, Section 1.3). Thus, the

band pass spectra were substantially reproduced during testing, although the stop band attenuation was further increased by the test rig response.

#### 4. DOUBLE RESONANCE POWER SPECTRA

The input command signal for the Keelavite  $\pm 3\frac{1}{2}$  Tr servo rig was obtained by filtering the output of a Solartron B01227 multilevel random sequency generator. The instrument uses digital and analog techniques to generate random signals and could be set to give output signals which satisfy the Gaussian amplitude probability distribution up to a defined crest factor.

Seven thyatron noise sources are available within the instrument. These are sampled simultaneously at a rate determined by the cut off frequency control. Each noise source has an associated bistable which uses the polarity information of the noise to generate binary numbers. These numbers are fed to an accumulator. Therefore, a seven bit random binary number is generated at the sampling instant. This number is converted to a voltage level and, since seven bistables are available with an equal probability of one of two states, a voltage level is produced proportional to  $2^7$  (128). The number of successive samples contributing to a single output level can be varied up to 32 by the iteration control. The crest factor is controlled proportionately by the number of iterations and crest factor switches. The generated power spectrum is flat down to zero frequency but in order to obtain a flat spectrum up to the highest significant frequency of the filter response it was necessary to select a considerably higher cut off frequency.

The following instrument settings were used:-

Number of iterations (N)	8
Crest Factor ( $\sqrt{3N}$ )	4.9
Cut off frequency	1000 Hz.

For these settings the output amplitude distribution would have been Gaussian, based on the Central Limit theorem, which states that if a *large* number of independent random sources contribute each a very small amount to the output then the output amplitude distribution will be Gaussian regardless of the distribution of the individual sources.

Two filters were synthesised from operational amplifiers with feedback circuits arranged to form resonances at approximately 5 Hz. and 28 Hz. The Q factor of the first resonance remained unaltered throughout the testing, and it is convenient to consider this resonance as providing the fundamental waveform of the signal which is modified by the second resonances. The effect is to produce a number of smaller high frequency peaks and notches between the fundamental zero crossings which, as the energy content of the second resonance is increased, dominate the signal more until a Rayleigh distribution of peaks is finally produced. The waveform traces of both signals in fig. 4.15 illustrate this linear superposition effect of high and low frequency resonance bands. The signal peak distribution is affected by the ratio of the two resonant frequencies, the ratio between the energies contained in the resonances and the steepness of the filter roll-off. One filter characteristic was designed to provide a signal with a peak distribution which was almost Rayleigh, i.e. with a ratio of positive zero crossings to peaks - or irregularity factor - of unity,

while the other filter was designed to give an irregularity factor of the order of 0.5.

The basic amplifier circuit (53) which was used to form a second order resonance is shown in fig. 4.16. Without the lowpass R-C input network the transfer function is expressed in terms of angular frequency,  $w$ , as:-

$$H(w) = \frac{-R_2}{R_1} \left[ \frac{1 + jw(C_2 + C_1) \cdot R}{1 + jw \cdot (C_2 + C_1) \cdot R - w^2 \cdot C_2 \cdot C_1 \cdot R \cdot R_2} \right] \quad (4.1)$$

The natural resonant frequency is:-

$$w_n^2 = \frac{1}{R R_2 C_1 C_2} \quad (4.2)$$

Equation 4.1 can be rewritten:-

$$H(w) = -\frac{R_2}{R_1} \left[ \frac{1 + j\alpha \frac{w}{w_n}}{1 + j\alpha \frac{w}{w_n} - \left(\frac{w}{w_n}\right)^2} \right] \quad (4.3)$$

where,

$$\alpha = (C_2 + C_1) \sqrt{\frac{R}{R_2 C_2 C_1}} \quad (4.4)$$

For high frequencies the attenuation is proportional to  $\frac{1}{w}$ .

A sharper cut-off is obtained by including the lowpass filter, where the sum of the input resistors is again  $R_1$ , so that:-

$$H(w) = -\frac{R_2}{R_1} \left[ \frac{1}{1 + j\alpha \frac{w}{w_n} - \left(\frac{w}{w_n}\right)^2} \right] \quad (4.5)$$

The equation for the amplitude response can, therefore, be written:-

$$H(w) = -\frac{R_2}{R_1} \left[ \frac{1}{1 + (\alpha^2 - 2) \left(\frac{w}{w_n}\right)^2 + \left(\frac{w}{w_n}\right)^4} \right]$$

Thus the parameter  $\alpha$  is similar to the reciprocal of the conventional Q-factor for a tuned circuit. If the feedback capacitors are made equal in value the resonant frequency and "Q factor" can therefore be written:-

$$w_n^2 = \frac{1}{R R_2 C^2} \quad \text{for } C_1 = C_2 = C \quad (4.6)$$

$$Q = 0.5 \sqrt{\frac{R_2}{R}} \quad (4.7)$$

The nominal resistance and capacitance values which were used for the synthesis of the two filters are shown in figs. 4.17 and 4.18. The additional amplifier in fig. 4.18 was used to "boost" the energy contained in the second resonance to help achieve the higher irregularity factor signal.

Amplitude probability density, peak probability density and power spectral density estimates were made of both filter outputs. Amplitude probability measurements are summarised in Tables 4.11 and 4.12 and graphical comparisons between the expected and actual distributions are shown in figs. 4.19 and 4.20. The hypothesis of normality was accepted for the amplitude probability measurements at the 5% level of significance. The graphs in figs. 4.21 and 4.22 show an accurate comparison between the theoretical and experimental peak probability density distributions. The expected and actual peak densities are given in Tables 4.13 and 4.14. The details of power spectral density measurements are presented in Table 4.15 and figs. 4.23 and 4.24.

Class Interval Midpoint (z)	Observed Frequency	Expected Frequency	Class Interval Midpoint (z)	Observed Frequency	Expected Frequency
-3.316	3	4.940	0.110	530	542.0
-3.145	1	3.933	0.281	563	525.0
-2.974	10	6.633	0.452	480	493.1
-2.802	7	10.87	0.624	426	449.8
-2.631	15	17.29	0.795	397	398.4
-2.460	25	26.70	0.966	334	342.3
-2.288	40	40.07	1.138	258	286.4
-2.117	68	58.38	1.309	243	232.3
-1.946	68	62.61	1.480	196	183.1
-1.775	118	113.5	1.651	138	140.1
-1.603	147	151.5	1.823	109	104.1
-1.432	187	196.4	1.994	69	75.14
-1.261	268	247.2	2.165	59	52.66
-1.089	312	302.1	2.337	39	35.85
-0.918	335	358.6	2.508	23	23.70
-0.747	397	413.5	2.679	21	15.21
-0.575	472	462.9	2.851	4	9.484
-0.404	518	503.3	3.022	3	5.742
-0.233	528	531.5	3.193	6	7.545
-0.062	542	545.0			

Amplitude resolution =  $0.323 = 0.171 \times \text{rms.}$

Signal rms. = 1.883 V.

Total no. of class intervals = 39

Total no. of samples = 8000

5% Value of chisquare = 51

Sample Chisquare value = 29.0

47 Hz. Centre Frequency Signal

Table 4.1

Class Interval Midpoint (z)	Observed Frequency	Expected frequency	Class Interval Midpoint (z)	Observed Frequency	Expected Frequency
-3.007	4	13.6	0.124	470	499.3
-2.851	10	8.7	0.281	426	479.9
-2.694	15	13.3	0.437	428	453.8
-2.537	22	20.1	0.594	417	418.7
-2.381	24	29.5	0.750	388	376.9
-2.224	43	42.3	0.907	346	351.2
-2.068	63	59.1	1.063	325	283.9
-1.911	80	80.7	1.220	244	237.6
-1.755	91	107.4	1.376	200	194.0
-1.598	144	139.6	1.533	157	154.5
-1.442	204	177.0	1.689	123	120.1
-1.285	222	219.0	1.846	110	91.1
-1.128	266	264.4	2.003	74	67.5
-0.972	325	311.5	2.159	49	48.7
-0.815	352	358.2	2.316	32	34.4
-0.659	403	401.9	2.472	14	23.6
-0.502	437	440.1	2.629	9	15.9
-0.346	469	470.2	2.785	8	10.4
-0.189	491	490.3	2.942	16	16.8
-0.033	499	498.9			

Amplitude resolution = 0.255 V. = 0.157 x rms.

Signal rms. = 1.499 V.

Total no. of class intervals = 59

Total no. of samples = 8000

5% Value of chisquare = 51

Sample chisquare value = 41.6

10 Hz. Centre Frequency Signal

Table 4.2

Class Interval Midpoint (z)	Observed Peak Frequency	Expected Peak Frequency	Class Interval Midpoint (z)	Observed Peak Frequency	Expected Peak Frequency
-6.85	0	0	0.11	808	925.2
-6.64	0	0	0.33	2493	2576.3
-6.42	0	0	0.54	3865	3907.3
-6.20	0	0	0.76	4742	4746.4
-5.98	0	0	0.98	5200	5055.3
-5.77	0	0	1.20	5028	4880.5
-5.55	0	0	1.42	4501	4346.1
-5.33	0	0	1.63	3661	3504.5
-5.11	0	0	1.85	2929	2801.0
-4.90	0	0	2.07	2045	2047.6
-4.68	0	0	2.29	1347	1412.0
-4.46	0	0	2.50	839	920.5
-4.24	0	0	2.72	528	568.0
-4.03	0	0	2.94	281	332.3
-3.81	0	0	3.16	144	184.4
-3.59	0	0	3.37	72	97.1
-3.37	0	0	3.59	24	48.6
-3.16	0	0	3.81	10	23.1
-2.94	0	0	4.03	2	10.5
-2.72	0	0	4.24	3	4.5
-2.50	0	0	4.46	0	1.8
-2.28	0	0	4.68	0	0.7
-2.07	0	0	4.90	0	0.3
-1.85	0	0	5.11	0	0.1
-1.63	0	0	5.33	0	0.0
-1.41	0	0	5.55	0	0.0
-1.20	0	0	5.77	0	0.0
-0.98	0	0	5.99	0	0.0
-0.76	0	0	6.20	0	0.0
-0.54	0	0	6.42	0	0.0
-0.33	0	0	6.64	0	0.0
-0.11	19	22.9	6.86	0	0.0

Signal rms. = 1.437 V.

Measurement time = 775 sec.

Peaks = 38541

Positive Zero Crossings = 38495

Irregularity Factor = 0.999

47 Hz. Centre Frequency Signal

Table 4.3

Class Interval Midpoint (z)	Observed Peak Frequency	Expected Peak Frequency	Class Interval Midpoint (z)	Observed Peak Frequency	Expected Peak Frequency
-5.09	0	0	0.08	202	201.1
-4.93	0	0	0.24	449	391.1
-4.76	0	0	0.40	583	600.4
-4.60	0	0	0.57	744	774.3
-4.44	0	0	0.73	899	897.5
-4.28	0	0	0.89	939	963.0
-4.12	0	0	1.05	955	973.5
-3.96	0	0	1.21	969	936.2
-3.80	0	0	1.37	860	861.5
-3.63	0	0	1.53	775	761.3
-3.47	0	0	1.70	621	649.0
-3.31	0	0	1.86	547	533.8
-3.15	0	0	2.02	477	424.6
-2.99	0	0	2.18	343	326.9
-2.83	0	0	2.34	240	243.9
-2.67	0	0	2.50	179	176.4
-2.50	0	0	2.67	125	123.8
-2.34	0	0	2.83	92	84.4
-2.18	0	0	2.99	38	55.8
-2.02	0	0	3.15	32	35.9
-1.86	0	0	3.31	23	22.4
-1.70	0	0	3.47	6	13.6
-1.53	0	0	3.63	6	8.0
-1.37	0	0	3.80	2	4.6
-1.21	0	0	3.96	2	2.6
-1.05	0	0	4.12	0	1.1
-0.89	0	0	4.28	1	0.7
-0.73	0	0	4.44	0	0.4
-0.57	1	0.2	4.60	0	0.2
-0.40	2	2.2	4.77	0	0.1
-0.24	13	16.3	4.93	0	0
-0.08	62	71.7	5.09	0	0

Signal rms. = 1.935 V.

Measurement time = 913 sec.

Peaks = 10167

Positive Zero Crossings = 9889

Irregularity Factor = 0.982

10 Hz. Centre Frequency Signal

Table 4.4

Degrees of Freedom	=	1064
Sampling Frequency	=	160 Hz.
Signal rms.	=	1.833 V.

47 Hz. Centre Frequency Signal

Degrees of Freedom	=	328
Sampling Frequency	=	50 Hz.
Signal rms.	=	1.499 V.

10 Hz. Centre Frequency Signal

Table 4.5

Class Interval Midpoint (z)	Observed Frequency	Expected Frequency	Class Interval Midpoint (z)	Observed Frequency	Expected Frequency
-3.431	5	3.342	0.190	554	566.8
-3.250	2	2.976	0.371	584	538.8
-3.069	7	5.265	0.552	521	495.7
-2.888	8	9.015	0.733	429	441.4
-2.707	13	14.84	0.914	382	380.4
-2.526	28	23.96	1.095	302	317.3
-2.345	27	37.20	1.276	270	256.1
-2.164	60	55.89	1.457	192	200.1
-1.983	89	61.26	1.639	164	151.3
-1.802	100	114.4	1.820	111	110.7
-1.621	177	155.8	2.001	84	78.42
-1.440	213	205.3	2.182	44	53.76
-1.258	262	262.0	2.363	37	35.67
-1.077	302	323.5	2.544	23	22.90
-0.896	385	336.6	2.725	20	14.23
-0.715	411	447.1	2.906	8	8.560
-0.534	522	500.5	3.087	5	4.983
-0.353	549	542.3	3.268	2	2.807
-0.172	561	568.6	3.449	2	3.133
0.009	575	577.1			

Amplitude resolution = 0.372 V. = 0.181 x rms.

Signal rms. = 2.052 V.

Total no. of class intervals = 39

Total no. of samples = 8000

5% value of chisquare = 51

Sample chisquare value = 33.3

5/52 Hz. Band Pass Signal

Table 4.6

Class Interval Midpoint (z)	Observed Frequency	Expected Frequency	Class Interval Midpoint (z)	Observed Frequency	Expected Frequency
-3.937	1	.4972	0.054	619	635.0
-3.738	1	.6022	0.254	623	615.8
-3.538	1	1.242	0.454	547	574.0
-3.339	2	2.461	0.653	519	514.1
-3.139	4	4.337	0.853	406	442.6
-2.939	2	8.530	1.052	362	366.2
-2.740	22	15.09	1.252	312	291.2
-2.540	24	25.52	1.451	217	222.6
-2.341	43	42.47	1.651	204	163.5
-2.141	63	64.76	1.851	106	115.4
-1.941	100	97.19	2.050	79	78.23
-1.742	137	140.2	2.250	54	51.04
-1.542	192	194.4	2.449	31	31.98
-1.343	258	259.0	2.649	14	19.26
-1.143	330	331.6	2.849	8	11.15
-0.944	389	408.1	3.048	4	6.201
-0.744	486	482.6	3.248	6	3.315
-0.544	556	548.6	3.447	0	1.703
-0.345	623	599.4	3.647	2	1.558
-0.145	648	629.3			

Amplitude resolution = 0.391 V. = 0.200 x rms.

Signal rms. = 1.959 V.

Total no. of class intervals = 39

Total no. of samples = 3000

5% value of chisquare = 51

Sample chisquare value = 36.7

25/52 Hz. Band Pass Signal

Table 4.7

Class Interval Midpoint (z)	Observed Peak Frequency	Expected Peak Frequency	Class Interval Midpoint (z)	Observed Peak Frequency	Expected Peak Frequency
-5.37	0	0	0.09	1414	1518.6
-5.20	0	0	0.26	1745	1884.2
-5.03	0	0	0.43	2050	2217.8
-4.85	0	0	0.60	2308	2481.3
-4.68	0	0	0.77	2469	2643.7
-4.51	0	0	0.94	2544	2687.8
-4.34	0	0	1.11	2491	2612.4
-4.17	0	0	1.28	2356	2432.0
-4.00	0	0	1.45	2235	2172.2
-3.83	0	0	1.62	1975	1864.4
-3.66	0	0	1.79	1588	1540.0
-3.49	0	0	1.96	1338	1225.6
-3.32	0	0	2.13	1141	940.8
-3.15	0	0	2.30	832	697.3
-2.98	0	0	2.47	641	499.3
-2.81	0	0	2.64	465	345.8
-2.64	0	0	2.81	304	231.6
-2.47	0	0	2.98	221	150.2
-2.30	1	0.1	3.15	135	94.3
-2.13	0	0.4	3.32	105	57.3
-1.96	1	1.1	3.49	56	33.8
-1.79	4	2.8	3.66	39	19.3
-1.62	14	6.8	3.83	23	10.7
-1.45	24	15.5	4.00	11	5.7
-1.28	40	33.1	4.17	7	3.0
-1.11	85	66.4	4.34	3	1.5
-0.94	126	124.8	4.51	2	0.7
-0.77	248	220.2	4.68	3	0.4
-0.60	333	364.9	4.86	2	0.2
-0.43	560	509.0	5.06	0	0.1
-0.26	795	836.0	5.26	0	0
-0.09	1072	1158.9	5.37	0	0

Signal rms. = 1.835 V.

Measurement time = 761 sec.

Peaks = 310806

Positive Zero Crossings = 24999

Irregularity Factor = 0.786

5/52 Hz. Band Pass Signal

Table 4.8

Class Interval Midpoint (z)	Observed Peak Frequency	Expected Peak Frequency	Class Interval Midpoint (z)	Observed Peak Frequency	Expected Peak Frequency
-4.97	0	0	0.05	1145	1034.1
-4.81	0	0	0.24	1576	1493.2
-4.65	0	0	0.39	2016	1971.8
-4.50	0	0	0.55	2521	2405.6
-4.34	0	0	0.71	2855	2737.5
-4.18	0	0	0.87	2982	2931.8
-4.02	0	0	1.03	3040	2977.4
-3.87	0	0	1.18	2897	2884.9
-3.71	0	0	1.34	2677	2679.8
-3.55	0	0	1.50	2334	2395.0
-3.39	0	0	1.66	1940	2064.9
-3.23	0	0	1.81	1625	1720.9
-3.08	0	0	1.97	1332	1338.5
-2.92	0	0	2.13	1042	1085.8
-2.76	0	0	2.29	797	823.7
-2.60	0	0	2.45	543	606.6
-2.45	0	0	2.60	354	434.0
-2.29	0	0	2.76	237	301.8
-2.13	0	0	2.92	164	204.0
-1.97	0	0	3.08	116	134.1
-1.81	0	0	3.23	60	85.8
-1.66	0	0	3.39	47	53.4
-1.50	0	0	3.55	29	32.4
-1.34	1	0.2	3.71	11	19.1
-1.18	1	0.8	3.87	9	11.0
-1.03	3	3.2	4.02	10	6.1
-0.87	13	10.7	4.18	3	3.3
-0.71	33	31.6	4.34	1	1.8
-0.55	85	81.1	4.50	0	0.9
-0.39	180	183.1	4.65	0	0.5
-0.24	371	365.2	4.81	0	0.2
-0.08	704	648.7	4.97	0	0.1

Signal rms. = 1.981 V.

Measurement time = 758 sec.

Peaks = 33834

Positive Zero Crossings = 31184

Irregularity Factor = 0.922

25/52 Hz. Band Pass Signal

Table 4.9

Degrees of Freedom	=	1040
Sampling Frequency	=	160 Hz.
Signal rms.	=	2.052 V.

5/52 Hz. Band Pass Signal

Degrees of Freedom	=	856
Sampling Frequency	=	160 Hz.
Signal rms.	=	1.959 V.

25/52 Hz. Band Pass Signal

Table 4.10

Class Interval Midpoint (z)	Observed Frequency	Expected Frequency	Class Interval Midpoint (z)	Observed Frequency	Expected Frequency
-3.620	1	.4190	0.080	142	146.2
-3.435	0	.4103	0.264	138	142.3
-3.250	4	.7601	0.449	141	133.3
-3.065	2	1.361	0.634	117	120.6
-2.880	3	2.355	0.819	100	105.5
-2.695	5	3.939	1.004	93	89.13
-2.510	4	6.366	1.189	67	72.30
-2.325	8	9.945	1.374	56	57.47
-2.140	12	15.01	1.559	41	43.84
-1.955	20	21.91	1.744	37	32.73
-1.770	40	30.89	1.929	21	23.04
-1.585	42	42.09	2.114	12	15.86
-1.400	51	55.44	2.299	7	10.56
-1.215	63	70.57	2.484	9	6.792
-1.030	68	86.81	2.669	5	4.222
-0.845	101	103.2	2.854	5	2.537
-0.660	123	118.5	3.039	1	1.473
-0.475	154	131.7	3.224	1	.8266
-0.290	153	141.3	3.409	1	.9103
-0.105	150	146.6			

Amplitude resolution = 0.284 V. = 0.185 x rms.

Signal rms. = 1.532 V.

Total no. of class intervals = 39

Total no. of samples = 2000

5% value of chisquare = 51

Sample chisquare value = 39.2

Low Irregularity Factor Signal

Table 4.11

Class Interval Midpoint (z)	Observed Frequency	Expected Frequency	Class Interval Midpoint (z)	Observed Frequency	Expected Frequency
-3.412	2	.8634	0.069	154	133.2
-3.238	2	.7426	0.243	138	134.7
-3.064	1	1.283	0.417	131	127.2
-2.890	2	2.152	0.591	112	116.5
-2.716	6	3.500	0.765	116	105.6
-2.542	10	5.525	0.939	77	89.56
-2.368	10	6.461	1.113	68	74.79
-2.194	11	12.57	1.287	67	60.75
-2.020	19	18.12	1.461	47	47.34
-1.846	20	25.35	1.635	27	38.57
-1.672	31	34.40	1.809	20	27.12
-1.498	39	45.30	1.983	20	19.51
-1.324	57	57.87	2.157	14	13.62
-1.150	57	71.73	2.331	15	9.227
-0.976	79	86.27	2.505	3	6.064
-0.802	96	100.7	2.679	5	3.867
-0.628	124	114.0	2.853	3	2.392
-0.454	132	125.2	3.027	1	1.436
-0.280	132	133.4	3.201	4	1.844
-0.106	148	137.9			

Amplitude resolution =  $0.254 \text{ V.} = 0.174 \times \text{rms.}$

Signal rms. = 1.460 V.

Total no. of class intervals = 39

Total no. of samples = 2000

5% value of chisquare = 51

Sample chisquare value = 34.6

High Irregularity Factor Signal

Table 4.12

Class Interval Midpoint (z)	Observed Peak Frequency	Expected Peak Frequency	Class Interval Midpoint (z)	Observed Peak Frequency	Expected Peak Frequency
-12.75	0	0	0.20	2029	2120.6
-12.33	0	0	0.61	2404	2471.7
-11.92	0	0	1.01	2282	2351.8
-11.52	0	0	1.41	1842	1844.3
-11.11	0	0	1.82	1334	1191.5
-10.71	0	0	2.22	744	637.9
-10.30	0	0	2.63	374	284.3
-9.89	0	0	3.03	146	105.8
-9.50	0	0	3.44	56	33.0
-9.10	0	0	3.84	10	3.6
-8.69	0	0	4.24	2	1.9
-8.28	0	0	4.65	2	0.4
-7.88	0	0	5.05	0	0.1
-7.48	0	0	5.46	0	0
-7.07	0	0	5.86	0	0
-6.67	0	0	6.26	0	0
-6.26	0	0	6.67	0	0
-5.86	0	0	7.07	0	0
-5.46	0	0	7.48	0	0
-5.05	0	0	7.88	0	0
-4.65	0	0	8.28	0	0
-4.24	0	0	8.69	0	0
-3.84	0	0	9.09	0	0
-3.45	0	0	9.50	0	0
-3.03	0	0.3	9.90	0	0
-2.63	2	1.9	10.30	0	0
-2.22	16	9.8	10.71	0	0
-1.82	56	41.7	11.11	0	0
-1.41	156	141.1	11.52	0	0
-1.01	348	333.5	11.92	0	0
-0.61	734	838.7	12.32	0	0
-0.20	1423	1461.2	12.73	0	0

Signal rms. = 0.773 V.

Measurement time = 766 sec.

Peaks = 13958

Positive Zero Crossings = 8160

Irregularity Factor = 0.585

Low Irregularity Factor Signal

Table 4-13.

Class Interval Midpoint (z)	Observed Peak Frequency	Expected Peak Frequency	Class Interval Midpoint (z)	Observed Peak Frequency	Expected Peak Frequency
-6.14	0	0	0.10	1023	899.1
-5.95	0	0	0.29	1277	1299.3
-5.75	0	0	0.49	1615	1686.6
-5.56	0	0	0.68	2068	1988.8
-5.36	0	0	0.88	2130	2153.9
-5.17	0	0	1.07	2107	2163.5
-4.97	0	0	1.27	1979	2032.4
-4.78	0	0	1.46	1786	1797.2
-4.58	0	0	1.66	1456	1503.5
-4.39	0	0	1.85	1155	1194.3
-4.19	0	0	2.05	866	903.4
-4.00	0	0	2.24	659	651.9
-3.80	0	0	2.44	417	449.5
-3.61	0	0	2.63	281	296.5
-3.41	0	0	2.83	191	187.2
-3.22	0	0	3.02	123	113.3
-3.02	0	0	3.22	92	65.7
-2.83	0	0	3.41	65	36.6
-2.63	0	0	3.61	43	19.5
-2.44	0	0	3.80	21	10.0
-2.24	0	0	4.00	17	4.9
-2.05	1	0	4.19	7	2.3
-1.85	0	0	4.39	1	1.1
-1.66	0	0.1	4.58	4	0.5
-1.46	0	0.3	4.78	0	0.2
-1.27	2	1.5	4.97	0	0.1
-1.07	1	5.9	5.17	0	0
-0.88	23	20.0	5.36	0	0
-0.68	73	57.2	5.56	0	0
-0.49	156	140.5	5.76	0	0
-0.29	330	298.6	5.95	0	0
-0.10	584	552.6	6.15	0	0

Signal rms. = 1.602 V.

Measurement time = 749 sec.

Peaks = 20553

Positive Zero Crossings = 18399

Irregularity Factor = 0.895

High Irregularity Factor Signal

Table 4.14.

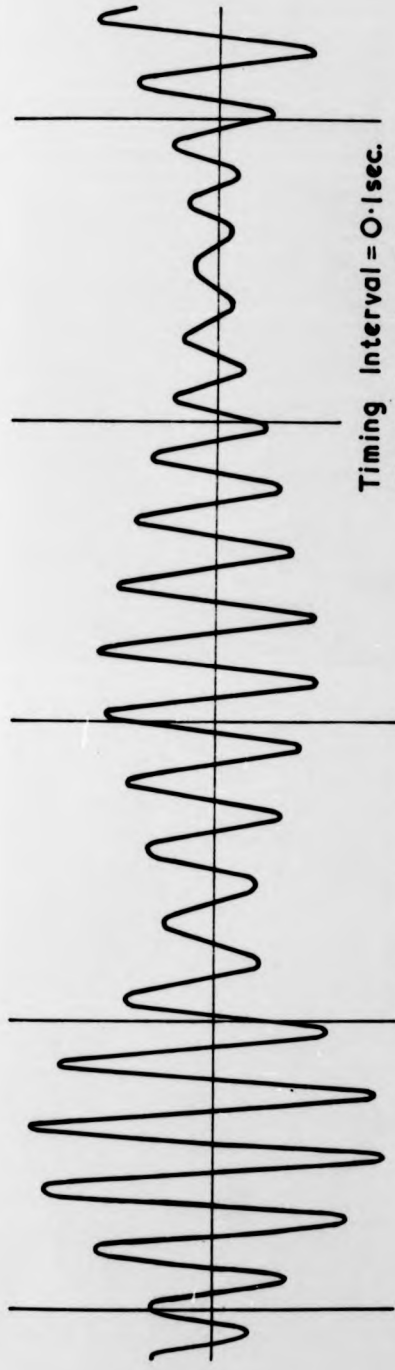
Degrees of Freedom	=	364
Sampling Frequency	=	100 Hz.
Signal rms.	=	1.532 V.

Low Irregularity Factor Signal

Degrees of Freedom	=	308
Sampling Frequency	=	100 Hz.
Signal rms.	=	1.939 V.

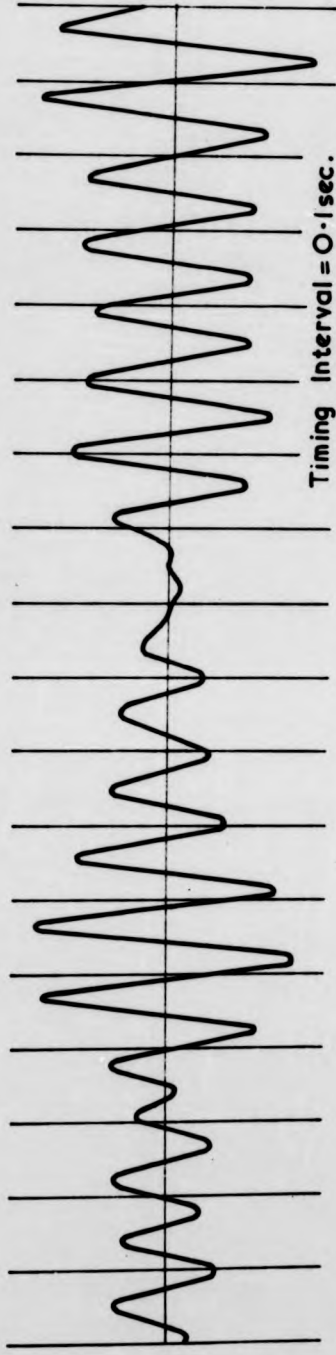
High Irregularity Factor Signal

Table 4.15



47Hz centre frequency signal

Timing Interval = 0.1 sec.  
Chart Speed = 500 mm/sec.

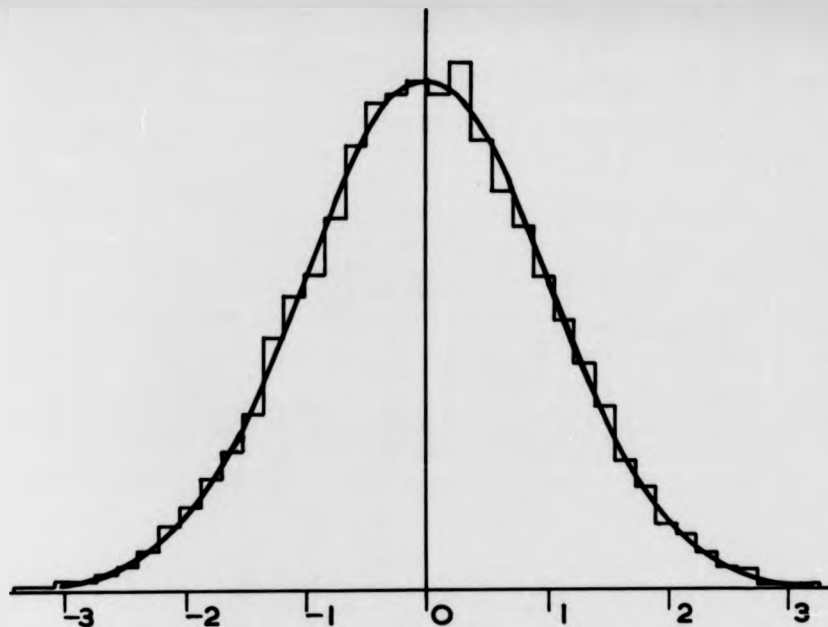


10Hz centre frequency signal

Timing Interval = 0.1 sec.  
Chart Speed = 125 mm/sec.

Waveform Traces

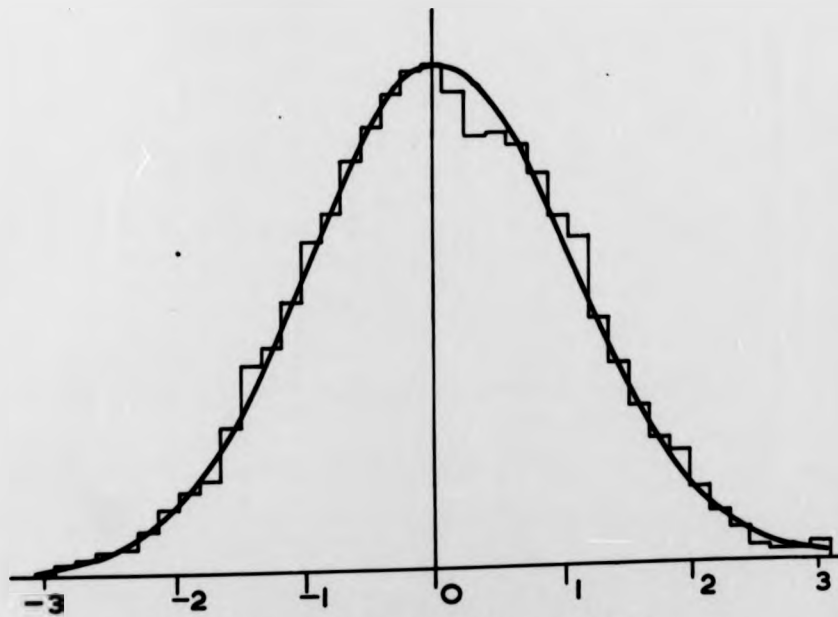
FIG. 4.1.



Standardised Probability Density

47Hz Centre Frequency Signal

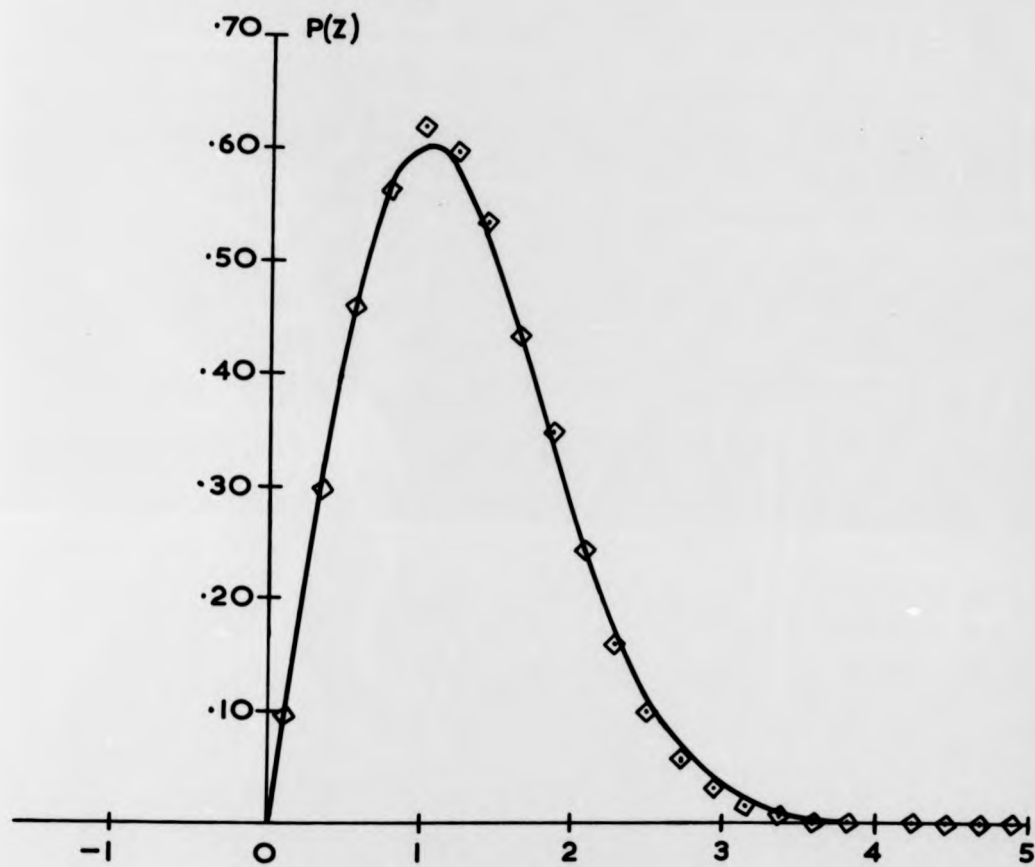
Fig. 4.2.



Standardised Probability Density

10Hz Centre Frequency Signal

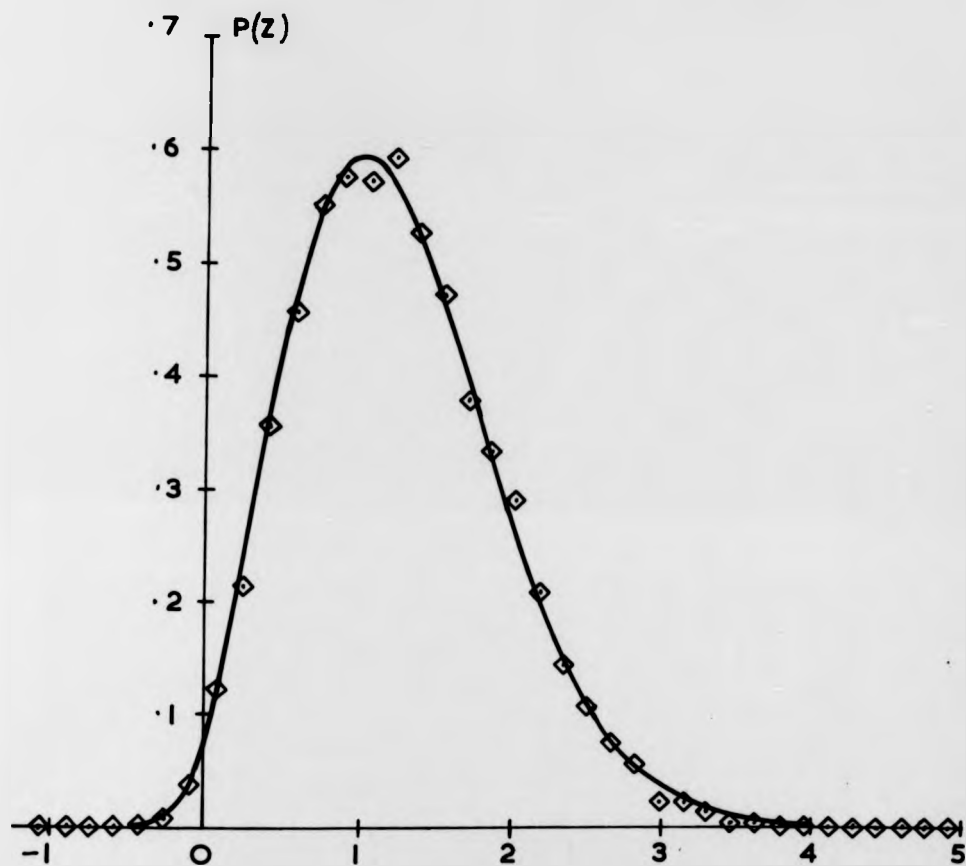
Fig. 4.3.



Standardised Peak Probability Density Function

47Hz Centre Frequency Signal

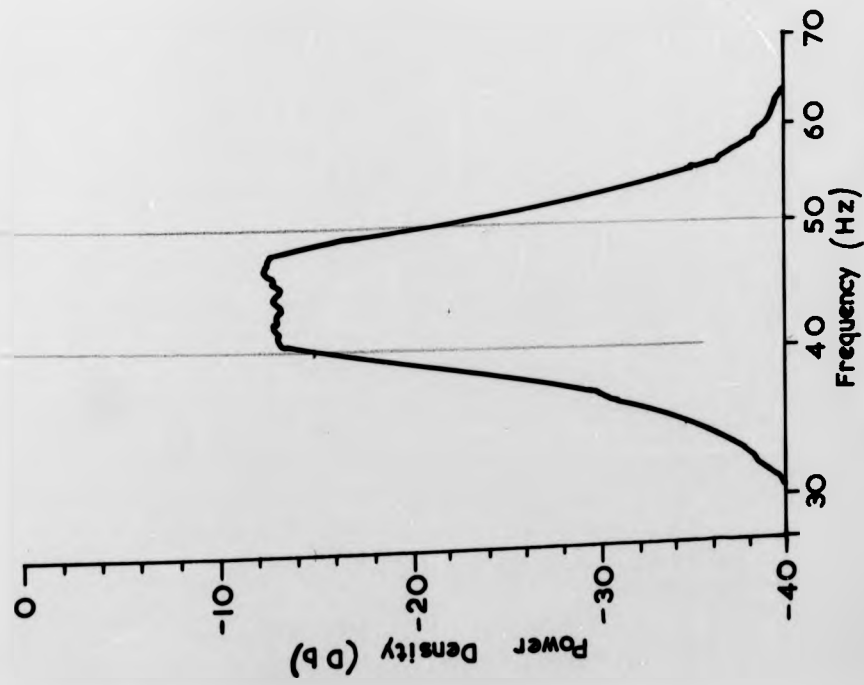
Fig. 4.4.



Standardised Peak Probability Density Function

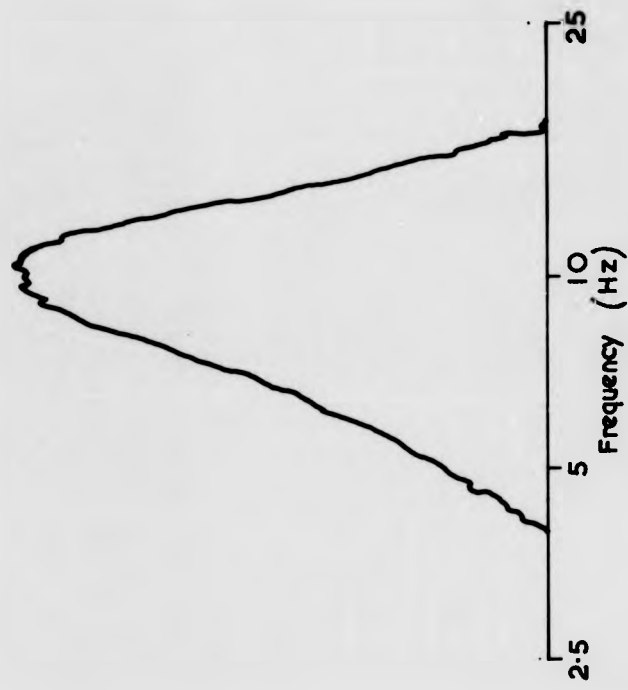
10Hz Centre Frequency Signal

Fig. 4.5.



47Hz Centre Frequency Signal

Fig. 4. 6.



10Hz Centre Frequency Signal

Fig. 4. 7.

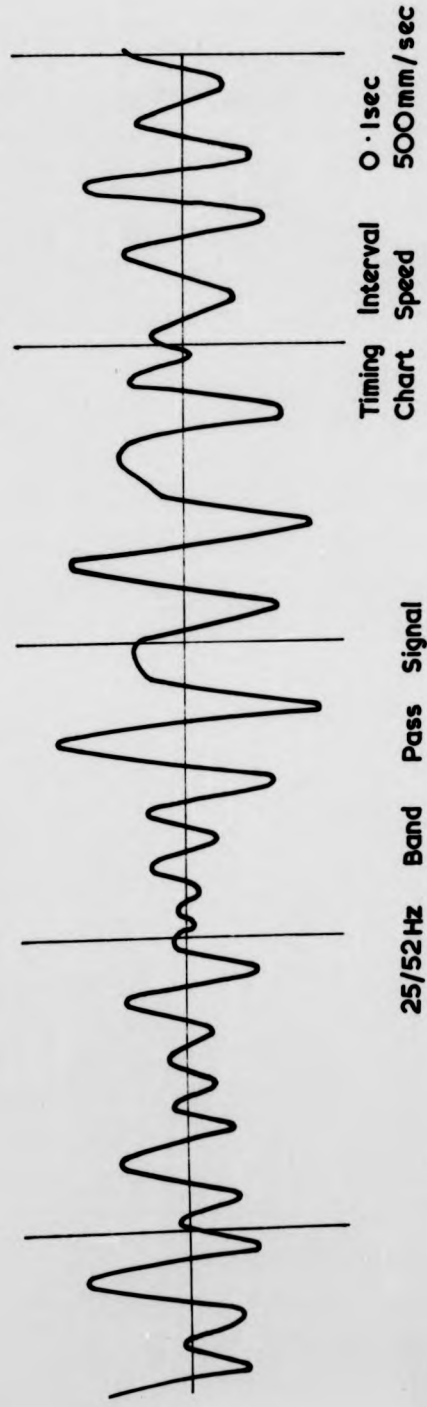
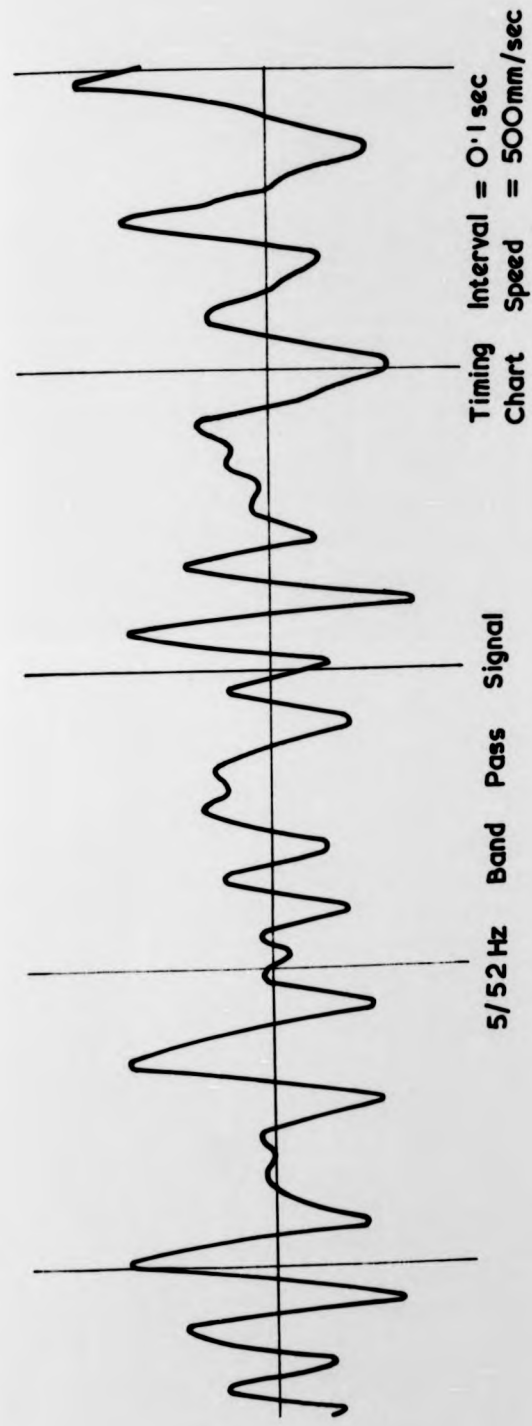
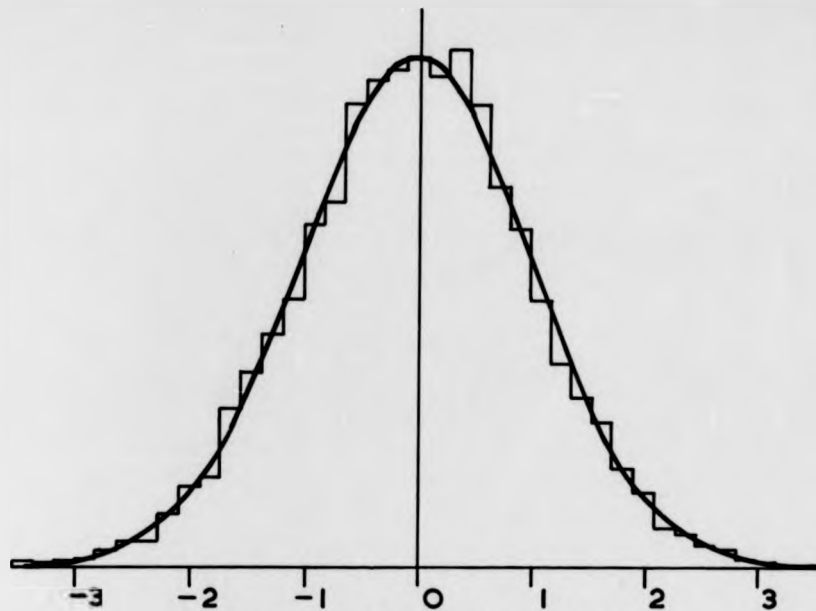


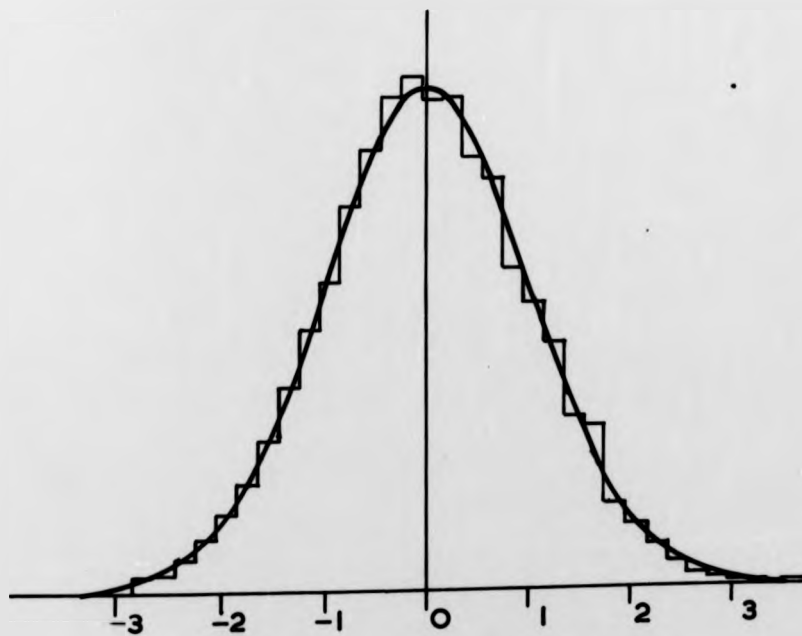
FIG. 4.8.



Standardised Probability Density

5/52Hz Band Pass

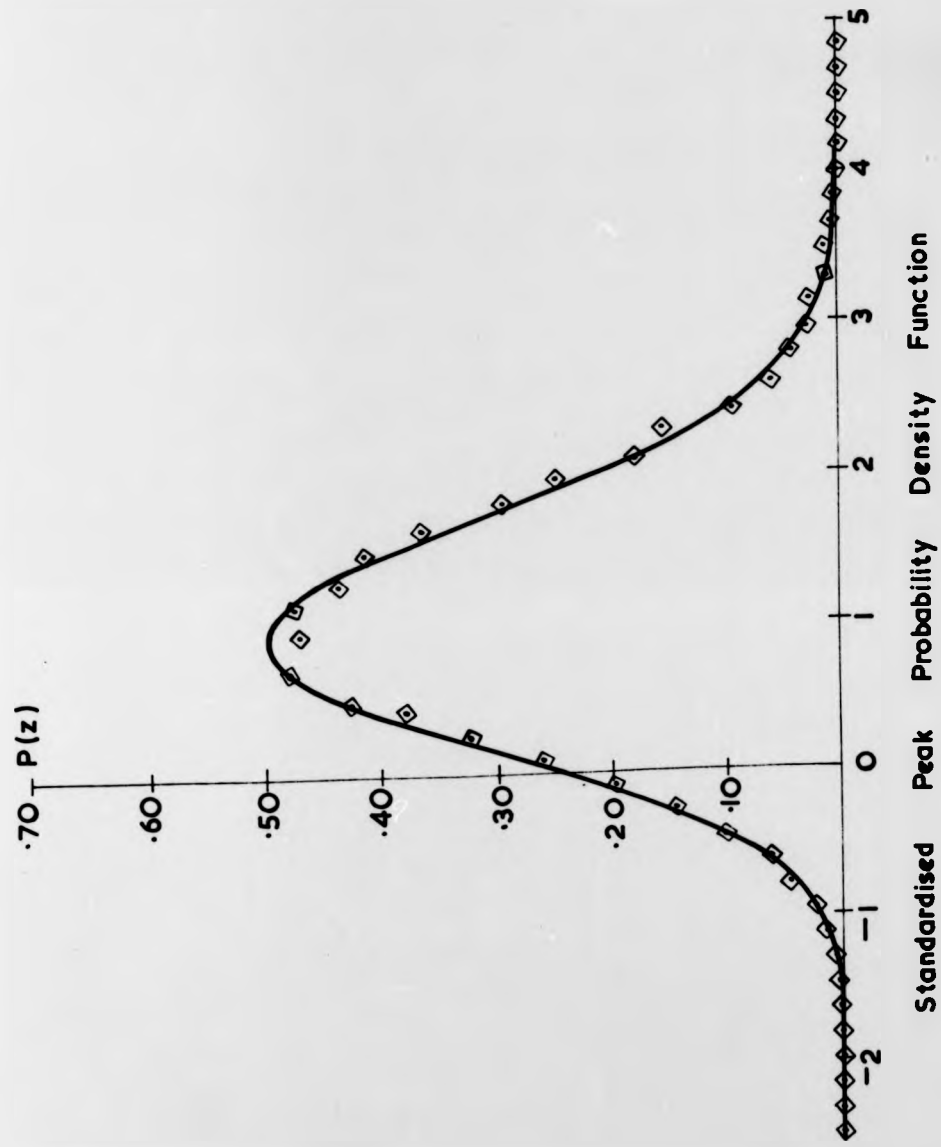
Fig. 4.9.



Standardised Probability Density

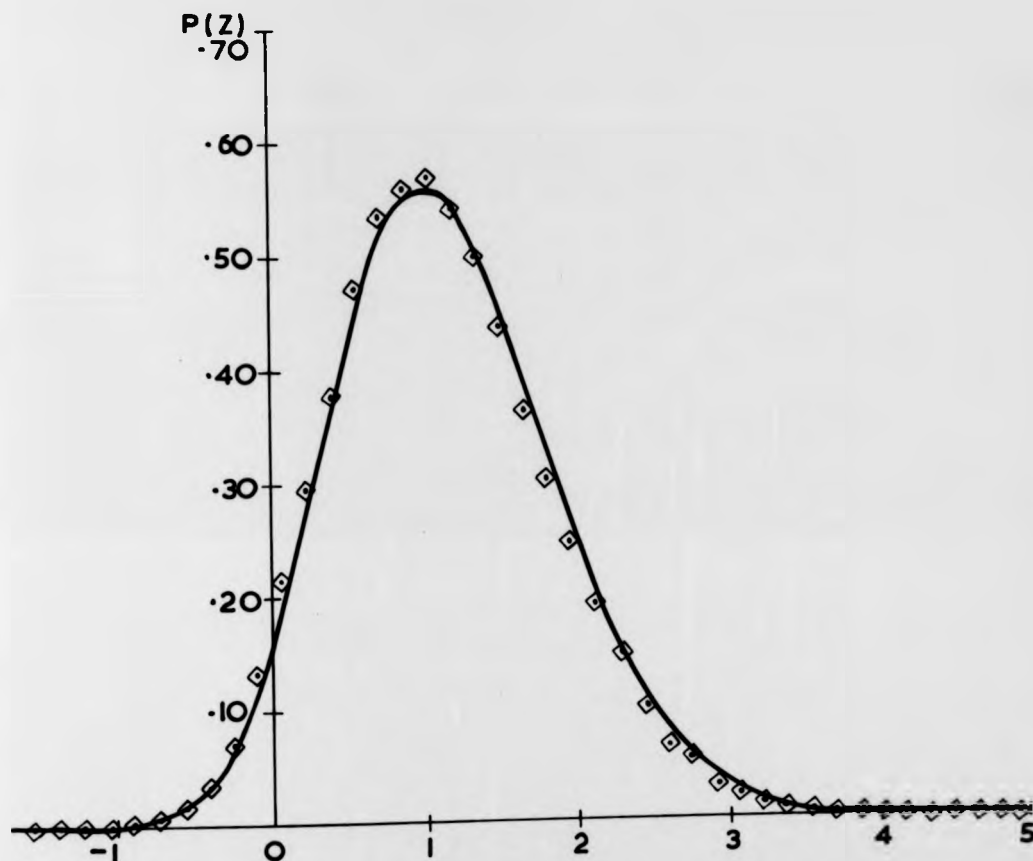
25/52 Hz Band Pass

Fig. 4.10.



Standardised Peak Probability Density Function  
5/52Hz Band Pass Signal

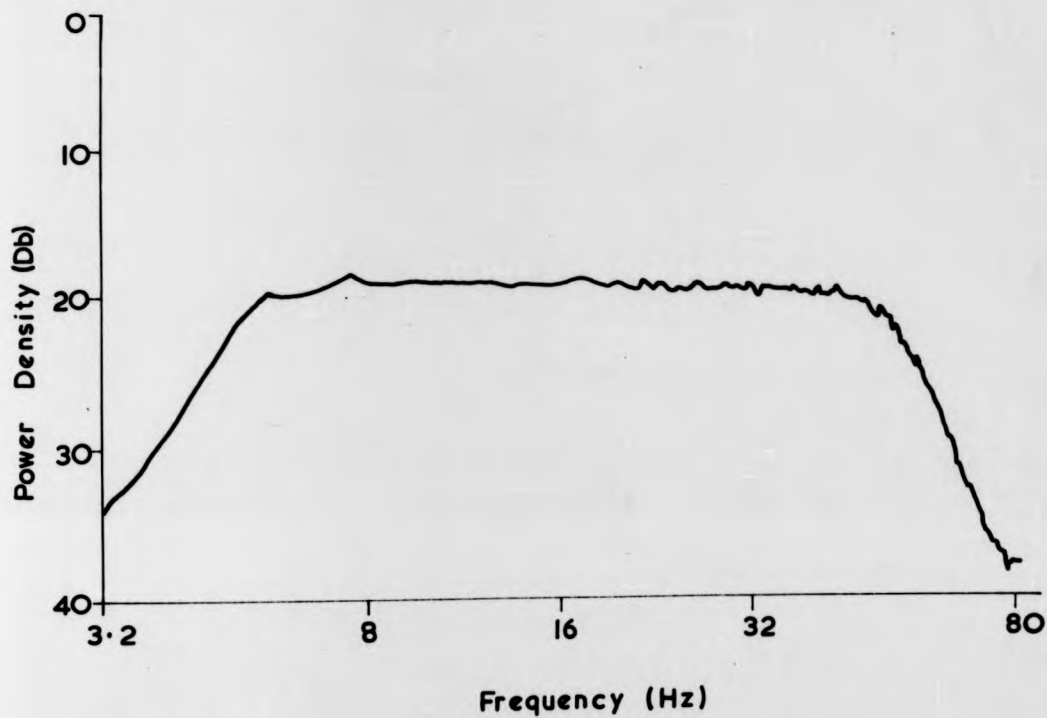
FIG. 4.11.



Standardised Peak Probability Density Function

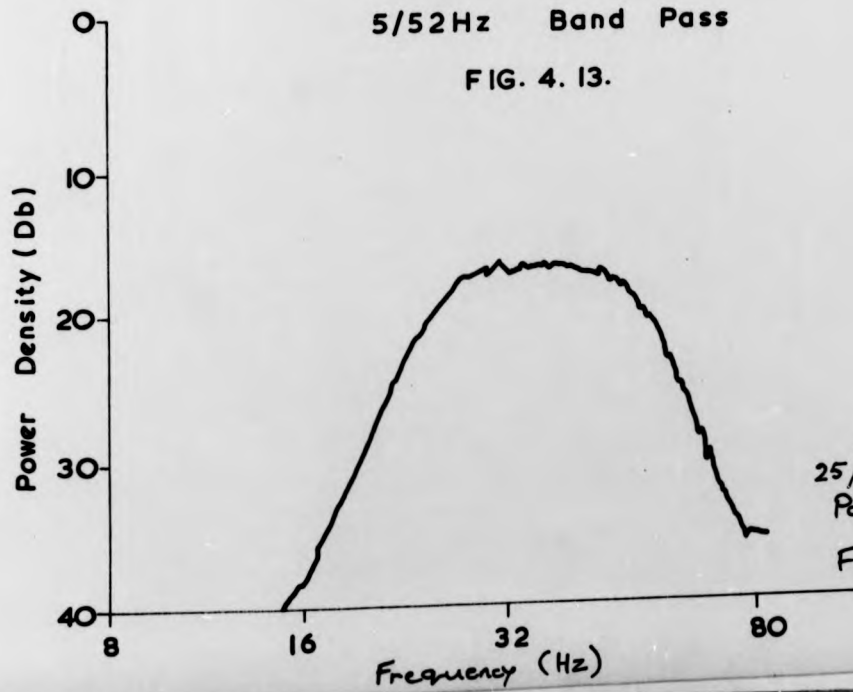
25/52Hz Band Pass

FIG. 4.12.



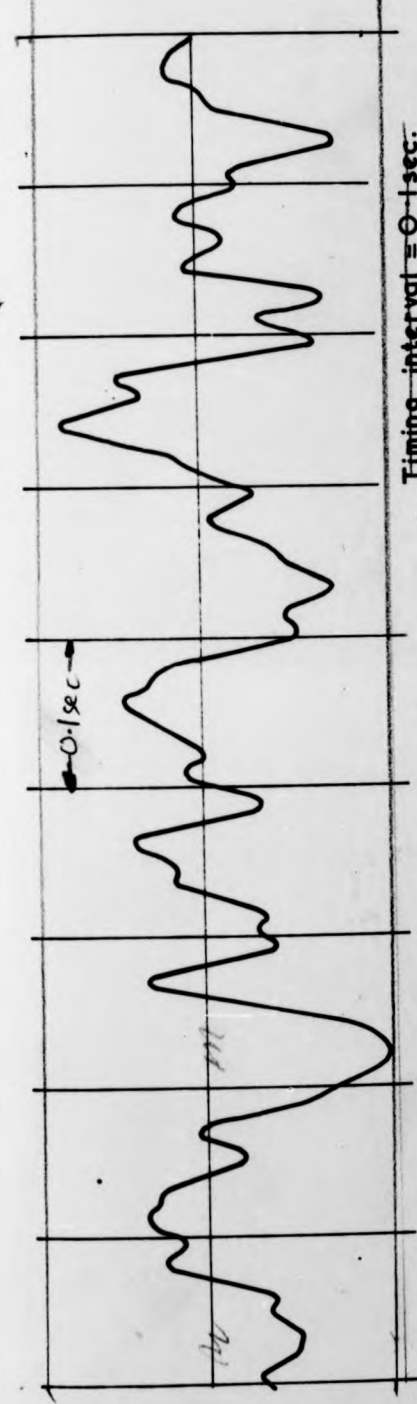
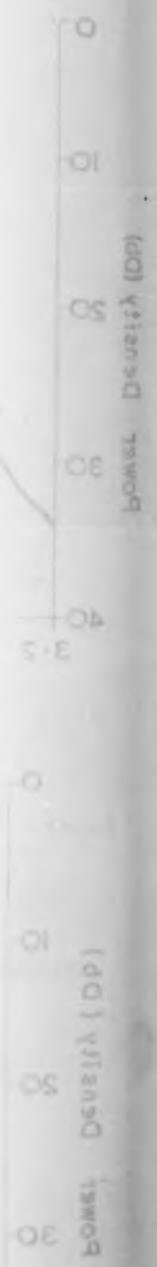
5/52 Hz Band Pass

FIG. 4.13.



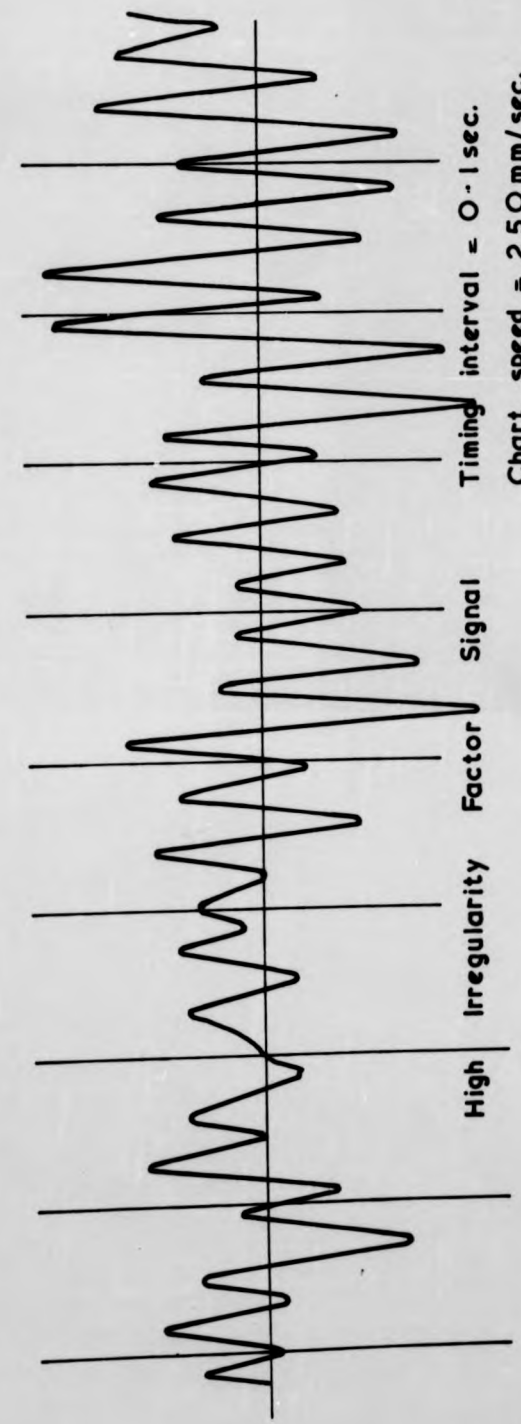
25/52 Hz Band  
Pass Signal.

FIG. 4.14.



Timing interval = 0.1 sec.  
Chart speed = 250 mm/sec.

Low Irregularity Factor Signal



Timing interval = 0.1 sec.  
Chart speed = 250 mm/sec.

High Irregularity Factor Signal

FIG. 4. 15.

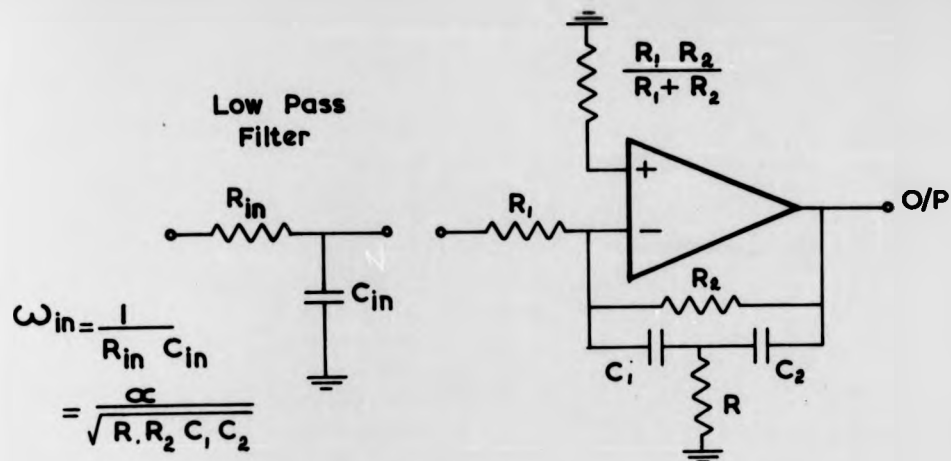
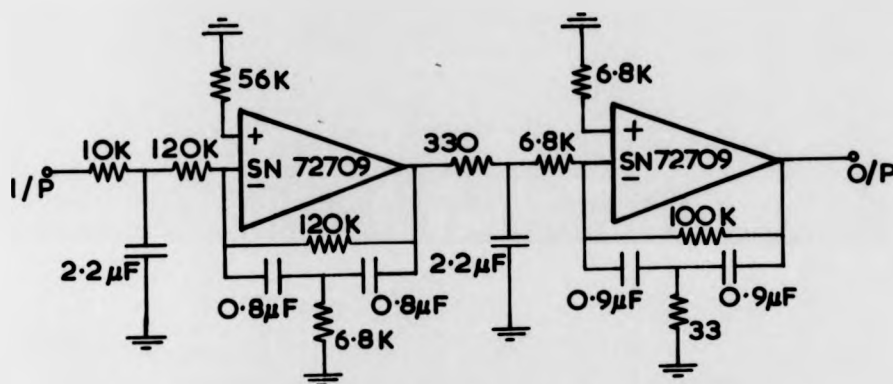
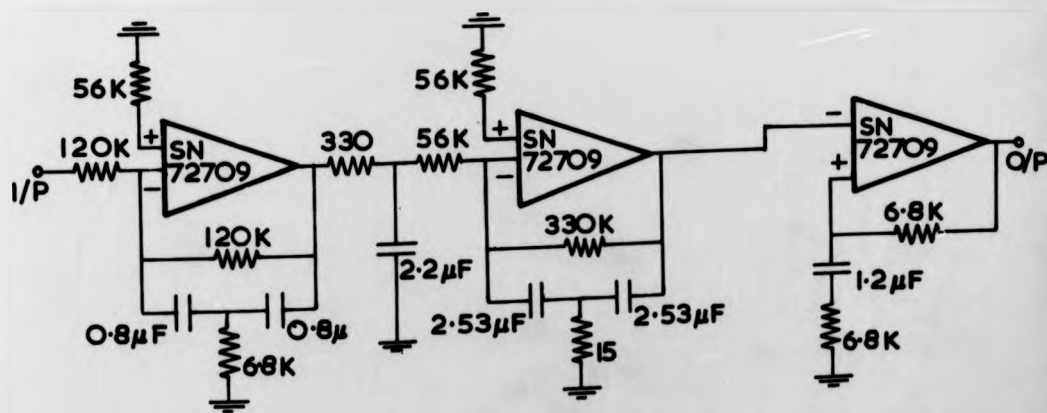


Fig. 4.16.



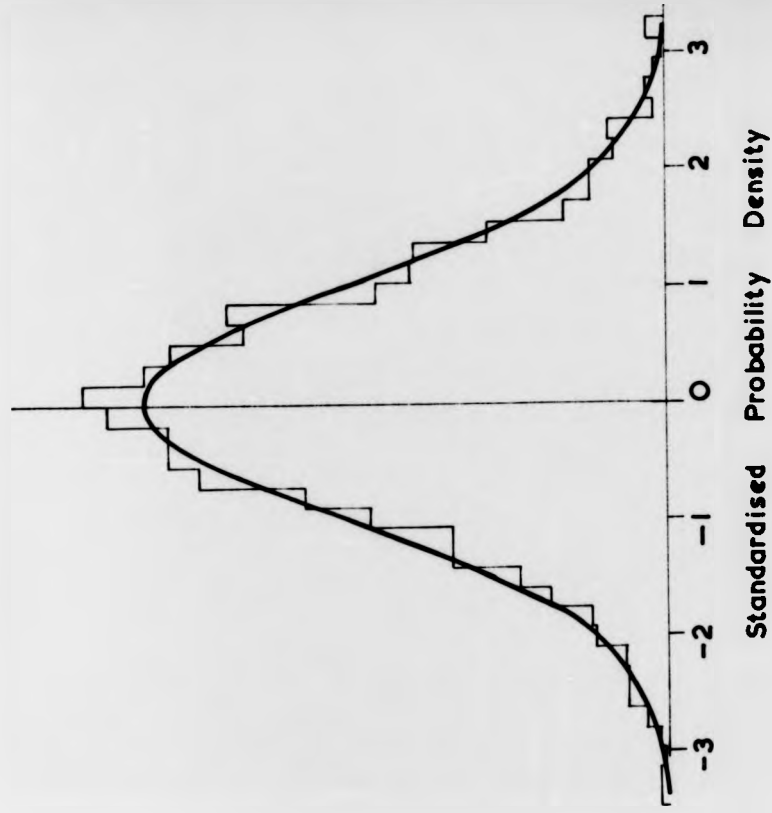
Low Irregularity Factor Filter

Fig 4.17.



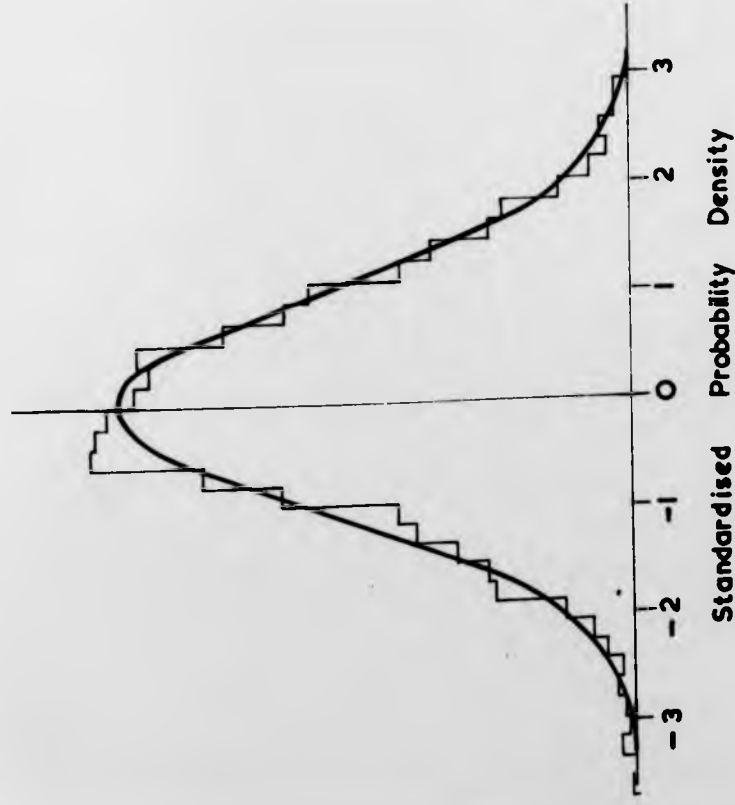
High Irregularity Factor Filter

Fig. 4.18.



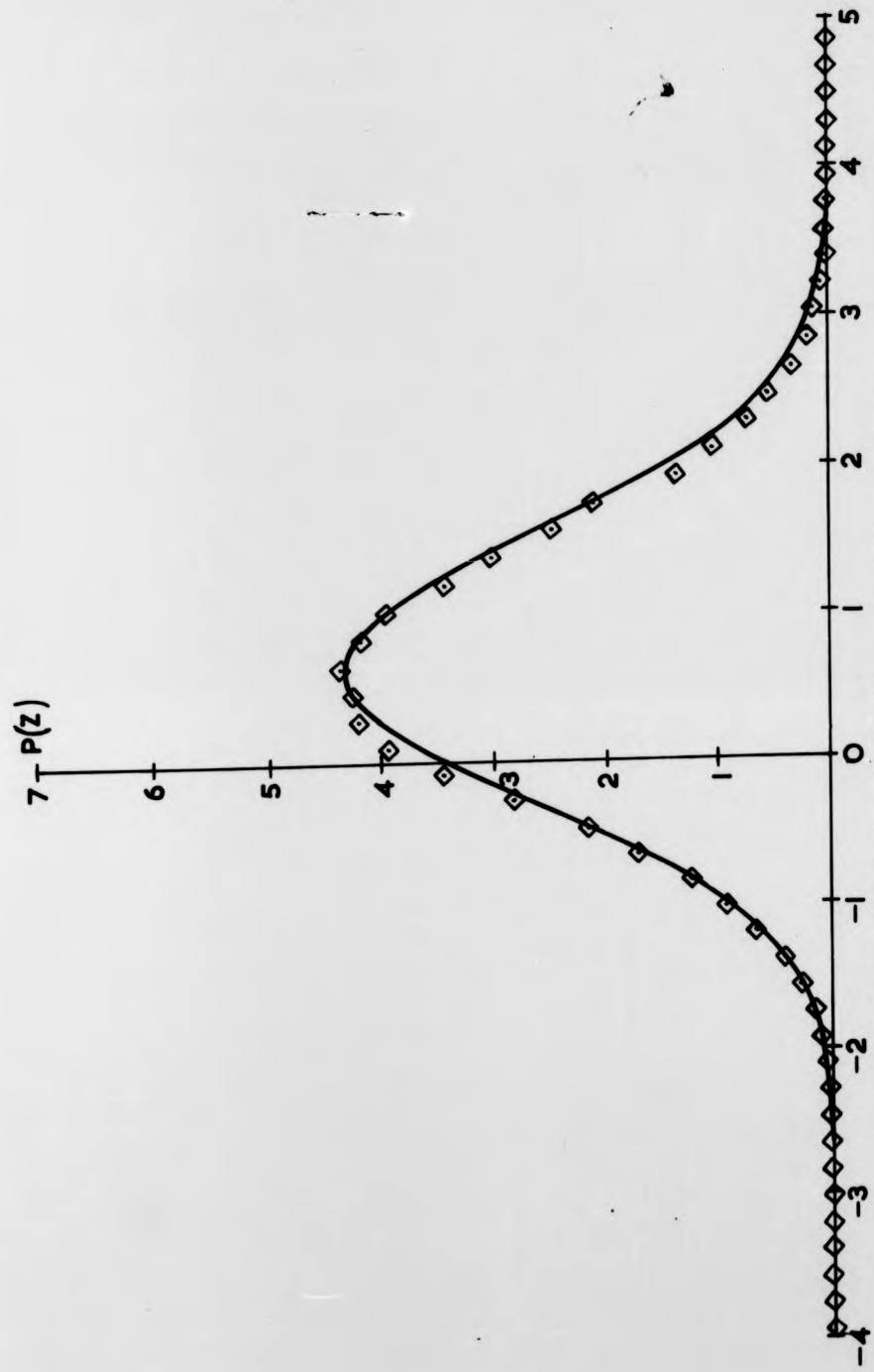
High Irregularity Factor  
Signal

FIG. 4.20.



Low Irregularity Factor  
Signal

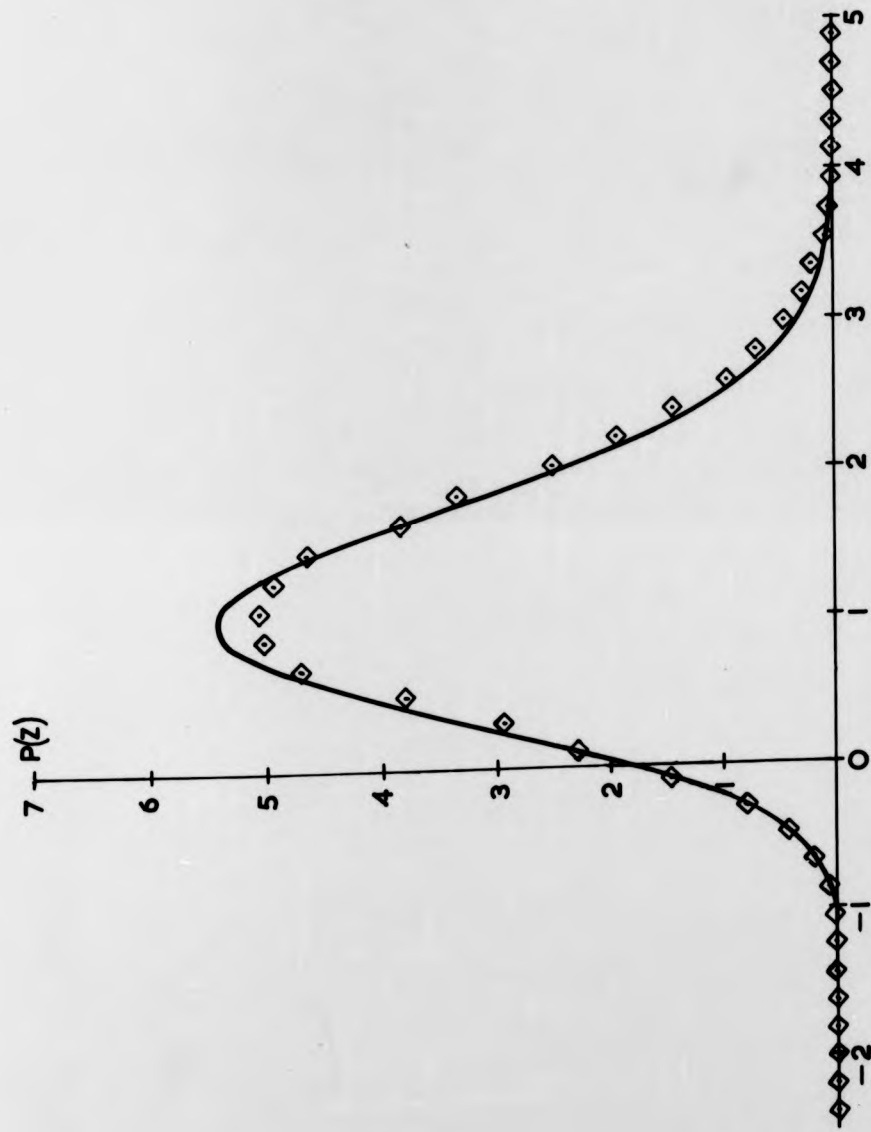
FIG. 4.19.



Standardised Peak Probability Density Function

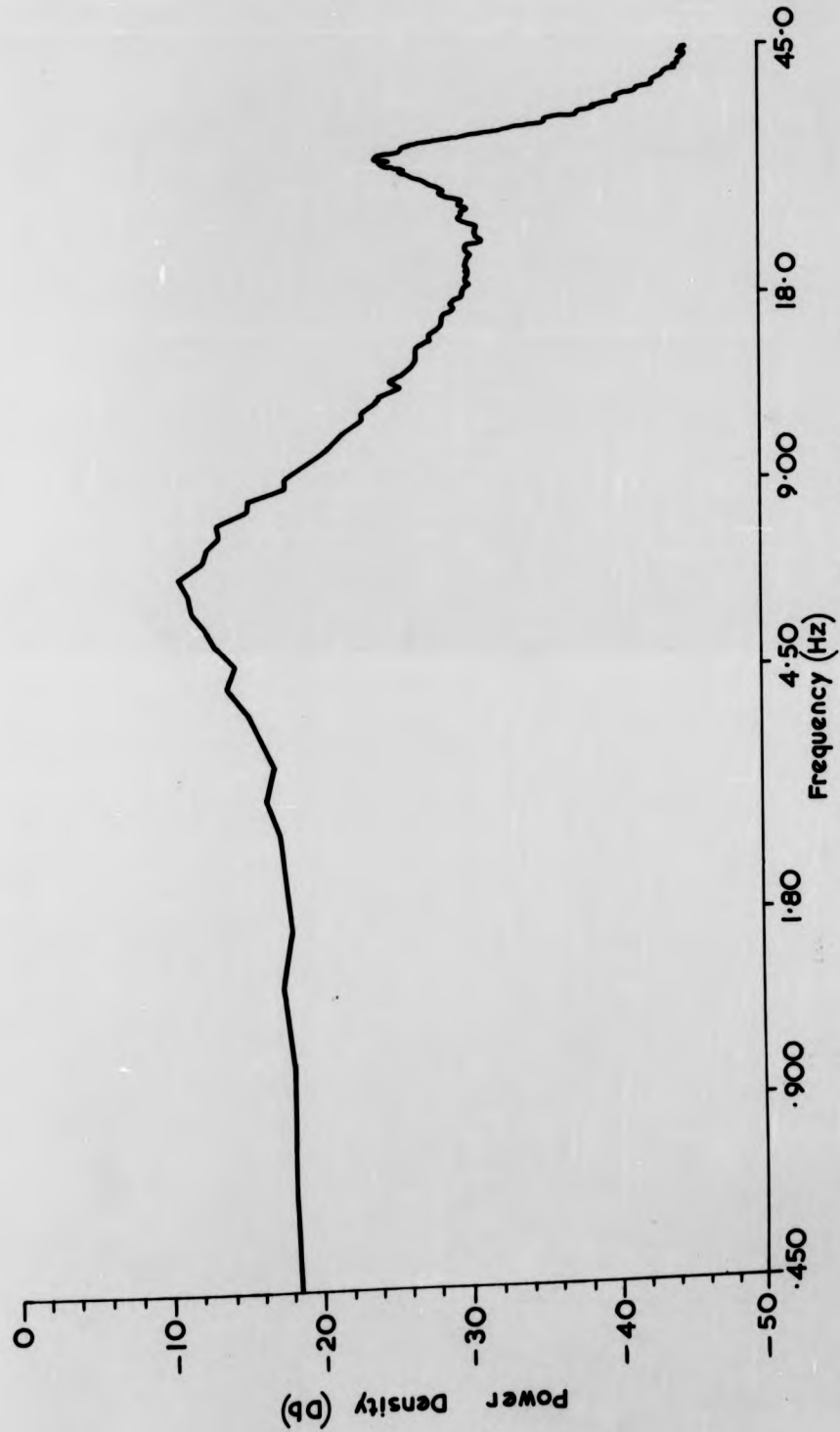
Low Irregularity Factor Signal

Fig. 4.21.



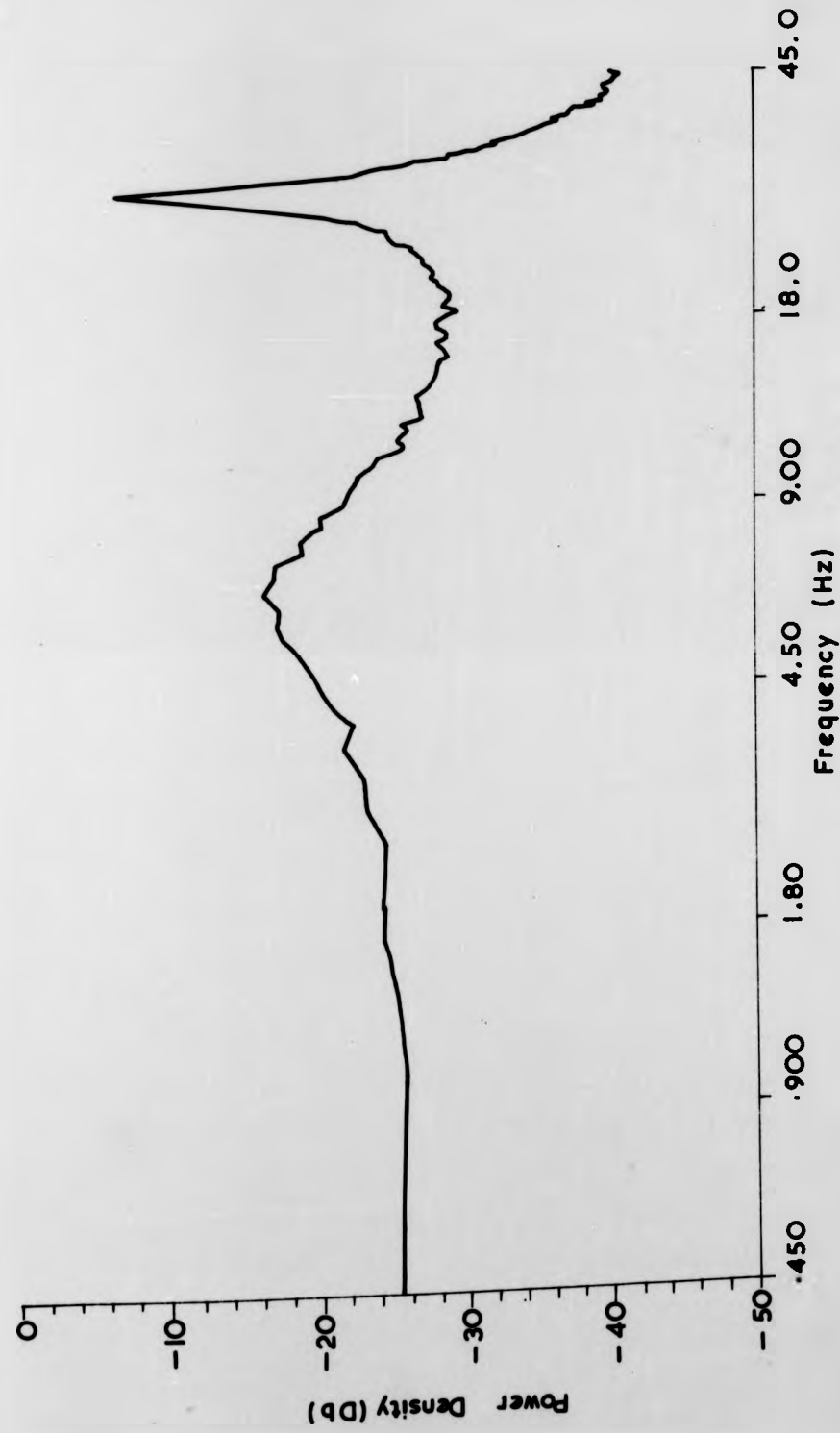
Standardised Peak Probability Density Function  
High Irregularity Factor Signal

Fig. 4.2.2.



Low Irregularity Factor Signal

FIG. 4.23.



High Irregularity Factor Signal

FIG. 4.24.

CHAPTER 5

FLAT STRIP CANTILEVER SPECIMEN

FATIGUE TEST RESULTS

1.	INTRODUCTION	91
2.	CONSTANT AMPLITUDE LIFE TESTS	91
3.	EDDY CURRENT CRACK DETECTION	94

## 1. INTRODUCTION

The test results presented in this chapter refer to the flat strip specimens shown in fig. 2.27, which were fatigued in cantilever bending using the servohydraulic test rig described in Chapter 2, Section 1.1. The test program was restricted to constant amplitude loading because of the significant amount of time which had to be spent on rig development, and because of the subsequent merging of this research project with the British Rail Contract. The fatigue test results can be grouped into two sections:-

2. Constant Amplitude Life Tests.
3. Eddy Current Crack Detection.

Constant amplitude test results are presented in a similar way in subsequent chapters, but the detail of this chapter is omitted.

## 2. CONSTANT AMPLITUDE LIFE TESTS

The objective of this part of the test program was to determine the specimen constant amplitude diagram. A series of 5 constant stress amplitude tests was conducted at a frequency of 20 Hz. with 4 specimens at each stress level. The results are summarised in Table 5.1. Test stress levels were chosen to carefully define the basic S/N diagram at the "knee of the curve". Out of 20 specimens tested seven failed from final fracture at the centre section; nine failed from fractures which were off-centre; and four specimens failed from cracks initiated at the top notch only.

Since it was intended to extend the testing to random loading, mathematical definition of this curve was necessary in order that subsequent cumulative damage calculations could be made. Thus, it is particularly important to realistically represent specimen behaviour for all stress levels encountered with random load waveforms, although in practice it is usually not possible to do this during a constant amplitude test program - as was the case here. It is required to extrapolate test data to establish the fatigue limit (for mild steels) and also to account for life at high peak stresses, a loading condition which is more usually described in terms of strain range because of the associated specimen plasticity. Nevertheless, suffice it to say that stress peaks high enough to cause failure on application of the first load cycle can be defined by the material ultimate tensile stress. This applies to axial loading conditions. In bending it is possible to sustain stresses which are above the UTS, so that specimen behaviour is then better described in terms of a collapse load stress. On this basis the estimated S/N diagram was represented by a Stussi type equation (27), where the static failure condition for this series of tests was represented by the specimen collapse load stress. The material was treated as being perfectly plastic at the point where bending stresses became equal to the ultimate tensile stress. Thus, for the case of a rectangular cross section cantilever beam the collapse stress then becomes  $1.5 \times \text{UTS}$  (54). Although this does not provide a true

description of the material behaviour under high dynamic loads it does provide a basis from which to define the experimental results in stress amplitude - cycles to failure terms.

The stress-life equation is written in the form:-

$$\frac{S - S_f}{S_u - S} = aN^{-b}$$

where,

- S = value of the stress peak
- S<sub>f</sub> = fatigue limit peak stress
- S<sub>u</sub> = material ultimate tensile stress or collapse stress
- a, b = constants
- N = mean life to failure (cycles)

Transforming the equation by taking logs gives a straight line:-

$$\log \left( \frac{S - S_f}{S_u - S} \right) = -b \log N + \log a$$

which is familiar in the form:-

$$y = mx + c$$

A computer program was written using an orthogonal polynomial least squares curve fit algorithm (55) to give the best fit to data straight line equation. The value of the fatigue limit (S<sub>f</sub>) was that value which gave the best fit to the data. The mean life at a given stress was determined as the antilog of the average log<sub>10</sub> of the specimen lives, where failure was defined as complete separation of the specimen. Therefore the S/N diagram was the 50% probability of failure curve. Statistical weights for the mean fatigue lives were inversely proportional to the estimated variance of log<sub>10</sub> cycles to failure for each test stress level.

The estimated 50% probability of failure equation is given in fig. 5.1, together with the plotted test data.

### 3. EDDY CURRENT CRACK DETECTION

The objective of this part of the program was to test the feasibility of using high sensitivity eddy current crack detection to establish a specimen fatigue life stage behaviour which could be correlated with the phases of crack initiation/microcrack propagation (associated with slip movement under resolved shear stresses) and macrocrack propagation (associated with principal tensile stresses).

A Forster Defectometer and hand probe were used for eddy current fatigue crack detection work, and instrument settings were made according to the manufacturer's instructions to give maximum defect sensitivity response. Defectometer readings were taken at regular intervals during the fatigue lives of 7 specimens. The results are summarised in Table 5.2 and typical Defectometer readings against life cycles are shown for different stress levels in figs. 5.2 and 5.3. The resulting Stage A/Total life behaviour was similar to that reported in earlier work (43). The data for the 7 specimens is shown in fig. 5.4 and provides good evidence of a linear relationship between Stage A and Total life for fatigue lives greater than about  $10^5$  cycles. The best straight line fit to the data was achieved by using an orthogonal polynomial curve fit with constraint algorithm (56). It was assumed that a constant proportion of life was spent in Stage A behaviour at all stress levels. Therefore, the best fit straight line was constrained to contain the origin. Mathematical definition of the straight line was

necessary to enable cumulative damage calculations to be extended to include the prediction of first cracking under random loading waveforms. Best fit straight lines without origin constraint generally resulted in relationships with positive abscissa intercepts. If this form of relationship is accepted, it raises particular life prediction problems since the implication is that above certain stress levels cracks are initiated immediately a stress cycle is applied. A possibility is that in this high stress/finite life range the Stage A/Total life relationship is non-linear. This possibility was not investigated, and it was considered that little error was introduced into cumulative damage calculations by assuming a linear relationship in this region.

Three specimens were part-fatigued and examined optically for the presence of fatigue cracks. The specimen which was sectioned while still in Stage A behaviour contained no cracks. The other two specimens were sectioned at the knee of the curve, i.e. Stage A/Stage B transition. The two Defectometer responses and corresponding crack lengths are shown in fig. 5.5. Photographs of fatigue cracks are shown in figs. 5.6 and 5.7. No Defectometer crack response calibration was carried out for this test program.

These results, together with the results of the constant amplitude tests reported in the following chapters, do indicate that by using high sensitivity eddy current crack detection techniques, the fatigue life can be split into two stages which accord with accepted fatigue crack growth (17):-

Stage A:- Microcrack Initiation and Propagation

Stage B:- Macrocrack Propagation.

It is in this respect that this work differs from that reported earlier (43), which concluded that usually cracks about 0.005 inches long were present when Stage B started, although this could vary from 0.003 to 0.010 ins.

Generally crack length definition in these and subsequently tested strip specimens was complicated by the fact that fatigue cracks within the detectable range of the Defectometer tended to propagate with non-uniform through-the-thickness lengths. This was particularly so with very small cracks, which tended to initiate as corner cracks. In general cracks of interest to this work, i.e. less than about 0.040 inches long, had the profiles shown in fig. 5.8, and their effective length was estimated as shown.



Nominal Peak Stress Tsi.	18.54	15.95	12.56	9.81	8.78
Mean of $\log_{10}$ of Lives	3.9441	4.3720	5.0434	5.6234	6.2471
Antilog of Mean Log Life (cycles)	8,792	23,552	110,514	420,093	1,766,300
Sample Variance	0.0043	0.0412	0.0140	0.0081	0.0733

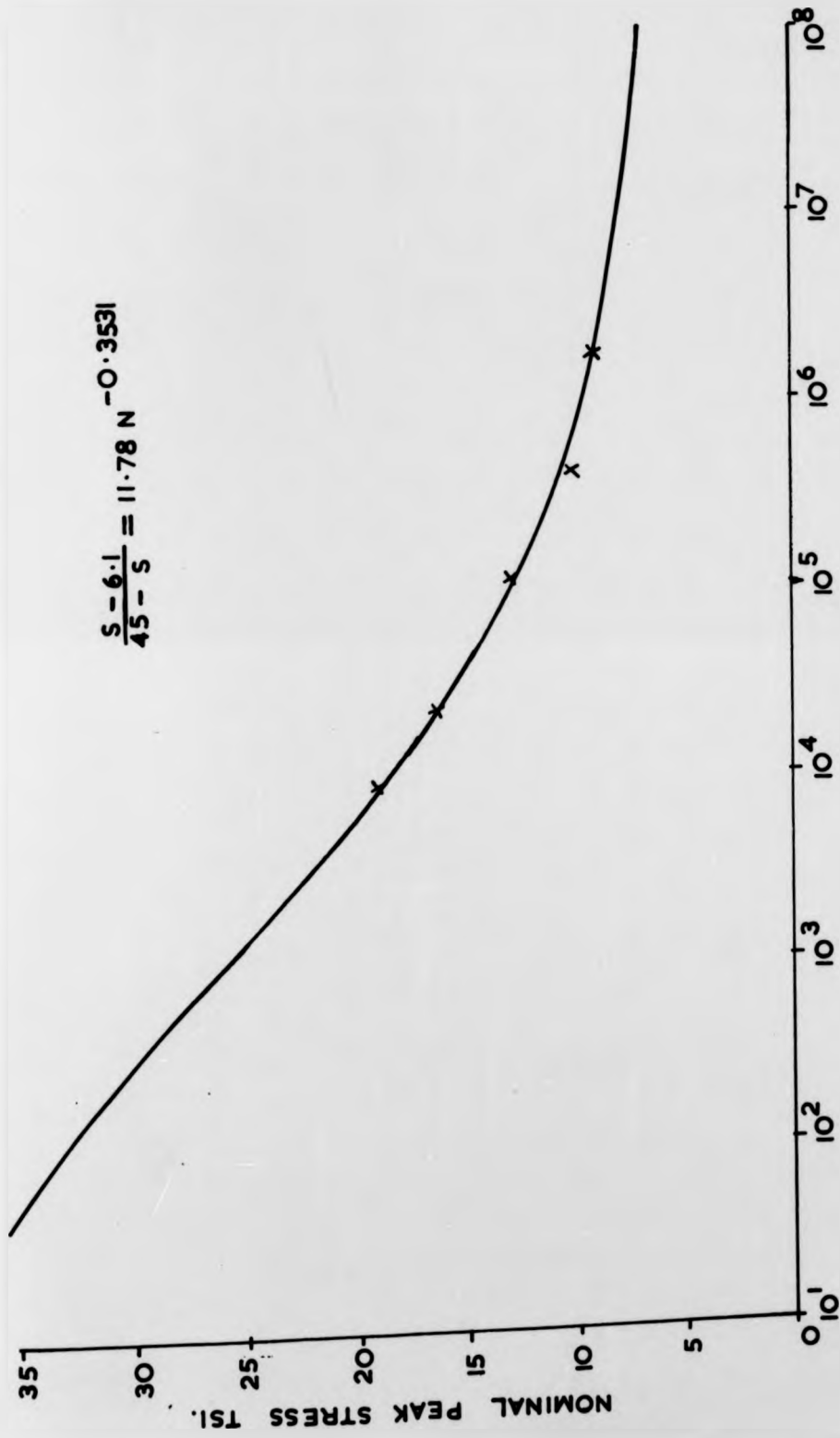
4 specimens tested at each stress level.

Table 5.1.

Specimen Identification	Nominal Peak Stress Tsi.	Stage A Life Cycles	Total Life Cycles
F20	12.14	38,000	103,000
F1	10.32	130,000	240,300
D15	9.92	220,000	340,000
C21	9.68	225,000	426,000
C16	9.45	315,000	518,500
E12	9.43	410,000	525,000
I16	9.45	580,000	890,000

Constant Amplitude Loading

Table 5.2.



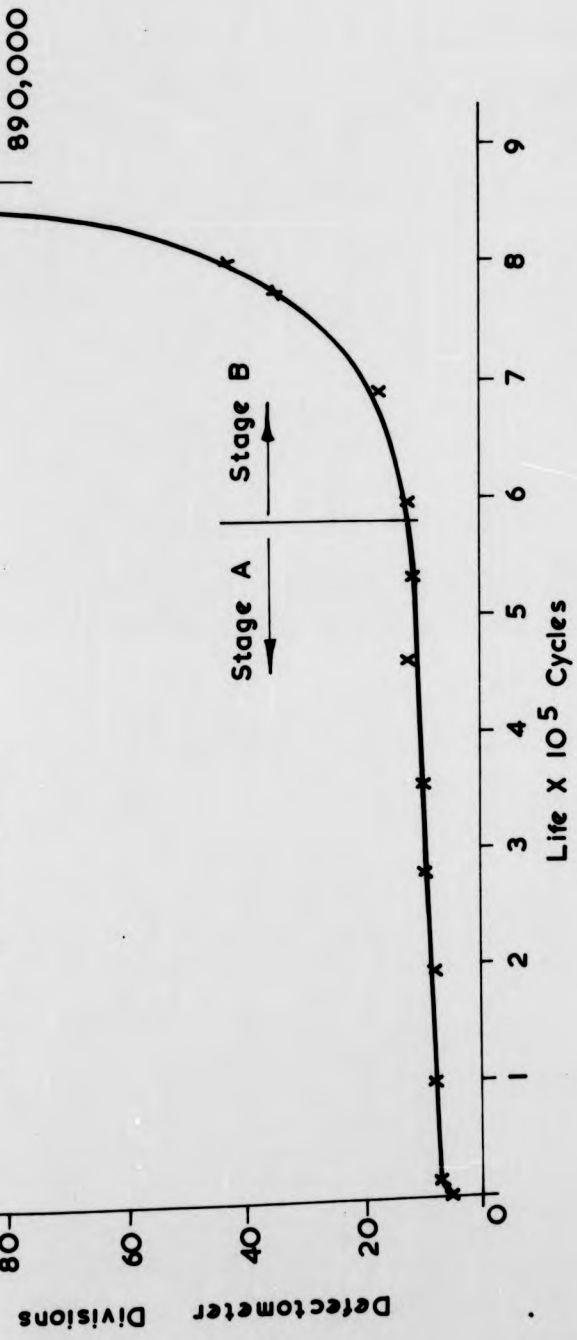
CYCLES TO FAILURE

FIG 5.1.

$\frac{12.5}{2-0.1} = 11.38 \text{ M} = 0.32 \text{ M}$

Specimen I16

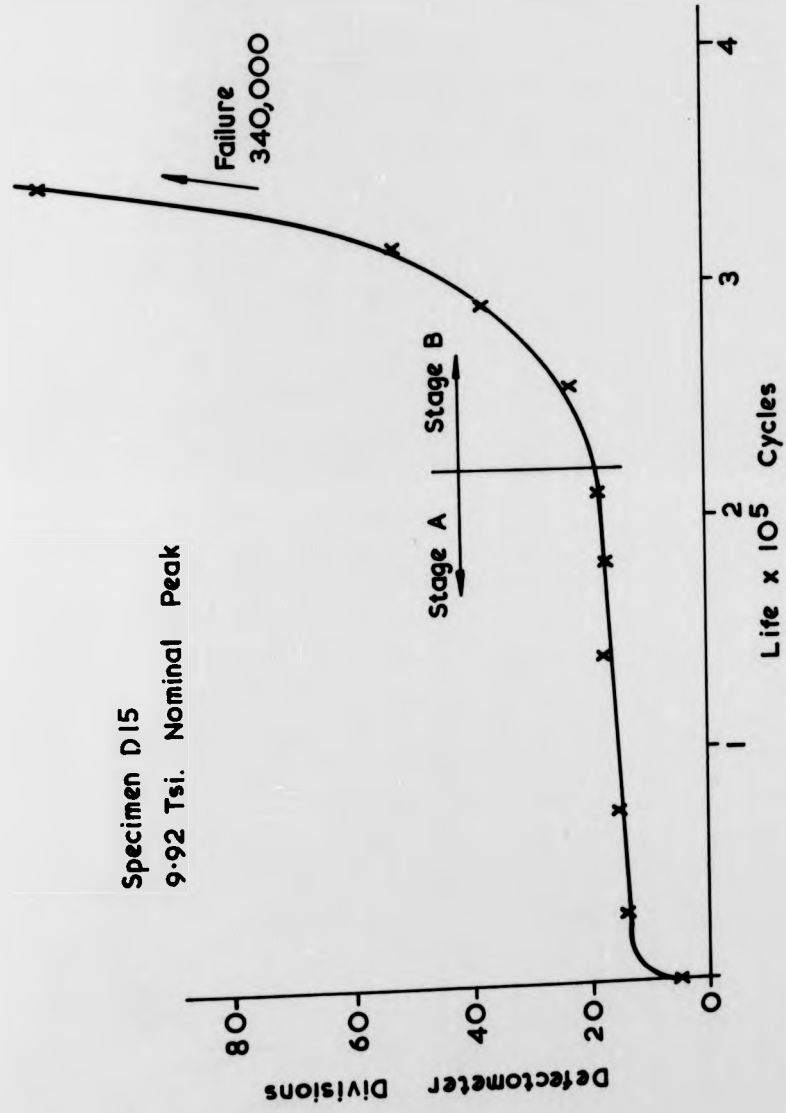
9.45 Tsi. Nominal Peak



Constant Amplitude Loading

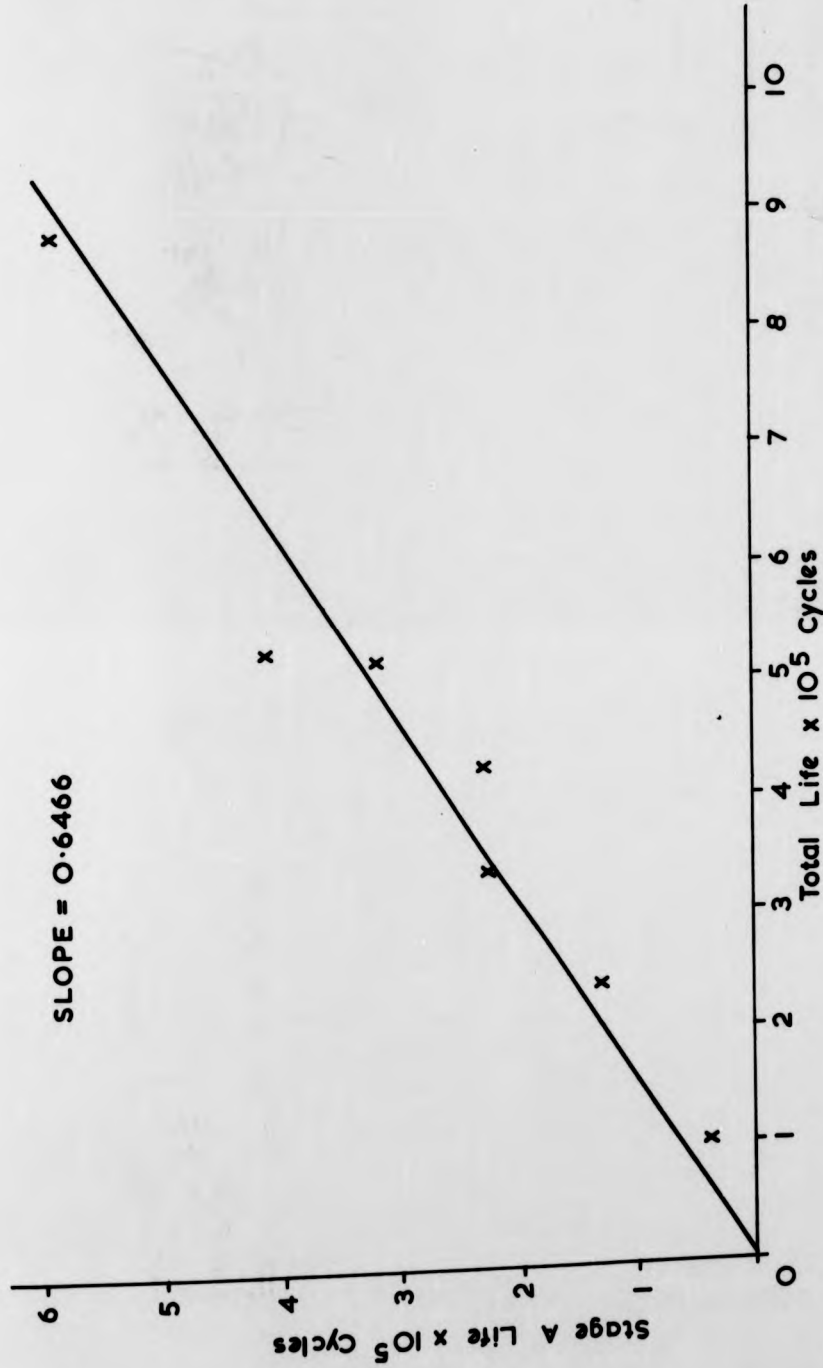
FIG. 5. 2.

Specimen D15  
9.92 Tsi. Nominal Peak



Constant Amplitude Loading

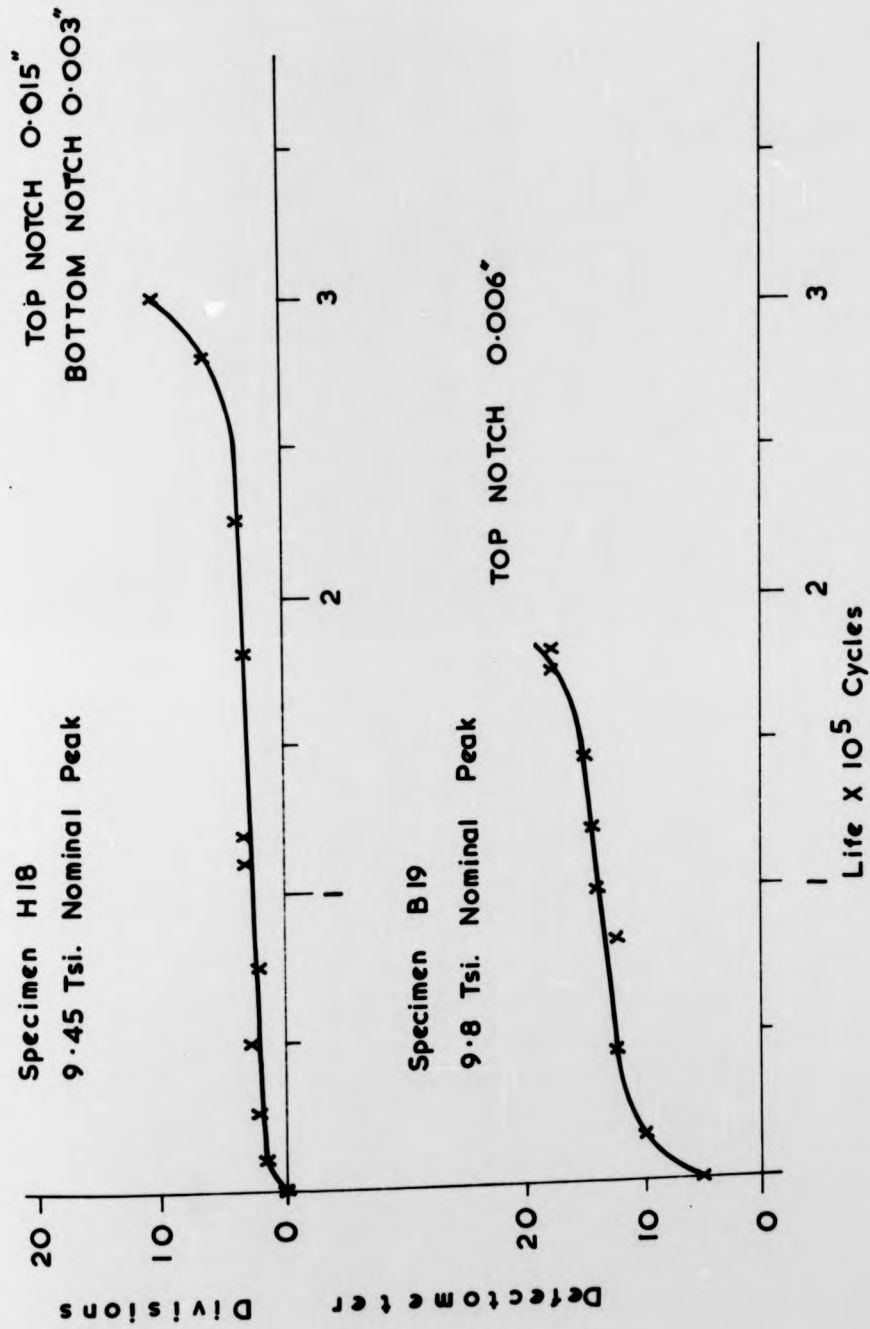
FIG. 5.3.



Constant Amplitude Loading

FIG. 5.4.

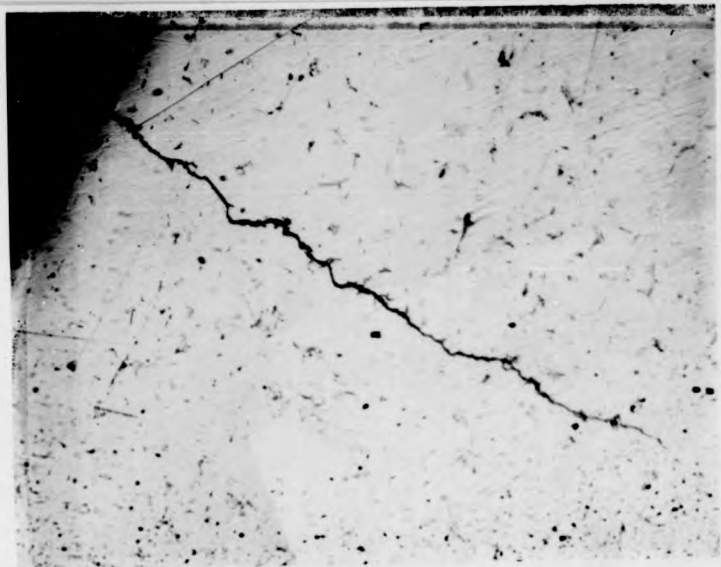
STOBE = 0.1119



Constant Amplitude Loading

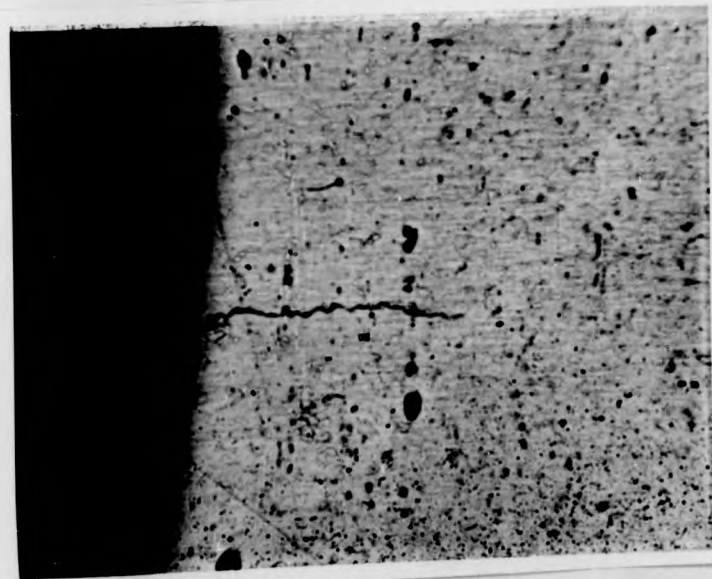
FIG. 5.5.

BOTTOM NOTCH 0.003,  
TOP NOTCH 0.012.

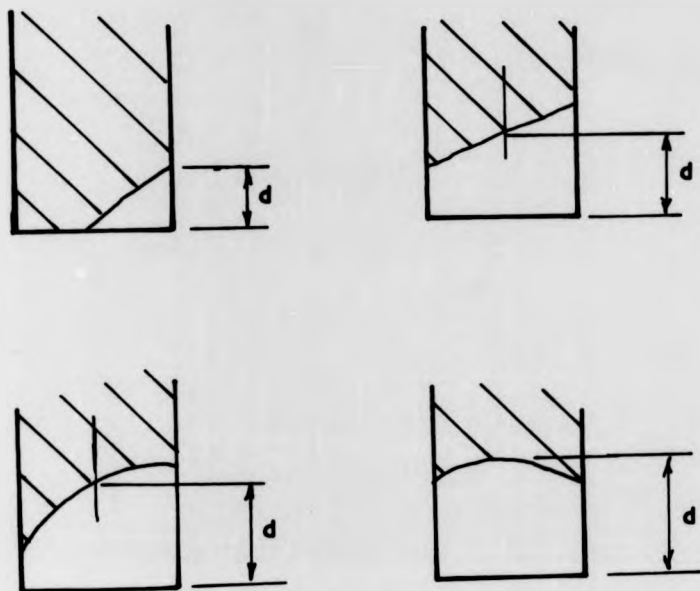


SPECIMEN H18 X 300  
0.015"  
FIG 5.6.

0.02 1st Notch of  
specimen H18



SPECIMEN B 19 X 300  
0.006"  
FIG 5.7.



**d - EQUIVALENT CRACK LENGTH**

**FIG 5.8.**

C H A P T E R 6

FLAT STRIP AXIAL SPECIMEN

FATIGUE TEST RESULTS

1.	INTRODUCTION	98
2.	CONSTANT AMPLITUDE LIFE TESTS	98
3.	CONSTANT AMPLITUDE EDDY CURRENT CRACK DETECTION	99
4.	RANDOM LOADING LIFE TESTS	100
5.	RANDOM LOADING EDDY CURRENT CRACK DETECTION	104

## 1. INTRODUCTION

The test results presented in this chapter refer to the flat strip specimens shown in fig. 2.28 which were fatigued in axial tension/compression about a small mean tensile load - 3 Tsi. nominal - using the servohydraulic test rig described in Chapter 2, Section 1.2. Fatigue testing was carried out under constant amplitude and two random loading waveforms. The fatigue test results can be grouped into the following sections:-

2. Constant Amplitude Life Tests.
3. Constant Amplitude Eddy Current Crack Detection.
4. Random Loading Life Tests.
5. Random Loading Eddy Current Crack Detection.

The general principles of presentation for constant amplitude results established in Chapter 5 apply here.

## 2. CONSTANT AMPLITUDE LIFE TESTS

The objective of this part of the test program was to determine the specimen constant amplitude diagram. A total of 27 specimens were tested at a frequency of 30 Hz. The test results are summarised in Table 6.1. Test stress levels were chosen to carefully define the basic S/N diagram, particularly at the "knee of the curve".

The equation of the S/N curve was determined by a least squares fit of lives to the Stussi equation, where static failure condition was represented by the material UTS. The equation together with the plotted test data is presented in fig. 6.1.

### 3. CONSTANT AMPLITUDE EDDY CURRENT CRACK DETECTION

Defectometer readings were taken at regular intervals during the fatigue lives of 10 specimens. The results are summarised in Table 6.2, and typical plots of Defectometer readings against life cycles are shown for different stress levels in figs. 6.2 and 6.3. The previously observed two stage fatigue behaviour was present in all specimens tested, and fig. 6.4 shows the best fit straight line through the origin for the Stage A/Total life data.

A further 10 specimens were part-fatigued and sectioned and examined for fatigue cracks. No cracks were found in the two specimens which were sectioned towards the end of their estimated Stage A behaviour. The remaining specimens were sectioned to examine crack lengths present at the Stage A/Stage B transition and when Stage B behaviour was established. Except for one case, all specimens contained cracks which increased in length with amount of time spent in Stage B. Crack lengths were defined as outlined in Chapter 5. Sometimes several through-the-thickness sections were taken in order to properly define the crack front. The results are summarised in Table 6.3. Two Defectometer responses and corresponding crack lengths at the point of specimen sectioning are shown in fig. 6.5, with photographs of the fatigue cracks in figs. 6.6 and 6.7. The linear relationship between crack length and Defectometer response shown in fig. 6.8 was established from these results and was in accordance with the manufacturer's description of instrument performance when used with a high defect sensitivity setting.

#### 4. RANDOM LOADING LIFE TESTS

The principal objective of this series of tests was to investigate the effect of variations in signal irregularity factor on overall fatigue life for two random loading waveforms of defined Gaussian amplitude distribution and a common fundamental power spectrum shape. It is convenient to present the data under two headings:-

4.1 Statistical definition of random loading waveforms.

4.2 Fatigue results.

##### 4.1. Statistical Definition of Random Loading Waveforms

Two series of random tests were carried out under loading waveforms having the same fundamental double resonance power spectrum but different peak probability density distributions (or irregularity factors). The signals were synthesised (Chapter 4, Section 4) to give major differences in the overall waveform shape, and consequently have been designated "high irregularity factor signal" and "low irregularity factor signal".

The test rig transfer function was modified in order to achieve a flat amplitude/frequency closed loop response over the frequency range of the random signals so that there would be as little rig modification of the input signal as possible (Appendix A. Part 2. "Design Example").

Nevertheless, the objective here is to present a statistical description of the achieved test rig random stress waveforms. The two loading waveforms are shown in fig. 6.9 and are of the same form as the synthesised signals. Statistical measurements of amplitude probability density, peak probability density and power spectral density were made from the test rig strain gauge load cell output using

the on-line computer techniques which have been set out in Chapter 3. The amplitude probability density measurements are presented in Tables 6.4 and 6.5, and the chi-square goodness-of-fit tests at the 5% level of significance show that the hypothesis of normality can be accepted for achieved test rig stresses under both loading waveforms. The results are presented graphically in fig. 6.10 and enable a visual comparison to be made between observed and expected amplitude distributions.

Power Spectral density analysis details are given in Table 6.6. The results are shown in figs. 6.11 and 6.12, and when compared with the respective synthesised power spectra show no apparent modification by the test rig transfer function. However, this is essentially a qualitative comparison and what is probably more significant in a fatigue context is the reproduction of waveform irregularity, especially with regard to the small stress ranges in a waveform, as illustrated by the low irregularity factor waveform trace in fig. 6.9. The method of analysis of random signals in terms of range probability density distributions is not reliably established (41) and therefore the peak probability density distribution has been used to describe waveform irregularity. The details of peak probability density measurements are listed in Tables 6.7 and 6.8, and the graphs in figs. 6.13 and 6.14 enable a visual inspection to be made between the theoretical and achieved distributions for peak excursions at least to 4 x signal rms.

Peak and zero crossing frequencies for both waveforms were extracted from the peak/trough on-line analyses and are summarised for both the synthesised and the test rig signals in Table 6.9. These results again show little modification of the input signal in both cases, although the achieved stress measurements have been used in the presentation of random fatigue data and for cumulative damage analyses.

#### 4.2. Fatigue Results

Four series of tests were conducted with 3 specimens at each stress level for both random waveforms. Stress levels were chosen to define the high cycle life regions of the rms. stress/life curves. Test results are summarised in Tables 6.10 and 6.11.

Mathematical definition of the rms. stress/life (seconds) curve was necessary for cumulative damage analysis purposes. It is usually not practicable to run tests of very long lives, e.g. greater than  $10^7$  zero crossings. Thus, it is necessary to extrapolate test data to establish behaviour in this region, and with random loading the stress/life relationship generally is represented by a slowly falling curve rather than by an abrupt S/N fatigue limit type of behaviour. In addition, realistic representation of rms. stress/life behaviour in terms of cumulative damage analyses based on S/N data is not possible for the high stress/low life region where peak stress excursions within a random loading waveform approach the specimen collapse load.

The following stress-life equation was chosen to represent fatigue behaviour under random loading, on a nominal rms. stress/life (seconds) basis:-

$$S - S_f = aN^{-b}$$

where,

S = value of rms. stress

S<sub>f</sub> = fatigue limit under random loading  
(rms. stress)

a, b = constants

N = mean life to failure (seconds)

Transforming the equation by taking logs gives a straight line:-

$$\log(S - S_f) = -b \log N + \log a$$

which is familiar in the form:-

$$y = mx + c$$

A computer program was used to give the best fit to data straight line, and the value of the fatigue limit (S<sub>f</sub>) was that value which gave the best fit to the data. The mean life at a given stress was determined as the antilog of the average log<sub>10</sub> of the specimen lives - in seconds - where failure was defined as complete separation of the specimen. Therefore, the rms. stress/life diagram was the 50% probability of failure curve. Statistical weights for the mean fatigue lives were inversely proportional to the estimated variance of log<sub>10</sub> life to failure for each test stress level.

The estimated 50% probability of failure equation is given in fig. 6.15 together with the plotted test data for both waveforms. The best fit to data was obtained with a fatigue limit of zero. The results are expressed in terms of peaks, positive zero crossings and positive peaks to failure in figs. 6.16, 6.17, and 6.18 by using the data of Table 6.9.

## 5. RANDOM LOADING LOW FREQUENCY SIGNAL BEHAVIOUR

The objective of this part of the test program was to investigate whether a two-stage behaviour similar to that present under constant amplitude loading could be established for random loading, and to examine the effect of variations in signal irregularity factor on this behaviour.

Defectometer responses were taken for 5 specimens fatigued under each random waveform. Typical plots for the high irregularity factor signal are shown in fig. 6.19 and 6.20 for two different stress levels, and fig. 6.21 shows the straight line best fit to data through the origin. Similar results for the low irregularity factor signal are presented in figs. 6.22, 6.23 and 6.24. The Stage A/Total life data is summarised in Tables 6.12 and 6.13 for both waveforms.

Specimen sectioning was carried out in order to determine the Defectometer crack length response as related to this two-stage behaviour. Sectioning and optical examination for cracks was carried out for 7 specimens fatigued by the low irregularity factor signal, and for 5 specimens fatigued by the high irregularity factor signal. Again, no cracks were found in the two specimens which were sectioned while still showing Stage A behaviour. Specimens sectioned at the Stage A/Stage B transition all contained cracks which increased in length as Stage B behaviour progressed. Typical Defectometer plots and associated crack lengths at sectioning are shown for the low irregularity factor in fig. 6.25, with photographs

of cracks in figs. 6.26 and 6.27. Similar results are shown for the high irregularity factor signal in figs. 6.28, 6.29 and 6.30. The crack length-defectometer response information is summarised in Table 6.14 for both signals. The linear relationship between crack length and instrument eddy current response is shown in fig. 6.31 which contains data for both signals. The graph suggests that there is no significant difference in terms of Defectometer reading for a given crack grown under either loading waveform.

Specimen Identification	Peak Nominal Stress Tsi.	Life Failure Cycles
F20	18.0	910
C1	16.5	3670
F6	15.5	4220
C10	14.25	5500
E9	13.5	12,471
E15	13.0	16,768
D19	11.83	26,961
H16	11.62	28,349
C6	11.45	32,631
E15	11.10	36,007
E6	10.5	52,115
A13	10.5	70,209
D4	9.21	81,998
F13	9.2	87,119
C4	9.83	94,420
D14	9.83	102,395
H14	9.04	114,130
D3	8.28	208,206
B10	8.75	260,409
B12	8.18	360,764
A7	7.85	488,795
E14	7.66	1,170,000
C19	7.55	1,339,700
C9	6.45	2,350,803
G17	7.0	2,644,411
C7	6.39	7,336,108
E12	6.4	12,647,829

Constant Amplitude Loading

Table G.1.

Specimen Identification	Nominal Peak Stress Tsi.	Stage A Life Cycles	Total Life Cycles
M4	11.5	29,000	46,300
G20	10.6	30,000	61,700
B11	9.74	58,000	91,000
E8	8.41	150,000	213,400
D21	8.15	130,000	216,200
E11	8.85	150,000	226,000
A3	8.19	280,000	444,500
H21	7.97	380,000	538,500
B19	7.97	550,000	757,100
C11	7.97	680,000	1,016,000

Constant Amplitude Loading

Table 6.2

Specimen Identification	Nominal Peak Stress Tsi.	Crack Length" Notch A		Crack Length" Notch B		Total Equivalent Crack Length	Total Defectometer Stage B Divisions
		Side 1	Side 2	Side 1	Side 2		
B4	9.5	-	-	-	-	0	3.0
D16	8.0	0.001	-	-	-	0.001	1.0
G6	9.75	-	-	0.011	0.016	0.011	6.0
D6	8.0	-	-	0.015	0.016	0.015	6.2
D18	8.2	-	-	0.036	0.014	0.025	10.6
F11	8.3	0.038	-	-	-	0.038	18.8
G18	8.7	-	0.012	0.037	-	0.049	18.4
G5	9.25	0.046	-	0.021	-	0.072	24.6
				0.005			

Constant Amplitude Loading

Table 6.3

Class Interval Midpoint (z)	Observed Frequency	Expected Frequency	Class Interval Midpoint (z)	Observed Frequency	Expected Frequency
-3.782	1	0.9	-0.037	594	596.4
-3.595	1	1.0	0.151	597	590.1
-3.408	1	1.8	0.338	515	563.0
-3.220	2	3.4	0.525	524	520.2
-3.032	5	6.1	0.712	467	463.4
-2.845	9	10.5	0.900	402	398.7
-2.659	17	17.6	1.087	354	331.2
-2.471	26	28.4	1.274	239	265.7
-2.284	35	44.3	1.461	213	205.8
-2.097	63	66.7	1.649	151	153.9
-1.909	88	96.9	1.836	104	111.2
-1.722	140	136.0	2.023	70	77.5
-1.535	190	184.4	2.211	60	52.2
-1.348	251	241.3	2.398	34	34.0
-1.160	320	305.0	2.585	27	21.3
-0.973	382	372.2	2.772	15	12.9
-0.786	456	438.7	2.960	9	7.6
-0.599	523	499.2	3.147	6	4.3
-0.411	543	548.5	3.334	5	4.8
-0.224	561	582.1			

Amplitude resolution = 0.381 V. = 0.187 x rms.

Signal rms. = 2.036 V.

Total no. of class intervals = 39

Total no. of samples = 8000

5% value of chisquare = 51

Sample chisquare value = 23.0

Low Irregularity Factor Signal

Table 6.4.

Class Interval Midpoint (z)	Observed Frequency	Expected Frequency	Class Interval Midpoint (z)	Observed Frequency	Expected Frequency
-3.384	1	3.9	0.045	573	545.8
-3.212	5	3.2	0.216	555	533.8
-3.041	5	5.4	0.387	493	507.0
-2.869	6	9.0	0.559	458	467.6
-2.698	14	14.5	0.730	453	418.6
-2.527	32	22.6	0.902	359	364.3
-2.355	35	34.4	1.073	286	307.7
-2.184	61	50.6	1.244	272	252.4
-2.012	80	72.5	1.416	188	201.1
-1.841	123	109.3	1.587	156	155.5
-1.670	135	136.0	1.759	117	116.8
-1.498	168	178.4	1.930	79	85.2
-1.327	193	227.1	2.101	63	60.4
-1.155	250	280.8	2.273	46	41.5
-0.984	361	337.1	2.444	31	27.8
-0.813	341	393.1	2.616	14	18.0
-0.641	463	445.1	2.787	12	11.3
-0.470	467	489.5	2.958	7	6.9
-0.298	545	522.7	3.130	5	9.3
-0.127	545	542.0			

Amplitude resolution = 0.332 V. = 0.171 x rms.

Signal rms. = 1.939 V.

Total no. of class intervals = 39

Total no. of samples = 8000

5% value of chisquare = 51

Sample chisquare value = 47.5

High Irregularity Factor Signal

Table 6.5.

Degrees of Freedom	=	792
Sampling Frequency	=	100 Hz.
Signal rms.	=	2.036 V.

Low Irregularity Factor Signal

Degrees of Freedom	=	800
Sampling Frequency	=	100 Hz.
Signal rms.	=	1.460 V.

High Irregularity Factor Signal

Table 6.6.

Class Interval Midpoint (z)	Observed Peak Frequency	Expected Peak Frequency	Class Interval Midpoint (z)	Observed Peak Frequency	Expected Peak Frequency
-5.77	0	0	0.092	1915	1777.0
-5.59	0	0	0.275	2047	1953.0
-5.41	0	0	0.458	2076	2062.8
-5.22	0	0	0.641	2124	2094.5
-5.04	0	0	0.825	2033	2044.3
-4.86	0	0	1.008	1915	1919.9
-4.67	0	0	1.191	1664	1734.1
-4.49	0	0	1.374	1467	1507.0
-4.31	0	0	1.558	1206	1260.5
-4.12	0	0	1.741	1030	1015.0
-3.94	0	0	1.924	665	786.9
-3.76	0	0	2.107	514	587.6
-3.57	0	0	2.291	351	422.7
-3.39	1	0.1	2.474	260	293.0
-3.21	1	0.3	2.657	152	195.7
-3.02	0	0.7	2.840	98	126.0
-2.84	1	1.5	3.024	56	78.3
-2.66	5	3.2	3.207	30	46.9
-2.47	7	6.5	3.390	16	27.1
-2.29	12	12.8	3.573	12	15.1
-2.11	24	24.0	3.757	7	8.1
-1.92	45	43.1	3.940	1	4.2
-1.74	79	74.3	4.123	1	2.1
-1.56	126	122.8	4.306	1	1.0
-1.37	203	194.8	4.490	0	0.5
-1.19	330	296.4	4.673	0	0.2
-1.01	463	432.7	4.856	0	0.1
-0.82	602	606.2	5.039	0	0
-0.64	857	815.2	5.223	0	0
-0.46	1066	1052.5	5.406	0	0
-0.27	1379	1304.8	5.589	0	0
-0.09	1678	1553.6	5.772	0	0

Signal rms. = 1.705 V.

Measurement time = 1475 sec.

Peaks = 26848

Positive Zero Crossings = 26521

Irregularity Factor = 0.506

Low Irregularity Factor Signal

Table 6.7.

Class Interval Midpoint (z)	Observed Peak Frequency	Expected Peak Frequency	Class Interval Midpoint (z)	Observed Peak Frequency	Expected Peak Frequency
-6.04	0	0	0.10	1528	1515.9
-5.85	0	0	0.29	1961	2165.6
-5.66	0	0	0.48	2548	2795.2
-5.47	0	0	0.67	3160	3292.7
-5.27	0	0	0.86	3371	3574.7
-5.08	0	0	1.06	3391	3608.7
-4.89	0	0	1.25	3309	3413.7
-4.70	0	0	1.44	3112	3044.7
-4.51	0	0	1.63	2569	2572.6
-4.32	0	0	1.82	2235	2066.8
-4.12	0	0	2.01	1666	1582.9
-3.93	0	0	2.21	1286	1158.1
-3.74	0	0	2.40	951	810.6
-3.55	0	0	2.59	638	543.4
-3.36	0	0	2.78	463	349.3
-3.16	0	0	2.97	301	215.4
-2.97	0	0	3.17	181	127.5
-2.78	0	0	3.36	116	72.5
-2.59	0	0	3.55	56	39.6
-2.40	0	0	3.74	36	20.8
-2.21	0	0	3.93	26	10.5
-2.01	0	0	4.12	9	5.1
-1.82	0	0	4.32	3	2.4
-1.63	1	0.2	4.51	2	1.1
-1.44	1	0.8	4.70	2	0.5
-1.25	1	3.5	4.89	0	0.2
-1.05	15	12.9	5.08	1	0.1
-0.86	46	40.4	5.28	0	0
-0.67	130	109.5	5.47	0	0
-0.48	276	257.0	5.66	0	0
-0.29	542	526.8	5.85	0	0
-0.10	978	949.2	6.04	0	0

Signal rms. = 1.629 V.

Measurement time = 1266 sec.

Peaks = 34911

Positive Zero Crossings = 31109

Irregularity Factor = 0.891

High Irregularity Factor Signal

Table 6.8.

		Irregularity Factor	Peaks /sec.	+ve Zero Crossings /sec.
Low Irregularity Factor Signal	Synthesised	0.585	10.22	10.07
	Achieved	0.506	17.97	9.09
High Irregularity Factor Signal	Synthesised	0.895	27.45	24.57
	Achieved	0.891	27.57	24.58
Constant Amplitude Signal		30 Hz.		

Table 6.9

Nominal Rms. Stress Tsi.	5.65	4.75	3.90	3.40
Mean of $\log_{10}$ of Lives	4.0281	4.3559	5.0071	5.4787
Antilog of Mean Log Life (seconds)	10,670	22,694	101,647	301,122
Sample Variance	0.0095	0.0057	0.0382	0.009

3 specimens tested at each stress level.

Low Irregularity Factor Signal

Table 6.10.

Nominal Rms. Stress Tsi.	4.95	3.70	3.0	2.7
Mean of $\log_{10}$ of Lives	3.5027	4.2498	4.7625	5.1099
Antilog of Mean Log Life (seconds)	3,182	17,776	57,870	128,791
Sample Variance	0.0102	0.0164	0.0004	0.0169

3 specimens tested at each stress level.

High Irregularity Factor Signal

Table 6.11.

Specimen Identification	Nominal Rms. Stress Tsi.	Stage A Life Seconds	Total Life Seconds
F15	5.05	7,000	13,400
D2	4.5	9,000	16,000
H15	4.0	22,500	35,250
A21	3.5	40,000	50,000
E1	3.4	60,000	86,400

Low Irregularity Factor Signal

Table 6.12

Specimen Identification	Nominal Rms. Stress Tsi.	Stage A Life Seconds	Total Life Seconds
F10	3.5	14,000	19,580
A14	3.2	30,000	44,500
F18	3.0	48,000	60,480
C18	2.85	72,500	99,460
E4	2.7	91,000	104,880

High Irregularity Factor Signal

Table 6.13

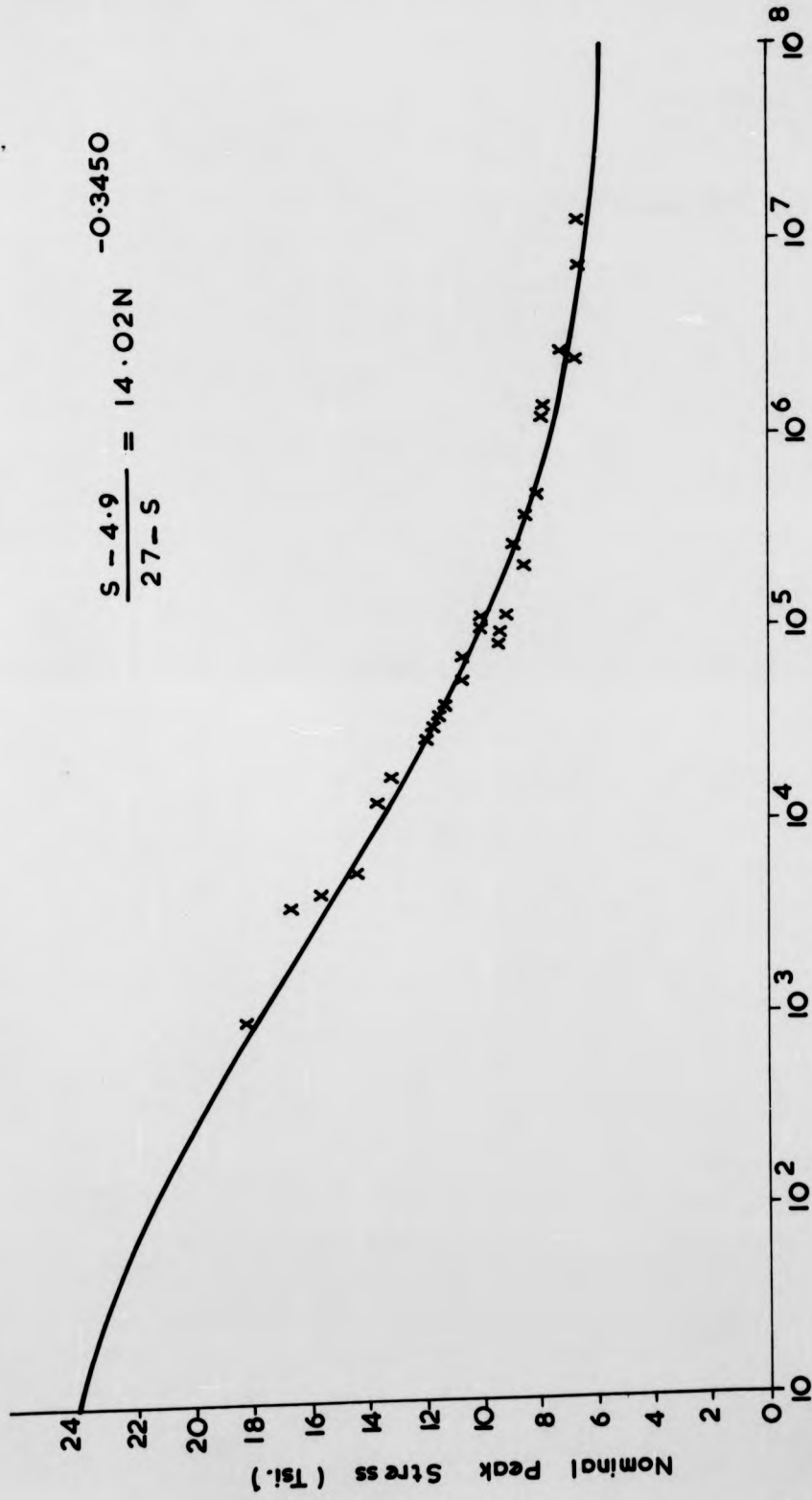
Specimen Identification	Nominal RMS Stress Tsi	Crack Length Notch A		Crack Length Notch B		Total Equivalent Crack Length	Total Defectometer Stage B Divisions
		Side 1	Side 2	Side 1	Side 2		
B14	3.85	-	-	0.001	0.0003	0.001	3
E5	3.7	0.006	-	-	-	0.006	9.2
A21	3.5	0.023	-	-	0.003	0.026	14.9
H17	3.7	-	0.027	-	0.003	0.030	25.6
F17	3.7	0.002	0.032	0.022	-	0.050	30
		0.002	0.024	0.014			
C15	3.65	0.002	0.024	0.040	0.043	0.065	42

Low Irregularity Factor Signal.

C3	3.75	-	2@ 0.001	2@ 0.003	0.007	0.008	6
D1	3.25	0.012	0.007	0.003	0.021	0.025	17
			0.001		0.004		
B17	3.5	0.002	-	0.001	0.030	0.032	31
					0.001		
A11	3.0	-	0.001	0.038	0.013	0.064	37
					0.021		
					0.019		
					0.001		

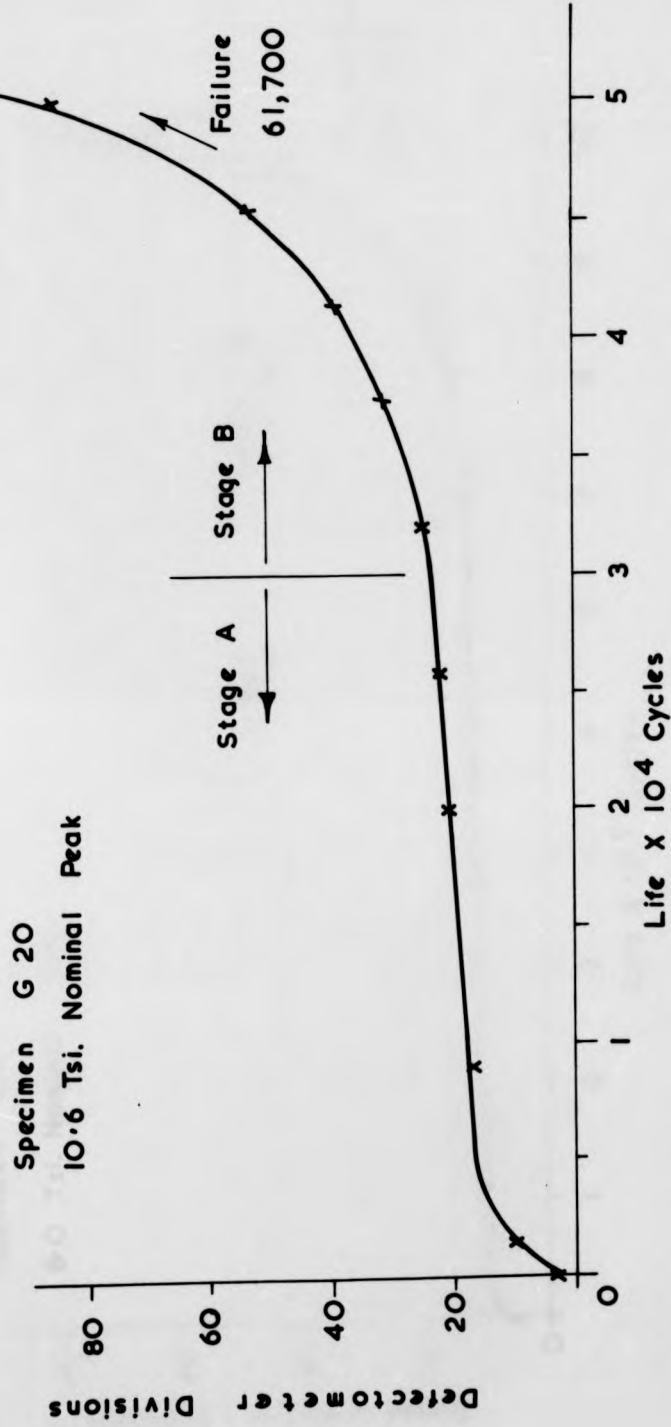
High Irregularity Factor Signal.

Table 6.14

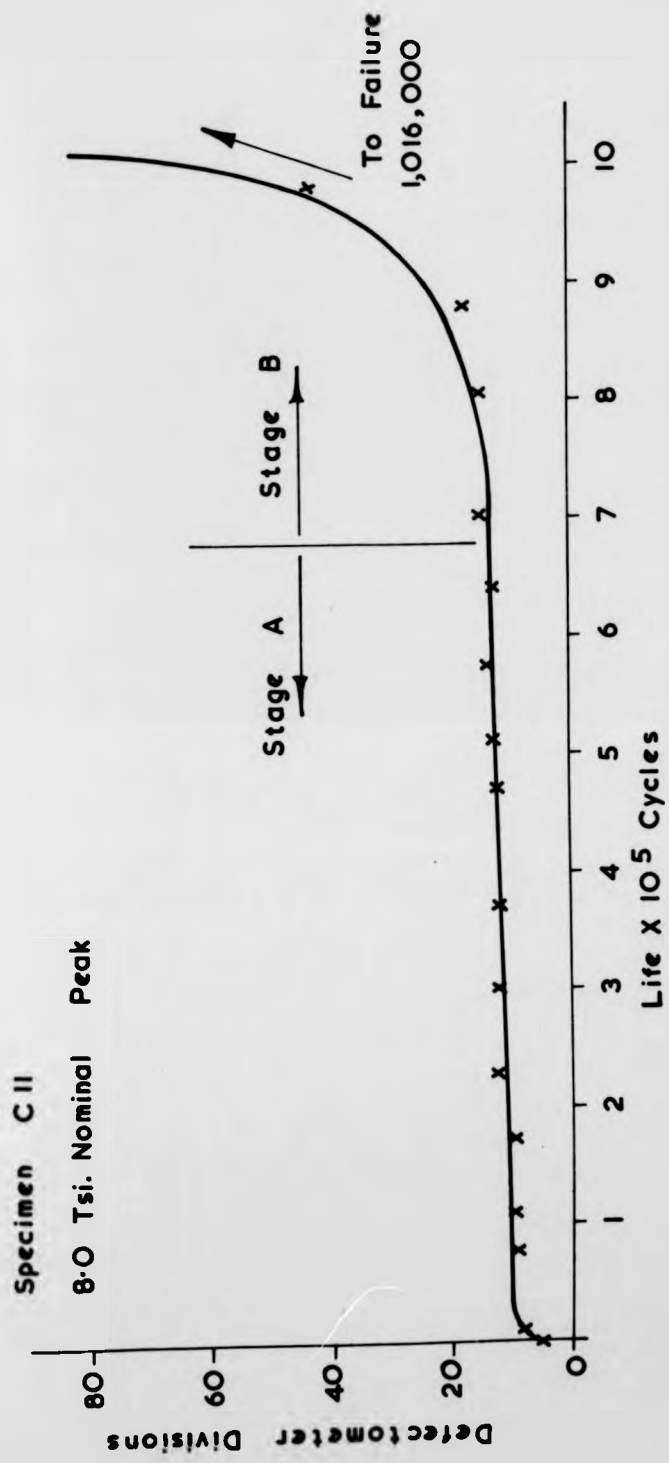


Cycles to Failure

FIG. 6.1

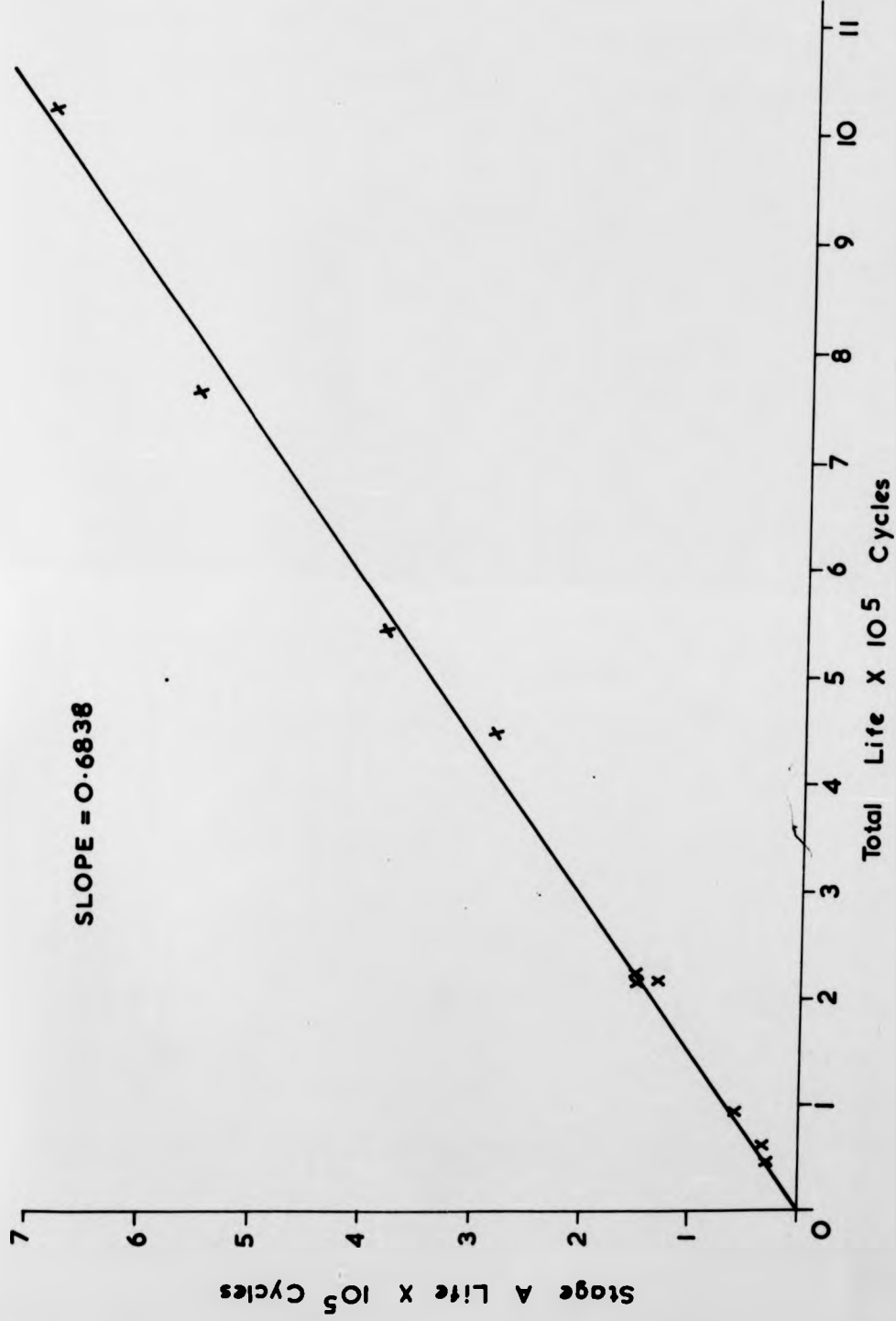


Constant Amplitude Loading  
FIG. 6.2.



Constant Amplitude Loading

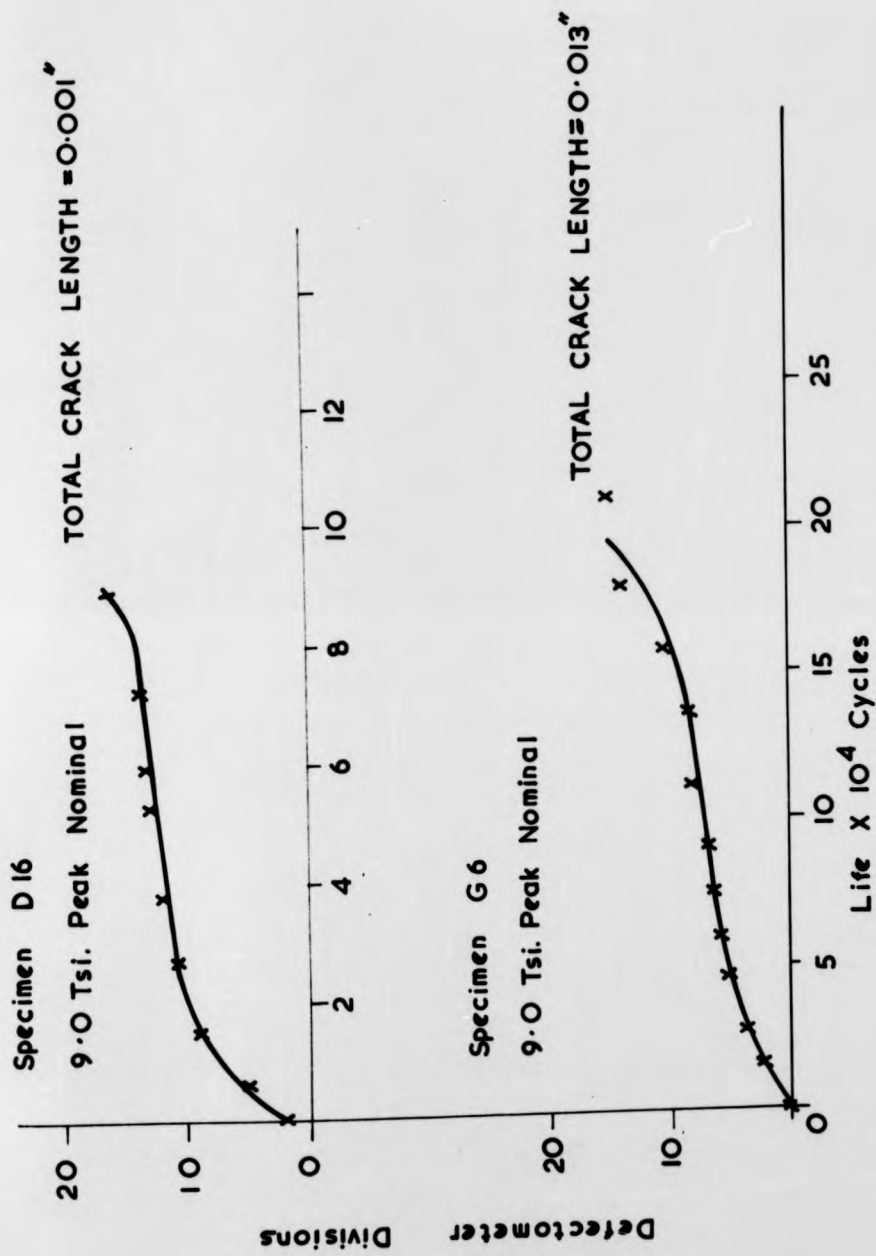
FIG. 6.3.



Constant Amplitude Tests

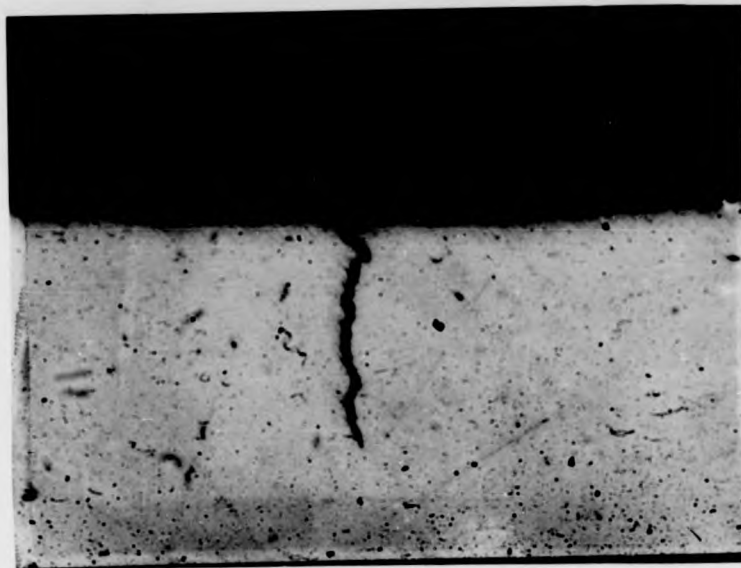
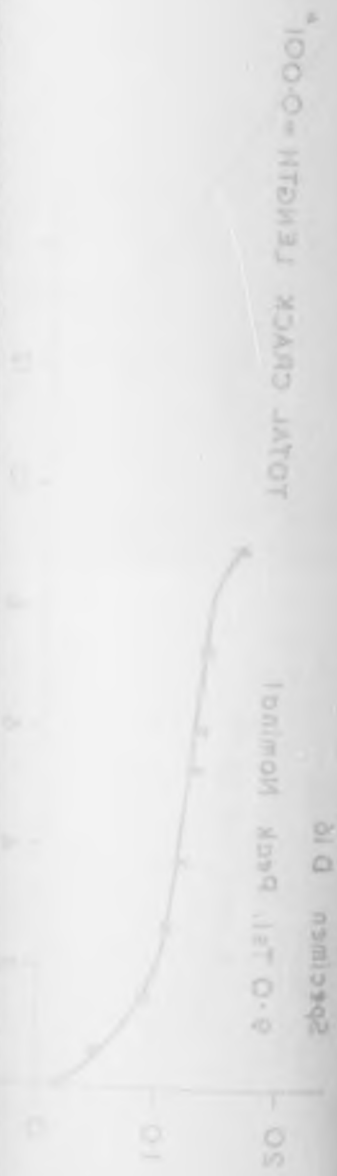
FIG. 6.4.

STOBE = 0.9838



Constant Amplitude Loading

FIG. 6.5.



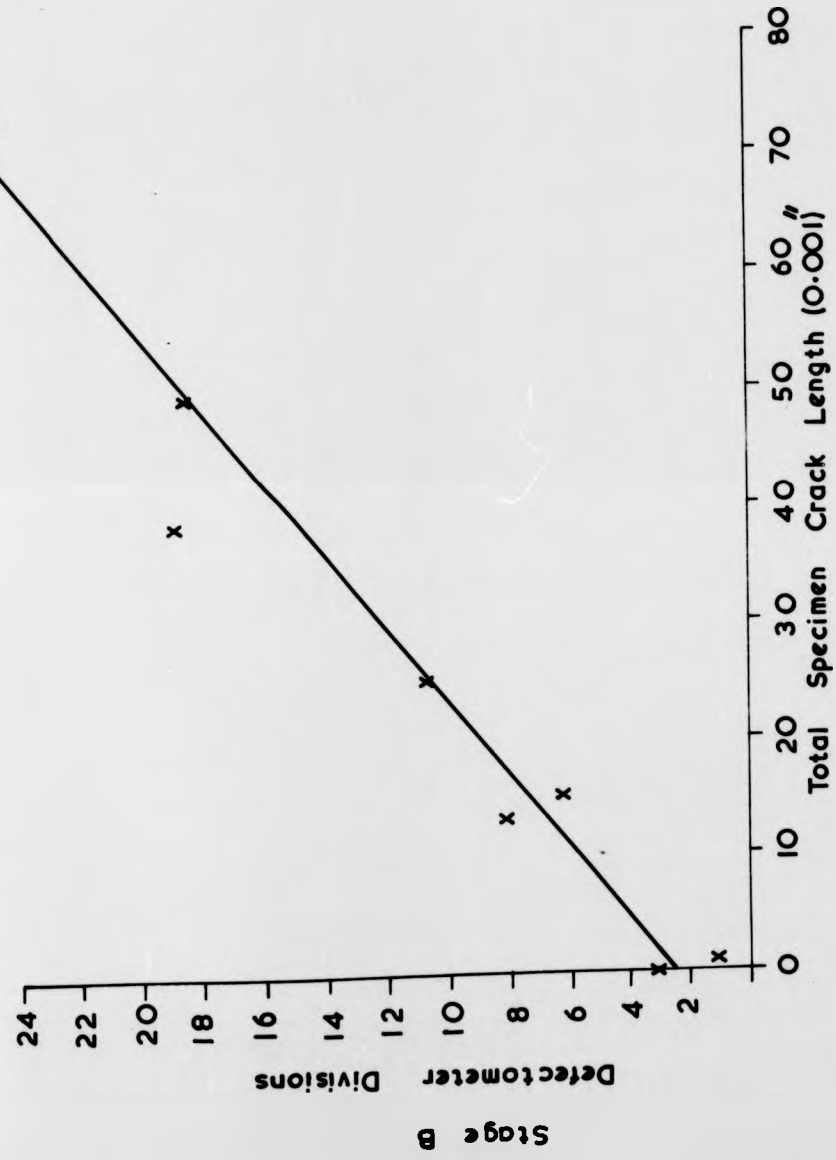
SPECIMEN G6 X160  
0.011"

FIG. 6.6.



SPECIMEN D16 X600  
0.001"

FIG. 6.7.



Constant Amplitude Tests.

FIG. 6.8.

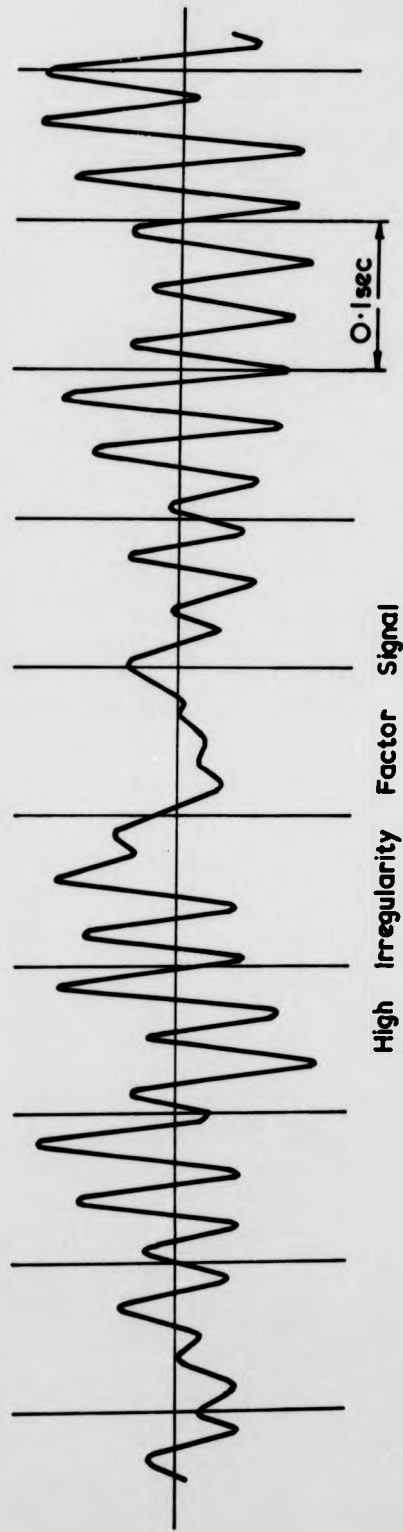
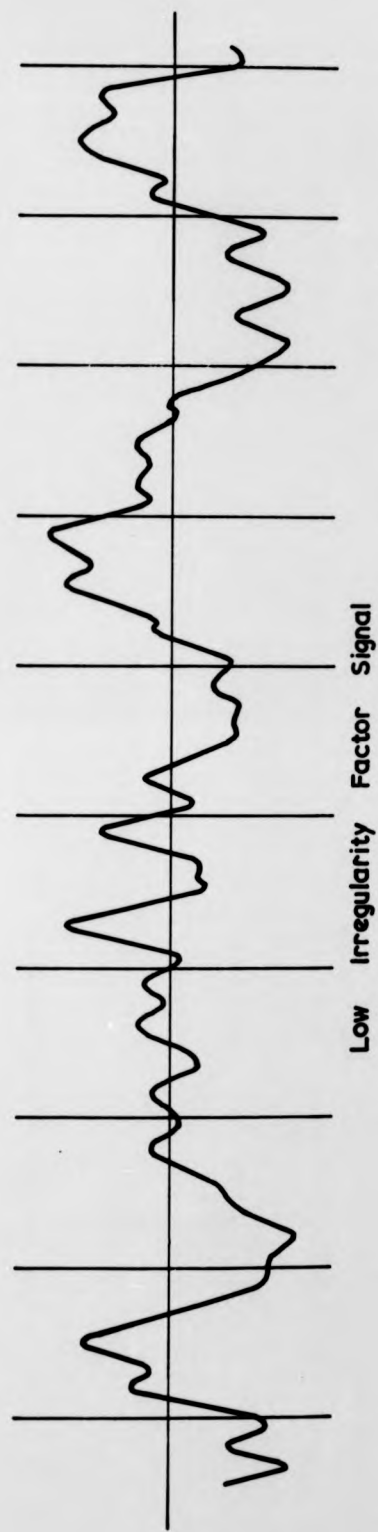


FIG. 6.9.

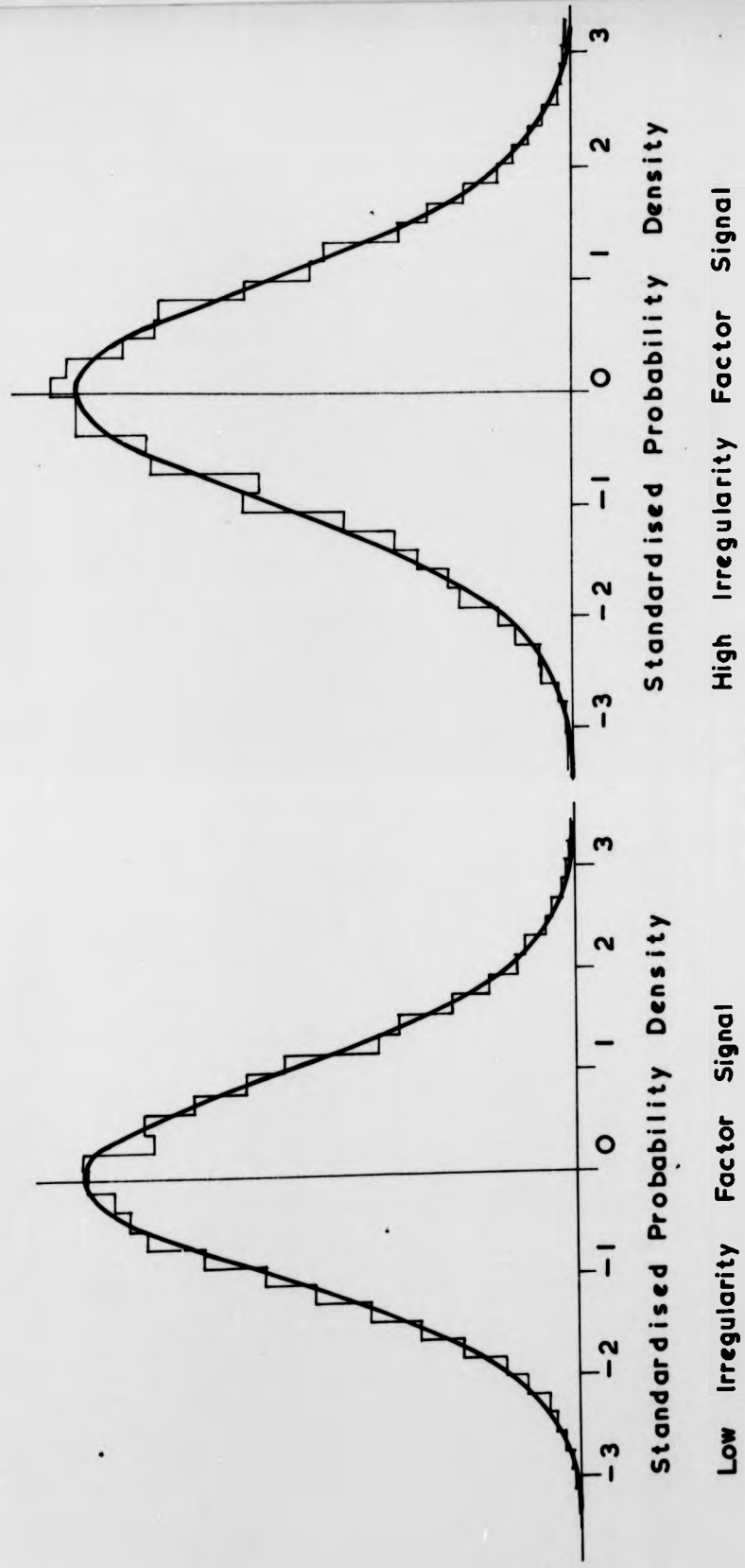
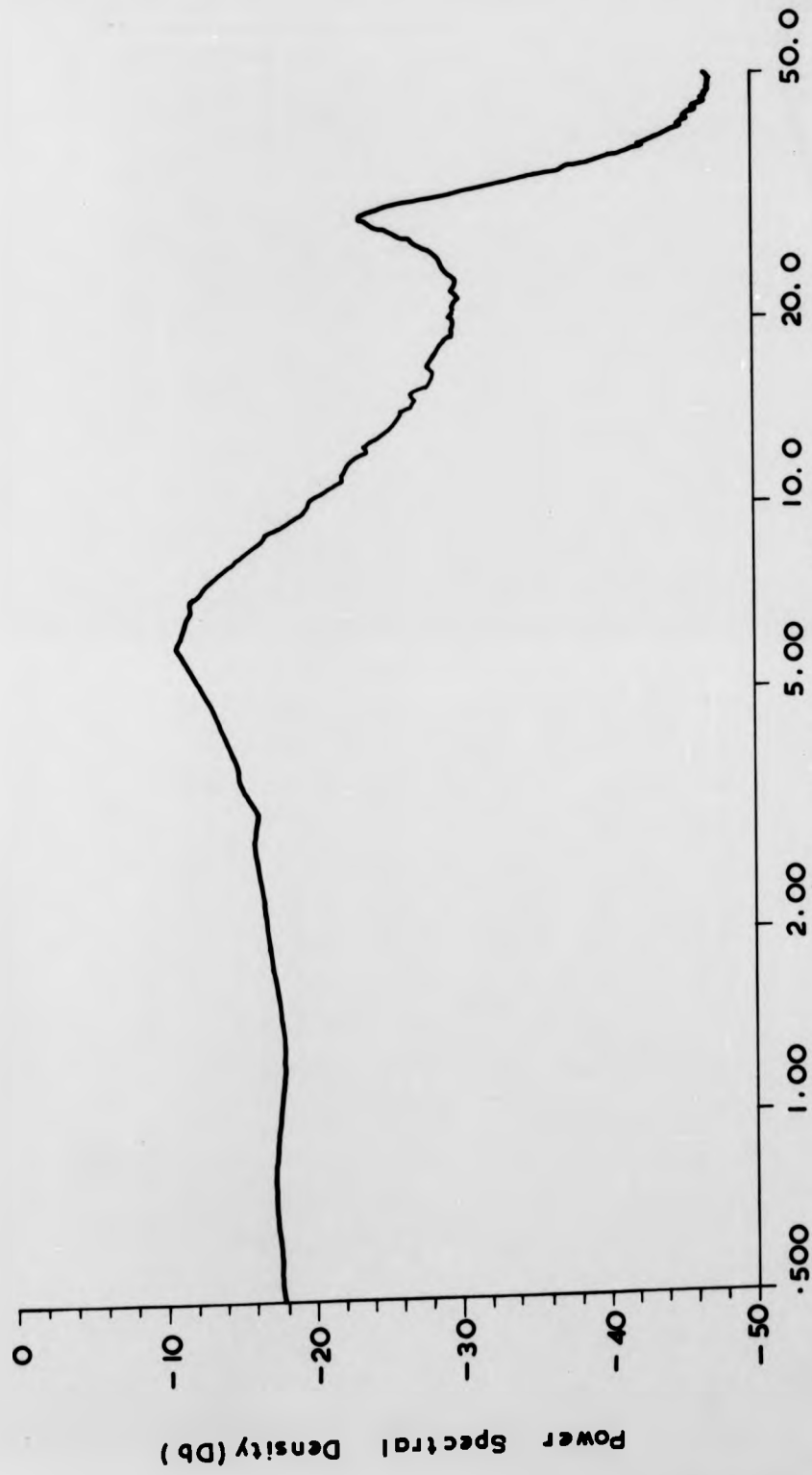
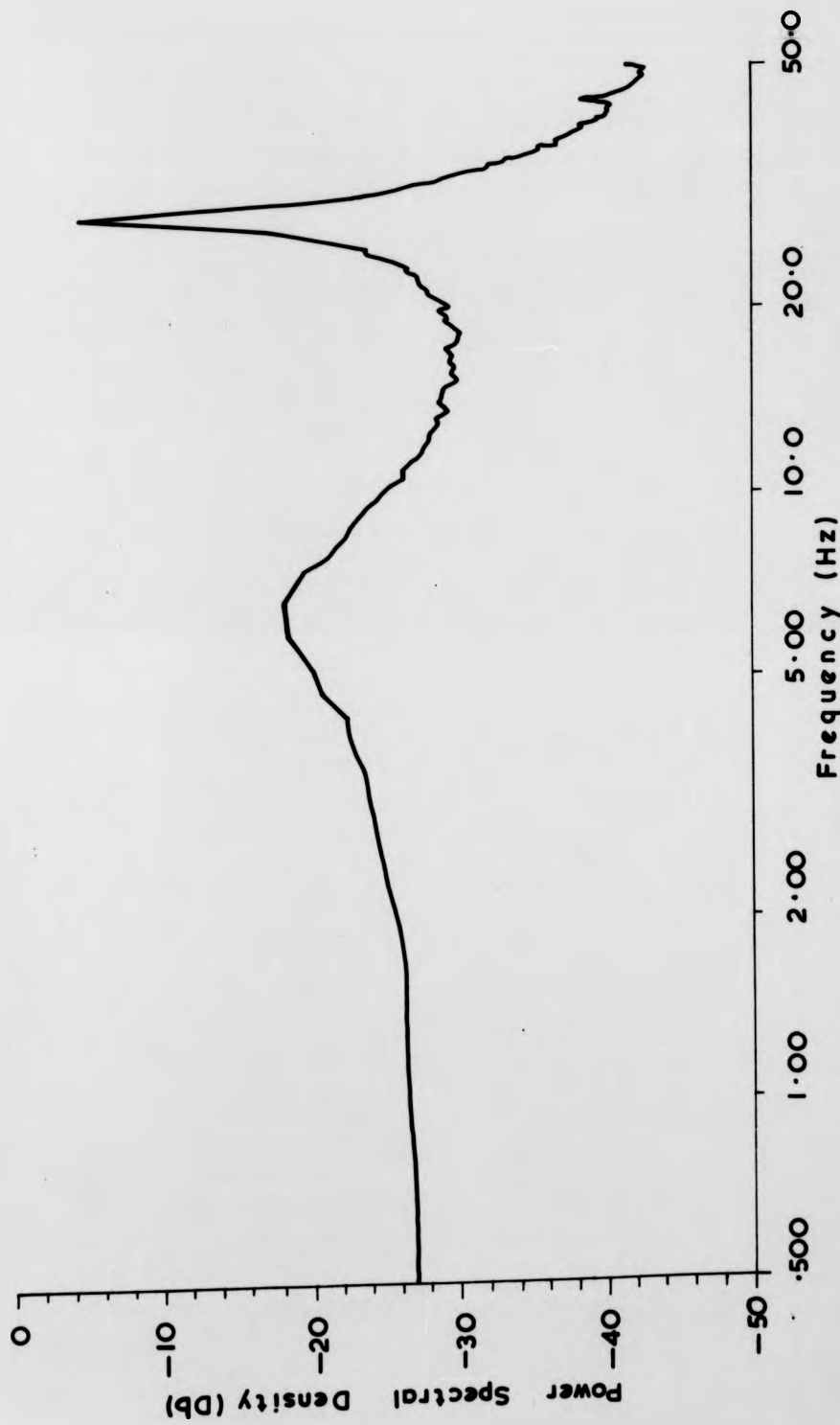


FIG. 6.10.

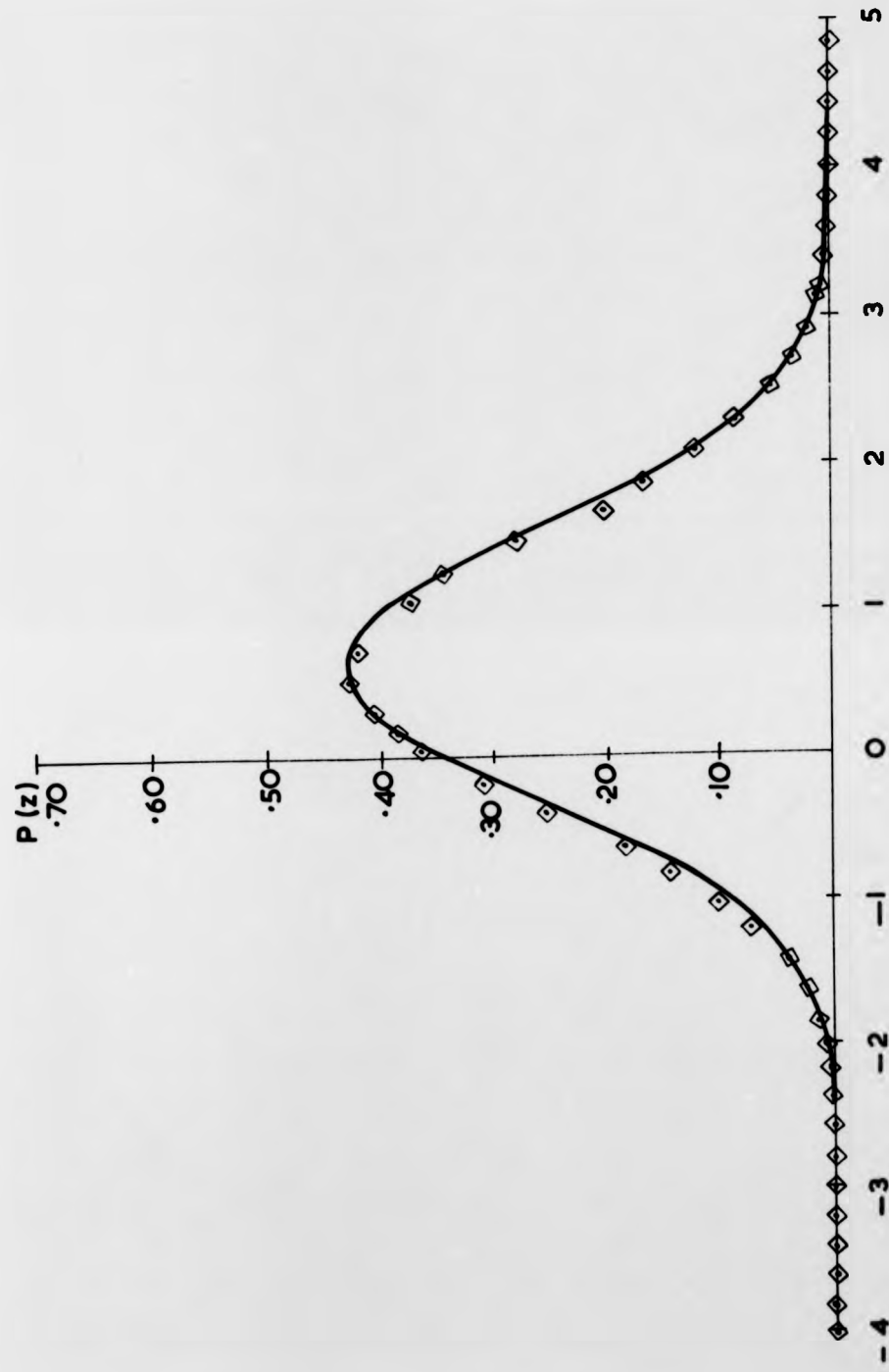


Low Irregularity Signal

FIG. 6.11.



High Irregularity Factor Signal  
FIG.6.12.



Standardised Peak Probability Density Function.  
Low Irregularity Factor Signal.

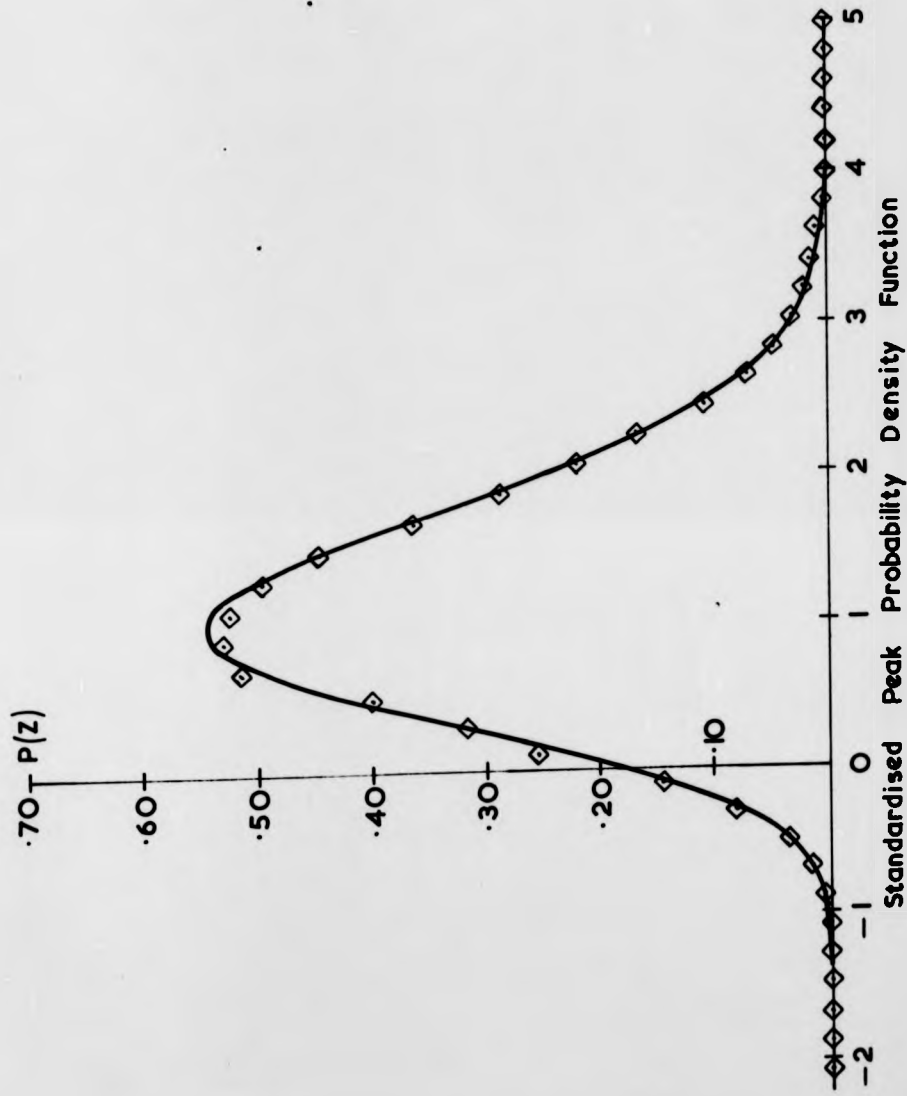


FIG. 6.14.

High Irregularity Factor Signal

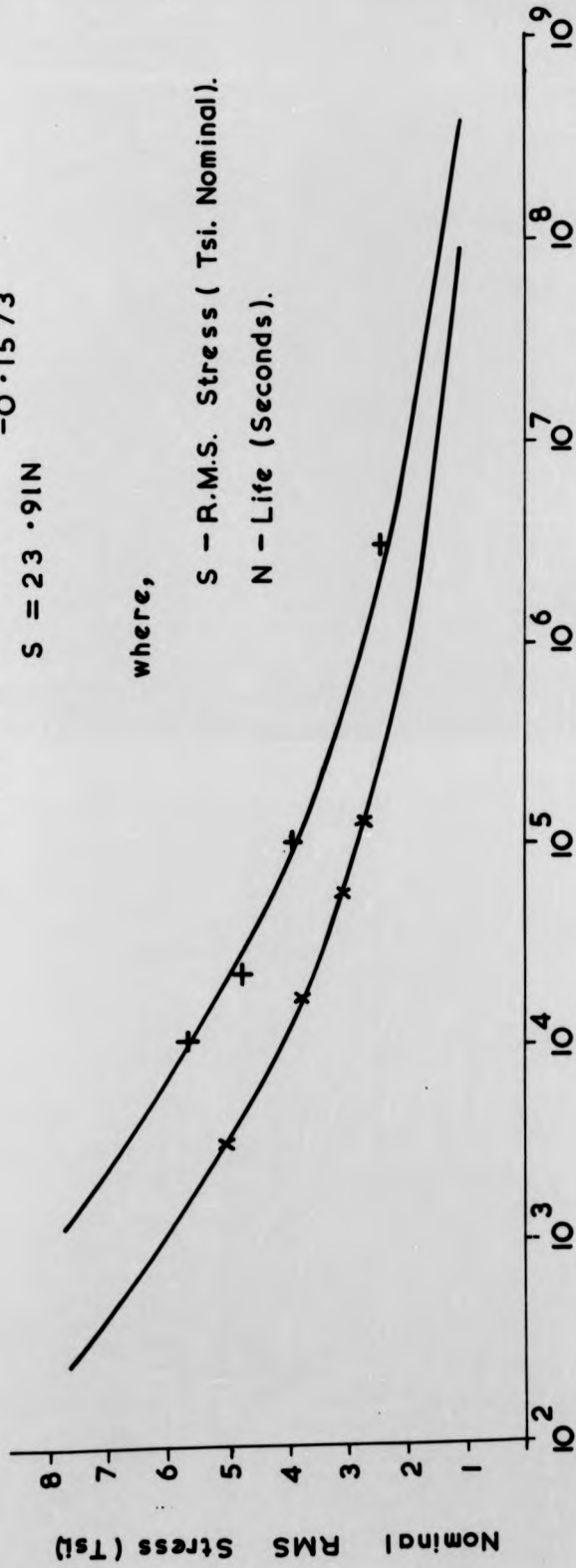
x - High Irregularity Factor Signal  
 $S = 18.38N$   
 $-0.1633$

+ - Low Irregularity Factor Signal  
 $S = 23.91N$   
 $-0.1573$

where,

S - R.M.S. Stress (Tsi. Nominal).

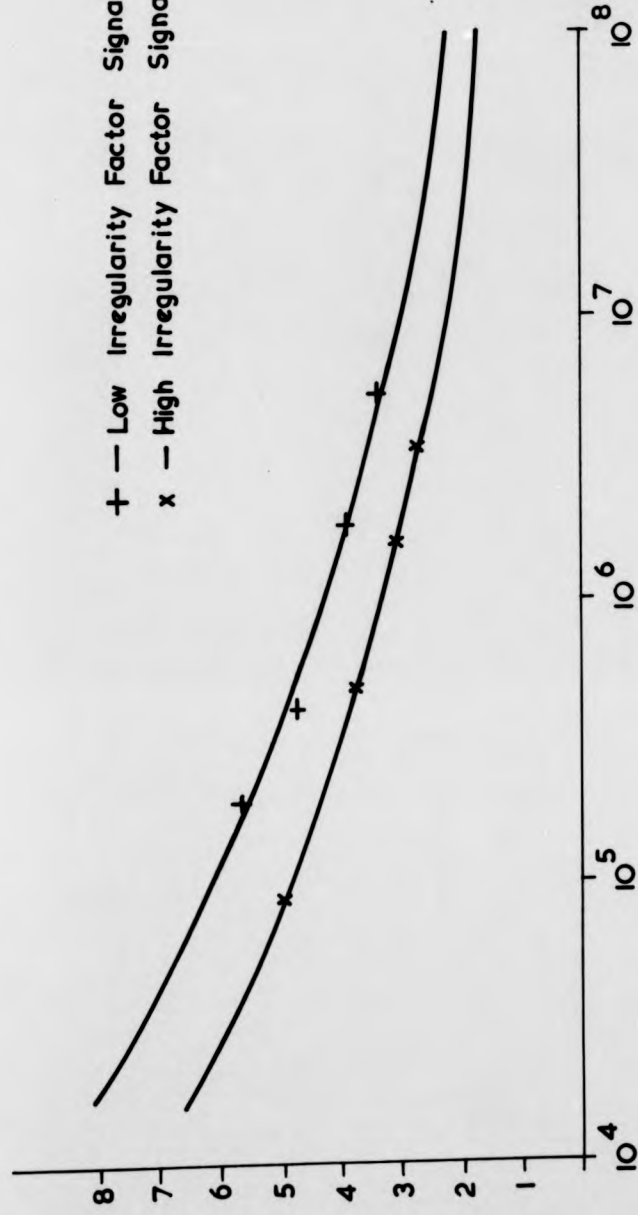
N - Life (Seconds).



Life to Failure (sec.)

FIG. 6.15

R.M.S. Stress (Tsi. Nominal)



Peaks to Failure

FIG. 6. 16

x - High Irregularity Factor Signal

+ - Low Irregularity Factor Signal

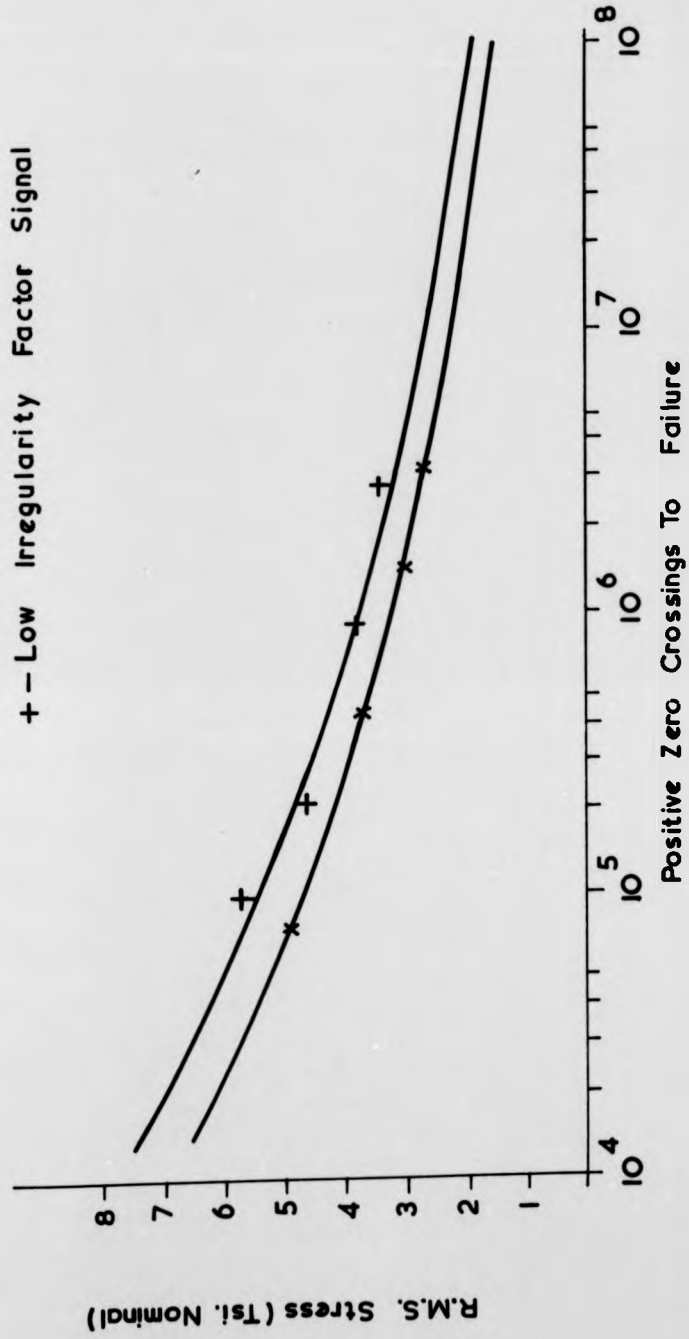


FIG. 6. 17.

R. M. S. Stress (Tsi. Nominal)

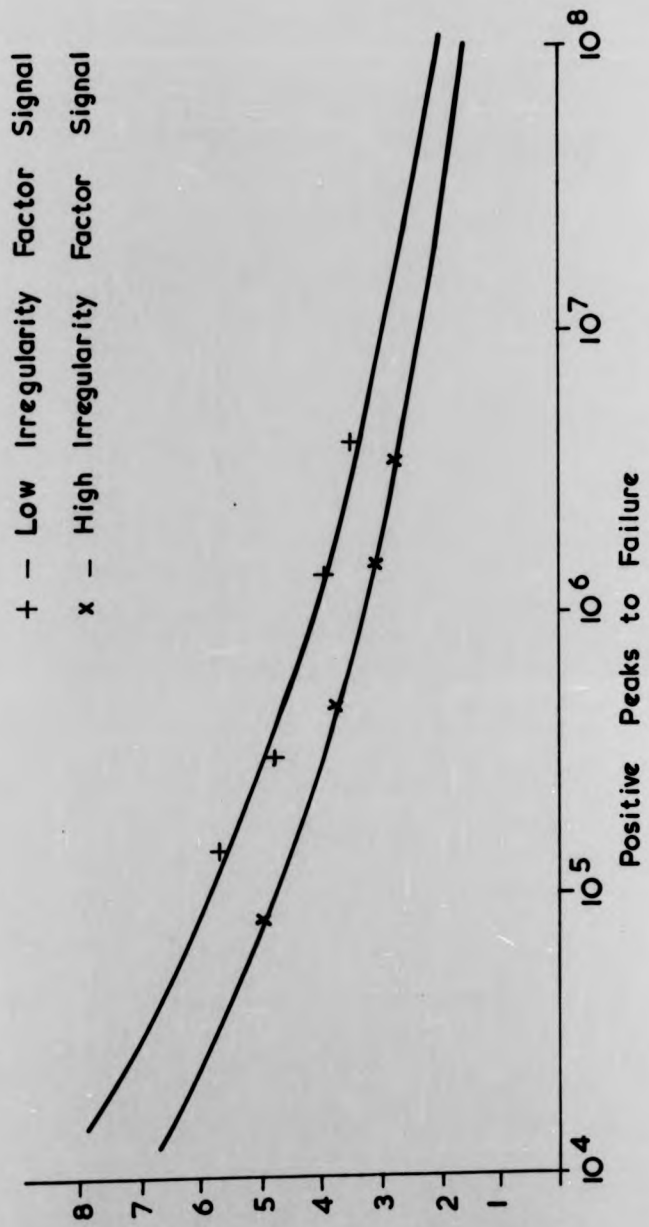
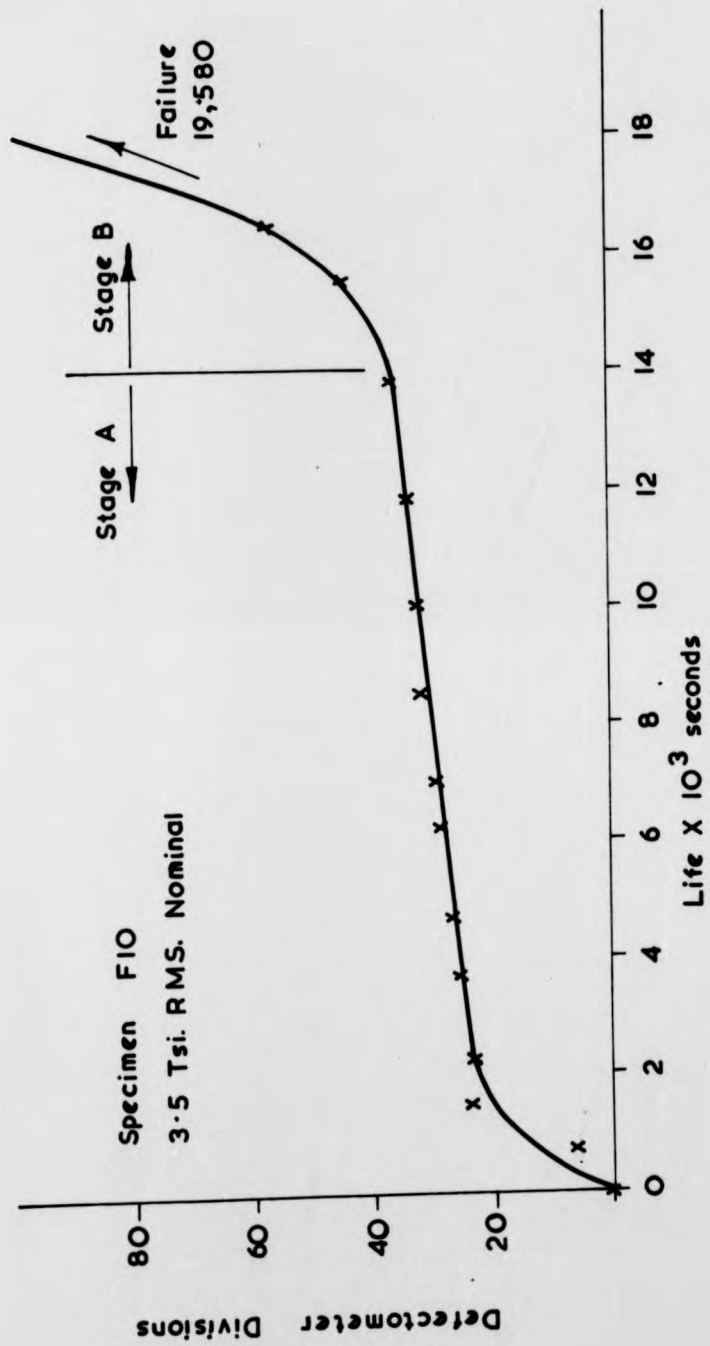


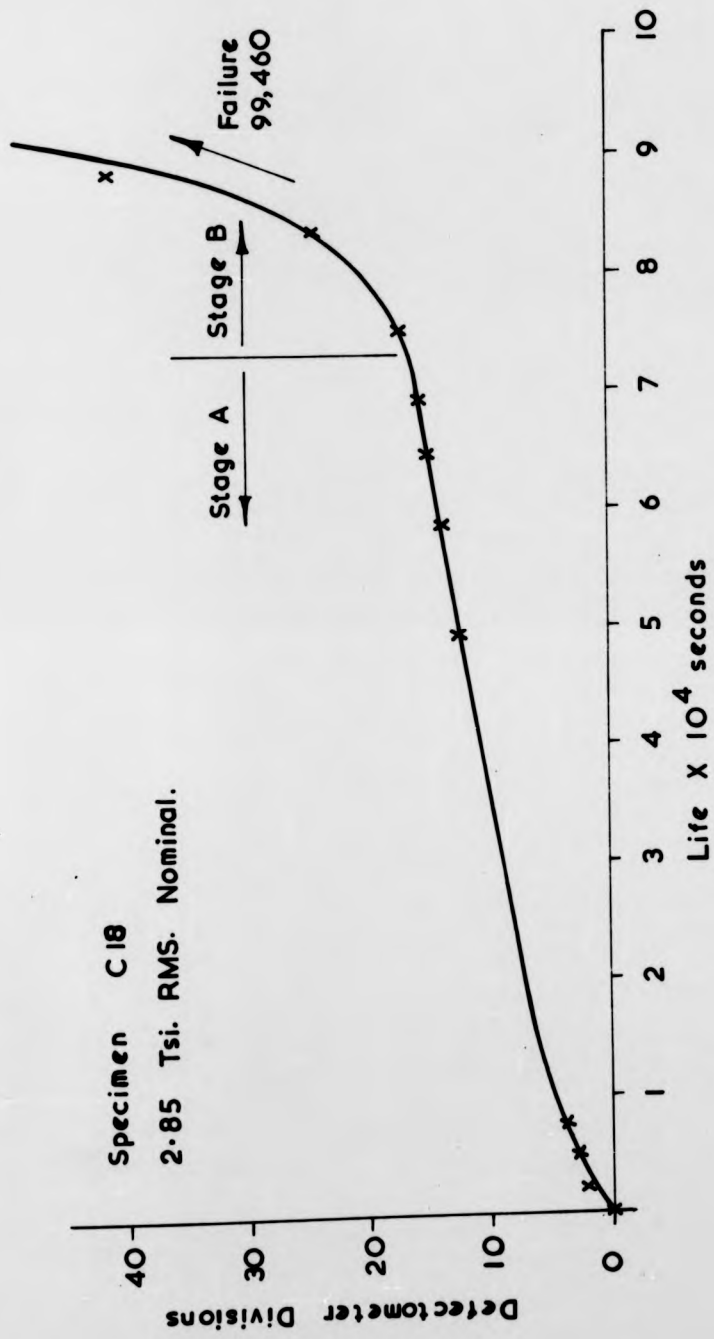
FIG. 6. 18



High Irregularity Factor Signal

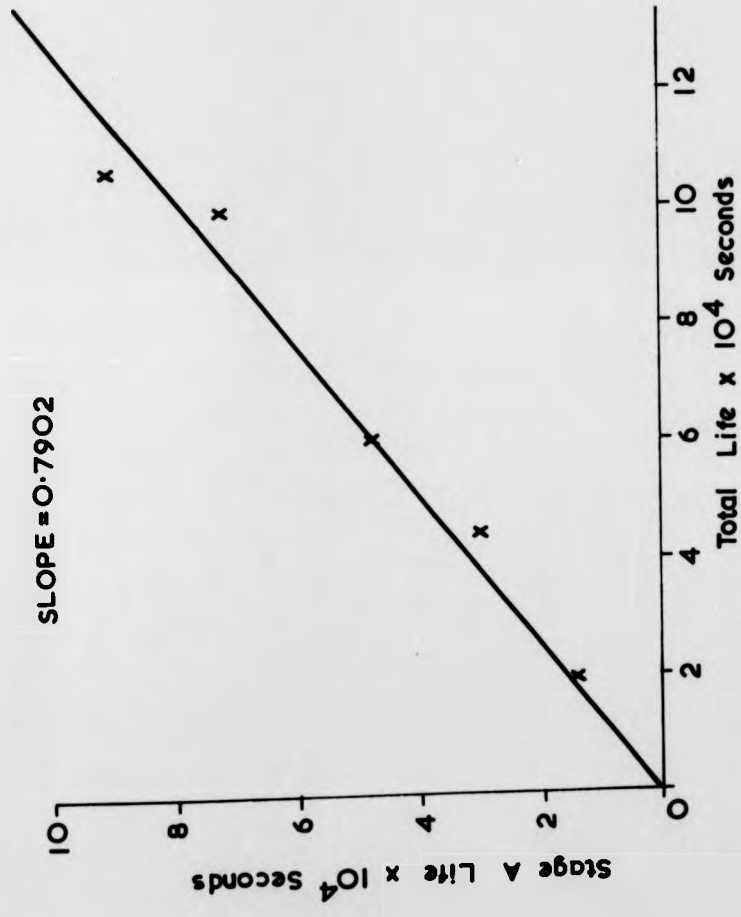
FIG. 6.19.

Specimen C18  
2.85 Tsi. RMS. Nominal.



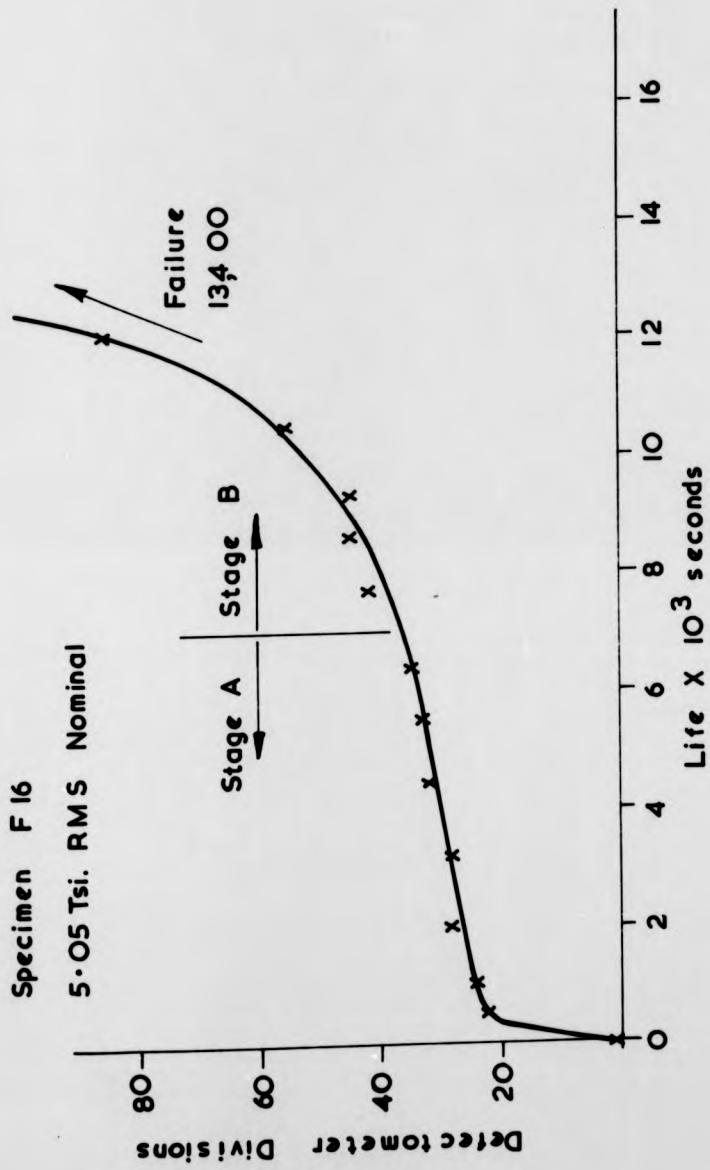
High Irregularity Factor Signal

FIG. 6.20.



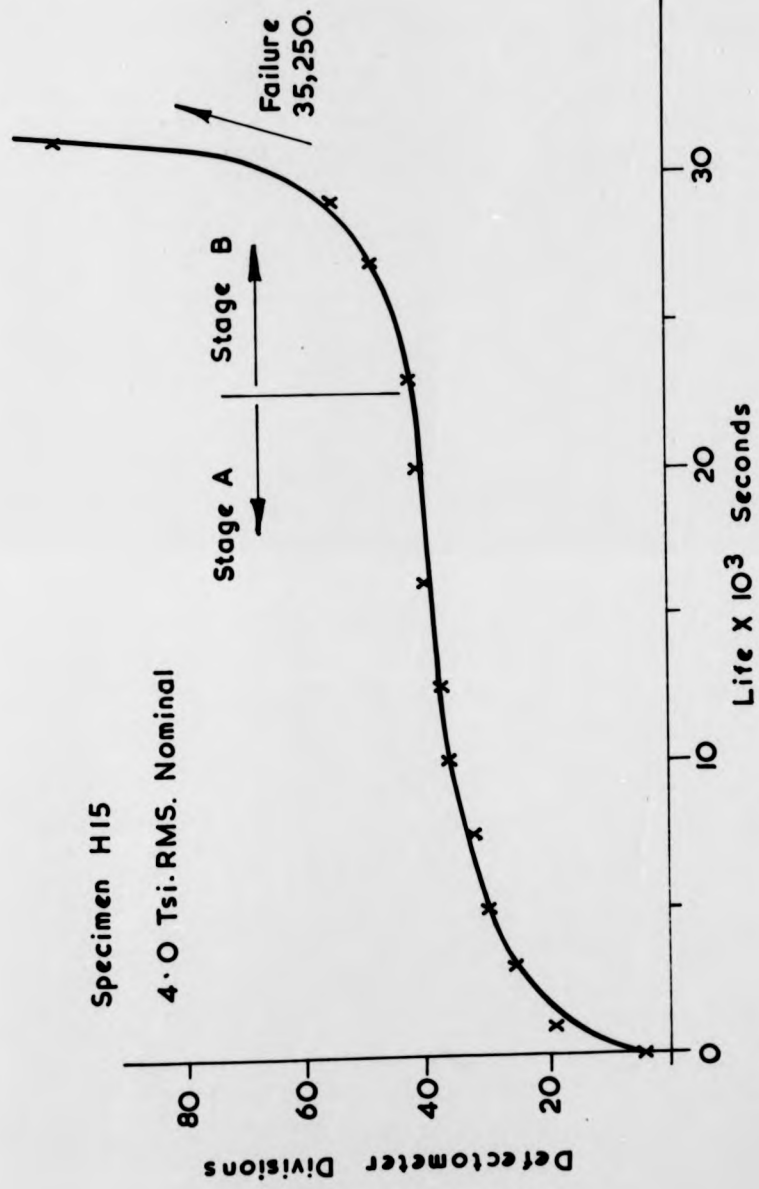
High Irregularity Factor Signal

FIG. 6.21.



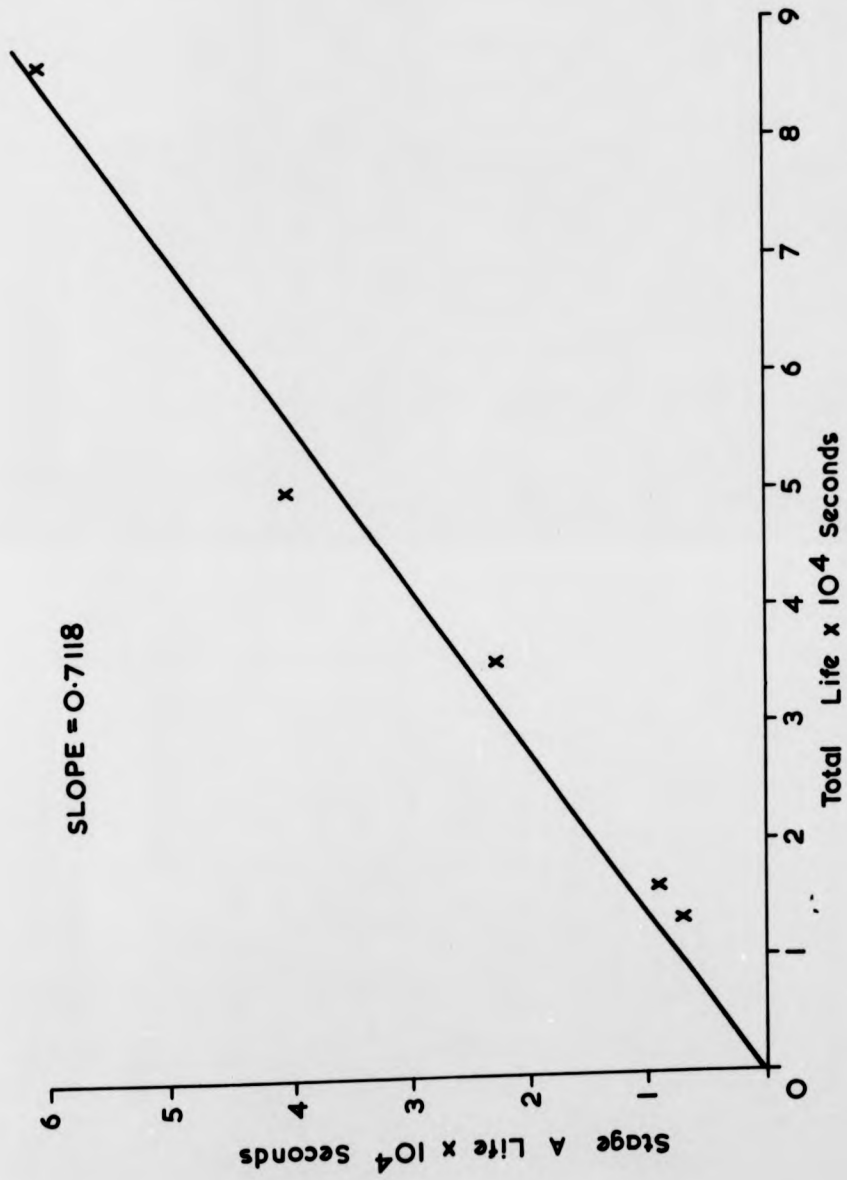
Low Irregularity Factor Signal

FIG. 6.22.



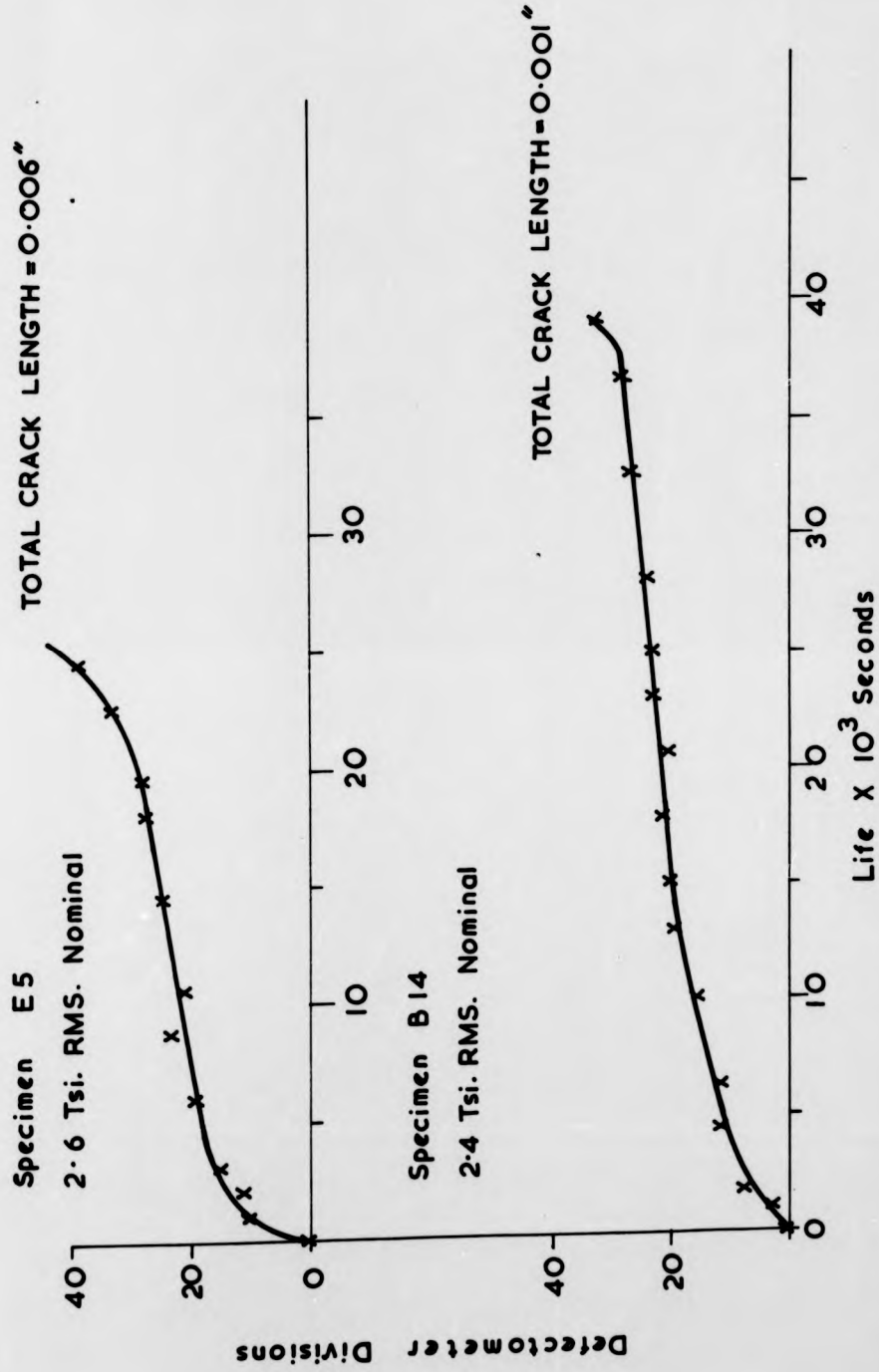
Low Irregularity Factor Signal

FIG. 6.23.



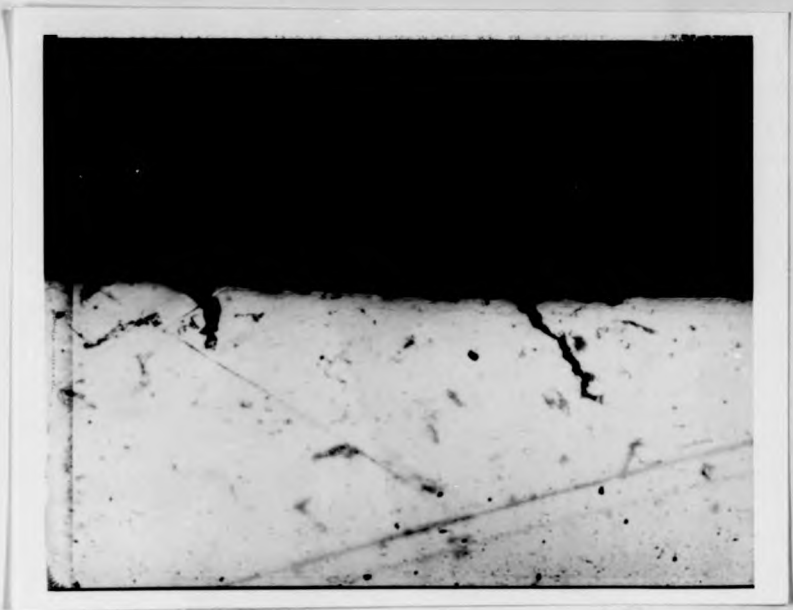
Low Irregularity Factor Signal

FIG. 6.24.

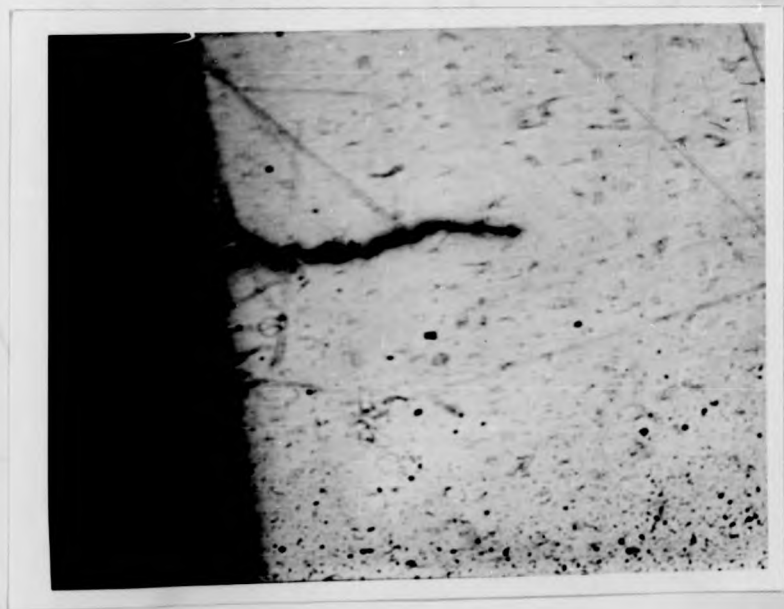


Low Irregularity Factor Signal

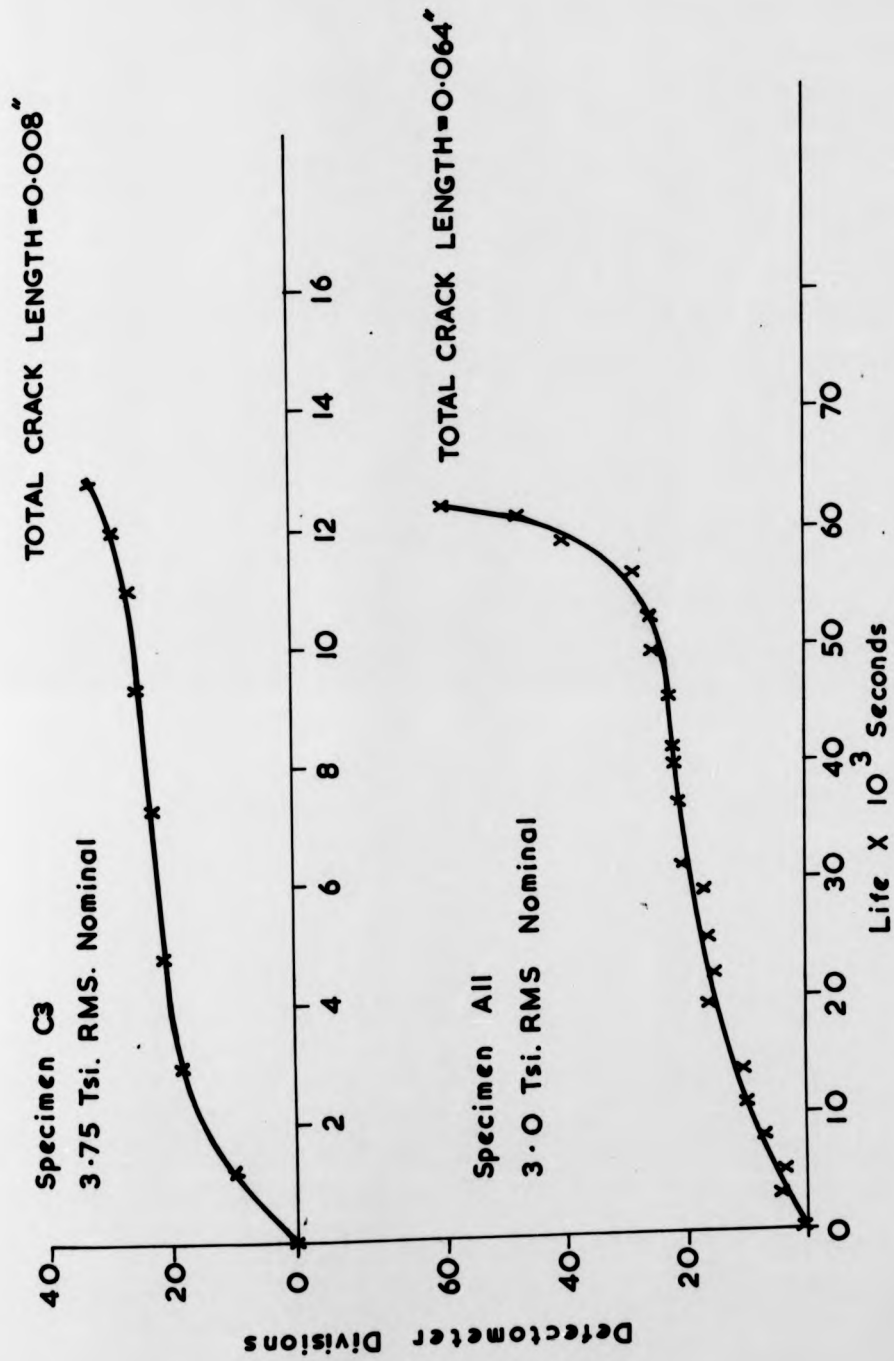
FIG. 6-25.



SPECIMEN B14 X500  
0.001"  
FIG 6.26.



SPECIMEN E5 X300  
0.006"  
FIG 6.27.

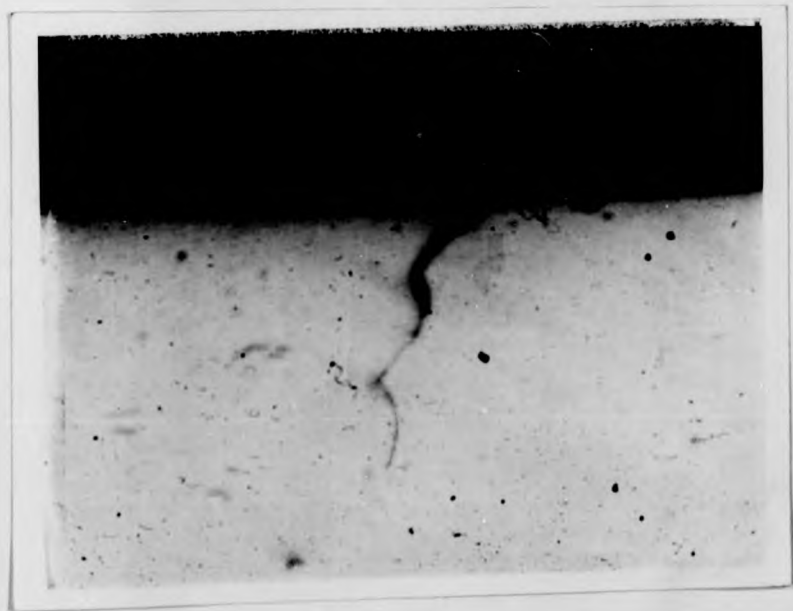


High Irregularity Factor Signal

FIG. 6.28.

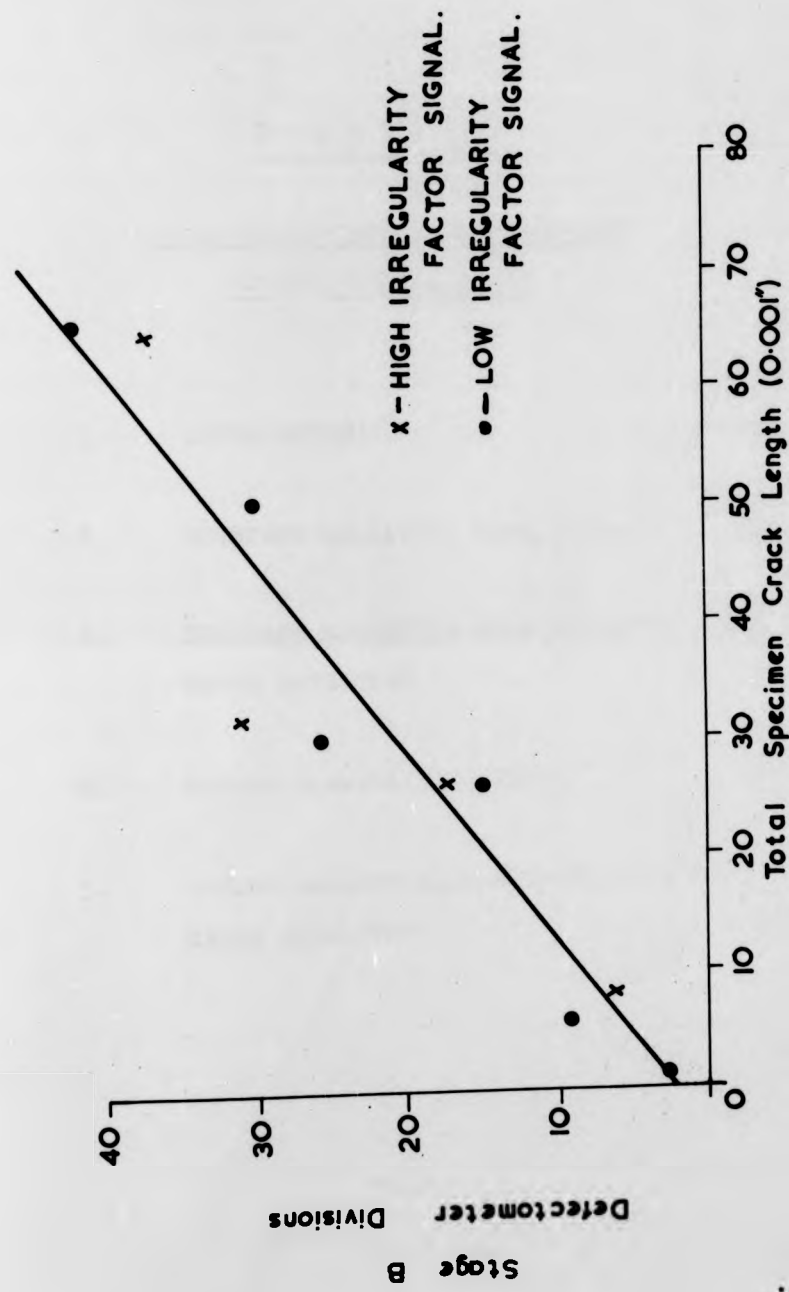


SPECIMEN A11 X75  
 0.038"  
 FIG. 6.29.



SPECIMEN C3 X800  
 0.003"  
 FIG. 6.30.





Random Loading Tests

FIG. 6.31.

C H A P T E R 7

SMALL BEAM CANTILEVER SPECIMEN

TABLE OF CONTENTS

1.	INTRODUCTION	107
2.	CONSTANT AMPLITUDE LIFE TESTS	108
3.	CONSTANT AMPLITUDE EDDY CURRENT CRACK DETECTION	109
4.	RANDOM LOADING LIFE TESTS	109
5.	RANDOM LOADING EDDY CURRENT CRACK DETECTION	113

## 1. INTRODUCTION

The test results presented in this chapter refer to the small round specimens shown in fig. 2.29 which were fatigued in cantilever bending using two electromagnetic vibrator test rigs described in Chapter 2, section 1.3.

This phase of the work came about from the joint SRC - British Rail Contract at a time when British Rail started work on a long term project aimed at establishing techniques to reliably predict the fatigue life of a component in its service environment. Part of this project was to synthesize random signals equivalent in terms of fatigue damage to service loading, and carry out fatigue tests in a multi-station testing machine. The work was then to be extended to larger test pieces and actual service components using a 50Tf. machine. The success of the extension from small to large specimens would depend very much upon the evidence of size effect under random loading. The joint SRC - British Rail Contract thus formed a sub-project of the main work and, at its simplest, was aimed at a qualitative observation of any size effect under identical random loading waveforms. However, during the test program it became clear that for the small specimens it was possible to extend the testing to additionally investigate the effect of signal irregularity factor on overall fatigue life and on the initiation of detectable fatigue cracks in much the same way as the work described in Chapter 6. The size effect investigation is, therefore, reported in Chapter 8.

Fatigue testing was carried out under constant amplitude and three random loading waveforms using two electromagnetic test rigs. The fatigue test results can be grouped into the following sections:-

2. Constant Amplitude Life Tests.
3. Constant Amplitude Eddy Current Crack Detection.
4. Random Loading Life Tests.
5. Random Loading Eddy Current Crack Detection.

The general principles of presentation of results established in Chapter 6 apply here.

## 2. CONSTANT AMPLITUDE LIFE TESTS

A total of 120 constant stress amplitude tests were conducted at a frequency of 47 Hz. to determine the basic S/N diagram. Six series of tests were conducted with 10 specimens from each machine. Checks were made at each stress level for significant differences between means using the t - distribution, and between variances using the F - distribution. It was assumed that the fatigue lives were lognormally distributed for this statistical analysis, and fig. 7.1 shows this to be a reasonable assumption. The results for each test rig are summarised in table 7.1. No significant difference between means and variances was found at the 5% level of significance and, therefore, the results from both rigs were combined at each stress level and are summarised in table 7.2.

The S/N diagram was determined by a least squares fit of mean lives to the Stussi equation, where static failure was represented by a collapse load stress as described in Chapter 5. Thus, for the case of a circular cross section cantilever specimen the collapse stress would then be  $1.7 \times \text{UTS} (54)$ . The equation together with the plotted test data is presented in fig. 7.2.

### 3. CONSTANT AMPLITUDE EDDY CURRENT CRACK DETECTION.

Eddy current crack detection work was carried out as previously outlined to establish whether the two stage behaviour was again present for these smaller specimens. Defectometer readings were taken during the fatigue lives of 13 specimens. Two typical plots are shown in figs. 7.3 and 7.4. The initial response of the Defectometer was slightly different to that found in other specimen tests. Generally, the eddy current readings dipped at the beginning of a specimen fatigue life before remaining constant throughout the dwell period of Stage A. Other tests have shown a slight increase in Defectometer readings before the Stage A dwell period. The results of the Stage A/Total life tests are summarised in table 7.3, and fig. 7.5 shows the best fit straight line constrained to the origin.

Sectioning and optical examination of 10 specimens was carried out in order to establish the Defectometer crack response for this specimen notch geometry. The results are summarised in table 7.4. No cracks were found in the specimen which was sectioned towards the end of its estimated Stage A life. Nine specimens were sectioned when Stage B behaviour became apparent. Those which were sectioned at the Stage A/Stage B transition all contained cracks in the 0.004/0.010 inches range, while specimens which showed established Stage B behaviour contained longer cracks. The linear relationship between crack length and Defectometer response shown in fig. 7.6 results from these tests.

### 4. RANDOM LOADING LIFE TESTS.

The objective of this series of tests was to investigate the effect of variations in signal irregularity factor on

overall fatigue life for three random loading waveforms of defined Gaussian amplitude distribution and a common fundamental power spectrum shape. It is convenient to present the data under two headings:-

4.1. Statistical definition of random loading waveforms.

4.2. Fatigue results.

4.1. Statistical definition of random loading waveforms.

Three series of random tests were carried out under loading waveforms, each having a fundamental band pass power spectrum shape and similar frequency content, and synthesised as described in Chapter 4, sections 2 and 3. The nominal half power bandwidths of the power spectra were synthesised as 10 Hz., 27 Hz. and 47 Hz., each with an upper cut off frequency of 52 Hz. The signals are therefore described respectively as the "47 Hz. centre frequency signal", "25/52 Hz. Band Pass Signal" and the "5/52 Hz. Band Pass Signal". Open loop frequency response modifications to both test rigs were carried out to achieve flat amplitude/frequency characteristics over the frequency range of the random signals, so that achieved specimen stress waveforms would only be slightly different from the input signals.

The main objective was to achieve an accurate statistical description of the random stress waveforms experienced by test specimens in each rig, and thus establish that both rigs were giving essentially identical testing conditions from a common input signal. Statistical measurements of amplitude probability density, peak probability density and power spectral density were made for both rigs under all three signals in a similar way to that described in Chapter 6. Goodness-of-fit tests showed that the hypothesis of normality for the amplitude distributions of all

waveforms could be accepted at the 5% level of significance. Traces of the load cell outputs of each rig for the three test waveforms are shown in figs. 7.7, 7.8 and 7.9. The complete series of random signal measurements is summarised in the following table:-

Signal Description	Amplitude Probability Density		Peak Probability Density		Power Spectral Density	
	Rig 1	Rig 2	Rig 1	Rig 2	Rig 1	Rig 2
	47 Hz. Centre Frequency Signal	fig.7.10 tab.7.5	fig.7.10 tab.7.6	fig.7.11 tab.7.7	fig.7.12 tab.7.8	fig.7.13 tab.7.9
25/52 Hz. Band Pass Signal	fig.7.14 tab.7.10	fig.7.14 tab.7.11	fig.7.15 tab.7.12	fig.7.16 tab.7.13	fig.7.17 tab.7.14	fig.7.17 tab.7.14
5/52 Hz. Band Pass Signal	fig.7.18 tab.7.15	fig.7.18 tab.7.16	fig.7.19 tab.7.17	fig.7.20 tab.7.18	fig.7.21 tab.7.19	fig.7.22 tab.7.19

Peak and zero crossing frequencies for both waveforms were extracted from the peak/trough on-line analyses and are summarised for both the synthesised and the test rig signals in table 7.20. These results show little modification of the input signal by either rig, although the achieved stress measurements have been used in the presentation of random fatigue data and for cumulative damage analyses.

The data presented in this section enabled a comparison to be made between each test rig performance under the three random waveforms. The results show that essentially the same random loading pattern was achieved by each rig from a given input signal. Therefore, fatigue testing was carried out assuming that there was no significant difference between the random loading produced by each rig for a given common input signal.

#### 4.2. Fatigue results

Five series of tests were conducted with 5 specimens at each stress level for each machine to determine basic rms. stress/life (seconds) curves, except that 6 series of tests were run for the 47 Hz. centre frequency signal. Test stress levels were chosen so that the high cycle life regions were well defined. Higher stress levels were chosen so that test rig clipping of high stress peaks did not occur.

Significance tests were made at each stress level for differences between machine means using the t - distribution and between variances using the F - distribution, assuming the fatigue lives to be lognormally distributed. The plots of the fatigue lives in figs. 7.23, 7.24 and 7.25 show that this is a reasonable assumption. There was no significant difference between means or variances at the 5% level for any one test level, so that results from both rigs were combined. The fatigue life data is summarised in the following table:-

Signal Description	Individual Test Rig Results	Combined Results
47 Hz. Centre Frequency Signal	table 7.21	table 7.22
25/52 Hz. Band Pass Signal	table 7.23	table 7.24
5/52 Hz. Band Pass Signal	table 7.25	table 7.26

The striking fact about these results is the similar fatigue life which is produced for similar stress levels regardless of testing waveform. This is emphasised in table 7.27 where results have been grouped according to test stress level, and lives expressed as peaks, positive zero

crossings and positive peaks to failure using the data from table 7.20. Because of the lack of any test variation in fatigue life it was decided to represent the results by one failure curve. The equation for the best fit to the rms. stress/mean life (seconds) data, as described in Chapter 6, is shown in fig. 7.25 together with the plotted test results. The best fit to data was obtained with a fatigue limit of zero. The results are expressed in terms of peaks, positive zero crossings and positive peaks to failure in figs. 7.27, 7.28 and 7.29 by using the data of table 7.20.

##### 5. RANDOM LOADING EDDY CURRENT CRACK DETECTION.

The objective of this part of the test program was to investigate whether the two stage behaviour present under previous random loading tests could be established for these small specimens, and also to examine the effect of variations in signal irregularity factor on this behaviour.

A series of Defectometer tests was carried out for specimens fatigued under each random waveform. The characteristic Stage A/Stage B behaviour was present in these small specimens under random loading, although the initial eddy current response was slightly different to that found in other specimen random load tests. The eddy current readings dipped at the beginning of a specimen fatigue life, as was the case with the constant amplitude tests with these small specimens. The results of the testing which was carried out in order to establish the stage behaviour are summarised in the following table:-

Signal Description	Typical Defectometer Response		Plot of Stage A/Total	Summary of Stage A/Total
	High Stress	Low Stress	Life Data	Life Data
47 Hz. Centre Frequency Signal	fig. 7.30	fig. 7.31	fig. 7.32	table 7.28
25/52 Hz. Band Pass Signal	fig. 7.33	fig. 7.34	fig. 7.35	table 7.29
5/52 Hz. Band Pass Signal	fig. 7.36	fig. 7.37	fig. 7.38	table 7.30

Other specimens were part fatigued and sectioned and examined in order to establish the Defectometer crack response under random loading for the small specimen notch geometry. This work was only carried out for the 47 Hz. centre frequency and 5/52 Hz. Band Pass signals. (If there was to be any significant difference in eddy current response under each waveform for this test series it was considered that it would show most clearly for the two signals of extreme waveform irregularity). The results are summarised in tables 7.31 and 7.32. No cracks were found in specimens fatigued under either waveform which were sectioned towards the end of their estimated Stage A life. Specimens sectioned after Stage B became apparent all contained cracks which increased in length as Stage B behaviour progressed. The interrelation of fatigue crack formation and growth with the two stage behaviour is most strikingly illustrated by a series of 4 tests with the 47 Hz. centre frequency signal whose Defectometer responses are shown in fig. 7.39. Photographs of fatigue cracks found in two of the specimens are shown in figs. 7.40 and 7.41. The eddy current responses and corresponding crack

lengths at the point of sectioning are shown in fig. 7.42 for two specimens fatigued under the 5/52 Hz. Band Pass signal. Photographs of fatigue cracks are shown in fig. 7.43 and 7.44. The linear relationship between crack length and instrument eddy current response is shown in fig. 7.45 which contains data for both signals. The graph suggests that there is no significant difference in terms of Defectometer reading for a given crack grown under either loading waveform.

Nominal Peak Stress Tsi.	30.1	23.9	21.0	17.4	15.7	14.6
Mean of $\log_{10}$ of Lives (cycles)	4.4845	4.8467	5.2053	5.6056	6.2617	6.4417
Sample Variance	0.0031	0.0052	0.0042	0.0113	0.0153	0.0274

Rig No. 1

Nominal Peak Stress Tsi.	30.1	23.9	21.0	17.4	15.7	14.6
Mean of $\log_{10}$ of Lives (cycles)	4.5176	4.8726	5.1686	5.6182	6.2333	6.3912
Sample Variance	0.0053	0.0034	0.0034	0.0059	0.0267	0.0407

Rig No. 2

Sample 'F' Value	1.71	1.53	1.24	1.92	1.57	1.49
Sample 't' Value	1.14	0.88	1.35	0.23	0.43	0.61

10 specimens tested at each stress level.

2-sided 5% F Value = 4.03 for (9,9) degrees of freedom.

2-sided 5% t Value = 2.10 for 18 degrees of freedom.

Constant Amplitude Loading

Table 7.1.

Nominal Peak Stress Tsi.	21.28 30.1	16.96 23.9	14.85 21.0	12.30 17.4	11.10 15.7	10.32 14.6
Mean of $\log_{10}$ of Lives (cycles)	4.5010	4.8596	5.1872	5.6134	6.2475	6.4185
Antilog of Mean log life (cycles)	31,698	72,384	153,886	410,610	1,768,000	2,691,200
Sample Variance	0.0040	0.0041	0.0035	0.0062	0.0207	0.0323

Combined results for 20 specimens at each stress level.

Constant Amplitude Loading

Table 7.2.

Specimen Identification	Nominal Peak Stress Tsi.	Stage A Life (seconds)	Total Life (seconds)
J	23.9	900	1,790
H	23.9	1,450	2,537
I	21.0	750	2,956
K	21.0	1,750	4,667
M	17.4	4,600	10,201
V	17.6	5,000	10,493
S	17.9	6,000	12,532
Q	16.8	6,000	14,360
U	17.0	8,200	15,371
N	17.4	7,000	16,927
R	16.6	12,700	20,709
O	15.7	13,000	22,174
T	16.3	15,000	27,323

Testing Frequency = 47 Hz.

Constant Amplitude Loading

Table 7.3.

Specimen Identification	Nominal Peak Stress Tsi.	Crack Length"		Total Equivalent Crack Length"	Total Defectometer Stage B Divisions
		Top Notch	Bottom Notch		
K1	21.0	0.004	0.005	0.010	3.5
K2	21.0	0.010	-	0.010	3.0
G	17.4	0.006	0.007	0.013	3.0
F	17.4	0.020	0.001	0.021	5.1
O1	15.7	0.014	0.013	0.027	5.2
D	17.4	0.015	0.018	0.033	5.6
E	17.4	0.019	0.018	0.037	7.1
K3	21.0	0.027	0.038	0.065	12.0
A	18.0	0.050	0.045	0.095	13.3

Constant Amplitude Loading

Table 7.4.

Class Interval Midpoint (z)	Observed Frequency	Expected Frequency	Class Interval Midpoint (z)	Observed Frequency	Expected Frequency
-3.653	1	0.7	0.202	651	633.0
-3.650	0	0.8	0.405	600	595.3
-3.447	0	1.7	0.607	505	537.5
-3.245	4	3.4	0.810	446	465.7
-3.042	5	6.4	1.015	386	387.4
-2.839	15	11.6	1.216	293	309.3
-2.636	19	20.2	1.418	252	237.0
-2.434	30	33.8	1.621	167	174.4
-2.231	52	54.1	1.824	119	123.1
-2.028	76	83.2	2.027	79	83.4
-1.825	126	122.8	2.229	56	54.3
-1.623	178	173.9	2.432	28	33.9
-1.420	226	236.5	2.635	21	20.3
-1.217	314	308.7	2.838	11	11.7
-1.014	370	336.8	3.040	10	6.5
-0.812	459	465.2	3.243	6	3.4
-0.609	585	537.0	3.446	0	1.7
-0.406	598	595.0	3.649	0	0.8
-0.204	662	632.8	3.851	2	0.7
-0.001	648	646.0			

Amplitude resolution = 0.215 V. = 0.203 x rms.

Signal rms. = 1.061 V.

Total no. of class intervals = 39

Total no. of samples = 8000

5% value of chisquare = 51

Sample chisquare value = 26.0

Rig No. 1

47 Hz. Centre Frequency Signal

Table 7.5.

Class Interval Midpoint (z)	Observed Frequency	Expected Frequency	Class Interval Midpoint (z)	Observed Frequency	Expected Frequency
-3.332	2	4.7	0.156	507	549.2
-3.157	3	3.9	0.331	594	526.4
-2.983	9	6.6	0.505	529	489.5
-2.808	17	10.9	0.680	412	441.5
-2.634	9	17.5	0.854	375	386.4
-2.460	33	27.2	1.028	323	328.0
-2.285	43	41.1	1.203	242	270.2
-2.111	55	60.2	1.377	229	215.8
-1.936	83	85.7	1.552	162	167.3
-1.762	141	118.2	1.726	131	125.8
-1.588	152	158.1	1.901	89	91.8
-1.413	208	205.3	2.075	67	64.9
-1.239	255	258.6	2.249	40	44.6
-1.064	304	316.0	2.424	37	29.7
-0.890	376	374.5	2.598	22	19.2
-0.716	404	430.6	2.773	11	12.0
-0.541	502	480.4	2.947	7	7.3
-0.367	496	519.9	3.121	2	4.3
-0.192	558	545.8	3.296	5	5.3
-0.018	566	555.8			

Amplitude resolution = 0.293 V. = 0.174 x rms.

Signal rms. = 1.681 V.

Total no. of class intervals = 39

Total no. of samples = 6000

5% value of chisquare = 51

Sample chisquare value = 47.2

Rig No. 2

47 Hz. Centre Frequency Signal

Table 76.

Class Interval Midpoint (z)	Observed Peak Frequency	Expected Peak Frequency	Class Interval Midpoint (z)	Observed Peak Frequency	Expected Peak Frequency
-6.28	0	0	0.10	351	937.3
-6.08	0	0	0.30	2669	2804.8
-5.88	0	0	0.50	4259	4318.8
-5.68	0	0	0.70	5468	5309.2
-5.48	0	0	0.90	6176	5892.2
-5.28	0	0	1.10	5577	5906.3
-5.08	0	0	1.30	5654	5506.3
-4.88	0	0	1.50	4809	4815.6
-4.68	0	0	1.69	4275	3976.2
-4.48	0	0	1.89	3164	3112.0
-4.28	0	0	2.09	2490	2315.1
-4.09	0	0	2.29	1738	1640.4
-3.89	0	0	2.49	1211	1108.8
-3.69	0	0	2.69	677	715.7
-3.49	0	0	2.89	476	441.7
-3.29	0	0	3.09	259	260.7
-3.09	0	0	3.29	126	147.3
-2.89	0	0	3.49	57	79.7
-2.69	0	0	3.69	35	41.3
-2.49	0	0	3.89	19	20.5
-2.29	0	0	4.09	6	9.8
-2.09	0	0	4.29	3	4.5
-1.89	0	0	4.48	1	2.0
-1.69	0	0	4.68	1	0.8
-1.49	0	0	4.88	0	0.3
-1.30	0	0	5.08	0	0.1
-1.10	0	0	5.28	0	0
-0.90	0	0	5.48	0	0
-0.70	0	0	5.68	0	0
-0.50	0	0	5.88	0	0
-0.30	0	0	6.08	0	0
-0.10	2	14.6	6.28	0	0

Signal rms. = 0.784 V.

Measurement time = 1048 sec.

Peaks = 49507

Positive Zero Crossings = 49478

Irregularity Factor = 0.999

Rig No. 1

47 Hz. Centre Frequency Signal

Table 7.7.

Class Interval Midpoint(z)	Observed Peak Frequency	Expected Peak Frequency	Class Interval Midpoint(z)	Observed Peak Frequency	Expected Peak Frequency
-7.94	0	0	0.13	412	976.0
-7.69	0	0	0.38	2668	2748.7
-7.43	0	0	0.63	3795	4037.4
-7.18	0	0	0.88	4597	4676.4
-6.93	0	0	1.13	4740	4669.9
-6.68	0	0	1.39	4123	4161.7
-6.43	0	0	1.64	3466	3366.7
-6.17	0	0	1.89	2733	2496.2
-5.92	0	0	2.14	1950	1706.6
-5.67	0	0	2.39	1257	1080.2
-5.42	0	0	2.65	719	634.7
-5.17	0	0	2.90	377	347.0
-4.91	0	0	3.15	235	176.7
-4.66	0	0	3.40	98	83.9
-4.41	0	0	3.65	35	37.2
-4.16	0	0	3.91	19	15.4
-3.91	0	0	4.16	11	6.0
-3.65	0	0	4.41	0	2.2
-3.40	0	0	4.66	0	0.7
-3.15	0	0	4.91	0	0.2
-2.90	0	0	5.17	0	0.1
-2.65	0	0	5.42	0	0
-2.39	0	0	5.67	0	0
-2.14	0	0	5.92	0	0
-1.89	0	0	6.17	0	0
-1.64	0	0	6.43	0	0
-1.39	0	0	6.68	0	0
-1.13	0	0	6.93	0	0
-0.88	0	0	7.18	0	0
-0.63	0	0	7.43	0	0
-0.38	0	0	7.69	0	0
-0.13	0	0	7.94	0	0

Signal rms. = 1.240 V.

Measurement time = 667 sec.

Peaks = 31236

Rig No. 2

Positive Zero Crossings = 31236

Irregularity Factor = 1.000

47 Hz. Centre Frequency Signal

Table 7.8.

Degrees of Freedom = 796

Sampling Frequency = 150 Hz.

Signal rms. = 1.061 V.

Rig No. 1

Degrees of Freedom = 816

Sampling Frequency = 160 Hz.

Signal rms. = 1.681 V.

Rig No. 2

47 Hz. Centre Frequency Signal

Table 7.9.

Class Interval Midpoint (z)	Observed Frequency	Expected Frequency	Class Interval Midpoint (z)	Observed Frequency	Expected Frequency
-4.064	1	0.3	0.170	674	664.8
-3.853	2	0.4	0.382	641	627.2
-3.641	3	0.9	0.594	566	565.9
-3.429	2	1.9	0.806	481	488.2
-3.217	8	3.9	1.017	404	402.3
-3.006	9	7.5	1.229	320	317.8
-2.794	18	13.8	1.441	235	239.8
-2.582	28	24.3	1.652	174	175.1
-2.371	51	41.1	1.864	125	119.4
-2.159	63	66.2	2.076	91	78.8
-1.947	100	102.1	2.288	44	49.7
-1.735	147	150.5	2.499	26	30.0
-1.524	204	212.2	2.711	15	17.3
-1.312	283	286.2	2.923	15	9.6
-1.100	362	369.1	3.135	6	5.0
-0.888	448	455.3	3.346	2	2.5
-0.677	531	537.0	3.558	2	1.2
-0.465	607	605.7	3.770	2	0.6
-0.253	641	653.3	3.982	1	0.4
-0.041	668	675.9			

Amplitude resolution = 0.381 V. = 0.212 x rms.

Signal rms. = 1.800

Total no. of class intervals = 39

Total no. of samples = 8000

5% value of chisquare = 51

Sample chisquare value = 34.4

Rig No. 1

25/52 Hz. Band Pass Signal

Table 7.10.

Class Interval Midpoint(z)	Observed Frequency	Expected Frequency	Class Interval Midpoint(z)	Observed Frequency	Expected Frequency
-3.461	5	3.0	0.310	589	572.8
-3.273	5	2.9	0.499	557	530.9
-3.084	5	5.2	0.687	469	474.9
-2.896	14	9.2	0.876	404	410.0
-2.707	18	15.6	1.064	338	341.7
-2.518	31	25.4	1.253	270	274.8
-2.330	45	40.1	1.441	205	213.3
-2.141	61	61.1	1.630	158	159.8
-1.953	82	89.8	1.819	114	115.6
-1.764	122	127.4	2.007	81	80.7
-1.576	160	174.3	2.196	48	51.3
-1.387	224	230.3	2.384	38	35.3
-1.198	276	293.7	2.573	22	22.2
-1.010	354	361.4	2.761	13	13.4
-0.821	417	429.3	2.950	12	7.8
-0.633	484	492.2	3.138	12	4.4
-0.444	546	544.6	3.327	1	2.4
-0.256	584	581.6	3.516	3	1.3
-0.067	593	599.6	3.704	2	1.2
0.121	638	596.5			

Amplitude resolution = 0.313 V. = 0.169 x rms.

Signal rms. = 1.659 V.

Total no. of class intervals = 39

Total no. of samples = 8000

5% value of chisquare = 51

Sample chisquare value = 36.1

Rig No. ?

25/52 Hz. Band Pass Signal

Table 7.11.

Class Interval Midpoint (z)	Observed Peak Frequency	Expected Peak Frequency	Class Interval Midpoint (z)	Observed Peak Frequency	Expected Peak Frequency
-5.11	0	0	0.08	833	1186.9
-4.95	0	0	0.24	1358	1770.0
-4.79	0	0	0.41	1991	2380.6
-4.63	0	0	0.57	2650	2927.2
-4.47	0	0	0.73	3168	3332.8
-4.30	0	0	0.89	3287	3553.7
-4.14	0	0	1.06	3549	3581.7
-3.98	0	0	1.22	3459	3436.4
-3.82	0	0	1.38	3290	3155.2
-3.65	0	0	1.54	2984	2782.8
-3.49	0	0	1.71	2532	2364.3
-3.33	0	0	1.87	2180	1938.7
-3.17	0	0	2.03	1819	1536.8
-3.00	0	0	2.19	1432	1179.0
-2.84	0	0	2.35	1052	876.2
-2.68	0	0	2.52	856	631.2
-2.52	0	0	2.68	600	441.1
-2.35	0	0	2.84	447	299.1
-2.19	0	0	3.00	294	196.9
-2.03	0	0	3.17	229	125.9
-1.87	0	0	3.33	130	78.2
-1.70	0	0	3.49	91	47.2
-1.54	0	0	3.65	62	27.7
-1.38	0	0.1	3.82	35	15.8
-1.22	0	0.3	3.98	16	8.8
-1.06	0	1.5	4.14	8	4.7
-0.89	0	6.4	4.30	7	2.5
-0.73	10	22.4	4.47	4	1.3
-0.57	41	66.7	4.63	1	0.6
-0.41	93	169.6	4.79	0	0.3
-0.24	235	371.7	4.95	1	0.1
-0.08	508	708.4	5.12	0	0.1

Signal rms. = 1.92 V.

Measurement time = 919 sec.

Peaks = 39255

Positive Zero Crossings = 36560

Irregularity Factor = 0.931

Reg No. 1

25/52 Hz. Band Pass Signal

Table 7.12.

Class Interval Midpoint (z)	Observed Peak Frequency	Expected Peak Frequency	Class Interval Midpoint (z)	Observed Peak Frequency	Expected Peak Frequency
-5.69	0	0	0.09	1607	1539.0
-5.51	0	0	0.27	2411	2295.6
-5.33	0	0	0.45	3013	3061.4
-5.15	0	0	0.63	3860	3702.6
-4.97	0	0	0.81	4173	4116.4
-4.79	0	0	0.99	4090	4256.8
-4.61	0	0	1.17	4147	4133.7
-4.42	0	0	1.36	3795	3797.3
-4.24	0	0	1.54	3340	3317.3
-4.06	0	0	1.72	2709	2766.5
-3.88	0	0	1.90	2150	2208.6
-3.70	0	0	2.08	1689	1691.3
-3.52	0	0	2.26	1228	1244.2
-3.34	0	0	2.44	865	830.4
-3.16	0	0	2.62	553	599.7
-2.98	0	0	2.80	441	393.5
-2.80	0	0	2.98	274	248.9
-2.62	0	0	3.16	157	151.9
-2.44	0	0	3.34	112	89.4
-2.26	0	0	3.52	65	50.8
-2.08	0	0	3.70	25	27.9
-1.90	0	0	3.88	20	14.8
-1.72	0	0	4.06	9	7.6
-1.54	0	0	4.24	7	3.7
-1.35	0	0.3	4.43	1	1.8
-1.17	0	1.5	4.61	1	0.8
-0.99	11	6.6	4.79	1	0.4
-0.81	18	24.8	4.97	0	0.2
-0.63	78	78.0	5.15	0	0.1
-0.45	171	207.0	5.33	0	0
-0.27	432	467.8	5.51	0	0
-0.09	875	909.6	5.69	0	0

Signal rms. = 1.730 V.

Measurement time = 955 sec.

Peaks = 42328

Positive Zero Crossings = 38935

Irregularity Factor = 0.920

Rig No. 2

25/52 Hz. Band Pass Signal

Table 7.13.

Degrees of Freedom . = 764  
Sampling Frequency = 160 Hz.  
Signal rms. = 1.801 V.

Rig No. 1

Degrees of Freedom = 744  
Sampling Frequency = 160 Hz.  
Signal rms. = 1.659 V.

Rig No. 2

25/52 Hz. Band Pass Signal

Table 7.14.

Class Interval Midpoint (z)	Observed Frequency	Expected Frequency	Class Interval Midpoint (z)	Observed Frequency	Expected Frequency
-3.913	1	0.6	0.232	605	642.7
-3.705	0	0.7	0.439	602	599.7
-3.498	0	1.5	0.646	553	536.1
-3.291	2	3.0	0.853	457	459.2
-3.084	3	5.8	1.061	346	376.9
-2.876	6	10.7	1.268	311	296.3
-2.669	13	19.0	1.475	255	223.3
-2.462	29	32.2	1.682	148	161.2
-2.255	58	52.4	1.890	104	111.5
-2.048	89	81.8	2.097	69	73.9
-1.840	112	122.1	2.304	57	46.9
-1.633	179	174.8	2.511	29	28.5
-1.426	234	239.7	2.718	14	16.6
-1.219	332	315.0	2.926	11	9.3
-1.011	386	396.5	3.133	8	5.0
-0.804	496	478.5	3.340	2	2.5
-0.597	562	552.7	3.547	0	1.2
-0.390	639	612.0	3.755	2	0.6
-0.183	634	649.3	3.962	1	0.5
0.025	646	660.0			

Amplitude resolution = 0.450 V. = 0.207 x rms.

Signal rms. = 2.170 V.

Total no. of class intervals = 39

Total no. of samples = 8000

5% value of chisquare = 51

Sample chisquare value = 34.8

Rig No. 1

5/52 Hz. Band Pass Signal

Table 7.15.

Class Interval Midpoint (z)	Observed Frequency	Expected Frequency	Class Interval Midpoint (z)	Observed Frequency	Expected Frequency
-3.210	5	7.3	0.542	504	516.4
-3.022	4	6.3	0.730	449	458.5
-2.835	7	10.9	0.917	397	393.0
-2.647	16	18.2	1.105	331	325.3
-2.459	27	29.3	1.292	258	260.0
-2.272	50	45.6	1.480	189	200.6
-2.084	63	68.6	1.667	142	149.5
-1.897	101	99.5	1.855	96	107.5
-1.709	131	139.4	2.043	65	74.7
-1.521	200	188.5	2.230	49	50.1
-1.334	255	246.2	2.418	43	32.4
-1.146	337	310.5	2.605	22	20.3
-0.959	373	378.1	2.793	13	12.2
-0.771	432	444.4	2.981	8	7.1
-0.584	514	504.5	3.168	3	4.0
-0.396	544	552.9	3.356	2	2.2
-0.208	594	585.0	3.543	3	1.1
-0.021	589	597.7	3.731	2	0.6
0.167	607	589.6	3.918	1	0.5
0.354	574	561.5			

Amplitude resolution = 0.381 V. = 0.188 x rms.

Signal rms. = 2.032 V.

Total no. of class intervals = 39

Total no. of samples = 8000

5% value of chisquare = 51

Sample chisquare value = 24.6

Rig No. 2

5/52 Hz. Band Pass Signal

Table 7.16.

Class Interval Midpoint (z)	Observed Peak Frequency	Expected Peak Frequency	Class Interval Midpoint (z)	Observed Peak Frequency	Expected Peak Frequency
-4.62	0	0	0.07	1540	1454.8
-4.47	0	0	0.22	1964	1778.8
-4.33	0	0	0.37	2284	2037.8
-4.18	0	0	0.51	2542	2354.9
-4.03	0	0	0.66	2710	2557.0
-3.89	0	0	0.81	2770	2676.4
-3.74	0	0	0.95	2777	2704.1
-3.59	0	0	1.10	2613	2541.0
-3.45	0	0	1.25	2443	2496.6
-3.30	0	0	1.39	2276	2287.1
-3.15	0	0	1.54	1869	2032.9
-3.01	0	0	1.69	1503	1754.8
-2.86	0	0	1.83	1329	1472.6
-2.71	0	0	1.98	1123	1202.3
-2.57	0	0	2.13	798	955.8
-2.42	0	0	2.27	669	740.2
-2.27	0	0.1	2.42	483	558.7
-2.13	0	0.2	2.57	362	411.3
-1.98	0	0.6	2.71	235	295.4
-1.83	1	1.5	2.86	184	207.0
-1.69	3	3.5	3.01	102	141.6
-1.54	5	7.6	3.15	78	94.6
-1.39	10	15.7	3.30	49	61.7
-1.25	20	30.6	3.45	33	39.3
-1.10	50	57.4	3.59	13	24.5
-0.95	70	101.7	3.74	15	14.9
-0.81	134	171.5	3.89	7	8.9
-0.66	269	275.2	4.03	5	5.1
-0.51	415	420.9	4.18	0	2.9
-0.37	596	614.2	4.33	0	1.6
-0.22	954	856.0	4.47	1	0.9
-0.07	1290	1140.5	4.62	2	0.5

Signal rms. = 2.130 V.

Measurement time = 909 sec.

Peaks = 36776

Rig No. 1

Positive Zero Crossings = 29371

Irregularity Factor = 0.799

5/52 Hz. Band Pass Signal

Table 7.17.

Class Interval Midpoint (z)	Observed Peak Frequency	Expected Peak Frequency	Class Interval Midpoint (z)	Observed Peak Frequency	Expected Peak Frequency
-4.70	0	0	0.08	1864	1844.0
-4.55	0	0	0.22	2226	2256.6
-4.41	0	0	0.37	2872	2647.8
-4.26	0	0	0.52	3097	2983.2
-4.11	0	0	0.67	3133	3232.0
-3.96	0	0	0.82	3253	3371.9
-3.81	0	0	0.97	3367	3392.7
-3.66	0	0	1.12	3357	3296.8
-3.51	0	0	1.27	3130	3098.0
-3.36	0	0	1.42	2833	2818.8
-3.21	0	0	1.57	2460	2486.4
-3.06	0	0	1.72	2098	2128.3
-2.91	0	0	1.87	1736	1769.5
-2.76	0	0	2.02	1403	1430.3
-2.61	0	0	2.17	1027	1124.7
-2.46	0	0	2.32	778	860.9
-2.31	0	0.1	2.46	641	641.8
-2.17	0	0.3	2.61	467	466.3
-2.02	0	0.7	2.76	335	330.2
-1.87	2	1.7	2.91	226	228.0
-1.72	3	4.0	3.06	163	153.6
-1.57	9	8.8	3.21	106	101.0
-1.42	11	18.5	3.36	66	64.7
-1.27	39	36.7	3.51	37	40.5
-1.12	85	69.3	3.66	18	24.8
-0.97	102	124.0	3.81	10	14.8
-0.82	214	211.0	3.96	5	8.6
-0.67	371	341.3	4.11	6	4.9
-0.52	527	525.6	4.26	4	2.7
-0.37	823	771.2	4.41	1	1.5
-0.22	1115	1079.3	4.55	2	0.8
-0.07	1458	1442.7	4.70	1	0.4

Signal rms. = 2.093 V.

Measurement time = 1069 sec.

Peaks = 45481

Rig No. 2

Positive Zero Crossings = 35969

Irregularity Factor = 0.796

5/52 Hz. Band Pass Signal

Table 7.18.

Degrees of Freedom = 1272  
Sampling Frequency = 160 Hz.  
Signal rms. = 2.170 V.

Rig No. 1

Degrees of Freedom = 1092  
Sampling Frequency = 160 Hz.  
Signal rms. = 2.032 V.

Rig No. 2

5/52 Hz. Band Pass Signal

Table 7.19.

SYNTHESIZED		Irregularity Factor	Peaks /sec.	+ve Zero Crossings /sec.
47 Hz. Centre Frequency Signal		0.999	49.74	49.68
25/52 Hz. Band Pass Signal		0.922	44.65	41.15
5/52 Hz. Band Pass Signal		0.786	41.79	32.85
ACHIEVED				
47 Hz. Centre Frequency Signal	Rig. No.1	0.999	47.24	47.21
	Rig. No.2	1.000	46.92	46.92
25/52 Hz. Band Pass Signal	Rig. No.1	0.931	42.75	39.78
	Rig. No.2	0.920	44.27	40.72
5.52 Hz. Band Pass Signal	Rig. No.1	0.799	40.47	32.30
	Rig. No.2	0.796	42.25	33.62
Constant Amplitude Signal		47 Hz.		

Table 7.20

Nominal Rms. Stress Tsi.	14.2	11.1	8.9	8.0	6.22	5.45
Mean of $\log_{10}$ of Lives (seconds)	2.8465	3.3327	3.5805	4.0495	4.6024	4.8220
Sample Variance	0.0027	0.0029	0.0016	0.0034	0.0040	0.0008

Rig No. 1

Nominal Rms. Stress Tsi.	14.2	11.1	8.9	8.0	6.22	5.45
Mean of $\log_{10}$ of Lives (seconds)	2.8862	3.3742	3.9395	4.0395	4.5192	4.8375
Sample Variance	0.0066	0.0101	0.0021	0.0061	0.0063	0.0207

Rig No. 2

Sample 'F' Value	2.49	3.49	2.18	1.80	1.27	1.04
Sample 't' Value	0.87	0.82	1.31	0.39	0.30	0.17

5 specimens tested at each stress level.

2-sided 5% F Value = 9.60 for (4,4) degrees of freedom.

2-sided 5% t Value = 2.31 for 8 degrees of freedom.

47 Hz. Centre Frequency Signal

Table 7.21.

Nominal Rms. Stress Tsi.	14.2	11.1	8.9	8.0	6.22	5.45
Mean of $\log_{10}$ of Lives (seconds)	2.8674	3.3534	3.9100	4.0412	4.6103	4.8299
Antilog of Mean log life (seconds)	737	2,257	8,129	10,994	40,811	67,569
Sample Variance	0.0045	0.0063	0.0026	0.0043	0.0070	0.0181

Combined results for 10 specimens at each stress level.

47 Hz. Centre Frequency Signal

Table 7.22.

Nominal Rms. Stress Tsi.	11.0	9.0	7.5	6.5	5.5
Mean of $\log_{10}$ of Lives (seconds)	3.3562	3.8285	4.2250	4.4345	4.9661
Sample Variance	0.0019	0.0024	0.0034	0.0231	0.0129

Rig No. 1

Nominal Rms. Stress Tsi.	11.0	9.0	7.5	6.5	5.5
Mean of $\log_{10}$ of Lives (seconds)	3.3693	3.7878	4.1414	4.5311	4.8596
Sample Variance	0.0023	0.0026	0.0070	0.0257	0.0157

Rig No. 2

Sample 'F' Value	1.24	1.09	2.07	1.11	1.22
Sample 't' Value	0.45	1.30	1.91	0.65	1.01

5 specimens tested at each stress level.

2-sided 5% F Value = 9.60 for (4,4) degrees of freedom.

2-sided 5% t Value = 2.31 for 8 degrees of freedom.

25/52 Hz. Band Pass Signal

Table 7.23.

Nominal Rms. Stress Tsi.	11.0	9.0	7.5	6.5	5.5
Mean of $\log_{10}$ of Lives (seconds)	3.3628	3.8081	4.1847	4.5078	4.9278
Antilog of Mean log life (seconds)	2,306	6,428	15,302	32,196	84,687
Sample Variance	0.0019	0.0027	0.0067	0.0170	0.0114

Combined results for 10 specimens at each stress level.

25/52 Hz. Band Pass Signal

Table 7.24.

Nominal Rms. Stress Tsi.	11.0	8.70	7.16	6.28	5.78
Mean of $\log_{10}$ of Lives (seconds)	3.5005	3.8395	4.3024	4.5258	4.8419
Sample Variance	0.0012	0.0053	0.0040	0.0026	0.0140

Rig No. 1

Nominal Rms. Stress Tsi.	11.0	8.70	7.16	6.28	5.78
Mean of $\log_{10}$ of Lives (seconds)	3.4820	3.7687	4.2679	4.4903	4.8632
Sample Variance	0.0011	0.0041	0.0043	0.0054	0.0095

Rig No. 2

Sample 'F' Value	1.14	1.27	1.06	2.06	1.54
Sample 't' Value	0.83	1.64	0.85	0.89	0.31

5 specimens tested at each stress level.

2-sided 5% F Value = 9.60 for (4,4) degrees of freedom.

2-sided 5% t Value = 2.31 for 8 degrees of freedom.

5/52 Hz. Band Pass Signal

Table 7.25.

Nominal Rms. Stress Tsi.	11.0	8.70	7.16	6.28	5.78
Mean of $\log_{10}$ of Lives (seconds)	3.4913	3.8041	4.2851	4.5080	4.8526
Antilog of Mean log life (seconds)	3,099	6,370	19,280	32,208	71,221
Sample Variance	0.0020	0.0056	0.0040	0.0039	0.0108

Combined results for 10 specimens at each stress level.

5/52 Hz. Band Pass Signal

Table 7.26.

Signal	Description	Nominal RMS Stress Tsi.	Total Life			
			Seconds	Peaks	Positive Zero Crossings	Positive Peaks
47Hz. Centre Frequency		14.2	737	34,650	34,650	34,650
47Hz. Centre Frequency		11.1	2,257	106,000	106,000	106,000
25/52Hz. Band Pass		11.0	2,306	102,000	93,900	98,400
5/52 Hz. Band Pass.		11.0	3,099	131,000	104,200	117,000
47 Hz. Centre Frequency		8.9	8,129	382,000	382,000	382,000
25/52 Hz. Band Pass		9.0	6,428	285,000	262,000	274,000
5/52 Hz. Band Pass		8.7	6,370	269,000	214,500	241,000
47 Hz. Centre Frequency		8.0	10,994	516,000	516,000	516,000
25/52 Hz. Band Pass		7.5	15,302	677,000	623,000	653,000
5/52 Hz. Band Pass		7.16	19,280	814,000	648,000	728,000
47 Hz. Centre Frequency		6.22	40,811	1,920,000	1,920,000	1,920,000
25/52 Hz. Band Pass		6.5	32,196	1,424,000	1,311,000	1,372,000
5/52 Hz. Band Pass		6.28	32,208	1,361,000	1,083,000	1,218,000
47 Hz. Centre Frequency		5.45	67,569	3,180,000	3,180,000	3,180,000
25/52 Hz. Band Pass		5.5	84,687	3,010,000	2,400,000	2,690,000
5/52 Hz. Band Pass		5.78	71,221	3,745,000	3,450,000	3,615,000

Combined Results for random Testing.

Table 7.27

Specimen Identification	Nominal Rms. Stress Psi.	Stage A Life (seconds)	Total Life (seconds)
5	11.1	500	2,321
4	9.79	1,300	4,161
2	8.85	1,400	5,218
EE	9.35	3,600	6,454
6	7.78	1,600	9,144
1	7.98	2,600	9,277
7	7.70	3,300	11,975
11	7.1	3,800	16,380
DD	7.34	4,800	18,977
9	7.1	5,800	19,794
CC	6.65	5,900	20,863
12	7.1	8,300	22,348
13	6.47	8,500	40,288

47 Hz. Centre Frequency Signal

Table 7.28

Specimen Identification	Nominal Rms. Stress Psi.	Stage A Life (seconds)	Total Life (seconds)
MB3	7.9	2,500	9,420
MB2	8.0	4,200	11,520
MB1	8.0	5,000	13,140
MB4	7.5	4,000	20,850
MB5	6.7	7,000	21,543
MB5	6.9	8,000	21,840
MB11	6.7	3,000	25,500
MB7	6.4	9,200	25,800
MB12	6.4	8,000	26,160
MB9	6.2	10,500	33,420
MB8	6.3	13,000	55,920
MB10	6.15	16,500	61,620

25/52 Hz. Band Pass Signal

Table 7.29.

Specimen Identification	Nominal Rms. Stress Psi.	Stage A Life (seconds)	Total Life (seconds)
BB8	7.5	2,500	8,700
BB7	7.85	3,500	15,060
BB3	6.9	8,000	25,728
BB6	6.65	9,000	30,180
BB9	6.4	12,000	30,350
BB5	6.27	18,000	41,220
BB4	6.15	28,000	60,520
BB2	6.9	34,000	63,372

5/52 Hz. Band Pass Signal

Table 7.30.

Specimen Identification	Nominal Rms. Stress Tsi.	Crack Length"		Total Equivalent Crack Length"	Total Defectometer Stage B Divisions
		Top Notch	Bottom Notch		
BB11	10.5	0.0005	-	0.0005	2.5
BB15	12.7	-	0.0005	0.0005	2.5
BB16	12.7	0.010	-	0.010	4.0
BB12	11.0	0.003	0.012	0.020	5.7
BB13	12.4	0.004	0.017	0.021	10.0
BB14	13.1	0.021	0.023	0.044	12.7
BB17	13.1	0.025	0.024	0.049	20.0

5/52 Hz. Band Pass Signal

Table 7.31.

Specimen Identification	Nominal Rms. Stress Tsi.	Crack Length"		Total Equivalent Crack Length"	Total Defectometer Stage B Divisions
		Top Notch	Bottom Notch		
1(b)	11.3	0.0006	-	0.0006	0.8
1	11.3	0.0025	0.0004	0.003	3.8
EE6	14.9	0.003	0.006	0.009	7.0
2	12.7	0.011	0.004	0.015	4.1
EE1	14.9	0.016	0.008	0.024	12.0
EE5	14.9	0.007	0.018	0.025	7.1
EE4	14.9	0.018	0.015	0.033	12.0
3	11.3	0.019	0.015	0.034	16.8
EE3	14.9	0.020	0.020	0.040	14.0

47 Hz. Centre Frequency Signal

Table 7.32.

Nominal Peak Stress

1 - 14.6 Tsi.

2 - 15.7 Tsi.

3 - 17.4 Tsi.

4 - 21.0 Tsi.

5 - 23.9 Tsi.

6 - 30.1 Tsi.

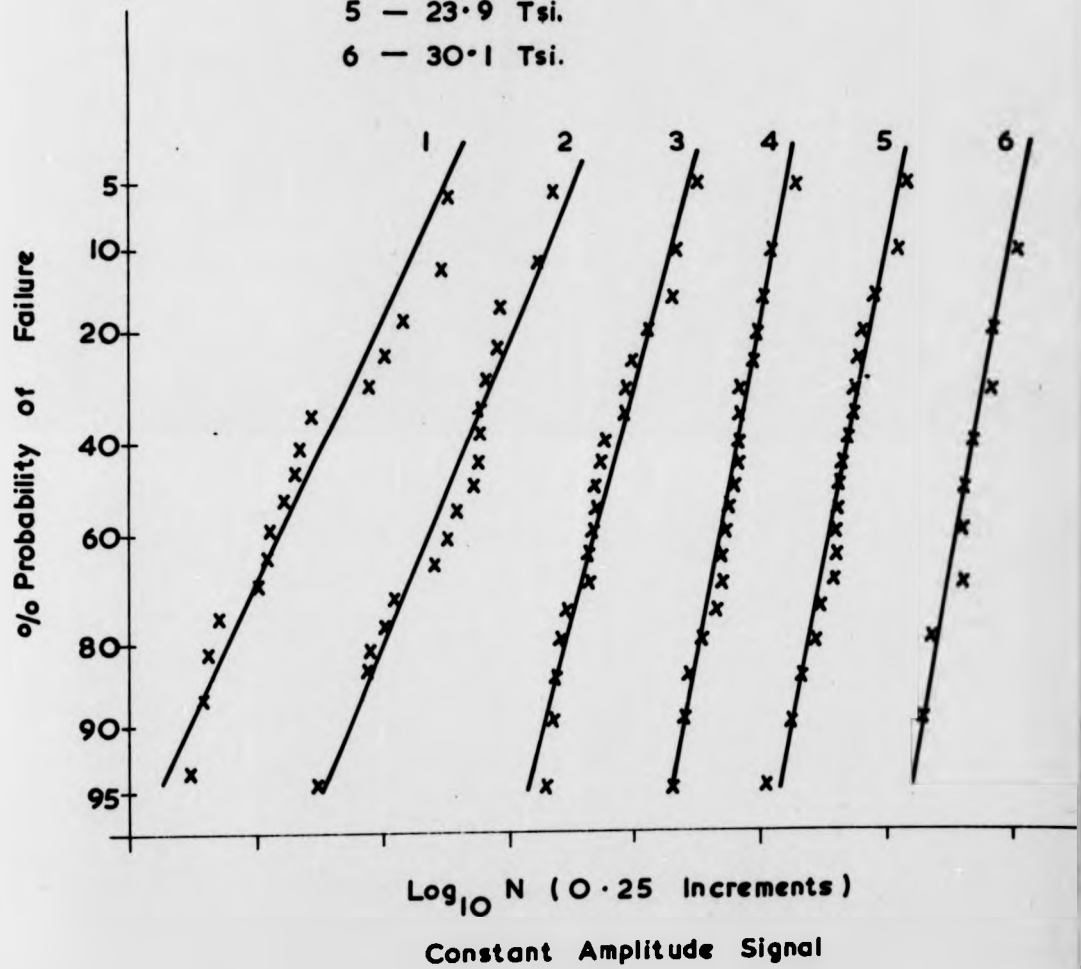
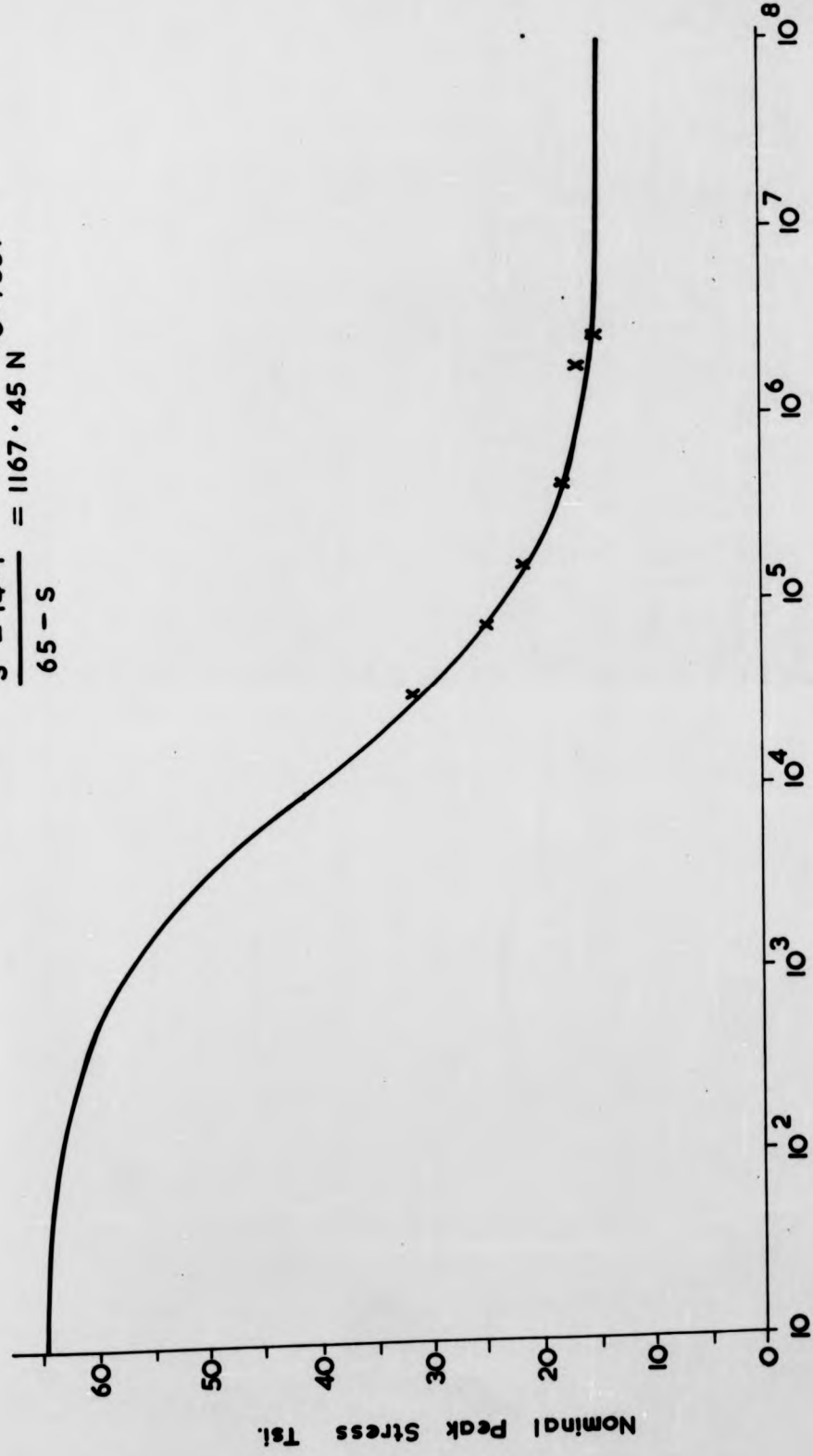


FIG.7.1.

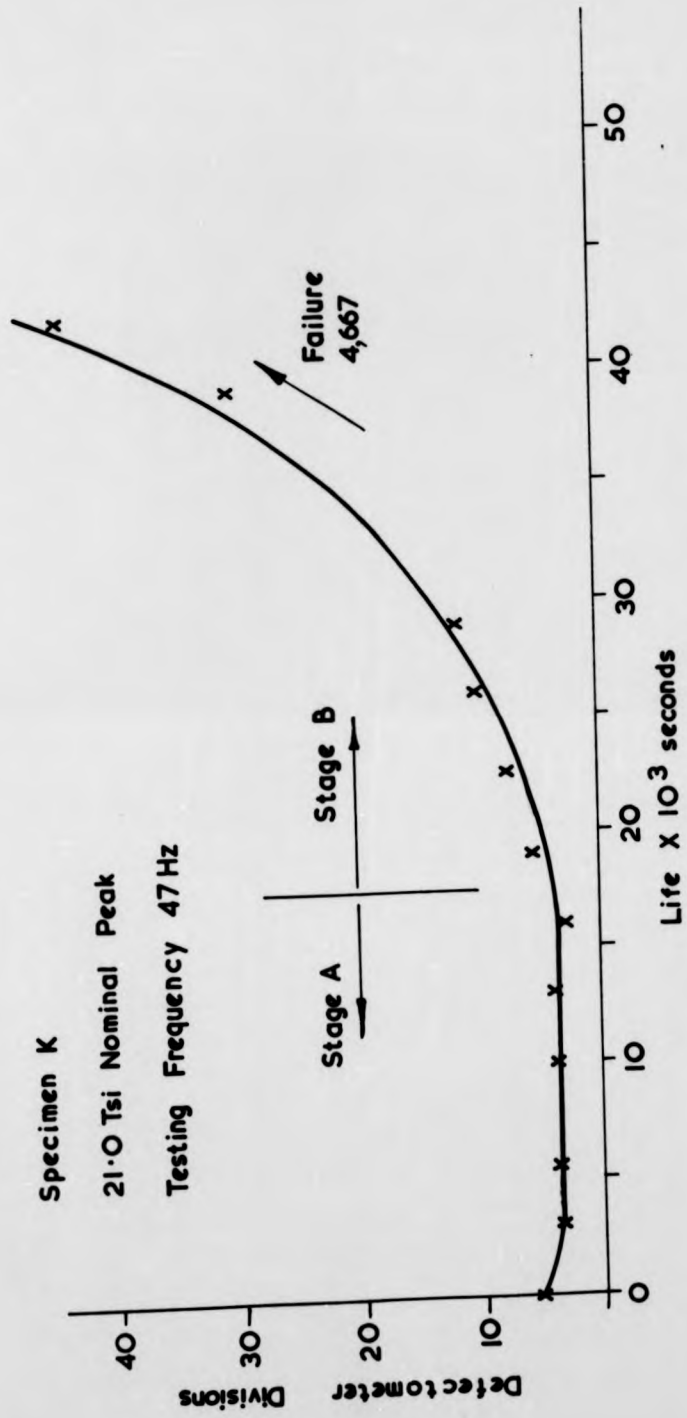
$$\frac{S - 14.1}{65 - S} = 1167 \cdot 45 N^{-0.7557}$$



Cycles to Failure

FIG. 7.2.

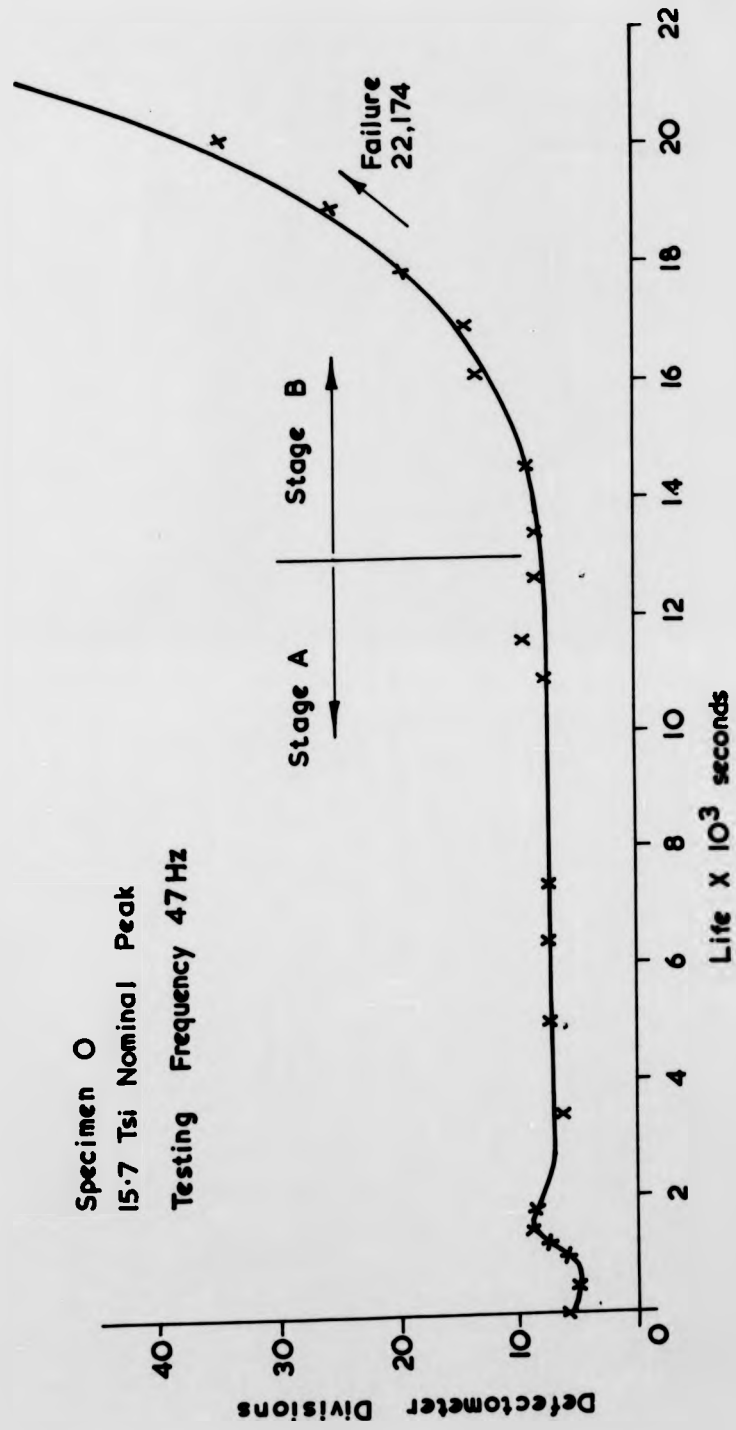
$$\frac{92 - 2}{2 - 14.1} = 1193.42 \text{ M} - 0.1221$$



Constant Amplitude Loading

FIG. 7. 3.

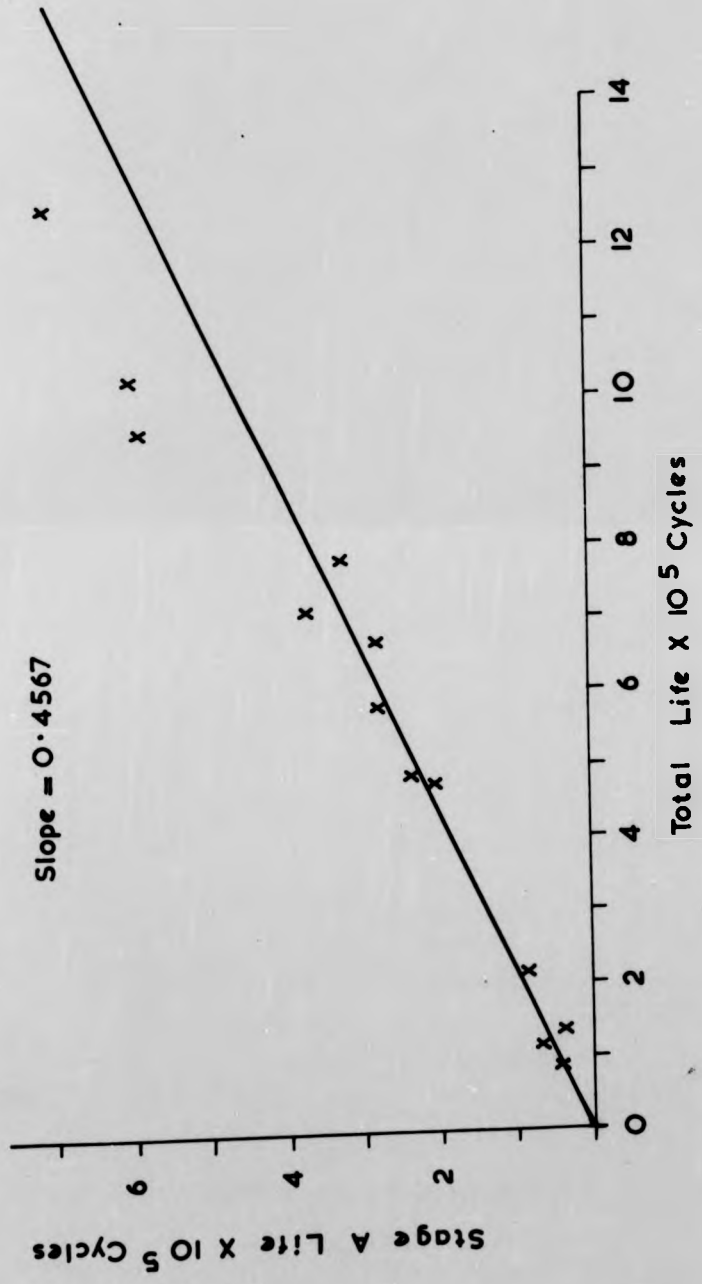
Specimen O  
15.7 Tsi Nominal Peak  
Testing Frequency 47 Hz



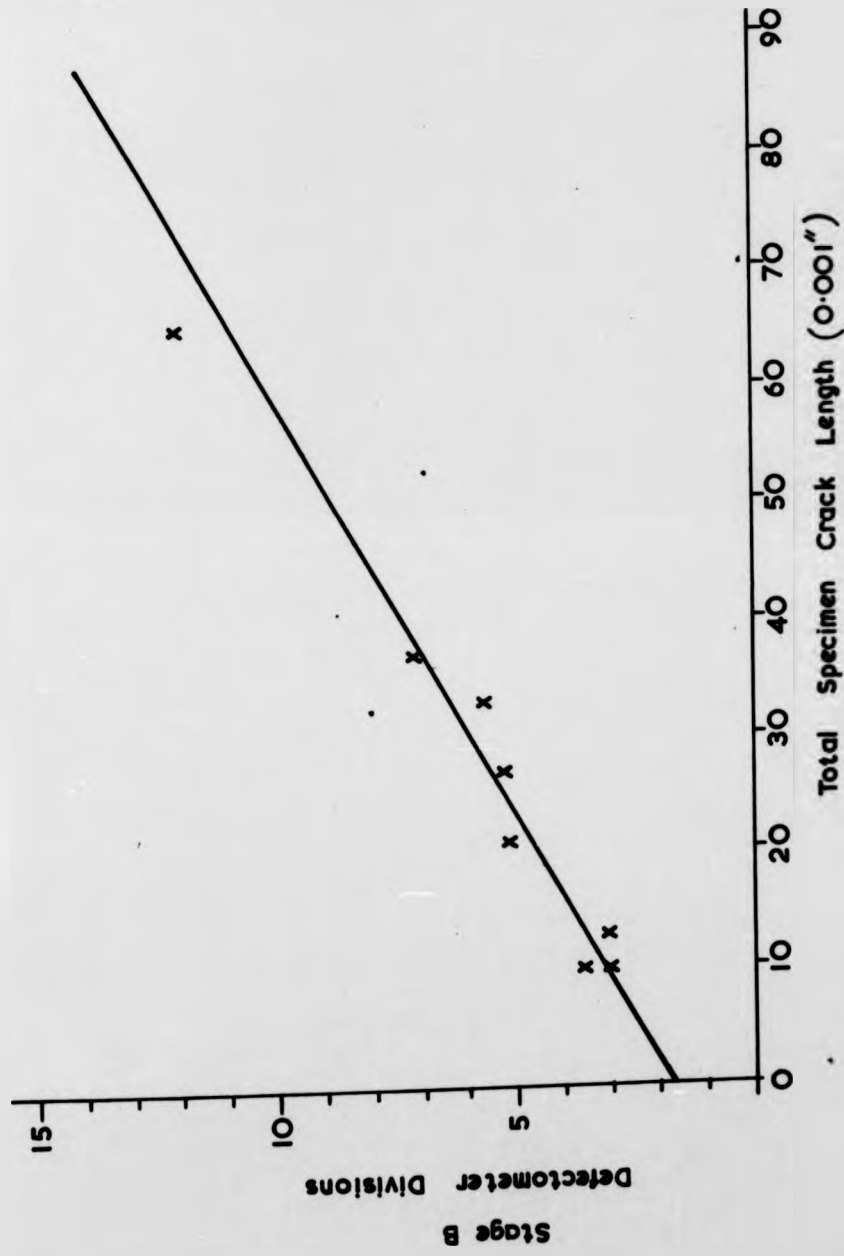
Constant Amplitude Loading.

FIG.7.4.

40  
STAGE A  
TOTAL LIFE  
STAGE B

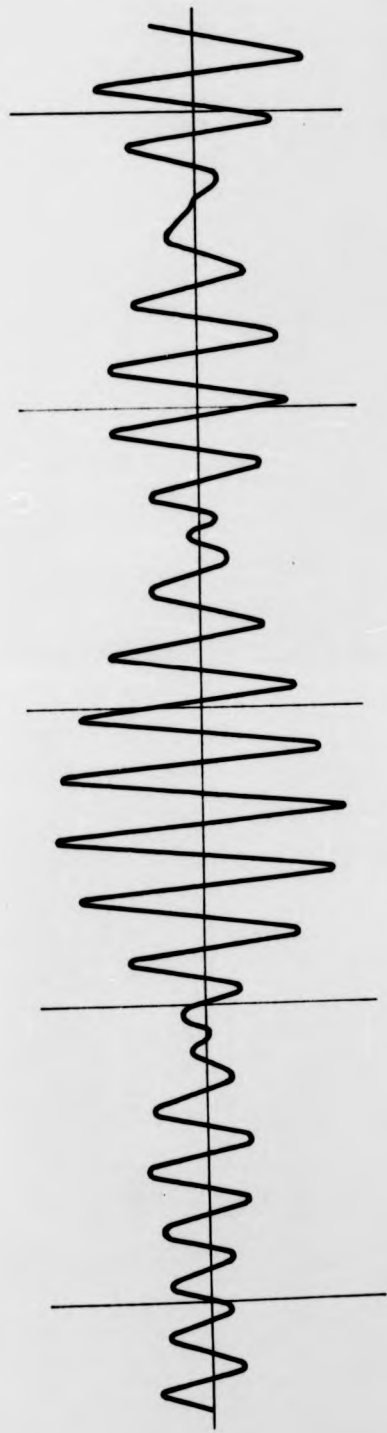


Constant Amplitude Loading  
FIG. 7.5.

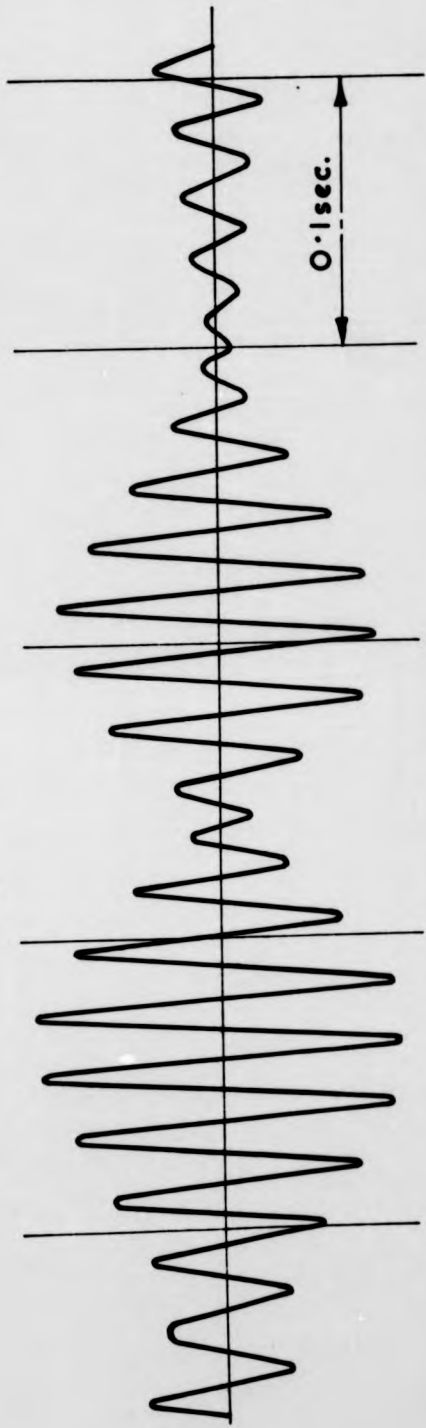


Constant Amplitude Loading

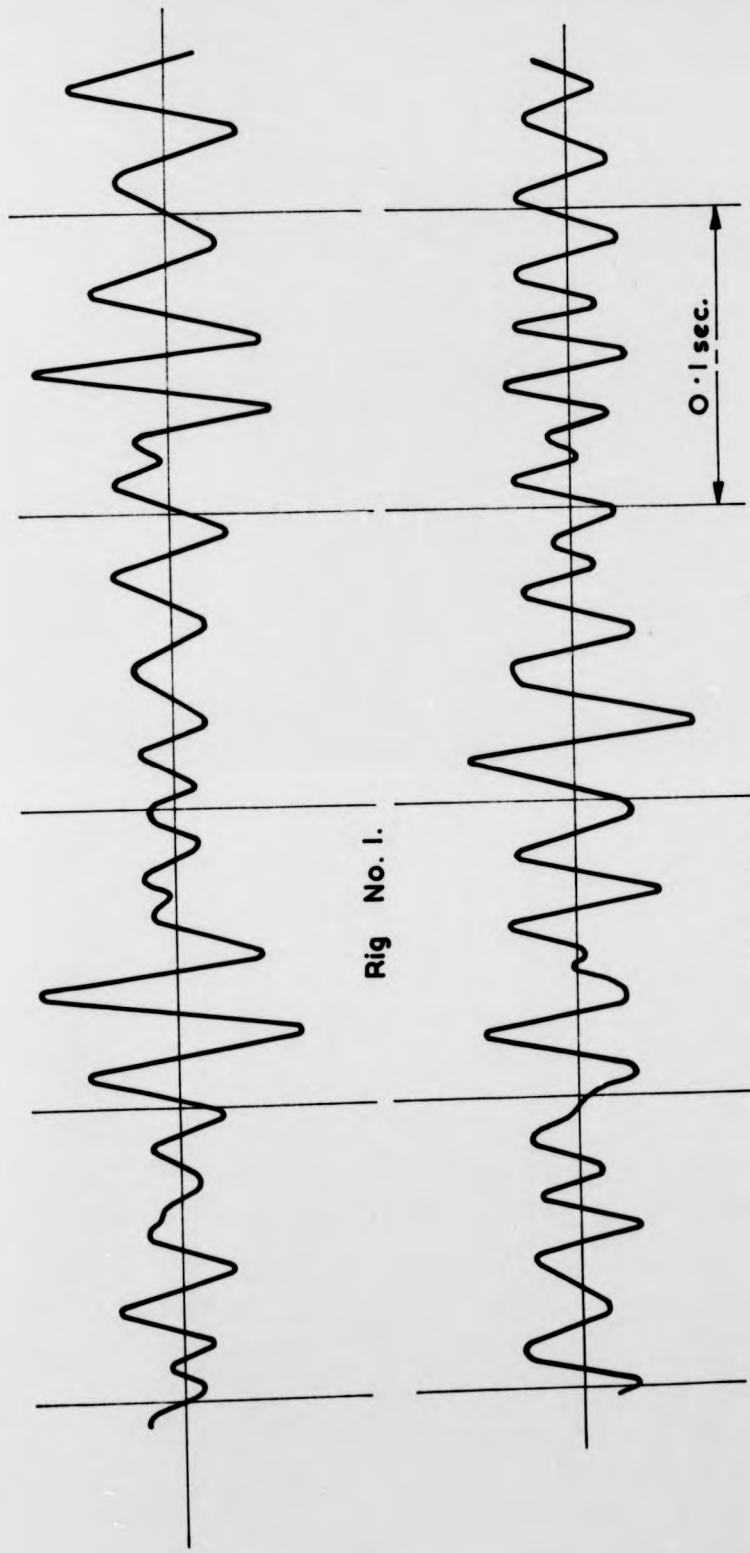
FIG. 7. 6.



Rig No. 1.



Rig No. 2.  
47 Hz Centre Frequency Signal.  
FIG.7.7.



Rig No. 1.

Rig No. 2.

25/52 Hz Band Pass Signal

FIG. 7.8.

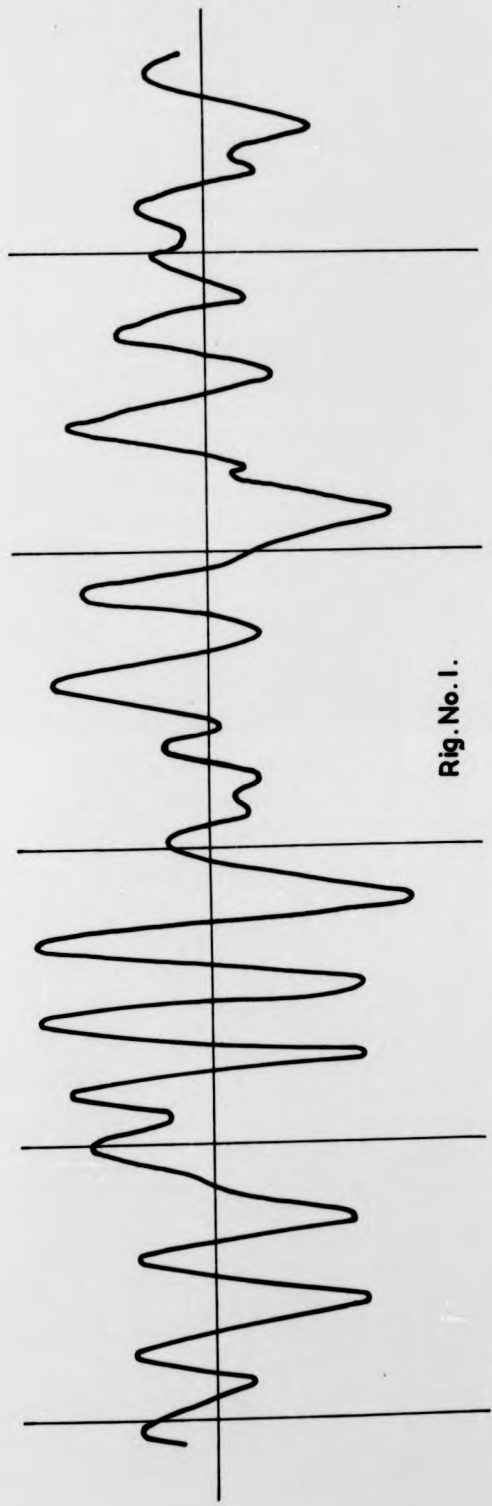


Fig. No. 1.

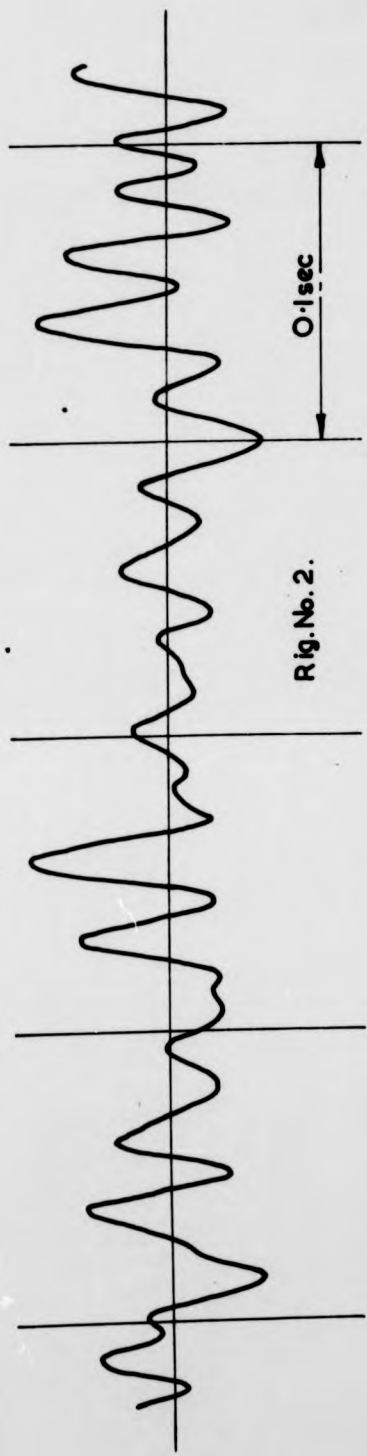
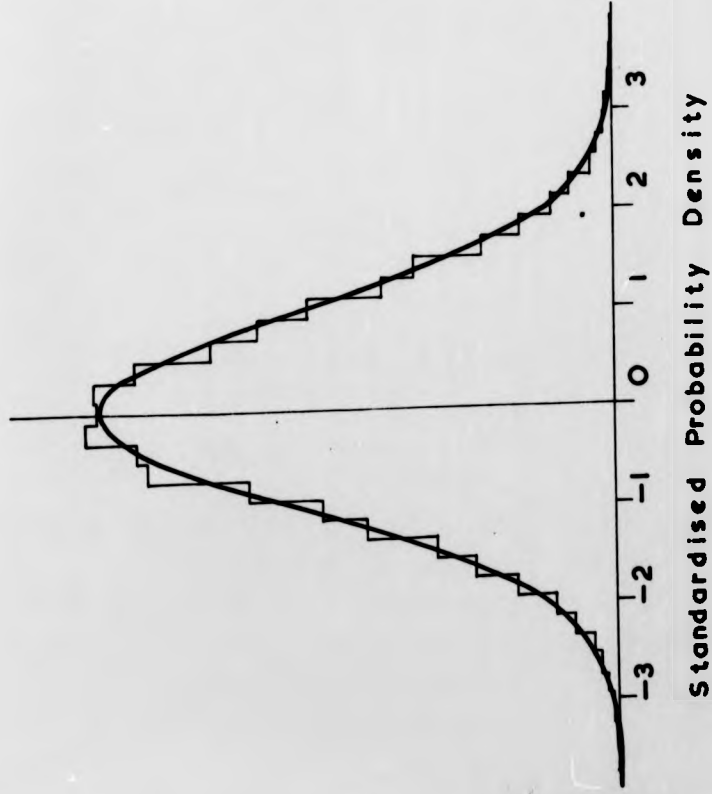


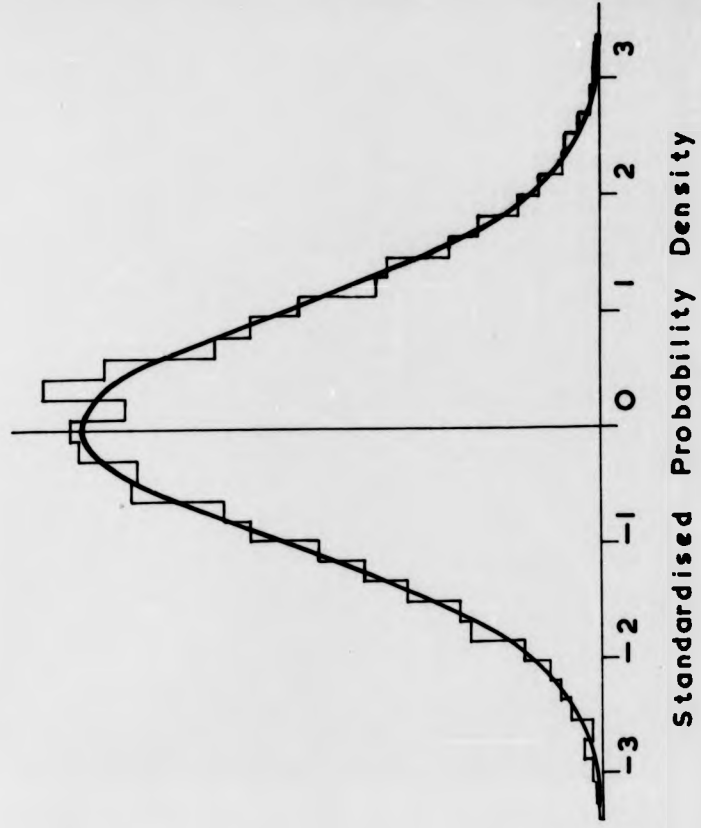
Fig. No. 2.

5/52Hz Band Pass Signal

FIG. 7.9.



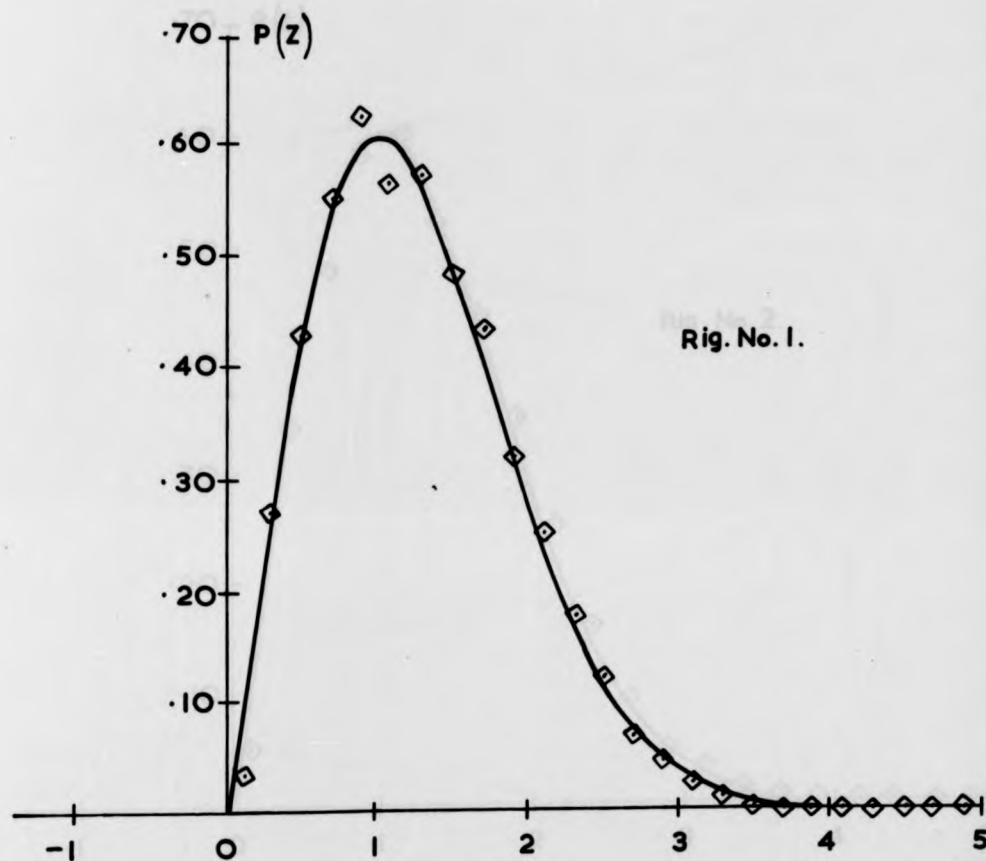
Rig No. 1.



Rig No. 2.

47 Hz Centre Frequency Signal

FIG.7.10.

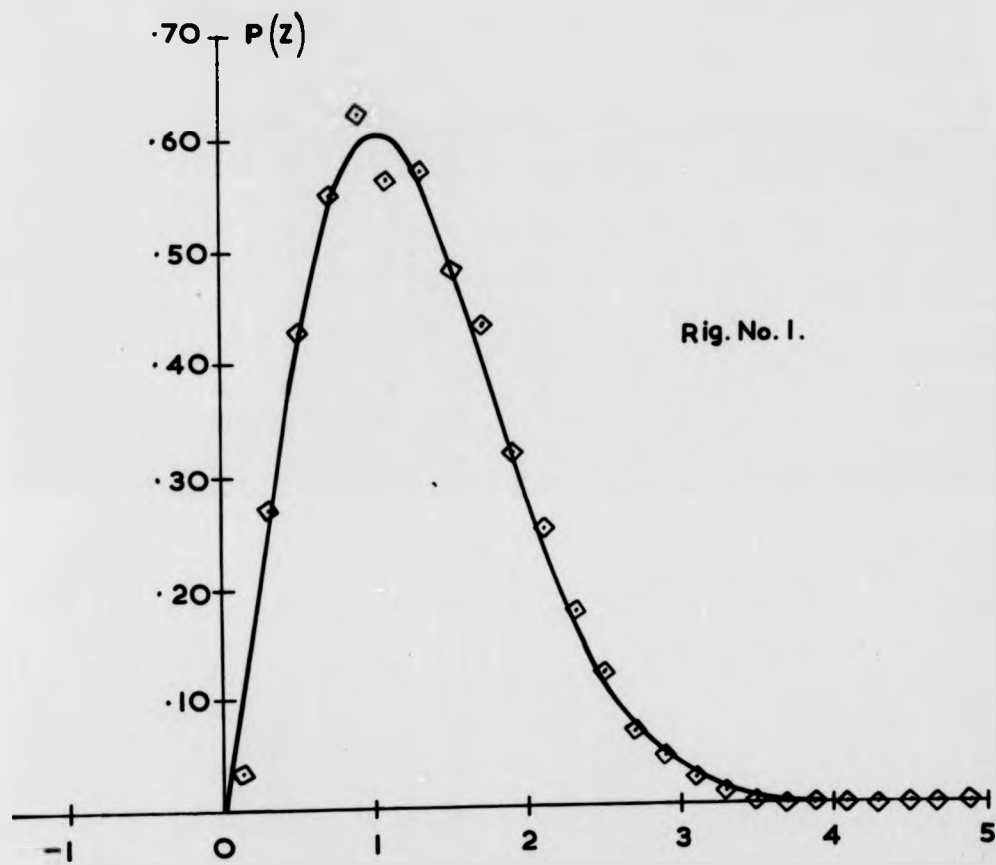


Rig. No. I.

Standardised Peak Probability Density Function

47Hz Centre Frequency Signal

FIG. 7. II.

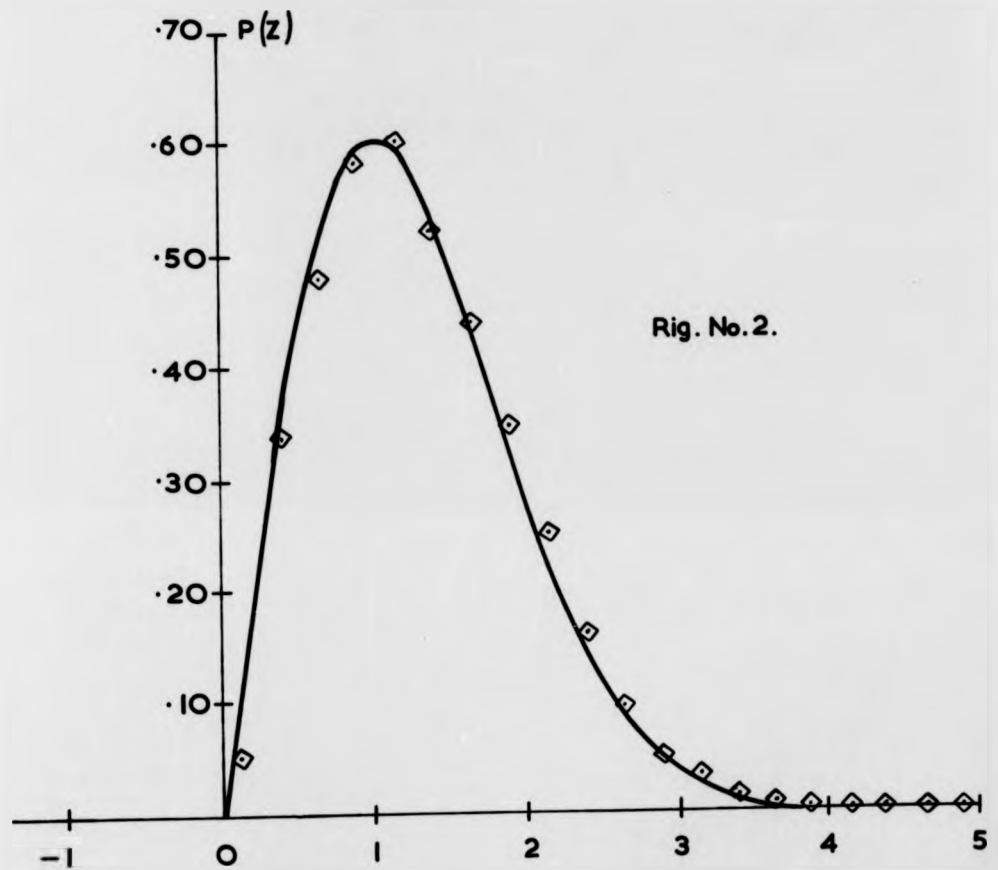


Rig. No. 1.

Standardised Peak Probability Density Function

47Hz Centre Frequency Signal

FIG. 7. II.



Standardised Peak Probability Density Function

47 Hz Centre Frequency Signal

FIG.7 12

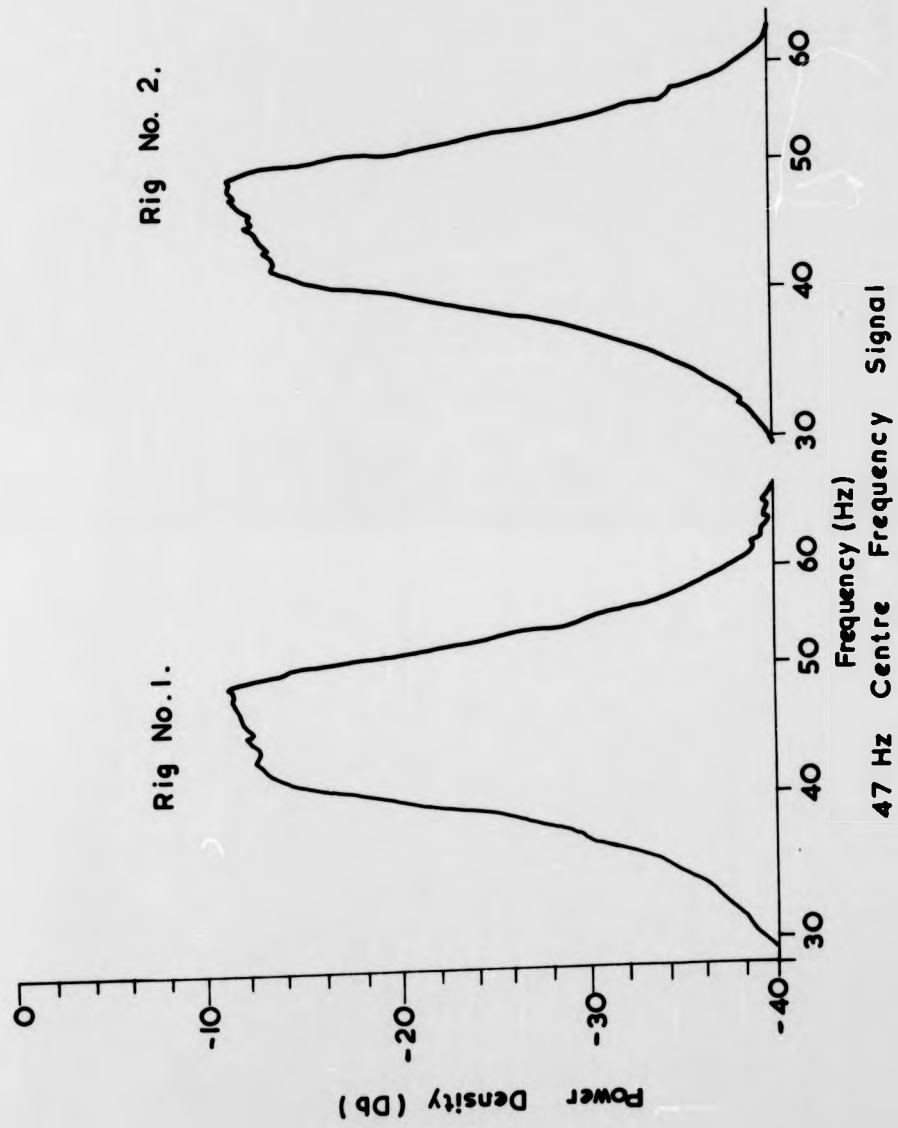


FIG.7. 13.

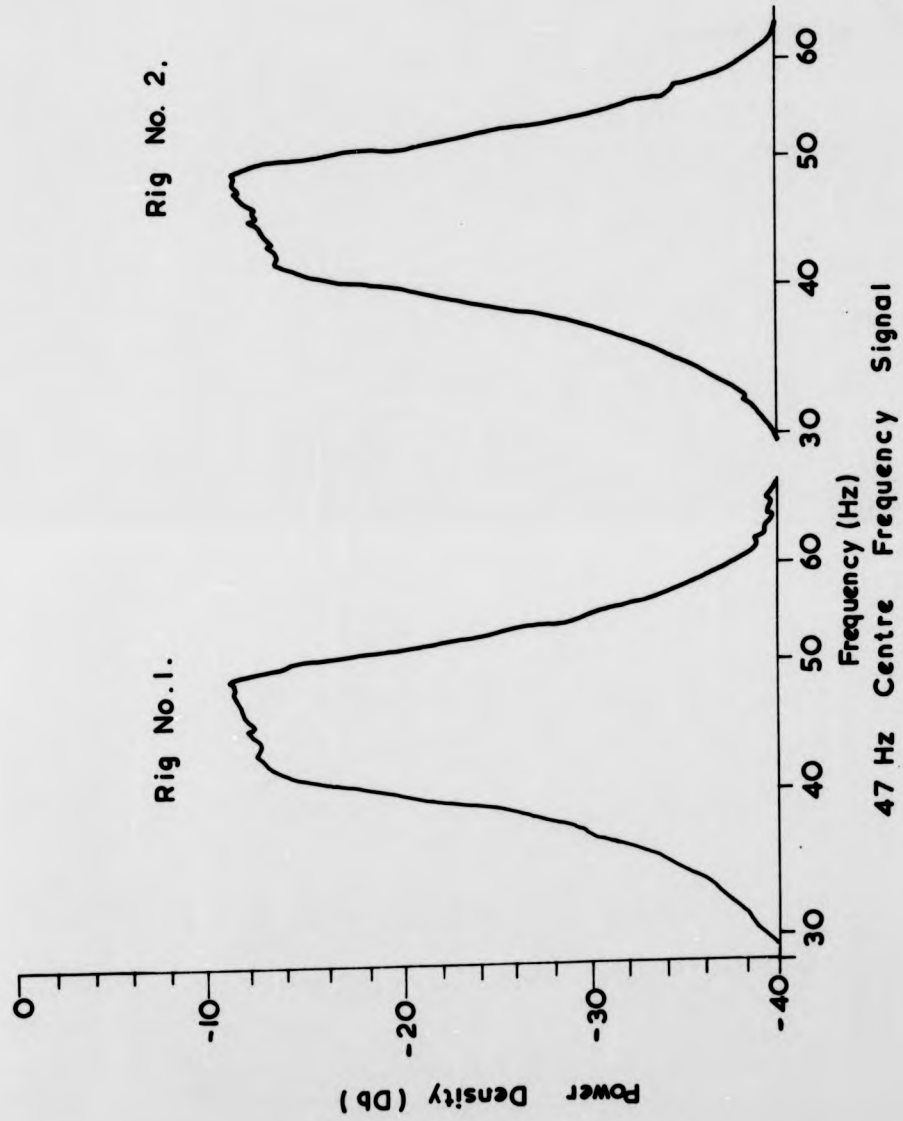
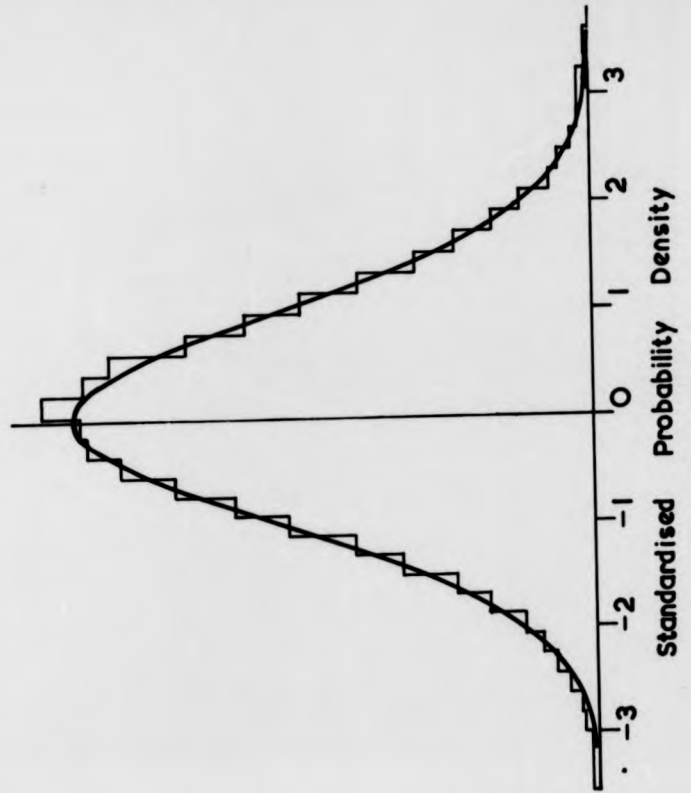


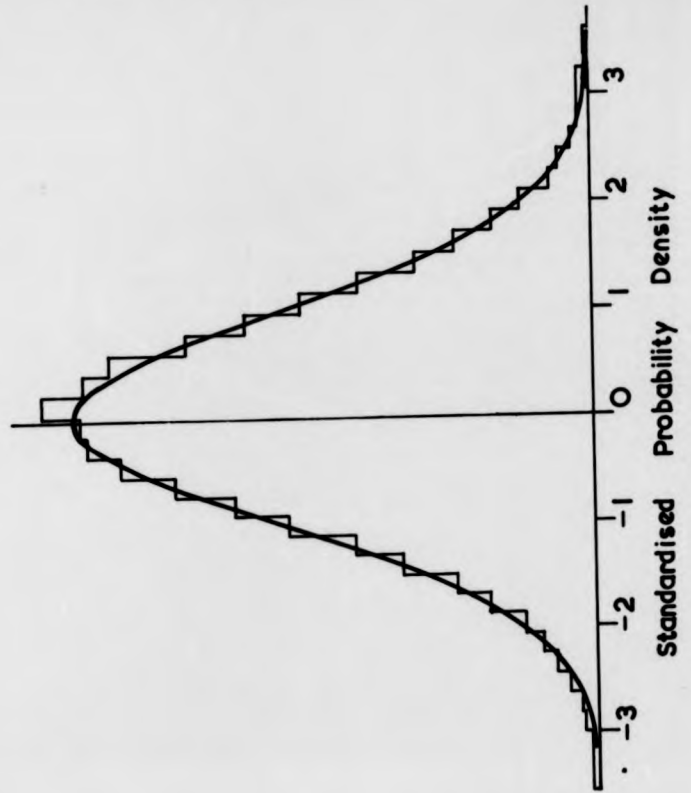
FIG. 7. 13.



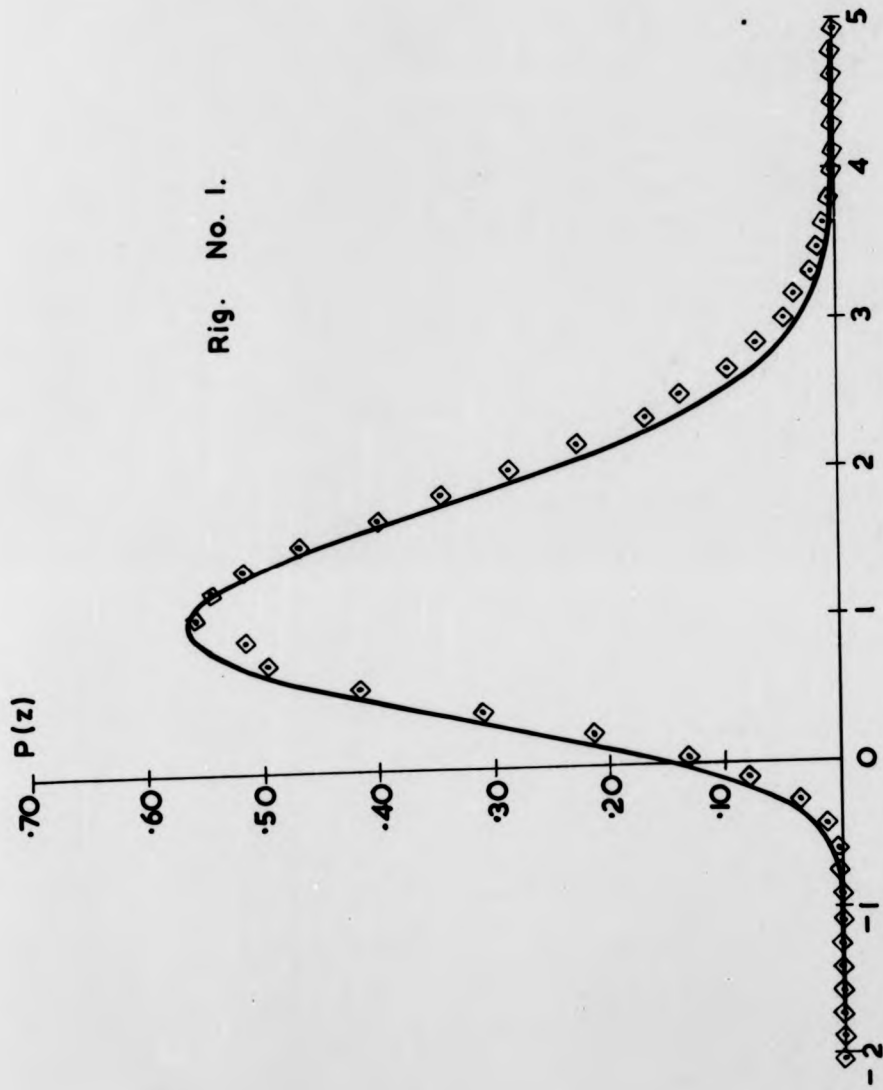
Rig. No.1.

25/52 Hz Band Pass Signal

FIG.7. 14.



Rig. No.2.



Standardised Peak Probability Density Function  
25/52 Hz Band Pass Signal

FIG. 7.15.

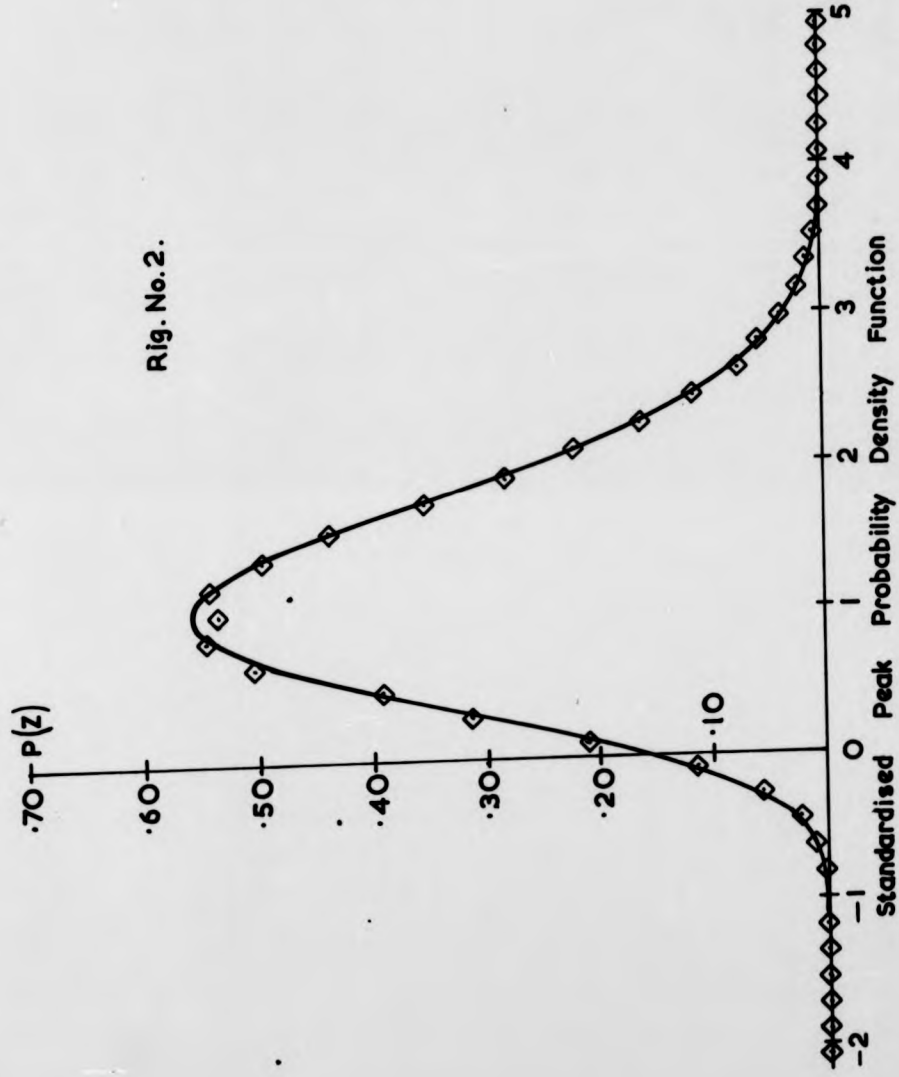
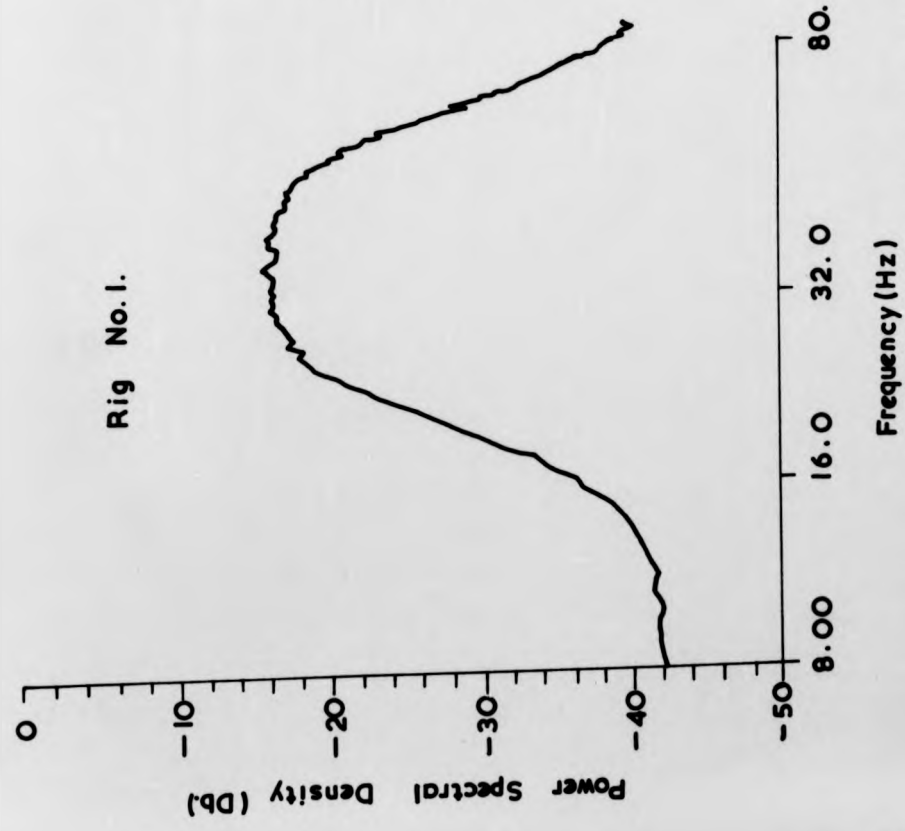
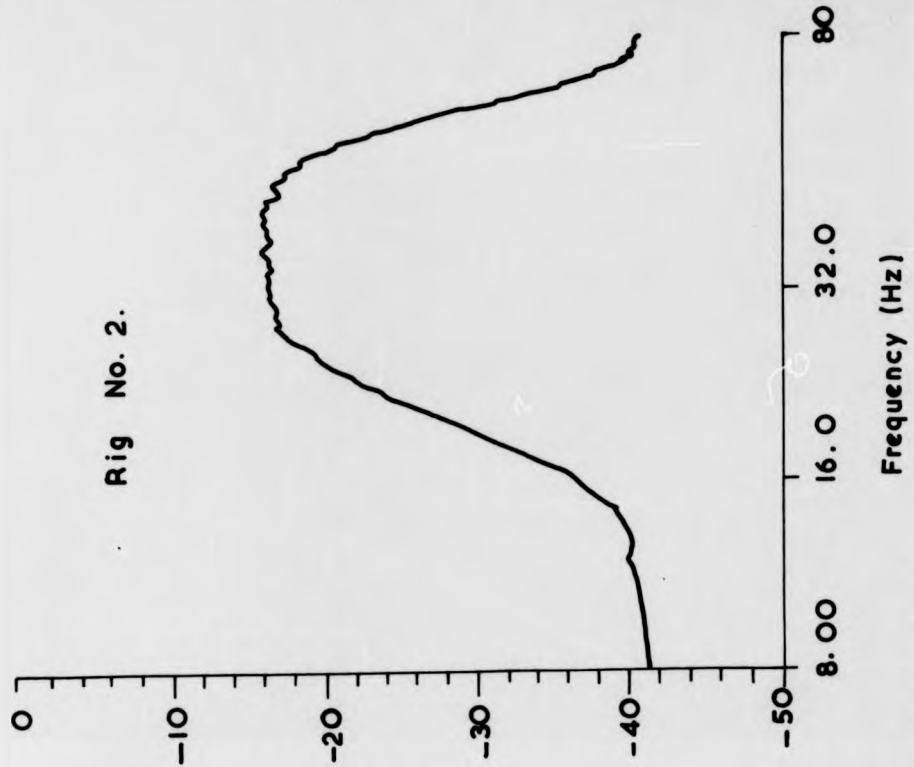


FIG. 7. 16.

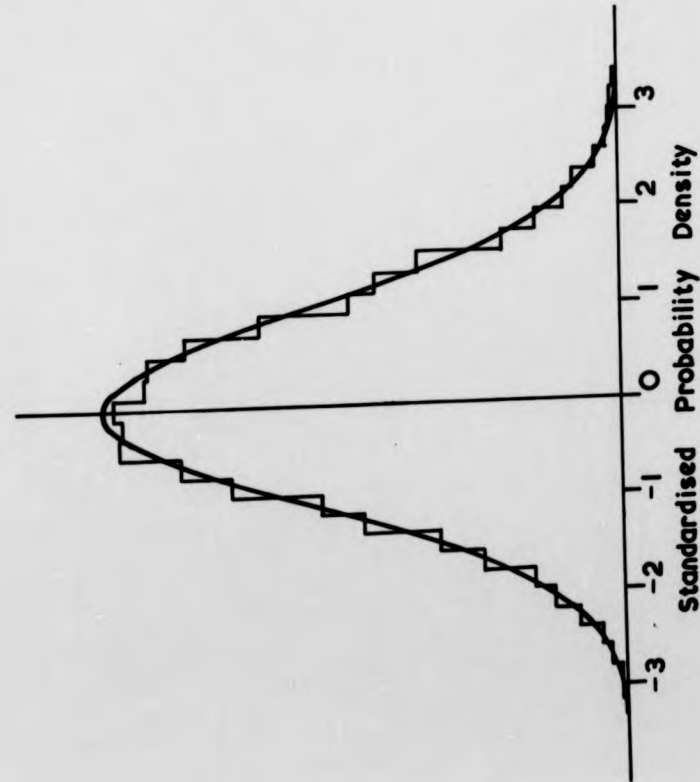
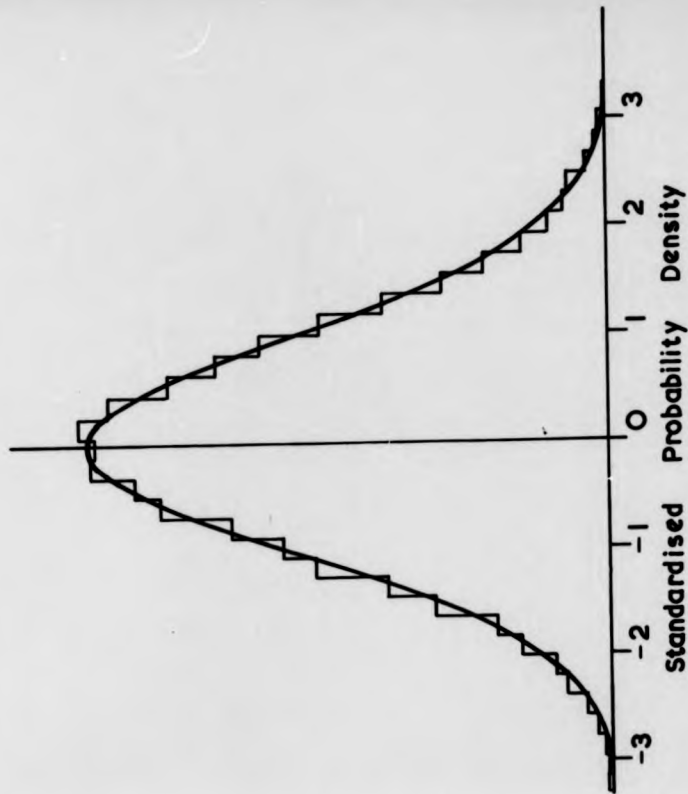


25/52 Hz Band Pass Signal

FIG. 7.17.

B16 No. 5

B16 No. 1



5/52 Hz Band Pass Signal

FIG.7.18.

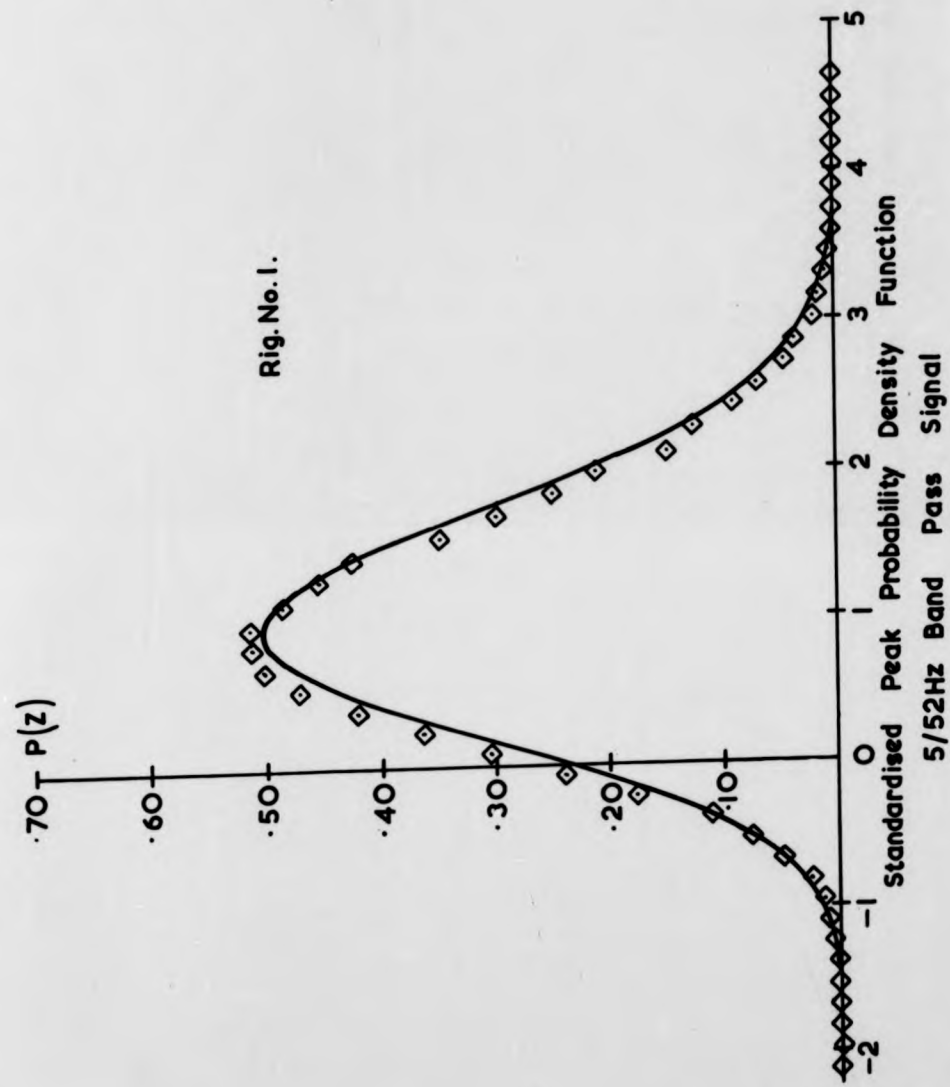


FIG. 7.19.

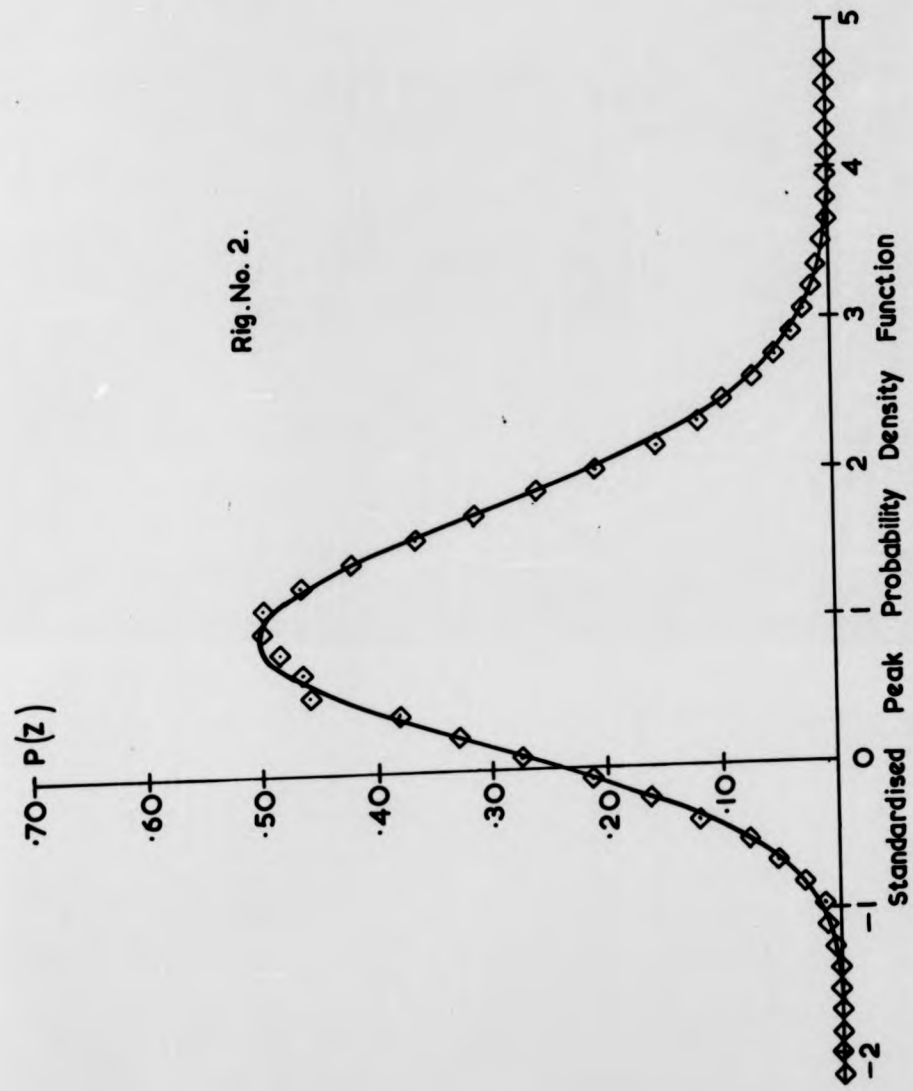
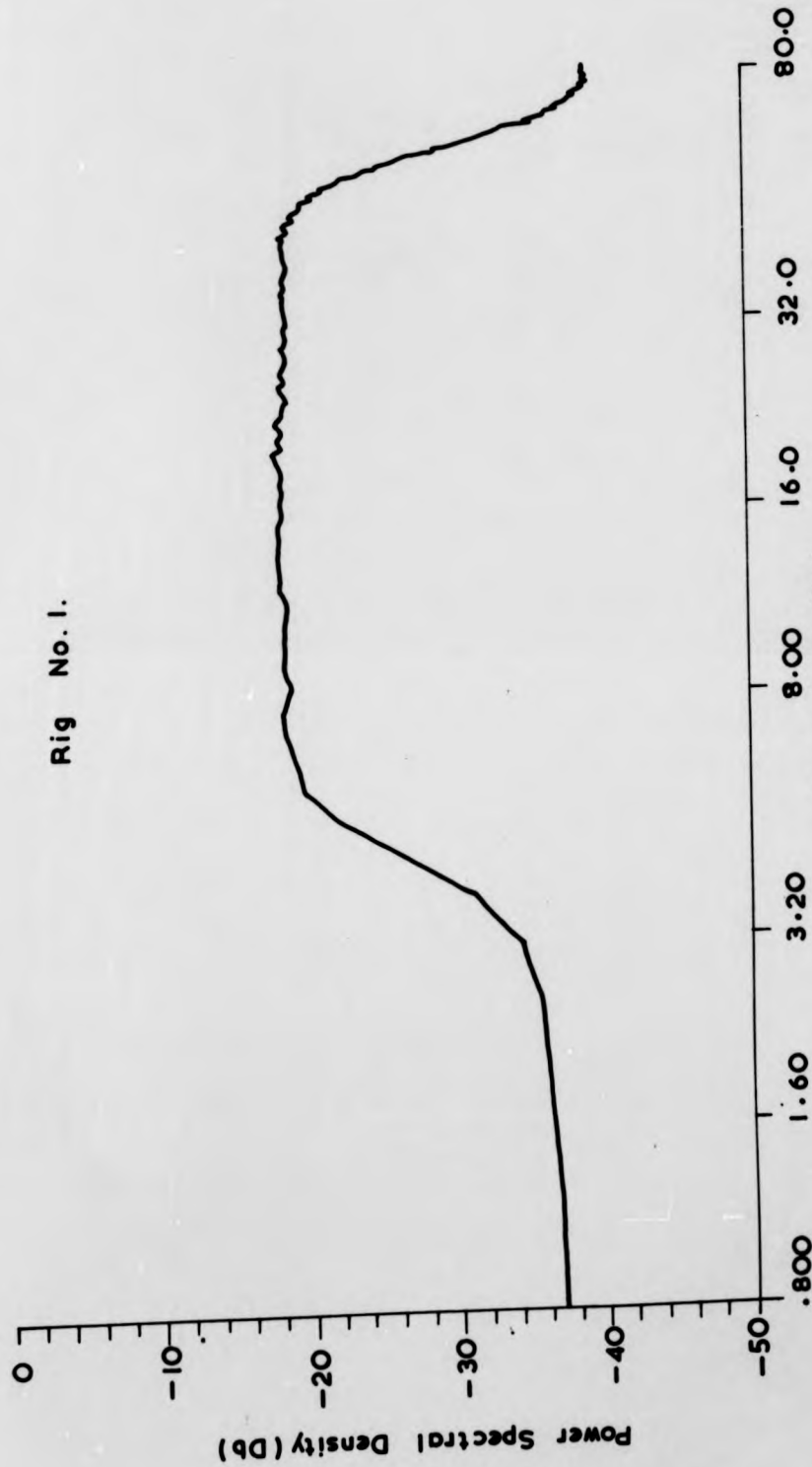


FIG. 7.20.



5/52 Hz Band Pass Signal

FIG. 7.21.

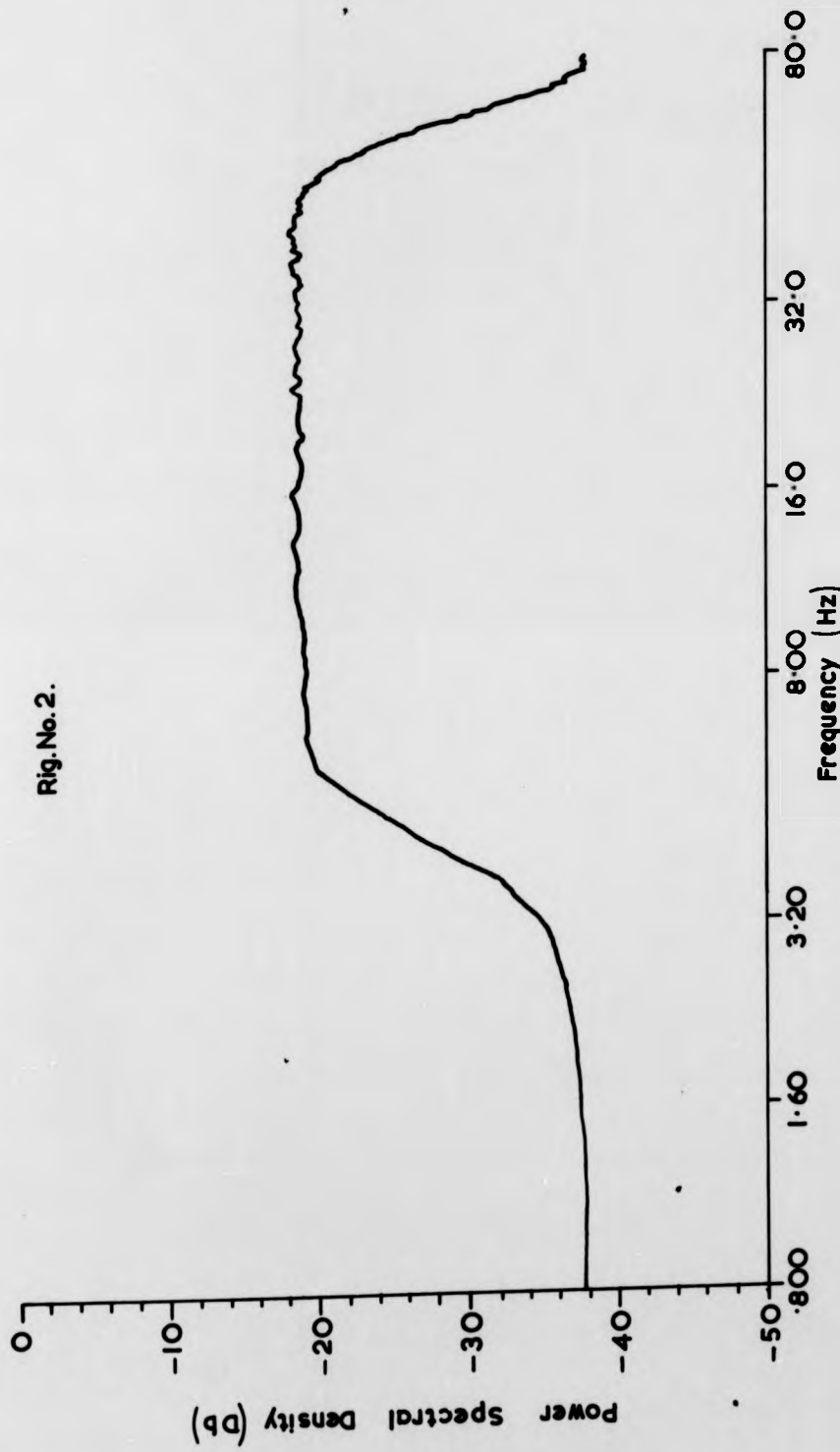


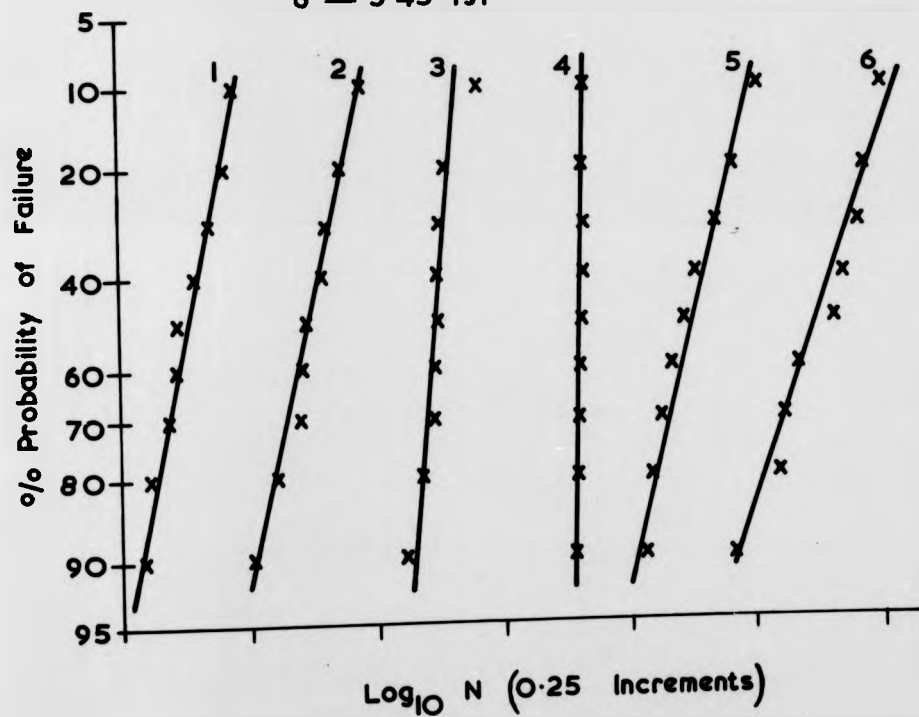
Fig. No. 2.

5/52Hz Band Pass Signal

FIG. 7.2 2.

Nominal R.M.S Stress

- 1 — 14.2 Tsi
- 2 — 11.1 Tsi
- 3 — 8.9 Tsi
- 4 — 8.0 Tsi
- 5 — 6.22 Tsi
- 6 — 5.45 Tsi



47Hz Centre Frequency Signal

FIG. 7. 23.

Nominal R.M.S. Stress

1 - 5.5 Tsi

2 - 6.5 Tsi

3 - 7.5 Tsi

4 - 9.0 Tsi

5 - 11.0 Tsi

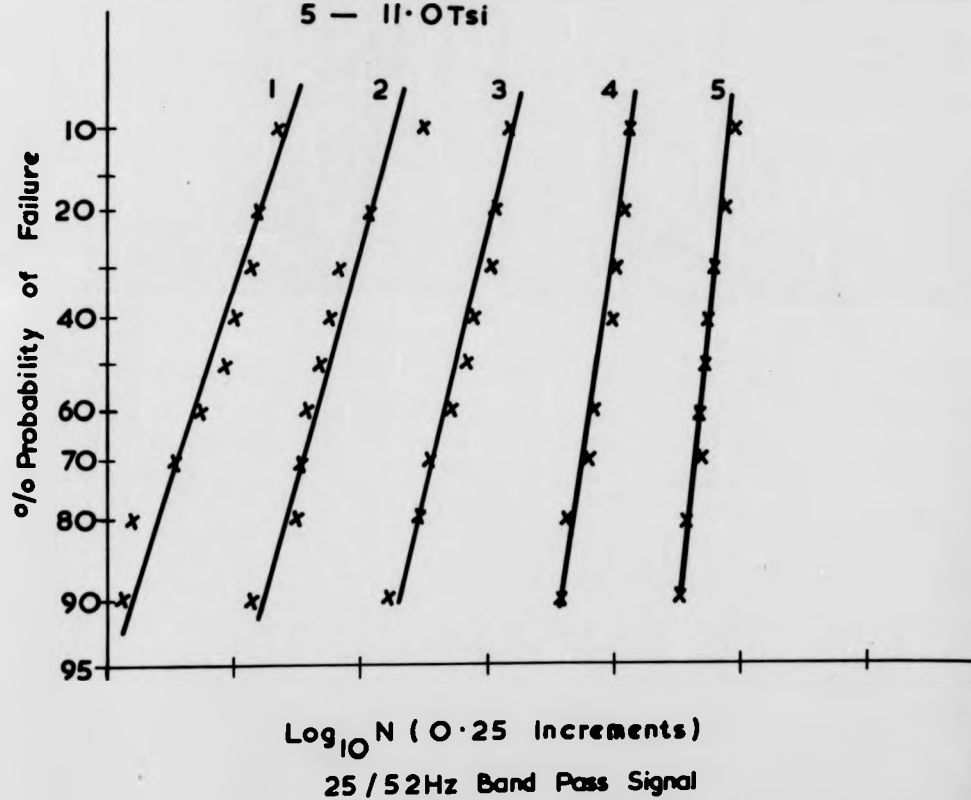


FIG. 7. 24.

Nominal R.M.S. Stress

- 1 - 5.78 Tsi.
- 2 - 6.28 Tsi.
- 3 - 7.16 Tsi.
- 4 - 8.79 Tsi.
- 5 - 11.0 Tsi.

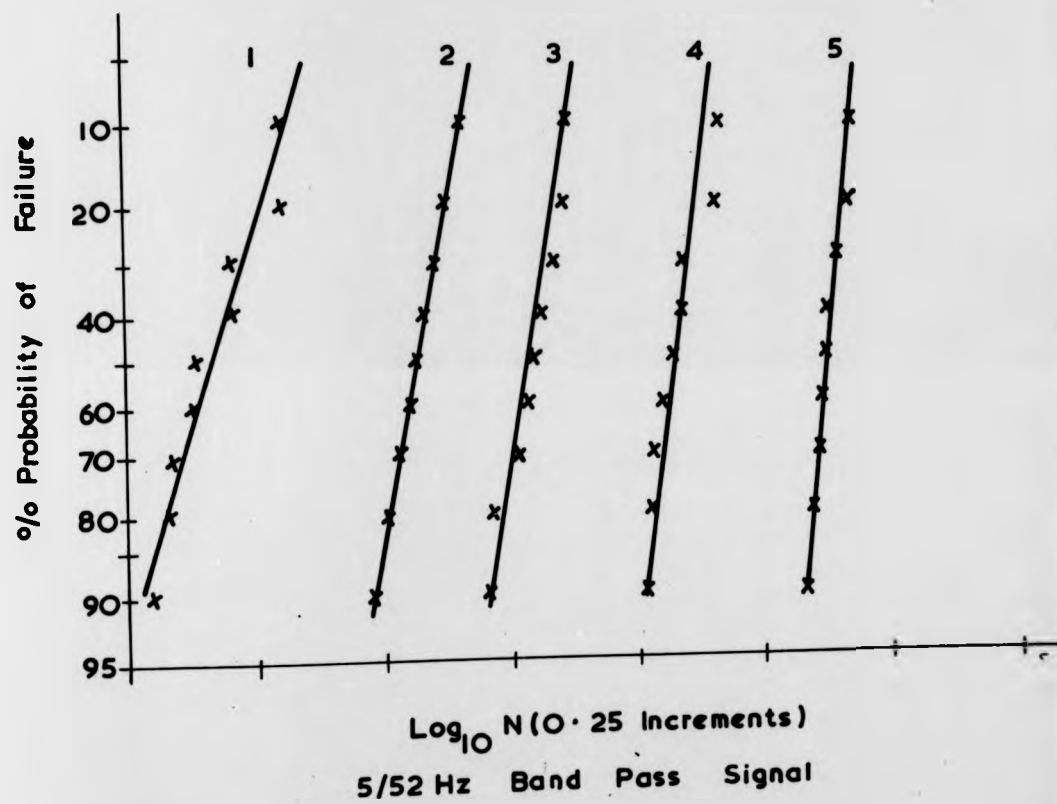


FIG. 7. 25.

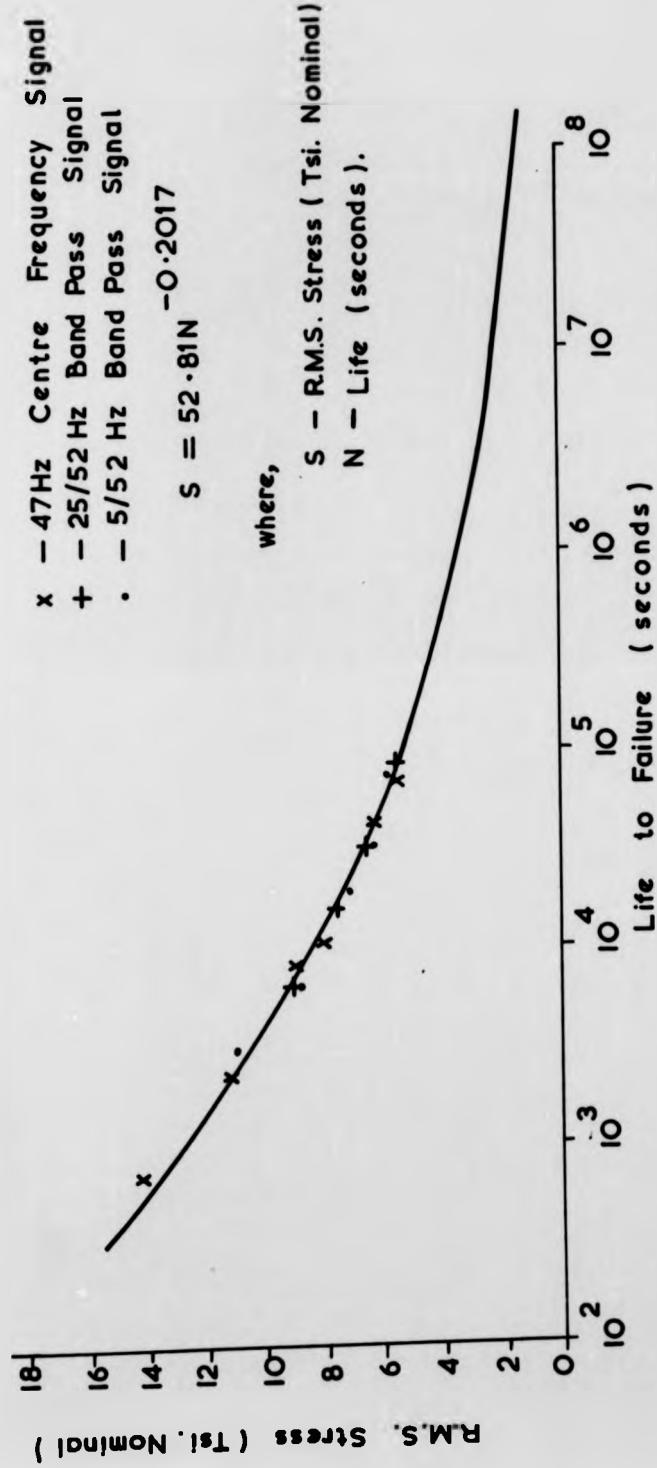


FIG. 7.26

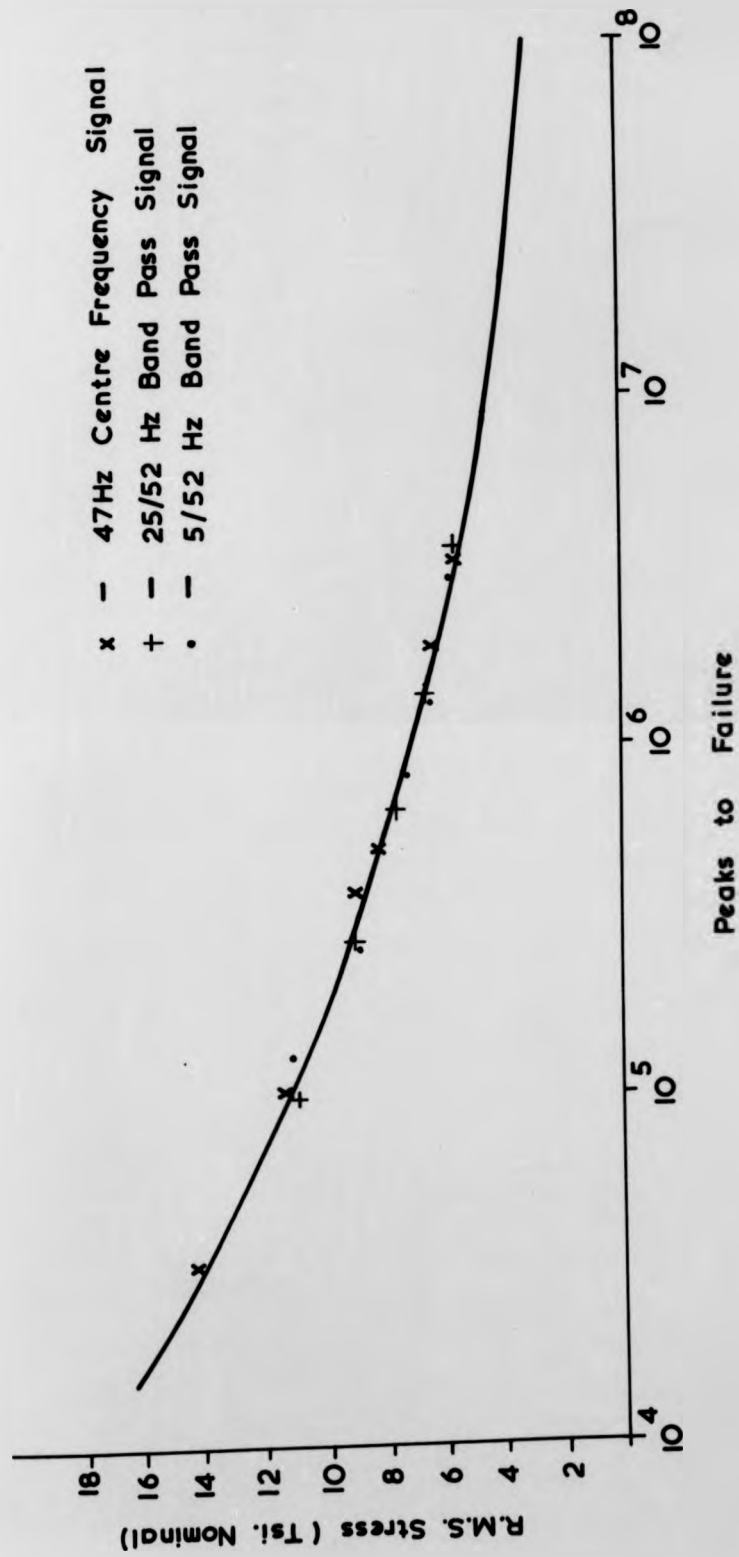


FIG. 7.27

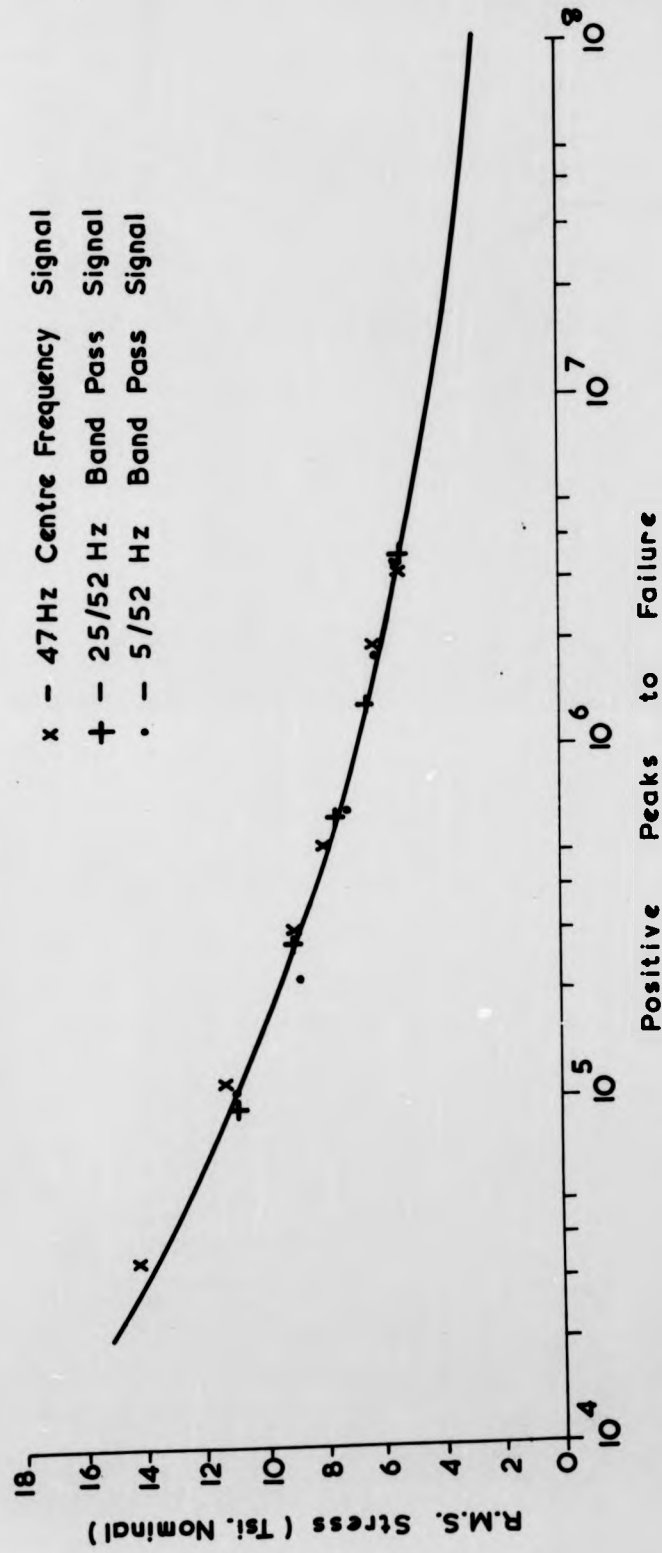


FIG. 7.28

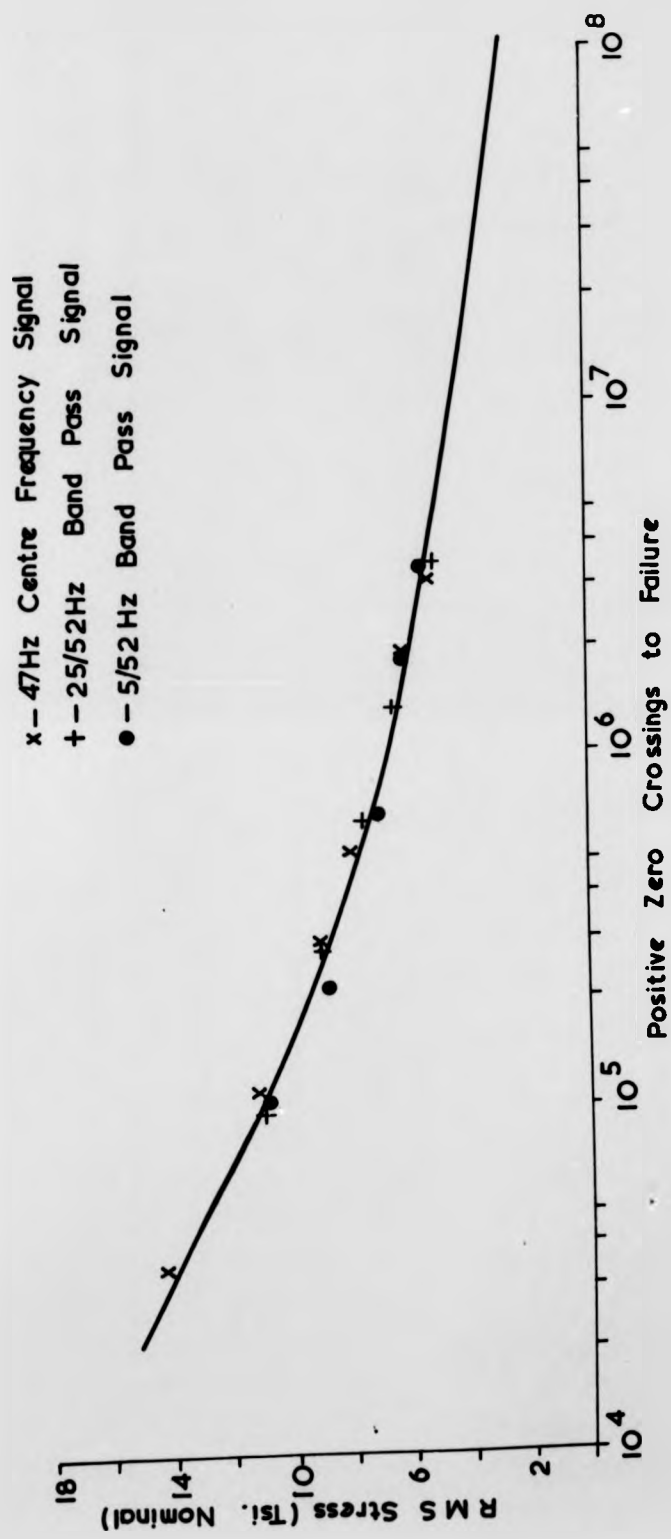
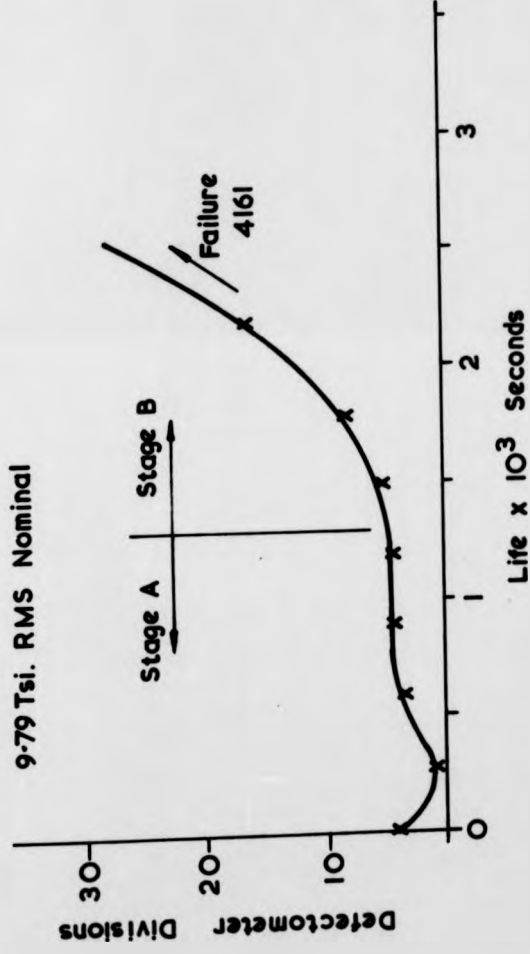


FIG. 7. 29

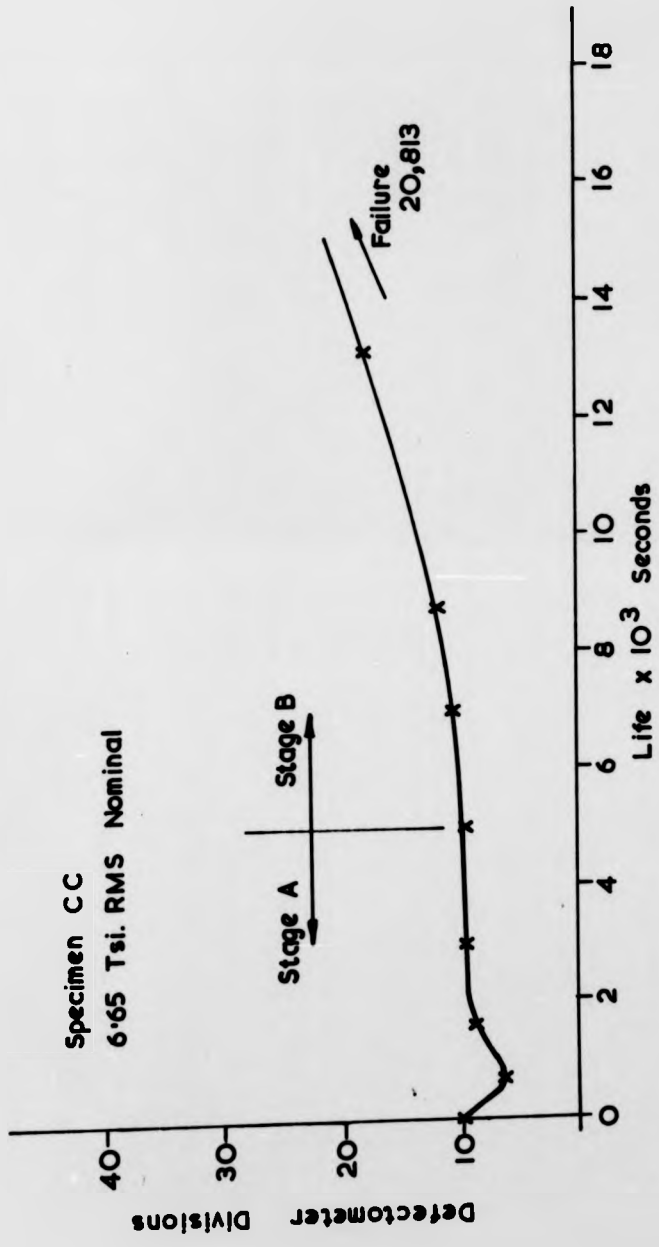
Specimen 4

9-79 Tsi. RMS Nominal



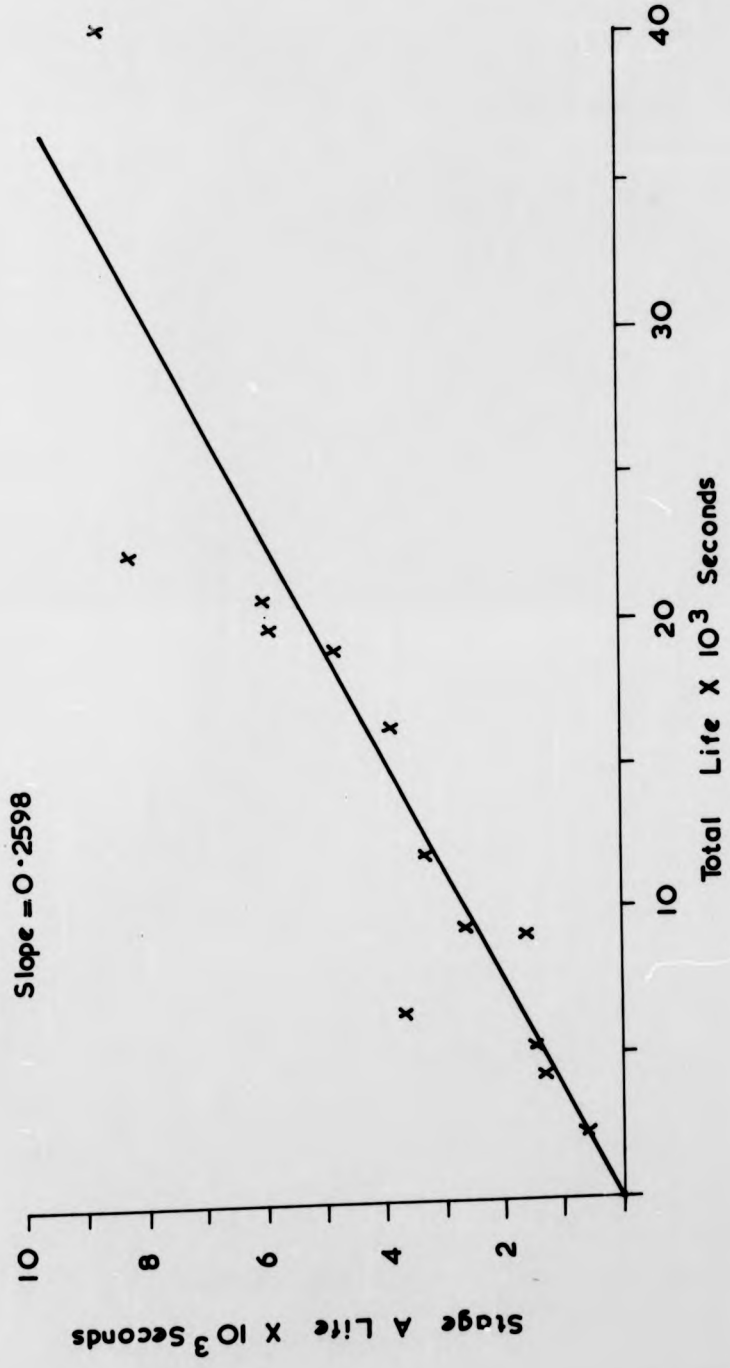
47Hz Centre Frequency Signal

FIG. 7. 30.



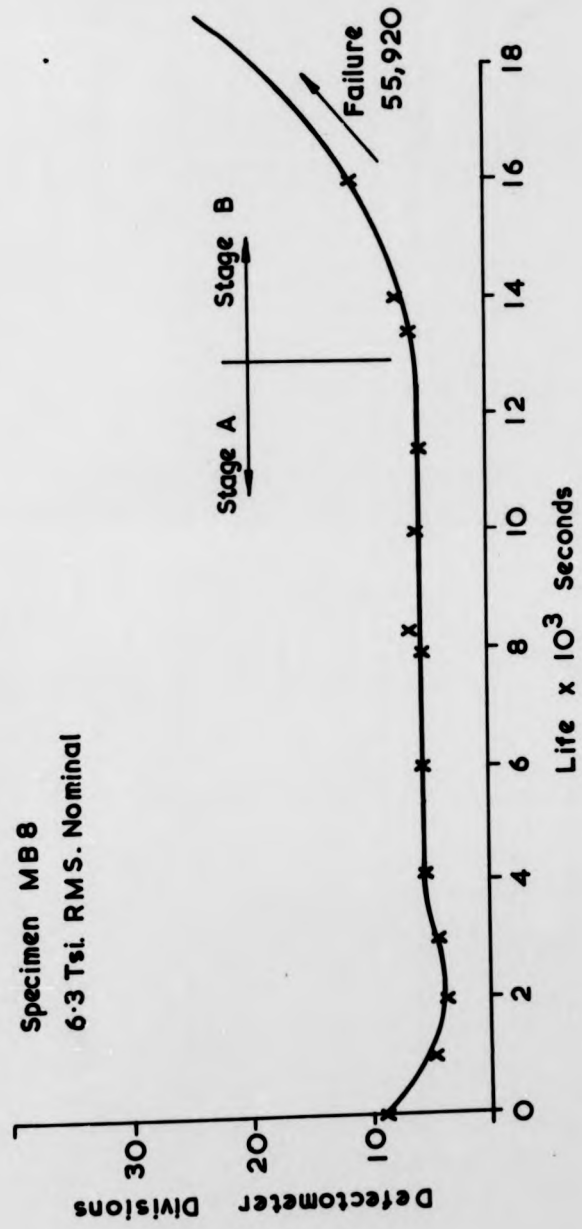
47 Hz Centre Frequency Signal

FIG. 7. 31.



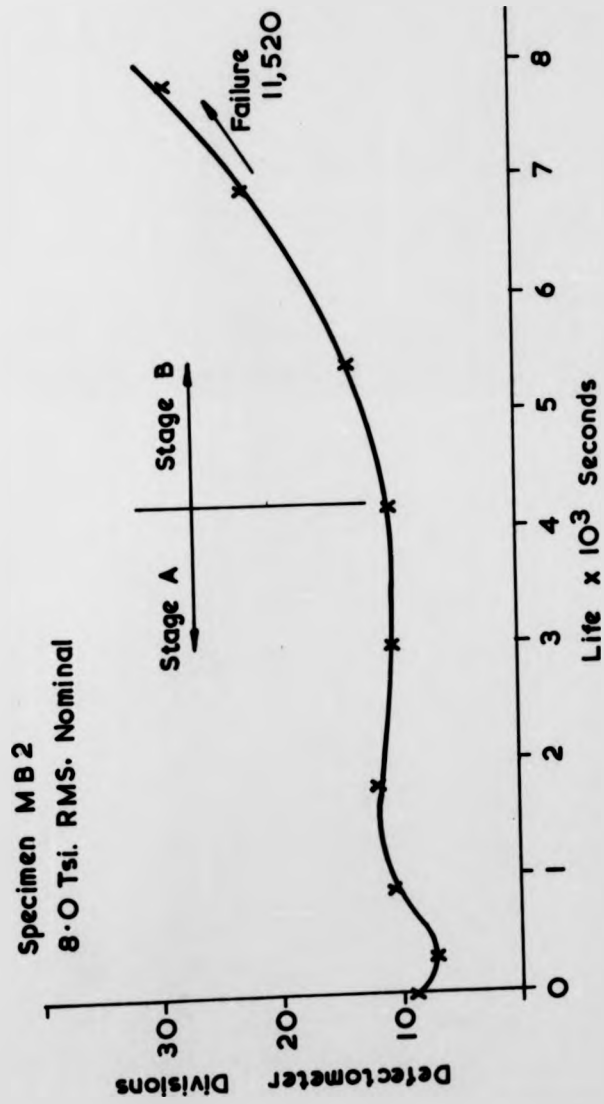
47 Hz Centre Frequency Signal  
 FIG. 7.32.

Specimen MB 8  
6.3 Tsi. RMS. Nominal



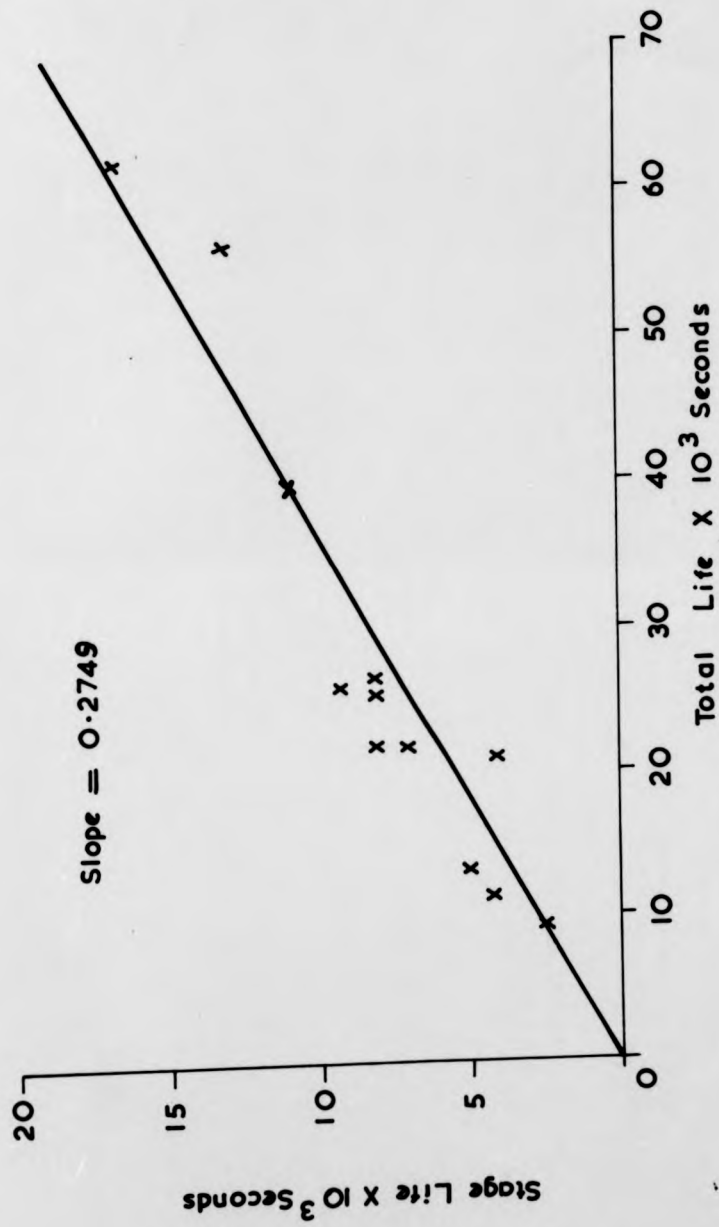
25/52 Hz Band Pass Signal

FIG. 7.33.



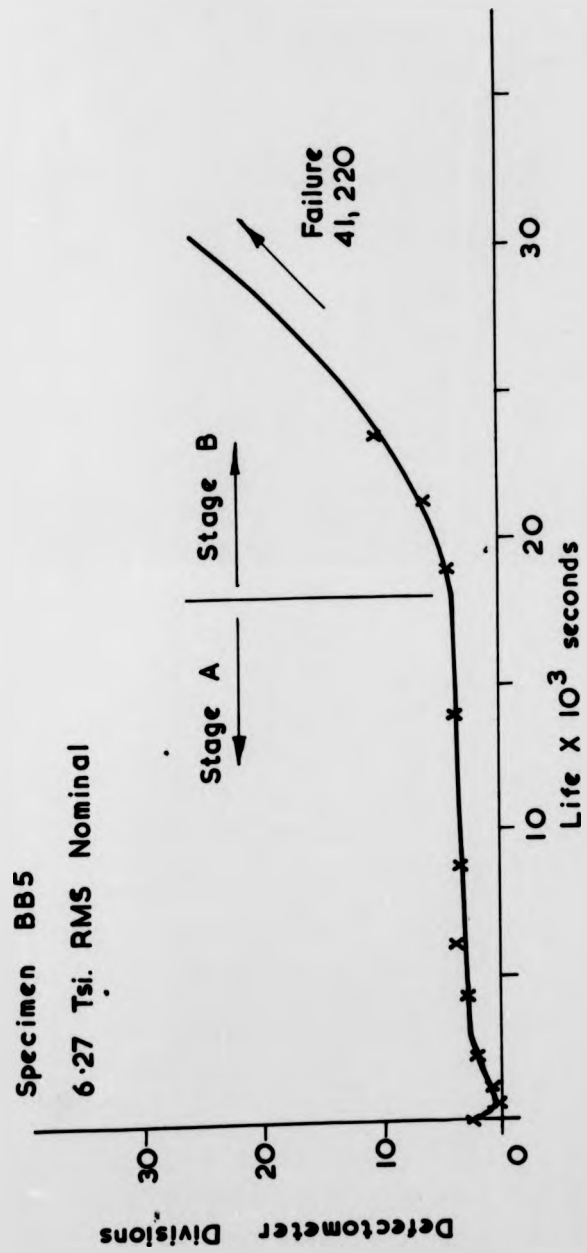
25/52 Hz Band Pass Signal

FIG. 7. 34.



25/52 Hz Band Pass Signal

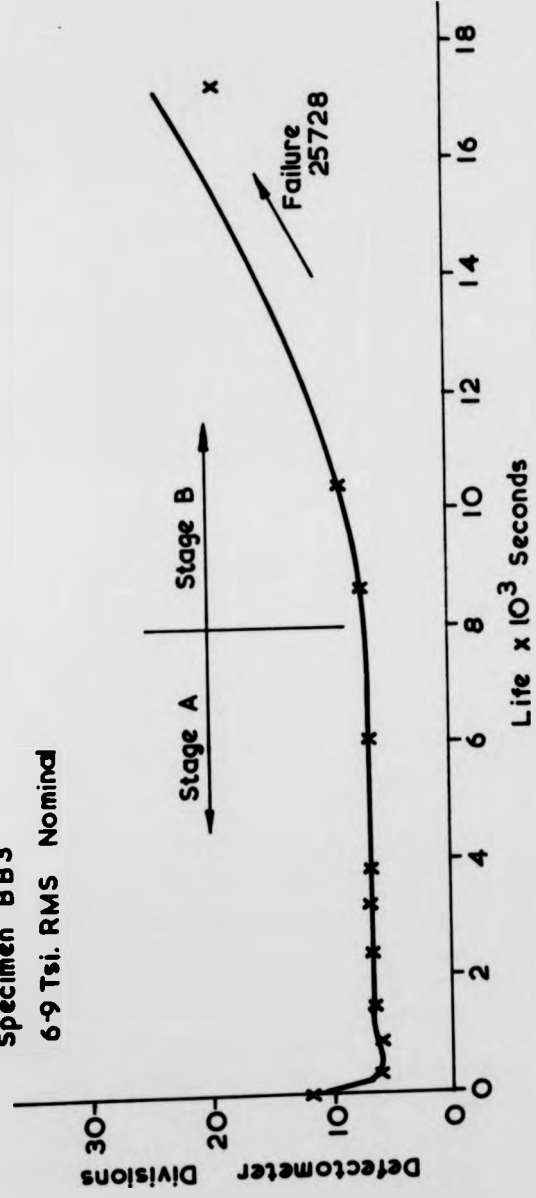
FIG. 7.35.



5/52 Hz Band Pass Signal

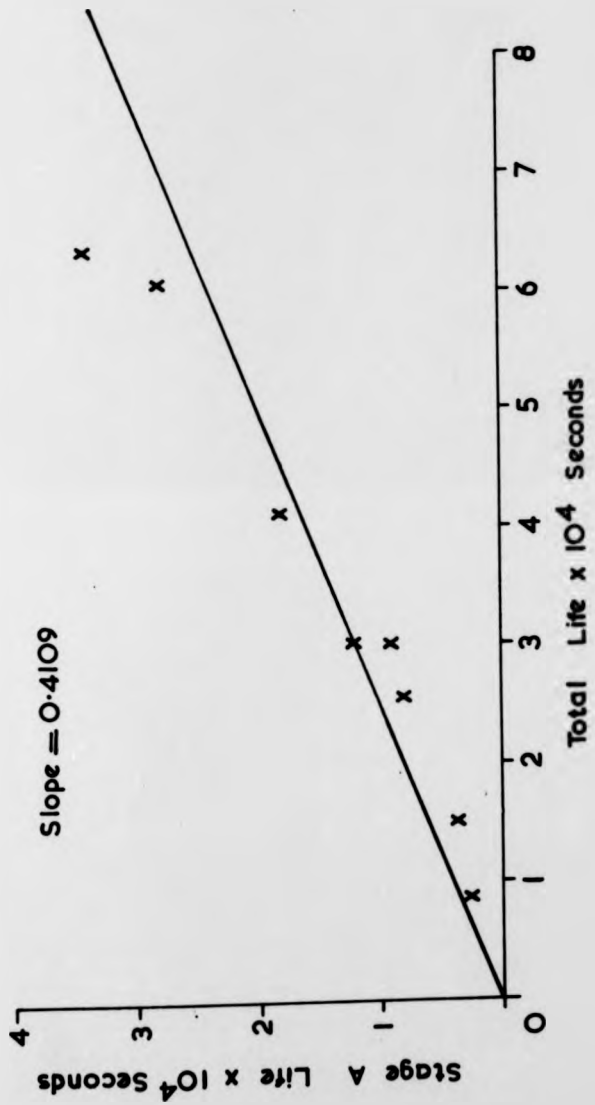
FIG. 7. 36.

Specimen BB3  
6.9 Tsi. RMS Nominal



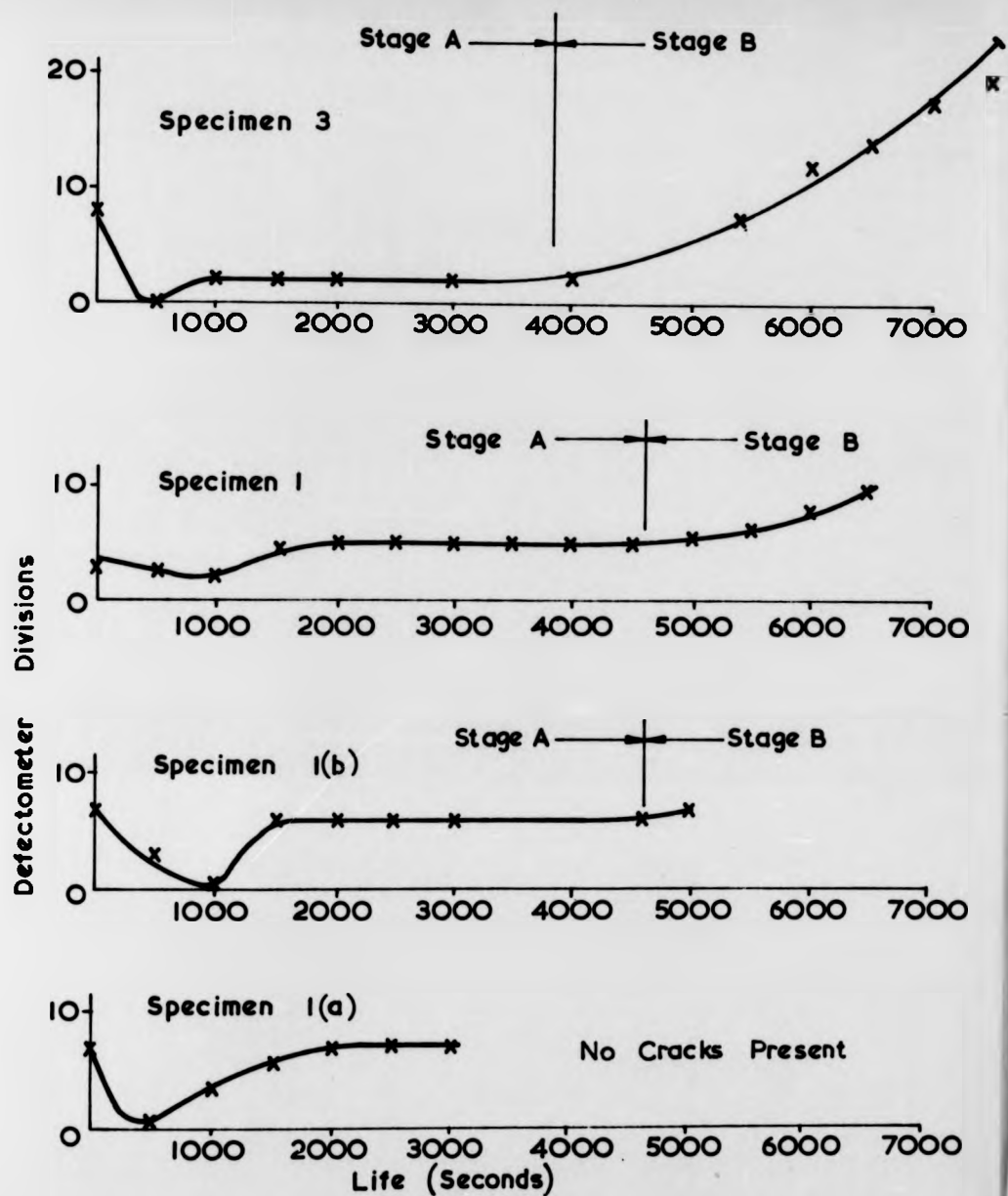
5/52Hz Band Pass Signal

FIG. 7. 37.



5/52Hz Band Pass Signal

FIG.7.38.



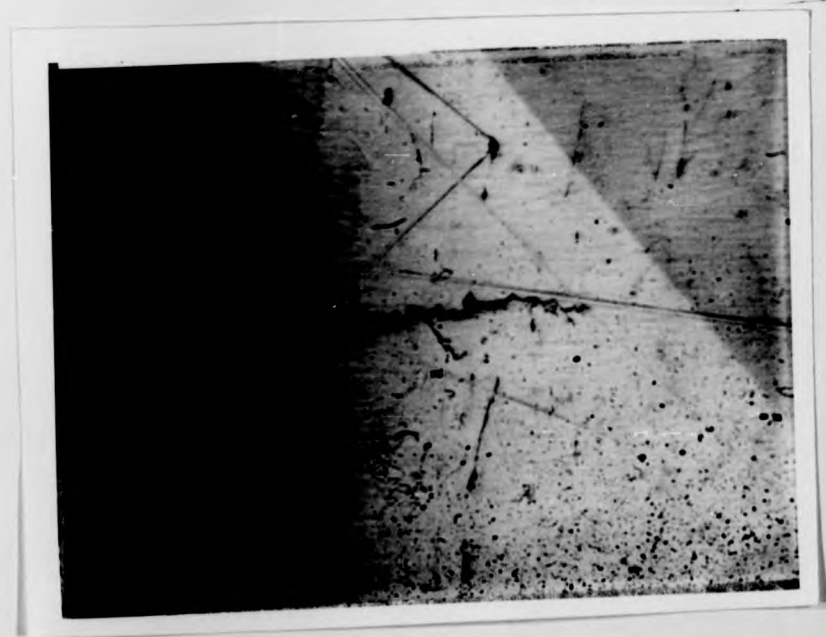
Specimen	Crack length 0.001"	
	Top notch	Bottom notch
1(b)	0.6	—
1	2.5	0.4
3	19	15

47Hz Centre Frequency Signal

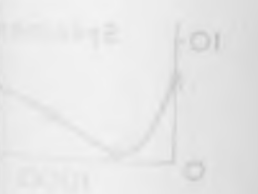
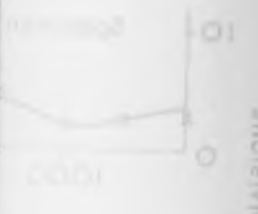
FIG. 7.39.



SPECIMEN 1(b) X750  
 0.0006"  
 FIG 7.40.

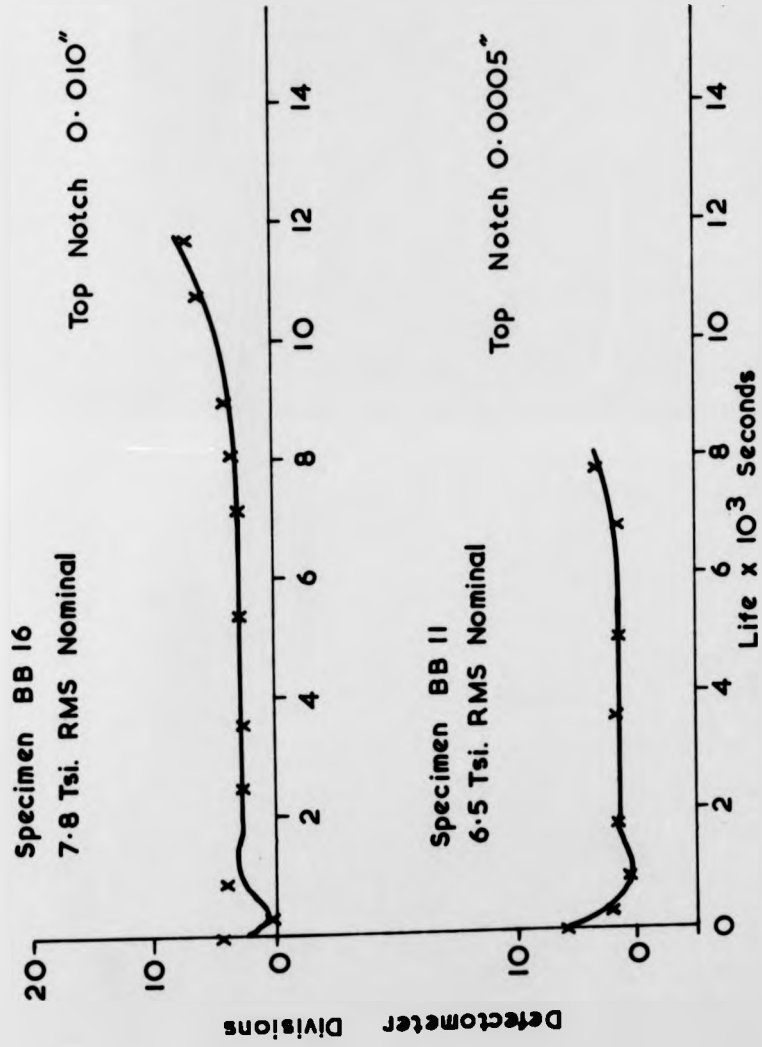


SPECIMEN 1 X600  
 0.003"  
 FIG 7.41.



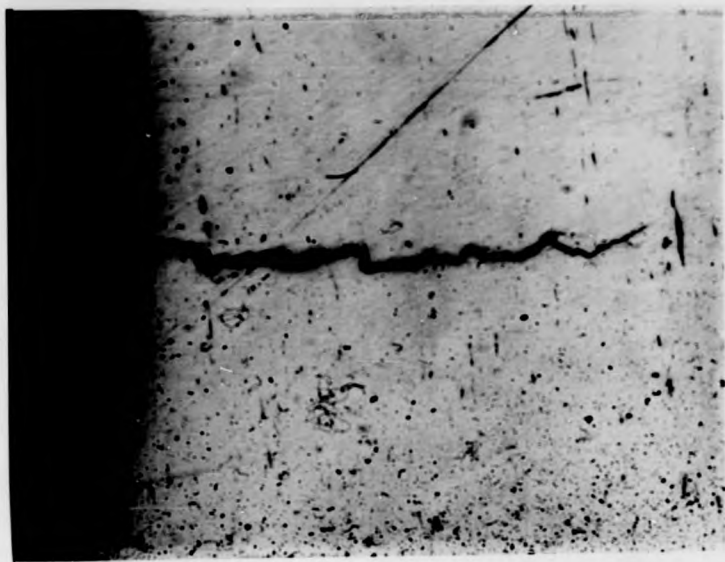
Specimen
1(b)
1
2

9176



5/52Hz Band Pass Signal

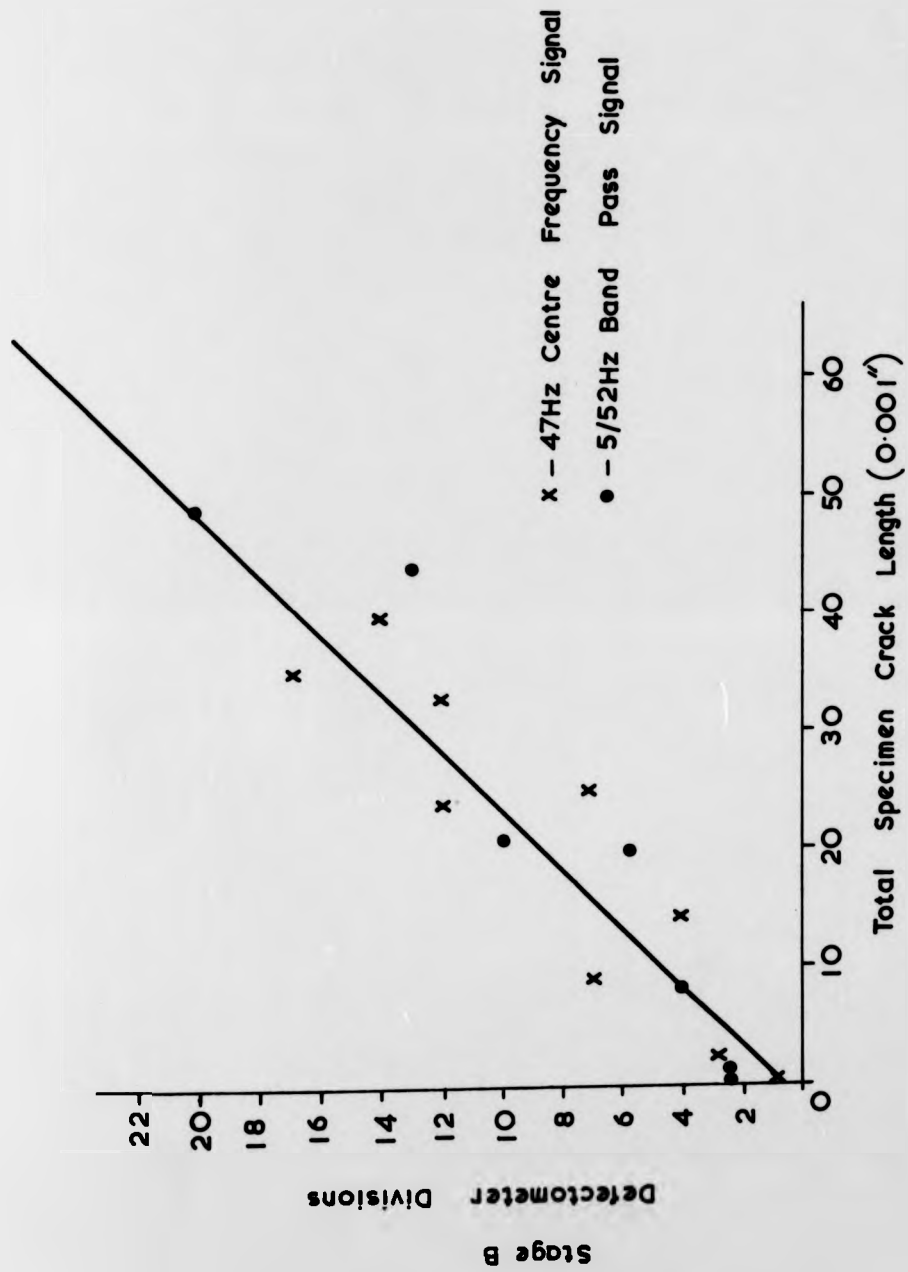
FIG.7.42.



SPECIMEN BB16 X340  
0.010"  
FIG 7.43.



SPECIMEN BB11 X975  
0.0005"  
FIG 7.44.



Random Loading Tests

FIG. 7. 45.

CHAPTER 8

SIZE EFFECT INVESTIGATION - LARGE ROUND  
3-POINT BENDING SPECIMEN FATIGUE TEST RESULTS

1.	INTRODUCTION	117
2.	CONSTANT AMPLITUDE LIFE TESTS	120
3.	CONSTANT AMPLITUDE EDDY CURRENT CRACK DETECTION	121
4.	RANDOM LOADING LIFE TESTS	121
5.	RANDOM LOADING EDDY CURRENT CRACK DETECTION	123
6.	ANALYSIS AND DISCUSSION OF RESULTS	124

1. INTRODUCTION

The work reported in this chapter resulted directly from the joint SRC - British Rail Contract and its associated size effect investigation. The test results refer to the round specimens shown in fig. 2.30, which were fatigued in three point bending using the servohydraulic test rig described in Chapter 2, section 1.4. These specimens were geometrically larger by a factor of ten than the small cantilever specimens of Chapter 7, and the elastic stress concentration factor of both specimens was 1.593. The fatigue testing was carried out with this particular bending configuration in order to enable size effect comparisons to be made for similar loading conditions.

For reasons of economy fatigue tests are usually conducted with small specimens, although the direct application of such fatigue data to the design of large parts may result in significant unconservative errors in life prediction of those parts. It is a well known fact that under constant amplitude loading the fatigue strength of geometrically similar specimens decreases as the size of the specimen increases. This phenomenon can be attributed to a "notch size effect" as well as to material effects to which fatigue strength becomes more sensitive as size increases. "Material size effects" result from such causes as the variation of material properties with increased cross section (i.e. mass effect), changes in residual stress distributions, surface finish, etc. It is standard design procedure to account for the influence of notch and material effects by one size effect factor. However, in laboratory tests it is usually the intention to eliminate extraneous material effects in order to investigate the notch size effect, as is the case with the work reported here.

Axially loaded unnotched specimens do not show a geometric size effect, although there is a size effect for plain specimens under bending. The distinguishing factor between the two loading conditions is the stress gradient, which is present with bending. Notched specimens loaded axially and in bending show size effects, and here a stress gradient is introduced in both specimen configurations and associated with the notch geometry. Stress gradients are higher for smaller geometrically similar specimens. Explanations for the size effect phenomenon are based largely on stress gradient and material inhomogeneity effects.

Neuber (57) proposed the concept that materials with metallic structures could be treated as a series of cubical blocks. It is then assumed that no stress gradient can develop across these individual material blocks and that the fatigue strength depends on the average stress acting over one block. Generally, for design applications, the empirical formula which results from Neuber's approach provides a satisfactory engineering method for size effect estimation. This is supported by Kuhn and Hardrath (58) who have made an evaluation of Neuber's proposal from a large amount of fatigue data for a variety of steels. The reduction in plain specimen fatigue strength for a notched component with an elastic stress concentration factor  $K_T$  is given by the equation:-

$$K_F = \frac{\text{Plain specimen fatigue strength}}{\text{Notched specimen fatigue strength}}$$
$$= 1 + \frac{K_T - 1}{1 + \frac{\pi}{\pi - \omega} \sqrt{\frac{K}{R}}}$$

The range of applicability of this equation is usually restricted to constant amplitude loading with peak concentrated

stresses that are within the elastic range to avoid the complication of corrections for plasticity effects, and to notches which have root radii greater than about 0.010 inches. The quantities  $\omega$  and  $R$  are the flank angle and radius of the notch respectively. Thus, for semicircular notches the equation then becomes:-

$$K_P = 1 + \frac{K_T - 1}{1 + \sqrt{\frac{A}{R}}}$$

The quantity  $A$  has the dimensions of length and is called the Neuber constant, and represents half the width of a block of material. If  $A$  is zero then  $K_P = K_T$  and, in terms of the widely used concept of notch sensitivity, the material has 100% notch sensitivity. If the constant  $A$  becomes large then  $K_P$  becomes independent of  $K_T$  and equal to unity, showing that the material is 100% insensitive to notches. This constant is evaluated as a function of material UTS. in reference 58 using a wide range of constant amplitude plain and notched specimen fatigue data. The relationship is shown by fig. 8.1. Similar relationships can be found elsewhere in the published literature, e.g. reference 59.

Thus it is established that the effect of specimen size on overall fatigue life can be accounted for by variations in the shape of the S/N curve, and it seems reasonable that a similar result applies for random loading R.M.S./life curves. However, it is possible that fatigue behaviour, as reflected for example by the proportions of life spent in crack initiation and propagation, differs for differently sized specimens and offers an additional explanation for the size effect phenomenon. Thus, part of the overall objective was to extend the eddy current crack detection techniques to these larger specimens.

Since this work is, to some extent, apart from that presented in Chapters 5, 6 and 7 it is relevant to include in this chapter a section which deals with the analysis of those aspects of the results which are directly relevant to size effect behaviour, rather than leave it to be included in Chapter 9. Thus the work is presented in the following sections:

2. Constant Amplitude Life Tests.
3. Constant Amplitude Eddy Current Crack Detection.
4. Random Loading Life Tests.
5. Random Loading Eddy Current Crack Detection.
6. Analysis and Discussion of Results.

The general principles of preparation of results established in previous chapters apply here.

## 2. CONSTANT AMPLITUDE LIFE TESTS

The objective of this part of the test program was to determine the specimen constant amplitude diagram. A series of 5 constant stress amplitude tests was conducted at a frequency of 10 Hz. with two specimens at each stress level. The results are summarised in table 8.1. Test stress levels were chosen to carefully define the basic S/N diagram at the "knee of the curve". Generally, specimen failure behaviour was similar at all stress levels. Failure resulted by complete specimen separation at one notch, accompanied by cracking in the other notch. Fatigue cracks grew symmetrically from the top and bottom of both notches.

The equation of the S/N curve was determined by a least squares fit of lives to the Stussi equation, where static failure condition was represented by the collapse load stress as described in Chapter 5. Thus, for the case of a circular

cross section 3-point bending specimen the collapse stress would then be  $1.7 \times \text{UTS}$ . The equation together with the plotted test data is presented in fig. 8.2.

### 3. CONSTANT AMPLITUDE EDGY CURRENT CRACK DETECTION

This part of the test program was aimed at establishing the pattern of two stage fatigue behaviour, as outlined in the test results of previous chapters. Defectometer readings were taken during the fatigue lives of 6 specimens, and the results are summarised in table 8.2. Two typical plots are shown in fig. 8.3 and 8.4 for different stress levels. The previously observed two stage fatigue behaviour was present in all specimens tested, and fig. 8.5 shows the best fit straight line through the origin for the Stage A/Total life data compared with the best fit straight line obtained from the small cantilever specimen data.

Specimen sectioning for crack examination was not carried out as described in previous chapters because of the cost and limited number of the specimens themselves. However, in order to partly check the actual fatigue behaviour against the Defectometer response one specimen was fatigued until just after the Stage A/Stage B transition, and then examined for fatigue cracks. The eddy current response together with the respective notch crack lengths are shown in fig. 8.6, and these results indicate a two stage behaviour corresponding to that found in previously mentioned constant amplitude tests. A photograph of one of the cracks is shown in fig. 8.7.

### 4. RANDOM LOADING LIFE TESTS

In order to effectively investigate size effect under random loading it is necessary to achieve similar modes of loading under stress waveforms which have similar statistical

properties. In this respect therefore, it is convenient to present the results of this section in two parts:-

- 4.1. Statistical definition of random loading waveforms.
- 4.2. Fatigue results.

#### 4.1. Statistical definition of Random Loading waveforms.

The size effect investigation was only carried out for the case of the Rayleigh peak distribution waveform. The results for the small specimens had been obtained under a 47 Hz. centre frequency signal of 10 Hz. bandwidth and, in order to achieve a loading waveform for the large specimens with the same signal rate of modulation but centred on 10 Hz. in order to test within the flat part of the rig amplitude/frequency response, it was necessary to use a 3 Hz. bandwidth signal. This rate of modulation effect is shown by the range/mean distributions of fig. 8.8 and 8.9 for signals from the Brüel & Kjaer sine-random generator type 1040, with different centre frequencies but similar bandwidth to centre frequency ratios.

The statistical description of the achieved test rig loading waveform, shown in fig. 5.10, was carried out in a similar way to that described in Chapter 6, with measurements of amplitude probability density, peak probability density and power spectral density. The goodness-of-fit test results in table 8.3 show that the hypothesis of normality for the waveform amplitude distribution can be accepted for the 5% level of significance. The expected and observed distributions are compared graphically in fig. 8.11. Table 8.4 presents details of peak probability measurements, and fig. 8.12 enables a visual comparison to be made between theoretical and achieved peak distributions. The analysis indicates an accurate comparison between theoretical and achieved peak stresses

for excursions at least to 4 x rms. levels. The power spectral density measurement details are presented in table 8.5 and fig. 8.13. This series of results can be compared with the measurements of Chapter 4, section 2, made on the synthesised signal, to show that there was little modification of the input signal by the rig transfer function.

Peak and zero crossing frequencies for both the synthesised and test rig signals are summarised in table 8.6. The test rig results were used in the presentation of random fatigue data and cumulative damage analyses.

#### 4.2. Fatigue Results.

Five series of tests were conducted with 2 specimens at each stress level in order to determine specimen fatigue life behaviour under random loading. Stress levels were chosen to define the high cycle life region of the rms. stress/life curve. Higher stress levels were chosen with due regard paid to the test rig dynamic force rating.

The test results are summarised in table 8.7 and the equation for the rms. stress/mean life (seconds) curve is shown in fig. 8.14, together with the plotted results. The results for both specimens are represented on a basis of stress peaks to failure in fig. 8.15.

#### 5. RANDOM LOADING EDDY CURRENT CRACK DETECTION

The objective of this part of the test program was to establish the pattern of two stage fatigue behaviour for these large specimens under random loading. Tests were carried out in a similar manner to those under constant amplitude loading described in section 3. The results for the Stage 1 Total life behaviour of 6 specimens are summarised in table 8.8 and the best fit to data straight line is shown in fig. 8.16, which

also shows the results for the small specimens under Rayleigh peak distribution loading. Two typical Defectometer plots at different stress levels are shown in figs. 8.17 and 8.18. The results of sectioning work for one specimen are shown in fig. 8.19, and this indicates a two stage behaviour which corresponds with that observed previously under random loading. A photograph of one of the cracks is shown in fig. 8.20.

## 8. ANALYSIS AND DISCUSSION OF RESULTS.

It is convenient to present those aspects of this work which are directly relevant to specimen size effects under two headings:-

6.1. Fatigue Strength Reduction.

6.2. Two-Stage Fatigue Life Behaviour.

### 6.1. Fatigue Strength Reduction.

Neuber's approach was used to assess the reduction in fatigue strength. The pattern of analysis has been to calculate the plain fatigue strength at a given life using the small notched specimen stress/life data, and then estimate the fatigue strength of the larger specimens. This enabled a comparison to be made between the actual and "predicted lives" for the large specimens under both random and constant amplitude loadings, although it is more usual for applications of Neuber's equation to be reported only for constant amplitude data. Both sets of results are shown in tables 8.9 and 8.10, and the analysis covers what is commonly termed the high cycle fatigue life range rather than being strictly limited to notch elastic behaviour, whereby maximum peak nominal stresses would be defined by the ratio of yield stress/stress concentration factor.

There is good agreement between actual and predicted

lives for both forms of loading, and this is to be expected from previous work in this field. However, it is relevant to mention several factors which affect the calculations themselves. Errors are inherent to the extrapolation of stress/life data to estimate fatigue behaviour for the long lives at which it is not usually practicable to test. This is particularly illustrated for the results in the region of the constant amplitude fatigue limit. In this respect also it should be commented that the best fit to data for the random loading test series indicated a fatigue limit of 2.8  $T_{0.1}$  rms. nominal. However, it was felt that insufficient data had been generated to justify this as an exception to previous random data best fit trends and, therefore, for the sake of consistency fatigue analyses have been made using the zero fatigue limit equation. Additional inaccuracies would result from the effects of differences between residual stress distributions for differently sized specimens, and from statistical fluctuations in data itself, although it would be expected that such factors are not significant for these laboratory controlled tests.

On this basis, therefore, it is reasonable to conclude that the Neuber approach gives satisfactory correlation with observed size effect behaviour in the high cycle fatigue life range, although the material block concept is not yet established in physical terms. Exceptions occur for this approach with the prediction of fatigue strength for "scratch-like" notches, where the notch depth may be less than the material block size itself. Modifications to the Neuber equation then more realistically describe behaviour under these conditions (6C). The redistribution of stresses in the notch which occurs at higher load levels is not

accounted for by the Neuber approach, although this in itself would not describe notch size effect since plastic flow should be similar for geometrically similar specimens.

### 6.2. Two-Stage Fatigue Life Behaviour.

The Stage A/Total life behaviour is shown for both the large and small specimens under constant amplitude and random loading in fig. 8.5. and fig. 8.16. respectively. There is a striking similarity of two stage fatigue behaviour for both specimens under similar loading patterns, although the overall fatigue life is shorter at a given stress level for the larger specimens. This two stage behaviour is reflected in the response of high sensitivity eddy current crack detection to fatigue damage accumulation and is analogous to the two stage behaviour referred to earlier (17). The stages have been defined:-

Stage A - Microcrack Initiation and Propagation.

Stage B - Macrocrack Propagation.

The results indicate that the proportion of life spent in crack initiation or crack propagation remains unaltered for geometrically similar specimens. However, there are some discrepancies in the results which affect this general conclusion. The larger specimen constant amplitude tests showed a tendency towards earlier initiation of cracks at higher stress levels than would be expected from the proposed straight line relationship, e.g. tests conducted at 15 and 16 Td. peak nominal. Under the Rayleigh loading waveforms there is good correlation between the observed two stage behaviour in both specimens, but there is a larger difference in the proportions of total life spent in the two stages when the comparison is made with the combined random results of the small specimens.

see fig. 8.15. Combining the Stage A/Total life results for the small specimens is referred to in Chapter 9. The results also suggest that cracks are initiated earlier in the larger specimens for tests of equal life under random loading, but later in tests under constant amplitude loading. It is thought unlikely that such an inconsistency of between waveform crack initiation behaviour exists, but that it results from statistically small test samples.

Thus, it is reasonable to conclude that although overall fatigue life is shorter for geometrically larger specimens, the proportions of life spent in Stage A and Stage B behaviour remain unaltered. In the light of this established two-stage fatigue behaviour it may be more realistic to assess size effect by taking into account only the uncracked state of the specimen. Estimates of large specimen cracked behaviour could be made through fracture mechanics, especially with regard to small cracks which, because of material constraint, have triaxial stress fields at the crack tip. This suggests therefore, using the Neuber approach to determine the reduction of fatigue strength for given Stage A lives. However, the ratio of predicted life to actual life obtained previously in tables 8.9 and 8.10 would still apply to the case of Stage A size effect behaviour, since it has been assumed that Stage A behaviour forms a constant proportion of total life, and total life decreases for the larger specimens anyway.

Nominal Peak Stress Tsi.	19.25	17.25	16.0	14.0	12.8
Specimen Lives (cycles)	56,410	137,300	183,500	563,700	1,369,100
Mean of $\log_{10}$ of Lives	4.7943	5.1403	5.2406	5.7708	6.2768
Antilog of Mean Log Life (cycles)	62,270	138,100	174,000	589,900	1,891,000

2 specimens tested at each stress level.

Table 8.1

Specimen Identification	Nominal Peak Stress Tsi.	Stage A Life Cycles	Total Life Cycles
K2	16.0	100,000	237,000
F4	15.0	100,000	270,000
F5	14.5	165,000	340,000
J5	14.0	290,000	514,400
E5	13.2	350,000	611,000
D3	12.4	435,000	802,000

Constant Amplitude Loading

Table 8.2

Class Interval Midpoint (z)	Observed Frequency	Expected Frequency	Class Interval Midpoint (z)	Observed Frequency	Expected Frequency
-3.497	4	2.6	0.135	585	573.5
-3.315	2	2.4	0.317	578	550.5
-3.133	5	4.3	0.499	518	511.3
-2.952	6	7.5	0.680	456	459.5
-2.770	10	12.6	0.862	369	399.6
-2.589	32	20.5	1.044	322	336.3
-2.407	35	32.2	1.225	277	273.8
-2.225	58	49.0	1.407	201	215.8
-2.044	71	72.1	1.588	160	164.5
-1.862	107	102.7	1.770	121	121.4
-1.681	134	141.5	1.952	97	86.7
-1.499	178	186.8	2.133	61	59.9
-1.317	237	243.6	2.315	43	40.0
-1.136	308	304.2	2.496	34	25.9
-0.954	347	367.6	2.678	15	16.2
-0.773	432	429.8	2.860	15	9.8
-0.591	493	486.3	3.041	7	5.7
-0.409	519	532.4	3.223	0	3.3
-0.228	557	564.0	3.404	5	3.7
-0.046	595	578.2			

Amplitude resolution = 0.284 V. = 0.132 x rms.

Signal rms. = 1.561 V.

Total no. of class intervals = 39

Total no. of samples = 8000

5% value of chisquare = 51

Sample chisquare value = 38.5

10 Hz. Centre Frequency Signal

Table 8.3.

Class Interval Midpoint (z)	Observed Peak Frequency	Expected Peak Frequency	Class Interval Midpoint (z)	Observed Peak Frequency	Expected Peak Frequency
-6.50	0	0	0.10	426	600.7
-6.29	0	0	0.31	1381	1256.8
-6.09	0	0	0.52	2078	1887.5
-5.88	0	0	0.72	2598	2324.6
-5.68	0	0	0.93	2619	2522.1
-5.47	0	0	1.14	2404	2493.2
-5.26	0	0	1.34	2239	2284.1
-5.06	0	0	1.55	1929	1953.1
-4.85	0	0	1.75	1543	1580.3
-4.64	0	0	1.96	1130	1205.5
-4.44	0	0	2.17	823	871.6
-4.23	0	0	2.37	599	598.5
-4.02	0	0	2.58	419	390.9
-3.82	0	0	2.79	244	243.2
-3.61	0	0	2.99	134	144.2
-3.41	0	0	3.20	61	81.5
-3.20	0	0	3.40	21	44.0
-2.99	0	0	3.61	18	22.7
-2.79	0	0	3.81	10	11.2
-2.58	0	0	4.02	0	5.3
-2.37	0	0	4.23	1	2.4
-2.17	0	0	4.43	2	1.0
-1.96	0	0	4.64	0	0.4
-1.75	0	0	4.85	0	0.2
-1.55	0	0	5.06	0	0.1
-1.34	0	0	5.26	0	0
-1.14	0	0	5.47	0	0
-0.93	0	0	5.68	0	0
-0.72	0	0	5.88	0	0
-0.52	0	1.6	6.09	0	0
-0.31	3	25.0	6.29	0	0
-0.10	50	172.3	6.50	0	0

Signal rms. = 1.514 V.

Measurement time = 2025 sec.

Peaks = 20732

Positive Zero Crossings = 20335

Irregularity Factor = 0.921

10 Hz. Centre Frequency Signal

Table 8.4.

Degrees of Freedom = 468  
Sampling Frequency = 50 Hz.  
Signal rms. = 1.561 V.

10 Hz. Centre Frequency Signal

Table 8.5.

		Irregularity Factor	Peaks /sec.	+ve Zero Crossings /sec.
10 Hz. Centre	Synthesised	0.982	11.03	10.85
Frequency Signal	Achieved	0.981	10.26	10.04
Constant Amplitude Signal		10 Hz.		

Table 8.6

Nominal Ras. Stress Tsi.	10	8.5	7.0	6.0	5.0
Specimen Lives (seconds)	5,250 4,800	12,840 10,320	32,700 24,720	54,000 54,320	234,000 205,380
Mean of log <sub>10</sub> of Lives	3.7007	4.0612	4.4539	4.7704	5.3415
Antilog of Mean Log Life (seconds)	5,020	11,510	28,440	58,940	219,530

2 specimens tested at each stress level

Table 8.7

Specimen Identification	Nominal Ras. Stress Tsi.	Stage A Life Seconds	Total Life Seconds
K5	7.0	5,000	18,540
E5	6.4	13,000	42,300
E2	6.0	13,000	53,720
C3	5.9	17,500	73,500
T4	5.6	20,000	83,880
J3	5.5	30,000	120,000

10 Hz. Centre Frequency Signal

Table 8.8

Small Specimen Life (cycles)	$5 \times 10^4$	$10^5$	$5 \times 10^5$	$10^6$	$5 \times 10^6$	$10^7$	$10^8$
Small Specimen Stress (Tsi. Peak.)	26.7	22.4	16.9	15.8	14.5	14.5	14.1
Large Specimen Fatigue Strength (Tsi. Peak)	24.8	20.8	15.7	14.7	13.5	13.5	13.1
Actual life of Large Specimen (cycles)	$2.3 \times 10^4$	$6 \times 10^4$	$3 \times 10^5$	$6 \times 10^5$	$10^6$	$10^6$	$2 \times 10^6$
Large Specimen <u>Predicted</u> Life Actual	2.2	1.7	1.7	1.7	5	10	50

Material Ultimate Tensile Strength = 38 Tsi. = 85 Ksi.

$$\sqrt{A} = 0.076 \text{ ins}^{\frac{1}{2}} \quad R_{\text{small}} = 0.035 \text{ ins.} \quad R_{\text{large}} = 0.35 \text{ ins.} \quad K_T = 1.593$$

$$K_F \text{ small} = 1.42 \quad K_F \text{ large} = 1.53$$

Constant Amplitude Loading.

Table 8.9

Small Specimen Life (Peaks).	$10^5$	$5 \times 10^5$	$10^6$	$5 \times 10^6$	$10^7$	$10^8$
Small Specimen Stress (Tsi. RMS)	10.8	7.9	7	5.1	4.5	2.9
Large Specimen Fatigue Strength (Tsi. RMS)	10.	7.35	6.5	4.7	4.2	2.7
Actual life of Large Specimen (Peaks).	$5 \times 10^4$	$2.5 \times 10^5$	$4.5 \times 10^5$	$2.5 \times 10^6$	$5 \times 10^6$	$5 \times 10^7$
Large Specimen Predicted Life Actual	2	2	2.2	2	2	5

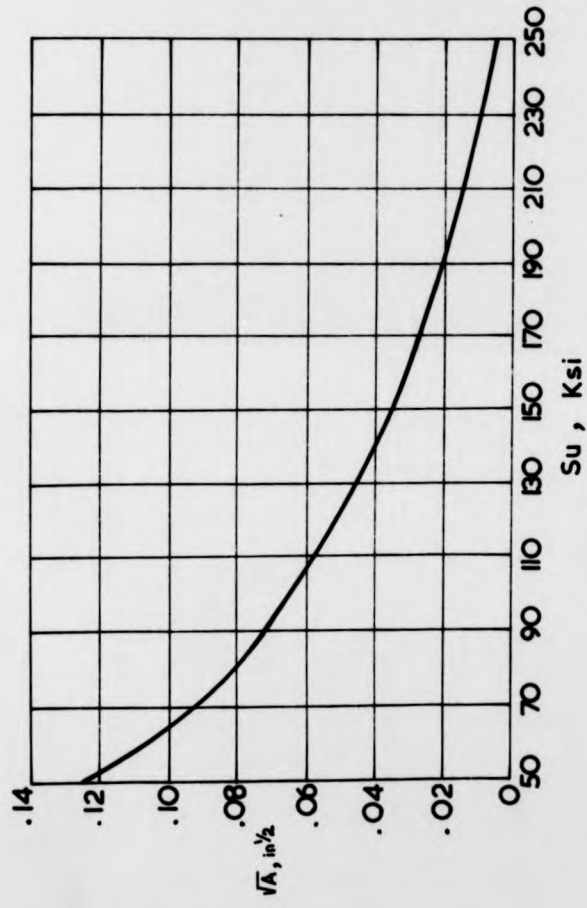
Material Ultimate Tensile Strength = 38 Tsi. = 85 Ksi.

$$\sqrt{K} = 0.076 \text{ ins}^{\frac{1}{2}} \quad R_{\text{small}} = 0.035 \text{ ins} \quad R_{\text{large}} = 0.35 \text{ ins.} \quad K_T = 1.593$$

$$K_T \text{ small} = 1.42 \quad K_T \text{ large} = 1.53$$

Random Loading

Table 8.10



Proposed relationship between the Neuber constant A and the ultimate strengths of steels ( ref. 58 )

FIG. 8.1

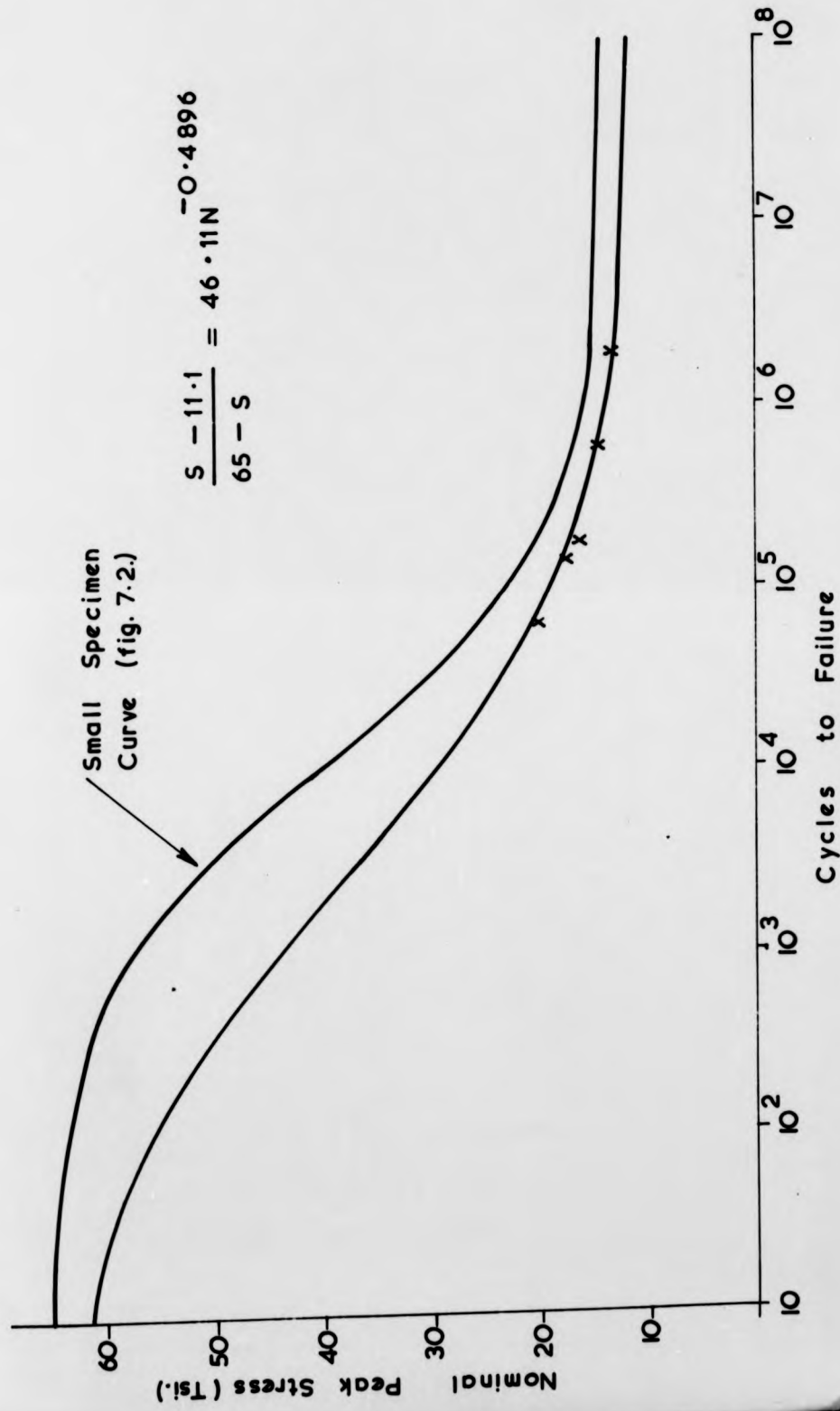
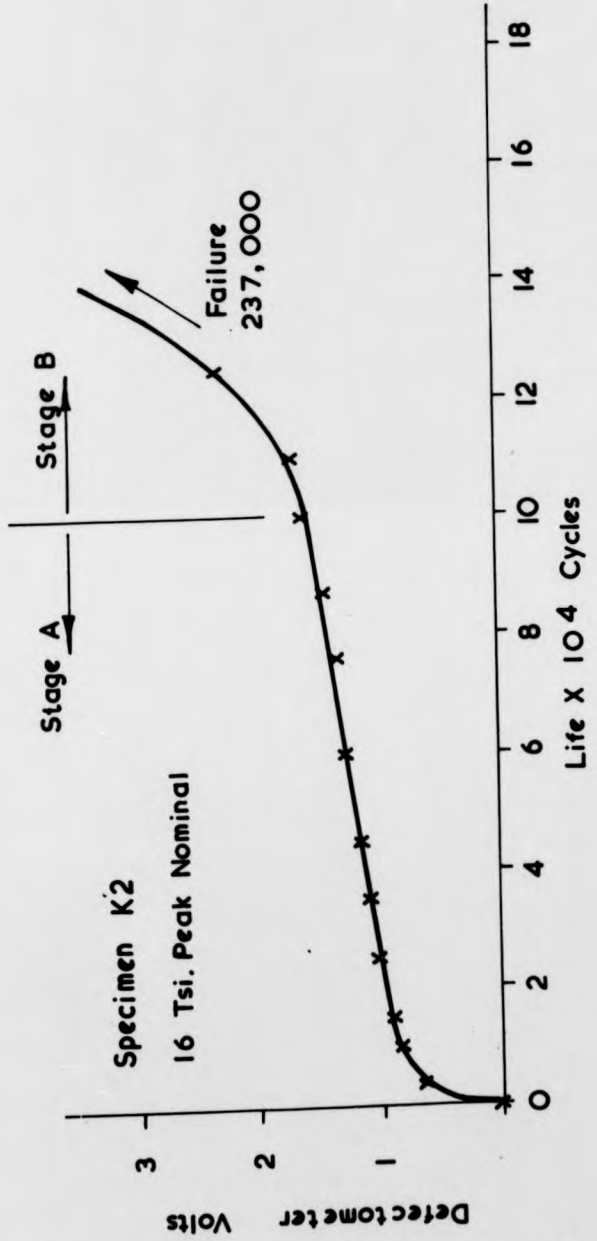
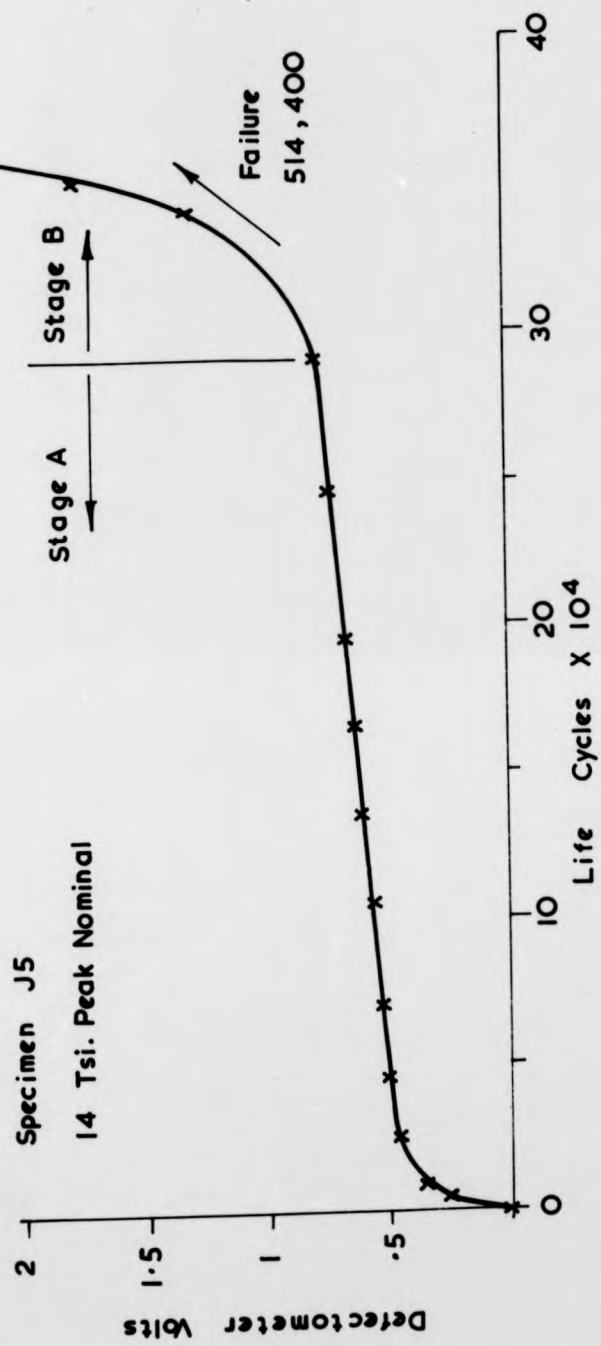


FIG. 8.2



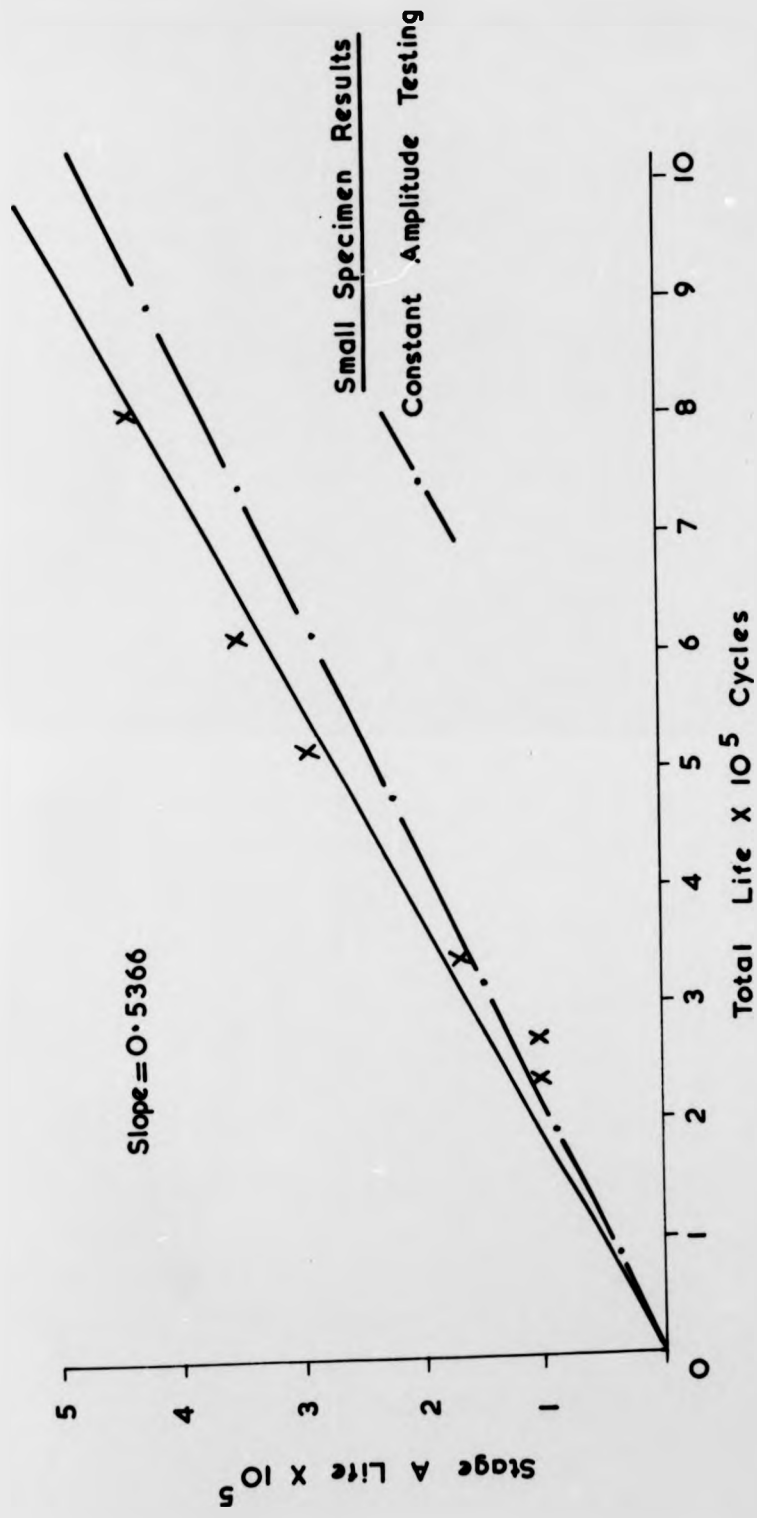
Constant Amplitude Loading

FIG. 8.3.

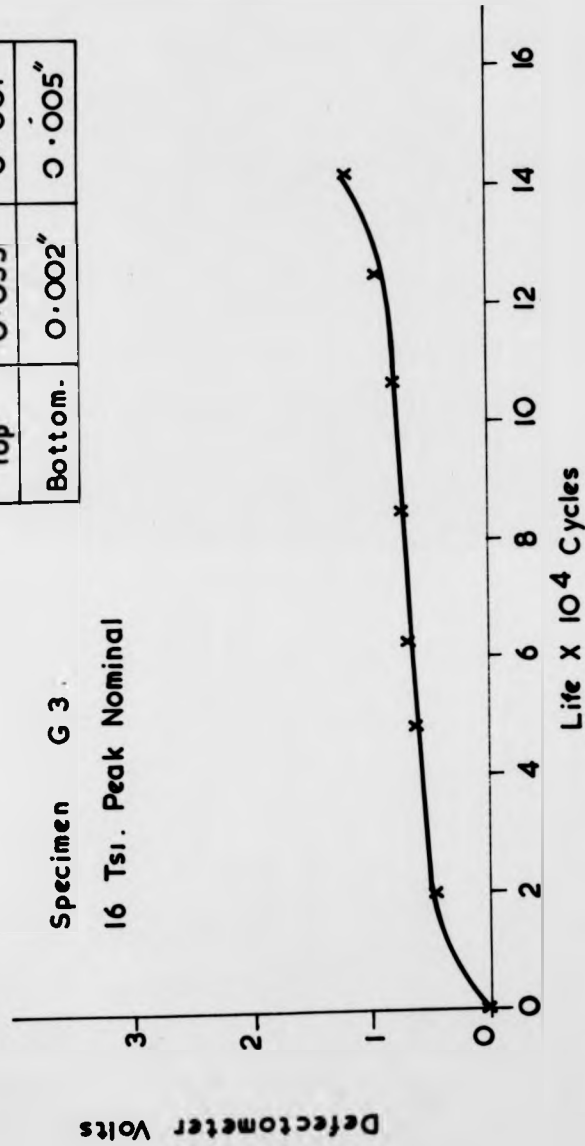


Constant Amplitude Loading

FIG. 8. 4.



Constant Amplitude Loading  
FIG. 8.5.



	Notch 1	Notch 2
Top	0.033"	0.001"
Bottom.	0.002"	0.005"

Constant Amplitude Loading

FIG. 8.6.

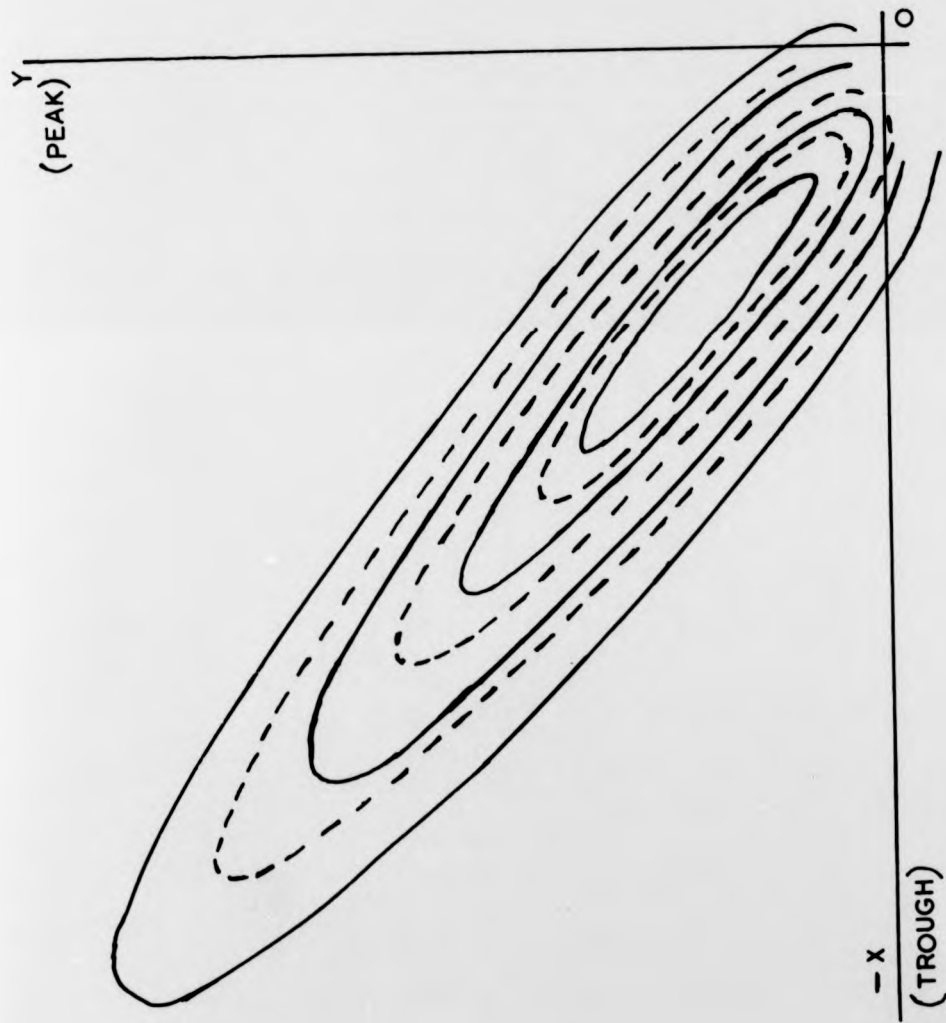


SPECIMEN G3 X125

0.033"

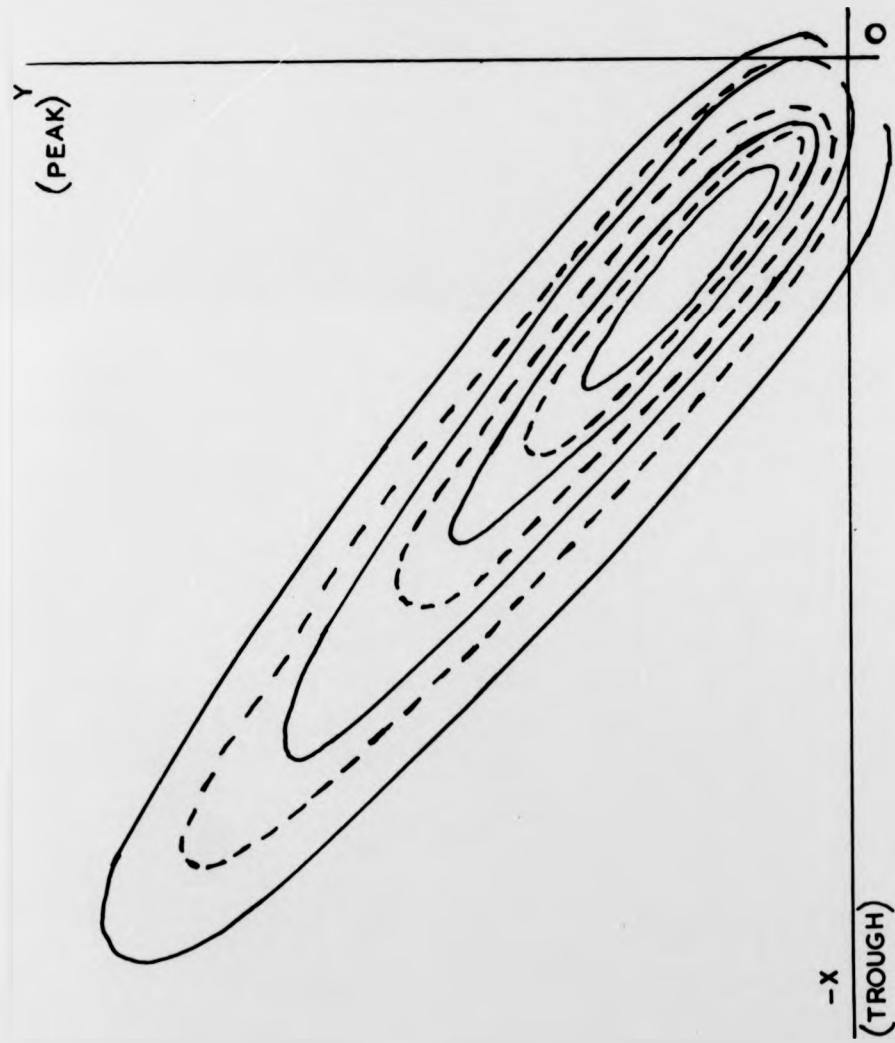
FIG. 8.7.

0.005	0.002
0.033	0.001
0.001	0.001



4.4 HZ. CENTRE FREQUENCY.  
10 HZ. BANDWIDTH.  
IRREGULARITY FACTOR=1.  
RMS. VOLTAGE = 2.2V.

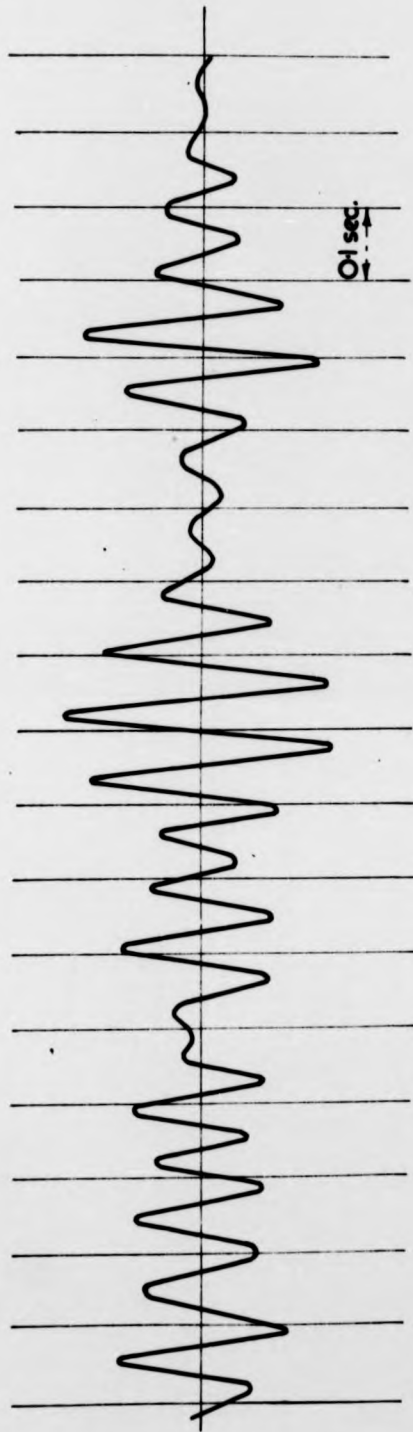
FIG. 8.8.



440HZ. CENTRE FREQUENCY.  
100HZ. BANDWIDTH.  
IRREGULARITY FACTOR = 1.  
RMS. VOLTAGE = 2.2V.

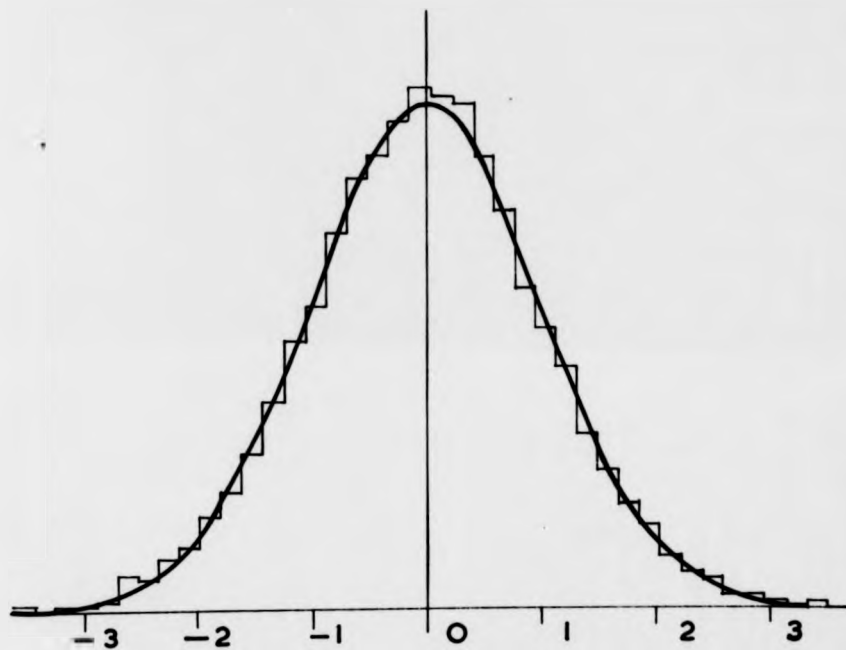
FIG. 8.9.

(SEVN)  
A



10 Hz Centre Frequency Signal

FIG. 8.10.



Standardised Probability Density  
10Hz Centre Frequency Signal

FIG. 8.11.

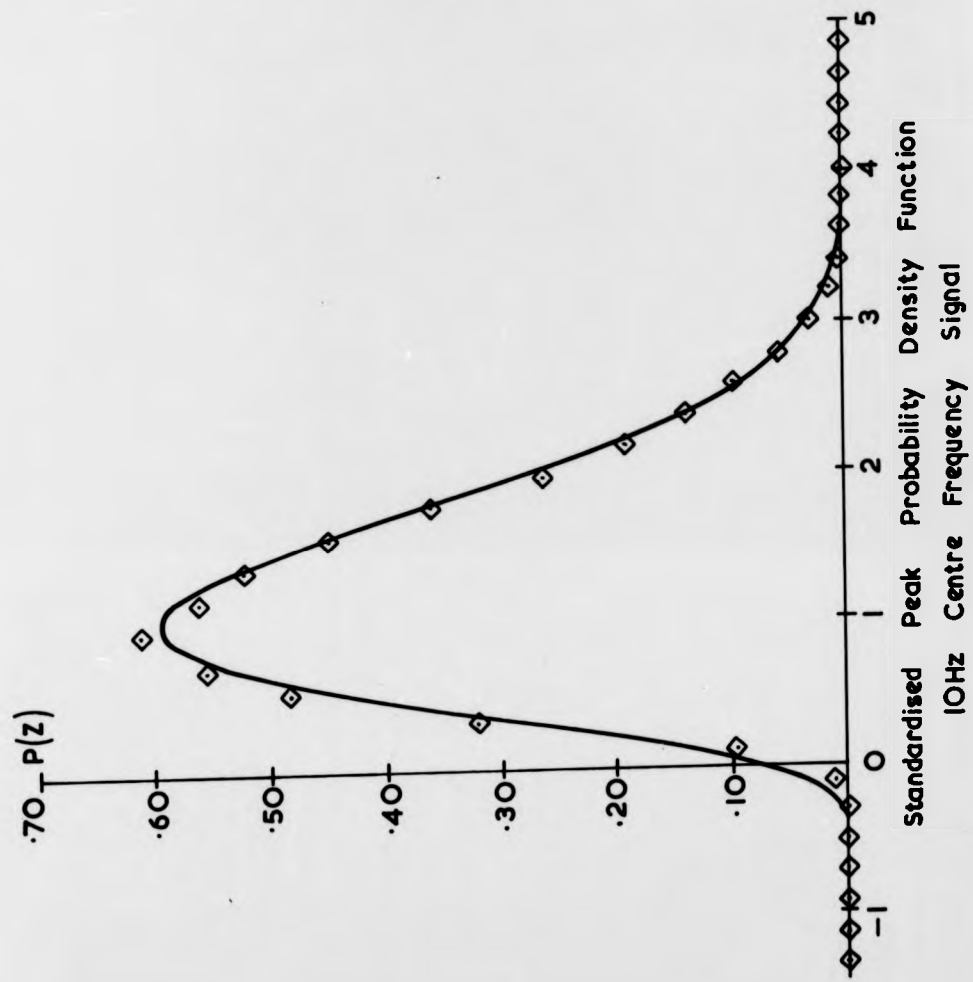
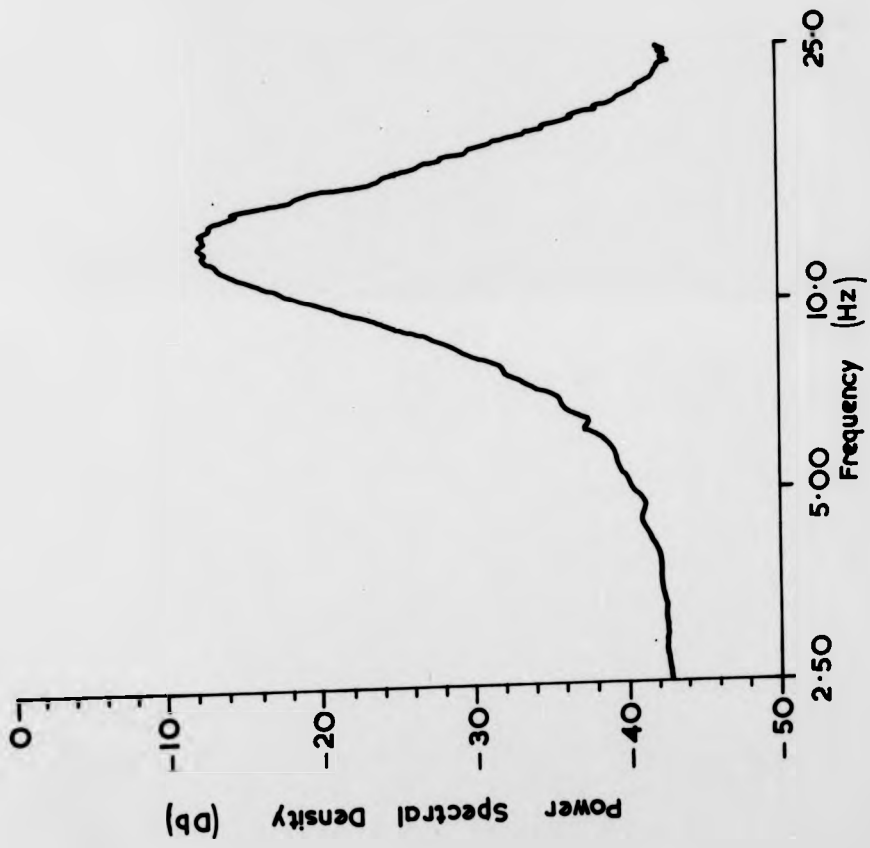


FIG. 8.12.



10Hz Centre Frequency Signal

FIG. 8. 13.

$$S = 48.50N^{-0.1871}$$

where,

$N$  = Life to failure (seconds)  
 $S$  = R M S Stress nominal (Tsi.)

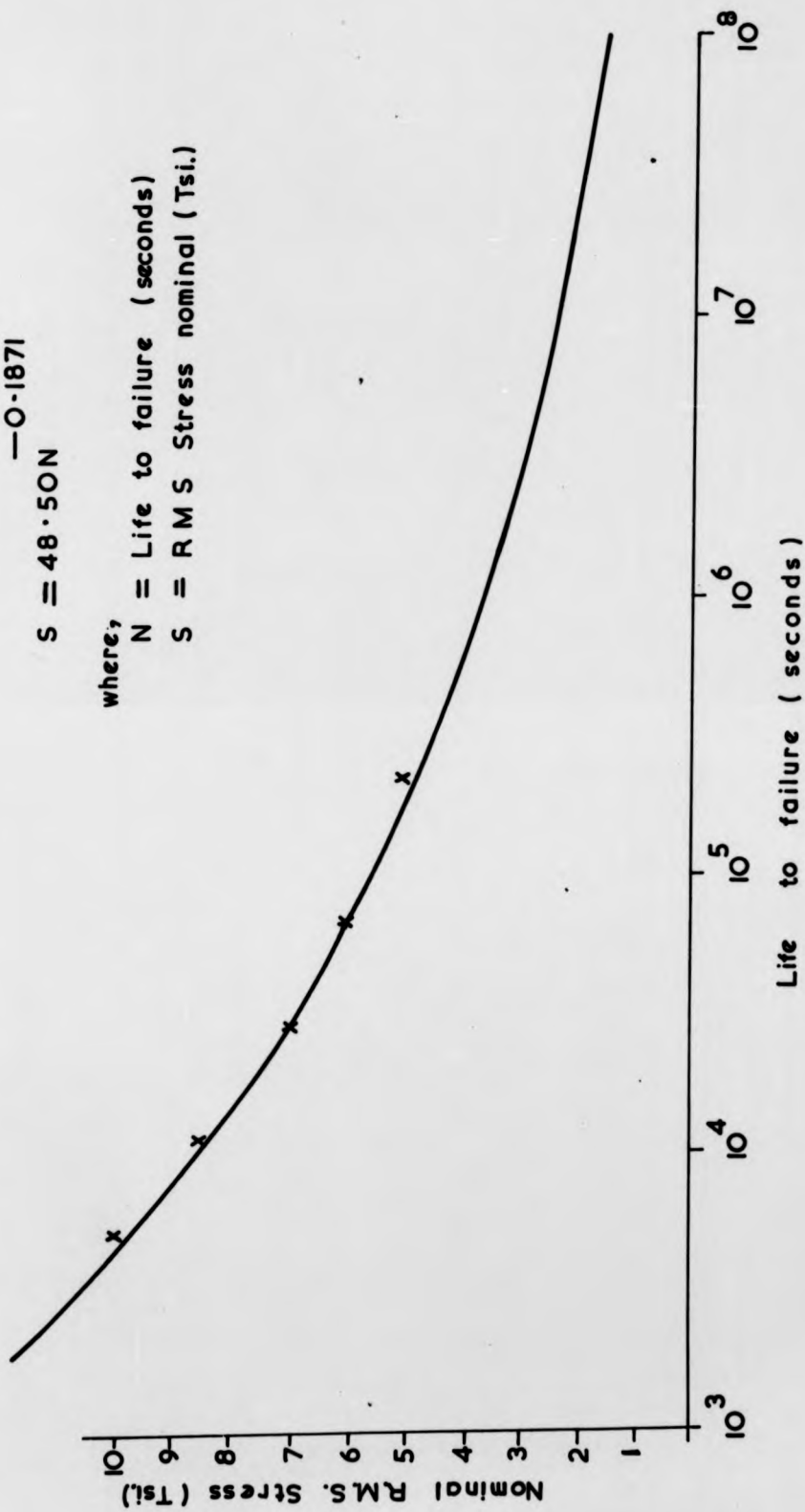
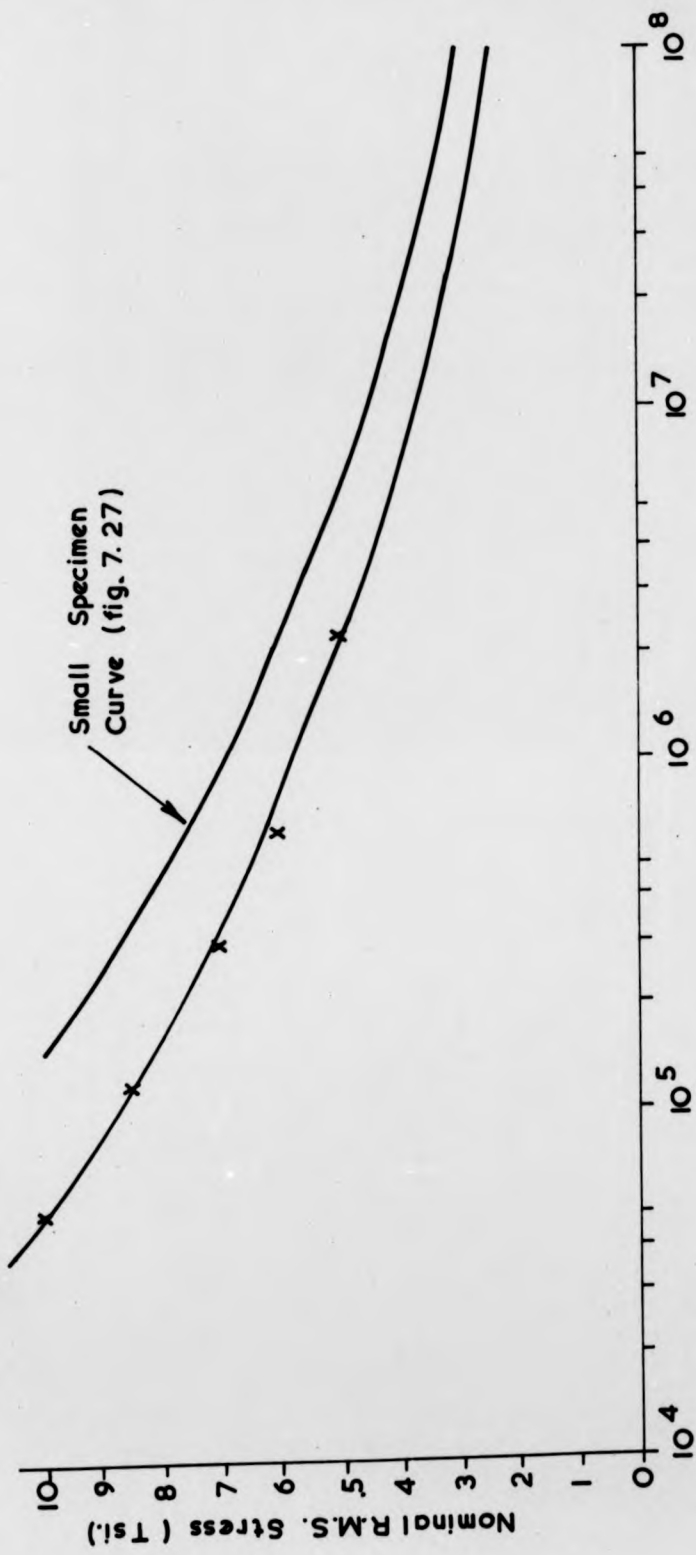


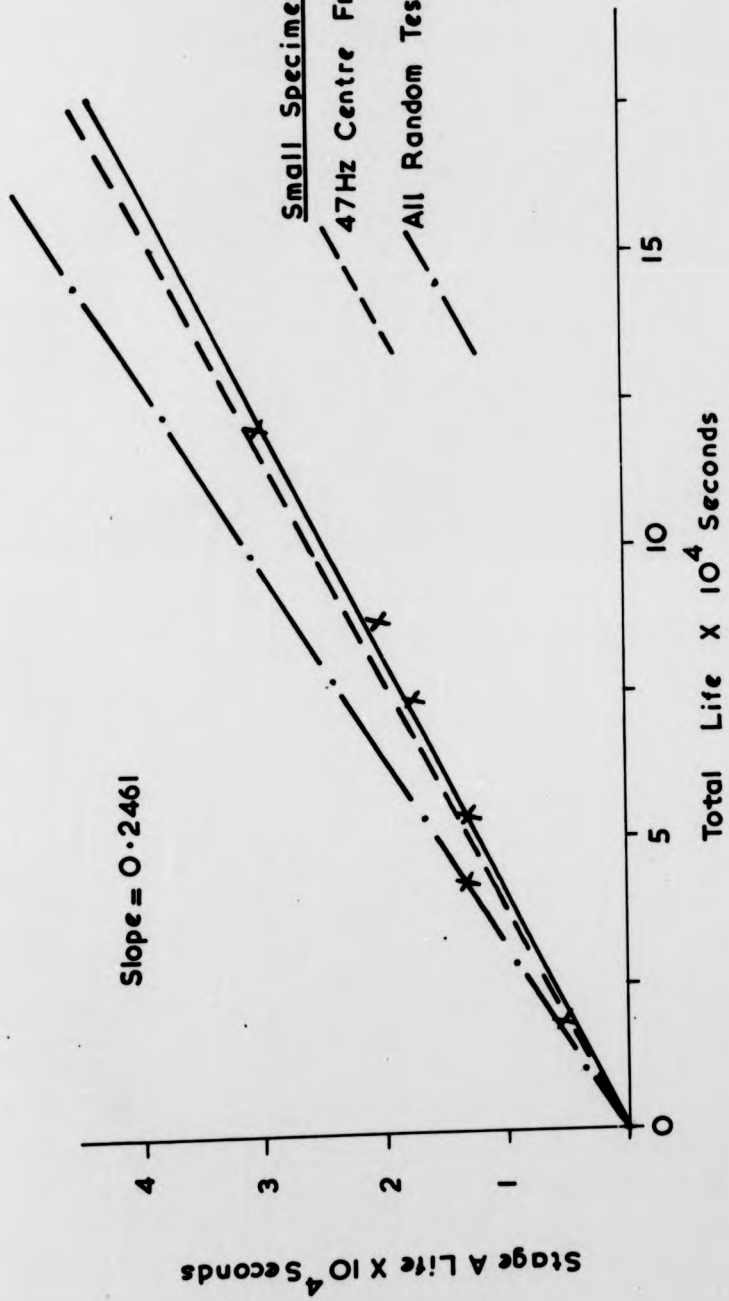
FIG. 8.14.

U.S. AIR FORCE RESEARCH AND DEVELOPMENT COMMAND  
WRIGHT-PATTERSON AIR FORCE BASE (CINCINNATI)  
RESEARCH CENTER

2-48-20M  
O-18A1



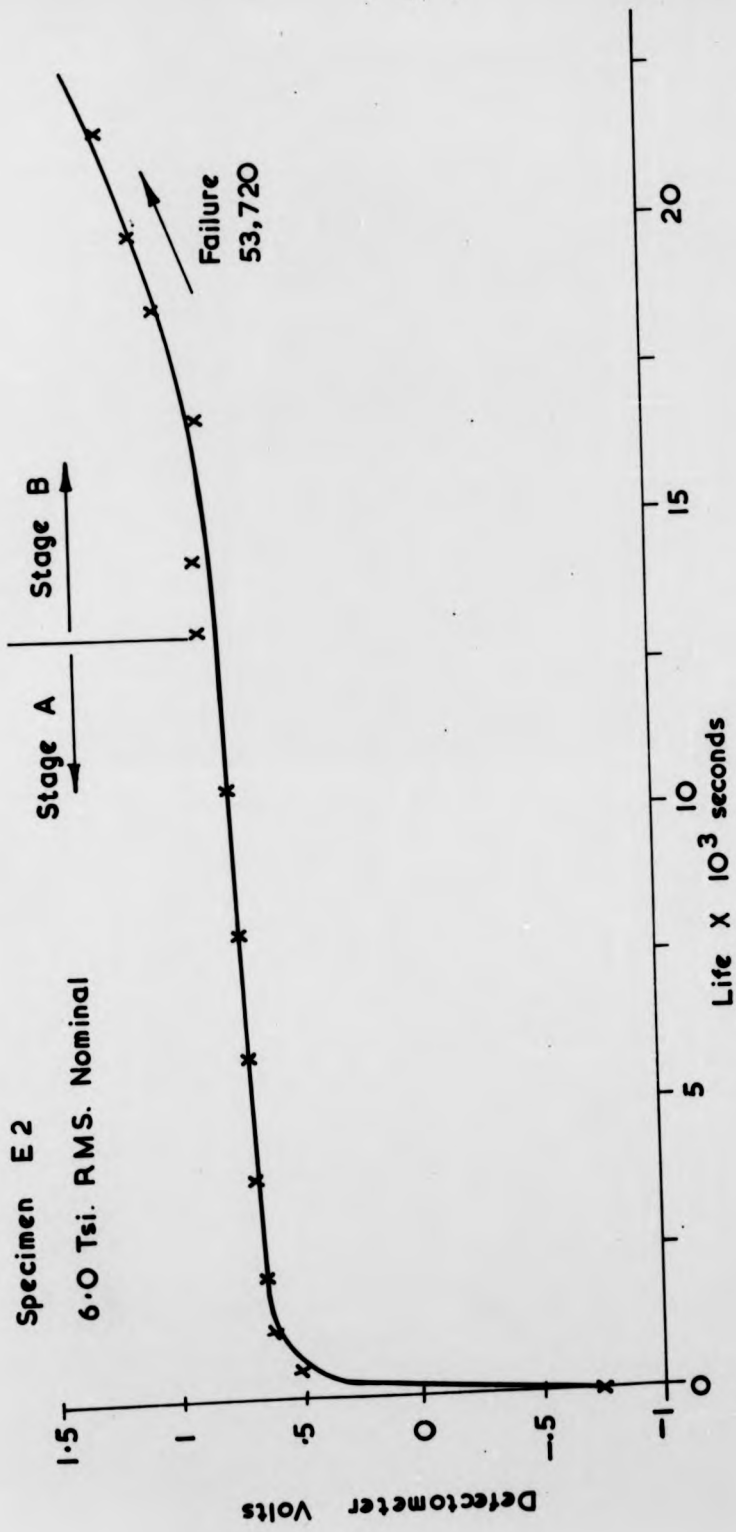
Peaks to Failure  
FIG. 8.15



10Hz Centre Frequency Signal

FIG. 8.16.

Specimen E2  
6.0 Tsi. RMS. Nominal



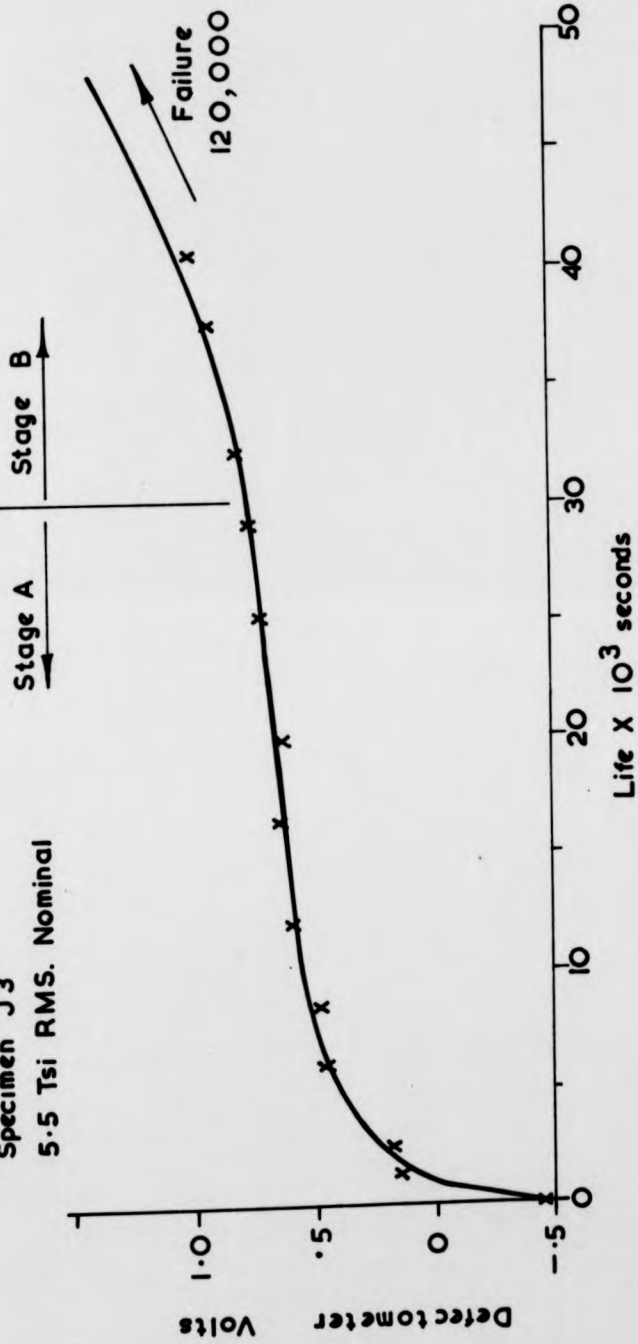
10Hz Centre Frequency Signal.

FIG. 8.17.

0.0 1.0 2.0 3.0 4.0 5.0 6.0 7.0 8.0 9.0 10.0  
Specimen E 5

Stage A Stage B

Specimen J 3  
5.5 Tsi RMS. Nominal

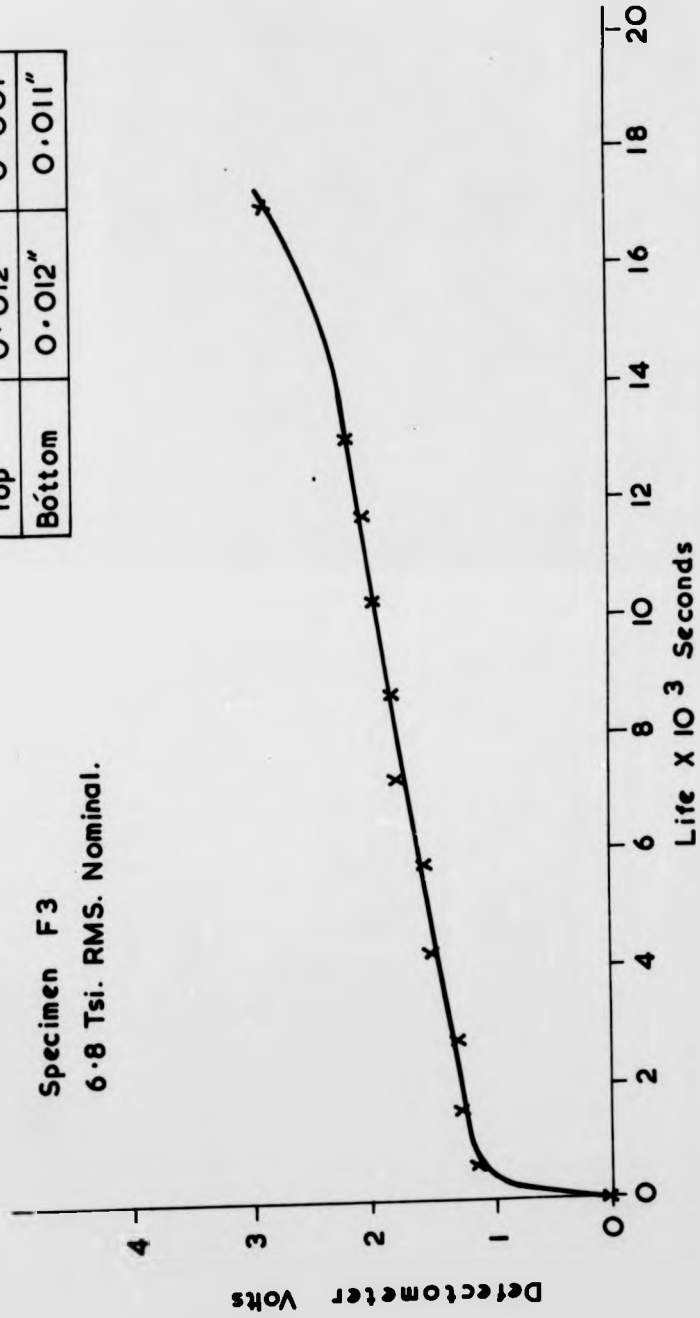


10Hz Centre Frequency Signal

FIG. 8-18.

Specimen F3  
6.8 Tsi. RMS. Nominal.

	Notch 1	Notch 2
Top	0.012"	0.001"
Bottom	0.012"	0.011"



10Hz Centre Frequency Signal

FIG. 8.19.

Bottom	0.015 <sub>2</sub>	0.011 <sub>1</sub>
Top	0.015 <sub>2</sub>	0.001 <sub>1</sub>
	Moist 1	Moist 5



SPECIMEN F3 X170  
0.012<sup>o</sup>

FIG. 8.20.

CHAPTER 9

ANALYSIS AND DISCUSSION  
OF RESULTS

1.	INTRODUCTION	129
2.	TWO STAGE FATIGUE LIFE BEHAVIOUR	129
3.	CUMULATIVE DAMAGE ANALYSIS	139
4.	CONCLUSIONS	144

1. INTRODUCTION.

The objective of the work in this chapter is to summarise the findings of the fatigue test results presented mainly in Chapters 5, 6 and 7, although there is some overlap with the work of Chapter 8. It is not intended to comment on the application of servocontrolled electrohydraulic systems to materials testing, since the techniques involved are now established - see Appendix A. Thus, the main aspects of this work can be presented in two sections followed by a summary of the findings:-

2. Two-Stage Fatigue Life Behaviour.
3. Cumulative Damage Analysis.
4. Conclusions.

2. TWO-STAGE FATIGUE LIFE BEHAVIOUR.

The results have established that by using high sensitivity eddy current crack detection, fatigue damage accumulation for both random and constant amplitude loading can be represented as occurring in two stages. These stages are analagous to those described by Forsyth (17), and here they have been defined:-

Stage A - Microcrack Initiation and Propagation.

Stage B - Macrocrack Propagation.

This is a similar finding to earlier work in this field (43), although there is a difference in that cracks upto 0.010 inches long were reported as being present in Stage A. There is a certain expertise involved in using eddy current crack detection, and it is additionally important to use correct instrument settings, especially with respect to suppressing lift-off effects at high sensitivity settings. This is supported by the work of Chatterjee (61), carried out

separately to that reported here, where similar fatigue stage behaviour is described. It is stated in the work of reference 43 that Defectometer instrument settings were not made in accordance with those recommended by the manufacturers, which may in part explain the discrepancy between the fatigue stage life crack definition adopted here.

Typical Defectometer responses have been shown in Chapters 5, 6, 7 and 8, and illustrate the two stage behaviour for several specimen shapes and loading waveforms. Generally, the same pattern of response has been recorded, whereby after an initial rise in eddy current reading, which is larger for higher stress levels, the response dwells and then climbs through the Stage A/Stage B transition into the macrocrack propagation phase. An exception in behaviour occurs for the small round cantilever specimens, where eddy current readings usually show an initial dip before remaining constant throughout the Stage A dwell period. The eddy current response is influenced chiefly by changes in specimen material electrical conductivity and magnetic permeability, and the presence of any cracks. The electrical performance of the Defectometer is such that its response to cracks is much more significant than to any associated material permeability or conductivity changes. However, since it has been established that no cracks are present at the beginning of Stage A, the Defectometer response in this stage can only be associated with permeability and conductivity changes. This reflects material internal changes. Thus, an initial dip in readings can be associated with work softening, and an initial rise in readings with work hardening. Cyclic stressing has been reported to cause work softening in previously work-hardened materials (62). The cold drawn material used for these

small specimens provides a similar situation. However, it is thought unlikely that the cold drawing effects associated with the material production process are significant in their effect on the results reported for the small specimens. Nevertheless it is interesting to reflect in this context that eddy current techniques offer a method of investigating the work hardening, work softening and ductility exhaustion phenomena which are responsible for setting up conditions favourable to crack initiation and which affect macrocrack propagation behaviour.

The test results for the Stage A/Total life behaviour shown under different random loading waveforms have been presented in Chapters 6 and 7, and the slopes of the best fit to data for all these results are summarised in table 9.1. The Stage A/Total life plots have been made with time as the fatigue life parameter, although the slope of the plot itself - i.e. the ratio of life spent in crack initiation to total life - is unaffected by the plot parameter. The small cantilever specimen results show a trend for crack initiation to occur earlier under higher irregularity factor waveforms for given fatigue lives. However, if all the test results are combined, the difference in the slopes for the three waveforms is not so apparent, perhaps partly because of the scatter in the data. The results are plotted for different fatigue life parameters in figs. 9.1, 9.2, 9.3 and 9.4. It therefore appears that the Stage A/Total life behaviour is more realistically represented by the best fit to the combined data, so that the proportion of time spent in crack initiation for a given fatigue life remains unaltered by waveform irregularity factor variations. This also is supported by the results for the axially loaded strip specimens, where

the results of both waveforms are plotted for different fatigue life parameters in figs. 9.5, 9.6, 9.7 and 9.8. Thus, within a given specimen configuration, the proportion of time spent in crack initiation for a given fatigue life remains unaltered by changes in waveform irregularity factor. This statement applies to two series of tests for loading waveforms of constant fundamental power spectrum shapes and Gaussian amplitude distributions. However, it could be stated that the small specimen power spectral shapes did change significantly within their band pass form, and that this could be attributed in part to the experienced variations in Stage A/Total life slope. However, it is probably more significant to comment on the likely effects of high peak stresses within a random waveform on this plot behaviour. The work of Booth et al (32) has shown that clipping stress peaks at above the 3.5 x rms. level negligibly affects total fatigue life, whereas clipping stress peaks at the 2.5 x rms. level results in considerably longer fatigue lives. The clipping ratios for the work reported here have not been exactly defined but the results of the peak probability measurements show accurately achieved peak stresses at the 4/4.5 x rms. level. Thus, the effect of the high stresses in a random waveform is probably more realistically assessed by considering the proportions of fatigue life spent in crack initiation and macrocrack propagation. Generally with specimens in the macrocrack propagation phase, beneficial compressive residual stresses are induced at the crack tip by high tensile loads which are not large enough to intrinsically damage the material, and this reduces subsequent crack growth rate. High compressive loads do not have the detrimental effect of inducing equivalent tensile residual stresses

because the crack faces come together and reduce the stress concentration at the root of the crack. Thus only a slight increase in growth rate is observed after high compressive loads. An uncracked component, however, would realise the notch stress concentration for compressive loads and harmful residual tensile stresses would be induced. With random loading there is an equal probability of occurrence of compressive and tensile load cycles, and it is thus possible that the beneficial effects of compressive residual stresses are not realised, so that the random loads with higher peak stresses initiate cracks more quickly. This behaviour would also be affected by the permanence of the residual stresses, which are more likely to fade in low yield stress materials like mild steels. If a test program were conducted to investigate the effects of low probability of occurrence high loads it would be particularly important to obtain accurate statistical definition of achieved stress waveforms, especially with regard to the reproduction of high peak stresses and fatigue machine test waveform limitations (see Appendix C), so that realistic between test correlations could be made. However, on the basis of the presented reasoning it is to be expected that the results of this work should show no significant difference in crack initiation behaviour for the different random loading waveforms considered.

The quantification of fatigue life under random loading into two distinct stages is important from a cumulative damage viewpoint, especially since it enables the accumulation of damage to be acknowledged in engineering terms, i.e. a period of life can be identified after which the onset of continuous and steady fatigue crack propagation occurs. It then becomes realistic to estimate whether life in either

stage is more accurately predicted than life as a whole. In this respect the damaging effect of stress peaks less than the constant amplitude fatigue limit can be assessed. It is possible that these low stresses are able to contribute to damage accumulation only when higher stress peaks are present to initiate damage, e.g. in the macrocrack propagation stage and, therefore, cumulative damage predictions are usually optimistic. Thus it could be expected that, in the absence of such damage, e.g. in the microcrack initiation and propagation stage, these low stresses are not so damaging and, therefore, life predictions should be more accurate for this stage alone. This aspect is investigated further in the next section.

The limited number of  $K_{T1}$  notch configurations tested under random loading precludes any attempt at the formulation of a general empirical relation describing crack initiation behaviour. However, some comparisons between the damaging effects of constant amplitude and random signals can be made. The small specimen rms. stress/life results have been described by one life curve, indicating little difference in overall life for waveforms with similar irregularity factor values and statistical properties. Therefore, for these results between test comparisons for the proportion of life spent in initiation could be made equally on a stress or life basis. For both the small and large round specimens crack initiation occurred more quickly under random loading than under constant amplitude loading. For example, with the cantilever specimens and the Rayleigh peak loading case, the proportion of time spent in each stage is shown in fig. 9.9, compared on a basis of equal lives. When the comparison is made on a basis of equal rms. stress, the proportion of time

spent in crack initiation is again shorter for the random tests, e.g. fig. 9.10, which again shows the Rayleigh loading case for the small cantilever specimens. However, the results for the axially loaded strip specimens show slightly different trends. The total life behaviour showed two distinct curves with the higher irregularity factor waveform more damaging for a given stress level. This suggests that major variations in the waveform shape (and the irregularity factor), e.g. see fig. 6.9, affect the total fatigue life, implying that less overall damage is caused when a large stress excursion is made up of a number of smaller stress ranges. When a comparison of the damaging effects of constant amplitude and random waveforms is made on a basis of equal rms. test stresses, the proportion of life spent in crack initiation is again shorter for the random tests. This can be seen by inspection of the Stage A/Total life data in tables 6.2, 6.12 and 6.13 in Chapter 6. But for a comparison based on equal fatigue lives, there is little difference in the time taken to initiate fatigue cracks under either constant amplitude or random loading. This is reflected in the slopes of the Stage A/Total life data in table 9.1, since the slope itself is unaffected by the fatigue life parameter.

Work carried out during sectioning and optical examination for cracks in all flat strip and round specimens part fatigued under constant amplitude loading, indicated a very quick transition from microcrack initiation and propagation to macrocrack propagation. Often constant amplitude specimens which were sectioned as soon as the Stage A/Stage B transition became apparent contained cracks upto 0.010 ins. long, indicating a rapid crack development into macrocrack propagation phase. However, under random loading the

transition to the establishing of macrocrack growth was slower than with constant amplitude loading, and macrocrack propagation rates for cracks within the detectable range of the Defectometer were also slower. It is likely that the slower development of the fatigue cracking process under random loading resulted from the residual compressive stresses left in the material immediately ahead of the crack tip after application of a high stress peak, so reducing the magnitude of the tensile stresses acting at the crack tip. The presence of a larger residual stress field at the crack tip was further evidenced by the Defectometer, which showed an increased response to an equivalent crack grown under random loading due to the additional effect of a larger plastically deformed zone of material on the eddy current distribution, see figs. 9.11 and 9.12. However, this larger residual stress field did not seem to inhibit some multiple crack initiation under random loading, as reported elsewhere (24). The best examples were found with the axially loaded strip specimens, see fig. 9.13, although it did occur with both the large and small round bending specimens.

Examination of the Stage A/Total life constant amplitude behaviour presented in this work shows that the slope of the plot is very similar for a wide range of test section sizes. This has been reported previously from similar work (43), suggesting that the proportion of life spent in crack initiation under constant amplitude loading is independent of specimen shape and only dependent on the specimen geometry and loading conditions as expressed through the  $K_T$  value of the notch. The total amount of available data describing this behaviour is listed in table 9.2. Since it has been established that there is a rapid crack development at the

Stage A/Stage B transition it is assumed that the validity of the work in reference 43 is little affected by the reported difference in Stage A behaviour. Therefore, that data has been reworked to obtain the best fit to data slopes constrained to the origin in order to retain consistency of data presentation. The results of the work by Frost (21) are included in table 9.2 to provide a description of the limiting case of Stage A behaviour expected under conditions favourable to the formation of non-propagating cracks. Plain specimen fatigue behaviour provides the other limiting condition for the Stage A/Total life concept. The philosophy behind the extension of the concept to these two extreme cases has been presented before (43) and is briefly outlined here:-

Non-propagating cracks.

Generally, it is assumed that for sharply notched specimens, crack initiation occurs early in the fatigue life and the majority of life is spent in macrocrack propagation. However, in terms of the Stage A/Stage B concept, Stage B is defined as starting when crack growth becomes a steady and continuous process so that the specimen is not regarded as being in the macrocrack propagation phase until the applied nominal stress is capable of propagating that crack to failure. The sharply notched specimen which is being stressed below the constant amplitude fatigue limit contains a small crack which will not propagate to failure unless the stress level is raised. This condition is defined as a microcrack propagation phase, or Stage A behaviour. For a specimen stressed near the fatigue limit damage will be initiated quickly, although the large variation in life occurs in propagating that initial damage into the macrocrack propagation phase, or Stage B behaviour. Therefore,

variations in the life of sharply notched specimens due to changes in stress level may be regarded as taking place for the major part in Stage A, i.e. the slope of the life in Stage A v. Total life plot for constant amplitude tests approaches  $45^\circ$ .

Plain Specimen Behaviour.

The absence of stress gradients with plain specimens means that immediately damage has been initiated the specimen behaviour passes into the macrocrack propagation or Stage B phase. The microcrack propagation phase dominated by specimen geometry is absent and the major variation in life occurs in Stage B behaviour. The slope in Stage A v. Total life plots for plain specimens in constant amplitude tests should then be parallel to the Total life axis, i.e. a slope of zero, but with an intercept on the Stage A life axis which denotes purely an initiation phase.

The adoption of this description of Stage A/Total life behaviour for these limiting cases enables an empirical relationship to be formulated linking the plot slope and specimen  $K_T$  for constant amplitude loading. Transforming the data to plot  $\log_{10} \frac{1}{K_T}$  v.  $\log_{10} \sec \theta$

- reference 43 - results in the best fit to data relationship shown in fig. 9.14. Results of tests carried out at small mean stresses also conform to this empirical relationship. This is supported by the results of Frost & Greenan (20) who report that crack propagation rates are insensitive to mean stress for mild steel. It could be expected, therefore, that Stage A behaviour is sensitive only to the range of resolved shear stress acting on slip bands, and not to the static shear stress.

### 3. CUMULATIVE DAMAGE ANALYSIS.

The objective of this section is to carry out Miner type life predictions for total life, and for Stage A and Stage B lives using the constant amplitude Stage A/Total life slope values, particularly to establish whether Miner can be used to more accurately predict life to crack initiation.

The constant amplitude and random loading results have been represented by best fit to data curves for the purposes of carrying out cumulative damage predictions. The adopted curve fitting procedures have been outlined in Chapters 5 and 6. Nevertheless, errors are involved in the representation of stress/life data by mathematical functions since it is usually not possible to obtain sufficient test results to adequately constrain the curve fitting over finite and infinite life ranges, and also because the analytical form of the equation itself is relied upon to realistically predict actual behaviour. The extrapolation of data for a wide range of stress and life values cannot be avoided for random load cumulative damage predictions, and the accuracy of the constant amplitude data itself is reflected in the calculations. The constant amplitude and random loading curves, together with other data which have been used in this cumulative damage analysis, are summarised in table 9.3.

The analysis has been based on the theoretical peak probability distribution and the assumption that the amplitudes of the stress cycles making up the random waveform can be accounted for by considering positive peaks only, see fig. 9.15. This is a similar counting method to that employed by some level crossing counters, except that then it is more usual for the largest peak and least subsequent trough between positive zero crossings to be recorded. However, it

is only likely that there is a significant difference between the two methods for low irregularity factor waveforms, when a large excursion is then made up of a series of smaller ranges. Thus, life predictions have been made using the positive area of the peak probability density curve, with stress amplitudes chosen in 0.1 x rms. level increments together with the corresponding probability of occurrence of the stress amplitudes, as shown by fig. 9.16.

The Miner summation for a given rms. stress level can therefore be written:-

$$N_T = \frac{1}{\sum \frac{P(z)}{N}}$$

where,  $N_T$  = predicted number of positive peaks to failure.

$P(z)$  = probability of occurrence of the standardised stress level,  $z$ .

$N$  = total number of positive peaks (cycles) to failure from S/N curve for standardised stress level,  $z$ .

The life fraction, i.e. the ratio of Miner life to actual life, is affected by the choice of maximum stress level to which the life summation is carried, and whether the peak distribution is truncated or clipped at this level, see fig. 9.17. For the clipped signal the number of peaks occurring at the clipping level is given by the total probability contained in the tail area. The effect of the choice has been investigated for the Rayleigh peak - 47 Hz. centre frequency signal loading of the small specimens. The choice of this waveform removes certain doubts about the definition of a stress cycle for random loading. It is also instructive to point out the possibility at high stress level life

summations of obtaining (mathematically) peak stresses in excess of the specimen static failure load. The results are summarised in table 9.4, showing ratios of Miner life to actual life in terms of positive peaks to failure. There is little difference between the summations on the truncated or clipped peak distributions, and similarly variations in maximum peak stress/rms. ratio do not have significant effects, as pointed out by White and Lewszuk (39). In terms of the Miner prediction clipping at 4.5 x rms. level proves to be most damaging and, therefore, since this clipping level realistically compares with that achieved in actual testing it was adopted for subsequent calculations. The calculations in tables 9.5 and 9.6 show Miner life fractions for the same waveform with three clipping ratios for Stage A and Stage B lives, but also comparing the effect of slight variations in the constant amplitude Stage A/Total life slope. For one set of calculations the experimentally determined constant amplitude Stage A/Total life slope has been used to determine the proportions of life spent in crack initiation and macrocrack propagation, and the other set uses the slope determined from the empirical relationship. It can be seen that the small variation in slope value has little effect on the resultant Miner fraction.

Thus, Miner life predictions were made for all the random load test series on a basis of positive stress peaks to failure, and using a clipping ratio of 4.5 with the experimentally determined values of constant amplitude Stage A/Total life slopes. The results are summarised in tables 9.7 to 9.11 inclusive, and presented graphically in figs. 9.18 to 9.22. Generally, for all these calculations, there appears to be little improvement over Miner predictions reported in

literature, either for total life or life in the respective stages. Fatigue lives are over predicted, although there is a tendency for Stage B, i.e. macrocrack propagation, to be most accurately assessed by Miner. The axial strip specimens are an exception to this statement, with Miner predictions being less than the actual life at higher rms. stress levels.

The Miner predictions are highly optimistic when more than about 90% of the peak stresses fall below the constant amplitude fatigue limit. This is shown by fig. 9.24. This indicates that Miner does not correctly estimate the damage contribution of small amplitude peak stresses for all stages of fatigue life. One way of overcoming this shortcoming in Miner is to choose a hypothetical S/N curve with a lower fatigue limit, e.g. reference 11 suggests a hypothetical fatigue limit of 0.8 x actual fatigue limit. This approach was adopted here, and the value of an artificial fatigue limit for the Stussi equation was selected so that the Miner life fraction was always between 1 and 1.5. A resulting set of hypothetical constant amplitude curves is shown in fig. 9.25 for the small cantilever specimens. However, the percentage number of peaks occurring below the hypothetical fatigue limit showed a similar trend to that with the real fatigue limit, see fig. 9.26. The details of the calculations are presented in tables 9.13 to 9.18, and the variation of the hypothetical fatigue limit with the percentage of peaks less than the constant amplitude fatigue limit is shown in figs. 9.27 to 9.32.

The conclusions which can be drawn from this analysis are themselves influenced by the form of the mathematical relationships chosen to represent the random and constant amplitude data. However, if the presentation of data is

accepted as being realistic it would seem that the adoption of a hypothetical fatigue limit concept does not satisfactorily account for the shortcomings in Miner's hypothesis. To some extent this reflects the comments in reference 14. Nevertheless, it is possible that by using other waveform parameters such as ranges, ranges and means, etc., more accurate predictions of random fatigue life could be obtained. The analysis here has been restricted to a positive peak interpretation of the waveform, although the available computer waveform analysis techniques (Appendix C) enable other parameters to be extracted. But even so, since analytical functions are only readily available to describe peak distributions for Gaussian signals, some recourse must be made to best-curve-fit procedures. Computer data capture can provide considerable quantities of data to accurately define functions at discrete points but, since such distributions as range probability distributions are of a double-exponential form, the application of standard curve fit procedures, such as orthogonal polynomials, to the data may not be straightforward because oscillations in the fitted polynomial can occur at extreme probability values. Thus, the application of computer techniques to data capture and interpretation becomes an area for research in itself.

In summarising, it can be stated that the Miner's Law predictions are in general agreement with the majority of published work, and there appears to be no significant gain in accuracy of life prediction by splitting the summation between the two stages of fatigue behaviour. Fatigue lives were usually optimistically predicted by a factor of about 3 to 4, although for waveforms with greater than about 90% of peaks less than the constant amplitude fatigue limit.

the prediction was grossly inaccurate. This illustrates that Miner seriously underestimates the damage contribution of low stress levels, both in the crack initiation and crack propagation phases of fatigue. Surprisingly, this is often regarded as not being too serious since, when a comparison is made on a stress basis between experimental and predicted behaviour at these low stress/long lives, the difference is perhaps of the order of 5%. Thus, to some extent, it is possible to achieve a safer life fraction by the addition of extra material to a component, although there is a tendency of this approach to lead to overdesign. However, inspection of the Miner life prediction and experimental data curves for the results presented here, figs. 9.18 to 9.23, show a greater discrepancy in stress levels in the long life region. Safe component life prediction under these conditions is more problematical. But even so, a lot of the doubt about the accuracy of cumulative damage predictions in this long life region must revolve around the lack of established component behaviour under these low stress/long life loading conditions, and the form of the mathematical representation of this data.

#### 4. CONCLUSIONS.

The findings of this research project are best framed around the two objectives which were stated in Chapter 1, section 1.7:-

a). To investigate the possibility of quantifying the fatigue process for random loading in terms of accepted two-stage behaviour and establish the realism of a life evaluation method based on an assessment of fatigue damage accumulation in these stages.

b). To make estimates of fatigue life using computer

techniques which enable accurate data acquisition from random stress waveforms.

It has been established that by using high sensitivity eddy current crack detection, fatigue damage accumulation for both random and constant amplitude loading can be represented as occurring in two stages:-

Stage A - Microcrack Initiation and Propagation.

Stage B - Macrocrack Propagation.

At the stage transition for constant amplitude loading there is a rapid fatigue crack growth to a length which is detectable and measurable by optical microscope methods. Under random loading the transition growth is not so quick, and cracks which were less than 0.001 inches long have been successfully detected at this phase in fatigue life. These results do tend to suggest a fatigue stage behaviour analogous to that established by Forsyth (17).

An empirical relationship has been restated for constant amplitude loading whereby the proportion of life spent in either stage can be estimated from the specimen elastic stress concentration factor. This relationship has been formulated from the behaviour of a wide range of specimen configurations.

The limited number of random load tests precluded any attempt at the formulation of a general empirical relationship describing crack initiation behaviour, but it has been established that, for a given specimen configuration, the proportion of time spent in Stage A behaviour for a given fatigue life remains unaltered for changes in waveform irregularity factor. This statement applies to two series of tests for loading waveforms of constant fundamental p.s.d.

shapes and Gaussian amplitude probability density distributions. It is suggested that the signal maximum peak/rms. ratio is a significant factor in determining the proportion of life spent in crack initiation, and that overall waveform shape plays an important part in determining total fatigue life. In this respect, it is felt that frequency effects, such as power spectral density variations, are of secondary importance.

On-line computer techniques have been used to accurately define the statistical properties of random loading waveforms, and also to provide the necessary signal data required for cumulative damage predictions. Fatigue lives were estimated using Miner's Hypothesis on a basis of positive peak stresses to failure for Stage A and Stage B lives, and overall fatigue life. The results were in general agreement with published work, showing highly optimistic predictions for waveforms with a significant number of stress peaks below the constant amplitude fatigue limit. This not only confirmed that Miner seriously underestimates the damage contribution of low peak stresses on fatigue life as a whole, but also showed that the damage contribution of low peak stresses is underestimated for the crack initiation phase of life. If anything, the Miner summations are more accurate for the macrocrack propagation stage than the microcrack initiation/propagation stage. This suggests that life to first cracking must take proportionately more account of low stress amplitudes. In a design sense, current practice is such that most components do, in fact, experience stress levels which are lower than the constant amplitude fatigue limit. In this respect, it is difficult to assess just how conservative component designs are because of the

lack of data describing crack initiation behaviour. However, it is probable that the tendency is for most designs to be too conservative, but this can only be answered when more information is available. It is suggested that the inadequacies in Miner's Hypothesis cannot always be accounted for by the adoption of a "hypothetical S/N curve" concept.

Together with the many other published findings, the results of this cumulative damage analysis emphasise the inability of Miner's Hypothesis to accurately assess fatigue lives for low stress levels. Part of the uncertainty in these predictions must be linked with the uncertainty of actual behaviour under low stress random loading; for example, is there a stress level similar to the constant amplitude fatigue limit at which no damage occurs? But apart from the low stresses, the effect of plastic flow and residual stress distributions caused by high loads is not entirely clear in a cumulative damage context. Therefore, the question must be asked as to whether the accuracy of cumulative damage predictions can be expected to show any significant improvement in accuracy while fatigue life is assessed by a Miner type summation from an S/N curve.

---

Specimen Description	Chapter	Stage A/Total life Slope
Cantilever Strip	5	0.6466
Axial Strip	6	0.6355
Small Cantilever Round	7	0.4567
Large Round 3 pt. Bending	8	0.5356

Constant Amplitude Loading

Signal Description	Irregularity Factor	Stage A/Total life Slope
Low Irregularity Factor	0.51	0.7116
High Irregularity Factor	0.89	0.7902

Combined Data Stage A/Total life Slope = 0.7646

Axial Strip Specimen (Chapter 6)

Signal Description	Irregularity Factor	Stage A/Total life Slope
47 Hz. Centre Frequency	1.0	0.2598
25/52 Hz. Band Pass	0.92	0.2749
5/52 Hz. Band Pass	0.80	0.4109

Combined Data Stage A/Total life Slope = 0.3142

Small Round Cantilever Specimen (Chapter 7)

Signal Description	Irregularity Factor	Stage A/Total life Slope
10 Hz. Centre Frequency	0.98	0.2461

Large 3 pt. Bending Specimen (Chapter 8)

SUMMARY OF STAGE A/TOTAL LIFE SLOPE DATA

Table 9.1

Fig. 9.14 reference	Mode of Loading.	Mean Load	Specimen Test Section Dims. (inches)	Elastic Stress Concentration Factor $K_t$ .	Stage A/Total Life Slope	$\log_{10} \frac{1}{K_t}$	$\log_{10} \text{sec } \theta$
1	Cantilever Bending (Chapter 7)	No	1.024 x 0.25	1.59	24° 34'	-0.2014	0.0412
2	3 pt. Plane Bending (Chapter 8)	No	1.8 dia.	1.59	28° 14'	-0.2014	0.0550
3	Rotating Bending (Ref. 43.)	No	0.531 dia.	2.0	27° 31'	-0.3010	0.0522
4	Cantilever Bending (Chapter 5)	No	0.198 dia.	1.95	32° 54'	-0.2878	0.0759
5	Axial Pulsating (Ref. 43)	Yes	1.0 dia.	2.17	31° 36'	-0.3365	0.0697
6	3 pt. Plane Bending (Ref. 43.)	Yes	4.3 dia.	2.21	30° 0'	-0.3444	0.0764
7	Axial push-pull (Chapter 6)	Yes	0.95 x 0.125	2.26	34° 22'	-0.3541	0.0833
8	See Test Results of Ref. 31.	-	-	3.42	45°	-0.5340	0.1505

Summary of Slope/ $K_t$  Data for Constant Amplitude Testing. Table 9.2

Signal Description.	Constant Amplitude Stage A/Life Slope	Constant Amplitude Equation.	Irregularity Factor	Positive Peaks/Sec.	Random Loading Stage A/Life Slope	Random Loading Equation.
10 Hz. Centre Frequency	0.5266	fig. 8.2	0.98	10.21	0.2461	fig. 8.14
47 Hz. Centre Frequency	0.4567	fig. 7.2	1.0	47.0	0.3142	fig. 7.26.
25/52 Hz. Band Pass	0.4567	fig. 7.2	0.92	42.64	0.3142	fig. 7.26.
5/52 Hz. Band Pass	0.4567	fig. 7.2	0.80	37.78	0.3142	fig. 7.26.
High Irregularity Factor	0.6838	fig. 6.1	0.89	26.0	0.7646	fig. 6.15.
Low Irregularity Factor	0.6838	fig. 6.1.	0.51	13.31	0.7646	fig. 6.15.

Summary of Data for Cumulative Damage Analysis.

Table 9.3

RMS Stress Tsi Nominal	Experimental Total Life Cycles	% Positive Peaks below Fatigue Limit for Clipped Signal	Signal Clipping Ratio			% Positive Peaks below Fatigue Limit for Truncated Signal	Signal Truncation Level		
			Signal Clipping Ratio				Signal Truncation Level		
			4.0	4.25	4.5		4.0	4.25	4.5
14	33,937	39.8	2.57	2.54	2.44	2.62	2.56	2.51	
13	49,004	44.5	2.7	2.46	2.45	2.50	2.48	2.46	
12	72,874	49.9	2.34	2.34	2.34	2.37	2.36	2.34	
11	112,183	56.0	2.23	2.23	2.23	2.25	2.24	2.23	
10	179,947	63.0	2.15	2.15	2.15	2.17	2.16	2.15	
9	303,390	70.7	2.14	2.14	2.13	2.16	2.15	2.14	
8	544,009	78.8	2.25	2.25	2.25	2.26	2.26	2.25	
7	1,054,677	86.8	2.64	2.64	2.64	2.69	2.66	2.65	
6	2,264,797	93.7	3.82	3.82	3.81	3.95	3.88	3.83	
5	5,592,363	98.1	8.38	8.37	8.29	9.12	8.70	8.43	
4	16,906,646	99.8	53.71	49.57	46.10	81.23	61.15	50.49	

Constant Amplitude Fatigue Limit = 14.1 Tsi, peak nominal

47Hz. Centre Frequency Signal  
Piner Total Life Summation

Table 9.4

RMS Stress Tsi. Nominal	Experimental Stage A Life Cycles	% Positive Peaks Below Fatigue Limit	Clipping Ratio for Miner Life Fraction in Stage A				Empirical Stage Life Slope	
			Experimental Stage Life Slope		Empirical Stage Life Slope			
			4.0	4.25	4.5	4.0		4.5
14	10,662	39.8	3.77	3.73	3.60	4.22	4.17	4.03
13	15,396	44.5	3.61	3.59	3.57	4.04	4.02	4.00
12	22,895	49.9	3.43	3.42	3.40	3.84	3.82	3.81
11	35,244	56.0	3.26	3.25	3.24	3.65	3.64	3.63
10	56,534	63.0	3.14	3.13	3.12	3.52	3.51	3.50
9	95,316	70.7	3.12	3.11	3.11	3.49	3.49	3.48
8	170,911	78.8	3.29	3.28	3.27	3.69	3.67	3.66
7	331,347	86.8	3.88	3.86	3.84	4.34	4.32	4.30
6	711,529	93.7	5.65	5.60	5.55	6.31	6.26	6.21
5	1,756,947	98.1	12.74	12.42	12.16	14.20	13.88	13.60
4	5,311,504	99.8	95.69	89.32	79.34	104.9	88.90	78.36

Constant Amplitude Fatigue Limit = 14.1 Tsi. peak nominal.

Random Loading Stage A / Total Life Slope = 0.3142

Constant Amplitude Stage A / Total Life Slope = 0.4567

Empirical S/N Stage A / Total Life Slope = 0.5113

47 Hz. Centre Frequency Signal

TABLE 9.5

RMS Stress Tsi. Nominal.	Experimental Stage B Life Cycles	% Positive Below Fatigue Limit.	Clipping Ratio for Miner Life Fraction in Stage B					
			Experimental Stage Life Slope			Empirical Stage Life Slope.		
			4.0	4.25	4.5	4.0	4.25	4.5
14	23,275	39.8	2.05	2.03	1.96	1.85	1.83	1.76
13	33,609	44.5	1.97	1.96	1.94	1.77	1.76	1.75
12	49,980	49.9	1.87	1.86	1.85	1.68	1.67	1.67
11	76,939	56.0	1.77	1.77	1.77	1.60	1.59	1.59
10	123,413	63.0	1.71	1.71	1.70	1.54	1.54	1.53
9	208,074	70.7	1.70	1.70	1.69	1.53	1.53	1.52
8	373,098	78.8	1.79	1.79	1.78	1.61	1.61	1.60
7	723,330	86.8	2.11	2.10	2.09	1.90	1.89	1.88
6	1,553,268	93.7	3.07	3.05	3.02	2.77	2.74	2.72
5	3,835,416	98.1	6.89	6.75	6.62	6.23	6.08	5.96
4	11,595,102	99.8	50.34	42.98	38.03	46.29	39.11	34.38

Constant Amplitude Fatigue Limit = 14.1 Tsi. peak nominal.

Random Loading Stage A / Total Life Slope = 0.3142

Constant Amplitude Stage A / Total Life Slope = 0.4567

Empirical S/N Stage A / Total Life Slope = 0.5113

47 Hz. Centre Frequency Signal

TABLE 9.6

RMS Stress Tsi. Nominal	% Positive Peaks Below Fatigue Limit	Total Life Summation		Stage A Life Summation		Stage B Life Summation	
		Experimental Life Cycles	Miner Life Fraction	Experimental Stage A Life Cycles	Miner Life Fraction	Experimental Stage B Life Cycles	Miner Life Fraction
14	39.8	33,937	2.44	10,662	3.60	23,275	1.96
12	48.9	72,875	2.34	22,895	3.40	49,980	1.85
10	63.0	179,947	2.15	56,534	3.12	123,413	1.70
8	78.8	544,009	2.25	170,911	3.27	373,098	1.78
6	93.7	2,264,797	3.81	711,529	5.55	1,553,268	3.02
4	99.8	16,906,646	46.11	5,311,544	70.34	11,595,102	38.03

Random Loading Stage A / Total Life Slope = 0.3142  
 Constant Amplitude Stage A / Total Life Slope = 0.4567  
 Constant Amplitude Fatigue Limit = 14.1 Tsi. peak nominal.  
 Irregularity Factor = 1.00

47 Hz Centre Frequency Signal

Table 9.7

RMS Stress Tsi. Nominal	% Positive Peaks Below Fatigue Limit	Total Life Summation		Stage A Life Summation		Stage B Life Summation	
		Experimental Life Cycles	Minor Life Fraction	Experimental Stage A Life Cycles	Minor Life Fraction	Experimental Stage B Life Cycles	Minor Life Fraction
14	42.3	30,788	2.92	9,673	4.32	21,116	2.35
12	51.9	66,115	2.30	20,771	4.08	45,343	2.22
10	64.5	163,254	2.57	51,289	3.74	111,964	2.04
8	79.7	493,543	2.69	155,056	3.92	338,487	2.14
6	93.9	2,054,701	4.56	645,523	6.65	1,409,178	3.62
4	99.8	15,338,284	55.24	4,818,813	84.27	10,519,471	45.57

Random Loading Stage A / Total Life Slope = 0.3142

Constant Amplitude Stage A / Total Life Slope = 0.4567

Constant Amplitude Fatigue Limit = 14.1 Tsi. peak nominal.

Irregularity Factor = 0.92

25/52 Hz. Band Pass Signal

Table 9.8

RMS Stress Tsi. Nominal	% Positive Peaks Below Fatigue Limit	Total Life Summation		Stage A Life Summation		Stage B Life Summation	
		Experimental Life Cycles	Miner Life Fraction	Experimental Stage A Life Cycles	Miner Life Fraction	Experimental Stage B Life Cycles	Miner Life Fraction
14	46.1	27,279	3.79	8,570	5.60	18,709	3.04
12	55.3	58,579	3.63	18,404	5.29	40,175	2.88
10	67.1	144,647	3.34	45,443	4.86	99,203	2.65
8	81.2	427,290	3.49	137,383	5.09	299,907	2.77
6	94.4	1,820,511	5.92	571,948	8.63	1,248,563	4.70
4	99.8	13,590,065	71.7	4,269,577	109.4	9,320,488	59.14

Random Loading Stage A / Total Life Slope = 0.3142

Constant Amplitude Stage A / Total Life Slope = 0.4567

Constant Amplitude Fatigue Limit = 14.1 Tsi. Peak nominal.

Irregularity Factor = 0.80

5/52 Hz. Band Pass Signal

Table 9.9

RMS Stress Tsi. Nominal	% Positive Peaks Below Fatigue Limit.	Total Life Summation		Stage A Life Summation		Stage B Life Summation	
		Experimental Life Cycles	Miner Life Fraction	Experimental Stage A Life Cycles	Miner Life Fraction	Experimental Stage B Life Cycles	Miner Life Fraction
8	62.2	155,779	2.73	38,331	5.97	117,448	1.68
7	71.8	348,056	3.02	78,261	6.61	239,795	1.86
6	82.1	725,048	3.78	178,406	8.26	546,642	2.33
5	91.6	1,921,451	6.09	472,794	13.3	1,448,657	3.76
4	97.9	6,333,750	17.5	1,558,489	38.7	4,775,261	10.9
3	99.9	29,479,478	251	7,253,751	604	22,225,727	173

Random Loading Stage A / Total Life Slope = 0.2461

Constant Amplitude Stage A / Total Life Slope = 0.5366

Constant Amplitude Fatigue Limit = 11.1 Tsi. peak nominal.

Irregularity Factor = 0.98

10 Hz. Centre Frequency Signal.

Table 9.10

RMS Stress Tsi. Nominal.	% Positive Peaks Below Fatigue Limit	Total Life Summation		Stage A Life Summation		Stage B Life Summation	
		Experimental Life Cycles	Miner Life Fraction	Experimental Stage A Life Cycles	Miner Life Fraction	Experimental Stage B Life Cycles	Miner Life Fraction
5	53.1	277,641	0.34	212,296	0.31	65,345	0.47
4	65.3	1,146,705	0.53	876,818	0.48	269,887	0.72
3	81.4	7,137,947	0.83	5,457,971	0.75	1,679,976	1.13
2	96.6	93,934,450	3.19	71,826,188	2.88	22,108,262	4.39

Random Loading Stage A / Total Life Slope = 0.7646

Constant Amplitude Stage A / Total Life Slope = 0.6838

Constant Amplitude Fatigue Limit = 4.9 Tsi. peak nominal.

Irregularity Factor = 0.51

Low Irregularity Factor Signal

Table 9.11

RMS Stress Tsi. Nominal.	% Positive Peaks Below Fatigue Limit	Total Life Summation		Stage A Life Summation		Stage B Life Summation	
		Experimental Life Cycles	Miner Life Fraction	Experimental Stage A Life Cycles	Miner Life Fraction	Experimental Stage B Life Cycles	Miner Life Fraction
5	41.7	75,530	0.72	57,753	0.65	17,777	1.00
4	55.5	296,296	1.19	226,560	1.07	69,736	1.62
3	75.2	1,725,907	2.00	1,319,700	1.79	406,207	2.71
2	95.3	20,684,054	8.32	15,815,88	7.52	4,868,166	11.45

Random Loading Stage A / Total Life Slope = 0.7646

Constant Amplitude Stage A / Total Life Slope = 0.6838

Constant Amplitude Fatigue Limit = 4.9 Tsi. peak nominal

Irregularity Factor = 0.89

High Irregularity Factor Signal.

Table 9.12

RMS Stress Tsi. Nominal.	% Positive Peaks Below S/N Fatigue Limit	Total Life Summation			Stage A life Summation		Stage B life Summation	
		Hypothetical Fatigue limit Tsi. Peak Nom.	Ratio of Hypothetical S/N Fatigue Limits	Hypothetical Fatigue Limit Tsi. Peak Nom.	Ratio of Hypothetical S/N Fatigue Limits	Hypothetical Fatigue Limit Tsi. Peak Nom.	Ratio of Hypothetical S/N Fatigue Limits	
14	39.8	9.5	0.674	6.3	0.446	11.4	0.809	
12	49.9	11.1	0.788	8.3	0.589	12.5	0.886	
10	63.0	12.0	0.850	10.1	0.716	13.1	0.929	
8	78.8	12.3	0.872	11.1	0.788	13.1	0.929	
6	93.7	11.6	0.822	10.8	0.765	12.3	0.872	
4	99.8	9.85	0.699	9.3	0.660	10.1	0.716	

Constant Amplitude Fatigue Limit = 14.1 Tsi. peak nominal

Irregularity Factor = 1.00

47 Hz. Centre Frequency Signal

Table 9.13

RMS Stress Tsi. Nominal	% Positive Peaks Below S/N Fatigue Limit	Total Life Summation		Stage A Life Summation		Stage B Life Summation	
		Hypothetical Fatigue Limit Tsi. Peak Nom.	Ratio of Hypothetical S/N Fatigue Limits	Hypothetical Fatigue Limit Tsi. Peak Nom.	Ratio of Hypothetical S/N Fatigue Limits	Hypothetical Fatigue Limit Tsi. Peak Nom.	Ratio of Hypothetical S/N Fatigue Limits
14	42.3	8.1	0.575	-	-	9.9	0.701
12	51.9	9.6	0.681	6.9	0.489	11.3	0.801
10	64.5	11.1	0.787	9.0	0.638	12.3	0.871
8	79.7	11.6	0.823	10.3	0.730	12.5	0.887
6	93.9	11.3	0.801	10.2	0.724	11.7	0.830
4	99.8	9.5	0.673	9.0	0.638	9.85	0.698

Constant Amplitude Fatigue Limit = 14.1 Tsi. peak nominal

Irregularity Factor = 0.92

25/52 Hz. Band Pass Signal

Table 9.14.

RMS Stress	Positive Peak's Below S/N Fatigue Limit	Total Life Summation		Stage A Life Summation		Stage B Life Summation	
		Hypothetical Fatigue Limit Tsi. Peak Non.	Ratio of <u>Hypothetical</u> S/N Fatigue Limits	Hypothetical Fatigue Limit Tsi. Peak Non.	Ratio of <u>Hypothetical</u> S/N Fatigue Limits	Hypothetical Fatigue Limit Tsi. Peak Non.	Ratio of <u>Hypothetical</u> S/N Fatigue Limits
14	46.1	5.7	0.404	-	-	7.8	0.553
12	55.3	7.8	0.553	-	-	9.5	0.674
10	67.1	9.6	0.661	7.5	0.532	10.8	0.766
8	81.2	10.7	0.758	9.3	0.660	11.6	0.822
6	94.4	10.5	0.744	9.6	0.681	11.1	0.787
4	99.8	9.1	0.645	8.6	0.610	9.5	0.674

Constant Amplitude Fatigue Limit = 14.1 Tsi. peak nominal

Irregularity Factor = 0.80

5/52 Hz. Band Pass Signal

Table 9.15

R/S Stress Tsi. Nominal	% Positive Peaks Below S/N Fatigue Limit	Total Life Summation		Stage A Life Summation		Stage B Life Summation	
		Hypothetical Fatigue Limit Tsi. Peak Nom.	Ratio of <u>Hypothetical</u> S/N Fatigue Limits	Hypothetical Fatigue Limit Tsi. Peak Nom.	Ratio of <u>Hypothetical</u> S/N Fatigue Limits	Hypothetical Fatigue Limit Tsi. Peak Nom.	Ratio of <u>Hypothetical</u> S/N Fatigue Limits
8	62.2	9.85	0.887	6.85	0.617	10.8	0.973
7	71.9	9.6	0.865	7.2	0.648	10.8	0.973
6	82.1	9.5	0.855	7.5	0.676	10.5	0.946
5	91.6	9.0	0.811	7.35	0.662	9.85	0.887
4	97.9	8.1	0.730	6.9	0.621	8.7	0.783
3	99.9	6.9	0.621	6.3	0.568	7.5	0.676

Constant Amplitude Fatigue Limit = 11.1 Tsi. peak nominal

Irregularity Factor = 0.98

10 Hz. Centre Frequency Signal.

Table 9.16

R/S Stress Tsi. Nominal	% Positive Peaks Below S/N Fatigue Limit	Total life Summation		Stage A Life Summation		Stage B Life Summation	
		Hypothetical Fatigue Limit Tsi. Peak Nom.	Ratio of <u>Hypothetical</u> S/N Fatigue Limits	Hypothetical Fatigue Limit Tsi. Peak Nom.	Ratio of <u>Hypothetical</u> S/N Fatigue Limits	Hypothetical Fatigue Limit Tsi. Peak Nom.	Ratio of <u>Hypothetical</u> S/N Fatigue Limits
5	53.1	6.3	1.287	6.4	1.308	5.7	1.153
4	65.3	5.4	1.101	5.65	1.152	5.1	1.040
3	81.4	4.9	1.000	4.9	1.000	4.6	0.939
2	96.6	4.0	0.816	4.1	0.837	3.9	0.797

Constant Amplitude Fatigue Limit = 4.9 Tsi. peak nominal

Irregularity Factor = 0.51

Low Irregularity Factor Signal

Table 9.17

RMS Stress Tsi. Nominal	% Positive Peaks Below S/N Fatigue Limit	Total Life Summation		Stage A Life Summation		Stage B Life Summation	
		Hypothetical Fatigue Limit Tsi. Peak Nom.	Ratio of <u>Hypothetical</u> S/N Fatigue Limits	Hypothetical Fatigue Limit Tsi. Peak Nom.	Ratio of <u>Hypothetical</u> S/N Fatigue Limits	Hypothetical Fatigue Limit Tsi. Peak Nom.	Ratio of <u>Hypothetical</u> S/N Fatigue Limits
5	41.7	4.9	1.000	5.1	1.040	4.6	0.939
4	55.5	4.6	0.939	4.6	0.939	4.15	0.847
3	75.2	4.0	0.816	4.15	0.847	3.7	0.755
2	95.3	3.4	0.694	3.4	0.694	3.1	0.633

Constant Amplitude Fatigue Limit = 4.9 Tsi. peak nominal.

Irregularity Factor = 0.89

High Irregularity Factor Signal

Table 9.18

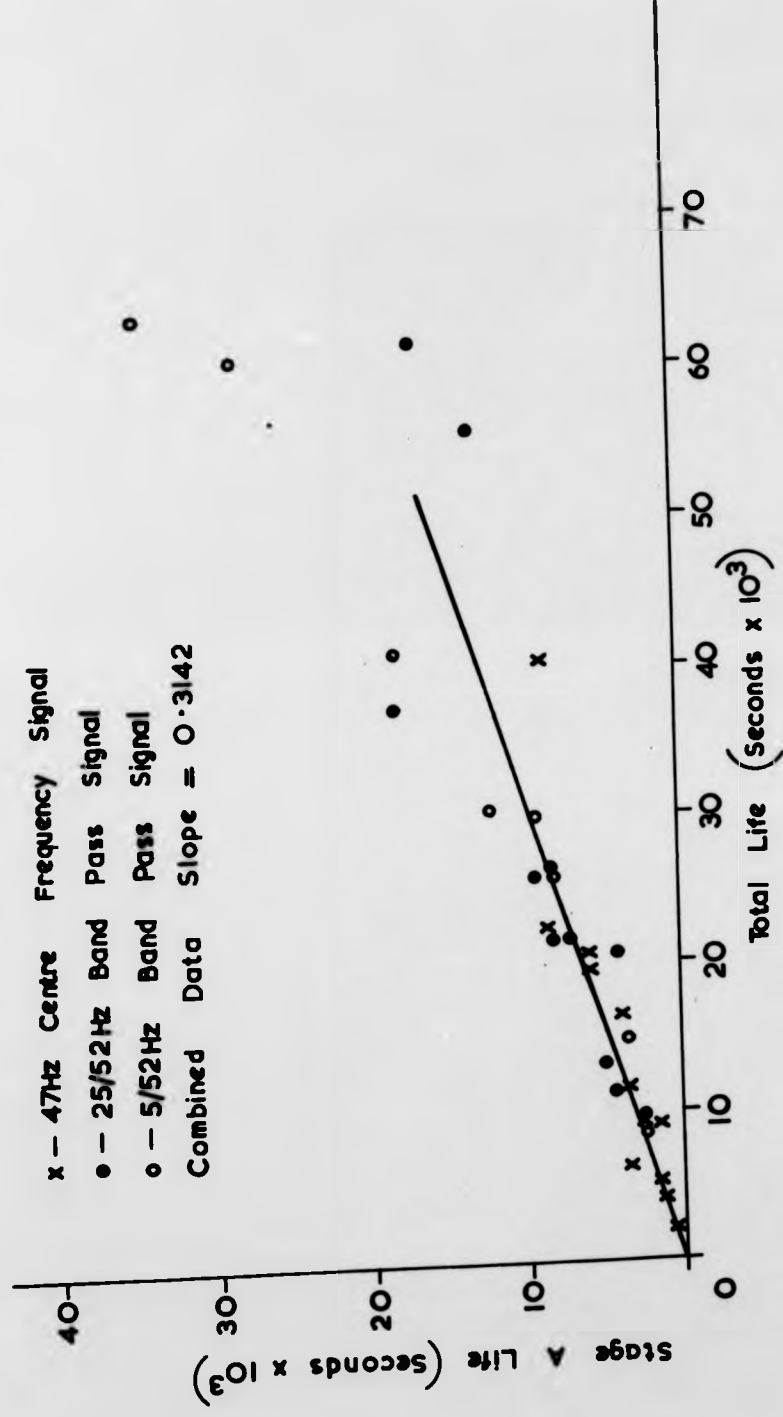


FIG. 9.1.

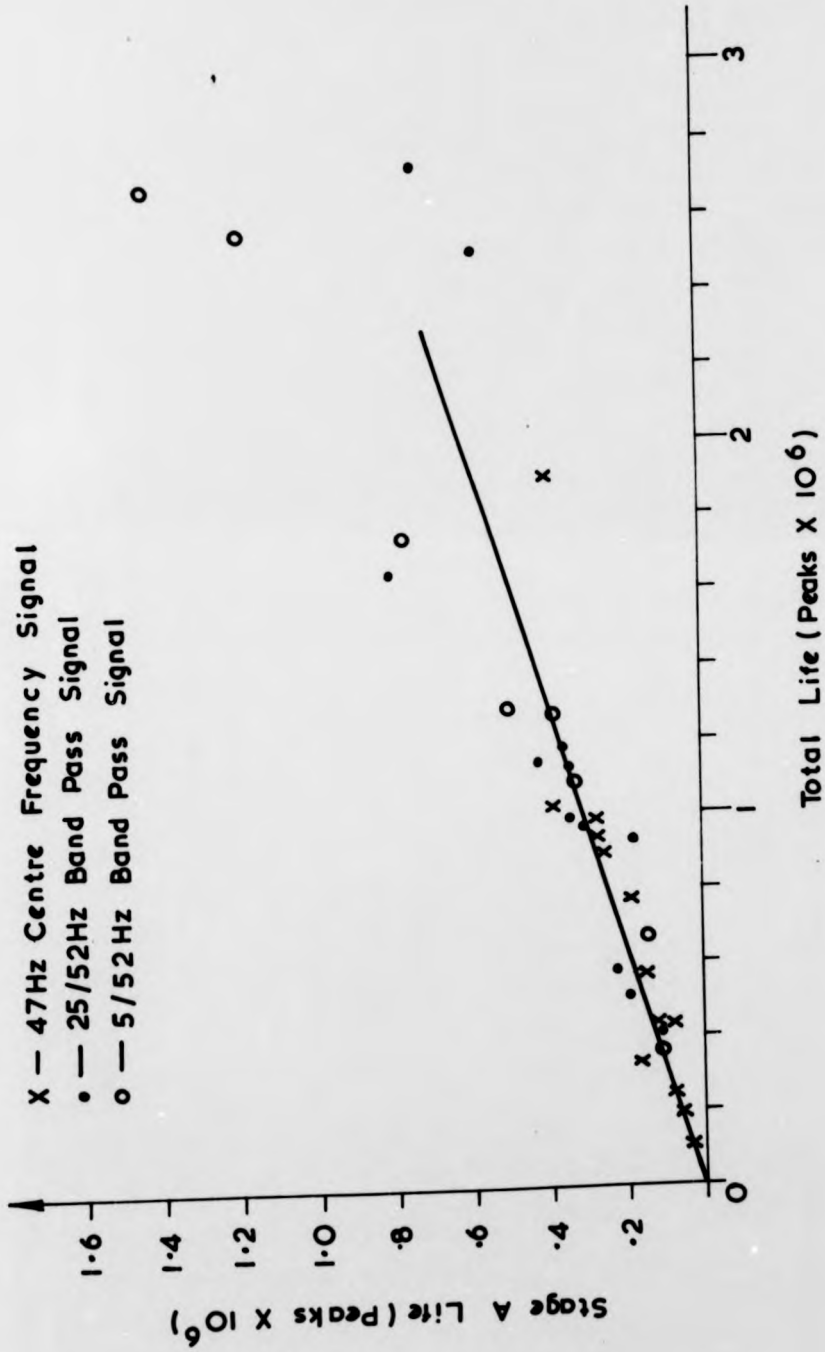


FIG. 9.2.

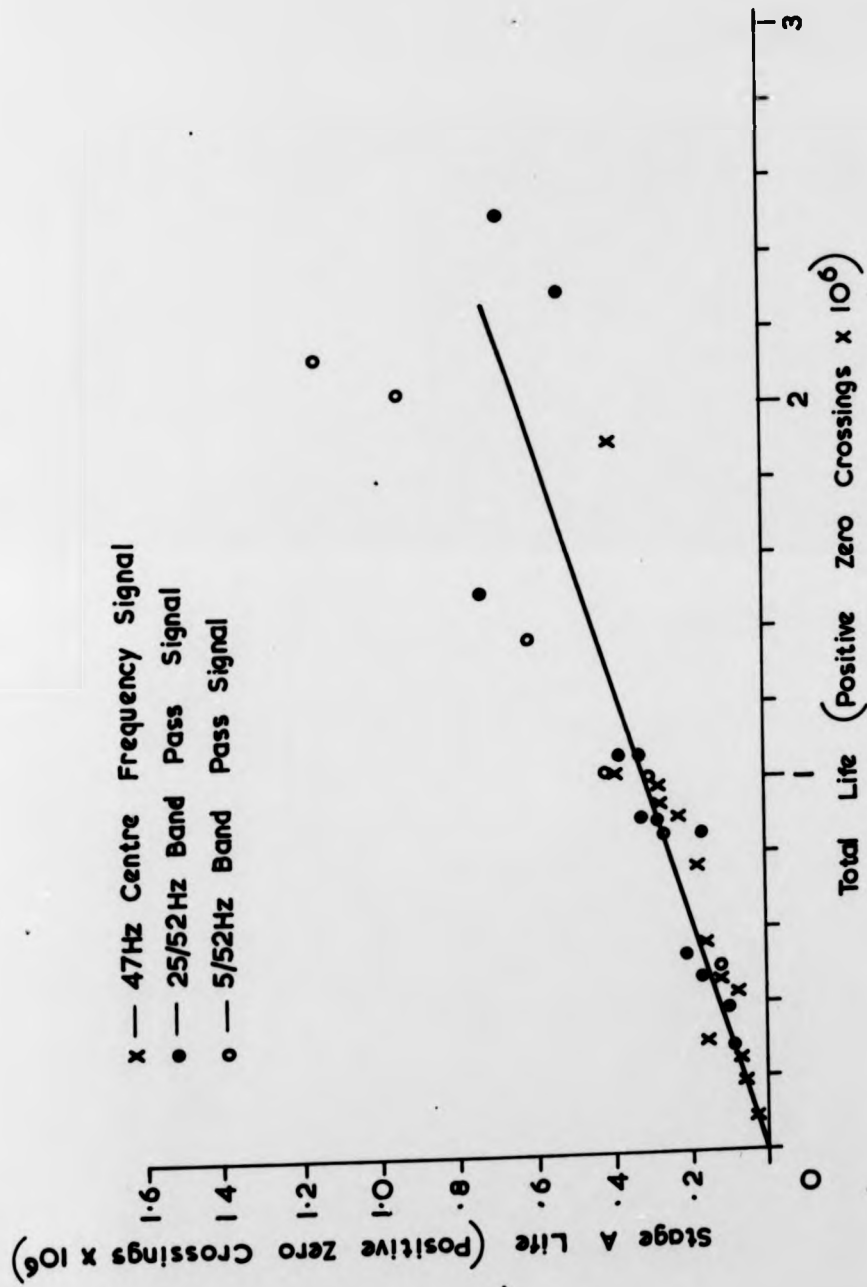


FIG. 9.3.

x — 47Hz Centre Frequency Signal  
 • — 25/52Hz Band Pass Signal  
 o — 5/52Hz Band Pass Signal

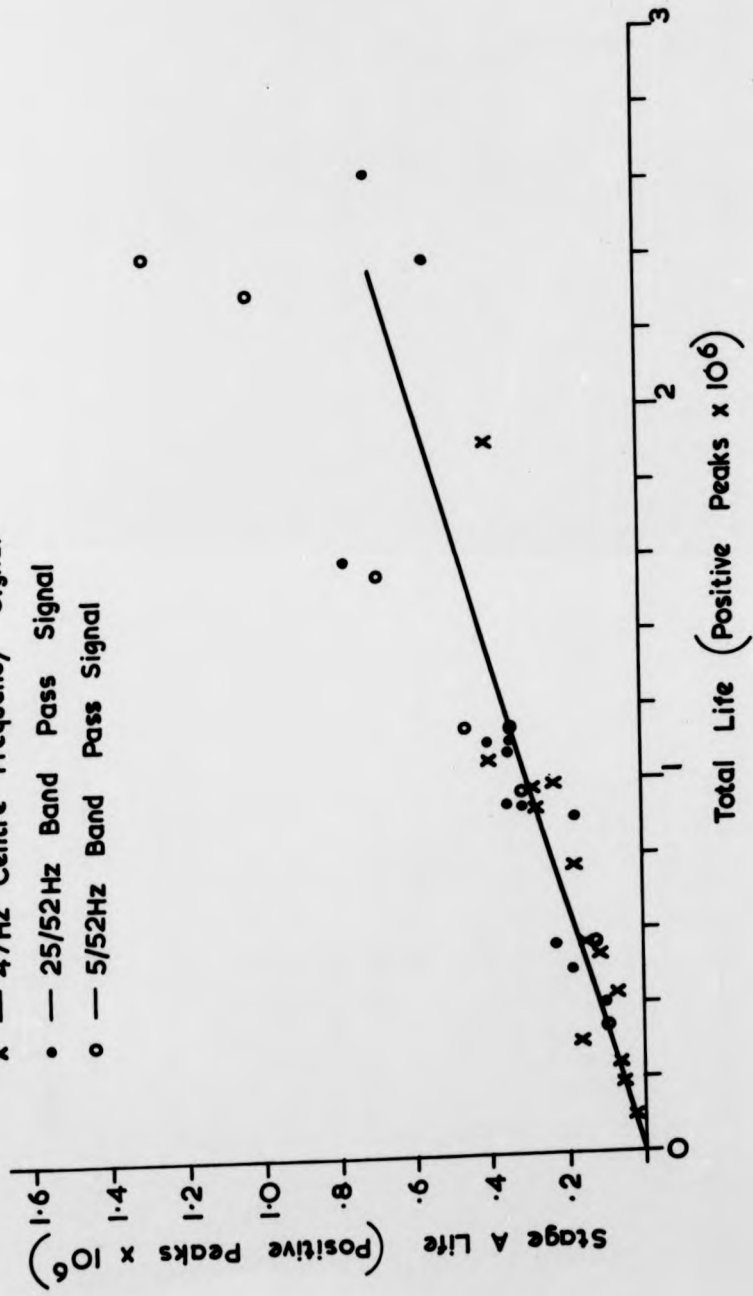


FIG. 9.4.

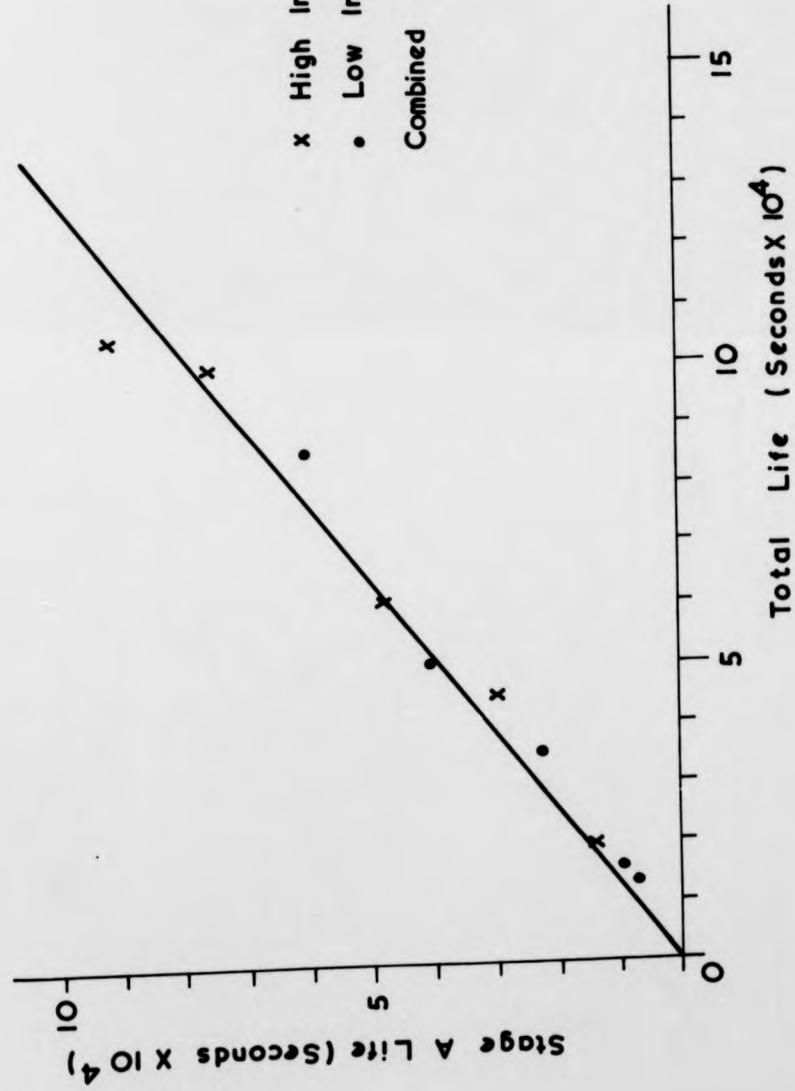
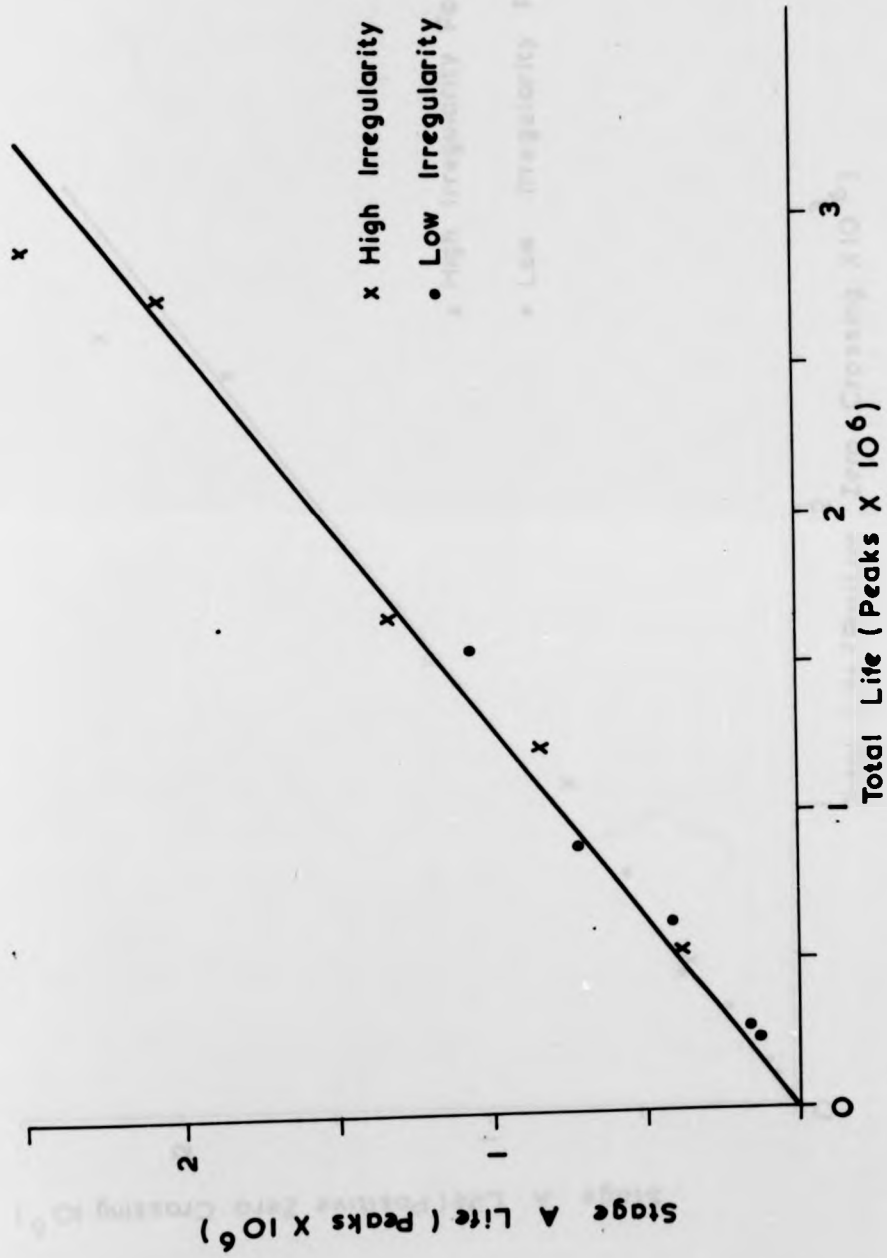


FIG. 9.5.



x High Irregularity Factor Signal  
 • Low Irregularity Factor Signal

FIG. 9.6.

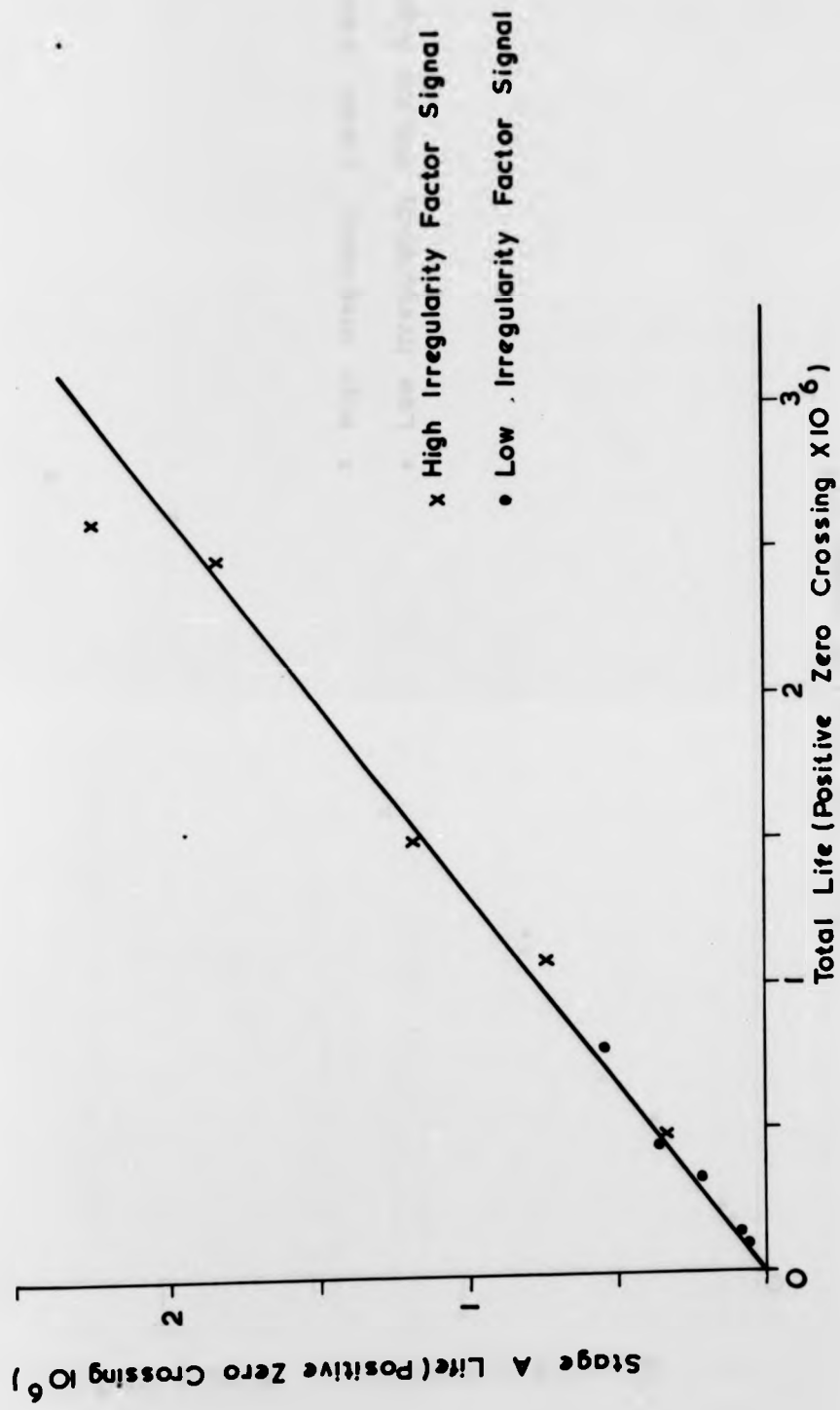


FIG. 9.7.

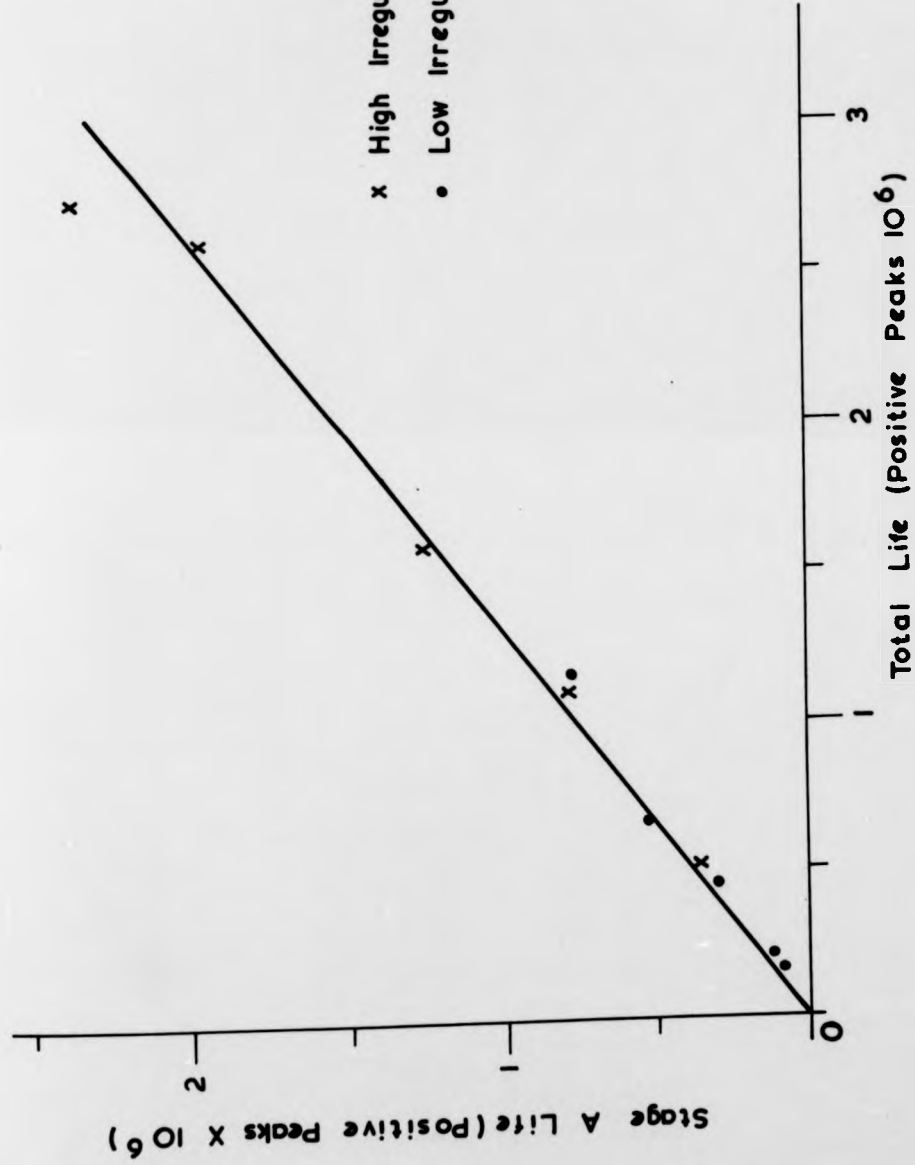
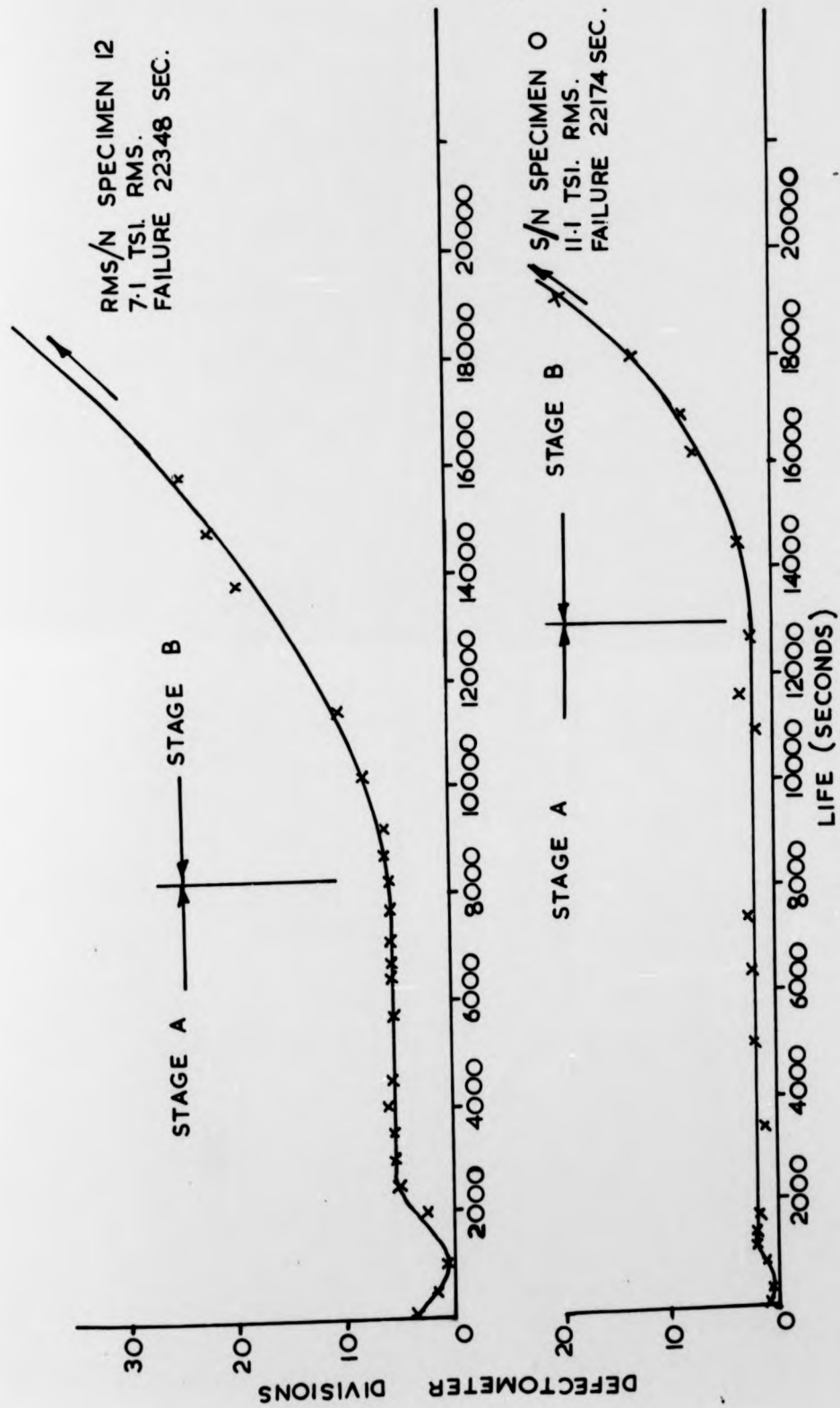


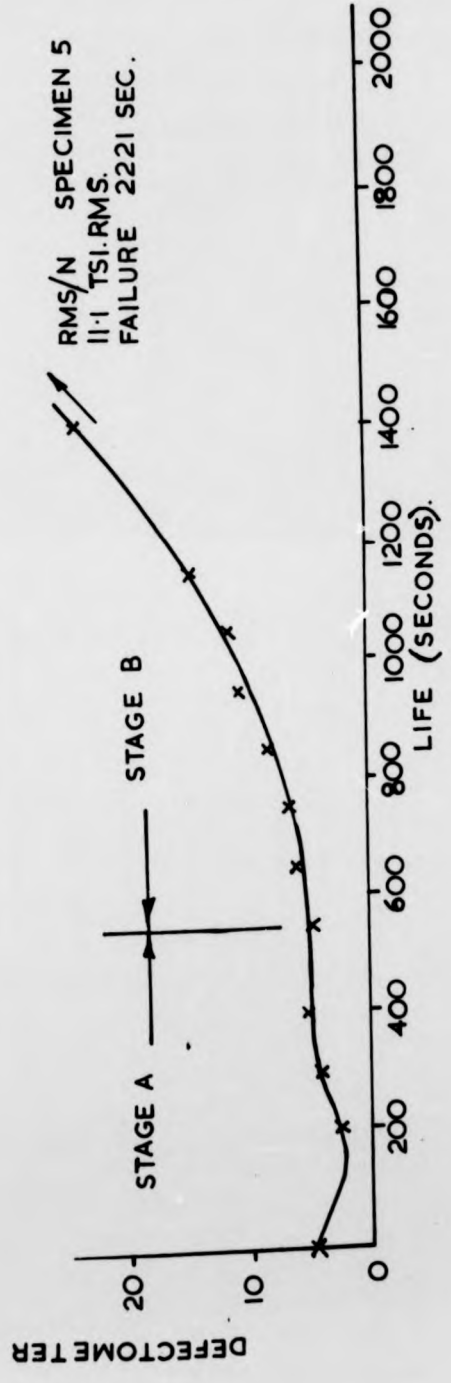
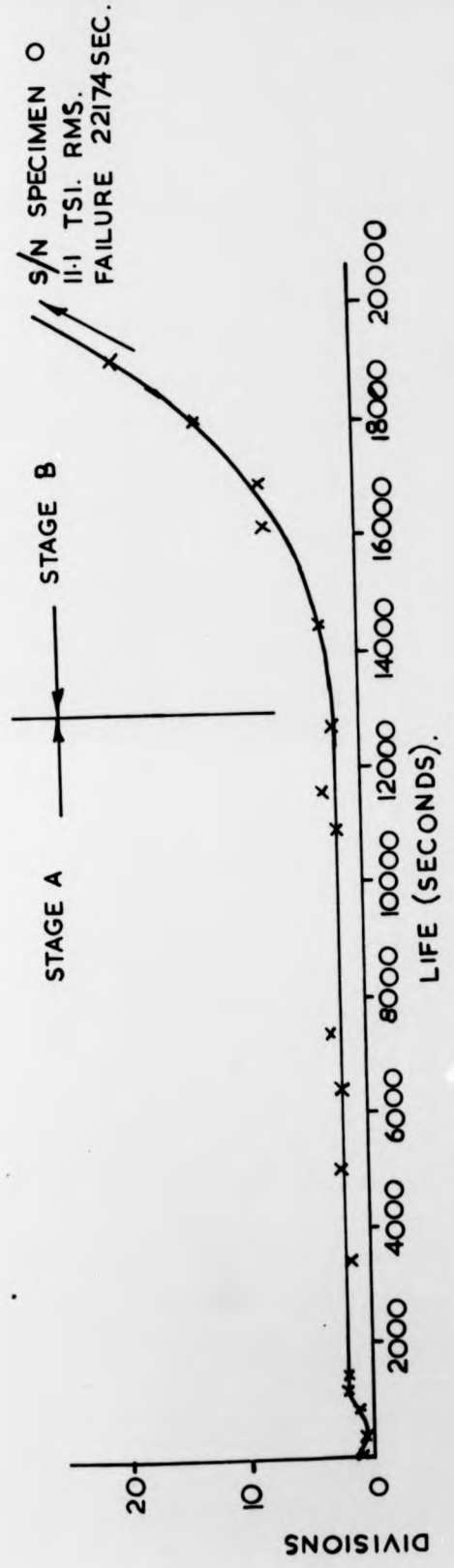
FIG. 98.



EQUAL LIFE COMPARISON

FIG. 9.9.

FIGURE 53348 SEC  
 31 JUL 54  
 RMS/N SPECIMEN 5

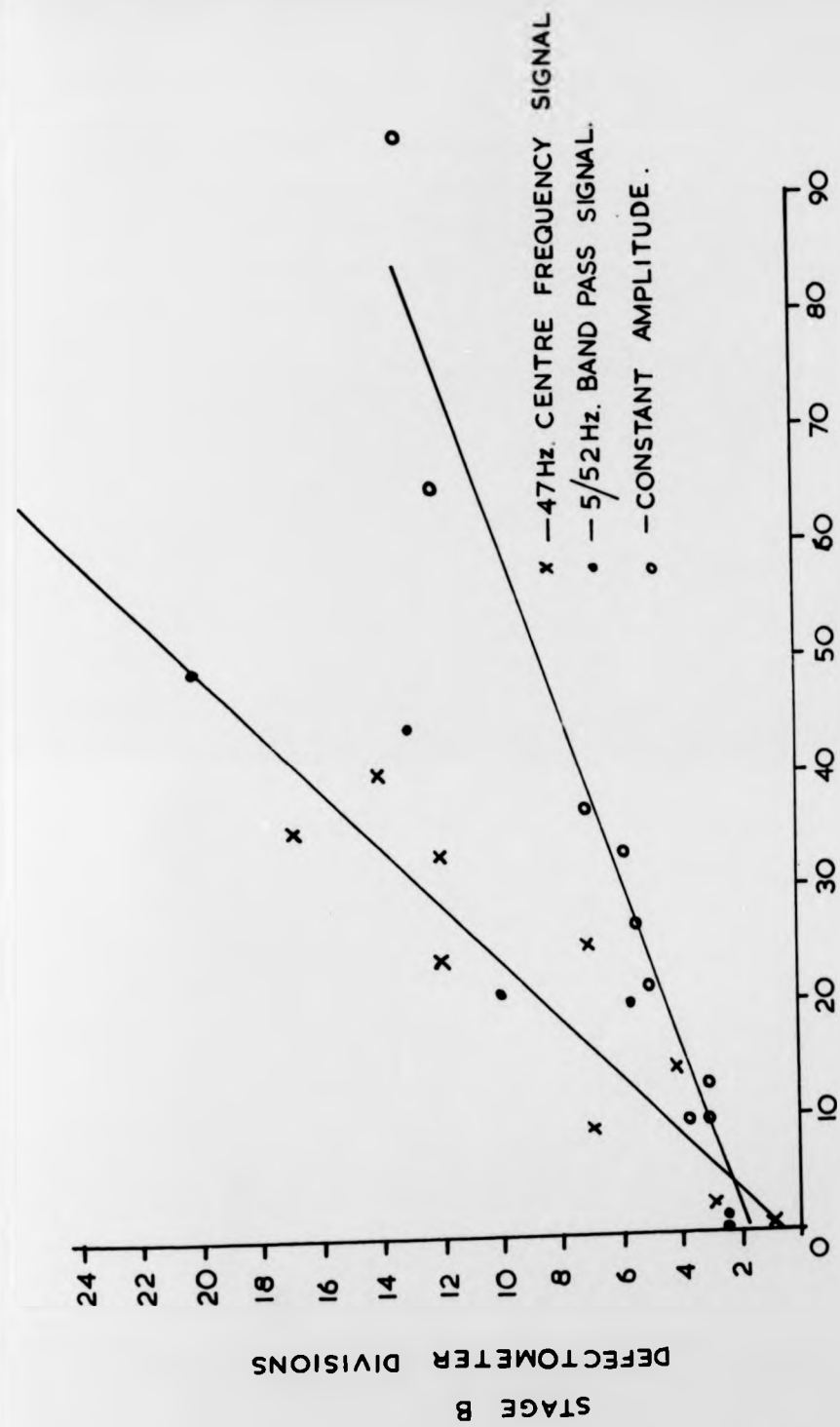


EQUAL STRESS COMPARISON

FIG. 9.10.

STAGE B  
 DEFLECTOMETER DIVISIONS

STAGE B  
 DEFLECTOMETER DIVISIONS



TOTAL SPECIMEN CRACK LENGTH (0.001").  
 SMALL CANTILEVER SPECIMENS.

FIG. 9.11.

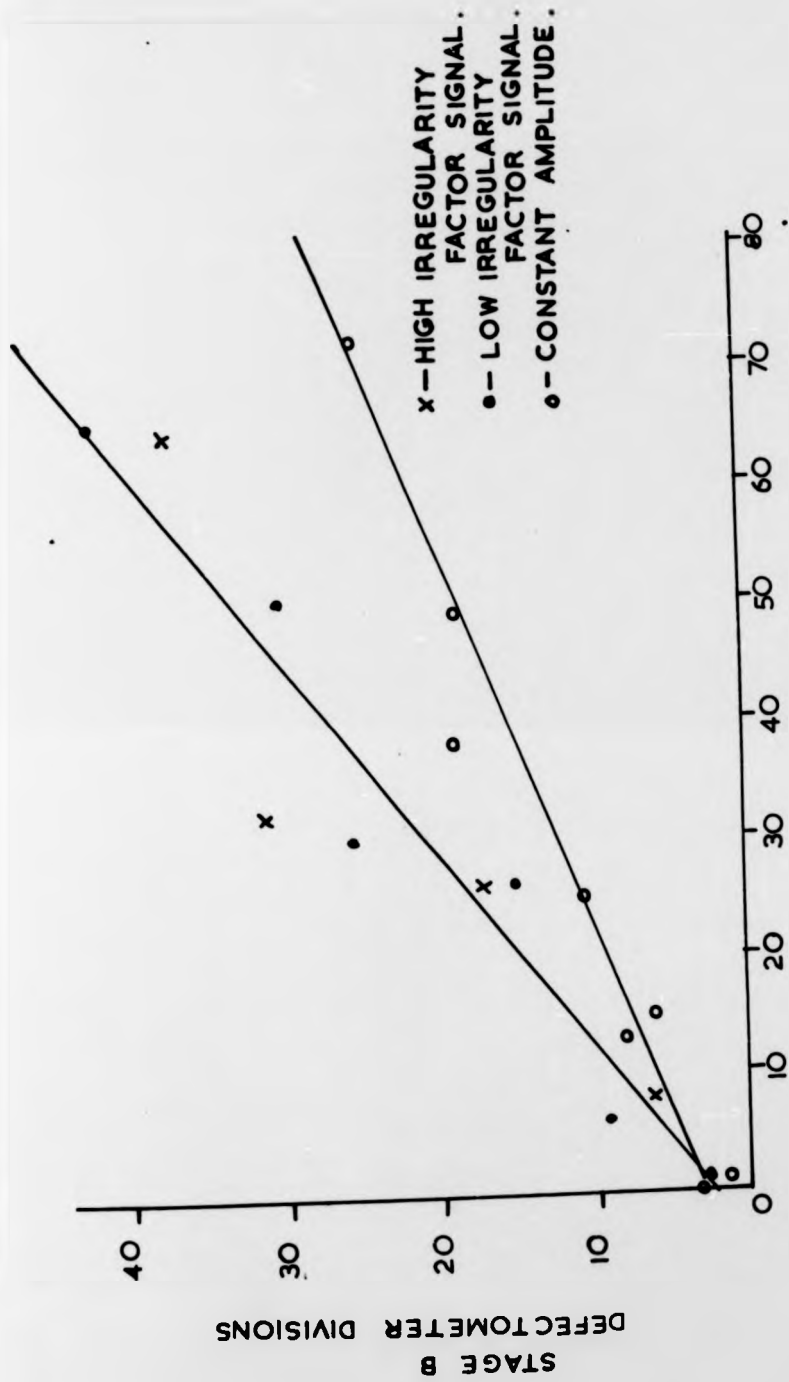
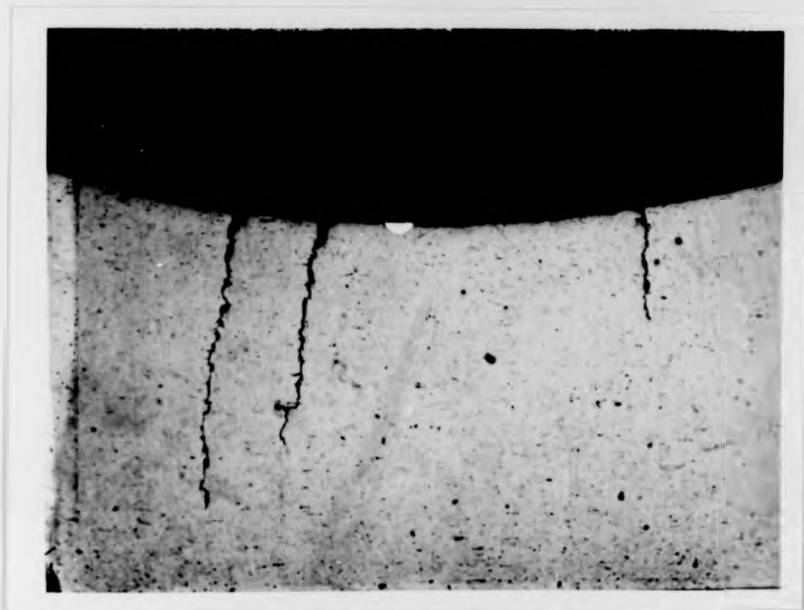
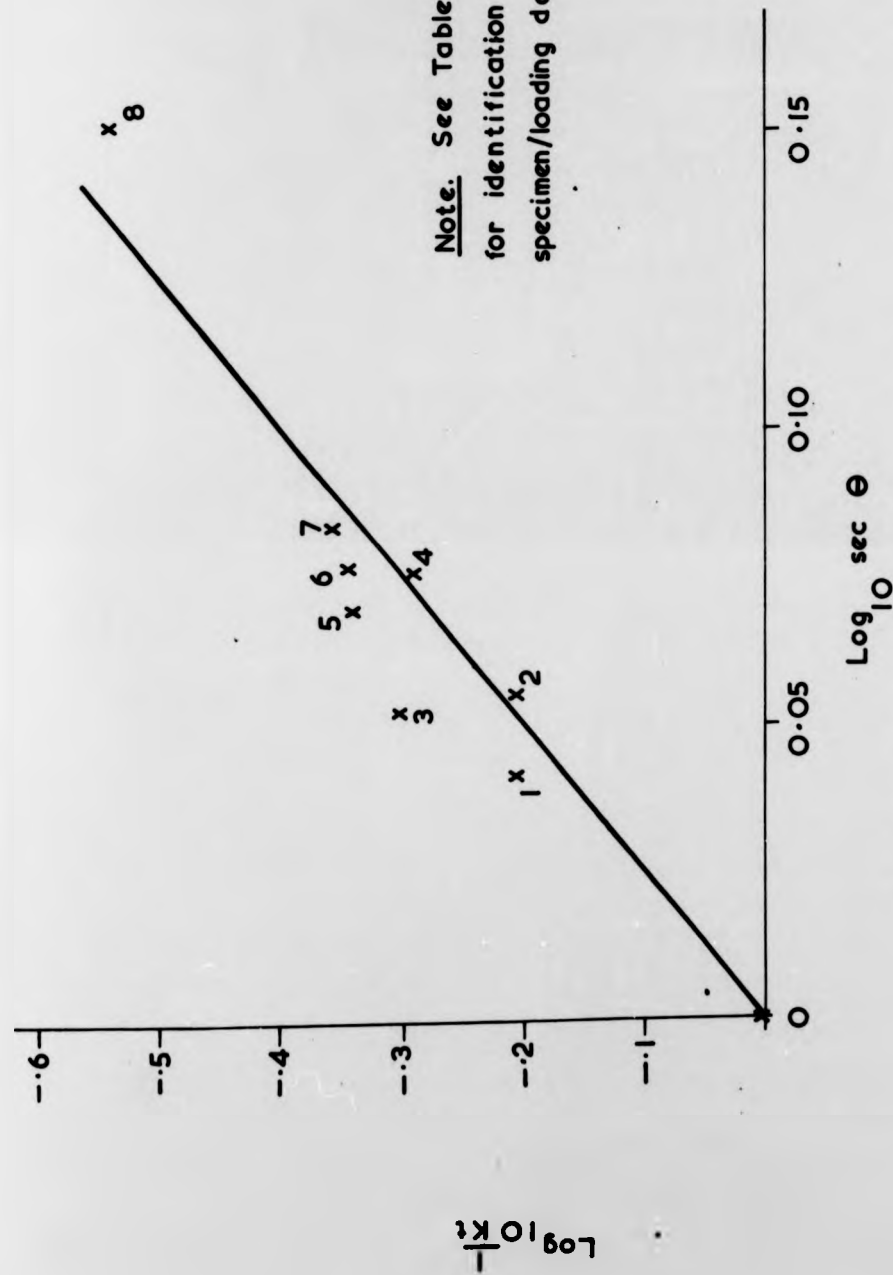


FIG. 9.12.



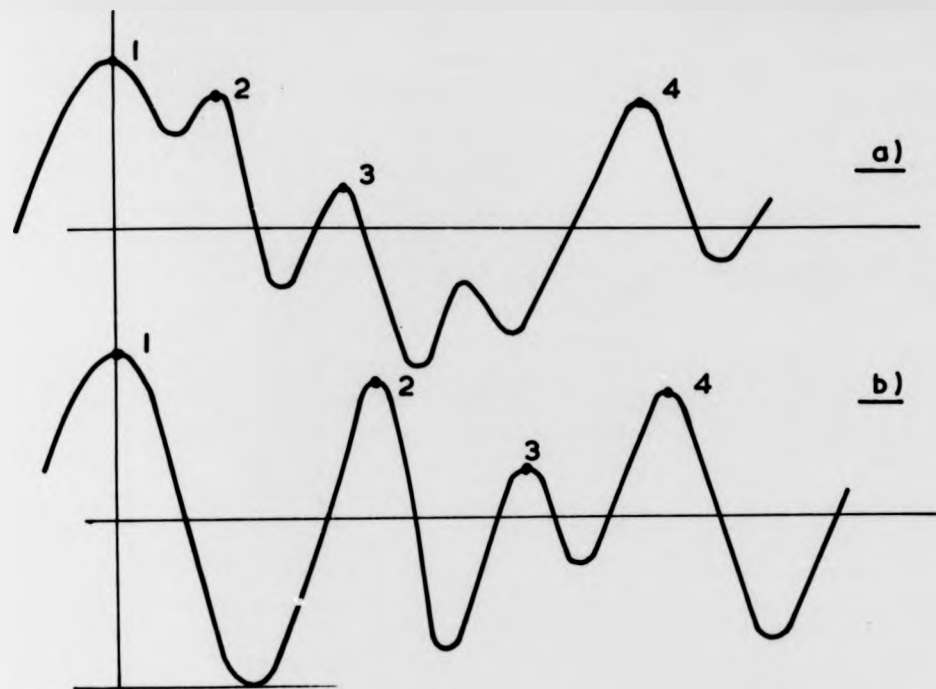
LOW IRREGULARITY FACTOR SIGNAL  
SPECIMEN F17 X55

FIG 9.13.



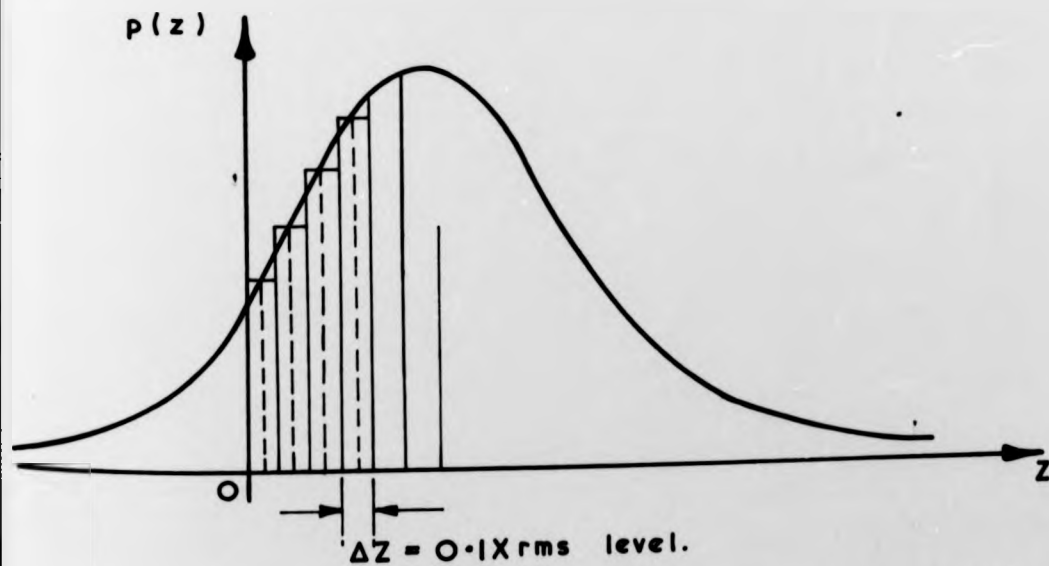
Note. See Table 9.2.  
for identification with  
specimen/loading data.

Plot of  $\text{Log} \frac{1}{K_t} V \text{ Log Sec } \theta$  for  
8 specimen configurations.



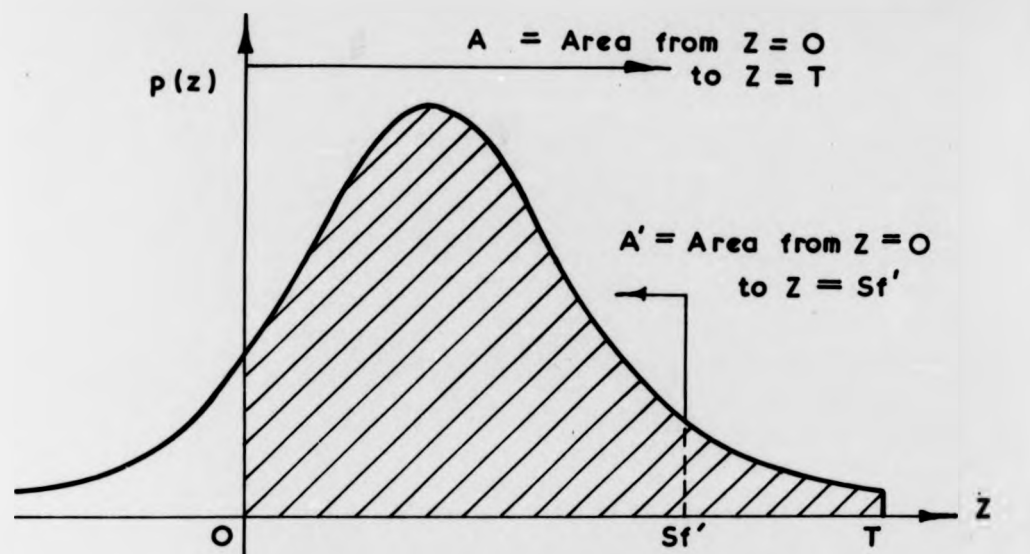
- a) Real Waveform  
 b) Positive Peak Waveform.

FIG. 9. 15



Standardised Peak Probability Density Distribution.

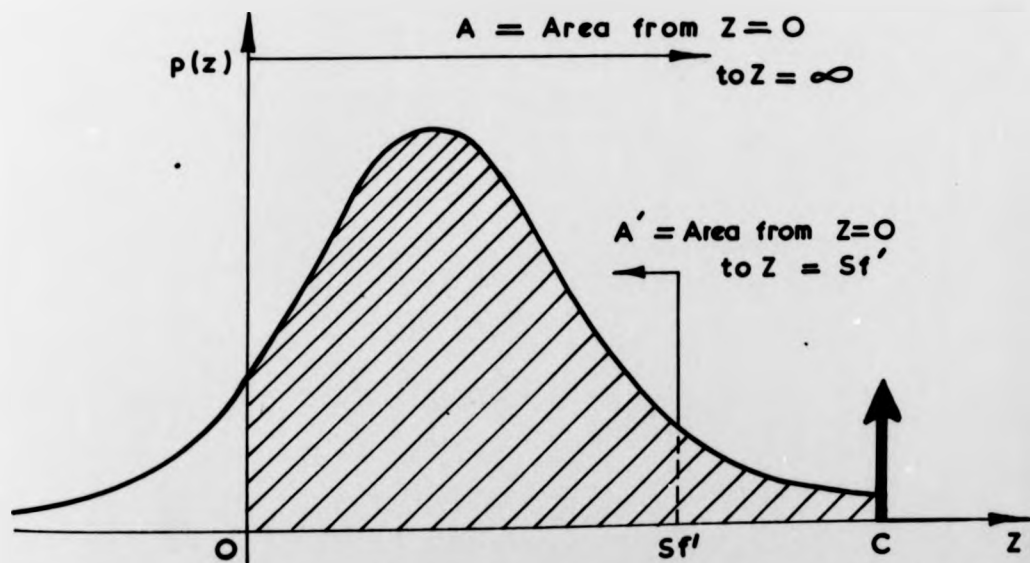
FIG. 9. 16



Standardised Peak Probability Density Distribution

$T = \text{Truncation Level}$

$$\% \text{ Peaks} < \text{S/N Fatigue Limit} = \frac{A'}{A} \times 100$$



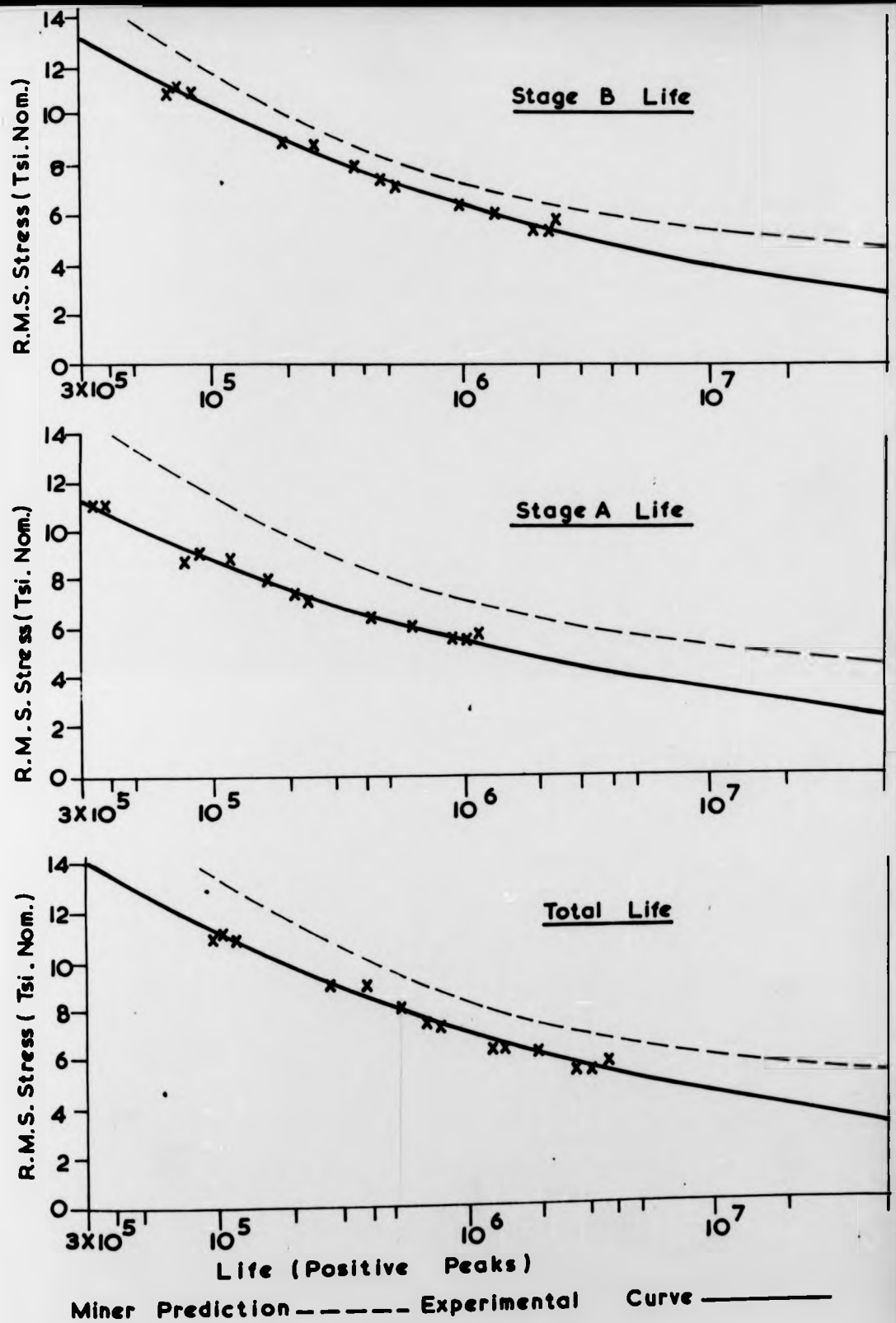
Standardised Peak Probability Density Distribution

$C = \text{Clipping Level}$

$$\% \text{ Peaks} < \text{S/N Fatigue Limit} = \frac{A'}{A} \times 100$$

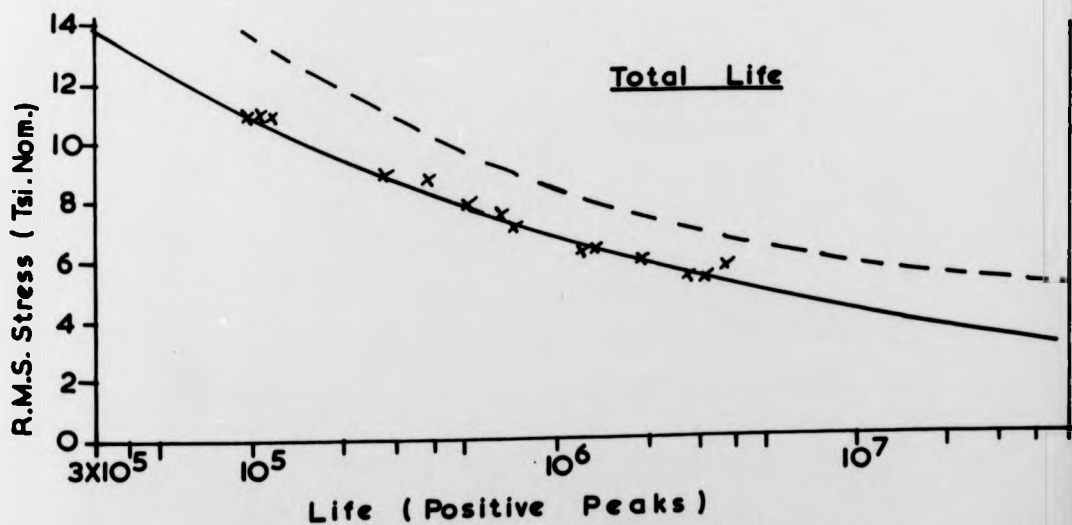
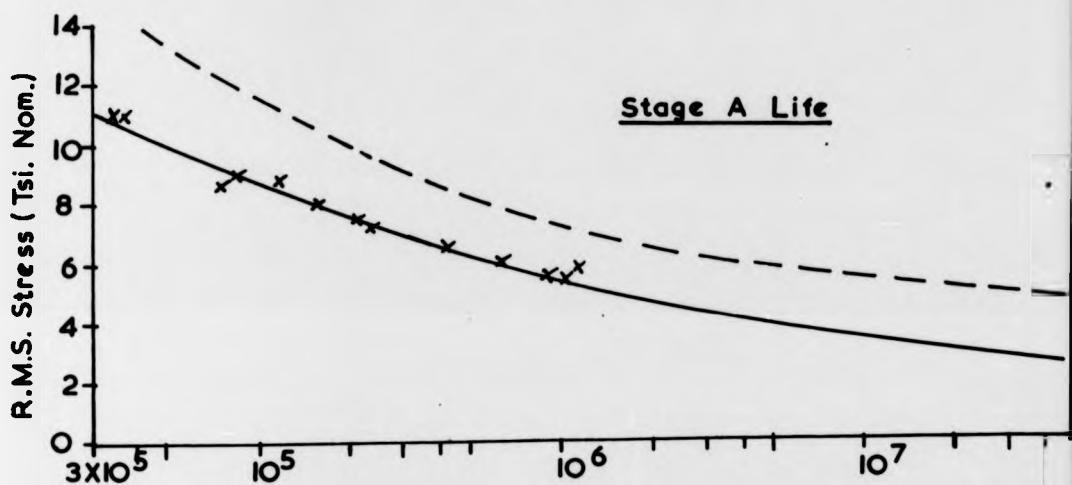
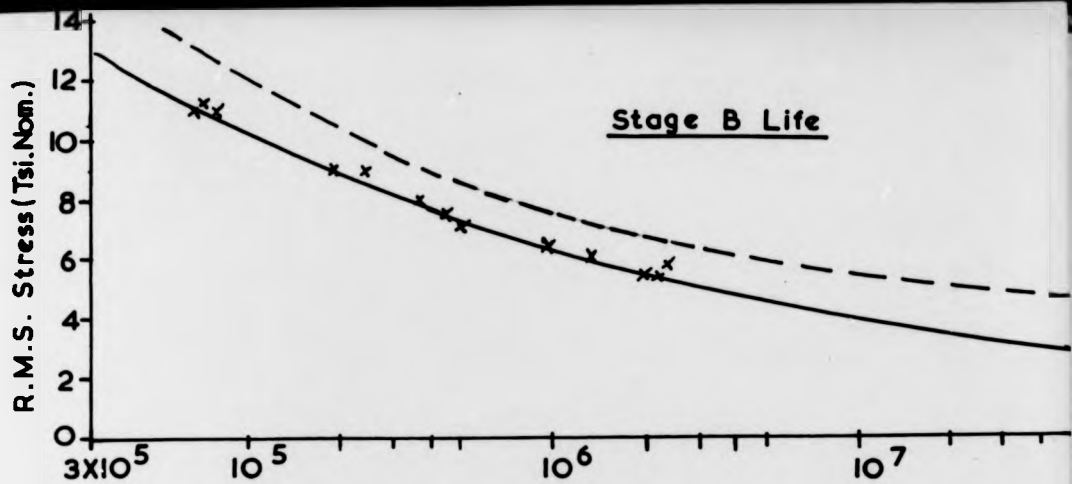
$$Sf' = \frac{\text{S/N Fatigue Limit}}{\text{Signal R.M.S. Stress}}$$

FIG. 9.17



47 Hz Centre Frequency Signal.

FIG. 9.18

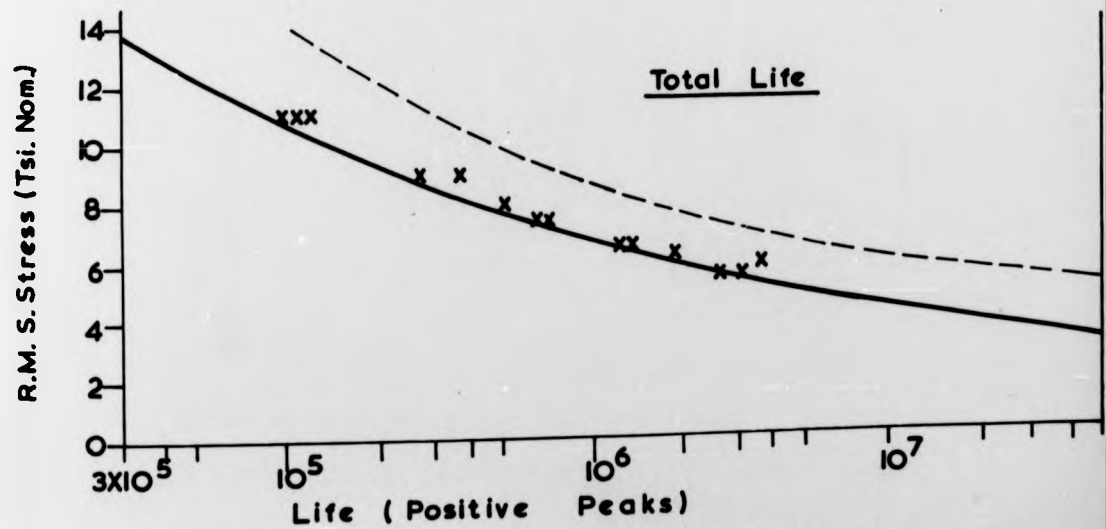
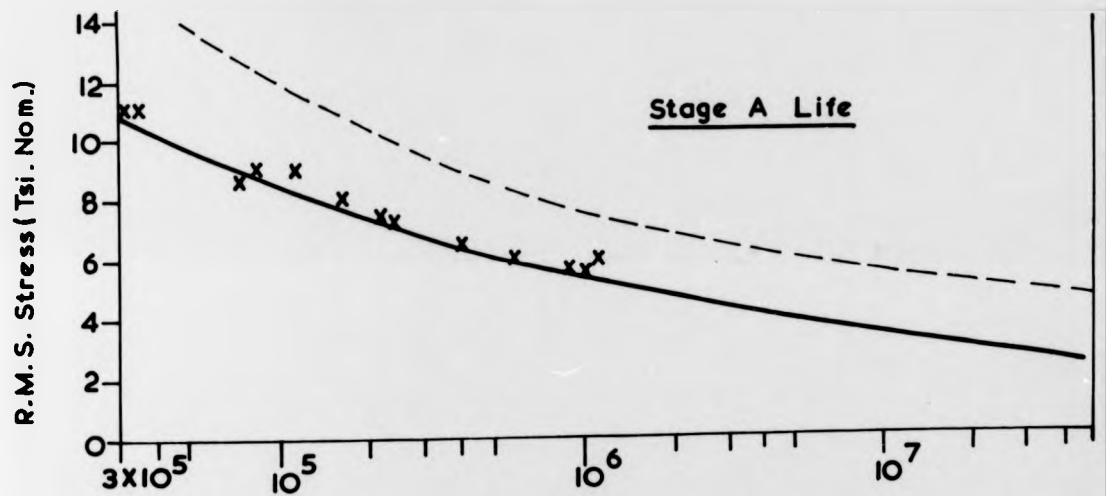
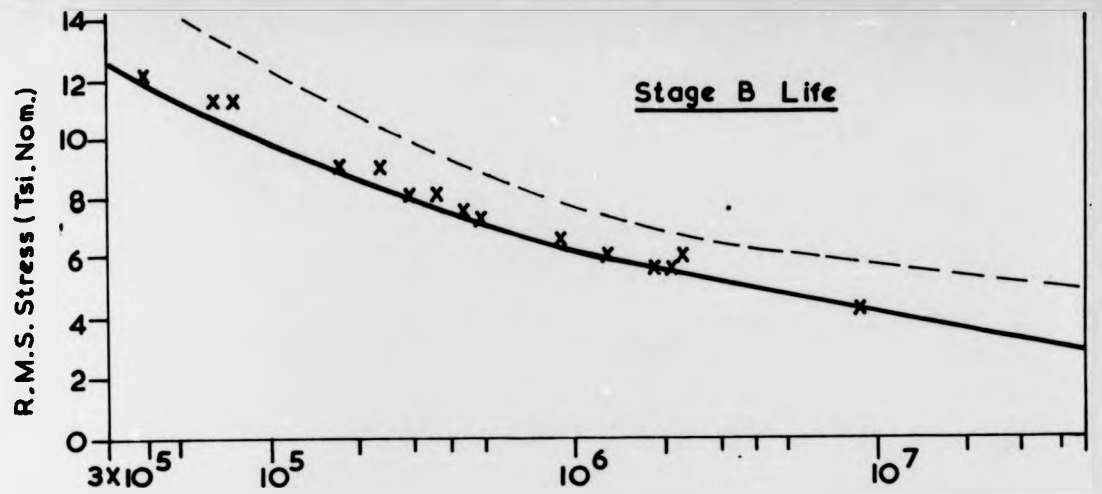


Life (Positive Peaks)

Miner Prediction ----- Experimental Curve —————

25/52Hz Band Pass Signal

FIG. 9. 19

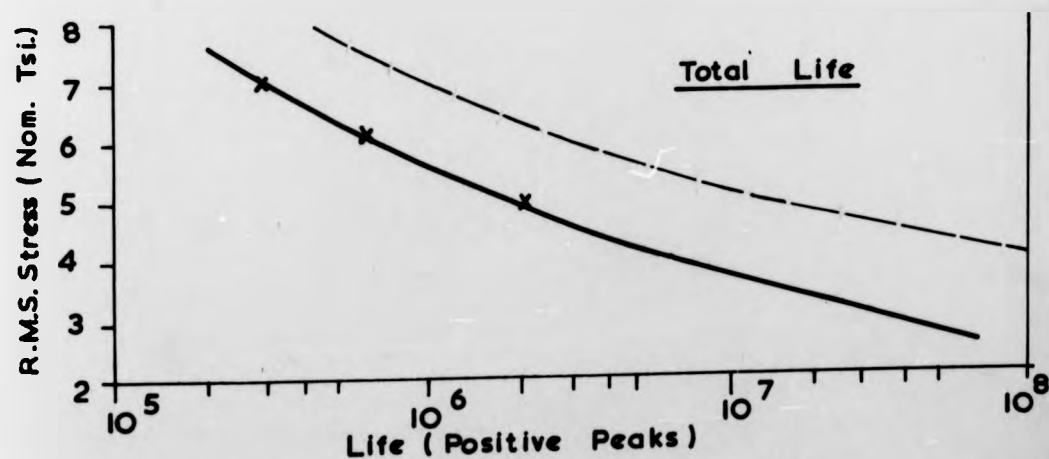
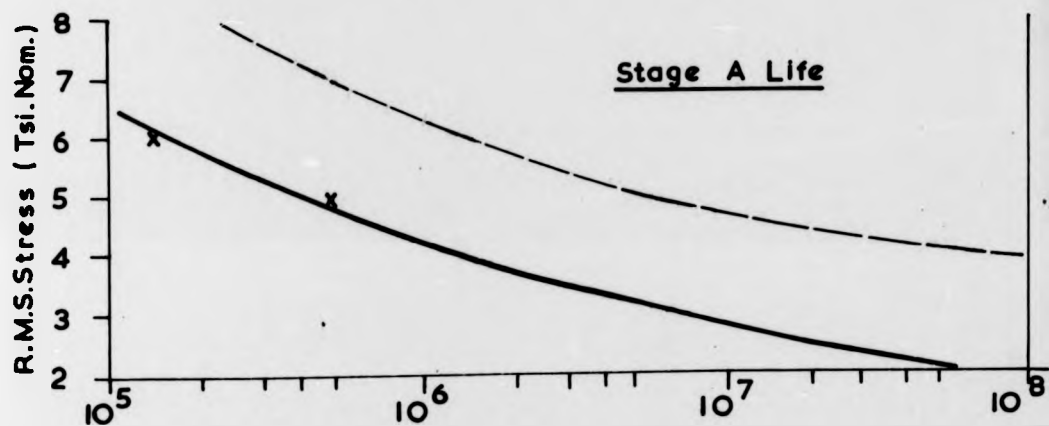
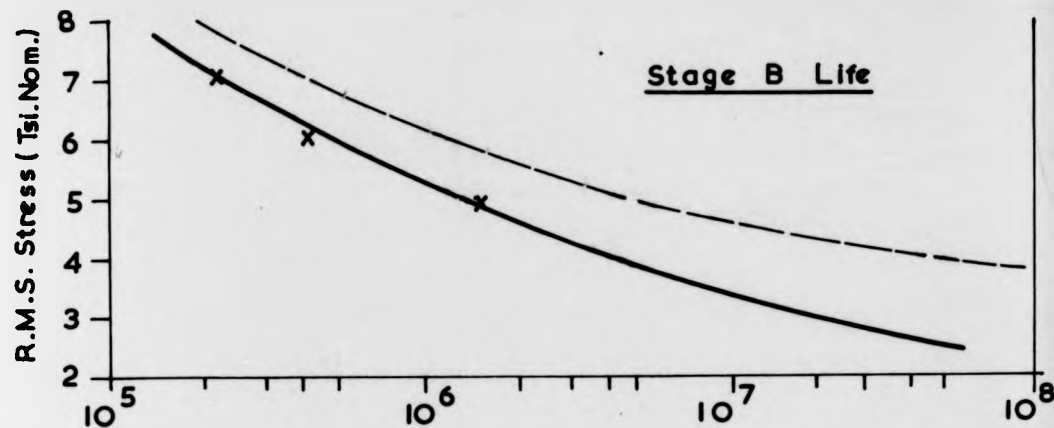


Miner Prediction ----- Experimental Curve ———

5/52Hz Band Pass Signal

FIG. 9. 20

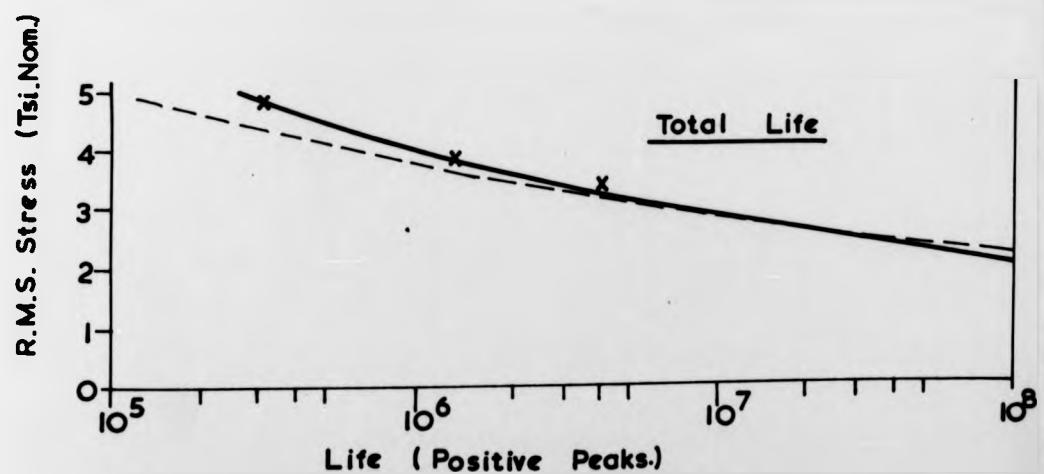
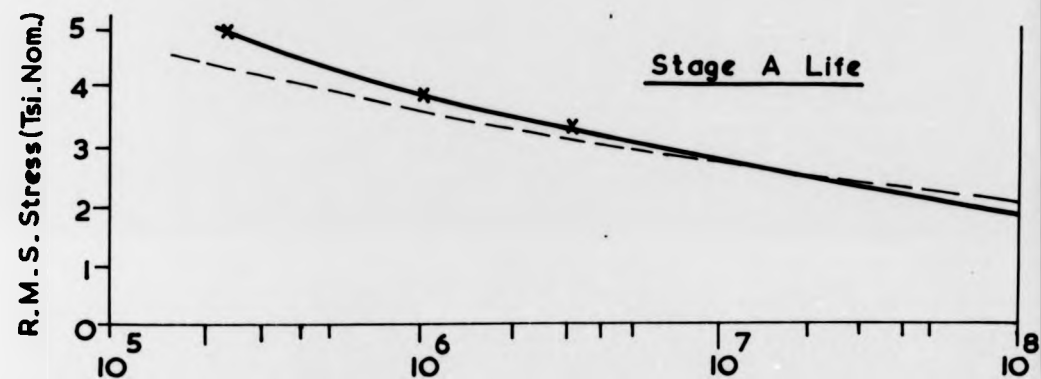
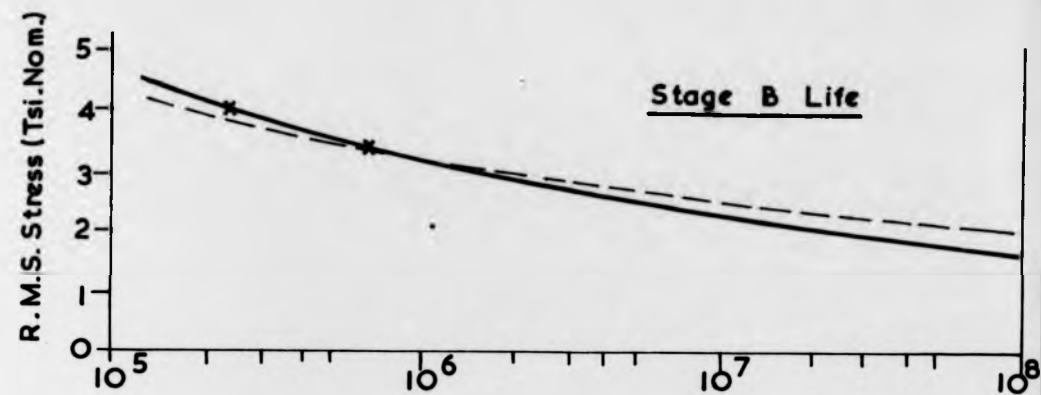
Miner Prediction - - - - - Experimental Curve - x - - - - -



(Large Specimen Experimental Data)

10Hz Centre Frequency Signal

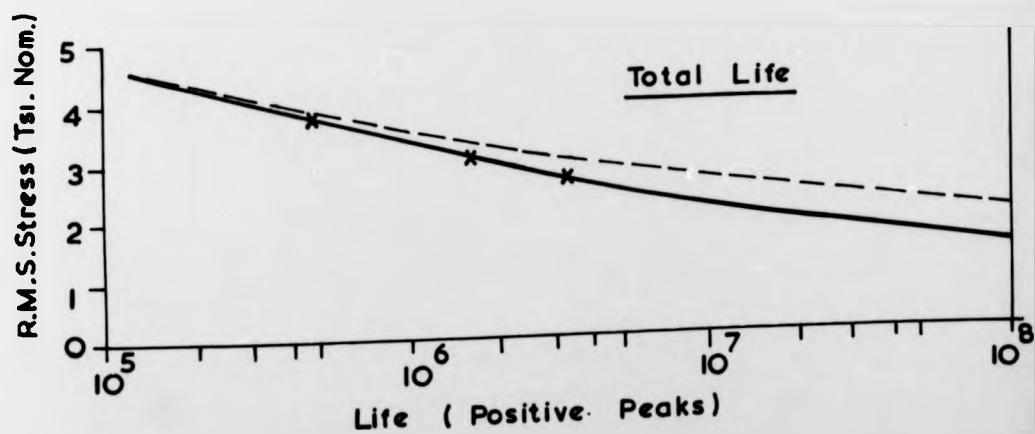
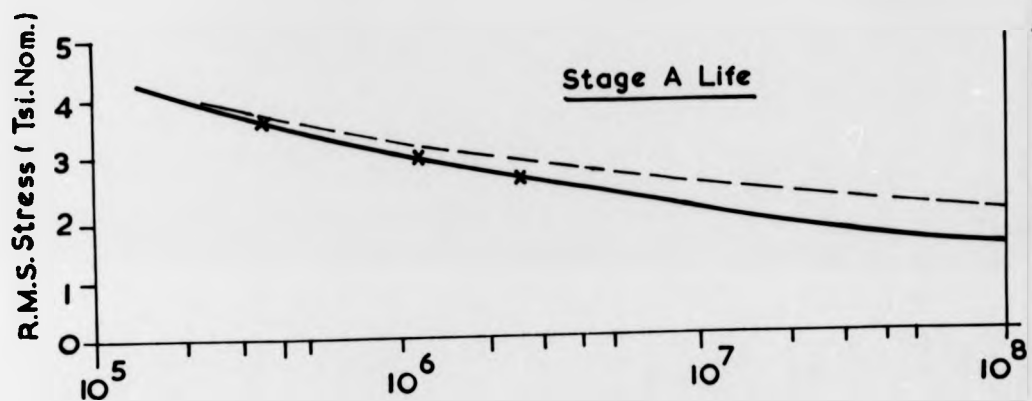
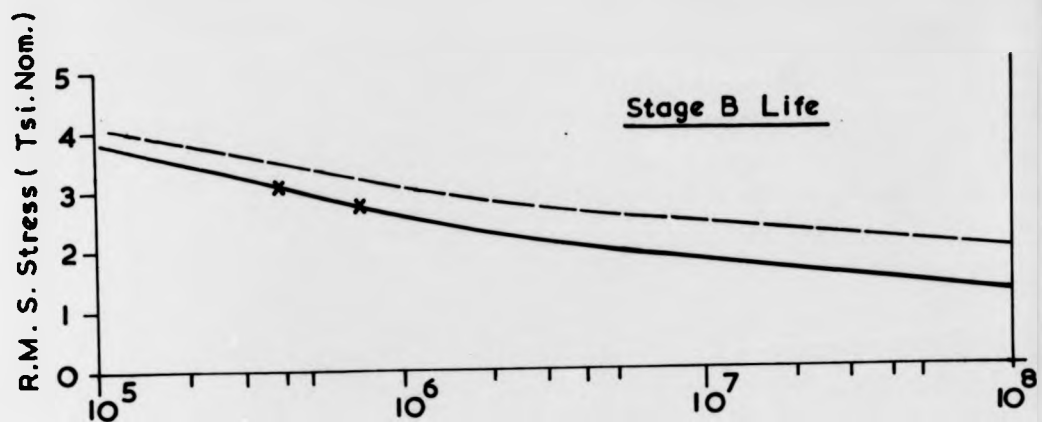
FIG 9. 21.



Miner Prediction - - - - - Experimental Curve ———

Low Irregularity Factor Signal

FIG. 9. 22.



Miner Prediction - - - - - Experimental Curve

High Irregularity Factor Signal

FIG. 9.23

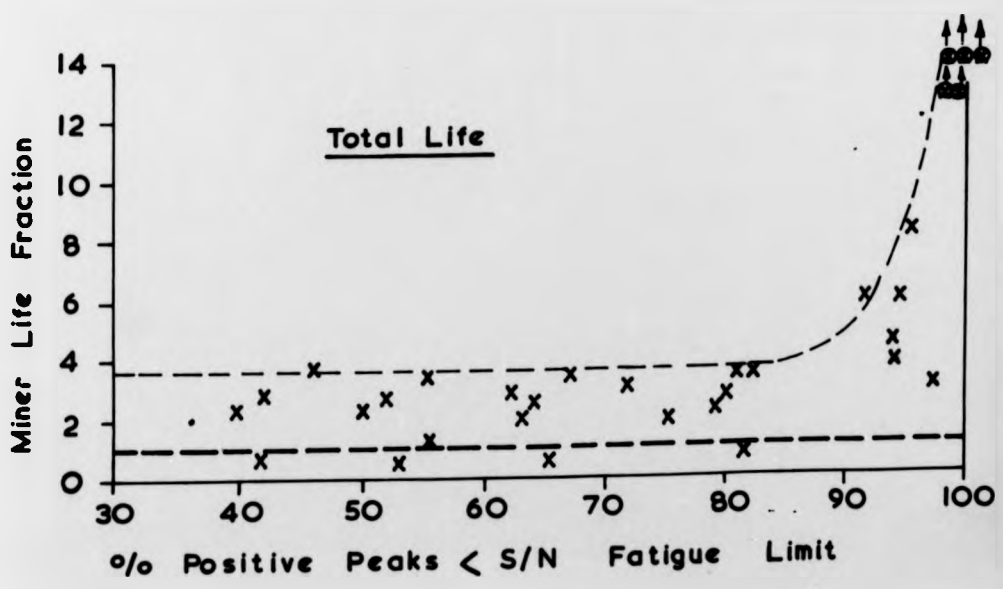
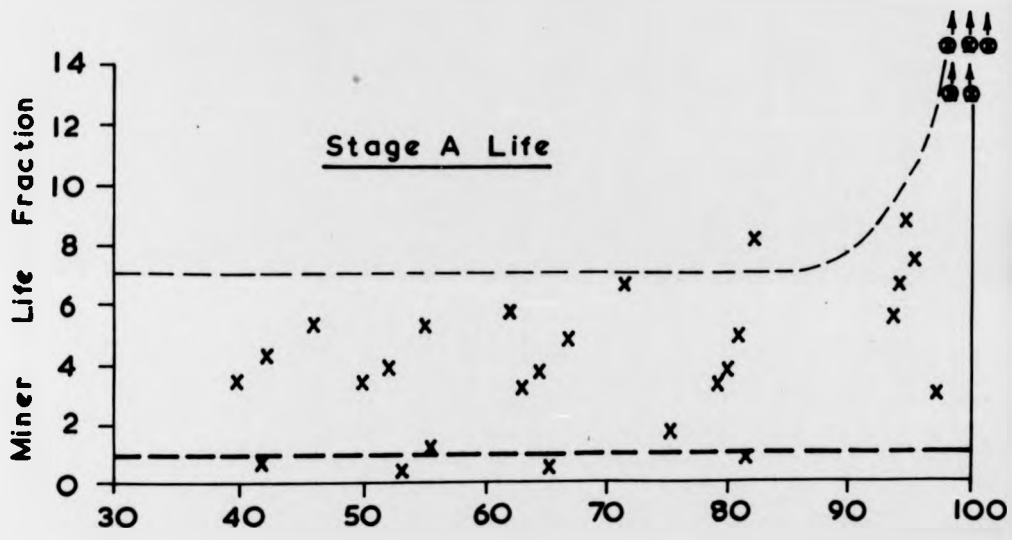
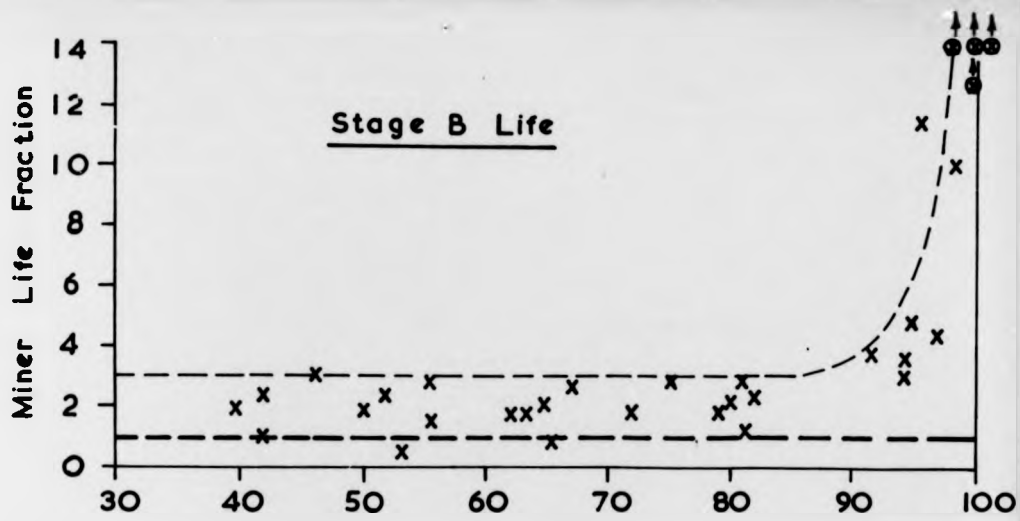
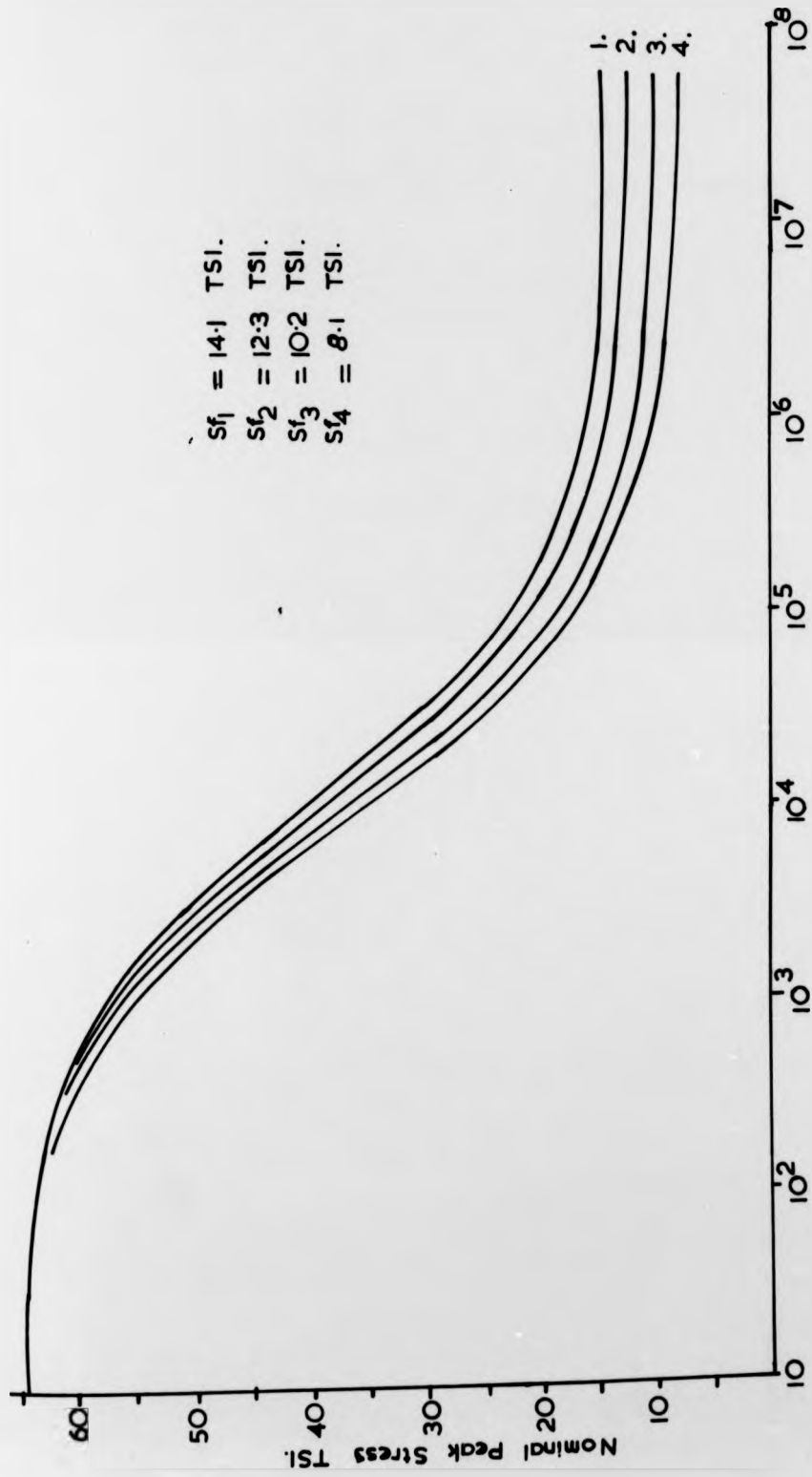


FIG. 9. 24.



Cycles To Failure  
 47Hz. CENTRE FREQUENCY SIGNAL

FIG. 9.25.

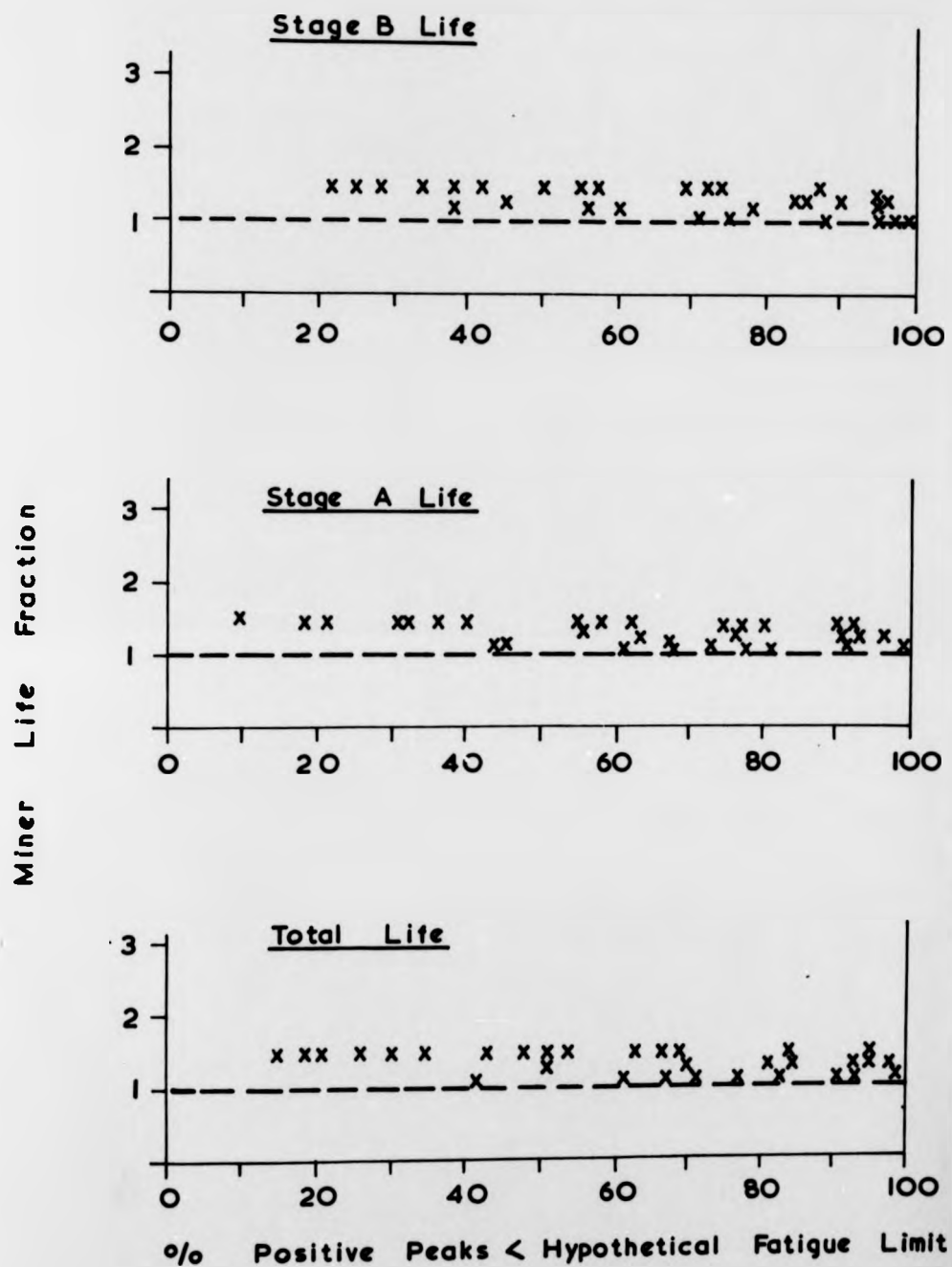
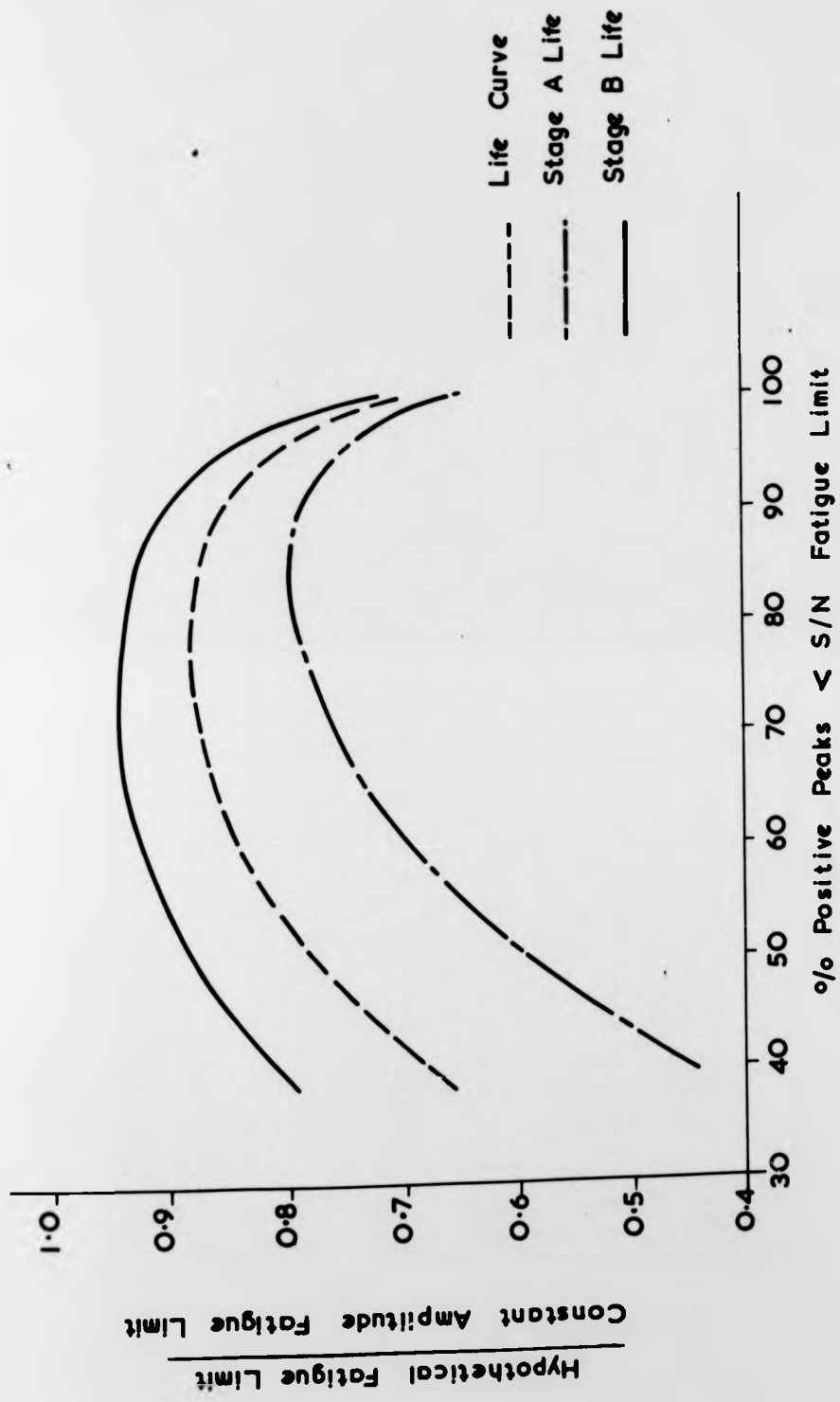
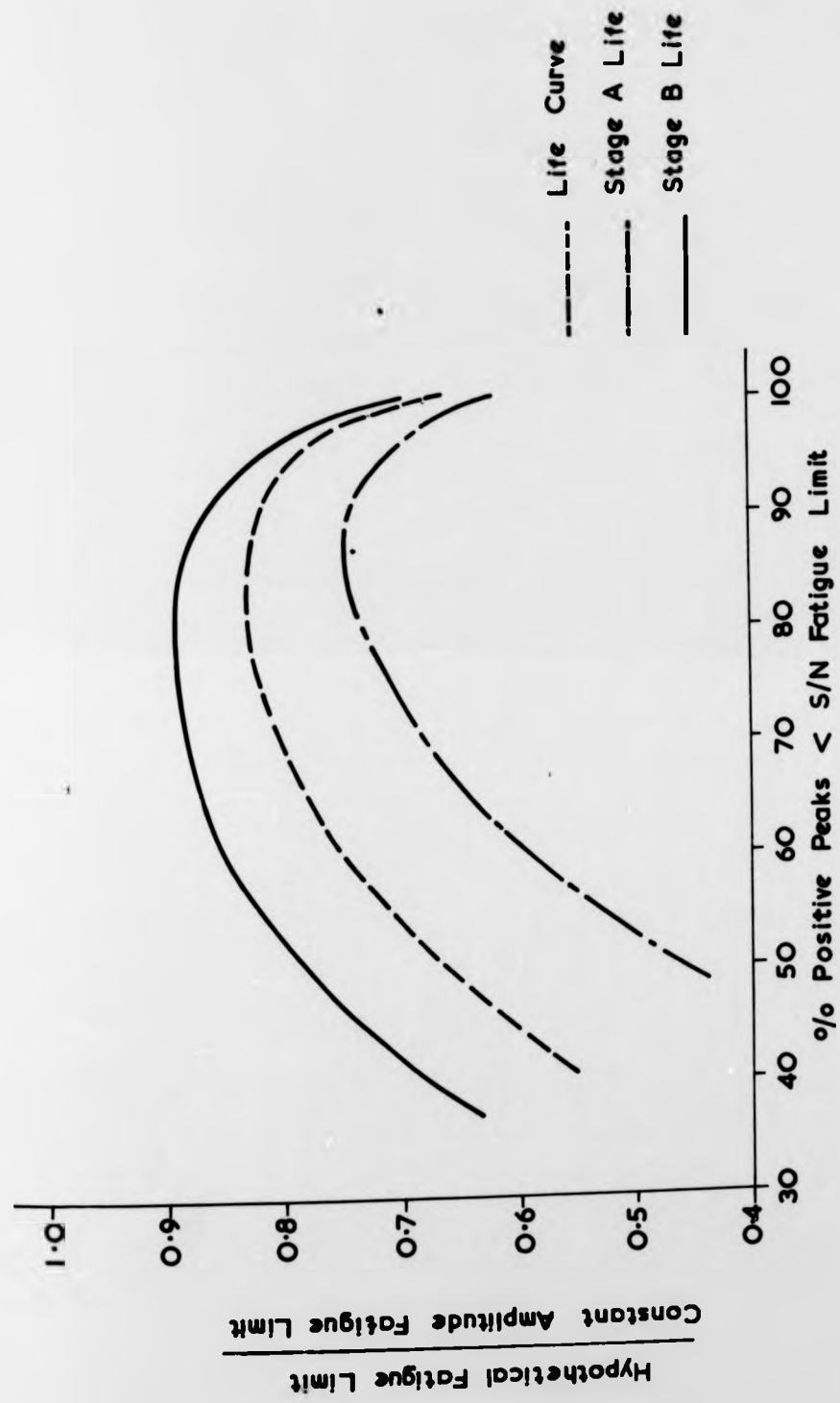


FIG. 9. 26



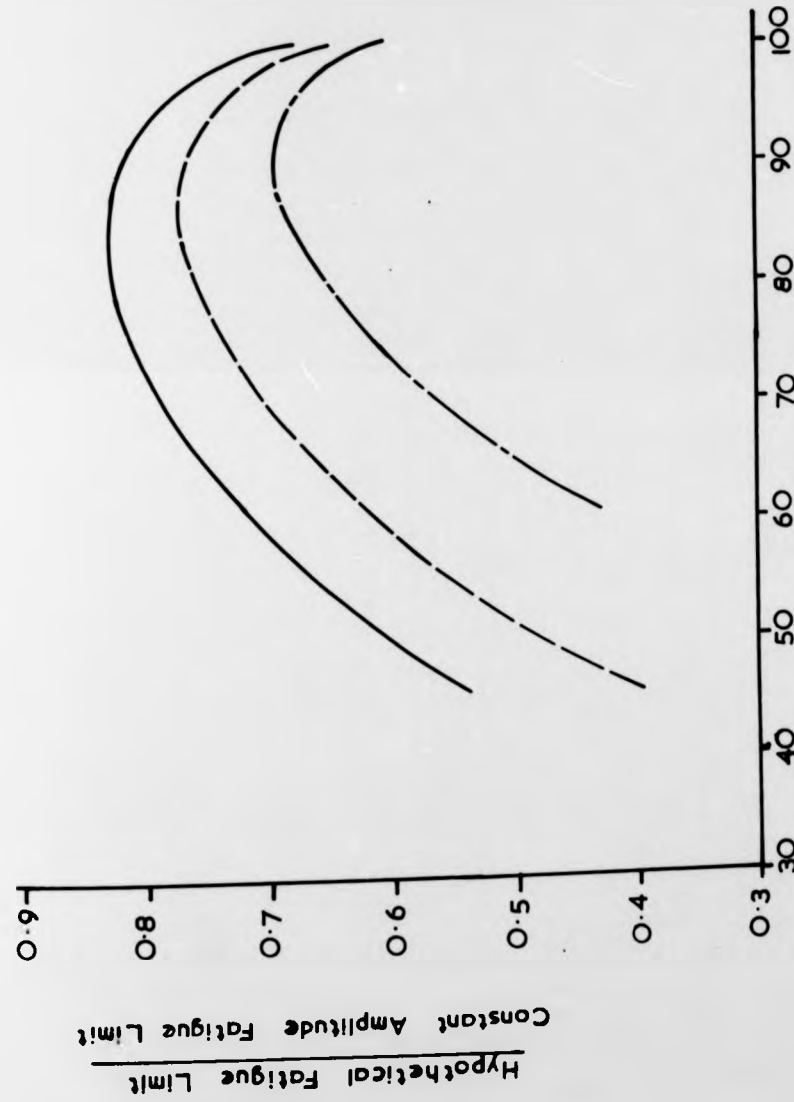
47Hz Centre Frequency Signal

FIG. 9. 27



25/52Hz Band Pass Signal

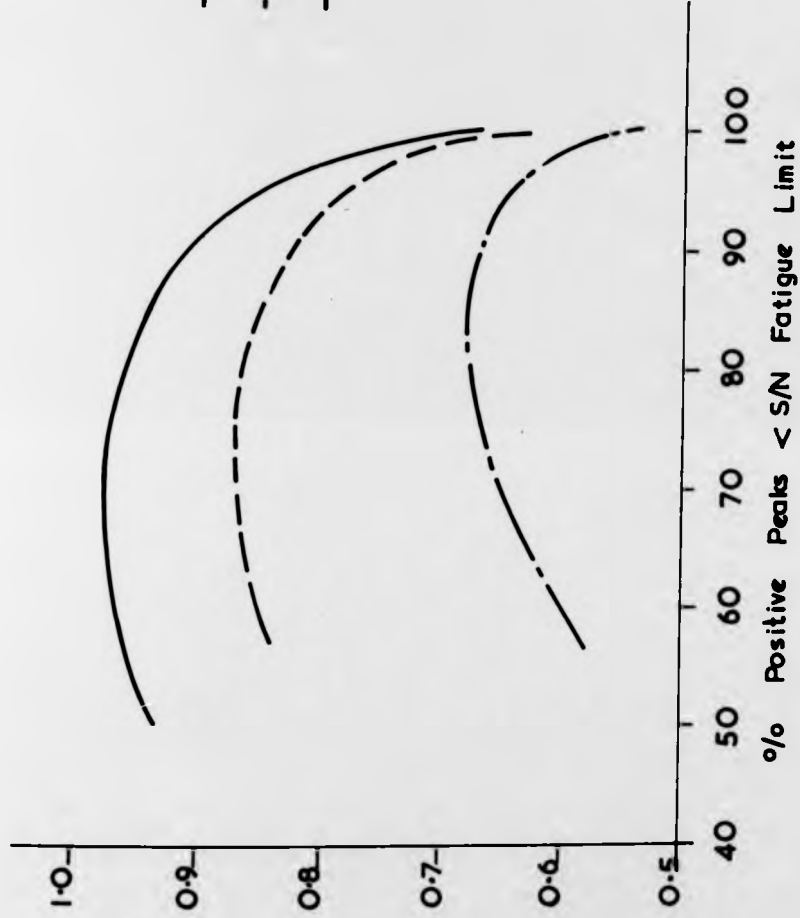
FIG. 9.28



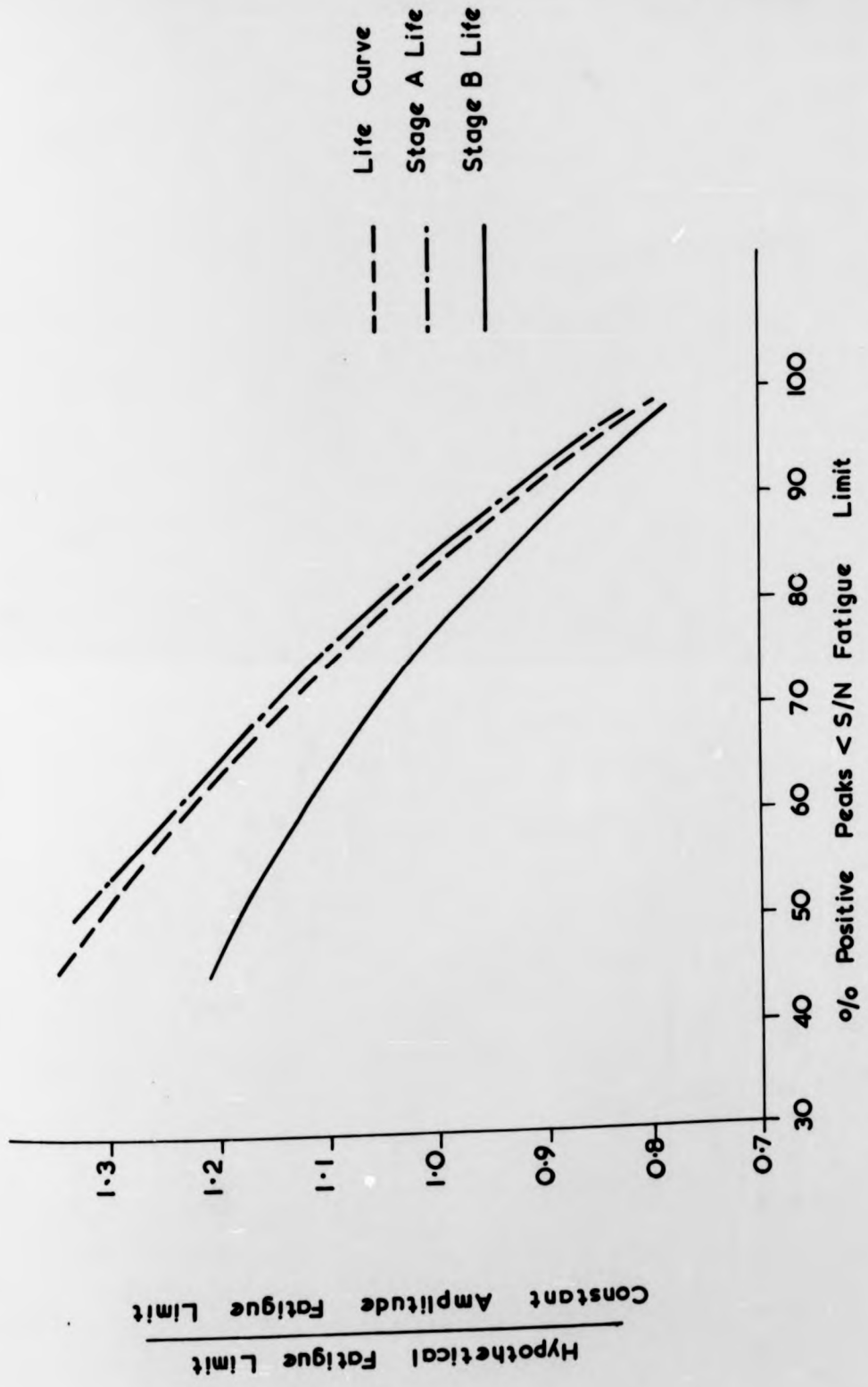
% Positive Peaks < S/N Fatigue Limit  
5/52 Hz. Band Pass Signal  
FIG. 9.29.

--- Life Curve  
- · - Stage A Life  
— Stage B Life

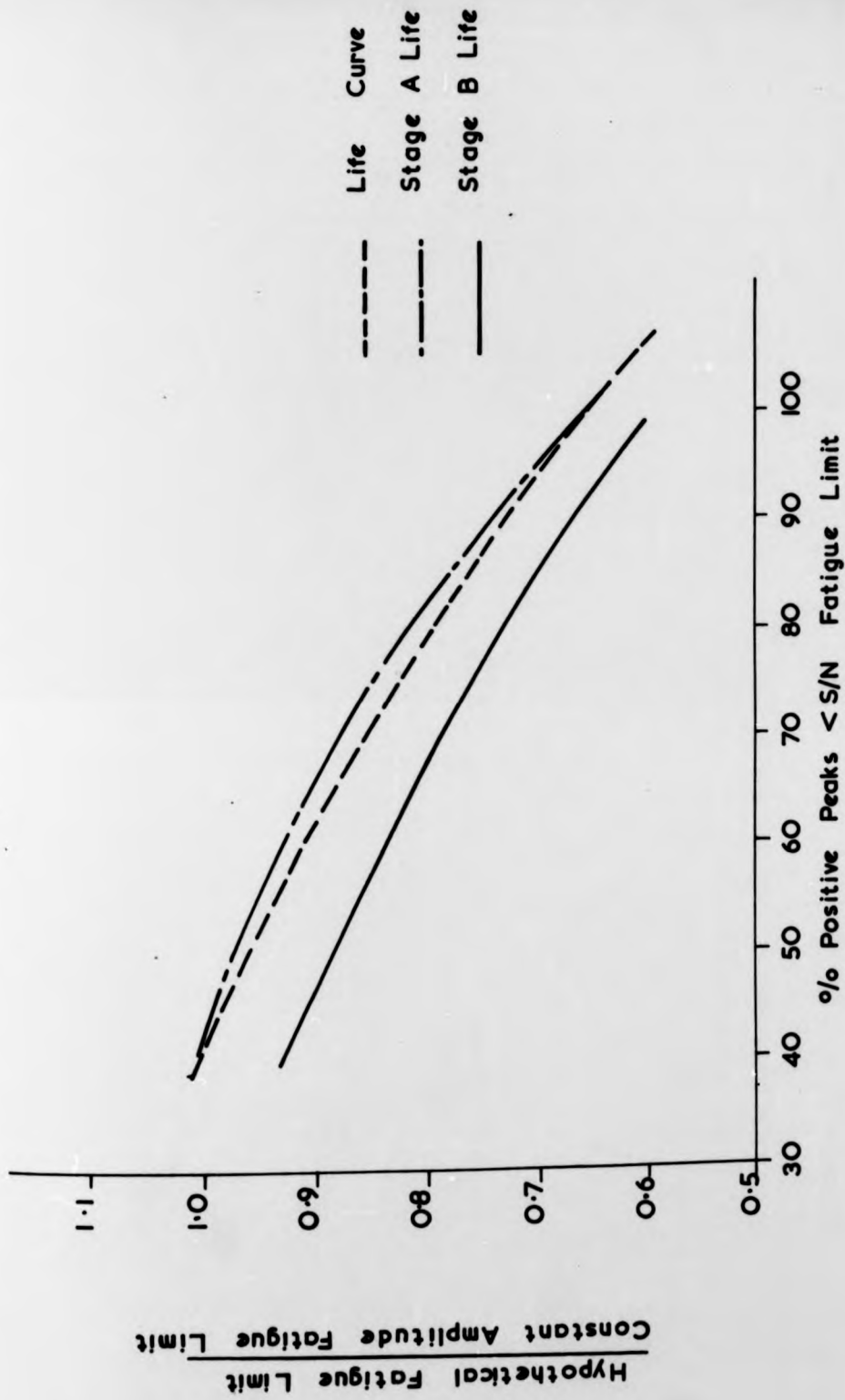
Hypothetical Fatigue Limit  
 Constant Amplitude Fatigue Limit



10 Hz Centre Frequency Signal  
 FIG. 9. 30



Low Irregularity Factor Signal  
 FIG. 9. 31



High Irregularity Factor Signal  
FIG. 9. 32

## REFERENCES

1. Miner, M.A. "Cumulative Damage in Fatigue"  
J. Appl. Mech., Vol.12, No.1, September 1945.
2. Kaechele, L. "Review and Analysis of Cumulative  
Fatigue Damage Theories" Memorandum RM-3650-PR,  
RAND Corporation, August 1963.
3. Stallmeyer, J.E. and W.H. Walter, "Cumulative Damage  
Theories and Application" Proc. A.S.C.E., Vol.94,  
No.ST12, December 1968.
4. Booth, R.T. "Variable-Load Fatigue Testing  
(Cumulative Damage - A Review and Proposals for  
Future Work)" Motor Industry Research Association,  
Report No. 1970/6.
5. Hardrath, H.F. "Cumulative Damage". Proceedings of  
10th Sagamore Army Materials Research Conference,  
Syracuse University Press, 1964.
6. Valluri, S.A. "A Unified Engineering Theory of High  
Stress Level Fatigue" Aerospace Eng., Vol.20, No.10,  
October 1961.
7. Shanley, F.R. "A Theory of Fatigue Based on  
Unbonding During Reversed Slip" Memorandum P-350,  
RAND Corporation, November 1952.
8. Corten, H.T. and T.J. Dolan, "Cumulative Fatigue  
Damage", International Conference on Fatigue of Metals,  
I. Mech. E and A.S.M.E., 1956.
9. Liu, H.W. and H.T. Corten, "Fatigue Damage During  
Complex Stress Histories", NASA TN D-256, November 1959.
10. Liu, H.W. and H.T. Corten, "Fatigue Damage Under  
Varying Stress Amplitudes", NASA TN D-647, November 1960.

11. Marsh, K.J. and J.A. Mackinnon, "Random-Loading and Block-Loading Fatigue Tests on Sharply Notched Mild Steel Specimens", J. Mech. Eng. Sci., Vol.10, No.1, 1968.
12. Freudenthal, A.M. and R.A. Heller, "On Stress Interaction in Fatigue and a Cumulative Damage Rule", J. Aerospace Sci., Vol.26, No.7, July 1959.
13. Grover, H.J., "An Observation Concerning the Cycle Ratio in Cumulative Damage", Symposium on Fatigue of Aircraft Structures, ASTM STP 274, 1960.
14. Frost, N.E. and K.J. Marsh, "Designing to Prevent Fatigue Fracture", Proceedings of 2nd Tewksbury Symposium, Butterworths, 1969.
15. Kirkby, W.T. and P.R. Edwards, "A Method of Fatigue Life Prediction Using Data Obtained Under Random Loading Conditions", R.A.E. Technical Report 66023, January 1966.
16. Thompson, N. and N.J. Wadsworth, "Metal Fatigue", Advances in Physics, Vol.7, p.72, 1958.
17. Forsyth, P.J.E., "The Physical Basis of Metal Fatigue", Chapter 4, "Fatigue Crack Growth", Blackie and Son Ltd., 1969.
18. Schijve, J. and P. De Rijk, "The effect of ground-to-air cycles on the fatigue crack propagation in 2024-T3 Alclad sheet material," National Aerospace Laboratory, NLR-TR M.2148, July 1966.
19. Paris, P.C. "The Fracture Mechanics Approach to Fatigue" Proceedings of 10th Sagamore Army Materials Research Conference, Syracuse University Press, 1964.
20. Frost, N.E. and A.F. Greenan, "Effect of a Tensile Mean Stress on the Alternating Stress required to Propagate an Edge-Crack in Various Materials", J. Mech. Eng. Sci., Vol.12, No.3, 1970.

21. Frost, N.E., "Significance of Non-Propagating cracks in the Interpretation of Notched Fatigue Data", J. Mech. Eng. Sci., Vol.3, No.4, 1961.
22. Harrison, J.D., "An Analysis of Data on Non-propagating Fatigue Cracks on a Fracture Mechanics Basis", Metal Construction and British Welding Journal, P.93, March 1970.
23. Schijve, J. "Significance of Fatigue Cracks in Micro-Range and Macro-Range". Symposium on Fatigue Crack Propagation, ASTM STP 415, 1967.
24. Swanson, S.R., "Random Load Fatigue Testing: A State of The Art Survey", Materials Research and Standards, April 1968.
25. Clevenston, S.A. and R. Steiner, "Fatigue Life Under Various Random Loading Spectra", Proceedings 35th Symposium on Shock and Vibration, October 1965.
26. Kowalewski, J., "On the Relation Between Fatigue Lives Under Random Loading and Under Corresponding Program Loading", Full Scale Fatigue Testing of Aircraft Structures, Pergamon Press, 1961.
27. Fuller, J.R., "Research on Techniques of Establishing Random Type Fatigue Curves for Broad Band Sonic Loading", SAE Paper 617 c, April 1963.
28. Hillberry, B.M., "Fatigue Life of 2024-T3 Aluminium Alloy Under Narrow and Broad-Band Random Loading", Symposium on Effects of Environment and Complex Load History on Fatigue Life, ASTM STP 462, 1970.
29. Bussa, S.L., "Effect of RMS Stress Level, Irregularity Factor and Power Spectrum Shape on the Fatigue Life of SAE 1006 Notched Specimens under Stochastic Loading Conditions", M.Sc. Thesis, Wayne State University, Detroit, Michigan. 1967.

30. Carse, A.M. "An Investigation into Testing Procedures Simulating the Effect of Fatigue in Small Steel Specimens Subjected to Random Loading", Ph.D. Thesis, Queen's University, Belfast, October 1970.
31. Broch, J.T. "Peak-Distribution Effects in Random-Load Fatigue", Symposium on Effects of Environmental and Complex Loading History on Fatigue Life, ASTM STP 462, 1970.
32. Booth, R.T., D.H. Wright and N.P. Smith. "Variable-Load Fatigue Testing". Motor Industry Research Association. Report No. 1969/9.
33. Jaeckel, H.R. and S.R. Swanson, "Random Load Spectrum Test to Determine Durability of Structural Components of Automotive Vehicles", 7th International FISITA Congress, May 1968.
34. Haas, T. "Loading Statistics as a Basis of Structural and Mechanical Design", The Engineer's Digest, Vol.23, No.3-5, 1962.
35. Schijve, J. "The Analysis of Random Load-Time Histories with Relation to Fatigue Tests and Life Calculations", National Aerospace Laboratory, NLR-TR MP.201, 1961.
36. Sherratt, F. "Random-Loading Fatigue Machines On-Line to a Digital Computer", I.E.R.E. Conference Proceedings, No.20, November 1970.
37. Fralich, R.W. "Experimental Investigation of Effects of Random Loading on the Fatigue Life of Notched Cantilever-Beam Specimens of SAE 4130 Normalised Steel", NASA TN D-663, February 1961.

38. White, D.J. and J. Lewszuk, "Narrow Band Random Fatigue Testing with Amsler Vibrophore Machines", J. Mech. Eng. Sci., Vol.11, No.6, 1969.
39. Williams, T.R.G., "Fatigue Under Sinusoidal and Narrow-Band Random Conditions", J. Sound Vib., Vol.11, No.2, 1970.
40. Hoblit, F.M. et al., "Development of a Power-Spectral Gust Design Procedure for Civil Aircraft", AD 651 152, January 1966.
41. Rice, J.R., F.P. Beer and P.C. Paris, "On the Prediction of Some Random Loading Characteristics Relevant to Fatigue", Acoustical Fatigue in Aerospace Structures, edited by W.J. Trapp and D.M. Forney, Syracuse Press, 1965.
42. Schjelderup, H.C. and A.E. Galef, "Aspects of the Response of Structures Subject to Sonic Fatigue", WADD Tech. Report 61-187, July 1961.
43. Ashby, D.J., "Cumulative Damage Fatigue in Notched Mild Steel Specimens", Ph.D. Thesis, University of Warwick, September 1969.
44. Wellstead, P.E., "Aspects of Real Time Digital Spectral Analysis", Ph.D. Thesis, University of Warwick, October 1970.
45. "Design Considerations for Diaphragm Pressure Transducers", Technical Note TN-129, Welwyn Electric Limited, January 1969.
46. Bendat, J.S. and A.G. Piersol, "Measurement and Analysis of Random Data", Wiley & Sons, New York, 1966.
47. Williams, C.A., "On the Choice of the Number and Width of Classes for Chi-Square Test of Goodness of Fit", J. Am. Statistical Assoc., Vol.45, March 1950.

48. Cooley, J.W. and J.W. Tukey, "An Algorithm for the Machine Calculation of Complex Fourier Series", Math. of Comput., Vol.19, April 1965.
49. Guerriero, J.R., "Computerizing Fourier Analysis", Control Engineering, p.90, March 1970.
50. Bendat, J.S., "Probability Functions for Random Responses: Prediction of Peaks, Fatigue Damage and Catastrophic Failures", NASA CR-33, April 1964.
51. Rice, S.O. "Mathematical Analysis of Random Noise". "Selected Papers on Noise and Stochastic Processes", edited by N. Wax, Dover Publications, New York, 1954.
52. Broch, J.T., "Peak Distributions of Random Signals", Brüel & Kjaer Technical Review 3, 1963.
53. Girling, F.E.J. and E.F. Good, "Active Filters", Wireless World, p.348, August 1969.
54. Hodge, P.G., "Plastic Analysis of Structures", Chapter 1, McGraw-Hill, 1959.
55. MacKinney, J.G., "Least Squares Fitting by Orthogonal Polynomials", CACM Algorithm No. 28.
56. Peck, J.E.L., "Curve Fitting with Constraints", CACM Algorithm No. 74.
57. Neuber, H., "Theory of Notch Stresses" published by J.W. Edwards Co., Ann Arbor, Mich. 1946.
58. Kuhn, P. and H.F. Hardrath, "An Engineering Method for Estimating Notch-Size Effect in Fatigue Tests on Steel", NACA TN-2805, 1952.
59. Heywood, R.B. "Designing Against Fatigue", Chapter 6, Chapman & Hall Ltd. 1962.
60. Reference 59, Chapter 5.
61. Chatterjee, N. "The Effect of Shot-Peening on the Initial Crack Propagation Rate & Fracture Surface Appearance in Metals", Ph.D. Thesis, University of Warwick, Nov.1970.

62. Polakowski, N.H. and A. Falchoudhuri, "Softening of Certain Cold Worked Metals under the Action of Fatigue Loads", A.S.T.M. Proceedings, P.701 V.54, 1954.

APPENDIX A

Fundamentals of Electro Hydraulic  
Servo Controlled Fatigue Test Rig Design

# The Fundamentals of Electrohydraulic Servo-controlled Fatigue Test Rig Design—Part 1

By B. C. FISHER, Senior Research Associate, and  
J. V. COMFORT, Research Graduate, School of Engineering Science, University of Warwick.

THE DEVELOPMENT of the electrohydraulic servo system was stimulated by the demands of the aerospace industry to solve control problems such as those presented by radar antenna drives and rocket steering systems. Low power level electrical signals are processed electronically to control high power, rapid response hydraulic equipment. The component which is vital to the closed loop chain is the servo valve, which transforms the electrical control signal into an hydraulic flow. Over the past few years the difficulties associated with the production of these valves have been overcome and the electronic techniques associated with closing the loop have been understood. This, backed by the flexibility of control offered by electrohydraulic servo systems has brought their use to other fields. Commercial electrohydraulic fatigue testing equipment has been available for several years for mechanical testing. The capabilities of this type of equipment have been outlined in Ref. 1.

The design and performance of an electrohydraulic servo-controlled fatigue test rig can be established from certain basic mechanical, electronic and control engineering principles without resorting to complex mathematics. The control system can be designed to allow for a considerable variety of test rig component layouts. Frequency responses flat from d.c. to about 25Hz are not uncommon.

The loop transfer function is the combined effect of the individual transfer functions of the mechanical and electrical components within the loop. The system design is simplified if these components have flat frequency responses and do not introduce significant phase lags within the frequency range mentioned. When this is the case, loop design and closed loop performance evaluation is relatively simple. Where significant phase lags do occur, the closed loop response can often be improved by closed loop transfer function measurement, which is used for the design of phase lead networks.

An extensive treatment of the analysis and design of hydraulic servo systems is given in Ref. 2, while the subject is treated more generally in Ref. 3. The basic electrohydraulic servo loop with component force as the controlled parameter is shown in Fig. 1.

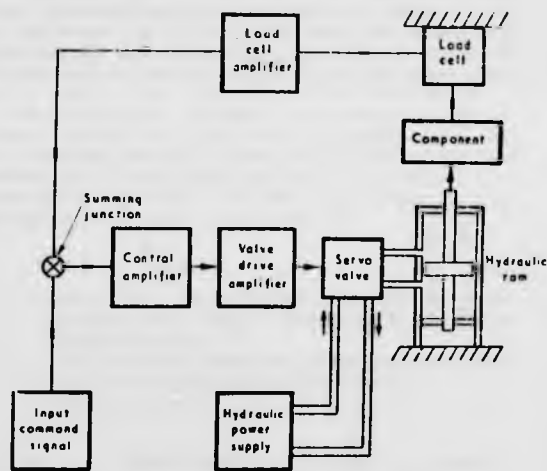


Fig. 1. Basic electrohydraulic servo loop

## Hydraulic Circuit Considerations

By far the largest number of hydraulic power supply units in electrohydraulic servo systems maintain a fixed pressure level regardless of the flow demand placed upon the supply by the load. Constant pressure supply units have the advantage that several loads can be paralleled from one supply unit, and they afford more linear characteristics from the servo valve. Self-contained hydraulic power packs can be bought from hydraulic equipment manufacturers complete with accumulators, microfilters, pressure relief valves, dump valves, etc., and fail-safe systems which cut out with excessive variations in oil temperature, level and pressure.

Most systems operate with 3000lb/in<sup>2</sup> supply pressure.

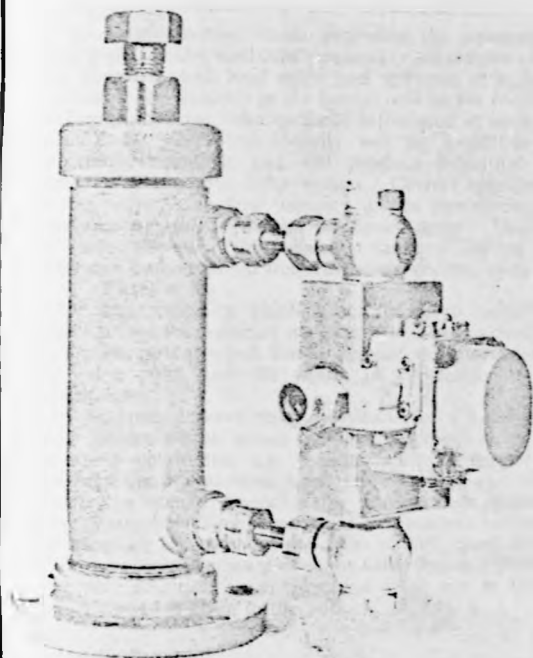


Fig. 2. Hydraulic ram and servo valve 2in dia. ram. Moog series 21 servo valve. (Courtesy Keelavite Hydraulics Ltd., Dowty Hydraulic Units Ltd.)

The maximum required delivery is dictated by the flow capacity of the servo valve. The power pack, servo valve and hydraulic ram should be compatible with the same hydraulic oil and supply pressure. The ram can be subjected to full supply pressure during slow cycling and static operation because then there is little pressure drop through the servo valve.

Oil system cleanliness is of utmost importance. The servo valve is most susceptible to particle contamination because of the small clearances between the spool and sleeve<sup>(4)</sup>. The chosen servo valve will dictate the system filtration level, usually of the order of 10 $\mu$ . A recommended practice is to install a filter in the pressure line, as near to the servo valve as practicable, in addition to that on the power pack, because particle contamination can originate in high pressure lines between the pump and servo valve.

Standard hydraulic pressure tube and couplings can be used to connect a servo valve mounting block to the ram, and the servo valve is then easily bolted to the mounting block, (Fig. 2). Alternatively, some ram bodies are drilled to provide fluid galleries which terminate in ports at a machined face and which mate with similar ports on the servo valve manifold. The ram/servo valve assembly is then connected to the power pack with standard flexible, hydraulic pressure hose and couplings to complete the hydraulic circuit.

Any disconnexions in the hydraulic circuit should be followed by a thorough circuit flushing. This involves replacing the servo valve with a flushing block and running at reduced pressure for about one hour to ensure that any particle contaminants are filtered from the oil supply.

### Servo Valves

There are many types of servo valve and an extensive review has been made by Kinney and Weiss<sup>(5)</sup>. The criteria which determine the performance specification of a servo valve are given in Ref. 6.

The basic servo valve is one in which the output flow to a constant load is proportional to the electrical input current. The most common arrangement consists of a low power electrical motor with two windings, known as the valve coils, and two stages of hydraulic power amplification, (Fig. 3). A signal applied to the motor deflects the flapper to provide a pressure difference proportional to the input signal which controls the second stage, consisting of a spool-sleeve assembly. A large group of valves use this principle. Valve weights are about 1lb and their flow capacities vary between 2 and 60in<sup>3</sup>/s for 3000 to 4000lbf/in<sup>2</sup> supplies, with internal leakage flows from 0.25 to 1.5in<sup>3</sup>/s. Electrical input powers are of the order 0.05 to 0.2W and 90° phase shift frequencies 100 to 2000Hz. The servo valve and ram together form an integrating component and cannot be used in an open loop without null shift. In fatigue testing it is usual to use this type of valve in a closed loop with component force feedback.

The required valve flow capacity can be determined from the maximum values of test frequency, ram displacement and net ram piston area. Reference 7 gives the necessary guide lines to be followed for the servo valve hydraulic ram specification, but note that flows are expressed in U.S. gallons. Errors introduced by the servo valve dead zone, hysteresis, null-shift and resolution characteristics are not usually significant in the overall system accuracy. However, the valve flow capacity should not be excessively greater than the maximum required flow since these errors will be roughly proportional to the valve flow capacity.

The next step is to establish the approximate dynamic response for the servo valve from the manufacturer's data. The frequency response between output flow at zero load pressure and a sinusoidally varying input current can be approximately described by a first order transfer function for the limited frequency range given by:

$$G(s) = \frac{K_v}{1 + sT}$$

$T$  = servo valve time constant; dictates the valve dynamics and is largely determined by valve flow capacity (seconds).

$K_v$  = servo valve static flow gain; determined from valve rated flow and input current (in<sup>3</sup>/s, mA).

$s$  = Laplace operator.

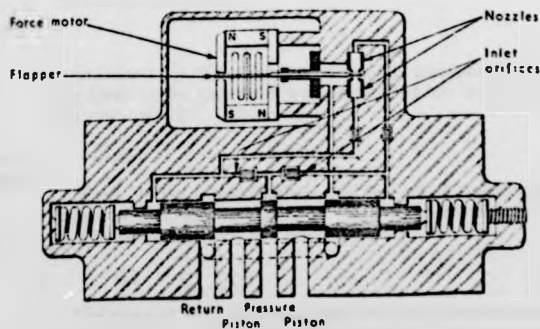


Fig. 3. Two-stage electrohydraulic flow control servo valve. (Courtesy of Moog Servo Controls Inc.)

This approximation holds providing the resonant frequency of the valve load combination (i.e. oil compressibility and damping, and load mass and stiffness) is high. A dominant non-linearity in the system will be the force rate of change limit (or velocity limit) introduced at maximum valve flow. This non-linearity will be amplitude and frequency dependent and will produce behaviour substantially like a first order system. Correct specification of the servo valve flow capacity avoids introducing this non-linearity within the test frequency range. Thus, for the initial design in the frequency range of interest here,  $G_v(s)$  can be considered frequency independent, and:

$$G_v(s) = K_v$$

The characteristics which affect the servo valve drive amplifier are the nominal maximum demand current, the maximum current which can be applied without damaging the valve coils, and the values of coil-resistances and inductances.

In practice, a servo valve proves to be a highly non-linear device whose actual dynamic response varies with operating conditions, e.g. hydraulic supply temperature and pressure, signal input level, valve loading, etc. These effects are usually negligible for performance about the valve design operating point, and linear analysis techniques are adequate for inputs of the order of 25% rated current. A more complete account of servo valve dynamic performance with empirical approximations which can be used in system design is given in the publication, Ref. 8.

#### Hydraulic Rams

The hydraulic ram dimensions are determined from the maximum force to be applied to the component, the ram differential pressure, and the ram stroke. Thus:

$$F = A P \text{ lbf.}$$

$F$  = output force (lbf).

$A$  = net piston area (in<sup>2</sup>).

$P$  = differential pressure (lbf/in<sup>2</sup>).

Oil-column resonant frequency is an important consideration in the use of hydraulic rams and can represent a limitation on the performance of the servo system. The overall apparent bulk modulus of the valve/ram combination will be considerably lowered by using flexible tubing between the valve and ram. The oil column stiffness combined in parallel with the component stiffness forms a resonant frequency which should be considerably higher than the desired system frequency response limit to avoid creating a closed loop stability problem. The ram stroke should in general be kept to a minimum in order to reduce the volume of oil enclosed in the ram. Neglecting load and piston damping, and assuming a rigid ram cylinder and valve connexions, the oil column stiffness is given:

$$K_o = \frac{A^2 B}{V} \text{ lbf/in.}$$

$B$  = oil bulk modulus (lbf/in<sup>2</sup>).

$V$  = total half volume of the ram, provided that piston movements are small and about the stroke centre position (in<sup>3</sup>).

The resonant frequency is:

$$F_n = \frac{1}{2\pi} \sqrt{\frac{(K_o + K_L)}{M}} \text{ Hz}$$

$K_L$  = component stiffness (lbf/in).

$M$  = load and piston effective dynamic mass (lb).

Usually the hydraulic stiffness is greater than the load stiffness, and the resonant frequency is well outside the frequency range of interest here.

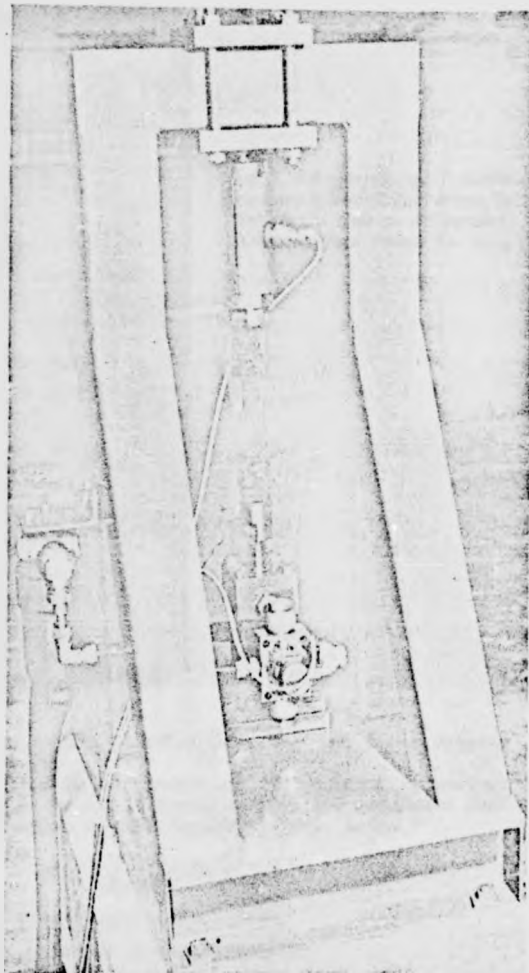


Fig. 4. Fatigue test rig. Frequency response up to 40Hz dynamic force  $\pm 3\frac{1}{2}$ tonf. (School of Engineering Science, University of Warwick.)

Dynamically the ram acts as a pure integrator, providing there is no excessive seal or bearing oil leakage from the ram cylinder. Thus:

$$G_R(s) = \frac{1}{sA}$$

Since the load combination will not affect the frequency range of interest, the gain of the hydraulic ram for the system design is:

$$K_R = \frac{1}{A} \left( \frac{1}{\text{in}^2} \right)$$

Differential area rams can be used and compensation of the unequal area is made by the closed loop control action. Static and dynamic forces can be applied together. The application of a static force gives a hydraulic pressure difference across the piston and thus the peak value of

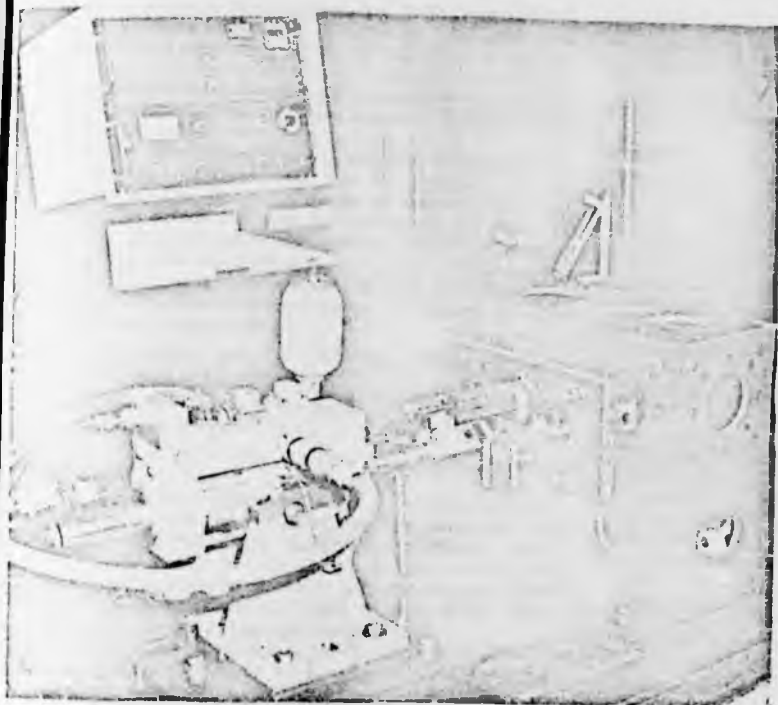


Fig. 5. Fatigue test rig. Trunnion mounted hydraulic ram driven by two servo valves in parallel. (Courtesy Ford Motor Co. Ltd.)

the dynamic load which can be applied about this static load is reduced. A wide range of commercial hydraulic rams with various types of mounting are available. Cylinder damping is recommended to prevent shock loading. Two other factors influence the choice of the hydraulic ram, viz ram friction and asymmetric load reaction forces.

Seal and bearing friction is important. It is preferable to use a combination of rubber wiper seals with p.t.f.e. lined bearings and p.t.f.e. piston seals. Excessive friction will cause non-linear stick-slip piston rod movement. The amount of friction does effect the system response to small input signals, i.e. system resolution, which is mentioned in Ref. 6. System resolution can be improved by dithering the valve. Four hundred Hertz is the usual order of valve dither frequency.

The other main factor is the severity of the component load reaction forces experienced by the ram. Ram performance is best when driving into structurally symmetrical loads, i.e. in the axial push-pull mode, when industrial rams can usually be employed. Alignment of the component drive with the ram is important to avoid excessive side loading. Satisfactory performance under cantilever loading is not easy to achieve because the ram is subjected to side loads and bending moments which have to be counterbalanced by the ram bearings. Special ram designs may have to be made to suit these conditions and the ram mounted on a swivel or pivot so that it can "follow" component deformation.

#### Test Frame Component Drive Considerations

The main point about the design of the test frame is to ensure that any mechanical resonant frequency falls outside the desired servo system frequency response limit by a factor of about ten. This avoids creating a closed

loop stability problem from the test frame dynamic behaviour.

Normally components are not designed to resonate within the test frequency range. The component itself will form a resonant frequency:

$$F_c = \frac{1}{2\pi} \sqrt{\frac{K_c}{M_c}} \text{ Hz}$$

$K_c$  = component stiffness (lbf/in).

$M_c$  = effective component mass (lb).

There are two approaches to the test frame design. The hydraulic ram and component can be mounted in a structural steel frame standing on an anti-vibration mounting. The framework can be welded and constructed from standard hollow tubular steel sections, making it stiff and light to give high natural frequencies, (Fig. 4). Alternatively, the design of mounting fixtures which can be clamped to a machined and keywayed base may be justified to give various component/ram layouts when many different components have to be tested (Fig. 5).

The component can be fixed between the ram and load cell, or the loadcell can be mounted on the piston rod. The load cell range determines the force capacity of the control system, and it should be closely matched to the test force range. Axial load cells should be compensated to eliminate any signal from bending due to misalignment. Achieved test rig component stresses are best measured by strain gauging the critical test areas and using a component static calibration to check the stresses achieved dynamically and calculated from the load cell output.

Difficulties with component drive attachments usually arise when loading is from tension to compression and allowance has to be made for rotational movement.

Backlash and waveform distortion can result from bearing drives. A spring steel strip clamped at both ends and designed to act as a strut is flexible and gives a solution under these conditions. With axial loading the component can be rigidly bolted in position but alignment is important to avoid inducing high clamping stresses. Useful design data is given in Ref. 9.

Assuming that the test frame is very stiff compared with the component stiffness, and that its dynamics do not contribute to the frequency range of interest, then the control loop design will only be affected by the load cell sensitivity and the component stiffness. The component is within the loop in a force control system. The load cell/component transfer function can be assumed frequency independent for the frequency range of interest here, so that for the system design:

$K_c$  = component gain or stiffness; slope of load/deflexion graph (lbf/in)

$K_L$  = load cell gain or sensitivity; depends on bridge supply volts ( $\mu\text{V}/\text{lbf}$ ).

### Trip Circuits

Trip circuits shut down equipment at component failure. The microswitch is a reliable electromechanical trip which is triggered from component deflexion, either directly or by a lever or cam to amplify component movement. A plunger opens or closes electrical contacts which make or break an electrical circuit to shut down timers, hydraulic power pack, signal excitation, etc.

Thin wire can be included in a trip circuit and glued to the component surface to be broken as a fatigue crack propagates, although it is important to ensure that the gluing process does not affect the test results.

Another method is to pass a d.c. voltage through the component, providing it is held in grips which are electrically insulated from the test rig, and component fracture breaks the circuit.

A reliable electronic circuit which works from the fall in load cell dynamic signal at component failure is shown in Fig. 6, and can be used except for very slow cycling tests. The load cell signal is rectified and amplified by a differential input operational amplifier to drive a transistor which provides the necessary current to energize a number of reed relay coils. The trips are set at the start of a test by a d.c. voltage and held by the dynamic signal. Low frequency signal components are blocked. For sine wave

testing the time constant of the feedback resistor/capacitor can be set to about 1s but for random signals it may need to be higher, perhaps between 5 and 10s, to prevent the circuit from tripping as the amplifier voltage falls during a period of low load signal.

### References

- (1) BUTZOW, G. N. AND CHURCHILL, R. W. Electrohydraulic Fatigue-Test-Systems Capabilities. Oct. 1964. MTS Systems Corporation, Minneapolis, Minnesota.
- (2) GUILLON, M. AND TRANSLATED BY GRIFFITHS, R. T. Hydraulic Servo Systems. Published by Butterworth & Co. Ltd., London. 1969.
- (3) MORSE, A. C. Electrohydraulic Servomechanisms. Published by McGraw-Hill. 1963.
- (4) OSGOOD, R. E. How Contamination Affects Servo Valve Design. *Applied Hydraulics & Pneumatics*. Feb. 1959. Vol. 12, No. 2, p. 79-82.
- (5) KINNEY, W. AND WEISS, P. What You Can Get in Electrohydraulic Servo Valves. *Applied Hydraulics & Pneumatics*. Feb. 1959. Vol. 12, No. 2, p. 67-78.
- (6) HOLZBOCK, W. G. Principles of Servo Valves—Part 1. *Hydraulics and Pneumatics*. Oct. 1960, Vol. 13, No. 10, p. 68-73.
- (7) JOHNSON, H. C. Application of Electro-Hydraulic Servo Control to Physical Testing. Proceedings of National Conference on Fluid Power. 1964. Vol. 18, p. 125-136.
- (8) THAYER, W. J. Transfer Functions for Dowty-Moog Servo Valves. Jan. 1965. Dowty Hydraulic Units Ltd., Tewkesbury, Gloucestershire.
- (9) HEYWOOD, R. B. Designing Against Fatigue. Published by Chapman & Hall Ltd., London. 1962.

## SIMA Metrication Guide

THE Scientific Instrument Manufacturers' Association, (SIMA), have published a "Metrication Guide" for the use primarily of member companies.

The guide was compiled by the Metrication Working Party at the request of the Sima technical and standardization committee and is based on an extremely practical and comprehensive approach to the problems.

The guide, which is extensively illustrated, is divided into five major sections:

- (1) Introduction to metric working.
- (2) Drawing office practice.
- (3) Reference material.
- (4) Managerial, commercial and clerical information.
- (5) Training and education.

Although the guide was produced as part of the service provided by Sima to all its members, it is considered that in view of the general interest throughout British industry in the complex issues involved, it should be made available to other organizations.

The price per copy to non-members of Sima, including packing and postage is 50/-d. Orders for single or multiple copies, which should be accompanied by the necessary remittance, should be addressed in writing to Scientific Instrument Manufacturers' Association, 20, Peel Street, London, W.8, and should be endorsed "Metrication Guide".

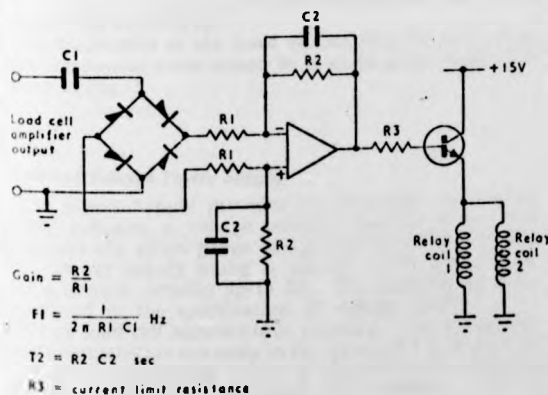


Fig. 6. Trip amplifier circuit

# The Fundamentals of Electrohydraulic Servo-controlled Fatigue Test Rig Design—Part 2

By **B. C. FISHER**, *Senior Research Associate and*  
**J. V. COMFORT**, *Research Graduate, School of Engineering Science, University of Warwick.*

AN ELECTROHYDRAULIC servo system has a high performance with an overall quick response. The hydraulic system operates at high power levels while the electrical system carries low energy signals, but both systems have rapid response speeds. The electrical system is flexible, and the overall system response may be compensated by additional electrical circuits rather than by their more complex hydraulic equivalents.

The availability of monolithic and integrated circuit operational amplifiers has greatly simplified the electronic design problems in electrohydraulic servo systems. Manufacturers' data sheets include recommended balancing and stabilization circuits for a range of feedback configurations and performance figures aid the choice of a suitable amplifier for different applications. Reference 1 gives a useful guide for the design and application of operational amplifier circuits.

The regulation of commercially available power supplies permits their direct use for amplifier drive and load cell excitation. Once designed, the electronic equipment can be arranged in separate modules—control amplifier, valve drive amplifier, power supply, *etc.*—and mounted in standard racks (Fig. 1). Multiway screened electrical cable is used to connect the remote load cell and servo valve to this equipment.

The electronics of the basic electrohydraulic servo loop with component force sensed by a strain gauge bridge are shown in Fig. 2.

### Stabilized Voltage Power Supply

The power supply provides the electronic component supply voltages, a voltage reference for the static load level, and the strain gauge bridge excitation for the load cell. Power supply rating is usually  $\pm 15V$  about earth with a current capacity up to 3A. The main factor to be considered in the specification of voltage stability is its effect on load cell measurement accuracy. Force measurement accuracies are normally in the region of 1% because of hysteresis and linearity errors of the load cell. Voltage changes on the load cell must not, therefore, cause a significant increase in this figure.

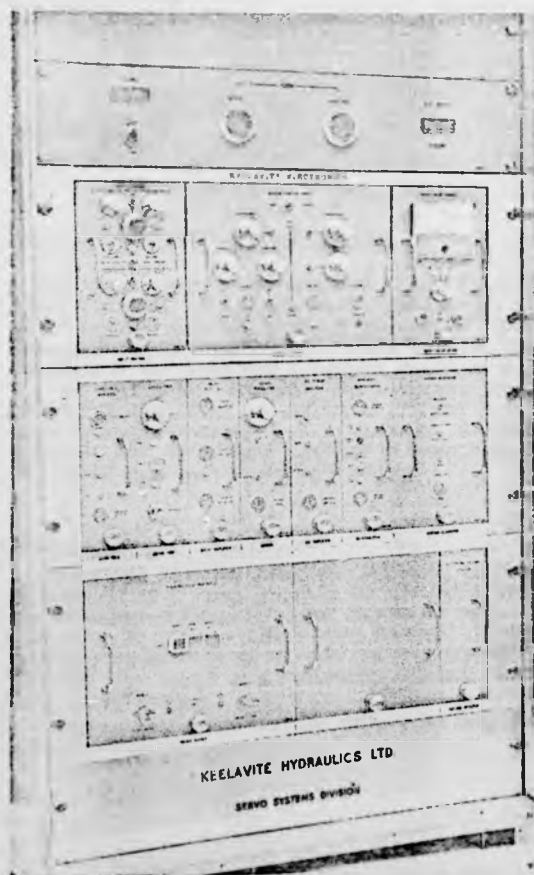


Fig. 1. Electronic control module. (Courtesy Keelavite Hydraulics Ltd.)

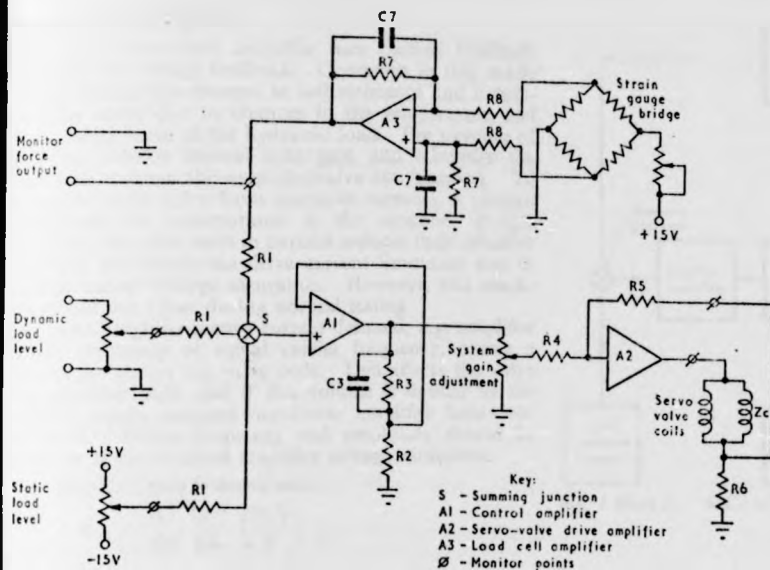


Fig. 2. Basic electronics of servo loop

Variations in stabilized voltage supply are due to:—

- mains voltage fluctuations;
- ripple and noise in regulating circuits;
- load regulation caused by the supply having a finite output impedance;
- temperature changes which affect supply reference voltages and control circuits within the power supply itself.

Their cumulative effect should be less than 0.25%. For a typical precision power supply available commercially the corresponding figures are:—

- 0.001% for  $\pm 10\%$  change in mains supply voltage;
- 0.002%;
- 0.01% no load to full load;
- 0.2% for 10degC temperature change.

No design problems should be encountered here.

#### Load Cell Amplifier/Load Cell

The accuracy of the control loop is principally determined by the accuracy of the force measurement. The use of strain gauges for force measurement involves a high gain differential input operational amplifier in order to increase the measurement signal level to that comparable with the control loop command signal. Adequate consideration must be given to the effects of temperature, electrical interference and noise, amplifier gain and the feedback configuration if acceptable accuracy of force measurement is to be achieved<sup>(2)</sup>. Drift at the load cell amplifier is seen at the summing junction as an error in the static load level. This error causes the servo system to alter the static load level until the drift signal has been cancelled. To achieve accurate results it will be necessary to use a low drift, chopperless, differential input operational amplifier to amplify the load cell signal, together with metal film or metal oxide resistors which define the amplifier closed loop gain.

For the system design here, the frequency invariant amplifier gain is:

$$K_{A3} = \frac{R7}{R8}$$

$K_{A3}$  = amplifier gain, usually 500 to 1000.

The strain gauge bridge resistance is usually about 250Ω. The bridge can be balanced by paralleling one arm with a variable resistance, usually of the order of 100kΩ. When the load cell amplifier output is monitored the input resistance of the monitoring equipment should be high, e.g. an oscilloscope; otherwise, the equipment causes electrical loading effects. A differential amplifier oscilloscope is required to monitor servo valve voltage. A voltage follower<sup>(1)</sup> is a useful buffer amplifier to insert between the control loop and monitoring equipment.

#### Control Amplifier

The control amplifier forms the difference or error between the input signal, which is the demanded force, and the measured force. The input may be the sum of a mean force level and a time varying demand. Similar considerations to those in the load cell amplifier design apply but since smaller gains are usually required, conditions are less stringent.

For the system design here the gain of the amplifier transfer function is:

$$K_{A1} = 1 + \frac{R3}{R2}$$

$K_{A1}$  = control amplifier gain, usually 1 to 10.

Adjustment of the system gain potentiometer fixes the level of the amplified error voltage signal available at the servo valve drive amplifier input.

### Servo Valve Drive Amplifier

The servo valve drive amplifier uses current feedback as opposed to voltage feedback. Operation in this mode helps to swamp any changes in coil resistance and inductance that occur due to changes in the temperature and reflected impedance of the hydraulic load. The purpose of this is to stabilize control loop gain and minimize the phase shift through the amplifier/valve combination. To protect the servo valve from excessive currents, a current limit should be incorporated in the amplifier design. Connecting the valve coils in parallel reduces their effective impedance and hence the drive current limitation due to amplifier output voltage saturation. However, this condition should not occur during normal testing.

Any small high frequency current demand, e.g. amplifier chopper frequency or signal carrier frequency, causes a high voltage across the valve coils. This affects the valve drive amplifier only, and if this voltage is limited by the amplifier supply voltages non-linear amplifier behaviour can result. Dither frequency and amplitude should be chosen so as not to cause amplifier voltage saturation.

The amplifier gain is expressed:

$$K_{As} = \frac{R5}{R4} \frac{10^{-3}}{R6} \left( \frac{mA}{V} \right)$$

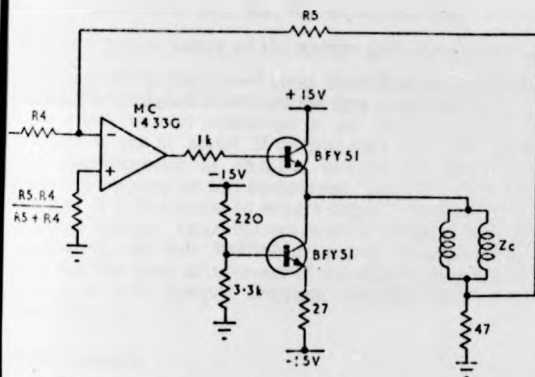


Fig. 3. Simple current amplifier circuit

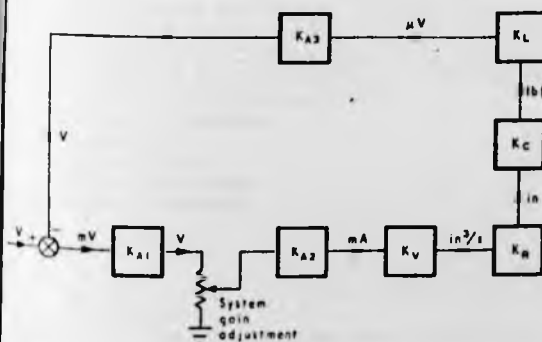


Fig. 4. Simplified block diagram of servo system

INSTRUMENT PRACTICE, JULY, 1970

C

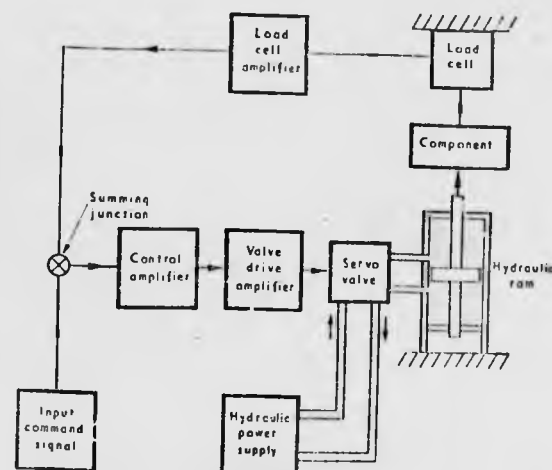
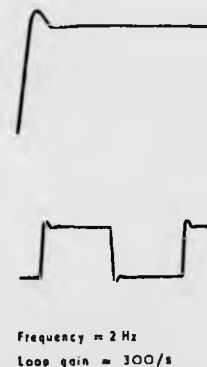


Fig. 1 (Part 1). Basic electrohydraulic servo loop

Fig. 5. Traces of servo system square wave response



Integrated circuits by themselves cannot normally be used to drive servo valves because of their limited output current. A useful circuit which will provide about  $\pm 15mA$  is shown in Fig. 3. This consists of an integrated circuit amplifier with a booster stage to supply the necessary current. The booster consists of a constant current emitter follower. The amplifier and booster stage is in itself a current control system and should be designed so as to ensure closed loop stability and an adequately damped transient response.

Servo valve manufacturers supply standard amplifier units to drive servo valves. The components in these amplifiers are readily accessible and adjustments to suit load impedance and gain are easily made.

### Initial Loop Gain Setting

The initial loop gain is set to the highest value to give an adequately damped transient response. An approximate method for obtaining this value is given by:

$$K = \frac{1}{T}$$

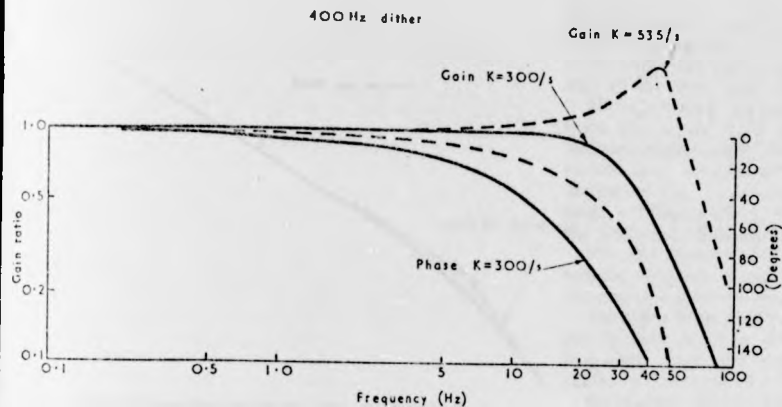


Fig. 6. Closed loop response (without compensation)

$K$  = loop gain.

$T$  = servo valve time constant obtained from manufacturer's data.

The units of loop gain are  $s^{-1}$  since the loop contains an integrating element. The loop gain is given (Fig. 4) by:

$$K = R \times K_{A1} K_{A2} K_V K_R K_C K_L K_{A3}$$

$R$  = attenuation factor of the system gain potentiometer.

Subsequent to the closed loop identification, compensation can be designed to extend the frequency response.

To check correct operation of the control system the pressure is set at about 500lb/in<sup>2</sup> and with the system gain potentiometer at about a quarter full turn, mean loads are applied to the component from the static level control. It is important to ensure negative feedback of the load cell voltage. Once correct control operation has been established, the full 3000lb/in<sup>2</sup> supply pressure can be used and the final adjustment of the system gain made to provide a well damped transient response from a step input (Fig. 5).

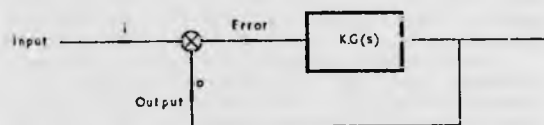
#### Design Example

A dynamic response from the fatigue test rig (Fig. 1, Part 1), was required which would substantially reproduce a random signal input with a frequency content from d.c. to 25Hz, and peak dynamic forces of 7000lb about a mean tensile load of 1000lb.

The hydraulic power supply working pressure is 3000lb/in<sup>2</sup>. The differential area hydraulic ram has a 2.5in dia. bore with a 1in dia. piston rod and 2in stroke. The servo valve is a Moog Series 22 with a rated flow of 40in<sup>3</sup>/s and a time constant of approximately 0.0026s. The gains of the loop components were given values:

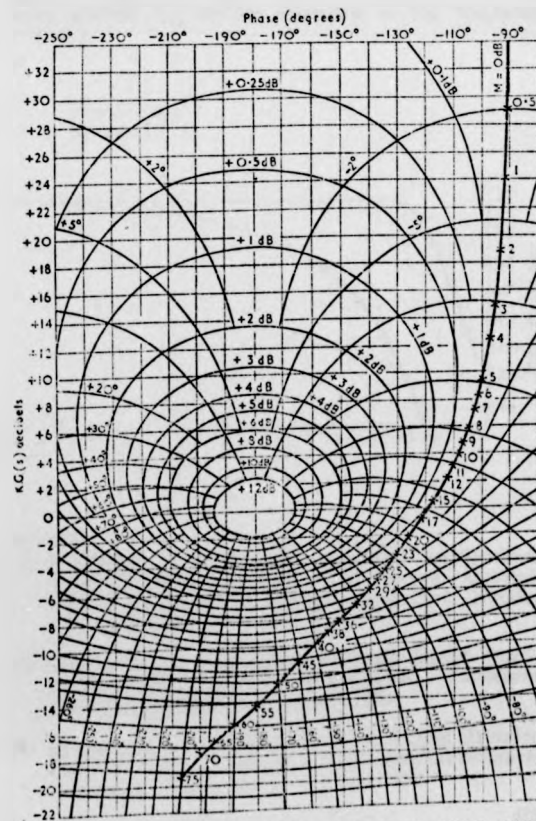
$$\begin{aligned} K_C &= 2 \times 10^3 \text{ lb/in} \\ K_{A1} &= 2 \\ K_{A2} &= 37 \text{ mA/V} \\ K_V &= 2.67 \text{ in}^3/\text{s/mA} \\ K_L K_{A3} &= 1.25 \text{ mV/lbf} \\ K_R &= 0.22 \frac{1}{\text{in}^2} \end{aligned}$$

Fig. 8. (right) Open loop—closed loop conversion (contours of constant gain and phase of  $\frac{K.G(s)}{1 + K.G(s)}$  for Input  $K.G(s)$ )



$$\text{System transfer function} = \frac{O}{I} = \frac{K.G(s)}{1 + K.G(s)}$$

Fig. 7. Simplified operational flow diagram of servo system:



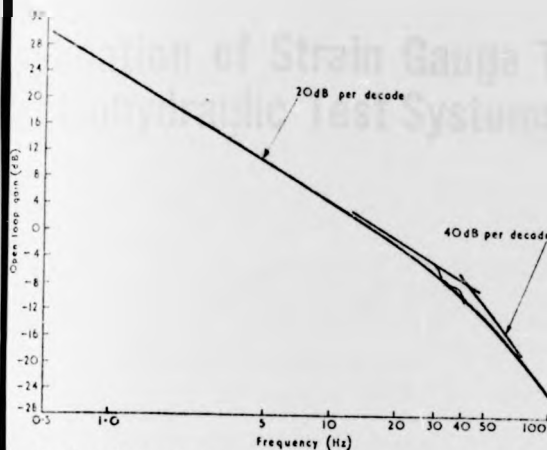


Fig. 9. Open loop response

The total loop gain is:

$$K = R \times 11000 \frac{1}{s}$$

Adjustment of R gave the closed loop response shown in Fig. 6.

To substantially reproduce a random input signal in a test rig, a loop transfer function is required which has a flat amplitude response and a phase lag not greater than about 45° within the input signal frequency range. The

analyser is not available, accurate measurements of the voltage feedback input signal amplitude ratio (dB) and phase displacement (degrees) can be made using an oscilloscope with time delay facilities, or from ultra-violet recordings of the input and feedback signals.

The open loop transfer function can be quickly derived from the closed loop transfer function using the Bode-diagram-phase-angle-Nichols-chart method. The servo system can be represented by the operational diagram shown in Fig. 7, a form which can be directly analysed using a Nichols chart, where K is the loop transfer gain and G(s) the frequency dependence of the loop transfer function.

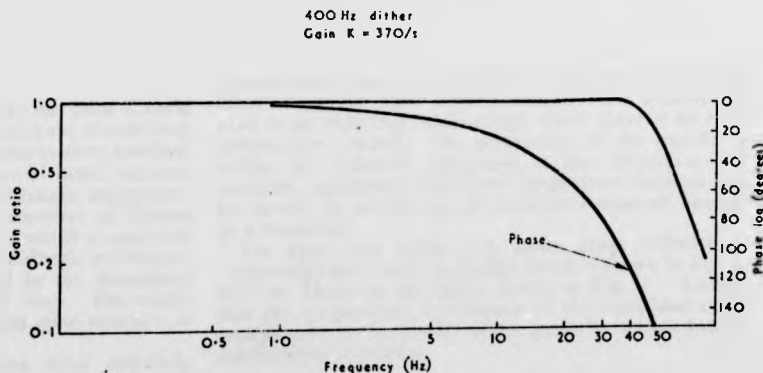
The flat closed loop response of Fig. 6 is plotted for specific frequencies on the Nichols chart, (Fig. 8), using the contour gain and phase lines.

The open loop response is determined by reverse use of the Nichols chart by reading the gain and phase for each frequency from the cartesian scale. This response is shown in the form of a Bode diagram, (Fig. 9).

Neglecting effects below 0.1 Hz where measurements were difficult the loop consisted of an integrator (the hydraulic ram) and a first order lag with a break frequency of about 40 Hz (the servo valve). These were the only significant dynamics in the frequency range of interest.

To compensate for this lag a lead term is introduced into the control amplifier with a breakpoint frequency of 40 Hz. This was done by paralleling the summing point feedback and dynamic input resistors with a capacitor. With a small increase in loop gain the closed loop response shown in Fig. 10 was achieved. Lags which are introduced into the measurement and control amplifiers to attenuate noise prevent any further extension of the frequency response.

Fig. 10. Closed loop response (with compensation)



servo system performance was improved to meet these demands by introducing electrical compensation networks. In force feedback systems the open loop transfer function is such that a simple compensating network can usually be employed, e.g. phase advance compensation. The required form of compensation is derived from the open loop transfer function.

For the purposes of analysis the assumption of linear operation can be made. The inherent integrating action of the servo valve/hydraulic ram combination makes it necessary for the open loop identification to be made under closed loop conditions. This was achieved using a digital transfer function analyser<sup>(3)</sup>. If a transfer function

#### References

- (1) Handbook of Operational Amplifier Applications. Published 1963, copyright Burr Brown Research Corporation. General Test Instruments Ltd., Hucclecote, Gloucester.
- (2) FISHER, B. C. Application of Strain Gauge Transducers to Electrohydraulic Test Systems. *Instrument Practice*, Vol. 24, No. 4. April, 1970.
- (3) ELSDEN, C. S. AND LEY, A. J. A Digital Transfer Function Analyser Based on Pulse Rate Techniques. *Automatica*, Vol. 5, No. 1. January, 1969.

# Application of Strain Gauge Transducers to Electrohydraulic Test Systems

By B. C. FISHER, School of Engineering Science, University of Warwick, Coventry.

## Introduction

OVER THE PAST FEW YEARS there has been a rapid advance in the application of electrohydraulic closed loop control systems to physical testing. These systems combine the advantages of electronic flexibility and rapid response with the high power level of hydraulic equipment. It is possible to closely control the parameter of interest in a test—for example, the force to which a specimen is subjected—by choosing the correct feedback transducer. The accuracy of control is determined by the transducer and the characteristics of the control loop. The transducer should have low output drift and good rejection of environmental electrical noise.

Resistance strain gauge transducers have relatively small electrical outputs. Consequently amplification of the order of one thousand is usual to ensure compatibility with the transducer control signal within the control loop. Procedures can be adopted to ensure that electrical pick up and drift do not form a significant percentage of the transducer/amplifier output signal.

## Temperature Effects

Temperature dependent behaviour of a resistance strain gauge transducer and its associated cable is the result of several cumulative minor effects. Adequate temperature compensation within the strain gauge bridge itself is only achieved if the transducer and the layers of adhesive bonding the gauges to the transducer behave linearly with temperature changes. Thermo-electric e.m.f.'s result from any temperature difference at the junctions of dissimilar metals, for example the bridge lead wires and gauge wire.

These effects may be minimal in constant temperature laboratories but often electro-hydraulic test systems are used in an industrial environment where there is no rigid temperature control. The positioning of the transducer within the hydraulic equipment is also important—for example, significant transducer temperature changes can be caused by oil heating an actuator connected directly to a transducer.

The basic four active arm strain gauge Wheatstone bridge/differential input amplifier circuit is shown in Fig. 1, with its Thévenin equivalent circuit in Fig. 2. Assume that the temperature dependence of the transducer/cable combination is represented in the gauge by a hypothetical coefficient of resistance.

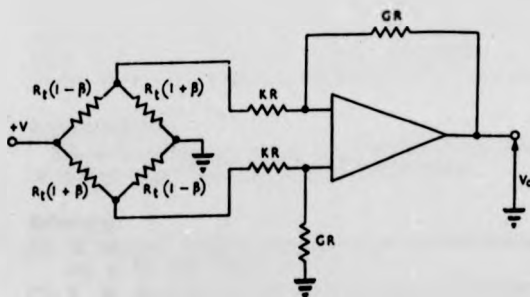


Fig. 1. Wheatstone bridge/differential input system

$R$  = strain gauge resistance at reference temperature.  
 $R_t$  = strain gauge resistance at temperature  $t$ .  
 $\alpha$  = coefficient of resistance.  
 $\delta R_t = \beta R_t$  = change in gauge resistance due to strain, where  $\beta$  is small.

The output of this circuit is:

$$V_o = \frac{V \beta GR}{R_t \left( \frac{1 - \beta^2}{2} \right) + KR}$$

$$V_o = \frac{2V \beta GR}{R(1 + \alpha)(1 - \beta^2) + 2KR}$$

$\beta^2$  is very small and can be neglected.

If  $K = 0$ , the amplifier gain can be markedly temperature dependent.

If  $K$  is sufficiently large the output becomes:

$$V_o = \frac{2V \beta G}{2K + 1}$$

A value of  $K$  between five and ten is suggested. Temperature variations also affect the properties of transistor amplifiers, and ref<sup>(1)</sup> gives useful guidelines in this respect.

#### Electrical Noise

Electrical noise picked up by the strain gauges and associated cable may form a significant part of the transducer amplifier input. The amount picked up depends on the intensity of the electromagnetic and electrostatic fields around the control equipment and the care taken with instrumentation, especially to ensure proper cable and

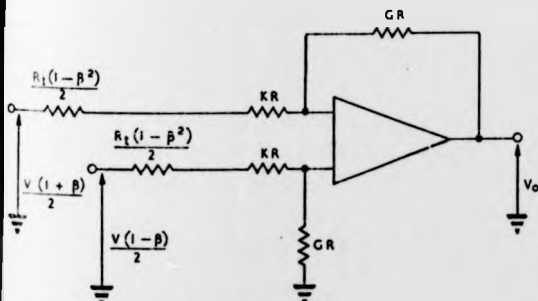


Fig. 2. Thévenin equivalent circuit

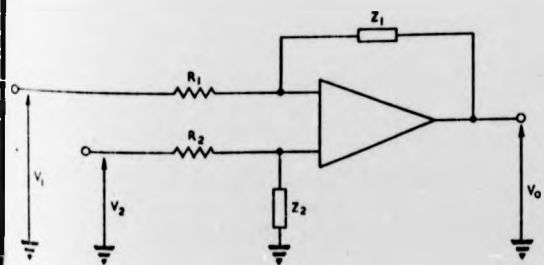


Fig. 3. Differential amplifier

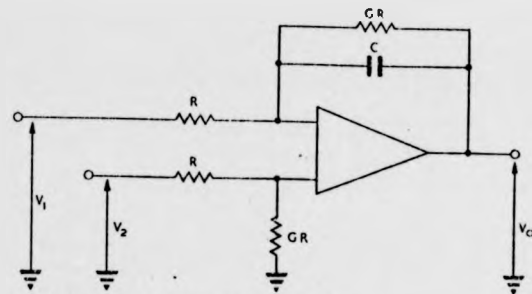


Fig. 4. Unbalanced differential amplifier

bridge screening, ref<sup>(2)</sup>. Rejection of noise by a differential amplifier depends on its ability to reject signals that appear between the two inputs together and ground reference, i.e., the common mode rejection of the amplifier. If the amplifier common mode balance is upset by the feedback circuits the resulting control signal can contain large noise components which impose severe loads on the specimen.

Electrohydraulic servo systems are essentially low frequency devices. Attenuation of high frequency noise at the transducer amplifier output can be achieved by placing a capacitor in the feedback loop. Referring to Fig. 3, the output of the circuit is:

$$V_o = \frac{Z_2}{R_2 + Z_2} \left( 1 + \frac{Z_1}{R_1} \right) V_2 - \frac{Z_1}{R_1} V_1$$

For this application  $R_1$  and  $R_2$  should be closely matched resistors and  $Z_1$  and  $Z_2$  should have matched resistive and reactive impedances.

In Fig. 4, resistive balance has been achieved with closely matched resistors but reactive unbalance exists because a capacitor has only been added to the negative feedback circuit. Using Laplace transforms the output is:

$$V_o = - \frac{(V_1 - V_2) G}{1 + Tp} + \frac{V_2 G Tp}{(1 + G)(1 + Tp)}$$

where  $T = GRC$  and is chosen so that the breakpoint frequency is five to ten times the limit of the frequency response of the electrohydraulic system for useful testing.

The first term describes the output of a differential input amplifier with a first order lag feedback network. The second term shows the effect of reactive unbalance where high frequency noise at the non-inverting input appears unattenuated at the output. This unattenuated noise signal can contribute severe components to the output from high frequency electrical "spike" pick-up.

#### Acknowledgment

The writer wishes to thank Mr. J. Monk of the School of Engineering Science for his helpful discussions.

#### References

- (1) W. MILLER. Use Op Amps in 8 ways. *Control Engineering*, p. 92, Feb. 1969.
- (2) K. W. READING AND L. HANDS. Systems Engineered for High Common Mode Rejection. *Instrument Practice*, p. 664, Aug. 1966.

APPENDIX B

The Autocorrelation Function Method of  
Power Spectral Density Estimation from  
a Discrete Sample Record of data

APPENDIX B

An estimate of the autocorrelation function at a displacement  $rh$  for a discrete sample record of  $N$  data values standardised to unit variance and zero mean is given by the formula (46):-

$$\hat{R}_r = \hat{R}_x(rh) = \frac{1}{N-r} \sum_{n=1}^{N-r} z_n z_{n+r} \quad (3.7)$$

where,

$h$  = sampling interval,

$r$  = lag number with values  $0, 1, 2 \dots m$

A "raw" estimate of the true power spectral density function is then given at  $m + 1$  discrete frequencies,  $f$ , by:-

$$\tilde{G}_x(f) = 2h \left[ \hat{R}_0 + 2 \sum_{r=1}^{m-1} \hat{R}_r \cos\left(\frac{\pi r f}{f_c}\right) + \hat{R}_m \cos\left(\frac{\pi m f}{f_c}\right) \right] \quad (3.8)$$

where,  $f_c$  defines the frequency interval  $(0, f_c)$  of the power spectral density function, and:-

$$f = \frac{K \cdot f_c}{m} \quad K = 0, 1, 2 \dots m \quad (3.9)$$

Equation 3.8 can be rewritten to give raw estimates from:-

$$\tilde{G}_k = \tilde{G}_x\left(\frac{K \cdot f_c}{m}\right) = 2h \left[ \hat{R}_0 + 2 \sum_{r=1}^{m-1} \hat{R}_r \cos\left(\frac{\pi r K}{m}\right) + (-1)^K \hat{R}_m \right] \quad (3.10)$$

These raw power estimates are not consistent estimates of the true spectral density in that their variance and bias do not tend to zero as the number of data values of the discrete sample record is increased. The process of obtaining consistent estimates is termed smoothing, and a satisfactory method of frequency smoothing can be obtained from Hanning. The smooth estimates of the power spectrum are then defined:-

$$\hat{G}_0 = 0.5 \tilde{G}_0 + 0.5 \tilde{G}_1 \quad (3.11)$$

$$\hat{G}_k = 0.25 \tilde{G}_{k-1} + 0.5 \tilde{G}_k + 0.25 \tilde{G}_{k+1}$$

where  $K = 1, 2, \dots, m-1$  (3.12)

$$\hat{G}_m = 0.5 \tilde{G}_{m-1} + 0.5 \tilde{G}_m \quad (3.13)$$

The sampling interval  $h$  should be chosen as close to  $\frac{1}{2f_c}$  as possible for computational economy. The desired equivalent resolution bandwidth is given from the maximum number of lag values:-

$$B = \frac{1}{mh} \quad (3.14)$$

and the normalised standard error for power spectral density calculations is defined:-

$$\epsilon = \sqrt{\frac{m}{N}} \quad (3.15)$$

with  $n = \frac{2N}{m}$  degrees of freedom.

A compromise choice for  $m$  is necessary since  $m \ll N$  gives small statistical uncertainty, but high resolution will only result if  $m$  is large, i.e.  $B$  small. A recommended rule is:-

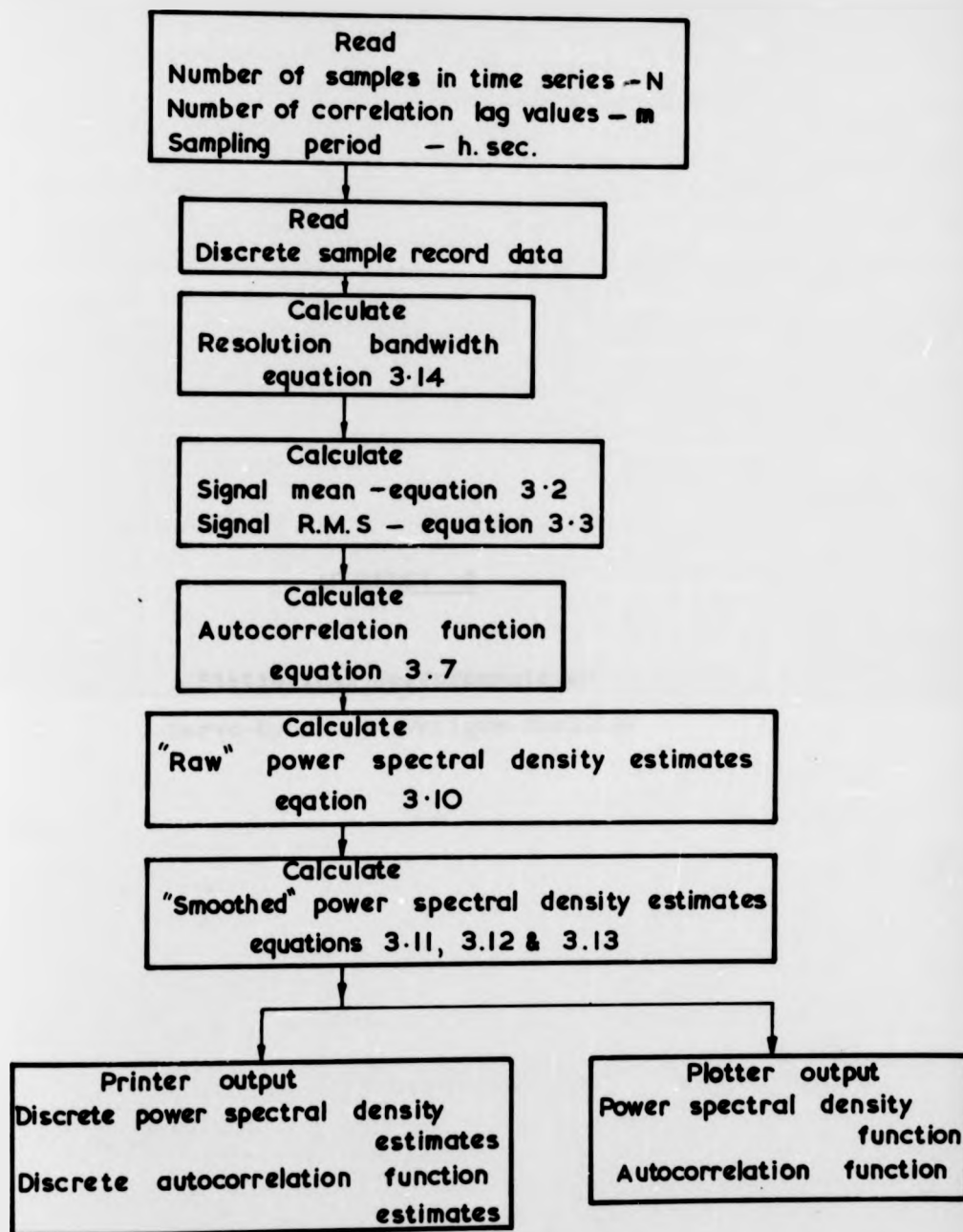
$$m \leq 0.1 N \quad (3.16)$$

The normalised standard error for p.s.d. function measurements involves both a bias term and a variance, both of which are influenced by the resolution bandwidth. The bias term is only negligible if the measurement is properly resolved and then equation 3.15 applies. This is particularly important for the spectra of random data which have abrupt changes and sharp peaks. A reasonable criterion for acceptable resolution in practice is:-

$$B < 0.25 B_p \quad (3.17)$$

### B.3

where  $B_p$  is the half power point bandwidth of a peak. If the spectrum is reasonably smooth larger resolution bandwidths can be used without introducing serious bias errors.



Flow Chart for Discrete Power Spectral Density Analysis based on the Procedure Outlined in Reference. 46

APPENDIX C

Statistical Measurements on  
Servo-Hydraulic Fatigue Machines

**"STATISTICAL MEASUREMENTS ON SERVO-HYDRAULIC  
FATIGUE MACHINES"**

*by*

**F. SHERRATT and B.C. FISHER**

**THE UNIVERSITY OF WARWICK**

*School of Engineering Science*

**MARCH, 1971**

## "STATISTICAL MEASUREMENTS ON SERVO-HYDRAULIC FATIGUE MACHINES"

### Calibration requirements of random-loading machines

Although random-load fatigue testing is well established, it is still new enough to lack agreed calibration techniques of the sort common in constant amplitude work. Certainly we usually have static or constant-amplitude calibrations of the force measuring devices, and also performance specifications of the servo system in frequency terms, but in the present state of knowledge these do not allow direct conclusions about the likely fatigue life deviation caused by machine error. The comparatively low scatter reported in random-load tests is encouraging, of course, and it may well be that achieving some nominally adequate frequency response is all that is necessary, but extensive comparisons are not yet being made between nominally identical tests in different laboratories. It was this requirement which forced more stringent standards on constant amplitude testing, and we ought probably to be looking for similar parameters for random work. Unfortunately random loading lacks the simple link between stress range and fatigue life which makes constant-amplitude calibration largely a matter of controlling the peak and trough values of a sine wave. Simply fixing the R.M.S. value of a random load still leaves too much freedom for such variables as peak distribution, crest factor, irregularity factor and amplitude distribution, and until we know how each of these affects life we will need to measure, control and report on them all. Signal analysis has advanced significantly in recent years, and many basic tools are now available, but there are drawbacks. The first arises directly from the statistical form of the measurements. An observer of a single cycle of a well-behaved sine wave knows all there is to know about it, but a random signal must be watched for much longer, and even then will only yield estimates of the relevant quantities. By properly choosing sample lengths, frequencies and intervals, the estimates can be made very reliable, but mastering the necessary theory can be pretty daunting to a researcher who already has the whole of fatigue literature to cope with. The second drawback is that most of the analysis has been derived in the vibration and automatic control fields, where frequency is the dominant factor. Translating the results into fatigue work, where absolute frequency is only a secondary factor compared with numbers of cycles, sometimes gives one a feeling that the information is not quite relevant. We need, then, to build up experience on this side, hoping eventually to identify measurements as helpful in random loading as correlation functions are in automatic control. Eventually we would hope to have something nearly as simple as specifying percentage error on stress amplitude and mean for constant amplitude loading. In the meantime some of our tests ought probably to be over-monitored, in the hope of identifying those factors which do not need close control. It is in this spirit that the results below are presented.

### Using digital computers

The amount of data needed for reliable measurements makes digital computers essential, and most modern analysis techniques assume their use. In the present work a small machine with 8k of 12-bit store was used on-line to signal generators and fatigue rigs, sampling with 10-bit plus sign accuracy at up to 20kHz. This allows measurements to be made over very long periods, compressing data for final output on to punched tape, and eventual analysis on a larger, 65k computer. Four programs, all in an assembler language, are used on the 8k machine :-

- (a) A basic sampling programme, storing and punching signal values at set intervals.
- (b) A power spectrum analysis based on the fast Fourier transform.
- (c) An amplitude probability density distribution program, which divides the range  $\pm 10v$  into up to 2024 intervals, samples the incoming signal at up to 5kHz, and records how often the signal was found in each interval.
- (d) A peak-trough probability program (equivalent to a range-mean count). This follows the signal until a peak is found, holds the value and tracks until the next trough is found, and then records the occurrence of the half cycle represented by this pair of values (Fig. 1). The signal field is divided into  $\pm 32$  intervals, the maximum excursion being selected at  $\pm 10, 5, 2.5$  or  $1.25$  volts. The results emerge as a  $64 \times 64$  matrix, from which contour plots of the joint probability of particular peaks occurring just after or just before particular troughs may be extracted (Fig. 2). Simplification of these plots gives the total numbers of peaks or troughs in any chosen interval, the usual dominant factor in fatigue work.

#### Routine use of the programs

About three-quarters of the tests using these programs at present are based on narrow band Gaussian input, the other quarter having more general power spectra still Gaussian in amplitude. The first overall requirement is therefore to check the amplitude probability density distribution against the normal distribution, and Fig. 3 gives the flow chart for this, using samples obtained by program (a) above. A chi-square test at the 5% significance level is used to check that the distribution is normal, and plots are prepared so that a visual check can also be made. Fig. 4 shows the plot for a 10Hz centre frequency input to a  $\pm 10$  tonf bending rig. This set of tests also gives some idea of the crest factor, that is the ratio of the most extreme signal value to the signal R.M.S. For Gaussian signals this is theoretically infinite, of course, but practically is usually limited to 4.5 or less in fatigue work. Program (a) samples are not usually long enough to give reliable data at these levels though, a point discussed in more detail below.

Power spectrum measurement with program (b) is monitored by oscilloscope during the run. As more data is acquired the calculation is up-dated, and choosing a sample length is simply a question of waiting until the display is smooth enough, usually about fifteen minutes or so. Smoothing routines are included to accelerate this if the operator wishes, with some danger of losing sharp resonances.

The remaining checks are carried out with program (d). The complete information this gives about the distribution of half-cycles is too unwieldy for general application at present, and so two main factors are used. Numbers of crossings of any chosen level can be extracted, but usually the input has zero mean and the leading figure is  $f_0$ , the number of zero crossings per second. Dividing this by the total number of peaks per second gives the irregularity factor. This we use as the leading classification figure, describing signals as of high irregularity factor when the bandwidth is narrow and the value approaches one. From this factor a theoretical curve for the probability distribution of peaks can be found, becoming the Rayleigh curve for high irregularity factors. Plots for visual comparison of theoretical and actual values can then be prepared for the peak distribution. Crest factor again emerges as part of the

routine, the value here being more reliable, with a half-hour or more of signal monitored. A flow chart for the calculations is shown in Fig. 5, and a typical peak probability density plot in Fig. 6.

By following this routine as each machine is brought into use, and at the start of any significantly new phase of testing (a major change of specimen shape, for instance) we feel that machine performance is reasonably under control. Certainly the results we are getting seem consistent and believable, but still some awkward questions remain. As an example, take the question of the frequency of the more extreme peaks, a factor likely to have very variable effects on life. Table I shows the actual and expected number of peaks in the  $3.6\sigma$  to  $5\sigma$  region for a particular test condition, assuming a Rayleigh distribution. Compared with the total of nearly 150,000 half-cycles in the sample the discrepancies are small, but it is disconcerting to see that many of these very high peaks occur about four times as often as theory predicts. The Rayleigh distribution seems well set to take over from the sine wave as the next level of complexity in fatigue testing, and getting it under control ought to be a high priority. With this in mind we have been considering plots of signal performance to bring out discrepancies in a way which might link with life testing. The remainder of this paper is devoted to one possibility, as yet untried against actual testing, but which does seem to be a very sensitive way of showing machine deviations.

Interval	31	30	29	28	27	26	25	24	23
s/ $\sigma$	4.92	4.76	4.60	4.45	4.29	4.14	3.98	3.82	3.67
Theoretical no. peaks	-	1	2	4	7	13	24	43	75
Actual peaks	12	12	12	18	32	52	76	125	188

**TABLE I** Number of peaks of very high value occurring in one hour of 20Hz running, compared with Rayleigh value. Axial machine of 20 tonf. capacity; measurements taken from load cell.

The cumulative peak probability plot

Cumulative probability plotting is a familiar technique in fatigue; to apply it to cycles of random amplitude involves dividing the signal excursion into a series of levels, and measuring the number of peaks greater than each level. Dividing this by the total number of peaks in the whole sample gives a cumulative probability value. If the level is  $s$  and the R.M.S. value of the signal is  $\sigma$ , we may designate the cumulative probability of peaks exceeding  $s/\sigma$  as  $P(s/\sigma)$ . Plotting this against  $s/\sigma$  would usually give a curve, but by specially scaling the axes for a given probability function a plot of this sort can be made to give a straight line if the desired distribution is achieved. Deviations from the ideal then show as deviations of plotted points from a straight line. In the Rayleigh case the plotting is reasonably simple, since expected cumulative probability at level  $s/\sigma$  is :-

$$P_{TH} \left( \frac{s}{\sigma} \right) = e^{-\frac{1}{2} \frac{s^2}{\sigma^2}}$$

Taking logs twice :-

$$\text{loglog } P_{TH} \left( \frac{s}{\sigma} \right) = k + 2 \log \left( \frac{s}{\sigma} \right) \quad \dots\dots\dots (1)$$

If we plot  $\text{loglog } P_p \left( \frac{s}{\sigma} \right)$  against  $\log \left( \frac{s}{\sigma} \right)$  for the measured values a straight line of slope  $\frac{2}{\sigma^2}$  should emerge. Deviations from this line then give a reasonably quantitative indication of discrepancies.

To demonstrate the use of a plot like this, a 20Hz Gaussian narrow-band signal was applied to a steel specimen of 12 mm. diameter in our 20 tonf. axial machine. Taking power spectra under the required input and two stiffness settings gives Fig. 7, which shows the performance as adequate at either setting. A more stringent test is to feed a wideband signal (in this case flat from 0 to 150Hz) to the input and obtain Fig. 8, which shows that at the intended test frequency the high setting gives too little and the medium setting too much damping. If this were a real test programme we would at present probably lower the test frequency, but if we wanted to retain 20Hz there seems a good possibility that the high stiffness setting will give too many high peaks. The row of dots on the cumulative probability plot, Fig. 9, based on a one hour sample of the load-cell output from the machine, confirms that this is so. Because the theoretical plot is straight the effect of shifting the R.M.S. can be represented by lines parallel to the original line. This extends the usefulness of the plot by giving an "equivalent" R.M.S. shift which would produce the observed deviation from the theoretical value of any load level. This is not a measure of how much the overall R.M.S. must be changed to correct the machine, since this would alter probabilities at all levels, but it is a good indication of how the balance of probabilities between different parts of the signal is distorted. While our knowledge of stress interaction is so poor it is essential for valid comparison between machines that this balance be kept under control.

A slightly more convenient form of the plot can be obtained by subtracting  $\text{loglog } P_{TH} \left( \frac{s}{\sigma} \right)$  from all values, effectively swinging the Rayleigh line on Fig. 9 to a horizontal position. Fig. 10 gives such plots of the 20Hz signal input used to drive the machine for Fig. 9, confirming that only a small part of the high load deviation is due to the input signal. At low  $s/\sigma$  values the plot is sensitive to mean stress, so that not too much significance should be read into the high deviations below  $s/\sigma = 1.0$ . Discrepancies at this level show up on plots like Fig. 6, though, and are in any case less likely to be important in fatigue.

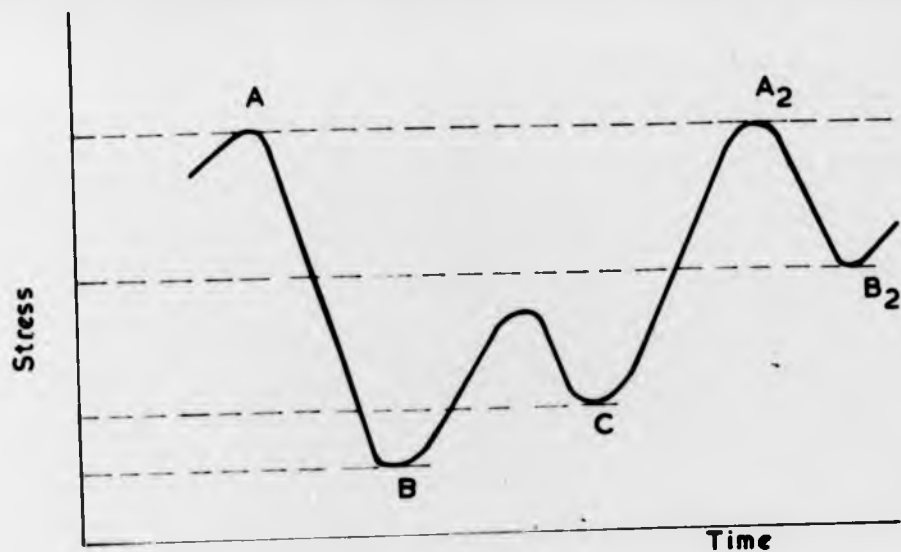
To complete the development Fig. 11 shows a few plots of this sort from measurements on two machines. Fig. 11(a) shows that on the 20 tonf. machine not only the high stiffness setting but also the medium stiffness setting causes high loads to occur too frequently, and confirms at a glance that this is not due to signal input error. Fig. 11(b) refers to specimen strain gauge readings from a 10 tonf. bending rig which has the shift in power spectrum seen in Fig. 12 when the R.M.S. is changed about 50%. The probability plot confirms that changing R.M.S. alters performance, but only by the same magnitude as the discrepancies which already exist between input and achieved loads for both high and low R.M.S. running.

Conclusion

There are still some difficulties in applying probability methods to random loading fatigue, but once random testing becomes general the monitoring systems will have to be built up if results are to be compared between laboratories. Apart from the methods described earlier in this paper, which are based firmly enough on existing data analysis to be recommended as routine, we should be looking for more sensitive ways of comparing machines with each other. The plc described has drawbacks, such as mean stress sensitivity at low loads, but offers a compact way of comparing performances at high loads. Similar criteria for wide-band work may emerge from studies of range-mean counting.

References

- F. Sherratt "Random loading fatigue machines on-line to a digital computer"  
I.E.R.E. Conference proceedings No. 20, Nov. 1970.
- D.J. White and J. Lewszuk "Cumulative damage in push-pull fatigue of fillet welded mild steel plate subjected to narrow-band random loading".  
I.Mech.E. Proceedings Vol. 185 28/71, 1970-71, p.339.



Joint Peak / Trough Pair Counting

FIG. 1

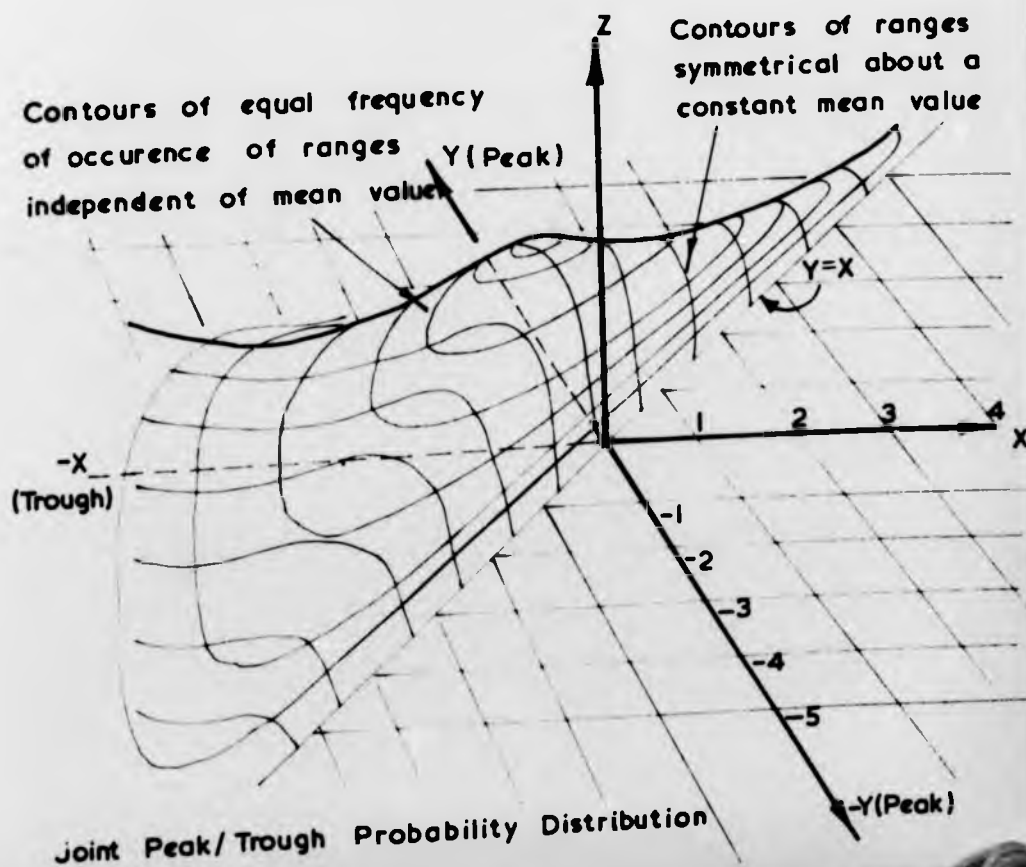
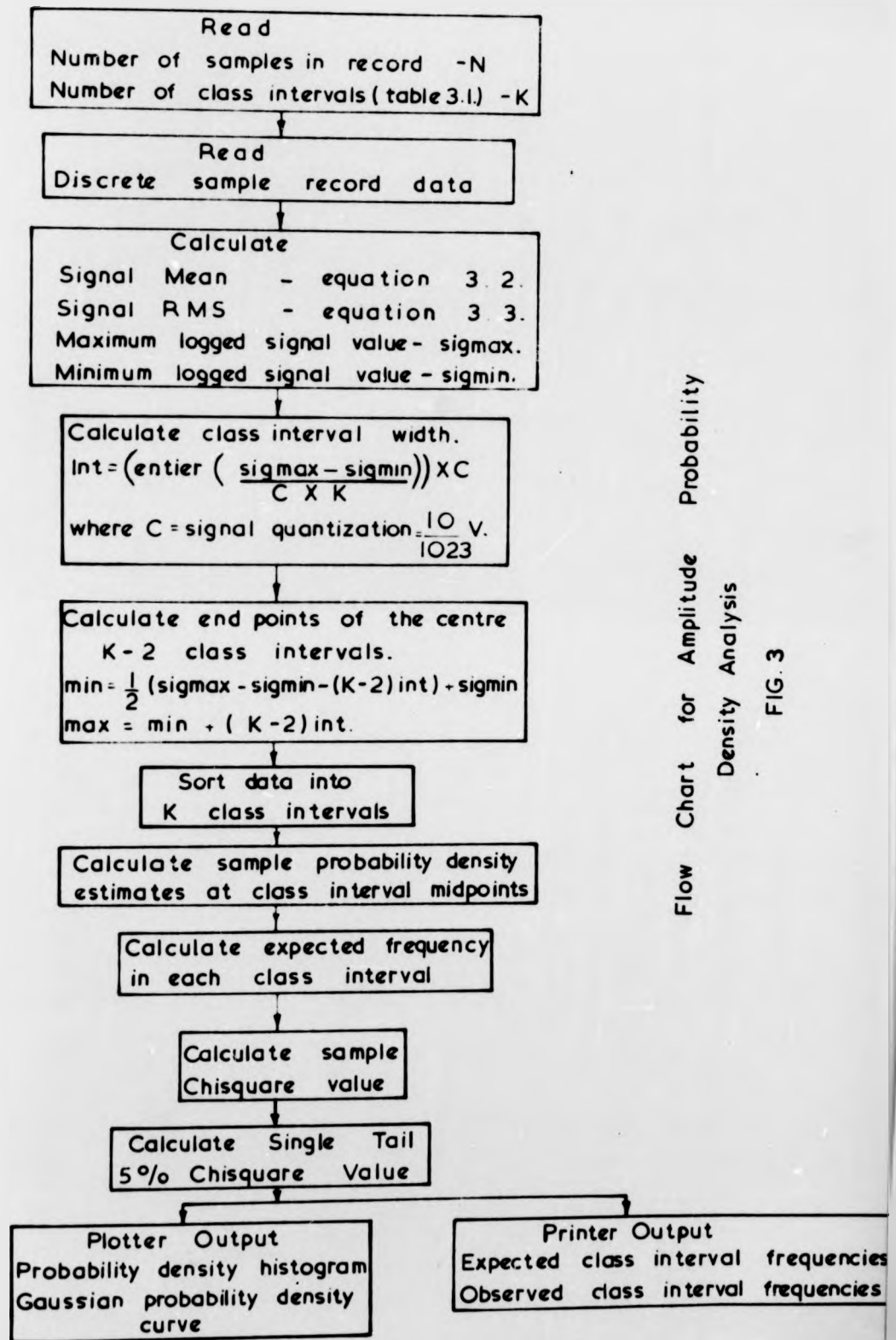
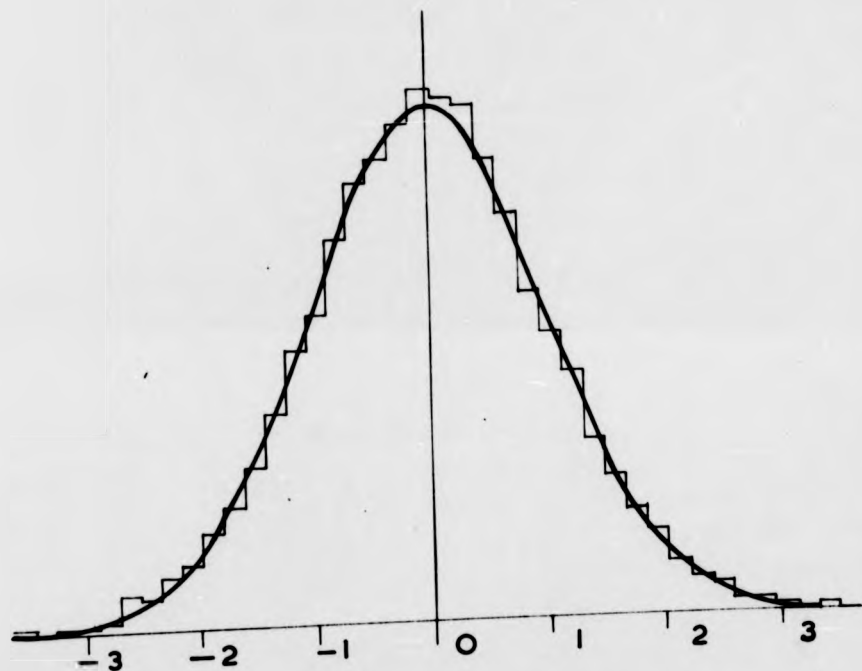


FIG. 2



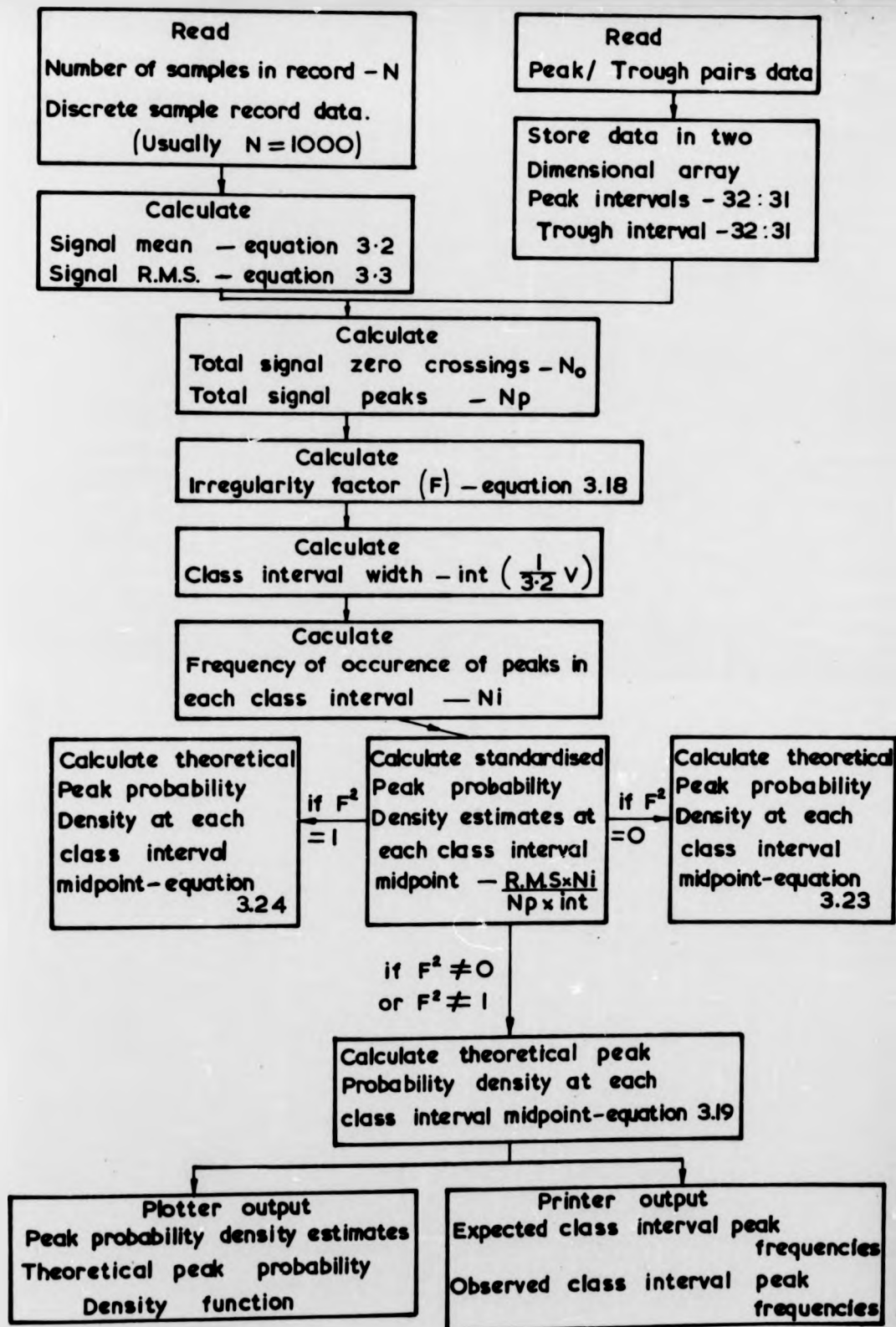
Flow Chart for Amplitude Probability  
Density Analysis

FIG. 3



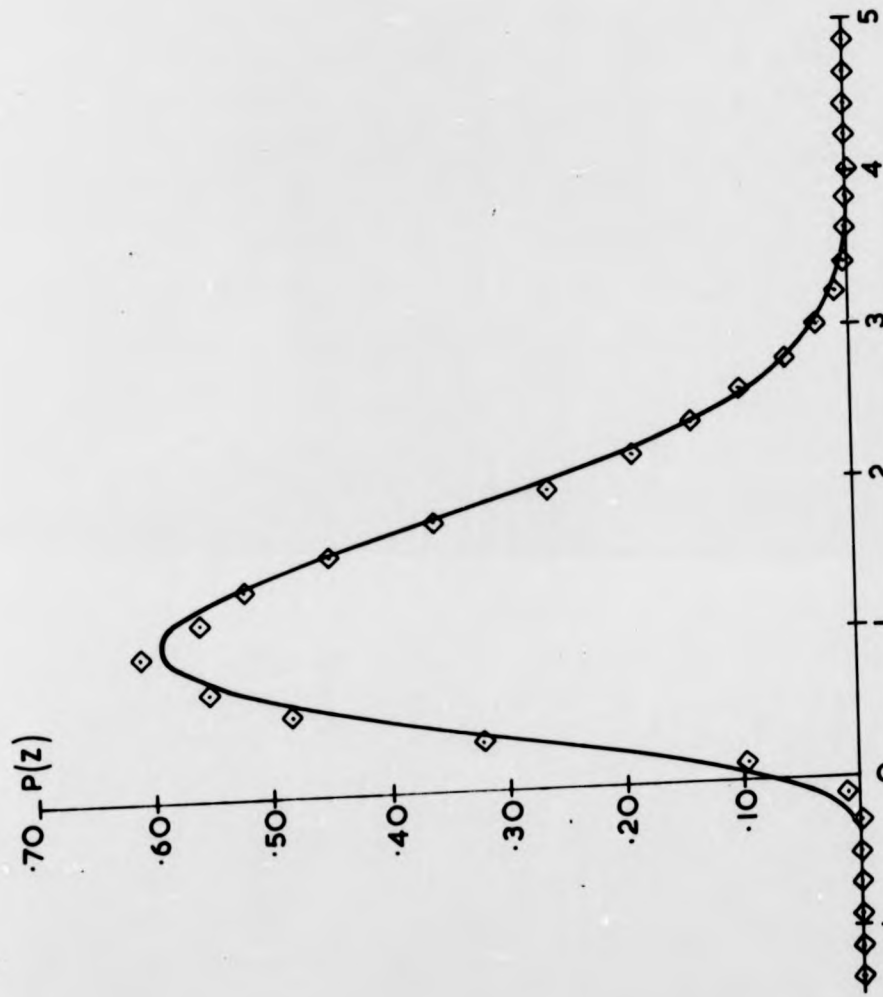
Standardised Probability Density  
10Hz Centre Frequency Signal

FIG. 4



Flow Chart for Peak Probability  
Density Analysis

Fig. 5



Standardised Peak Probability Density Function  
10Hz Centre Frequency Signal

FIG. 6

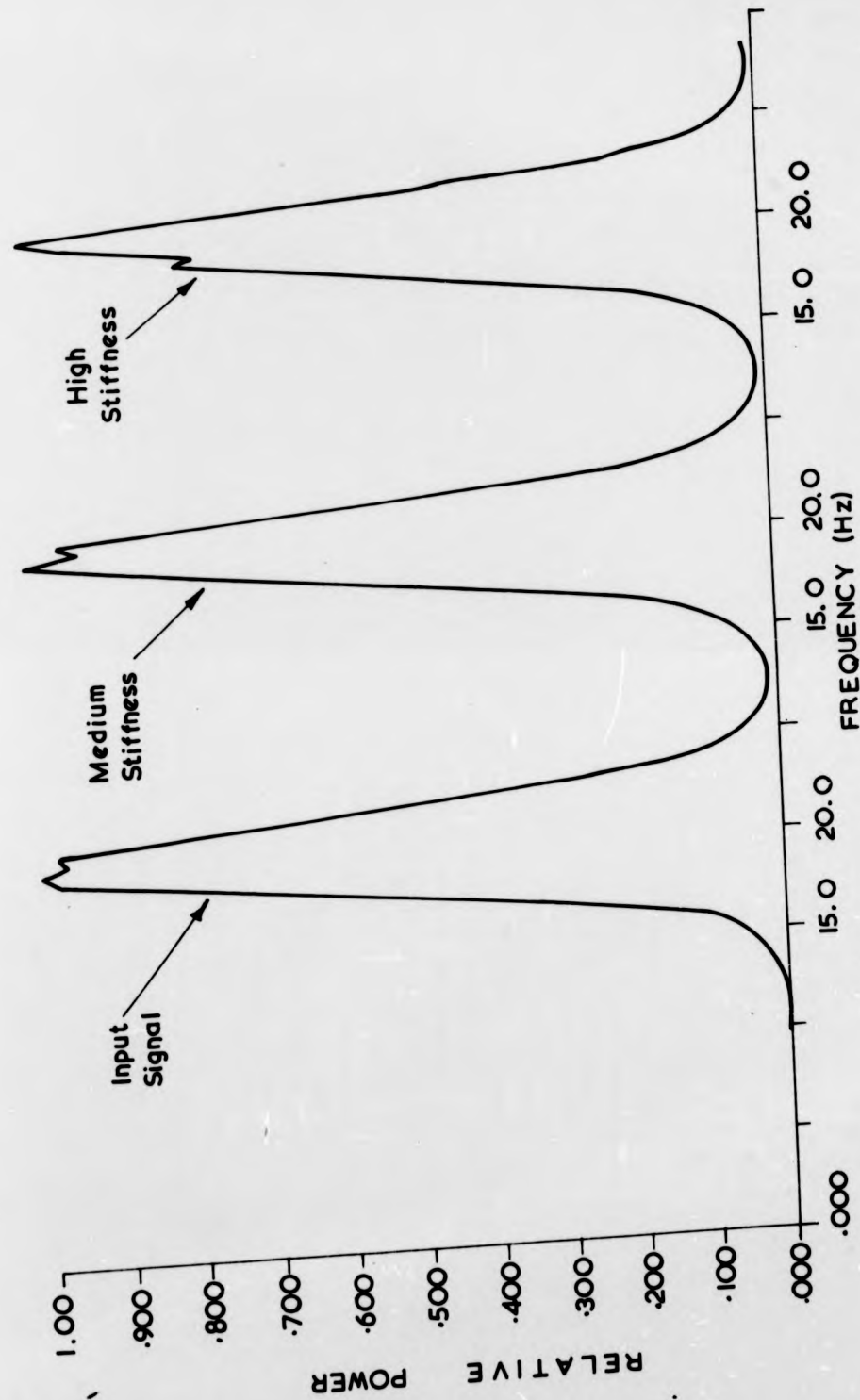


FIG. 7. Response of 20 ton.f machine to narrow-band input.

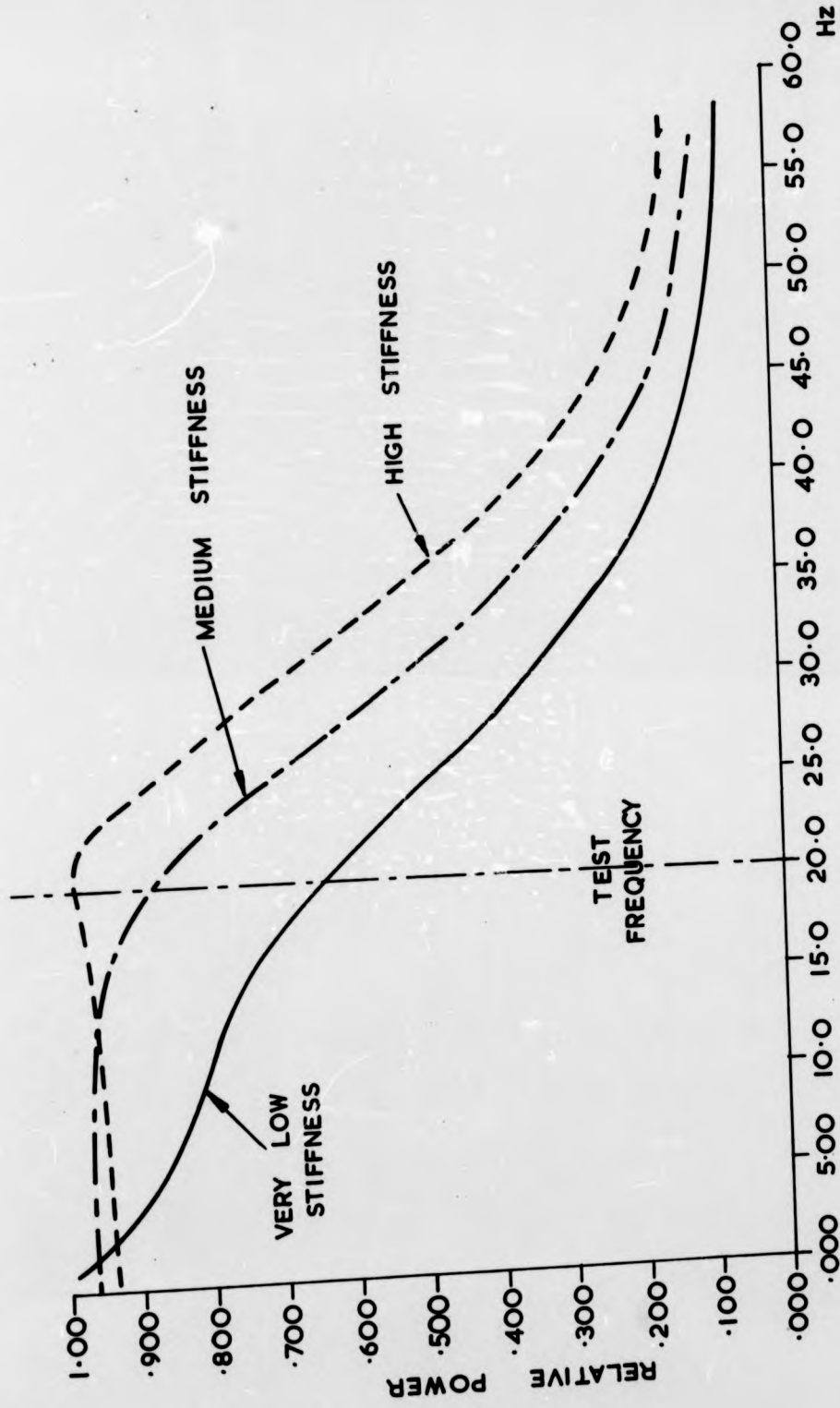


FIG. 8. Response of 20ton.f. machine to 0-150Hz input

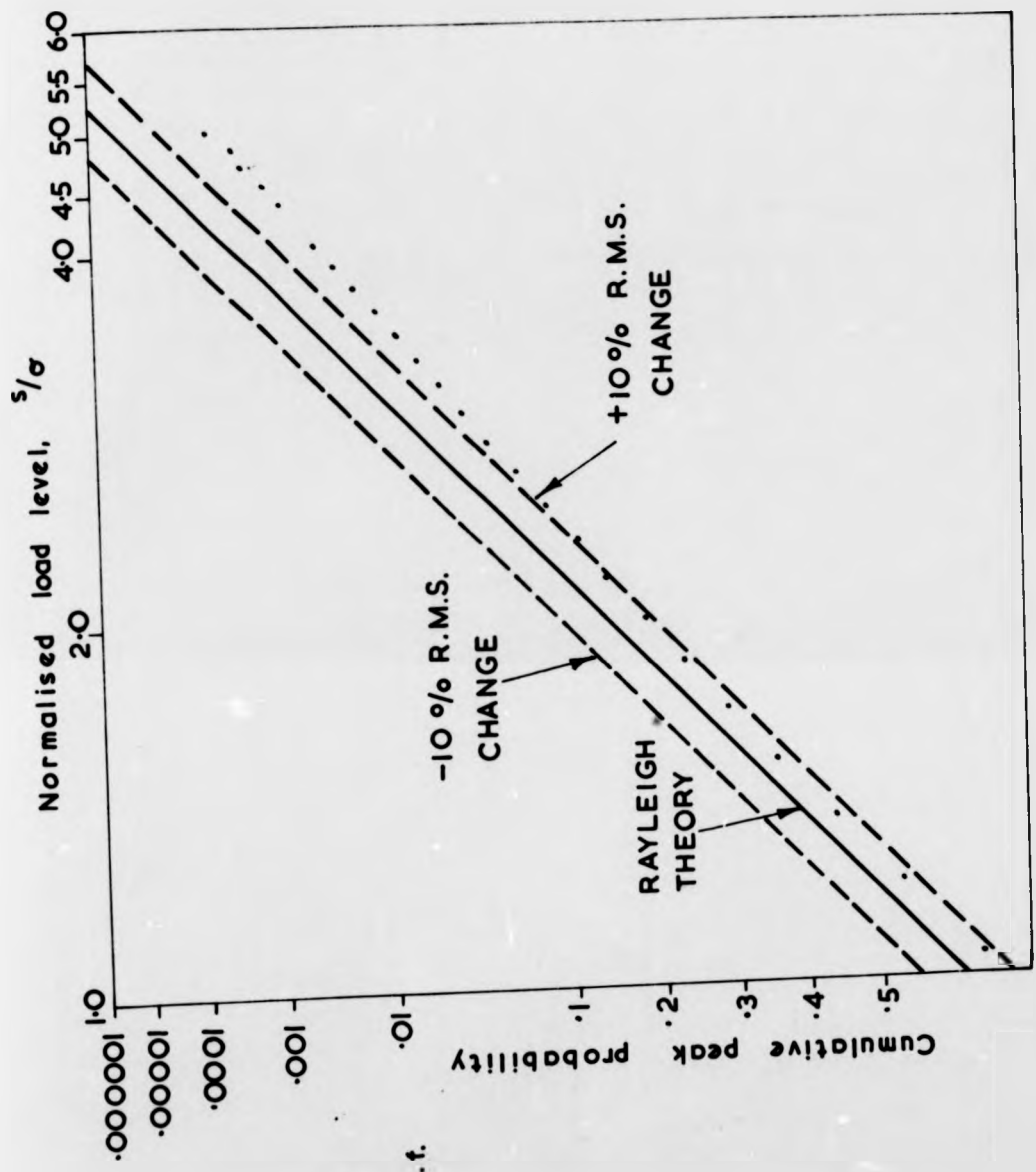
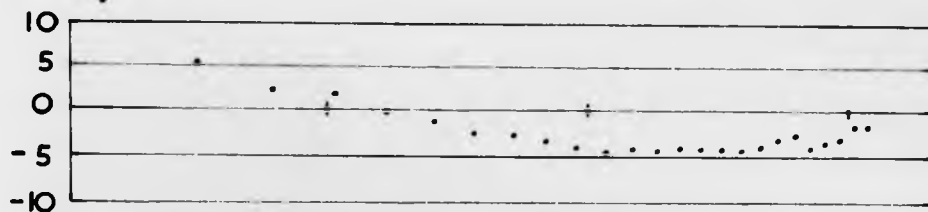


Fig. 9. Cumulative probability plot of peaks for 20 ton.f. machine on high stiffness ( 20 Hz input.)



(a) Sample length 2179 seconds



(b) Sample length 4745 seconds



(c) Sample length 17,790 seconds



FIG. 10 Performance of signal generator and filter from normal and very long samples. Frequency 20 Hz, irregularity factor  $> 0.99$ , nominal crest factor 4.90.

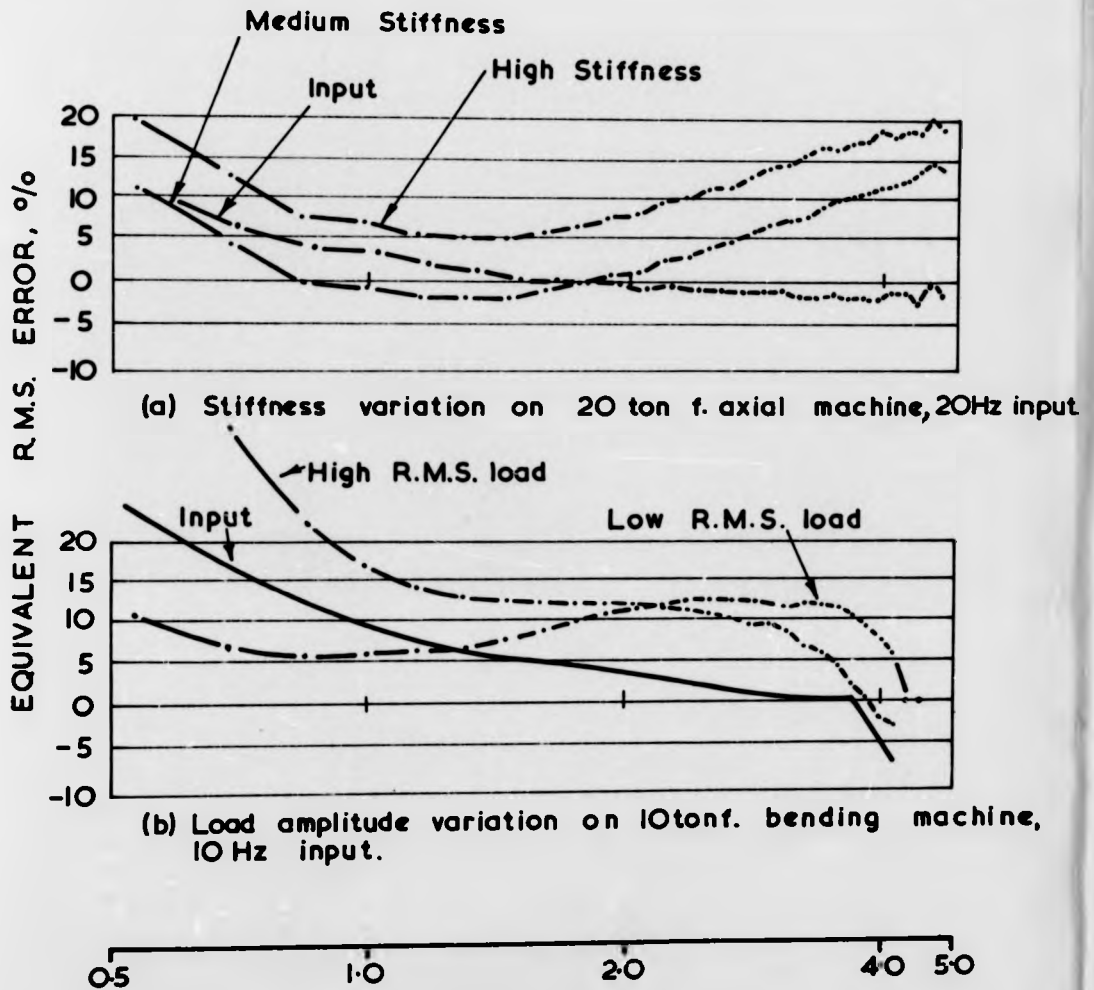


FIG 11. Evaluation of machine performance factors by modified probability plot.

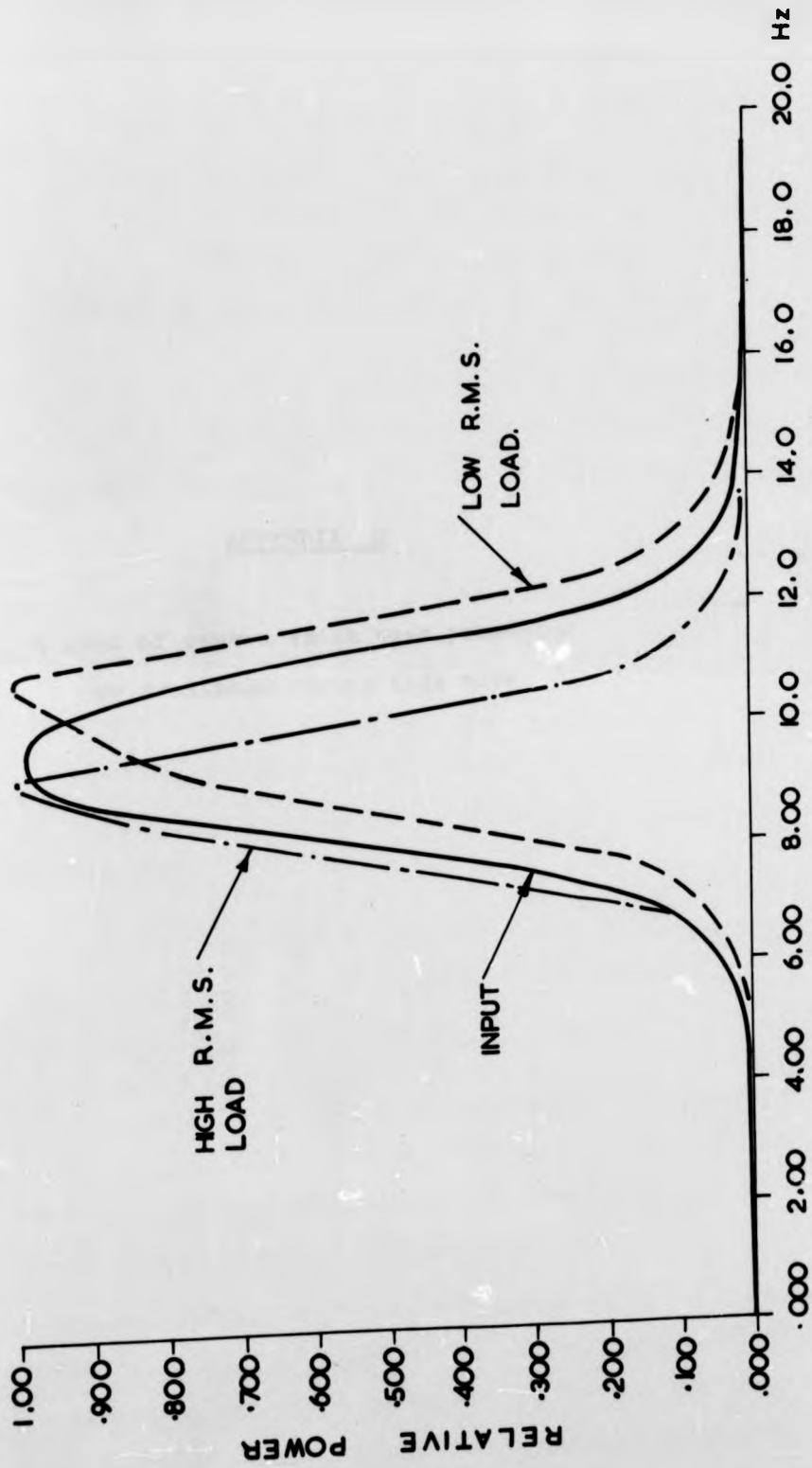


FIG.12. Bending rig response to 10Hz input at different R.M.S. Loads.

APPENDIX D

A list of papers which were presented  
or published during this work

1001

APPENDIX D

The following is a list of papers which have been presented or published during the course of this research project:

1. "Application of Strain Gauge Transducers to Electrohydraulic Test Systems", B.C. Fisher, Instrument Practice, April 1970.
2. "Fundamentals of Electrohydraulic Servo-controlled Fatigue Test Rig Design", B.C. Fisher and J.V. Comfort, Instrument Practice, Parts 1 and 2, June & July 1970.
3. "An Analysis of Fatigue Damage", B.C. Fisher, presented to Symposium on Fatigue, British Society for Strain Measurement, Trent Polytechnic, June 1970.
4. "Investigation of cumulative fatigue damage with special reference to railway components", B.C. Fisher and F. Sherratt, 2nd Report of British Rail Contract, October 1970.
5. "Fatigue Testing with Servohydraulics", B.C. Fisher, Successful Hydraulics (Keelavite Hydraulics Ltd., Coventry), March 1971.
6. "Statistical Measurements on Servohydraulic Fatigue Machines", F. Sherratt and B.C. Fisher, presented to Conference on Dynamic Testing with Electrohydraulic Servo-Systems, City University, April 1971.
7. "Extracting Fatigue Testing and Design Data from Service Loading Records", F. Sherratt and B.C. Fisher, to be presented to the Joint Committee for Stress Analysis Conference on Recording and Interpretation of Engineering Measurements, to be held at Institute of Marine Engineers, April 1972.

Attention is drawn to the fact that the copyright of this thesis rests with its author.

This copy of the thesis has been supplied on condition that anyone who consults it is understood to recognise that its copyright rests with its author and that no quotation from the thesis and no information derived from it may be published without the author's prior written consent.